①

AD-A219 741

AGARD

ADVISORY GROUP FOR AEROSPACE RESEARCH & DEVELOPMENT

7 RUE ANCELLE 92200 NEUILLY SUR SEINE FRANCE

AGARD CONFERENCE PROCEEDINGS No.468

Unsteady Aerodynamic Phenomena in Turbomachines

DTIC
S ELECTE
MAR 2 2 1990
D
E

NORTH ATLANTIC TREATY ORGANIZATION

DISTRIBUTION AND AVAILABILITY
ON BACK COVER

90 03 22 036

AGARD-CP-468

NORTH ATLANTIC TREATY ORGANIZATION

ADVISORY GROUP FOR AEROSPACE RESEARCH AND DEVELOPMENT

(ORGANISATION DU TRAITE DE L'ATLANTIQUE NORD)

AGARD Conference Proceedings No.468

UNSTEADY AERODYNAMIC PHENOMENA IN TURBOMACHINES

X

A-1

THE MISSION OF AGARD

According to its Charter, the mission of AGARD is to bring together the leading personalities of the NATO nations in the fields of science and technology relating to aerospace for the following purposes:

— Recommending effective ways for the member nations to use their research and development capabilities for the common benefit of the NATO community;

— Providing scientific and technical advice and assistance to the Military Committee in the field of aerospace research and development (with particular regard to its military application);

— Continuously stimulating advances in the aerospace sciences relevant to strengthening the common defence posture;

— Improving the co-operation among member nations in aerospace research and development;

— Exchange of scientific and technical information;

— Providing assistance to member nations for the purpose of increasing their scientific and technical potential;

— Rendering scientific and technical assistance, as requested, to other NATO bodies and to member nations in connection with research and development problems in the aerospace field.

The highest authority within AGARD is the National Delegates Board consisting of officially appointed senior representatives from each member nation. The mission of AGARD is carried out through the Panels which are composed of experts appointed by the National Delegates, the Consultant and Exchange Programme and the Aerospace Applications Studies Programme. The results of AGARD work are reported to the member nations and the NATO Authorities through the AGARD series of publications of which this is one.

Participation in AGARD activities is by invitation only and is normally limited to citizens of the NATO nations.

ii

RECENT PUBLICATIONS OF THE PROPULSION AND ENERGETICS PANEL

Conference Proceedings

Helicopter Propulsion Systems
AGARD Conference Proceedings No.302, 57th Meeting, May 1981

Ramjets and Ramrockets for Military Applications
AGARD Conference Proceedings No.307, 58th Meeting, October 1981

Problems in Bearings and Lubrication
AGARD Conference Proceedings No.323, 59th Meeting, May/June 1982

Engine Handling
AGARD Conference Proceedings No.324, 60th Meeting, October 1982

Viscous Effects in Turbomachines
AGARD Conference Proceedings No.351, 61st 4 Meeting, June 1982

Auxiliary Power Systems
AGARD Conference Proceedings 352, 61st *B* Meeting, May 1983

Combustion Problems in Turbine Engines
AGARD Conference Proceedings 353, 62nd Meeting, October 1983

Hazard Studies for Solid Propellant Rocket Motors
AGARD Conference Proceedings 367, 63rd *A* Meeting, May/June 1984

Engine Cyclic Durability by Analysis and Testing
AGARD Conference Proceedings No.368, 63rd *B* Meeting, May/June 1984

Gears and Power Transmission Systems for Helicopters and Turboprops
AGARD Conference Proceedings No.369, 64th Meeting October 1984

Heat Transfer and Cooling in Gas Turbines
AGARD Conference Proceedings No.390, 65th Meeting, May 1985

Smokeless Propellants
AGARD Conference Proceedings No.391, 66th *A* Meeting, September 1985

Interior Ballistics of Guns
AGARD Conference Proceedings No.392, 66th *B* Meeting, September 1985

Advanced Instrumentation for Aero Engine Components
AGARD Conference Proceedings No.399, 67th Meeting, May 1986

Engine Response to Distorted Inflow Conditions
AGARD Conference Proceedings No.400, 68th *A* Meeting, September 1986

Transonic and Supersonic Phenomena in Turbomachines
AGARD Conference Proceedings No.401, 68th *B* Meeting, September 1986

Advanced Technology for Aero Engine Components
AGARD Conference Proceedings No.421, 69th Meeting, September 1987

Combustion and Fuels in Gas Turbine Engine
AGARD Conference Proceedings No.422, 70th Meeting, October 1987

Engine Condition Monitoring — Technology and Experience
AGARD Conference Proceedings No.448, 71st Meeting, May/June 1988

Application of Advanced Material for Turbomachinery and Rocket Propulsion
AGARD Conference Proceedings No.449, 72nd *A* Meeting, October 1988

Combustion Instabilities in Liquid-Fuelled Propulsion Systems
AGARD Conference Proceedings No.450, 72nd *B* Meeting, October 1988

Aircraft Fire Safety
AGARD Conference Proceedings No.467, 73rd Meeting, May 1989

Working Group Reports

Through Flow Calculations in Axial Turbomachines
AGARD Advisory Report 175. Results of WG 12 (October 1981)

Alternative Jet Engine Fuels
AGARD Advisory Report 181. Vol.1 and Vol.2. Results of WG 13 (July 1982)

Suitable Averaging Techniques in Non-Uniform Internal Flows
AGARD Advisory Report 182 (in English and French). Results of WG 14 (June/August 1983)

Producibility and Cost Studies of Aviation Kerosines
AGARD Advisory Report 227. Results of WG 16 (June 1985)

Performance of Rocket Motors with Metallized Propellants
AGARD Advisory Report 230. Results of WG 17 (September 1986)

Recommended Practices for Measurement of Gas Path Pressures and Temperatures for Performance Assessment of
Aircraft Engines and Components
AGARD Advisory Report 245. Results of WG 19 (In production, 1990)

The Uniform Engine Test Programme
AGARD Advisory Report 248. Results of WG 15 (In production, 1990)

Test Cases for Computation of Internal Flows in Aero Engine Components
AGARD Advisory Report 275. Results of WG 18 (In production, 1990)

Lecture Series

Aircraft Fire Safety
AGARD LS 123 (June 1982)

Operation and Performance Measurement of Engines in Sea Level Test Facilities
AGARD LS 132 (April 1984)

Ramjet and Ramrocket Propulsion Systems for Missiles
AGARD LS 136 (September 1984)

3-D Computation Techniques Applied to Internal Flows in Propulsion Systems
AGARD LS 140 (June 1985)

Engine Airframe Integration for Rotorcraft
AGARD LS 148 (June 1986)

Design Methods Used in Solid Rocket Motors
AGARD LS 150 (April 1987)
AGARD LS 150 (Revised) (April 1988)

Blading Design for Axial Turbomachines
AGARD LS 167 (June 1989)

Other Publications

Rocket Altitude Test Facility Register
AGARD AG 297 (March 1987)

Manual for Aeroelasticity in Turbomachines
AGARD AG 298/1 (March 1987)
AGARD AG 298/2 (June 1988)

Application of Modified Loss and Deviation Correlations to Transonic Axial Compressors
AGARD Report 745 (November 1987)

Measurement Uncertainty within the Uniform Engine Test Programme
AGARD AG 307 (May 1989)

Rotorcraft Drivetrain Life Safety and Reliability
AGARD R 775 (In production 1990)

THEME

At present, for calculating the flow in turbomachines, averaging in time and location is applied and corrections due to unsteadiness are incorporated afterwards. The results are not satisfactory. We are now at a turning point for the understanding of the unsteady flow in and around the turbomachinery and it is hoped that in future unsteady flow calculations could be applied directly. The purpose of the meeting was to bring together specialists for unsteady flow calculation methods and experimentalists for turbomachinery. The main issue should lie in the basic physical understanding of unsteady flow effects in the turbomachinery surroundings and their description. 2D and 3D calculation methods for inviscid as well as for viscous flows were incorporated.

<p style="text-align:center">*   *   *</p>

A l'heure actuelle, le calcul des écoulements dans les turbomachines se fait par application de la moyenne spatio-temporelle, les rectifications demandées pour compenser les effets des phénomènes instationnaires étant apportées ultérieurement. Les résultats ainsi obtenus ne sont pas satisfaisants. Aujourd'hui, nous vivons un moment décisif pour ce qui est de la compréhension des écoulements instationnaires à travers et autour des turbomachines et nous espérons qu'à l'avenir les calculs des écoulements instationnaires pourront être appliqués directement. L'objet de la réunion fut de rassembler les spécialistes en matière de calcul des écoulements instationnaires et les expérimentalistes dans le domaine des turbomachines. Les discussions ont porté principalement sur la définition physique de base des effets des écoulements instationnaires en environnement turbomachine et leur description. La réunion a examiné également les méthodes de calcul bidimensionnelles et tridimensionnelles des écoulements visqueux et non-visqueux.

CONTENTS

EVALUATION REPORT

by

J.Fabri

1. INTRODUCTION

Purely empirical at its start, the design and realization of turbomachines became more and more rationalized as the Designer was able to use sophisticated theories and high performance computers.

However, this is true for the design point of operation only, for which theory and numerical computation may be considered as perfectly operational. If a proof is needed, one has just to consider the decrease in size and weight and the increase in power and efficiency of the present time jet propulsion engines, as compared to earlier designs.

On the other hand, the off-design operation of turbomachines and, even more, the unsteady phenomena that take place during the transients, and even during the steady operation of the machine, is less well known and did not attain, up-to-now, the same degree of advancement than the steady state operation.

As a matter of fact, a distinction has to be made between the various non-steady operations of turbomachines

- -- the most spectacular ones correspond to the highly off-design operating conditions, when surge, blade flutter, rotating stall or any other undesirable behaviour of the engine can be observed.

- — less deteriorating, for the performances or the structure, are the stage interactions, which may, however, affect even the design point of operation;

- — finally, the unsteadiness of the flow during supercritical operating conditions give rise to undesirable pressure fluctuations, which the designer has to avoid.

At the present time, there is no sufficiently reliable experimental investigation of unsteady flows in turbomachines, whereas around isolated airfoils much sophisticated research was already conducted in such regimes. Therefore, most of the time it is possible only to compare computational codes between themselves, in order to find the most suitable one for the task required

This is the reason for which PEP, the Propulsion and Energetics Panel of AGARD has decided to organize a series of Conferences on Unsteady Phenomena in Turbomachines in order to compare the degree of advancement of theoretical and experimental research conducted in this field not only in the NATO Countries, but also in Switzerland and Austria, whose industries work in close cooperation with those of the NATO countries.

This report gives a critical survey of the content of the papers presented during the meeting in order to emphasize the main points of interest and indications for future research and development that would be useful in the coming years in order to improve our knowledge of unsteady aerodynamics in turbomachines and avoid their hindering effects

2. CRITICAL SURVEY OF THE PRESENTATIONS

2.1 Unsteady Aerodynamics of Blade Cascades

It is quite unexpected that in most of the unsteady phenomena studies for turbomachines, there is no or almost no confrontation between theory and experiment, at least outside of the domain of research on aeroelasticity, a main that was excluded from the scope of the meeting.

Theories are therefore compared between themselves and this is namely the case of the presentation of A.Klose and K.Heinig (M.T.U., Germany) who did not hesitate to study one of the most difficult problems of turbomachinery, the blade flutter. Apparently, this problem is solved in the case of isolated airfoils, but in the case of blade rows, the great number of configurations, due to the blade interaction and inter-blade phase angles, makes it really more difficult. The conclusion of the authors is that for the present time blades, the weight of which is much higher than the aerodynamical forces acting on them, and the energy balance methods are sufficiently accurate to define the vibration frequencies of the blades. But for future engines, with light weight, hollow blades, new methods are required and the eigenvalue method proposed by the authors seems more appropriate for the determination of the critical blade frequencies.

In the meantime, the experimental investigation conducted by A.Bölcs, T.H.Fransson, D.Schäfli (EPFL, Lausanne, Switzerland) comforts the designers who are accustomed to the superposition method, using results obtained on simplified cases, either by theory or by means of experiments. These authors have tested an annular blade cascade, i.e. a fixed blade row as similar as possible to an actual rotor, without the difficulty of experimenting a moving cascade, and have shown that in many cases results obtained with intricated vibrating modes could be also obtained by superposing simple vibrating modes. It is certainly a relief for research as well as for industry, where this result was taken a priori.

The test results presented by H.P.Kau and H.E.Gallus (R.W.T.H., Aachen, Germany) were obtained on a more simplified test facility, a straight blade cascade, but on the other hand have been successfully compared to computational results of the authors. Although the theory resolves only the non-viscous, two dimensional Euler equations (whereas the flow is viscous and more or less three dimensional) the effect of blade geometry on the unsteady flow phenomena in blade cascades has been emphasised and the use of flat plate cascades rejected.

Computation on blade cascades in a compressible, viscous flow by means of the coupling between free-stream and boundary layer has been presented by M.Gazaix, P.Girodroux-Lavigne and J.C.Le Balleur (ONERA, France). The leading edge closed separation bubble, that is a separate boundary layer that reattaches further downstream, was especially studied. Experimental results comforting theory have been obtained, up to now, on isolated flat plates only, and the audience is longing for more complete comparison between theory and experience, wondering namely if in the blade cascade the separated flow can really reattach or not.

Such a theory is in advance on experimental results and it might be interesting to compare it to the work of J.de Ruyck, B.Hazarika, and Ch.Hirsch (Vrije Universiteit, Brussels, Belgium) who gave a much detailed experimental analysis of the flow and the boundary layer for an oscillating isolated aerofoil, with large amplitude of oscillation. The separation and reattachment of the boundary layer near the leading edge is similar to what the above paper was expecting, however the Mach number is very low and it is not sure at all that such results can be generalised to real compressor or turbine bladings.

It is surprising that so many authors did not understand the difference between isolated airfoils and fixed or rotating blade cascades. This is again the case of K.M.Forster (Stuttgart University, Germany) who computes the flow around a cambered isolated blade, without even asking himself if, in the case of a cascade, the higher pressure gradients would not lead to strong flow separations on the blade pressure side.

2.2 Blade Row Interaction

One of the major novelties of this meeting was the fact that several papers were considering the effect of the interaction between two adjacent blade rows.

In any real turbomachine, outside of a single blade row, one of the blade rows is attacked by a uniform flow, and the wakes or the shock-waves issued from the trailing edge of the upstream blade row interacts with the downstream one. But pressure waves or even shocks issued from the leading edge of the downstream row may also interact with the upstream one.

Furthermore, one of these blade rows is usually a moving one, and therefore these interactions result in time dependent pressure fluctuations.

As a matter of fact, nobody knows at the present time, if these pressure fluctuations improve or deteriorate the performance of a compressor or a turbine, since apparently in the case of a helicopter rotor, the boundary layer separation is hindered by the flow unsteadiness and, paradoxically, improves the performance.

However, to be on the safe side, R.E. Henderson (Penn State University, USA) and J.H.Horlock (The Open University, UK) devised a theory for minimising the flow unsteadiness due to blade row interaction, in order to avoid at least, the forced vibration of the blades.

This coupling between aerodynamical forces and blade structure has been thoroughly tested by H.Joubert and V.Ronchetti (SNECMA, France) who, using advanced computational codes both for the aerodynamics of the bladings and for the structural forces, compare the vibration of a stator blading under the effect of the wakes issued from the upstream rotor. This research can be considered as the starting point of a long duration research program that would eventually lead to a better understanding of these interaction effects.

It is even more difficult to understand what happens when the moving blade row induces shock waves that sweep the stator blade suction side. A clever experimental set-up devised at Oxford University by A.B.Johnson (presently at Cambridge University, UK), M.J.Rigby (Rolls Royce, UK) and M.G.Oldfield (Oxford University) reproduces the passage of a shock wave on the suction side of a blade in a kind of shock tube type experiment, the shock wave being induced by a high speed moving body in front of a fixed blade in a transonic wind-tunnel.

Large, time-consuming computational codes, written for high performance computers are developed on both sides of the ocean. K.C.Hall and J.M.Verdon at United Technologies, Hartford, USA, H.V.McConnaughey and I.W.Griffin at NASA Marshall Flight Center, USA and A.Fourmaux, G.Billonnet, A.LeMeur and A.Lesain at ONERA, France, are, each one in a different way, attacking, with success, the difficult problem of the interaction of blade rows. They all show the change in blade surface pressure distribution, as a blade row passes in front of another, without being able to state whether this interaction effect is negligible or has to be taken into account if overall performances are considreed. This same problem appears in the next section, devoted to testing.

In the same area, S.Servaty (MTU, Germany) and H.E Gallus (RWTH, Germany) analyse the response of a linear blade cascade to a wavy perturbation. This approach is interesting, but needs some development before being able to describe real compressor operation.

2.3 Advanced Testing

In most of the presentations, computations were ahead of the experimental evaluation of unsteady aerodynamics in turbomachinery, whereas in single blade aerodynamics theory and tests are on the same level. Therefore, all experimental results on unsteady flows in rotors, stators or blade cascades are of paramount interest.

An interesting contribution to unsteady flow testing is the one by A.H.Epstein et al. (MIT, USA), who justify the test methods used since the beginning of the turbomachinery era. For that purpose they make a detailed analysis of the flow field and show that the effect of rotor stator interaction on mean performances is eliminated if pressure and temperature measurements are made on angular locations similar relative to the stator blades.

Test equipment is still in progress: the semiconductor probe developed by R.W.Ainsworth et al. (Oxford University, UK) is miniaturised and gives accurate pressure and heat transfer coefficients, as shown by tests made in a calibration wind tunnel. Another temperature probe, developed by S.C Cook (Rolls Royce, UK) and R.L.Elder (Cranfield Institute of Technology, UK) is also designed in order to give accurate and reliable mean values in a fluctuating flow. This is not the least difficulty in unsteady aerodynamics and the number of questions asked during the discussion period shows the high interest for such probes.

The test facilities especially designed for unsteady flows or vibrating bales in cascades are rare. This gives even more value to the work of H.D.Schulz and H.E.Gallus (WRTH, Germany) and to that of A.Bölcs et al. (Ecole Polytechnique de Lausanne, Switzerland) who give detailed test results obtained either on cascade under the influence of wakes or on vibrating blades in an annular cascade.

3. CONCLUSIONS TO BE DRAWN FOR FUTURE RESEARCH AND DEVELOPMENT

At the end of the meeting it might be interesting to draw some conclusions of the impact of the lectures on future work.

3.1 Future Development of Theoretical Research

The large numerical codes for viscid or inviscid, unsteady flows in turbomachinery will be more and more developed, although the experimental work for validation of these codes is lagging behind them.

It is clear that a great effort has to be made, and is already made in the major industries and research centres, in order to give descriptions of the time dependent flows, showing the effect of flow unsteadiness on performance.

As long as the tedious, time consuming and sometimes doubtful test results will not be available, numerical computation will be the only tool the designer will have to improve his product. Such politics have been *fruitful during the last years and will be* even more in the future.

The blade profiles, that at present time are optimized in terms of

    smooth pressure distributions

   -- correct radial total pressure distributions, in order to allow the stacking of the blade profiles

    sufficiently large throat sections, in order to avoid chocking.

will be optimized in the future in order to minimize the effect of flow unsteadiness i.e. take advantage of the renewal of the boundary layer but avoid early stall.

The development of large computers and the improvement of the codes will reduce the computation times without hindering the accuracy of the computations.

3.2 Test Facilities

The large component test facilities fashionable for many years seem to be on the decline.

The highly sophisticated test methods, that have given outstanding results for many years are presently less used, due to the tremendous number of test data, the experimenter not knowing how to use them.

Effort will be made on clever test facilities designed for the purpose of validating details of calculations rather than to investigating the whole flow field.

And finally, it will be only through the cooperation of theoreticians and experimenters, each of them understanding the work of the other, that further progress will be obtained in this difficult field of Unsteady Aerodynamics in Turbomachinery.

A COMPARISON OF FLUTTER CALCULATIONS
BASED ON EIGENVALUE AND ENERGY METHOD

by A.Klose and K.Heinig
MTU Motoren- und Turbinen-Union München GmbH
Dachauer Str. 665
8000 München 50
Federal Republic of Germany

Summary

The effect of unsteady aerodynamic loads on the natural modes and frequencies of unshrouded blades of axial flow turbomachinery is investigated. It is shown that significant shifts in eigenfrequencies and aerodynamic coupling between different modes do not occur for blades with a large mass ratio. Even for compressor and turbine bladings of recent design, it is generally possible to neglect the effect of unsteady aerodynamic forces on the vibration characteristics. Therefore, the Energy Method is applicable for the theoretical flutter investigation of these machines. However, for future light-weight designs, e.g. hollow fan blades or blades made of fibre-reinforced plastics, the effects of unsteady airloads on the vibration characteristics will be larger. In these cases, the Eigenvalue Method will have to be employed for flutter prediction as well as for the calculation of eigenfrequencies and natural modes.

Nomenclature

k	reduced frequency
L_{se}	generalized airload coefficient
m	mass per unit area
M_s	generalized mass of s-th in-vacuo eigenmode
$\vec{n}$	outward directed unit vector normal to blade surface
p'	unsteady pressure amplitude
p_e	pressure amplitude due to e-th eigenmode
Q_s	generalized unsteady airload
$x, r\theta, r$	coordinates of blade surface
e, s	indices denoting in-vacuo eigenmodes
t	time
V_{ref}	velocity at a reference radius
$\vec{z}$	local deflection of blade surface
δ_l	logarithmic decrement of l-th eigenmode
μ^*	mass ratio
μ_s	generalized mass ratio of s-th in-vacuo eigenmode
ω	circular frequency
ω_1	circular frequency of lowest in-vacuo eigenmode
Ω_l	circular frequency of l-th eigenmode
φ_s	generalized coordinate
$\vec{\Phi}_s$	in-vacuo eigenmode
ρ_{ref}	density at a reference radius

Introduction

Precise knowledge of the vibration characteristics of the   des is of paramount importance in the design of axial flow turbomachinery. Eigenfrequencies have to be tuned to avo   engine order resonances, which might cause fatigue failure, and blade vibrations must be shown not to be excited by self-induced unsteady aerodynamic forces, causing unstable oscillations called flutter.

Eigenfrequencies, eigenmodes and flutter stability can be calculated from the balance of dynamic forces acting upon the blades, i.e. inertial, elastic and unsteady aerodynamic forces (see fig. 1). A flutter prediction method taking into account all three kinds of forces is called Eigenvalue Method. The unsteady aerodynamic forces are often neglected in the balance of forces, i.e. eigenfrequencies and eigenmodes are calculated as if the blading would work in vacuum. This permits a complete decoupling of the calculation of eigenfrequencies and eigenmodes from the flutter calculation. The flutter stability in this case is determined by calculating the energy that is transfered from the flow to the vibrating blades by unsteady aerodynamic forces. This method is called Energy Method. When employing this method for flutter prediction, possible coupling of different in-vacuo eigenmodes by unsteady aerodynamic forces as well as modifications of eigenfrequencies are neglected. The aim of the study presented herein is to compare the results of the two different flutter prediction methods in order to assess the range of applicability of the simpler Energy Method.

In the following chapters, the equations of motion of a blade, taking into account inertial, elastic and unsteady aerodynamic forces, will be presented first. The solution of these equations will be formulated as an eigenvalue problem, and general expressions for eigenfrequencies and aerodynamic damping will be given. Subsequently, the expression for aerodynamic damping used in the Energy Method will be derived as a limiting case to the general expression derived before. To assess the effect of different parameters, comparisons of flutter calculations based on Eigenvalue- and Energy Method will be performed for a simple two-degree-of-freedom (TDOF)- flat plate cascade model. Comparison of eigenfrequency and aerodynamic damping calculated with Energy- and Eigenvalue Method will also be presented for a wide-chord-fan and a propfan rotor, in order to assess the order of magnitude of differences in cases of practical importance.

Equations of Motion - Eigenvalue Method

For the problem under discussion, it is convenient to approximate the motion $\vec{Z}(x,r\theta,r,t)$ of a blade by a finite modal series, the advantage of this choice being that no inertial coupling does occur among different degrees of freedom. Assuming harmonic motion,

$$\vec{Z}(x,r\theta,r,t) = Re\left\{ e^{i\omega t} \cdot \sum_{s=1}^{S} \varphi_s \cdot \vec{\Phi}_s(x,r\theta,r) \right\} \tag{1}$$

where for each mode, $\vec{\Phi}_s$ is the in-vacuo vibration mode and ω_s the generalized coordinate of modal motion. Neglecting structural damping, the equations of motion for these degrees of freedom can be deduced by considering Lagrange's equations:

$$M_s (\omega_s^2 - \omega^2) \; \varphi_s = Q_s \qquad ; \qquad s = 1, \ldots, S \tag{2}$$

Here,

$$M_s = \iint_A m(x\,r\theta,r) \cdot \vec{\Phi}_s^2(x,r\theta,r) \; dA \tag{3}$$

is the generalized mass

and

$$Q_s = \iint_A -p' \cdot \vec{n} \cdot \vec{\Phi}_s(x,r\theta,r) \; dA \tag{4}$$

is the generalized unsteady airload.

ω_s is the eigenfrequency of the s-th in-vacuo eigenmode, m is the blade mass per unit area, p' is the unsteady static pressure amplitude on the blade surface and $\vec{n}$ is the outward directed unit vector normal to the blade surface.

Assuming a linear relation between static pressure and amplitude of motion, p' can be expressed as

$$p' = \sum p_e \cdot \varphi_e \qquad ; \qquad e = 1, \ldots, S \tag{5}$$

where p_e is the pressure amplitude acting upon the blade during oscillation in the e-th eigenmode. Using eq. (5), the generalized unsteady airloads can be expressed as

$$Q_s = \sum_{e=1}^{S} \varphi_e \iint_A -p_e \cdot \vec{n} \cdot \vec{\Phi}_s(x,r\theta,r) \; dA \tag{6}$$

or, with

$$L_{se} = \frac{1}{\rho_{ref} \cdot V_{ref}^2} \cdot \iint_A -p_e \cdot \vec{n} \cdot \vec{\Phi}_s(x,r\theta,r) \; dA \tag{7}$$

as

$$Q_s = \rho_{ref} \cdot V_{ref}^2 \cdot \sum L_{se} \cdot \varphi_e \qquad ; \qquad e = 1, \ldots, S \tag{8}$$

where ρ_{ref} and V_{ref} are density and relative flow velocity at a reference radius.

Thus, the equations of motion (2) can be written as

$$M_s (\omega_s^2 - \omega^2) \; \varphi_s = \rho_{ref} \cdot V_{ref}^2 \cdot \sum_{e=1}^{S} L_{se} \cdot \varphi_e \tag{9}$$

Introducing the abbreviations $\mu_s = M_s / (\rho_{ref} \cdot c_{ref}^2)$, $\lambda = (\omega_1/\omega)^2$ and $k = \omega \cdot c_{ref}/V_{ref}$, the equations of motion read

$$(\lambda - \frac{1}{(\omega_s/\omega_1)^2}) = \frac{1}{\mu_s k^2 (\omega_s/\omega_1)^2} \cdot \sum_{e=1}^{S} L_{se} \cdot \varphi_e \tag{10}$$

or

$$(\underline{A} - \lambda \underline{I}) \; \vec{\varphi} = \vec{0} \tag{11}$$

where $\underline{I}$ is the unit matrix and $\underline{A}$ is a matrix with the elements

$$a_{se} = \begin{cases} \dfrac{1}{(\omega_s/\omega_1)^2} + \dfrac{L_{ss}}{\mu_s k^2 (\omega_s/\omega_1)^2} & \text{for } e = s \\[4mm] \dfrac{L_{se}}{\mu_s k^2 (\omega_s/\omega_1)^2} & \text{for } e \neq s \end{cases} \tag{12}$$

The vibration characteristics of the blades under consideration of the unsteady aerodynamic forces can be deduced from these equations. The eigenmodes are described by the eigenvectors of the system of equations (11); the eigenfrequencies Ω_l and the aerodynamic damping δ_l of the different eigenmodes can be calculated from the eigenvalues of eq. (11) according to the formulae

$$\Omega_l = \frac{Re \sqrt{\lambda_l}}{|\lambda_l|} \cdot \omega_l \qquad\qquad \delta_l = -2\pi \frac{Im \sqrt{\lambda_l}}{Re \sqrt{\lambda_l}} \tag{13}$$

As the eigenfrequencies Ω_l are not necessarily equal to the eigenfrequencies ω_s of the in-vacuo eigenmodes, the unsteady airloads can be seen to influence the vibration characteristics of the blade.[3]

Energy Method

For large values of μ_s, the elements off the leading diagonal of $\underline{A}$ will be small when compared to the elements on the leading diagonal. In these cases, the eigenvalues of $\underline{A}$ can be approximated by the elements on the leading diagonal, i.e.

$$\lambda_s = \frac{1}{(\omega_s/\omega_l)^2} + \frac{L_{ss}}{\mu_s k^2(\omega_s/\omega_l)^2} = \frac{1}{(\omega_s/\omega_l)^2} + \frac{Re\{L_{ss}\}}{\mu_s k^2(\omega_s/\omega_l)^2} + i \frac{Im\{L_{ss}\}}{\mu_s k^2(\omega_s/\omega_l)^2}$$

Again, if μ_s is large, the above equation is approximately equivalent to

$$\lambda_s \approx \frac{1}{(\omega_s/\omega_l)^2} + i \frac{Im\{L_{ss}\}}{\mu_s k^2(\omega_s/\omega_l)^2} \tag{14}$$

Here, the imaginary part is small when compared to the real part, and $\sqrt{\lambda_s}$ can be approximated by

$$\sqrt{\lambda_s} = \sqrt{|\lambda_s|} \cdot e^{i\psi/2} = \sqrt{|\lambda_s|} \cdot (\cos(\psi/2) + i \cdot \sin(\psi/2)) \tag{15}$$
$$\approx \sqrt{|\lambda_s|} \cdot (1 + i \cdot \psi/2)$$

where

$$\psi = \frac{Im\{L_{ss}\}}{Re\{L_{ss}\}} \approx \frac{Im\{L_{ss}\}}{\mu_s \cdot k^2} \tag{16}$$

When introducing this result into eq. (13), the eigenfrequencies are found to be almost unchanged from their in-vacuo value by the presence of the flow around the blades:

$$\Omega_s \approx \omega_s \tag{18}$$

The same, of course, holds for the eigenvectors.

Taking into account the results obtained above, the following expression can be deduced for the aerodynamic damping:

$$\delta_s = -2\pi \cdot \frac{Im \sqrt{\lambda_s}}{Re \sqrt{\lambda_s}} \approx -2\pi \cdot \frac{Im\{L_{ss}\}}{2\mu_s k^2} = -\pi \frac{Im\{L_{ss}\} \cdot 2 \cdot q_{ref}}{2\mu_s \cdot k^2 \cdot q_{ref}} \tag{19}$$

This is identical to the expression

$$\delta_s = -\frac{W_s}{4 K_{Es}} \tag{20}$$

given by F.O. Carta (1) for the aerodynamic damping. Here, W_s is the work done by the aerodynamic forces on the oscillating blades, and K_{Es} is the mean kinetic energy of the blade[3] when oscillating in the s-th vacuum eigenmode.

For large values of μ_s, thus, an eigenvalue calculation as described in the previous chapter is not necessary. As eigenvectors and eigenfrequencies are almost identical to their in-vacuo values, the aerodynamic damping can be determined from eq. (20) after the aerodynamic work W_s has been calculated.

Mass Ratio

As has been shown in the previous chapter, the Energy Method is applicable for large values of μ_s. However, as the value of μ_s depends on the way the eigenvectors are normalized, μ_s is not suitable for an à priori decision about the applicability of the Energy Method. For that purpose, it is more convenient to use the mass ratio

$$\mu^* = \frac{m_{Blade}}{\varrho_{ref} \cdot c_{ref}^2} \tag{21}$$

which is roughly proportional to μ_s. Here, m_{Blade} is the blade mass per unit span and ϱ_{ref} and c_{ref} are gas density and chord, respectively. μ^* can be taken at a reference radius, or as blade-height averaged value.

The effect of μ^* on the applicability of the Energy Method will be discussed in the following chapter, along with the effects of some other parameters, by aid of a simple two-degree-of-freedom (TDOF-) flatplate cascade model.

TDOF - Flat Plate Cascade Model

The cascade model used for the parameter variation is shown in fig. 2, along with its geometrical parameters. The cascade consists of flat plates with a translational degree of freedom normal to chord and a torsional degree of freedom about the elastic axis. As there is an offset between center of gravity (c.g.) and elastic axis (e.a.), coupling between bending and torsion occurs even for the in-vacuo eigenmodes due to inertia effects.

In fig. 3, $\delta \cdot \mu^*$ of the predominantly torsional eigenmode is shown for different mass ratios as a function of relative flow velocity at M = 0.0 . As can be seen, the differences are small if the cascade operates far below flutter speed. When the flutter speed is approached, the curves diverge. The differences are small for very large mass ratios, e.g. $\mu^* = \frac{\pi}{2} \cdot 10^4$ or $\mu^* = \frac{\pi}{2} \cdot 10^3$, which indicates that the high mass ratio limit has been reached, for which the Energy Method is valid. Similar calculations have been performed for different Mach-numbers. The relative effect of the mass ratio on the flutter speed at these Mach numbers is shown in fig. 4. It can be seen that, when increasing the Mach number from 0.0 to 0.5, the sensitivity to mode coupling increases. If a 5‰ error margin in flutter speed is considered acceptable, the Energy Method would be applicable if $\mu^* > 160$ for M = 0.0 , and if $\mu^* > 560$ for M = 0.5. For supersonic relative flow, the range of applicability of the Energy Method extends to far lower values of μ^*. However, it should be pointed out, that these results are by no means generally valid. A change in the ratio of bending to torsional stiffness is only one further parameter affecting the applicability of the Energy Method. In fig. 5, valid for M = 0.5, it is shown that the sensitivity to mode coupling is the larger the closer the eigenfrequencies for pure bending and pure torsion are.

Although the example discussed above is quite instructive, the results are not generally valid. As it is impossible to derive general conclusions from such parameter studies, any à priori decision about the applicability of the Energy Method has to be based largely on experience gained from earlier calculations. Two example results for turbomachinery bladings believed to be more or less typical for modern configurations shall be presented subsequently.

Results for Wide-Chord-Fan and Propfan

Example calculations for real turbomachinery rotors have been performed for a modern Wide-Chord-Fan built from titanium and a CRISP-blade built of CFRP (carbon-fibre-reinforced-plastic). The fan is operating at supersonic relative flow velocities, and the radius-averaged mass ratio at the flow conditions investigated is approximately $\mu^*=80$. The CRISP-blade operates at tip Mach numbers close to 1.0, and the radius-averaged mass ratio is approximately $\mu^*=40$. In both examples, the generalized aerodynamic forces have been calculated with D.S. Whitehead's FINSUP code (2), applied in a strip-theory manner. For both blades, the components of the lowest three eigenvectors are shown in the complex plane in figs. 6-11. As can be seen, mode coupling is small for the titanium fan blade, but is relevant in some eigenmodes of the CRISP blade. These trends are similar for the eigenfrequencies and the predicted aerodynamic damping, as is shown in tables 1 and 2.

It should be noted, that the results presented are valid for an operating condition which is far from the flutter boundary. Calculations indicate that no unstalled flutter has to be expected within the respective flight envelopes, so that no effects can be studied close to the flutter boundary. From the results obtained in the previous chapter, however, it may be expected, that the differences between Eigenvalue- and Energy-Method become more substantial when approaching a flutter boundary. Nonetheless, the differences are expected to be negligible for the titanium fan blade, whereas for the CRISP-blade the differences are expected to be relevant. In this case, any flutter calculation has to be performed with the eigenvalue method.

Conclusions

The range of applicability of the Energy Method for flutter prediction of axial flow turbomachinery has been investigated. The Energy Method was shown to be the limiting case of the Eigenvalue Method for high mass ratio. However, a study performed with a flat-plate-cascade model showed other parameters to have an equally important effect. Thus no generally valid rule for the à priori decision about the applicability of the Energy Method could be derived. Results for real turbomachinery rotors, however, show that the Energy Method is applicable for wide-chord titanium fan blades, whereas the Eigenvalue Method has to be applied for blades made of CFRP. It is believed that these conclusions are more or less generally valid.

References

(1)   F.O. Carta   Coupled Blade-Disk-Shroud Flutter Instabilities in Turbojet Engine Rotors
                           J. Eng. Power, July 1967

(2)   D. S. Whitehead   Program FINSUP: Steady and Unsteady Supersonic Flow in Cascades by a Finite Element
                           Method
                           CUED/A-TURBO/TR-105-1981

- ELASTIC FORCES

- INERTIAL FORCES

- UNSTEADY
    AERODYNAMIC FORCES

Figure 1: Dynamic Forces acting upon Blade
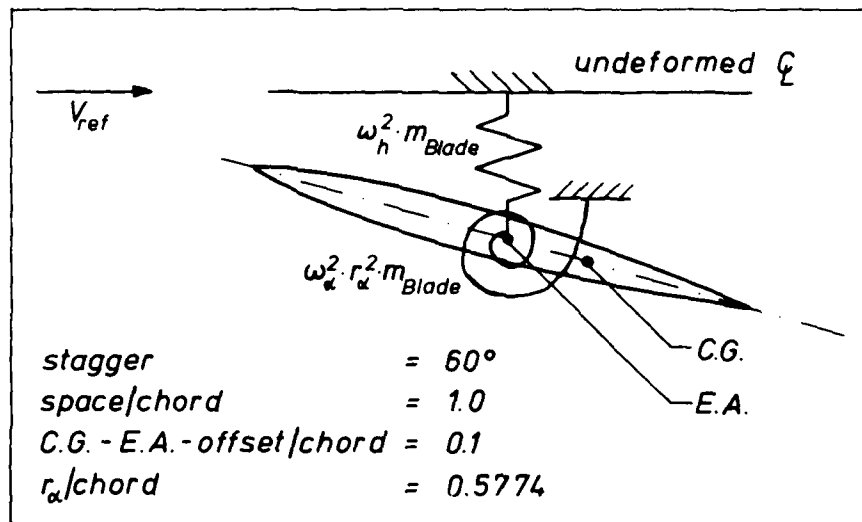
Figure 2: TDOF - Flat Plate Cascade Model
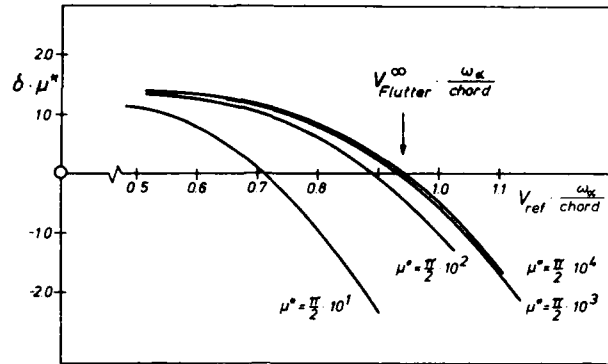
Figure 3: Effect of Mass Ratio μ^* on Aerodynamic Damping δ
(Mach No = 0 , ω_h/ω_α = 0.7)
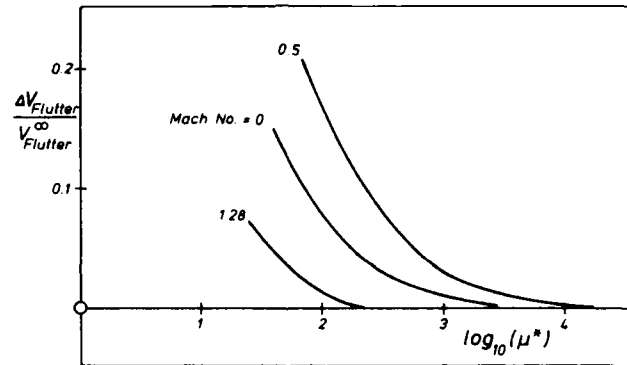
Figure 4: Effect of Mass Ratio μ^* on Error in Flutter Velocity
predicted by Energy Method (ω_h/ω_α = 0.7)
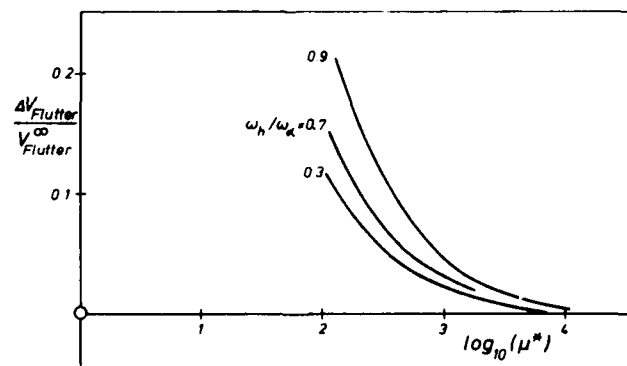
Figure 5: Effect of Frequency Ratio (ω_h/ω_α) on Error in
Flutter Velocity predicted by Energy Method
(Mach No = 0.5)
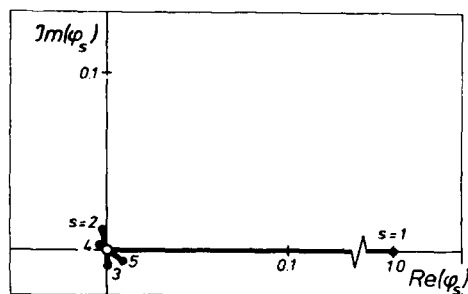
Figure 6 : Components of 1st Eigenvector
(Fan Blade)
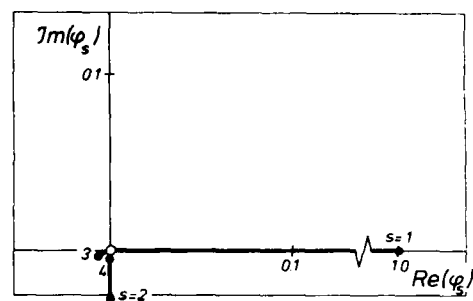
Figure 9 : Components of 1st Eigenvector
(Propfan Blade)
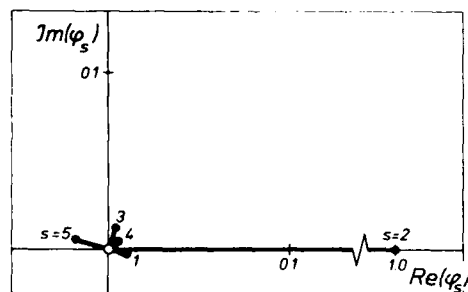
Figure 7 : Components of 2nd Eigenvector
(Fan Blade)
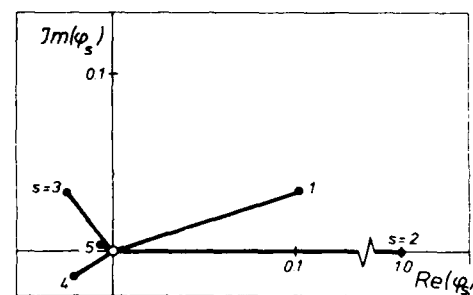
Figure 10 : Components of 2nd Eigenvector
(Propfan Blade)
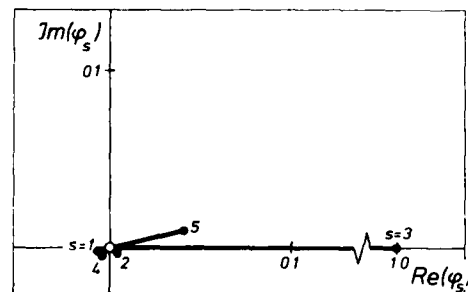
Figure 8 : Components of 3rd Eigenvector
(Fan Blade)
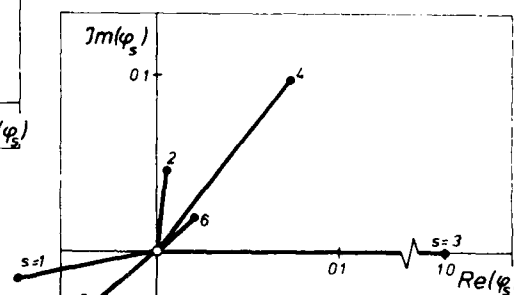
Figure 11 : Components of 3rd Eigenvector
(Propfan Blade)

1-8

Eigenmode l, s	$\dfrac{\Omega_l - \omega_s}{\omega_s}$
1	$-0.8\ \%$
2	$-0.2\ \%$
3	$+0.03\%$

Table 1 : Fan Blade – Difference of Eigenfrequencies
predicted with (Index l) and without (Index s)
Consideration of Unsteady Aerodynamic Forces

Eigenmode l, s	$\dfrac{\Omega_l - \omega_s}{\omega_s}$	$\dfrac{\delta_l - \delta_s}{\delta_s}$
1	$+0.4\ \%$	-3.8%
2	$+3.2\ \%$	$+5.5\%$
3	$-1.7\ \%$	-3.2%

Table 2 : Propfan Blade – Difference in Eigenfrequencies and
Aerodynamic Damping predicted with (Index l) and
without (Index s) Unsteady Aerodynamic Forces

DISCUSSION

H.Joubert - SNECMA, Villaroche, France
        Could the author give more details on the unsteady aerodynamic method he is using in order to obtain the unsteady forces?

Author's response :
        As indicated in the paper, D.S.Whitehead's FINSUP code is used to calculate aerodynamic forces for flutter prediction. The flat blade cascade results shown in the paper were obtained with linear, small perturbation singularity methods.

W.G.Alwang - Pratt & Whitney, USA
        Is there any experimental confirmation of the flutter calculation presented?

Author's response :
        The unsteady aerodynamics code was validated by comparison of calculations and experimental results for the Lausanne Standard Configuration (see reference below). The capability to predict accurately the onset of flutter was confirmed by checking prediction against experience for a titanium fan blading.

Reference : Bölcs A., Fransson T 1986
Aeroelasticity in Turbomachines: Comparison of theoretical and experimental cascade results-Communication N°13 of Laboratoire de Thermique Appliquée et de Turbomachines de l'Ecole Polytechnique Fédérale de Lausanne, Switzerland.

NUMERICAL INVESTIGATION OF UNSTEADY FLOW IN OSCILLATING

TURBINE AND COMPRESSOR CASCADES

H.P. Kau and H.E. Gallus
Institut für Strahlantriebe
und Turboarbeitsmaschinen
RWTH Aachen
Templergraben 55, 5100 Aachen
W.-Germany

Summary

A method of computing the unsteady two-dimensional, inviscid subsonic flow through oscillating compressor and turbine cascades is presented. The non-linear Euler-equations in conservative law form are solved taking into account the time-dependent geometry. For interior points MacCormack's explicit predictor-corrector scheme is used. Boundary conditions are formulated by characteristics methods.

A comparison of computational results and experimental data is given. A study is performed showing the influence of important aerodynamic and geometric parameters on the time-dependent forces and moments.

Nomenclature

a	velocity of sound	U	flow values (ρ, ρu, ρv, e)
$\vec{c}$	velocity	v	velocity in y-direction
c	chord length	x,y	coordinates
e	energy	ξ,η	coordinates for transformation
E,F	flux vectors	$\vec{\xi}$	local normal vector
h	bending amplitude dimensionless		$\xi = (\xi_1,\xi_2)^T$
	with chord	$\vec{n}$	local tangential vector
J	Jacobian		$\eta = (\eta_1,\eta_2)^T$
k	reduced frequency	α	upstream flow angle
p	pressure	γ	ratio of specific heats
t	time	ν	frequency
$\vec{t}$	tangential vector	ρ	density
u	velocity in x-direction	σ	interblade phase angle
		λ	stagger angle

Subscripts

B	blade
n	numerical
ref	reference value:
	turbine cascade: downstream
	compressor cascade: upstream
t	total value

Superscripts

n	value at time t
n+1	value at time t+Δt
^	value after the transformation
——	value after the predictor step
	of the MacCormack scheme
*	value at boundary after the
	MacCormack iteration

Introduction

The reliability of modern axial-flow turbomachines is particularly influenced by flow-induced vibrations. They may be caused through blade row interactions, turbulence, stall, inlet distortion and self-excited blade vibrations.

This paper presents a non-linearized method for calculating the unsteady two-dimensional, inviscid subsonic flow through oscillating compressor and turbine cascades.

The two-dimensional unsteady Euler-equations in conservative form are solved on a time-dependent grid, using the MacCormack scheme /1/ at interior points. The boundary conditions are taken into account by a post-correction-method and one-dimensional characteristics /2/. The moving computational grid is generated once per unsteady time-step using the Laplace-equations corresponding to the method of Thompson, Thames and Mastin /3/.

The algorithm has been checked first computing the steady flow through compressor and turbine cascades showing the local accuracy. The prediction capability of the algorithm for time-dependent values is shown by comparisons with several experimental data in bending and simultaneous bending-pitching mode. The algorithm was applied to both influence wave mode and travelling wave mode. The first part of a systematic variation of important parameters shows their influence on the aerodynamic forces and moments coefficients.

Governing Equations

The unsteady flow is modelled by the two-dimensional, inviscid and compressible Euler-equations written in conservative form. They are formulated on a cartesian coordinate grid with x being the axial direction:

$$\frac{\partial}{\partial t} U + \frac{\partial}{\partial x} E(U) + \frac{\partial}{\partial y} F(U) = 0 \tag{1}$$

where

$$U = \begin{pmatrix} \rho \\ \rho u \\ \rho v \\ e \end{pmatrix} \qquad E(U) = \begin{pmatrix} \rho u \\ \rho u^2 + p \\ \rho uv \\ (e+p)u \end{pmatrix} \qquad F(U) = \begin{pmatrix} \rho v \\ \rho uv \\ \rho v^2 + p \\ (e+p)v \end{pmatrix}$$

They are closed with the assumption of perfect gas:

$$e = \frac{p}{\gamma - 1} + \frac{\rho}{2}(u^2 + v^2)$$

This system of four partial differential equations forms an initial-/boundary value problem. It is solved by a combined algorithm, using MacCormack's explicit algorithm at interior points of the computational grid and a post correction method taking into account the boundary conditions in a formulation of one-dimensional characteristics. The following chapter will describe these algorithms in detail.

Mathematical Transformation

To solve the Euler-equations for a time-dependent geometry, a moving computational grid (x,y,t) has to be used, where at each time step the physical boundaries coincide with the grid lines (Fig. 1). To avoid space interpolations on these grids, for the formulation of the derivatives $\partial/\partial x$ and $\partial/\partial y$ a mathematical model is used, transforming the physical coordinates (x,y) at a fixed time on a new set (ξ, η). From there the Euler-equations will be solved in this transformed region. They can be written as

$$\frac{\partial}{\partial t} \hat{U} + \frac{\partial}{\partial \xi} \hat{E} + \frac{\partial}{\partial \eta} \hat{F} = 0 \tag{2}$$

where

$$\hat{U} = U/J$$
$$\hat{E} = (U \ \xi_t + E\xi_x + F\xi_y) / J$$
$$\hat{F} = (U \ \eta_t + F\eta_x + G\eta_y) / J$$

with the Jacobian

$$J = \xi_x \ \eta_y - \xi_y \ \eta_x = \frac{1}{x_\xi \ y_\eta - x_\eta \ y_\xi}$$

Expressing all terms in dependence of ξ and η and t the Jacobian can be eliminated from $\hat{E}$ and $\hat{F}$. The equations can be remodelled analytically for $\hat{E}$ and $\hat{F}$ giving:

$$\hat{E} = U * U_x + p \begin{pmatrix} 0 \\ y_\eta \\ -x_\eta \\ (uy_\eta - vx_\eta) \end{pmatrix}$$

$$\hat{F} = U * V_x + p \begin{pmatrix} 0 \\ -y_\xi \\ x_\xi \\ (vx_\xi - uy_\xi) \end{pmatrix}$$

with the abbreviations

$$U_x = x_\eta \ (y_t - v) + y_\eta \ (u - x_t)$$
$$V_x = x_\xi \ (v - y_t) + y_\xi \ (x_t - u) \ .$$

Interior points

This transformed Euler-equation can now easily be solved at interior points by the explicit predictor/corrector MacCormack scheme.

Predictor step:

$$\overline{U_{i,j}^{n+1}} = J_{i,j}^{n+1} \left\{ \frac{U_{i,j}^n}{J_{i,j}^n} - \frac{\Delta t}{\Delta \xi} \left[\hat{E}_{i+1-\delta,j}^n - \hat{E}_{i-\delta,j}^n \right] - \frac{\Delta t}{\Delta \eta} \left[\hat{F}_{i,j+1-\epsilon}^n - \hat{F}_{i,j-\epsilon}^n \right] \right\} \tag{4}$$

Writing this equation in a detailed finite difference form it can be seen that $\Delta\hat{F}$, $\Delta\hat{E}$ and J contain terms with $\Delta\xi$ and $\Delta\eta$ and that the whole equation is independent from these values.

The predictor step gives a first approximation $\overline{U_{i,j}^{n+1}}$ of the values $U_{i,j}^{n+1}$ at time t^{n+1}.

The corrector step gives a second approximation and includes averaging:

$$U_{i,j}^{n+1} = J_{i,j}^{n+1} + \frac{1}{2} \left\{ \frac{\overline{U_{i,j}^{n+1}}}{J^{n+1}} + \frac{U_{i,j}^n}{J_{i,j}^n} - \frac{\Delta t}{\Delta \xi} \left[\overline{\hat{E}_{i+\delta,j}^{n+1}} - \overline{\hat{E}_{i-1+\delta,j}^{n+1}} \right] - \frac{\Delta t}{\Delta \eta} \left[\overline{\hat{F}_{i,j+\epsilon}^{n+1}} - \overline{\hat{F}_{i,j-1+\epsilon}^{n+1}} \right] \right\} \tag{5}$$

The time step Δt is bounded by the CFL criterion /4/.

Using a proposal of MacCormack /5/ the four possible choices for approximating the derivatives $\partial\hat{E}/\partial\xi$ and $\partial\hat{G}/\partial\eta$ are cycled through during the course of a calculation (Fig. 2). This rotation introduces a numerical oscillation with the frequency

$$\nu_m = \frac{1}{4 \ \Delta t} \ . \tag{6}$$

To ensure that the physical phenomena to be computed are not influenced by these effects, the frequency ν_m of the blade vibration must have a certain distance from ν_m. In practice one period of blade oscillation will be divided into 200 or more time steps depending on the allowed maximum of Δt, so that

$$\nu_m \geq 50 \ \nu_b \ . \tag{7}$$

Boundary Points

The MacCormack algorithm yields only the solution at inner points. At the boundaries of the area (B1 to B8 in Fig. 3) a special treatment is necessary. The number of boundary conditions to be specified is given by an analysis of the physical area of dependence. For example, Fig. 4 shows the situation at the upstream boundary.

- At B1 the stagnation values p_t, T_t and the flow angle α are prescribed.
- At B2 the static pressure p is assumed known.
- At the blade profiles the flow tangency condition is used, i.e. $\vec{c} * \vec{\xi} = \vec{c_m} * \vec{\xi}$ where $\vec{c} = (u,v)^t$ denotes the velocity of flow at the solution point, $\vec{c_m} = (u_m,v_m)^t$ describes the local velocity of the blade and $\vec{\xi}$ is the normal vector to the profile.
- Downstream of the blading, the boundaries B5 and B6 are represented by the slip-streams leaving the trailing edge of each blade.
- At B7/B8 a special periodicity condition is used, which is explained later on.

The algorithm for the boundary points consists of two main steps. First, the MacCormack scheme is used, where the unknown space derivatives normal to the boundaries are formulated as one-sided finite difference approximations. These values are not correct, because they do not satisfy the boundary conditions, but their Riemann variables are already well computed. These values have to be changed in the second step taking into account the boundary conditions and the Riemann variables. In detail, the following system of equations in which the * denotes the results of the first step, is solved .

Inlet surface (B1):

$$-(\rho a)^* \ (u^{n+1} - u^*) + (p^{n+1} - p^*) = 0 \tag{8}$$

and p_t, T_t, α as boundary conditions.

As p^{n+1} depends from u^{n+1}, Eq. 8 must be solved with an iteration. To improve convergence, the equation is remodelled to the type $p_{new}(p_{old}) - p_{old} = 0$ and can be solved with a Newton iteration.

Outlet surface (B2):

$$-(a^2)^n (p^{n+1}-p^n) + (p^{n+1}-p^n) = 0 \qquad (9)$$

$$v^{n+1} - v^n = 0$$

$$(\rho a)^n (u^{n+1}-u^n) + (p^{n+1}-p^n) = 0$$

with p^{n+1} or a nonreflecting equation as boundary condition. The system can easily be solved.

Solid wall (B3, B4):

$$-(\rho a)^n \vec{\xi} \ (c^{n+1}-c^n) + (p^{n+1}-p^n) = 0 \qquad (10)$$

$$-(a^2)^n (p^{n+1}-p^n) + (p^{n+1}-p^n) = 0$$

$$\vec{n} \ (\vec{c}^{n+1}-\vec{c}^*) = 0$$

$$\vec{\xi} \ \vec{c} = \vec{\xi} \ \vec{c}_w$$

with $\vec{\xi}$ as local normal vector and vertical to $\vec{n}$.

Slipline (B5, B6):

Downstream of the blades, a slipline leaves the trailing edge of each blade. This model has been used by Butler /6/, Pandolfi /7/ and other authors. At each point of this line pressure and normal velocity are continuous while the tangential velocity will show a jump to simulate the effect of vorticity (Fig. 5).

The describing equations are:

$$(\rho a)_1 \ \vec{\xi}_1 \ \vec{c}_1^{n+1} + p^{n+1} = (\rho a)_1 \ \vec{\xi}_1 \ \vec{c}_1^* + p_1^* \qquad (11)$$

$$(\rho a)_2 \ \vec{\xi}_1 \ \vec{c}_2^{n+1} - p^{n+1} = (\rho a)_2 \ \vec{\xi}_1 \ \vec{c}_2^* - p_2^*$$

$$\vec{\xi}_1 \ \vec{c}_1^{n+1} - \vec{\xi}_1 \ \vec{c}_2^{n+1} = 0$$

$$\vec{n}_1 \ \vec{c}_1^{n+1} = \vec{n}_1 \ \vec{c}_1^*$$

$$\vec{n}_1 \ \vec{c}_2^{n+1} = \vec{n}_1 \ \vec{c}_2^*$$

This system of equations can be reduced analytically.

Periodicity condition (B7, B8):

When computing the steady state solution, the numerical grid can be closed at the lines B7/B8 with a simple periodicity condition. Computing unsteady phenomena, a special treatment has to be found to take into account the time-dependent fluctuation on these lines. If one is interested in the real physical phenomena during the transition from the initial values to the periodic state, the discretisation can not be limited to one channel. It must be extended over as many channels as are needed due to a geometry similarity that allows to close the computational domain with the simple periodic condition. If only the periodic state has to be computed, a distinction can be made in the treatment of the periodic lines (B7, B8 in Fig. 3) depending on the wave mode of the grid.

To compute the influence wave mode i.e. the case of all blades having a steady position except one /8/, it is necessary to discretise not only the channel of the moving air foil but the whole cascade. With only little loss of accuracy, the computational domain can be reduced to 7 or 5 channels, omitting some steady blades. In travelling wave mode, all the blades vibrate at the same frequency and amplitude, but there exists a circumferential constant phase lag between each blade and its neighbours.

A special treatment of the boundaries B7/B8 first introduced by Erdos and Alzner /9/ reduce the computational domain to a single channel. This special treatment of the periodicity condition takes advantage of the periodically identical states in the channel and its neighbours having only a constant time delay. This formulation is only valid for periodic conditions and cannot be used to compute the transition from steady initial conditions to the periodically fluctuating state reproducing the real physical phenomena. Besides, for reasons of stability it is necessary to introduce an additional damping coefficient, which depends on the difference between the values on the periodic lines at the last time step and those computed at the last period of the corresponding time. It drives the numerical scheme to the periodic state and vanishes after the transition. In addition to the original idea, the derivatives of these values in n-direction on these lines B7/B8 are stored, too. These derivatives can directly be used

2-5

to complete the MacCormack steps at the periodic lines. The entire formulation yields a stable transition to the periodic state.

Results

Steady Cascade Flow

Before the presentation of results with oscillating blades, computed steady-state solutions will be presented to show the 2D prediction capability of the algorithm. Fig. 6 shows the time averaged pressure coefficients for the "Fourth Standard Configuration No. 4" /10/, using a mesh with 51 x 17 points (Fig. 1). This grid represents a typical section of modern free standing turbine blades. It operates under high subsonic flow conditions. The agreement between measured and calculated results is fairly good, but in the region of high Mach numbers (Ma ~ 1) there exists a minor deviation. Fig. 7 shows the comparison between calculation and experiment for a low subsonic compressor cascade. Due to the inviscid mathematical model the calculation shows a greater lift than the experimental results.

Oscillating Cascades

The developed algorithm was applied to both influence (IWM) and travelling wave mode (TWM). Fig. 8 shows a selected result for the introduced compressor cascade bending in TWM with the frequency ν = 132 Hz, the upstream Mach number M_1 = 0.228 and the inter-blade phase angle σ = 180°. The unsteady pressure was measured in five positions D1 to D5 on the pressure side and in six positions S1 to S6 on the suction side. The comparison with computed results shows a very good agreement in amplitude and phase, exept for D1. Unfortunately, the pressure transducer S1 was out of order. The acceleration measured in the experiment shows a second, higher frequency corresponding to the first torsional mode. Therefore all measured results have a high oscillation. The difference at point D1 is caused by the relatively coarse grid.
For the same profile, there exist experimental data in influence wave mode. Fig. 9 shows the comparison between measured and computed results for a combined bending/pitching motion with 370 Hz. The prediction capability of the algorithm is not as good as in Fig. 8. Especially the deviation at the leading edge is increased, but now the computed results are higher than the measured ones. There also seem to be certain deviations in the measured results, because there is no physical explanation for the measured great amplitude at transducer D3, which is located nearby the torsional axis. On the whole, the accuracy is fairly well, and will increase with a finer computational grid and a better analysis of the results of the moving pressure transducers.

Influence of important parameters

With the presented method a systematic study of the influence of important parameters on the aeroelastic behaviour of a cascade has been performed. The most important parameters are the reduced frequency, the interblade phase angle and the Mach number. Fig. 10 shows in the upper two diagrams a comparison of the influence of Mach number on the aerodynamic force coefficients at constant other data for a flat plate cascade. The influence of the interblade phase angle is demonstrated in the diagrams 2, 3 and 4 of this figure at constant stagger and Mach number. These results can also be achieved by a linearized algorithm, such as LINSUB from Smith/Whitehead /11,12/. Nevertheless, the influence of important geometric parameters, such as thickness and camber, can only be studied by nonlinear methods. Fig. 11 shows in the lower right corner real- and imaginary part of the unsteady force coefficient depending on reduced frequency for the "Fourth Standard Configuration" in bending mode. Because of the wide range of the local Mach number of the turbine cascade these results are compared in the other three diagrams of Fig. 11 with those of a flat plate at different Mach numbers computed with LINSUB. Because of the strongly differing geometry of the turbine blade profile and a flat plate the different course of the curves in these diagrams becomes obvious.

Conclusion

The presented method computes the two-dimensional, unsteady, subsonic flow. The non-linear Euler-equations in conservative form are solved at interior points with the MacCormack's predictor-corrector scheme. Boundary conditions are handled with a post correction method using one-dimensional characteristics.
Results for bending and pitching motion of compressor and turbine cascades show a good agreement with experimental data.
The aeroelastic behaviour of a turbomachinery cascade mainly depends on the frequency, the interblade phase angle and the Mach number. Important geometric parameters are camber, thickness and stagger. To study the influence of these parameters in detail, comprehensive investigations are planned for the near future.

References

/1/ MacCormack, R.W.: "The Effect of Viscosity in Hypervelocity Impact Cratering", AIAA-Paper No. 69-354, May 1969

/2/ Veuillot, J.P., Meauze, G.: "A 3d Euler Method for Internal Transonic Flows Computation with a Multi-Domain Approach", AGARD-LS No. 140, 1985

/3/ Thompson, J.F., Thames, F.C., Mastin, C.W.: "Boundary-Fitted Curvilinear Coordi-
nate Systems for Solution of Partial Differential Equations on Fields Containing
Any Number of Arbitrary Two-Dimensional Bodies", NASA CR-2729, 1977

/4/ Courant R., Friedrichs, K., Lewy, H.: "Über die partiellen Differentialgleichun-
gen der mathematischeu Physik", Math. Ann., Vol. 100, 1928, pp. 32-74

/5/ MacCormack, R.W.: "Current Status of Numerical Solutions of the Navier Stokes
Equations", AIAA-Paper No. 85-0032, Jan. 1985

/6/ Butler, D.S.: "The Numerical Solution of Hyperbolic Systems of Partial Differ n-
tial Equations in Three Independent Variables", Proceedings of the Royal Society,
Vol. A255, 1960

/7/ Pandolfi, M.: "Numerical Experiments on Unsteady Flows through Vibrating Cas-
cades", Proceedings of the Symposium on Aeroelasticity in Turbomachines held in
Lausanne, Swi zerland, September 8-12, 1980, pp. 211-228

/8/ Gerolymos, G.A.: "Periodicity, Superposition and 3D Effects in Supersonic Com-
pressor Flutter Aerodynamics", ASME-Paper 88-GT-136

/9/ Erdos, J.I., Alzner, E.: "Numerical Solution of Periodic Transonic Flow through a
Fan Stage", AIAA-Journal, Vol. 15, No. 11, Nov. 1977

/13/ Bölcs, A., Fransson, T.H. (eds.): "Aeroelasticity in Turbomachines - Comparison of
Theoretical and Experimental Cascade Results", Communication du Laboratoire de
Thermique Appliquée et de Turbomachines, No. 13, Lausanne, EPFL 1986

/11/ Smith, S.N.: "Discrete Frequency Sound Generation in Axia! Flow Turbomachines",
University Engineering Dept., Cambridge, Report and Memoranda No. 3709, 1972

/12/ Whitehead, D.S.: "Classical Two-Dimensional Methods", AGARD Manual on Aeroela-
sticity in Axial-Flow Turbomachines, AGARD-AG-298, Vol. 1, 1987
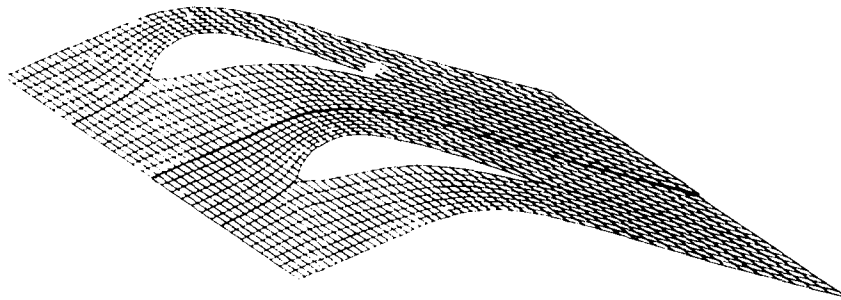
Fig. 1: Typical computational grid for a turbine cascade
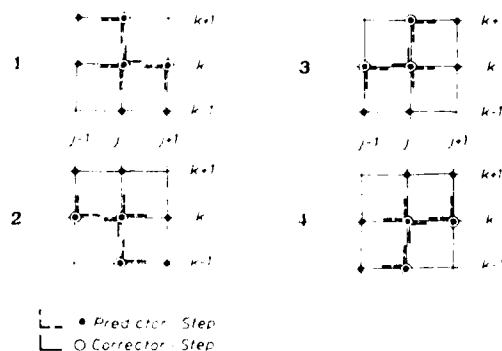
Fig. 2: Discretisation of the derivatives in the MacCormack-scheme
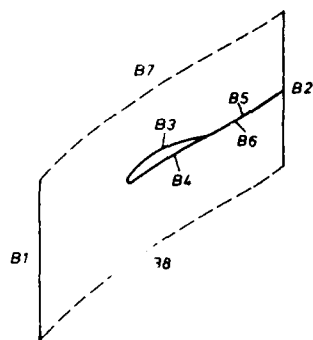
B1   - Upstream boundary
B2   - Downstream boundary
B3,B4 - Blade surface
B5,B6 - Slipstream
B7,B8 - Periodical boundary

Fig. 3: Location of boundaries
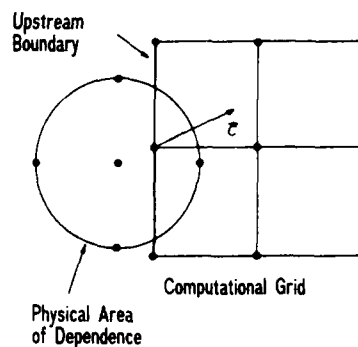
Fig. 4: Upstream boundary with physical area of dependence

$\vec{c}_n$ normal velocity
$\vec{c}_t^+$ upper tangential velocity
$\vec{c}_t^-$ lower tangential velocity
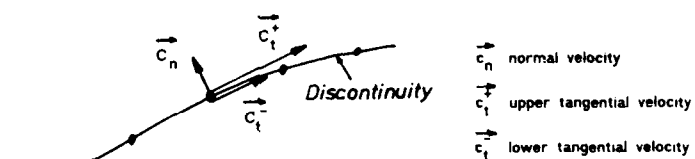
Fig. 5: Numerical model of the slipline

— PRESENT METHOD

$\bar{c}_p$

AEROELASTICITY IN TURBOMACHINE - CASCADES
STANDARD CONFIGURATION NUMBER 4

□ = US DATA
X = LS DATA
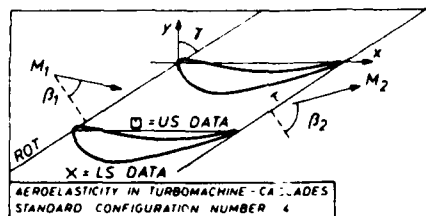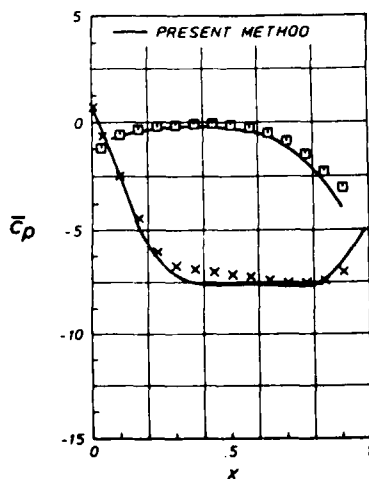
c   0744
τ   .76
γ   56.6
x_α - - -
y_α - - -
M_1 .28
β_1 -44.5
i
M_2 .90
β_2 -71.

□   upper side
X   lower side

Fig. 6: Data and steady state solution of the "Fourth Standard Configuration"

2-8

COMPARISON BETWEEN CALCULATION (——)
AND EXPERIMENT (— —)
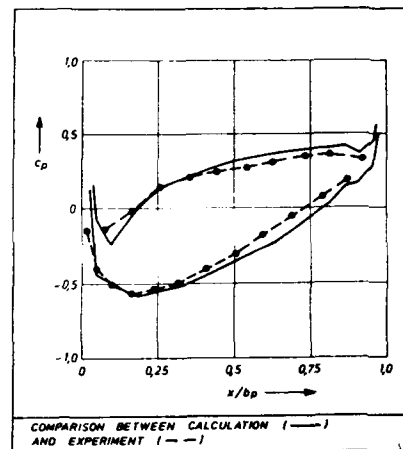
Fig. 7: Steady state solution of
a compressor cascade –
comparison between
experiment and presented
method

dynamic pressure
(N/m^2)
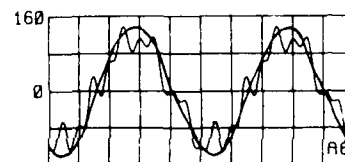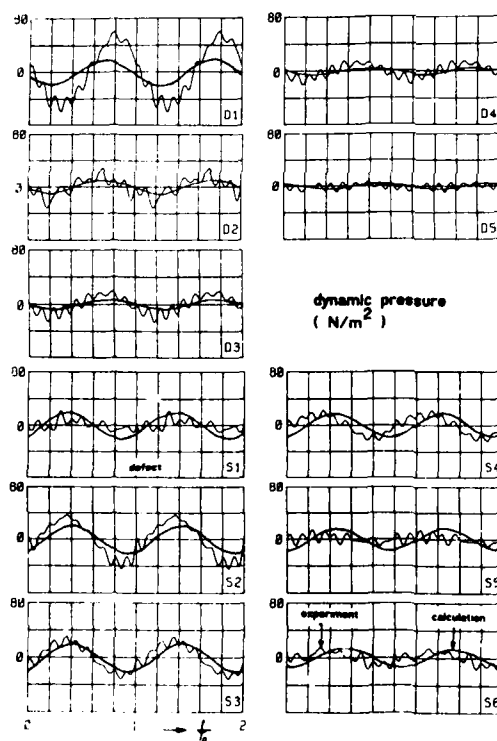
measured acceleration (m/s^2)
in comparison with
the calculation
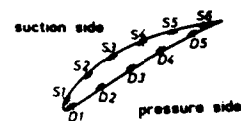
locations of the pressure
transducers

Fig. 8: Dynamic pressure for the compressor cascade bending in TWN; e - 180°,
v - 132 Hz, M$_1$ - 0,228 - comparison between measured and calculated results

bending:
   amplitude: h = 0.5 mm normal to chord

torsion:
   amplitude: α = 0.65°
   phase lag to bending: 10°

+ upper side ⎫
o lower side ⎬ measurement
        ⎭
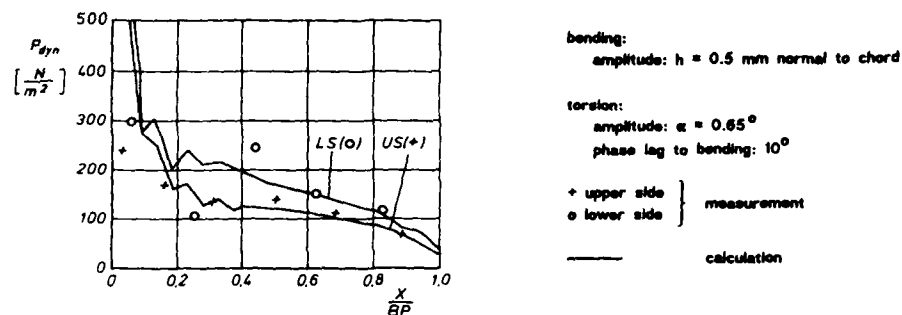
——— calculation

Fig. 9: Dynamic pressure for the compressor cascade in IWM, simultaneous bending/pitching, ν = 370 Hz, Ma$_1$ = 0,234 – comparison between measured and calculated results

O real part
Δ imaginary part

$$K_A = \frac{\int \tilde{p}(x,t) \cdot (\vec{e}_n \cdot \vec{e}_f) \frac{dx}{c}}{h \cdot (\bar{p}_{1-\infty} - \bar{p}_{-\infty})}$$

$$k = \frac{c \cdot \pi \cdot \nu}{2 \cdot v_{ref}}$$
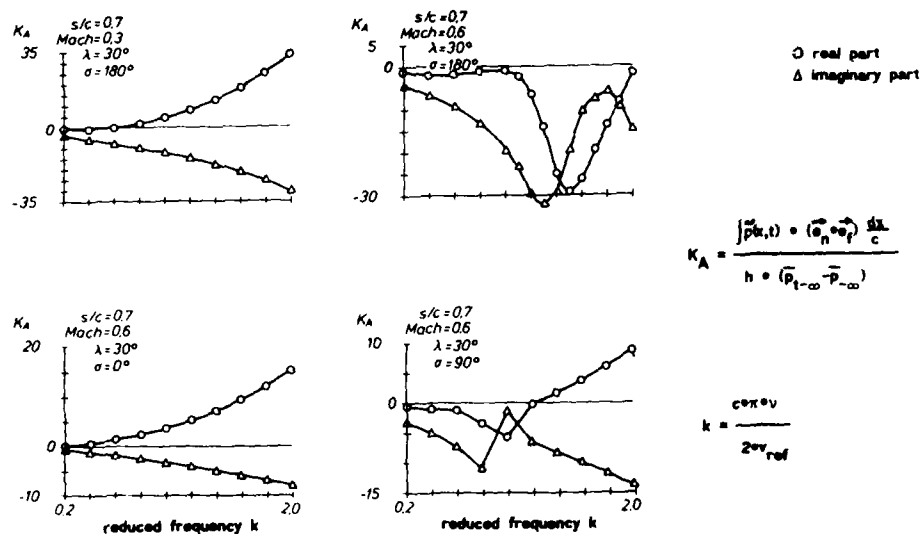
Fig. 10: Influence of frequency, Mach number and interblade phase angle on the aerodynamic force coefficient of a flat plate cascade
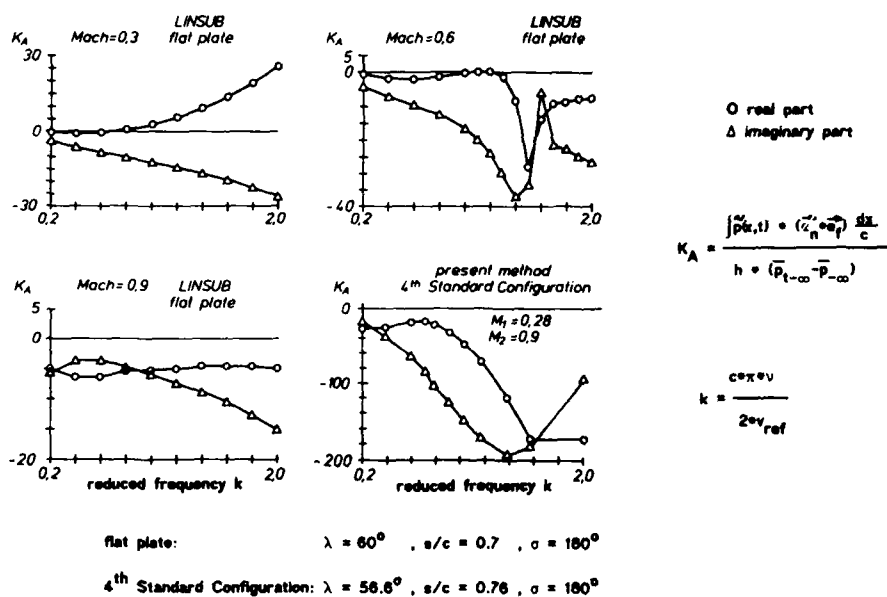
Fig. 11: Calculated aerodynamic force coefficient in dependence from frequency for the high subsonic "Fourth Standard Configuration" - comparison with the linearized method LINSUB (flat plate)

DISCUSSION

N.A.Ahmed, Cranfield Institute of Technology, U.K.

With reference to figure 7 of the paper, there is some discrepancy between experiment and calculation. Could the authors give some explanation? How much does the choice of the grid system contribute to this discrepancy?

Author's response :

There are two reasons for these discrepancies:

1) The computation is made with an inviscid mathematical model whilst the experiment is viscous: the calculations give a greater lift than the tests.

2) There might be a small effect of the coarseness of the computational grid, especially concerning the modelling of the leading edge and trailing edge regions.

Y.N. Chen - Sultzer Brothers, Switzerland

How many computational steps are required in order to obtain a periodical flow.

Author's response :

For the case presented, the computation required 5 periods.

Since the frequency was 130 Hz, the computation required 4 000 steps per period, hence a total of 20 000 time steps.

CALCUL INSTATIONNAIRE EN FLUIDE VISQUEUX

DES GRILLES D'AUBES A DECOLLEMENTS INDUITS PAR LES BORDS D'ATTAQUE.

M. Gazaix, P. Girodroux-Lavigne, J.C. Le Balleur

O.N.E.R.A.
B.P. 72, 92322 - Chatillon cedex (France)

RESUME.

Une méthode numérique d'interaction visqueux-non visqueux instationnaire pour le calcul des grilles d'aubes à bords d'attaques aigus décollés est présentée.

La méthode est fondée sur l'approche de "Formulation Déficitaire", dans son approximation de couche mince, avec modélisation paramétrique des profils de vitesse moyenne. Elle fait appel à la technique de couplage fort "Semi-Implicite", temporellement consistante. Le décollement est forcé au bord d'attaque. La méthode permet de calculer la zone décollée située en aval, ainsi que le point de recollement.

Des comparaisons calculs-expérience favorables sont obtenues à l'état stationnaire, sur une plaque plane en incidence et sur des grilles d'aubes. Les premiers résultats instationnaires dans le cas d'un mouvement de tangage sont présentés, aussi bien sur des profils isolés à bord d'attaque aigu en incidence que sur des configurations de grilles d'aubes.

UNSTEADY VISCOUS CALCULATION METHOD

FOR CASCADES WITH LEADING EDGE INDUCED SEPARATION.

ABSTRACT.

The recent progress in viscous-inviscid interaction methods for computation of unsteady separated flows over airfoils, in forced oscillations as well as in the buffet regime, make it possible to develop a numerical method for computations of unsteady flows over airfoils and cascades where the flow separation or stall is induced by sharp leading-edges. The aptitude of the method to describe the leading-edge separation in unsteady flow gives some hope for the prediction of subsonic flutter in cascades.

The method solves unsteady thin-layer integral viscous equations, in "Defect-Formulation", including two transport equations for turbulence. The equations are closed by turbulent mean velocity profiles which are modelled and discretized along the normal. The viscous method is strongly coupled time-consistently, by the so-called "Semi-Implicit" numerical technique, with a pseudo-inviscid solver based on potential small perturbations approximations. The numerical technique is able to enforce the separation at a sharp leading-edge.

A viscous calculation method for airfoils is first shown to predict the leading-edge separation over a sharp flat plate at incidence, and over isolated compressor blades. Steady and unsteady computations are presented, and compared with experimental results. A numerical method for internal flows, including conditions of periodicity in space for steady flows, and in space-time for unsteady flows, is secondly obtained to compute separated flows in a cascade configuration. Steady and preliminary unsteady results are shown.

INTRODUCTION.

Les écoulements de grilles d'aubes à bords d'attaques aigus, en incidence, sont caractérisés par le développement d'une couche limite turbulente sur l'extrados de l'aube qui est décollée dès le bord d'attaque, le point de recollement se situant sur le profil ou bien dans le sillage. Les études expérimentales montrent que les effets visqueux qui en résultent sont très importants. En particulier, ces écoulements peuvent dans certaines conditions être le siège d'instabilités aéroélastiques, et conduisent au phénomène de flottement de décrochage des aubes de compresseur.

Ces problèmes de flottement, qui apparaissent aussi bien en régime subsonique que transsonique, dépendent directement de l'évolution instationnaire de la couche limite à l'extrados, et notamment du déplacement du point de recollement. Jusqu'à présent, il n'existait pas véritablement d'outil numérique pour la prévision de ce type d'écoulement, dont la connaissance est cependant primordiale dans la définition des grilles d'aubes. Les premières études, menées par des méthodes instationnaires de fluide-parfait, se sont révélées inadaptées pour le calcul de ces écoulements, où les effets de la viscosité dominent.

La possibilité de décrire des écoulements instationnaires décollés complexes par une méthode numérique d'interaction visqueux-non visqueux temporellement consistante, Le Balleur, Girodroux-Lavigne [1], a déjà été démontrée aussi bien sur des profils d'ailes

en oscillation de tangage, que sur des profils d'ailes fixes où le régime instationnaire est induit par le tremblement aérodynamique [1,2,3,4,5]. Les progrès réalisés ont permis d'étendre la méthode au calcul du décollement induit par un bord d'attaque aigu. Des résultats préliminaires démontrant la faisabilité de tels calculs, avaient déjà été obtenus dans le cas d'un profil isolé à bord d'attaque aigu en incidence, Girodroux-Lavigne, Le Balleur, [6].

La méthode est basée sur la "Formulation Déficitaire" proposée par Le Balleur [7,8,9], simplifiée dans son approximation de couche mince, avec modélisation paramétrique des profils de vitesse moyenne. Elle fait appel, pour le couplage fort visqueux-non visqueux, à la technique numérique temporellement consistante dite "Semi-Implicite", Le Balleur, Girodroux-Lavigne [1]. Le champ pseudo-fluide-parfait est calculé par résolution de l'équation des petites perturbations potentielles transsoniques [10,11].

Le décollement est numériquement forcé au bord d'attaque. La méthode permet de calculer l'évolution de la couche limite décollée et du sillage situés en aval, ainsi que le point de recollement. Des comparaisons calculs-expérience favorables sont obtenues à l'état stationnaire. Les premiers calculs instationnaires dans le cas d'un mouvement de tangage sont présentés, aussi bien sur des profils isolés (plaque plane en incidence, aube isolée symétrique) que sur des configurations de grilles d'aubes.

1 - DESCRIPTION DE LA METHODE NUMERIQUE.

La méthode de calcul développée est basée sur une technique d'interaction visqueux-non visqueux instationnaire, et s'appuie sur la technique numérique de couplage "Semi-Implicite" temporellement consistante définie par Le Balleur, Girodroux-Lavigne [1,2,3,4,5]. La méthode numérique comprend essentiellement une méthode de calcul de "couche visqueuse", une méthode de "couplage fort", et un solveur "pseudo-fluide-parfait".

1.1 Méthode de calcul des couches visqueuses.

Le calcul des couches visqueuses est fondé sur l'approche de "Formulation Déficitaire", Le Balleur [7,8,9]. Celle-ci est utilisée ici seulement dans son approximation de couche mince, avec résolution d'équations intégrales et avec modélisation paramétrique des profils de vitesse moyenne. Numériquement, les profils de vitesse modélisés sont discrétisés selon la normale [16], ce qui conduit à une technique numérique hybride entre méthode intégrale et méthode locale, donnant accès non seulement aux grandeurs intégrales visqueuses, mais aussi au champ des vitesses.

Désignant par x, y un système de coordonnées respectivement tangent et normal à la surface du corps ou à la ligne de coupure du sillage, t le temps, $\bar{u}$, $\bar{v}$, $\bar{p}$, $\bar{\rho}$ les composantes de la vitesse, la pression, la masse volumique, par u, v, p, ρ les quantités correspondantes du pseudo-fluide-parfait, par $\bar{\tau}$ la contrainte de cisaillement, les équations intégrales déficitaires de continuité, de quantité de mouvement et d'entrainement s'écrivent [9,1,16] :

$$\left\{ \frac{\partial}{\partial t}[\rho\delta_o] + \frac{\partial}{\partial x}[\rho q \delta_1] - [\rho v - \bar{\rho}\bar{v}] \right\}_{(x,0,t)} = 0 \quad (1)$$

$$\left\{ \frac{\partial}{\partial t}[\rho q \delta_1] + \frac{\partial}{\partial x}[\rho q^2(\delta_1+\theta_{11})] - [\rho u v - \bar{\rho}\overline{uv}] = \rho q^2 \frac{Cf}{2} \right\}_{(x,0,t)} \quad (2)$$

$$\bar{p}(x,y,t) \approx p(x,y,t) \quad (3)$$

$$\left\{ \frac{\partial}{\partial t}[\rho(\delta-\delta_o)] + \frac{\partial}{\partial x}[\rho q(\delta-\delta_1)] = \rho q [E + \frac{\bar{\rho}\bar{v}}{\rho q}] \right\}_{(x,0,t)} \quad (4)$$

$$\delta_{o_{(x,t)}}[\rho]_{(x,0,t)} = \int_0^\bullet [\rho - \bar{\rho}]_{(x,y,t)} \, dy$$

$$\delta_{1_{(x,t)}}[\rho q]_{(x,0,t)} = \int_0^\bullet [\rho u - \bar{\rho}\bar{u}]_{(x,y,t)} \, dy$$

$$\delta_{1i_{(x,t)}}[q]_{(x,0,t)} = \int_0^\bullet [u - \bar{u}]_{(x,y,t)} \, dy$$

$$[\delta_1 + \theta_{11}]_{(x,t)}[\rho q^2]_{(x,0,t)} = \int_0^\bullet [\rho u^2 - \bar{\rho}\bar{u}^2]_{(x,y,t)} \, dy$$

$$E_{(x,t)} = \left\{ \frac{\frac{\partial \bar{\tau}}{\partial y}}{\rho q \frac{\partial}{\partial y}[u - \bar{u}]} \right\}_{(x,\delta,t)} \quad , \quad \left[\frac{Cf}{2}\right]_{(x,t)} = \left[\frac{\bar{\tau}}{\rho q^2}\right]_{(x,0,t)} \quad , \quad q^2 = u^2 + v^2 \quad (5)$$

Notons que ρ et u sont fonction de y dans le choix des épaisseurs intégrales.

La fermeture du système déficitaire approché ci-dessus fait appel à la modélisation des profils de vitesse turbulents de Le Balleur [8,9,16,17], modélisation dépendant de deux paramètres en bidimensionnel, valable pour les écoulements attachés et décollés. Le calcul de l'entrainement $E_{(x,t)}$, issu de cette même modélisation, fait de plus appel, dans l'hypothèse d'une turbulence d'équilibre, à un modèle de longueur de mélange [8,16]. Il peut aussi faire appel au modèle à deux demi-équations de transport de Le Balleur [8,16], dans l'hypothèse d'une turbulence hors-équilibre (2 équations intégrales pour l'énergie turbulente k et la tension de Reynolds τ).

En définitive, les équations déficitaires peuvent s'écrire, après transformation, aussi bien pour une couche limite que pour un sillage, sous la forme suivante :

$$\left\{ \frac{1}{q} C_j^i \,_{(a,m,b)} \frac{\partial \hat{f}^j}{\partial t} + A_j^i \,_{(a,m,b)} \frac{\partial \hat{f}^j}{\partial x} - b^i \right\}_{(x,0,t)} \quad (6)$$

$$f^j = \begin{bmatrix} \hat{m} \\ \hat{h}_t \\ \delta \\ a \\ \hat{k} \\ \hat{\tau} \end{bmatrix} \quad , \quad b^i = \begin{bmatrix} \dfrac{\hat{v}}{q} \\ \dfrac{Cf}{2} \\ E \end{bmatrix} \quad , \quad \begin{matrix} i = 1,5 \\ j = 1,6 \end{matrix}$$

Les sept inconnues du problème sont l'épaisseur de couche limite δ, le paramètre de forme $a = \delta_{1i}/\delta$, les paramètres intégraux de turbulence $\hat{k}$, $\hat{\tau}$, le nombre de Mach réduit $\hat{m} = .5(\gamma-1)\hat{M}^2$, l'enthalpie totale $\hat{h}_t$, et la vitesse de transpiration $\hat{v}$. Afin d'obtenir le couplage fort, les trois inconnues $\hat{m}$, $\hat{h}_t$, $\hat{v}$, doivent être couplées aux variables correspondantes du problème pseudo-fluide-parfait :

$$\hat{h}_t = h_t \quad \hat{m} = m \quad \hat{v} = v \quad (7)$$

Une résolution découplée du système visqueux (6) est d'abord réalisée, soit en mode Direct (écoulements attachés), en imposant $\hat{m} = m$, $\hat{h}_t = h_t$, soit en mode Inverse (écoulements décollés), en imposant $\hat{v} = v$, $\hat{h}_t = h_t$. La commutation Direct-Inverse permet dans tous les cas de résoudre les équations par une technique de marche en espace, même en présence de courants de retour. L'influence aval-amont dans les régions décollées, qui est éliminée par la résolution en mode Inverse, est récupérée dans l'étape de couplage fort. La discrétisation numérique utilisée est implicite en espace et en temps [1].

1.2 Méthode numérique de couplage fort.

La méthode de couplage fait appel à la technique numérique temporellement consistante dite "Semi-Implicite" de Le Balleur, Girodroux-Lavigne [1]. La méthode est une technique de relaxation, construite après détermination de l'opérateur numérique "visqueux" qui agit dans le problème de couplage. Cet opérateur, qualifié de "fonction d'influence numérique visqueuse" est déduit du système visqueux (6), après résolution découplée en mode direct ou inverse, par élimination des inconnues purement visqueuses δ, a, $\hat{k}$, $\hat{\tau}$. Cette fonction d'influence peut s'écrire au pas de temps n et au noeud $i,1$ sous la forme suivante :

$$R_{i,1}^n \left(\frac{\hat{v}}{q}, f^j \right) = \left[\frac{\hat{v}}{q} + \alpha_j \frac{\partial f^j}{\partial t} + \beta_j \frac{\partial f^j}{\partial x} \right]_{i,1}^n = 0 \quad (8)$$

$$[f^j = \hat{m}, \hat{h}_t] \quad j = 1,2$$

Tant que le couplage n'est pas convergé, les quantités "fluide-parfait" v/q, f^j ne vérifient pas la relation (8), et conduisent à des résidus $R_{i,1}^n(v/q, f^j)$ non nuls. La méthode de couplage "Semi-Implicite" effectue, au sein d'un même pas de temps, une itération de couplage afin de relaxer ces résidus. L'équation de relaxation à l'itération $v+1$ y est écrite :

$$\left[\frac{\Delta v}{q} + \alpha_j^v \frac{\partial}{\partial t} \Delta f^j + \beta_j^v \frac{\partial}{\partial x} \Delta f^j \right]_{i,1}^n = -\bar{\omega} \left[R^v \right]_{i,1}^n$$

$$\frac{\Delta v}{q} = \left(\frac{v^{v+1}}{q} - \frac{v^v}{q} \right) \qquad j = 1,2 \qquad\qquad (9)$$

$$\Delta f^j = (f^{j,v+1} - f^{j,v}) \qquad \bar{\omega} = 1$$

$$\left[R^v \right]_{i,1}^n = \left[\frac{\hat{v}}{q} - \frac{v^v}{q} \right]_{i,1}^n + \left[\alpha_j^v \frac{\partial}{\partial t} \left(f^j - f^{j,v} \right) + \beta_j^v \frac{\partial}{\partial x} \left(f^j - f^{j,v} \right) \right]_{i,1}^n$$

Après une discrétisation de type Gauss-Seidel des termes de conditionnement du premier membre, l'équation de relaxation de couplage (9) et le pas en y de la méthode ADI du pseudo-fluide-parfait sont résolus en marchant itérativement en espace, d'amont en aval, jusqu'à convergence du couplage.

La discrétisation centrée des résidus R et la consistance en temps de l'itération de couplage, menée à convergence à chaque pas de temps, permettent de prendre en compte totalement l'influence aval-amont, donnant ainsi accès au calcul en instationnaire des phénomènes de forte interaction visqueuse, du type décollement et interaction choc-couche limite.

1.3 Problème Pseudo-Fluide-Parfait.

Le sous-programme pseudo-fluide-parfait est traité par une technique ADI en petites perturbations potentielles transsoniques instationnaires, aussi bien pour les profils d'ailes [10], que pour les grilles d'aubes, [11]. Dans le cas des grilles d'aubes, des conditions de périodicité spatiales en stationnaire, et spatio-temporelles en instationnaire, sur les frontières hautes et basses du domaine de calcul, permettent de limiter celui-ci à deux canaux inter-aubes.

Les conditions aux limites ont été modifiées pour le couplage par adjonction d'un terme de vitesse normale sur le profil et d'un saut de vitesse normale dans le sillage [1].

1.4 Calcul du décollement forcé au bord d'attaque.

La méthode numérique d'interaction visqueux-non visqueux temporellement consistante [1] avait jusqu'à présent été utilisée pour calculer des écoulements instationnaires décollés sur des profils d'ailes où le décollement prenait naissance sur une surface régulière, et généralement dans la région de bord de fuite ou au pied de choc.

Dans le cas de profils ou de grilles d'aubes minces à bord d'attaque "aigu" en incidence, le décollement visqueux apparaît comme un processus forcé et prend naissance sur l'arête même du bord d'attaque. En fait, physiquement, le calcul du décollement de bord d'attaque nécessiterait un calcul visqueux coûteux sur un maillage fin à l'échelle du rayon de courbure réel du bord d'attaque, ainsi qu'un traitement correct du point d'arrêt situé à l'intrados du profil, actuellement non-accessible du fait des approximations du pseudo-fluide-parfait.

Une modélisation du décollement de bord d'attaque est alors proposée, en négligeant le rayon de courbure du bord d'attaque et en forçant numériquement le décollement de la couche limite extrados au premier noeud de calcul. En pratique, cette modélisation revient à imposer les conditions "amont" du calcul de couche limite, c'est à dire le profil de vitesse de la couche visqueuse décollée, qui est déterminée ici par l'épaisseur de déplacement δ_{1_o} et le paramètre de forme incompressible Hi_o. La valeur de cette modélisation repose sur l'hypothèse que le détail du processus local du décollement, d'échelle très petite, n'a qu'une influence réduite et négligeable sur l'écoulement global, dominé par le processus de mélange et de recollement.

Si on admet que la couche limite décolle sous un angle fini, l'épaisseur de déplacement δ_{1_o} est de l'ordre de grandeur de la taille de la première maille de calcul au bord d'attaque. Hi_o est naturellement choisi dans la gamme des paramètres de forme décollés. La couche limite extrados a été de plus supposée ici entièrement turbulente au premier noeud de calcul, ce qui revient à négliger l'étendue de la transition en aval du décollement. Bien que l'étendue de la transition soit nécessairement faible en raison du décollement, cette hypothèse d'absence d'influence de la zone de transition reste cependant à confirmer.

Une étude paramétrique portant sur les conditions amont du calcul de couche limite extrados a été réalisée afin de mettre en évidence leur influence sur la solution numérique obtenue.

Cette étude a permis de montrer que la forme du profil de vitesse moyenne décollé imposé à l'amont, déterminé par le paramètre de forme amont Hi_o a très peu d'influence sur la solution. Par contre la solution semble dans une certaine mesure dépendre du choix du maillage et de l'épaisseur très faible de la couche visqueuse, dans la région immédiatement voisine du bord d'attaque. Ce point semble montrer que le calcul serait encore plus délicat pour des solveurs "Direct" d'équations de Navier-Stokes, généralement plus imprécis pour les épaisseurs de couche limite, notamment aux bords d'attaque où les épaisseurs sont faibles.

L'étude a cependant mis en évidence que des solutions quantitatives correctes pouvaient être obtenues, à condition d'utiliser des maillages suffisamment fins dans la région de bord d'attaque, la taille de la première maille de calcul Δx_o au bord d'attaque devant être de l'ordre de 0,001 corde, et de choisir une épaisseur δ_{1_o} inférieure à Δx_o (le rapport $\delta_{1_o}/\Delta x_o$ étant d'ordre unité), voir figures 1 et 2.

2 - RESULTATS NUMERIQUES A L'ETAT STATIONNAIRE.

2.1 Plaque plane en incidence.

La méthode de calcul a été utilisée pour prédire l'état stationnaire sur une plaque plane biseautée en incidence, étudiée expérimentalement à l'ONERA/CERT, Bonnet, Houdeville [12,13]. La corde du profil est égale à 0,2m, l'incidence expérimentale est de 4 degrés, la vitesse de référence est de 30m/s, et le nombre de Reynolds est égal à 4 10^5. La divergence de veine expérimentale est prise en compte dans les calculs.

L'intérêt de la configuration réside principalement dans le fait que l'écoulement est très semblable à celui rencontré dans les grilles d'aubes à bord d'attaque aigu. De plus la taille importante de la maquette permet d'obtenir des résultats expérimentaux plus complets que sur une aube de petite dimension, comprenant des distributions de pression et des grandeurs de couche limite.

Le maillage utilisé comporte 180 points dans la direction longitudinale, avec 100 points disposés sur le profil de part et d'autre, et 40 points le long du sillage. Le fluide-parfait comporte 2 x 50 points dans la direction normale. Les profils de vitesse discrétisés dans les couches visqueuses utilisent 37 noeuds selon la normale. On a donc un total de 28360 noeuds pour le maillage visqueux. Les frontières du domaine de calcul dans la direction longitudinale ont été choisies à -4 et +5 cordes. Dans la direction normale, elles sont situées à +/- 0,75 cordes, ce qui correspond aux parois hautes et basses de la soufflerie.

La figure 3 visualise les champs de lignes iso-Mach obtenus par le calcul pour deux incidences, et met en évidence l'étendue de la zone décollée qui prend naissance au bord d'attaque.

La figure 4 compare avec les résultats expérimentaux trois calculs, utilisant le niveau de turbulence d'équilibre "habituel" de la fermeture turbulente [16,17], complété respectivement par les modèles de turbulence à 0, 1, et 2 équations. Des différences importantes entre les calculs et l'expérience apparaissent au niveau de la survitesse de bord d'attaque ainsi que sur la position du recollement. Par contre les trois calculs fournissent des résultats très peu différents en ce qui concerne l'écoulement moyen.

Les expériences de l'ONERA/CERT semblent indiquer qu'un niveau de turbulence exceptionnellement fort est présent dans la région décollée. Compte tenu de cette donnée et de l'insuffisance actuelle des modèles de turbulence, des calculs ont été réalisés en maintenant la même modélisation et les mêmes équations de transport de turbulence, mais en augmentant heuristiquement le niveau de turbulence d'équilibre de la couche limite. Cette augmentation de turbulence est obtenue en multipliant à l'extrados le niveau de longueur de mélange d'équilibre d'un facteur K, ce qui revient à multiplier l'entrainement d'équilibre par K^2 (notons que la longueur de mélange locale dépend en plus du modèle d'équations de transport).

Des essais ont conduit à adopter un coefficient multiplicatif $K = 1,1$, correspondant à une longueur de mélange d'équilibre $l = 0.091\delta$ accrue de 10% par rapport à la valeur standard utilisée dans la méthode, $l = 0,083\delta$.

Un très bon accord calcul-expérience est alors obtenu sur les distributions du coefficient de pression à l'extrados de la plaque, même si le calcul ne reproduit pas parfaitement l'aspect observé expérimentalement au voisinage immédiat du bord d'attaque, figure 5. Le calcul prédit correctement la survitesse de bord d'attaque, le niveau de pression en aval du recollement et au bord de fuite, ainsi que la position du point de recollement, situé à 35% de corde.

Les distributions des épaisseurs de déplacement (figure 6), de quantité de mouvement (figure 7), du paramètre de forme incompressible (figure 8) à l'extrados de la plaque, confirment cette valeur de K. Les épaisseurs de déplacement et de quantité de mouvement calculées sont qualitativement et quantitativement similaires aux valeurs expérimentales, bien que légèrement inférieures en niveau. Un bon accord calcul-expérience est observé sur le paramètre de forme incompressible, en particulier dans la zone de recollement et dans la région de bord de fuite.

La figure 9 visualise l'excellent accord calcul-expérience sur les profils de vitesse moyenne à l'extrados de la plaque. De même, les répartitions de l'énergie cinétique turbulente et du cisaillement turbulent, en valeurs moyennes sur l'épaisseur de la couche limite, représentées sur les figures 10 et 11, se comparent très favorablement avec l'expérience.

2.2 Profil d'aube isolée

Des calculs ont été réalisés sur une aube de compresseur isolée symétrique et effilée , pour laquelle on dispose également de résultats expérimentaux d'origine ONERA, Notin [14].

Le maillage de calcul est identique à celui utilisé sur la plaque plane en incidence. Les calculs ont été conduits en utilisant la même constante d'accroissement de la longueur de mélange d'équilibre $K = 1,1$ et le modèle à 2 équations de transport. L'écoulement a été calculé pour un nombre de Mach égal à 0,3 , et pour des incidences comprises entre 3 et 7 degrés.

La figure 12 représente les distributions du coefficient de pression obtenues pour les différentes incidences. Contrairement à d'autres méthodes de couplage simplifiées, le calcul prédit ici correctement l'effet d'incidence mis en évidence expérimentalement, qui se traduit par une diminution de la survitesse de bord d'attaque, ainsi qu'une augmentation de l'étendue du décollement, pour des incidences croissantes.

A partir de l'incidence de 6 degrés, l'écoulement est décollé depuis le bord d'attaque jusqu'au bord de fuite, le recollement R se produisant dans le sillage. Ceci explique la tendance à l'obtention d'un plateau de pression observé sur la figure 12 pour les deux incidences les plus élevées. Ce résultat est encourageant en ce qui concerne la prédiction du flottement de décrochage, qui apparait dans le cas d'un décollement généralisé de l'aube.

La figure 13 montre l'influence de l'incidence sur l'épaisseur de déplacement, qui passe au bord de fuite de 1% à 13% quand l'incidence croit de 3 à 7 degrés.

La figure 14 montre une comparaison calcul-expérience pour 4 et 5 degrés. On constate que le calcul numérique a ici tendance à surestimer le décollement. Un ajustement différent de la longueur de mélange ainsi que des corrections de soufflerie pourrait sans doute améliorer l'accord expérience-calcul.

2.3 Grille d'aubes de compresseur

La méthode a été utilisée pour prédire l'écoulement, à l'état stationnaire, dans une grille d'aubes de compresseur. Les calculs ont ici été réalisés simplement dans l'hypothèse d'une turbulence d'équilibre (modèle à 0 équation de transport), les constantes du modèle de longueur de mélange étant modifiées comme dans le cas des profils d'aubes isolés ($l = 0,091\delta$).

Le maillage comporte 340 points dans la direction longitudinale. 83 points sont disposés sur l'aube de chaque côté, et le sillage comporte 94 noeuds de calcul. Le fluide parfait comporte 20 points suivant la hauteur du canal (2 × 10). Avec une discrétisation de 37 noeuds selon la normale pour les couches visqueuses, le maillage visqueux total est environ 20000 noeuds. Les conditions du calcul correspondent à un nombre de Mach égal à 0,704 et à une incidence de 5,78 degrés. Le nombre de Reynolds basé sur la corde est de 2,19 10^6. Le calage de l'aube est $\gamma = 64°$ et le pas relatif est égal à 0,8.

La figure 15 visualise le champ des lignes iso-Mach issu du calcul visqueux. L'agrandissement de la zone de bord d'attaque met en évidence la poche de décollement qui s'étend sur environ 30% de corde.

Les distributions de pression expérimentales et issues du calcul numérique sont représentées sur la figure 16. Un accord qualitatif encourageant est obtenu par ce premier calcul de grille d'aube, même si des différences subsistent avec l'expérience sur les niveaux de pression. Il faut cependant noter que le calcul à été effectué dans les conditions nominales de l'ex, ´rience, et qu'un meilleur accord pourrait probablement être obtenu en introduisant des corrections de Mach et d'incidence.

3 - RESULTATS PRELIMINAIRES INSTATIONNAIRES.

Pour tous les calculs présentés ici, le calcul visqueux a été effectué simplement dans l'approximation quasi-stationnaire visqueuse, ce qui revient à négliger les dérivées temporelles des grandeurs visqueuses, les dérivées temporelles des grandeurs non-visqueuses étant conservées.

3.1 Aube isolée

Des calculs instationnaires ont été effectués pour 4 et 5 degrés d'incidence moyenne. On impose un mouvement de tangage harmonique d'amplitude 0.5 degrés, autour d'un axe à mi-corde. Dans les 2 cas, on effectue d'abord un calcul stationnaire, suivi de plusieurs périodes instationnaires. Deux ou trois périodes suffisent pour obtenir le régime permanent. Le nombre de pas de temps par période est de 256. La fréquence réduite d'oscillation basée sur la corde, $f = \omega c / U_\infty$ est égale à 1.

A 4 degrés, le point de recollement stationnaire est situé vers 25% de corde. Au cours d'une période de tangage, on observe sur la figure 17 que le point de recollement oscille entre 15% et 37%. Les évolutions du module et de la phase du coefficient de pression extrados instationnaire sont représentées sur la figure 18. Le module présente un pic dont la largeur correspond au déplacement du point de recollement. Pour avoir une comparaison significative avec les résultats expérimentaux, il faudrait que le point de recollement calculé en stationnaire soit voisin du point de recollement moyen expérimental. Malheureusement, d'une part l'expérience ne fournit pas la valeur du point de recollement, et d'autre part les résultats instationnaires expérimentaux sont limités à quelques incidences seulement. Il a été choisi ici de comparer les résultats de calcul à quatre degrés d'incidence avec les résultats expérimentaux à 5.75 degrés, qui présentent une évolution du module du coefficient de pression assez semblable à la répartition calculée. On observe une phase décroissante sur la majeure partie de la corde, qualitativement voisine de la phase mesurée expérimentalement. L'écart en incidence est à rapprocher de l'effet constaté en stationnaire (figure 14).

A 5 degres, le point de recollement stationnaire est situé vers 50%. Le module et la phase du coefficient de pression instationnaire sont représentés sur la figure 19. La phase est cette fois décroissante sur tout le profil, ce qui est observé expérimentalement à partir de 6,5 degrés.

Pour ces deux incidences, si on admet une correction d'incidence, l'accord calcul-expérience est donc correct pour le module, et plus grossier sur la phase. Une cause probable du résultat moins satisfaisant sur la phase est sans doute à rechercher dans l'approximation quasi-stationnaire qui a été retenue pour le calcul des couches visqueuses dans cette étape préliminaire.

3.2 Grille d'aubes

La figure 20 présente les premiers résultats instationnaires de calcul obtenus en configuration de grille d'aubes, prenant en compte des conditions aux limites périodiques instationnaires [11]. L'incidence moyenne est de 5 degrés, et on impose un mouvement harmonique de tangage autour d'un axe situé à mi-corde. La fréquence réduite est fixée à 1. Il y a 128 pas de temps par période. Le maillage est identique à celui utilisé en stationnaire. Le point de recollement varie au cours du cycle entre 20 et 30 % de corde. La figure 20 montre les distributions du module et de la phase du coefficient de pression extrados instationnaire, pour un mouvement de tangage harmonique autour d'un axe à mi-corde, avec un déphasage inter-aubes nul.

CONCLUSIONS.

Une méthode numérique de calcul des écoulements instationnaires visqueux dans les grilles d'aubes à décollements induits par des bords d'attaque aigus , en sub- ou trans-sonique, est présentée.

La méthode de calcul, basée sur une technique numérique d'interaction visqueux-non visqueux "instationnaire", s'appuie sur la méthode numérique de couplage "Semi-Implicite" temporellement consistante, précédemment proposée pour le calcul des écoulements transsoniques instationnaires sur profils d'ailes. Le décollement est numériquement forcé au bord d'attaque. Il est modélisé en imposant les conditions aux limites "amont" du calcul de couche limite extrados. La méthode permet de calculer l'évolution de la couche limite partout en aval, et notamment de déterminer la zone décollée, ainsi que le point de recollement, celui-ci pouvant très bien être rejeté dans le sillage visqueux.

Une étude numérique paramétrique, portant sur les conditions "amont" du calcul visqueux et sur les maillages dans la zone de décollement forcé de bord d'attaque a été effectuée, afin de préciser l'échelle minimale de résolution.

Des calculs numériques, réalisés sur une plaque plane en incidence placée dans une veine de soufflerie, ont permis d'ajuster les constantes du modèle de turbulence, et d'obtenir dans ces conditions d'excellents accords calcul-expérience en stationnaire. Des résultats de calcul stationnaires, et les premiers résultats instationnaires, en oscillation harmonique forcée, ont été obtenus aussi bien sur un profil d'aube isolé que sur des configurations de grilles d'aubes.

Références

[1] LE BALLEUR J.C., GIRODROUX-LAVIGNE P. - A semi-implicit and unsteady numerical method of viscous-inviscid interaction for transonic separated flows. - La Recherche Aerospatiale 1984-1, p.15-37, English and French editions, (1984).

[2] LE BALLEUR J.C., GIRODROUX-LAVIGNE P. - A viscous-inviscid interaction method for computing unsteady transonic separation. - Proceed. 3rd Symp. Numerical and Physical Aspects of Aerodynamics Flows, Long-Beach (jan.1985), T. Cebeci ed., Springer-Verlag (1986).

[3] LE BALLEUR J.C., GIRODROUX-LAVIGNE P. - Prediction of buffeting and calculation of unsteady boundary layer separation over airfoils. IUTAM symp. "Boundary layer separation", London, August 26-28, (1986), or ONERA TP 1986-95.

[4] GIRODROUX-LAVIGNE P., LE BALLEUR J.C. - Unsteady viscous-inviscid interaction method and computation of buffeting over airfoils. Proceed. Springer Verlag joint IMA/SMAI Conf. "Computational Methods in Aeronautical Fluid Dynamics", University of Reading, 6-8 April (1987), or ONERA TP 1987-58.

[5] GIRODROUX-LAVIGNE P., LE BALLEUR J.C. - Time-consistent computation of transonic buffet over airfoils - Proceeding of ICAS-1988, Jerusalem, Israel, August-Sept 1988.

[6] GIRODROUX-LAVIGNE P., LE BALLEUR J.C. - Développement d'une méthode de calcul des écoulements instationnaires de grilles d'aubes décollés au bord d'attaque. - Rapport ONERA RTS no 37/1621 RY (Janvier 1987).

[7] LE BALLEUR J.C. - Computation of flows including strong viscous interactions with coupling methods. - AGARD-CP-291, General Introduction, Lecture 1, Colorado-Springs (1981), or ONERA TP 1980-121.

[8] LE BALLEUR J.C. - Strong matching method for computing transonic viscous flows including wakes and separations. Lifting airfoils. - La Recherche Aerospatiale 1981-3, p.21-45, English and French editions, (1981).

[9] LE BALLEUR J.C. - Numerical viscid-inviscid interaction in steady and unsteady flows. - Proceed. 2nd Symp. Numerical and Physical Aspects of Aerodynamic Flows, Long-Beach, (1983), Springer-verlag, T. Cebeci ed., chapt.13, p.259-284 (1984), or ONERA-TP 1983-8.

[10] COUSTON M., ANGELINI J.J. - Solution of nonsteady two-dimensional transonic small disturbances potential flow equation. - ASME Conf., San Francisco (1978) or J. of Fluids Engin., vol.101, no 3, (1979).

[11] MORTCHELEWICZ G.D., ANGELINI J.J. - Calcul des coefficients de pression instationnaire dans une grille droite. - La Recherche Aerospatiale 1984-3, p.211-221, English and French editions, (1984).

[12] BONNET J.L., HOUDEVILLE R. - Ecoulement autour d'une plaque plane en incidence. - Rapport Technique ONERA-CERT RTS no 12/5014 DN (Juillet 1985).

[13] BONNET J.L., HOUDEVILLE R. - Ecoulement à l'extrados d'une plaque plane à bords aigus. - Rapport Technique ONERA-CERT RTS no 14/5014 DN (Août 1986).

[14] NOTIN CL. - Etude de l'écoulement autour d'un profil s'aube de compresseur en régime subsonique. - Rapport ONERA RTS no 33/1621 RY (Juin 1985).

[15] SZECHENYI E. - Etude du flottement de décrochage du fan du compresseur M53 P2 en régime d'écoulement subsonique. - Rapport ONERA RTS no 71/7108 RY (Mars 1981).

[16] LE BALLEUR J.C. - New possibilities of Viscous-Inviscid numerical techniques for Solving Viscous flow equations, with massive separation. - Fourth Symposium "Numerical and Physical Aspects of Aerodynamic Flows", Long Beach, USA (16-19 January 1989). ONERA TP no 1989-24 (and Springer-Verlag to appear).

[17] LE BALLEUR J.C. - Viscous-Inviscid Interaction Solvers and Computation of Highly Separated Flows. - Symposium ICASE, NASA-Langley (July 9-10,1985), Proceed. "Studies of Vortex Dominated Flows", Chap. 3, p. 159-192, editors M. Hussaini and M Salas, Springer-Verlag 1987 (or ONERA TP no 1986-4).
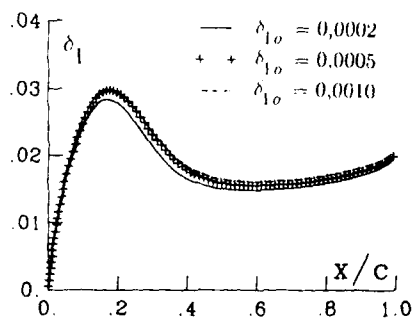
Figure 1. Plaque plane en incidence. Epaisseur de déplacement. Influence de l'épaisseur de déplacement initiale ($\Delta x_o = 0,001$). $U = 30m/s$; $\alpha = 4^o$; Re = 4 10^5.
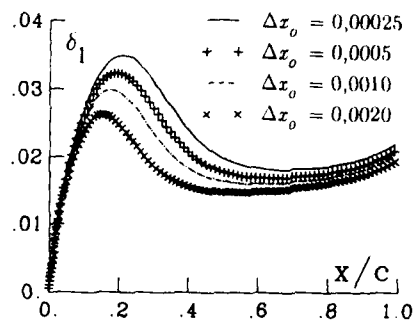
Figure 2. Plaque plane en incidence. Epaisseur de déplacement. Influence du maillage au bord d'attaque ($\delta_{1o}/\Delta x_o = 1$). $U = 30m/s$; $\alpha = 4^o$; Re = 4 10^5.

$\alpha = 4,25^o$

$\alpha = 5,25^o$
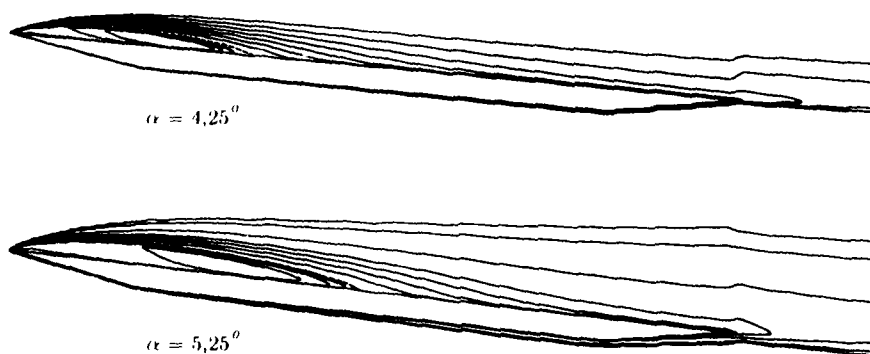
Figure 3. Plaque plane en incidence. Lignes iso-Mach calculées. $U = 30m/s$; Re = 4 10^5.
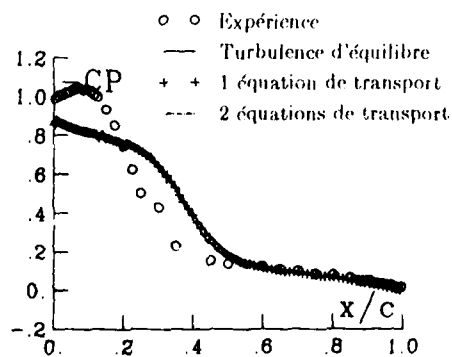
Figure 4. Plaque plane en incidence. Coefficient de pression. Longueur de mélange d'équilibre standard ($l = 0,083\delta$). Influence du modèle de transport de turbulence. $U = 30m/s$; $\alpha = 4^o$; Re = 4 10^5.
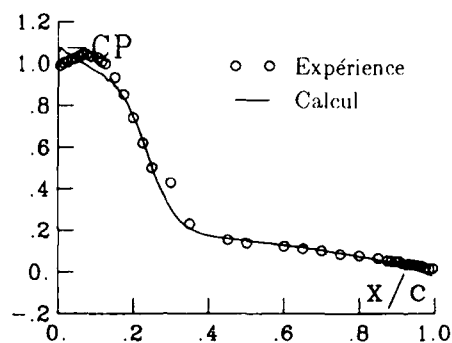
Figure 5. Plaque plane en incidence. Coefficient de pression.
Modèle 2 équations de transport
Longueur de mélange d'équilibre modifiée ($l \approx 0,091\delta$).
$U = 30m/s$; $\alpha = 4^o$; $Re = 4\ 10^5$.
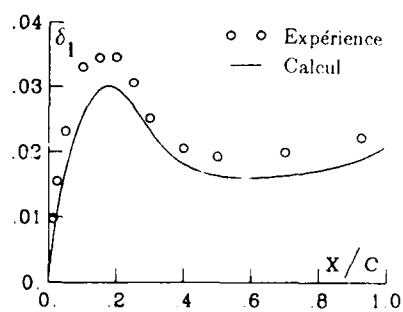
Figure 6. Plaque plane en incidence. Epaisseur de déplacement.
Modèle 2 équations (avec $l\ equilibre \approx 0,091\delta$).
$U = 30m/s$; $\alpha = 4^o$; $Re = 4\ 10^5$.
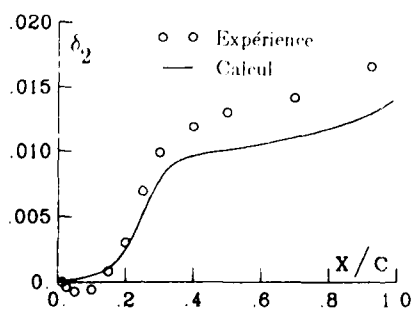
Figure 7. Plaque plane en incidence. Epaisseur de quantité
de mouvement. Modèle 2 équations (avec $l\ equilibre \approx 0,091\delta$).
$U = 30m/s$; $\alpha = 4^o$; $Re = 4\ 10^5$.
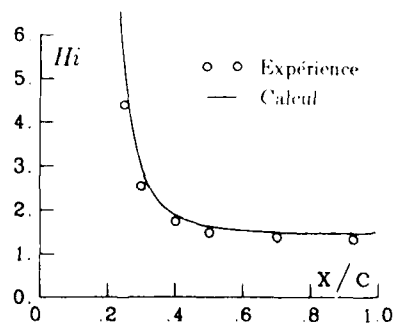
Figure 8. Plaque plane en incidence. Paramètre de forme
incompressible. Modèle 2 équations (avec $l\ equilibre \approx 0,091\delta$).
$U = 30m/s$; $c = 4^o$; $Re = 4\ 10^5$.
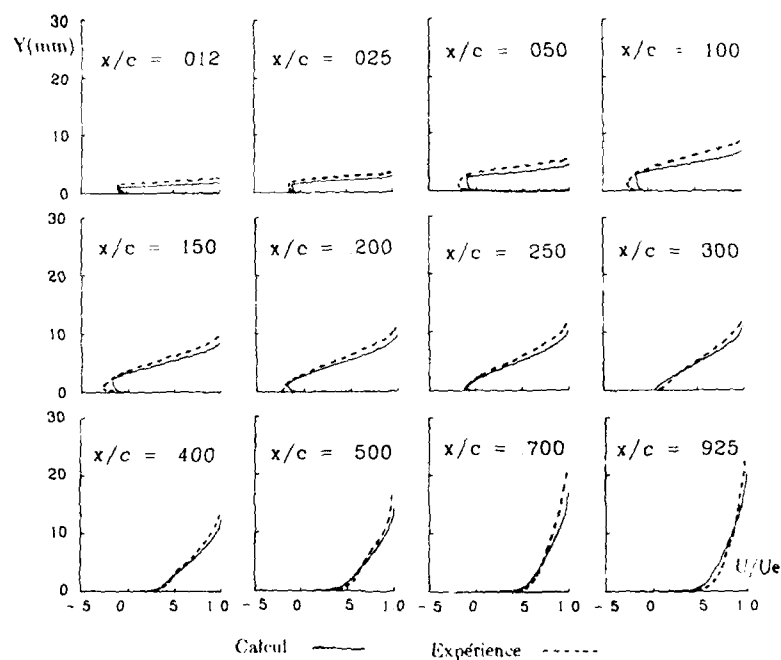
Figure 9. Plaque plane en incidence. Profils de vitesse moyenne (extrados).
Modèle 2 équations (avec $l_{equilibre} \approx 0,091\delta$).
$U = 30m/s$; $\alpha \approx 4^o$; Re = 4 10^5.
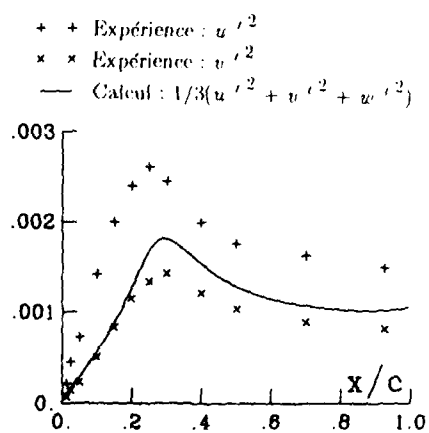
Figure 10. Plaque plane en incidence. Energie cinétique
turbulente moyennée sur l'épaisseur de couche limite.
Modèle 2 équations (avec $l_{equilibre} \approx 0,091\delta$).
$U = 30m/s$; $\alpha \approx 4^o$; Re = 4 10^5.
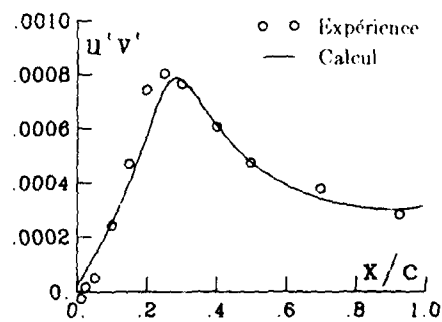
Figure 11. Plaque plane en incidence. Contrainte de
cisaillement moyennée sur l'épaisseur de couche limite.
Modèle 2 équations (avec $l_{equilibre} \approx 0,091\delta$).
$U = 30m/s$; $\alpha \approx 4^o$; Re = 4 10^5.
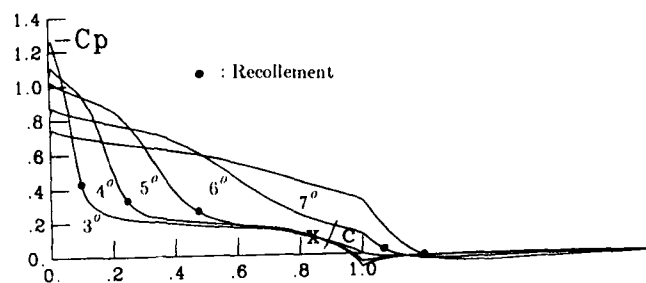
Figure 12. Profil d'aube isolé.
Effet de l'incidence sur les distributions de pression extrados.
$M = 0,3$; $Re = 2,2\,10^6$.
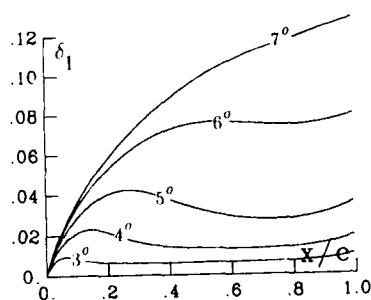
Figure 13. Profil d'aube isolé.
Variation de l'épaisseur de déplacement avec l'incidence.
$M = 0,3$; $Re = 2,2\,10^6$.
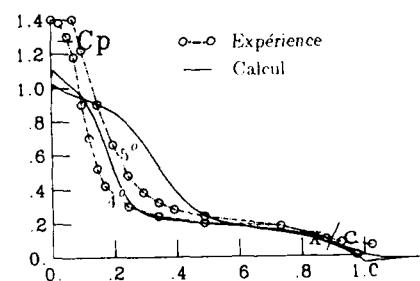
Figure 14. Profil d'aube isolé.
Comparaison calcul-expérience (pression extrados).
Modèle 2 équations (avec $l\ equilibre = 0,091\delta$).
$M = 0,3$; $Re = 2,2\,10^6$.

agrandissement du bord d'attaque
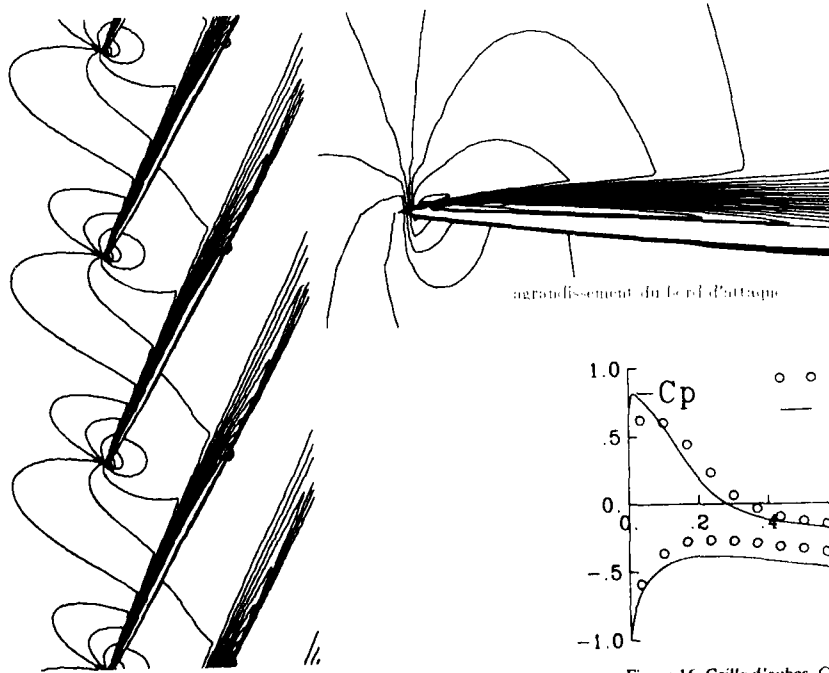
Figure 15. Grille d'aubes. Lignes iso-Mach calculées.
$M = 0,7$; $Re = 2,2\,10^6$; $\alpha = 5,78^o$.
$\gamma = 64^o$; $r = 0,8$
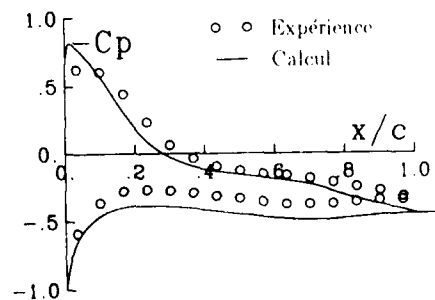
Figure 16. Grille d'aubes. Coefficient de pression.
$M = 0,7$; $Re = 2,2\,10^6$; $\alpha = 5,78^o$.
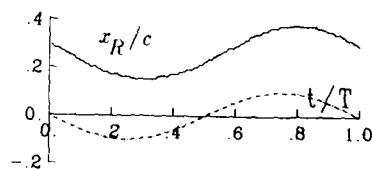
Figure 17. Profil d'aube isolée en mouvement de tangage
Evolution sur une période T du point de recollement,
et de l'incidence du profil.

$\alpha = 4^o + 0,5^o\ sin\,(\omega t)$; $M = 0,3$; $f = 1,0$.
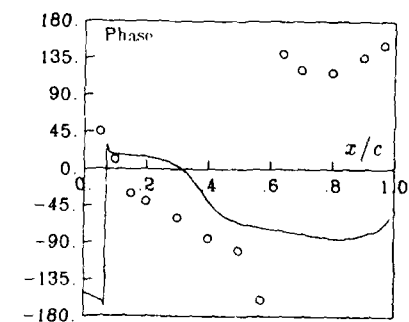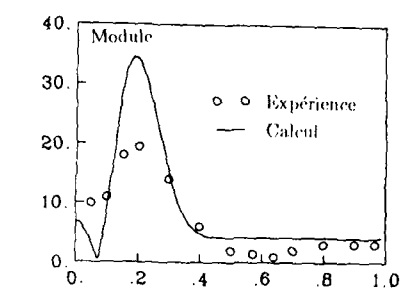
Figure 18. Profil d'aube isolée en mouvement de tangage.
Premier harmonique du coefficient de pression extrados.

$\alpha = 4^o + 0,5^o\ sin\,(\omega t)$; $M = 0,3$; $f = 1,0$.
Re = 2,2 10^6.
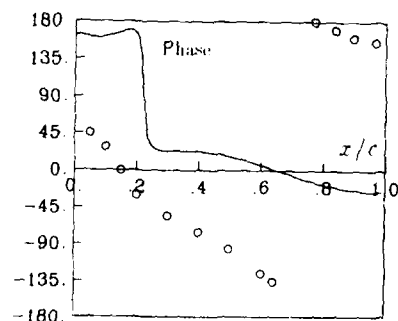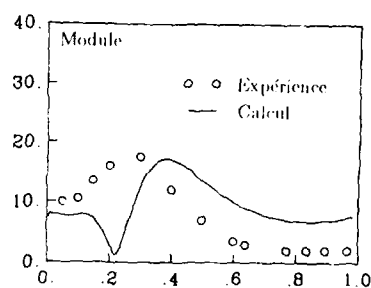
Figure 19. Profil d'aube isolée en mouvement de tangage.
Premier harmonique du coefficient de pression extrados.

$\alpha = 5^o + 0,5^o\ sin\,(\omega t)$; $M = 0,3$; $f = 1,0$.
Re = 2,2 10^6.
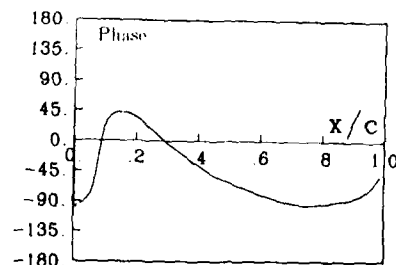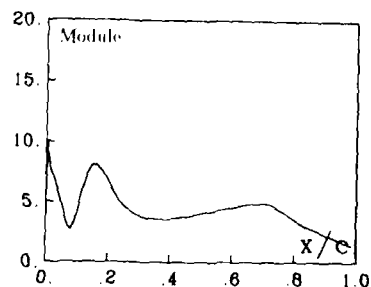
Figure 20. Grille d'aubes en mouvement de tangage.
Premier harmonique du coefficient de pression extrados.

$\alpha = 5^o + 0,5^o\ sin\,(\omega t)$; $M = 0,7$; $f = 1,0$.
Re = 2,2 10^6

DISCUSSION

N.A.Ahmed - Cranfield Institute of Technology, U.K.

Is it correct to state that, according to the theory presented, the choice of shape parameter (H) and displacement thickness (δ_*) does not have any influence on the calculations. Since the shape parameter ($H = \delta_*/\theta_{**}$) is a ratio of displacement thickness and momentum thickness, it could then mean that the value of momentum thickness is also immaterial. Could the authors explain the physical significance of this assumption.

Author's response :

In the calculation method presented, the normalized viscous velocity profile is imposed at the first station of the grid, near the leading edge. The choice of the shape parameter H is equivalent to the choice of the initial velocity profile. Of course, as it is assumed that the flow is separated at the leading edge, a velocity profile with reverse flow, H>2.6 is chosen.

It is observed numerically that the overall solution at the global scale, and the reattachment length are almost not affected by the choice of the initial profile and of H. The choice of the initial profile is however influent in a very small region, close to the leading edge, and especially for the maximal shape parameter, H_{max}, in this area.

Physically, the flow is dominated by the length scale of the separated zone, determined by this method. As this length scale is of the order of magnitude of the chord of the blade, the position of the reattachment point, and the global solution, seem rather independant of the details of the separation process at the leading edge, which occurs over a very small length scale.

The numerical method seems however somewhat more sensitive to the initial thickness of the boundary layer than to the shape of the initial velocity profile. This corresponds to the second viscous parameter prescribed at the first grid station, for example the displacement thickness δ_1. The value of this displacement thickness has to be discussed in relation with the mesh size near the leading edge. This parameter has in general some influence on the solution, but it could be shown that this influence is minimized if a very small grid spacing at the leading edge is used, and if the value of δ_1 is smaller than the size of the first mesh interval.

This result, which must be confirmed, would suggest that direct Navier-Stokes solvers must also require very fine meshes at the leading edge in order to give accurate estimation of the initial boundary layer thickness downstream of the separation point.

CALCULATION OF THE UNSTEADY TWO-DIMENSIONAL, INVISCID, COMPRESSIBLE FLOW
AROUND A STRONGLY CAMBERED OSCILLATING SINGLE BLADE
by

K.M.Förster, Dr.-Ina., Prof.i.R
formerly:
Institut für Aerodynamik und Gasdynamik der Universität Stuttgart
Pfaffenwaldring 21,   D - 7000 Stuttgart 80

Abstract

The paper describes some numerical experiments done with a computational method which was developed recently by the author and his co-workers. Its main features are an extension of the computational domain to infinity and a moving grid fixed to the body in question. The first part of the paper describes this method in some detail. The second part presents some results about the aerodynamic characteristics of an oscillatina blade with respect to the reduced frequency, to the free stream Mach Number and to the oscillation amplitude, including an investigation of the higher harmonics introduced by the nonlinearity of the problem.

1. Scope

Aerodynamic phenomena, and especially unsteady ones are characterized by many parameters and we select a very confined problem only:

- inviscid flow   around a
- single blade   or airfoil of
- one distinct shape   which oscillates
- harmonically   and
- perpendicular to its chord.

Nevertheless there are still some free parameters:

- the onflow Mach Number,
- the reduced frequency of the oscillation and
- its amplitude,

the latter being of influence because of the problem's nonlinearity, and our aim is to examine and present the effect of these parameters upon the blade's lift coefficient.

2. The computational method

2.1 Design philosophy

Truly unsteady problems are completely hyperbolic with respect to the type of the governing partial differential equations and they stay hyperbolic in contrast to e.g. such transient problems which lead asymptotically to elliptic regimes. This makes them much more sensitive to even slight errors in the treatment of boundaries. So to avoid sources of numerical and methodical errors as far as possible we developed our scheme (see /1a/,/1b/) according to the following rules:

- physical boundaries should be rigidly connected to the computational arid,
- artificial boundaries with nonphysical boundary conditions are banned.

To fulfill the first rule, the simplest way is to connect a rigid contour-aligned grid with the moving body in question. To care for the second rule means in our case to extend the computational domain right to infinity. Both concepts will be detailed in the following sections.

2.2 Moving systems

According to the first rule we have to compute the flow in a moving arid whose motion is identical with that of the moving body and so is assumed to be known. Then it is a straightforward procedure to transform the differential equations

$$U_t + F_\zeta + G_\eta = 0$$

with the (conservative) solution vector $U = (\rho, \rho U, \rho V, e)^T$

(ρ denoting density, e total energy, U,V velocity components)

and $F = \begin{bmatrix} \rho U \\ \rho U^2 + p \\ \rho VU \\ hU \end{bmatrix}$, $G = \begin{bmatrix} \rho V \\ \rho UV \\ \rho V^2 + p \\ hV \end{bmatrix}$ with $p = (\varkappa - 1)(e - \frac{\rho}{2}(U^2 + V^2))$

$h = e + p$

$\varkappa$ ratio of specific heats

from the original ξ, η, τ-space into the moving one with the coordinates x,y,t.

In doing so, however, quite a number of variants is possible: one may choose for instance between cartesian or polar or other systems, or between different forms of the solution vector. To present just one example out of many - and by far not the most abundant one - we get for a solution vector with the velocity components of the moving cartesian x,y,t-frame

$$W = (\ \rho,\ u,\ v,\ p)^{\mathsf{T}}$$

the system $W_t + \mathbb{A}\ W_x + \mathbb{R}\ W_y = Q$

with $\mathbb{A} = \begin{bmatrix} u & \rho & 0 & 0 \\ 0 & u & 0 & 1/\rho \\ 0 & 0 & u & 0 \\ 0 & \varkappa p & 0 & u \end{bmatrix}$, $\mathbb{R} = \begin{bmatrix} v & 0 & \rho & 0 \\ 0 & v & 0 & 0 \\ 0 & 0 & v & 1/\rho \\ 0 & 0 & \varkappa p & v \end{bmatrix}$

and $Q = \begin{bmatrix} 0 \\ -U_n C - \dot{V}_n S + x\omega_n^2 + 2v\omega_n + y\dot{\omega}_n \\ \dot{U}_n S - \dot{V}_n C + y\omega_n^2 - 2u\omega_n - x\dot{\omega}_n \\ 0 \end{bmatrix}$ with ξ_n, η_n, σ_n position and angle of moving x,y,t-system,

$U_n = \dot{\xi}_n$, $V_n = \dot{\eta}_n$, $\omega_n = \dot{\sigma}_n$,

$C = \cos\sigma_n$, $S = \sin\sigma_n$

A careful evaluation of all possibilities has to regard accuracy and computational efficiency as well as the formulation of the boundary conditions; it turns out that the overall optimum choice is, in spite of all transformations, the original conservative solution vector U (see above).

2.2 The mapping

Now we turn to the realization of the second rule of the design philosophy: the moving grid in the infinite physical plane must be mapped onto a finite computational plane - preferably rectangular. For this we design a suitable chain of transformations:

Blade   Near Circle   Unit Circle   Inversion   cartesian map
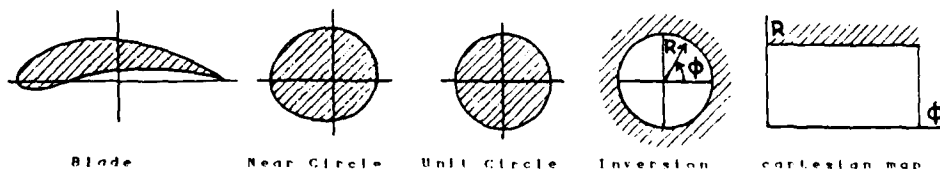
Fig. 1   Transformation from physical to computational domain

The first two steps in this chain, from the physical space around the blade onto the exterior of a unit circle, are best done by some conformal mapping (leading in general to a near circle) followed by Theodorsen's scheme to produce (up to some order of approximation) the unit circle. To avoid this approximation and to save the computational expense we adopted for the purpose of this paper a special conformal mapping combining the well-know Karman-Trefftz formula with an extension, suggested by Jones and McWilliams /2/, of Joukowski's mapping. With suitable parameter values the result is as shown in fig 2 (farther below).

Due to this specialization the whole chain of transformations is purely analytical (with one singular point at the trailing edge). Consequently the transformation coefficients which appear in the transformed system of equations can be evaluated with arbitrary accuracy.

2.3 Implementation and efficiency

The implementation of the method sketched above is straightforward:
The R,Φ-plane is discretized by a regular cartesian grid and the system of equations is integrated in time by a standard finite difference scheme of second order of accuracy, in our case the Lax-Wendroff-Richtmyer scheme. The

only detail worth mentioning is the treatment of the trailing edge point where
the transformation coefficients are singular. Here we adopted a method
developed by Theilemann /3/: the point in question is considered as a field
point and updated by a "grilless" scheme using a suitable cluster of
neighboring points to compute the spatial derivatives.

Due to the relatively small meshes along the surface of the blade (see fig.2
displaying the grid with our choice of $\Delta R, \Delta \Phi$) the time step of the explicit
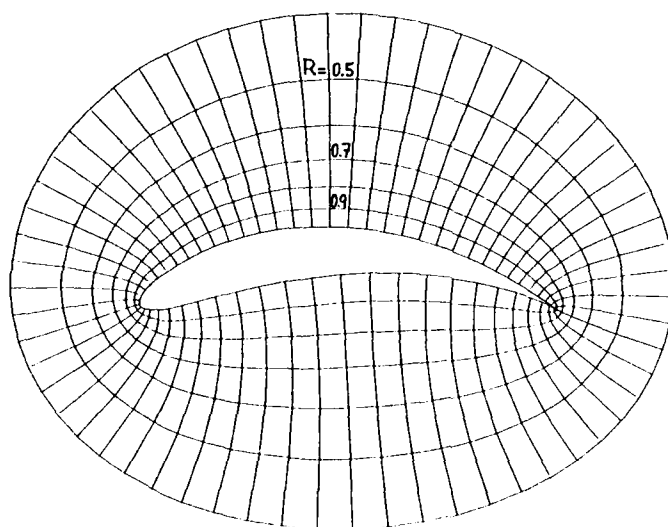
Fig.2 Computational grid around blade

scheme which is governed by the CFL-condition with a maximum Courant Number of
one is small too; typically, we need about 2000 steps for one period of
oscillation whereas about 400 steps would provide a sufficient resolution in
time. Therefore we plan to implement a flux-splitting scheme using a purely
onesided algorithm with third-order accuracy which permits a maximum Courant
Number of three and consequently the computation of the same period with about
700 time steps.

3. Results of numerical experiments

3.1 Phenomenological theory

For a very slow oscillation, with a reduced frequency $k = \omega c / u_{\infty}$ (ω fre-
quency, c length of chord, u_{∞} upstream velocity) much smaller than one, one
can compute the quasi-steady lift coefficient $c_{L,qs}$ by the well-known
steady-state theory which is nothing but the first member of a Taylor
expansion:

$$c_{L,qs}(\alpha) = c_L(0) + \frac{\partial c_L}{\partial \alpha} \alpha(t) \qquad \text{with } c_L(0) = c_L(\alpha=0)$$

or, in the case of a harmonic oscillation with an amplitude α_{mx}:

$$c_{L,qs}(t) = c_L(0) + \frac{\partial c_L}{\partial \alpha} \alpha_{mx} \cos(\omega t) .$$

In our case of a translational motion with amplitude y_{mx}, α and α_{mx} are given
by: $\alpha = \operatorname{atan}(y_{mx}\omega \sin(\omega t)/ u_{\infty})$, $\alpha_{mx} = \operatorname{atan}(y_{mx}\omega / u_{\infty}) = \operatorname{atan}(y_{mx}k/c)$.

For higher reduced frequencies one expects a change in amplitude and a phase

shift, so, following McCroskey /4/, one has to write

$$c_L(t) = c_L(0) + \frac{\partial c}{\partial a}\Big|. \; R \; a_{max} \cos(\omega t + \Delta\varphi)$$

or, expanding and combining,

$$c_L(t) = c_L(0) + \frac{\partial c}{\partial a}\Big|. \; a_{max} \; (\; f \cos(\omega t) - g \sin(\omega t) \;).$$

f is the amplitude of an oscillation in phase with the motion of the blade, g is the amplitude of an oscillation shifted in phase by $\pi/2$, and the f,g-diagram is the commonly adopted means for the description of the behaviour of a harmonically oscillating airfoil.

We extend this concept by considering the possibility that in spite of the harmonic motion of the body the flow variables will in general not vary harmonically due to the nonlinearity of the problem. Then $c_L(t)$ can be described by a Fourier series and we write accordingly

$$c_L(t) = c_L(0) + \frac{\partial c}{\partial a}\Big|. \; a_{max} \; (\; \sum_1^\infty f_i \cos(i\omega t) - \sum_1^\infty g_i \sin(i\omega t) \;) \; ,$$

thus splitting up the one f,g-diagram into a manifold.

3.2 Influence of the nonlinearity

What we have to do is just a spectral analysis of the computed curve $c_L(t)$, directly giving the f_i, g_i. Of course, some care is necessary in processing the raw data (for instance, interpolating for the exact period boundaries, and correcting for the eventually not yet reached exactly periodic state).

We present the results for an upstream Mach Number $M_\infty = 0.4$ which for our highly cambered blade is rather near the (lower) critical Mach Number signalling the first appearance of sonic flow in the steady case. The reduced frequency was given the values $k = 0.25, 0.5, 1, 2, 3, 4, 6$ and 8, for each of these frequencies the amplitude was varied according to

$y_{max} k/c =$	0.1	0.2	0.3	0.4	0.5	0.6	0.8	1.0
giving $\quad a_{max} \sim$	1.43	2.86	4.29	5.71	7.13	8.53	11.31	14.04	grd.

The overall results are not spectacular. Let us first examine the influence of the amplitude upon f_i and g_i in fig.3:
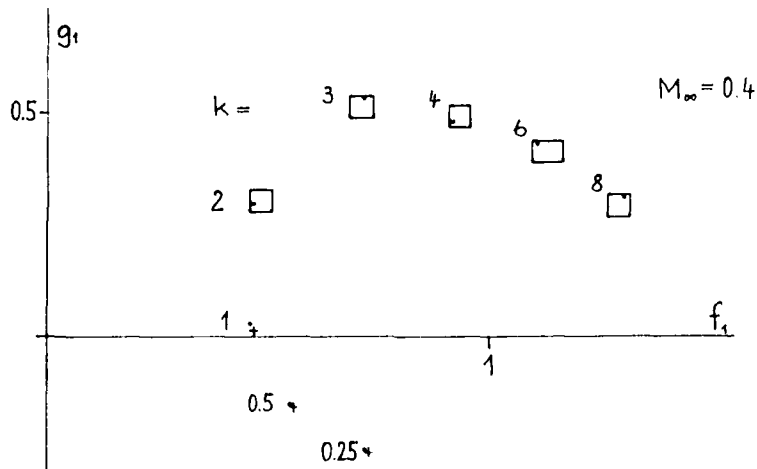
Fig 3 f_i, g_i-diagram for different oscillation amplitudes

The variations are so small that it takes enlarged diagrams to show details: fig.4 displays four of the five rectangles indicated in fig.3:
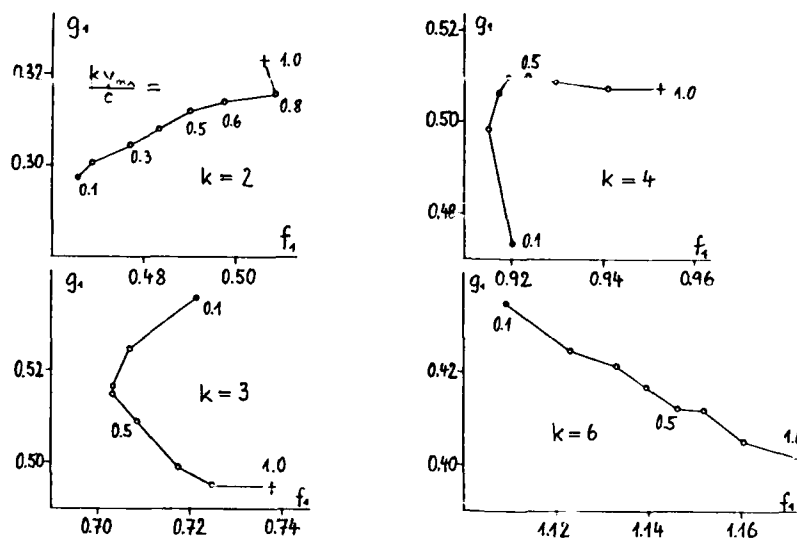
Fig.4   Details of fig.3

There is a distinct effect of the oscillation's amplitude but it is rather
divers with different reduced frequencies, and it is very small compared with
the effect of the reduced frequency itself and, as we will see later, the Mach
Number.

Let us turn next to the other nonlinear effect: the higher harmonics. We
computed them up to fourth order but, as fig.5 shows, already f_2 and q_2 are in
the order of one percent of f_1, q_1 so we did not display the higher ones.
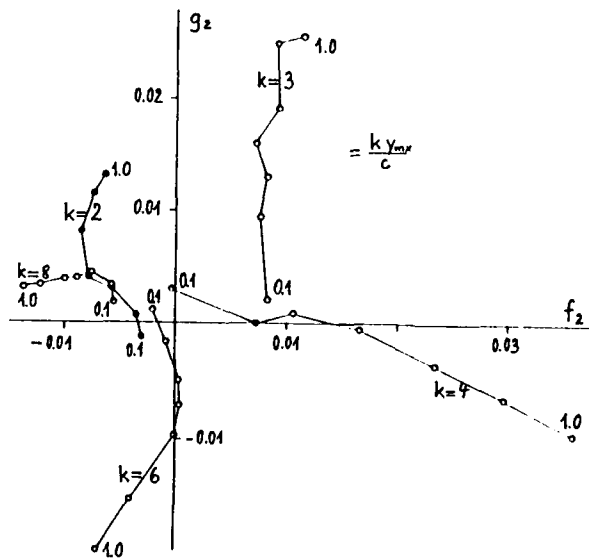
Fig.5   The second harmonics (f_2, q_2-diagram)

3.3 Influence of the Mach Number

From this investigation we show only $f_1 \cdot g_1$ which, as we have seen, already give the main effect. The picture, shown in fig.6, is rather impressive, at least compared with the meager one of the previous section.
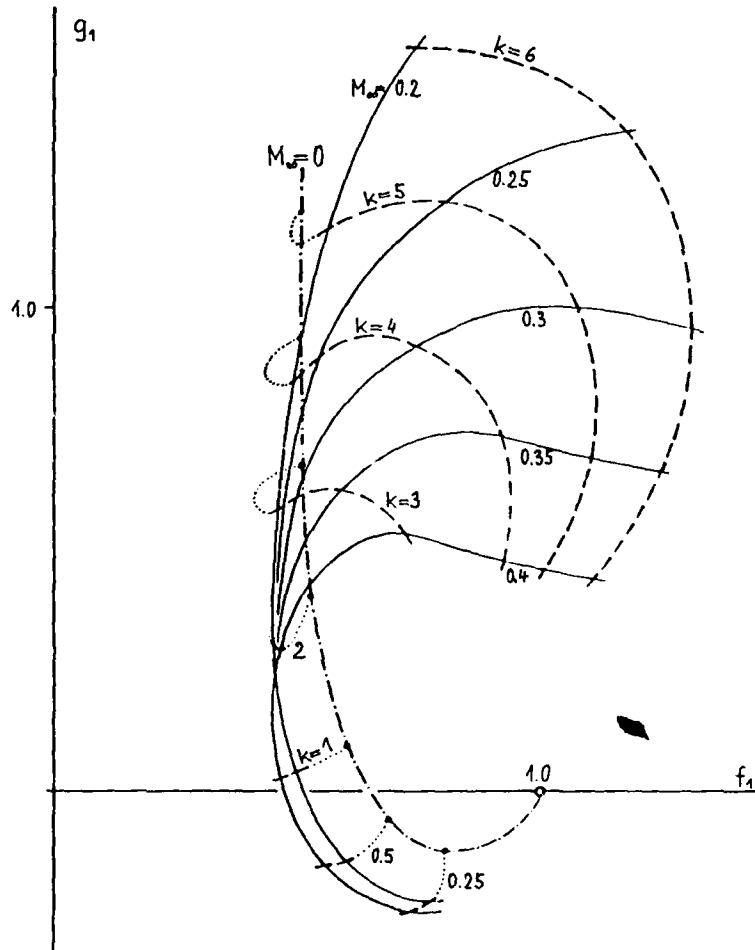
Fig.6 Influence of Mach Number and reduced frequency

For comparison we included the well-known case of a flat plate with Mach Number zero (dash-dotted line). The connections of the computed iso-k-lines for Mach Numbers between 0.2 and 0.4 (broken) to the corresponding points on the flat-plate-line are dotted - nevertheless they are realistic because they are based on further computed cases with lesser Mach Numbers which we do not display because of numerical uncertainties in some places.

4. Summary

The results of extended computer studies of the flow around an oscillating
blade show that
- the importance of the nonlinearity of the problem on the aerodynamic
  characteristics seems small generally,
- the influence of the onflow Mach Number, however, is moderate for reduced
  frequencies below three but becomes progressively larger for higher
  frequencies.

5. Acknowledgment

6. References

/1a/ Förster,K. and F.W.Li, A numerical scheme for the unsteady transonic
     flow around an oscillating airfoil.
     Proc. of the X.ICNMFD, Beijing June 23-27, 1986, p.276-282

/1b/ Li,F.W., Ein Beitrag zur Berechnung der instationären, transsonischen,
     reibungsfreien Strömung um ein Tragflügelprofil.
     Dissertation, Universität Stuttgart 1986

/2/ Jones,R.T. and R.McWilliams, Design your own airfoil - the Oshkosh
    airfoil program. July 1983

/3/ Theilemann,L., Ein gitterfreies Differenzenverfahren.
    Dissertation, Universität Stuttgart 1983

/4/ McCroskey,W.J., Unsteady airfoils.
    Ann.Rev.Fluid Mech. 14

DISCUSSION

Y.N.Chen Sulzer Brothers Ltd, Winterthur, Switzerland
The author presented an interesting view of calculating the flow field of an oscillating single blade (in the case of a strongly cambered airfoil). He considers the flow field of the airfoil as an independent one and neglects the unsteady flow in the wake, correcting this assumption with the McKroskey method and stressing out that this method applies to small perturbations only.

On the other hand, von Karman and Sears considered very early an oscillating plate with small amplitude oscillations by taking into account the wavy wake with positive and negative vorticities distributed alternately along it, and established a corresponding $f - g$ diagrame

Recently, del Hak and Ho measured the flow field around an oscillating airfoil (i.e. undergoing dynamic stall). The emission of a Karman vortex has been found in the wake, during an oscillating cycle.

Thus, shedding of a wavy wake with Karman-vorticity distribution for weak oscillations, and an established Karman vortex street in the wake for a strong oscillation are obvious.

The inclusion of the Karman vortices in the wake may therefore contribute to the refinement of the calculations.

Author's response :
The way von Karman and Sears considered the oscillating blade can not be compared with the point of view of modern **Computational Fluid Dynamics**
von Karman presupposed the existence of vortices and then - of course quite correctly for the case of incompressible flow - established their connection with the flow field.
Our more general method makes no assumptions whatsoever about the structure of the flow field and just solves the differential equations for the given **Boundary** conditions. Hence, eventual vortices are a consequence rather than a presupposition. They do of course come out (even in the case of Euler equations, due to numerical viscosity), but wether they show up or not depends on the mesh width of the computational grid.
We could easily trace them already under conditions of massive stall where their diameter is roughly three times the mesh length, but in the case of the shedding of a small vortex street from the trailing edge , our grid is much to coarse to resolve such a small scale phenomenon. Nevertheless their effect upon the whole flow field is taken into account, and one possibility to prove their existence is - next to the variation of the lift coefficient - would be to show the variation in time of the instantaneous circulation around the blade, but we did not yet extract this from the result files.

B.H. Becker , Siemens AG, West Germany
Since the paper deals with isolated blade, the results cannot be directly applied to turbomachinery cascades. Could the Author comment on the possibility to use nevertheless his results to explain, for instance, the pressure fluctuations near the leading edge where the effect of other blades might be small.

Author's response :
Mr Becker's assumption that the flow in the vicinity of the leading edge of our single blade will be similar to the flow in a cascade is certainly correct. In both cases the pressure fluctuations near the leading edge can be traced back to the migration of the stagnation point, which in turn is caused by the variation of the angle of attack. This is clearly displayed in the isobar sequences in the numerical computation film made using the method described and could quantitatively be extracted from the result files recorder during the computations.

Aerodynamic Superposition Principle in Vibrating Turbine Cascades

A. Bölcs, T. H. Fransson, D. Schläfli

Ecole Polytechnique Fédérale de Lausanne

Lausanne, Switzerland

Abstract

In unsteady aerodynamics the superposition principle states that the unsteady aerodynamic perturbations generated in a vibrating cascade are the same as the sum of the perturbations generated by vibrating single blades. This principle has been subject to controversy in the past; today it has been verified experimentally by different authors for torsional vibration modes in linear compressor cascades in subsonic and incompressible flow.

The present paper describes experiments on turbine cascades performed in an annular non-rotating test facility in order to validate the above mentioned superposition principle. Using an annular test facility eliminates the problems with lateral boundaries encountered in linear cascades: the annular cascade flow is truly periodic both for steady and unsteady flow. In the following, we present experiments

- performed with three different cascades, vibrating in a translational mode, simulating a bending vibration

- that cover supersonic, transonic and subsonic flow

- that cover the entire interblade phase angle range possible with 20 blades

The blade sections of the cascades are typical for the last stage of gas- and steam-turbines. The results obtained show that, within the limitations of experimental accuracy, the superposition principle is valid, i.e. from experiments with single vibrating blades the same conclusions can be drawn as from experiments with the whole cascade vibrating at constant amplitudes and interblade phase angles.

Nomenclature

Symbol	Explanation	Dimension
A	Blade amplitude	mm
B_n	Blade number "n"	-
c	Blade chord length	mm
$\tilde{c}_h$	Unsteady force coefficient in direction of bending vibration $$\tilde{c}_h = \sum_i \tilde{c}_{pi}\, \Delta\, (x/c)_i$$	-
$\tilde{c}_p$	Unsteady perturbation pressure coefficient $$\tilde{c}_p(x,t) = \frac{1}{h}\frac{\tilde{p}(x,t)}{p_{w1}\text{-}p_1}$$	

de mouvement. Modèle 2 équations (avec *l équilibre* ≈ 0,0918).
$U = 30m/s$; $\alpha = 4^o$; Re = 4 10⁵.

incompressible. Modèle 2 équations (avec *l équilibre* ≈ 0,0918).
$U = 30m/s$; $c = 4^o$; Re = 4 10⁵.

c_w Aerodynamic work coefficient per cycle of blade vibration in travelling wave mode   -

D_i Pressure transducer number "i" on blade pressure surface   -

f   Blade vibration frequency   Hz

h   Dimensionless (with chord) bending vibration amplitude   -

k   Reduced frequency $k = \dfrac{\omega c}{2 w_\infty}$ -

M   Mach Number   -

$\tilde{p}$ Unsteady perturbation pressure   mbar

S_i Pressure transducer number "i" on blade suction surface   -

β Flow angle   deg

$\Lambda (x/c)$ Normalized blade surface element normal to vibration direction   -

γ Cascade stagger angle   deg

ω Natural frequency of the blades   s⁻¹

σ Interblade phase angle. σ is positive when blade "n+1" leads blade "n"   deg

σ_p Pressure phase angle. Positive when pressure leads blade motion   deg

Ξ Aerodynamic damping coefficient in travelling wave mode   -

$\Xi_h = -Im(\tilde{c}_h)$ for pure bending

Subscript

h   Bending motion

i   Pressure transducer number i

ic   Influence coefficient

ls   Blade lower surface (=suction surface)

ps   Blade pressure surface

s   Isentropic

ss   Blade suction surface

twm   Travelling wave mode

us   Blade upper surface (=pressure surface)

1   Upstream flow conditions

2   Downstream flow conditions

1B   First bending mode

2B   Second bending mode

1T   First torsion mode

Superscript

m   Blade number "m"

n   Blade number "n"

k   Interblade phase angle wave number

-    Approximate value

Introduction

Aeroelastic experiments as well as numerical predictions are often performed in the "travelling wave" formulation, in which all blades vibrate with constant interblade phase angles and identical blade vibration amplitudes (see for example [Bölcs and Schläfli, 1987, Carstens, 1984; Carta, 1982; Fran on and Pandolfi, 1986. Gerolymos, 1988a,b. Kobayashi, 1988, 1984; Riffel and Rothrock, 1980; Servaty, Gallus and au, 1987; Verdon, 1987, Whitehead, 1987]). Results from such investigations give necessary useful information to the aeroelastician-designer, but the physical reasons for the specific aeroelastic behaviour of a certain cascade are not easily identified. Furthermore results from the "travelling wave" formulation are rather difficult to integrate into the structural analysis of a rotor

A different approach consists of the "influence coefficient" technique, where the unsteady forces acting on a blade in a particular vibration mode are considered as the sum of unsteady forces generated specifically by each blade of the cascade, much the same as structural coupling terms in a structural analysis. Crawley [1984] has demonstrated that the aeroelastic formulations as influence coefficients or travelling wave mode are mathematically identical; Gerolymos [1988a] has shown that, in a numerical example based on an inviscid blade-to-blade solution, the combined effect of influence coefficients computed from 7 blades gives similar results as the calculations in the travelling wave mode.

Experiments have recently started to be performed with only one blade in a cascade vibrating, while measuring the unsteady response on all neighbour blades (see for example [Davies and Whitehead, 1984; Hanamura et al, 1980; Schläfli, 1989; Szechenyi, 1980, 1983, 1984, 1985]). These responses are thereafter linearly summed up to yield the total influence on one blade, with this as well as all the other blades vibrating [Szechenyi, 1980, 1984]. From the purely analytical (linearized theories) point of view, such an approach may be questionable if only a limited number of blades is taken into account, while acoustic resonances [Samoloivich, 1967; Verdon, 1977a,b] will not be considered.

Attempts to prove the validity of the superposition principle experimentally have been published by several authors ([Hanamura et al., 1980; Bölcs and Schläfli, 1987; Buffum and Fleeter, 1988]). The results of these tests are only partly conclusive: The work by Hanamura was performed in incompressible flow in a linear test facility; Bölcs and Schläfli presented one single test case in an annular test facility. Buffum and Fleeter performed their study in subsonic flow and also used a linear cascade for their experiment, where the limited number of blades in the cascade (9) a priori precludes the detection of the influence of distant blades, if present. Their results presented also show some unexplained discrepancies, and the possible effect of the lateral boundaries on the unsteady flow in a linear cascade remains uncertain.

The objectives of the present study are to verify the validity of the superposition principle at sub-, trans- and supersonic flow regimes on turbine cascades, vibrating in the first bending mode, in an annular test facility.

Fundamentals of influence coefficients

The mathematical formulation of time dependent aeroelastic influence coefficients as the coupling terms between vibrating blades is well known and widely used for taken into account unsteady aerodynamic effects into structural dynamic models (see for example [Bendiksen and Friedmann, 1980; Crawley, 1984; Bloemhof,1988; Hoyniak and Fleeter, 1986; Topp and Fleeter, 1986]). However, the formulation is not as often employed for explaining the physical reasons for aerodynamic instabilities of cascades, with a few exceptions [Szechenyi et al, 1984; Hall and Crawley, 1983; Hanamura et al, 1980; Davies and Whitehead, 1984]. The influence coefficients will be used as the principal basis for the comparison of the experimental data below. The fundamentals of the diagrams used for the physical interpretation of the results will thus briefly be discussed here.

For this purpose the "2N+1" blades in a cascade are assumed to be numbered from "-N" to "+N", according to Fig. 1a, and it is assumed that the influence from all the blades can be linearly summed up to yield the global influence exercised on each blade in the travelling wave mode, i. e. with constant interblade phase angle between vibrating blades and with identical blade vibration amplitudes. This formulation has been given by Széchényi et al [1984] as[1]:

$$\tilde{c}_{h,twm}^{m,\sigma}(t) = \sum_{n=-N}^{N} \tilde{c}_{h,ic}^{n,m}\, e^{i\omega t}\, e^{i\sigma n} \qquad (1)$$

where

- $\tilde{c}_{h,twm}^{m,\sigma}(t)$ is the unsteady aerodynamic force coefficient in the direction of the bending vibratrion, acting on blade "m", with the blades oscillating in the travelling wave mode with interblade phase angle σ.

- $\tilde{c}_{h,ic}^{n,m}$ is the unsteady aerodynamic force influence coefficient of the vibrating blade "n", acting on the blade "m".

---

[1] The example is here given for the aerodynamic force coefficient in the bending direction but the procedure can be employed for any unsteady aerodynamic coefficient

- σ_n is the phase angle between blade "n" and the reference blade "m".
- $e^{i\omega t}$ is the unitary harmonic motion of the blade n.

If the blade vibrate in the travelling wave mode, the interblade phase angle is constant and it is possible to express eq. (1) as:

$$\tilde{c}_{h,twm}^{m,\sigma} \, e^{i\omega t} = \sum_{n=-N}^{N} \tilde{c}_{h,ic}^{n,m} \, e^{i(\omega t + (n-m)\sigma)} \tag{2}$$

and thus

$$\tilde{c}_{h,twm}^{m,\sigma} = \sum_{n=-N}^{N} \tilde{c}_{h,ic}^{n,m} \, e^{i(n-m)\sigma} \tag{3}$$

While assuming the reference blade to be blade "m"= blade "0", this expression becomes

$$\tilde{c}_{h,twm}^{0,\sigma} = \sum_{n=-N}^{N} \tilde{c}_{h,ic}^{n,0} \, e^{i n\sigma} \tag{4}$$

The relation between influence coefficients and the travelling wave forces has the form of a Fourier transform. It is a special case of the more general formulation given e.g. by Crawley [1984].

The influence exercised by one vibrating blade (reference blade "0": n=0 in eq. 4) on itself is independent of the interblade phase angle. Fig 1b shows an example for the superposition of the contributions from blades "+1" and "-1": According to eq. 4, the contributions of blade "+1" can be represented as a vector rotating in clockwise direction with increasing interblade phase angle σ; the influence of blade "-1" results in a vector rotating in counterclockwise direction with increasing σ. The resulting vector of blade forces or pressures describes an ellipse in the complex plane in case only direct neighbor blades are considered. With the inclusion of the effects of more distant blades, the resulting diagram becomes more complicated (Fig 1c).

The above discussion has been conducted based on the global unsteady force coefficient, but the same holds for the local unsteady pressure coefficients on each blade surface. These then allow to establish the relationship between the response on a certain part of a blade and the vibrating neighbour blades.

Test facility and model cascades

Test facility

The tests on the present cascade were performed in the non-rotating annular cascade tunnel at the Ecole Polytechnique Fédérale de Lausanne [Bölcs, 1983].

The annular set-up presents the advantage of a "closed" cascade without the lateral boundaries of a linear cascade. Therefore both the steady and unsteady flow periodicity establishes itself, and no interaction of the flow (steady and unsteady) with tailboards or other boundaries has to be accounted for. In particular unsteady perturbations can travel along the cascade without being cut off by tailboards. It is because of this feature that the annular set-up is best suited for the experimental verification of the superposition principle.

The flow is created in a radial-axial annular nozzle shown in Fig. 2. The velocity and flow angle profiles in the test section are obtained by the regulation of the two separate inlet valves ("1", "2") and the two independent inlet guide vanes ("5", "6").

The velocity profile in the inlet section can furthermore be influenced by two separate suctions immediately downstream of the preswirl vanes. Four independent suctions up and downstream of the test cascade can act on the velocity profile as well as on the boundary layer on the outer and inner tunnel walls.

As the annular cascade is "closed" circumferentially the inlet and outlet flow velocities as well as the flow angles adjust themselves in relation to the pressure ratio. The inlet flow angle in the test section can be adjusted continuously between -78° and -20° (measured from axial), and the inlet Mach number varied from 0.3 to 1.6.

The flow conditions are measured with two aerodynamic probes ("8") which can traverse over the channel height as well as in the circumferential direction.

Pressure taps ("10") are located on the inner and outer walls in order to determine the periodicity and the static pressure in the flow field. The test facility is also equipped with Schlieren optic and laser holography for flow visualization ("9").

The compressed air for the test facility is produced by a continuously running four stage radial compressor which has a maximum mass flow rate of 10 kg/s and a maximum pressure ratio of 3.5. The suction of the wall boundary layers can be performed with a second compressor (2 kg/s, pressure ratio 8).

Model Cascades

The annular cascades presented here are derived from gas- and steam turbine blades, operating in high subsonic or supersonic flow regimes. They consist of 20 prismatic blades each. They have a tip diameter of 0.4 m, a hub diameter of 0.32 m and a blade height of 0.04 m (see Fig. 3 and Table 1 for cascade geometries). The nominal flow conditions of the sections under investigation are also given in Table 1. The vibration directions are chosen as to reproduce the first bending mode, and the corresponding reduced vibration frequencies of the real blading are conserved for the model cascade.

Machine type		Cascade I Gas turbine	Cascade II Steam turbine	Cascade III Steam turbine
Stagger angle	(°)	49.0	56.6	73.4
Blade chord	(mm)	78.5	74.4	52.8
Profile thickness	(%)	10	17	5.2
Pitch/chord ratio	(-)	0.72	0.74	1.07
Upstream Mach number (M_1)	(-)	0.34	0.31	0.40
Inlet flow angle (β_1)	(°)	10	-44	-62
Downstream Mach number (M_2)	(-)	0.95	0.90	1.34
Outlet flow angle (β_2)	(°)	-58	-72	-71
Vibration direction (δ)	(°)	90	61	43
Vibration frequency (f_{1B})	(Hz)	210-230	140-150	220-230
Reduced frequency	(-)	0.14-0.21	0.08-0.13	0.08-0.17
Pressure transducers suction side		6	6	5
Pressure transducers pressure side		5	5	5

Table 1: Cascade data

Vibration and control system

The blades are elastically suspended on a spring-mass system, which allows vibrations in two translational and one torsional mode, of which only the first translational mode is considered in these experiments. They are forced into vibration by means of electromagnetic exciters (Fig 4a) [Kirschner et al, 1980]. These exciters consist of electromagnets made out of transformer kits. Part of the plates is fixed on the mass piece of the blade, closing the magnetic flux across the gap. The blade vibration is measured by inductive displacement transducers or strain gages on the spring, depending on the cascade. The measurement system is dynamically calibrated with miniaturized accelerometers mounted at midspan of the blade. The overall calibration precision is of the same order as the precision of the accelerometer (ca. 2%). The transducers are fixed on an impact ring ("6" in Fig. 4a) (which is also used as a mechanical limit for the blade vibration amplitudes), that is positioned axially by an hydraulic system. An electromagnetic control system allows to establish and maintain a pre-defined vibration mode of the cascade: Each blade has its own feedback control loop. The interblade phase angle and blade vibration amplitude can thus be selected individually and almost any cascade vibration pattern can be realized. The disadvantage of the versatile electromagnetic system is the limited forces that can be generated by the electromagnets of a given size. The blade

vibration amplitude and phase angles are therefore not rigorously constant in time and between the blades, but subject to fluctuations that depend on the mechanical properties of the cascade (such as coupling between the blades) and the vibration mode selected, as well as non periodic flow perturbations. An example of the vibration amplitude and interblade phase angle for seven adjacent blades is given in Fig. 4b. It is seen that both the blade amplitudes and the interblade phase angles can be controlled with a high accuracy.

Data acquisition and reduction

Data acquisition

The steady state flow conditions are established by means of probe measurements both up- and downstream of the cascade and static pressure taps on two adjacent blades, located at midspan. These taps are connected to a precision pressure acquisition system which permits a quick analysis of the steady state flow during the tests.

For the purpose of unsteady pressure measurements two blades in each cascade are equipped with high frequency response piezoresistive pressure transducers[1]. These have a diameter of 6 mm and a thickness of 0.6 mm. The pressure membrane has a diameter of 3 mm. One of the blades has the transducers on the pressure surface and a second has them on the suction side at midspan height of the blade. The locations of the pressure transducers correspond to locations of steady state pressure taps. All transducers are situated, as for the steady-state pressure instrumentation, in the same interblade channel (see Fig. 3) and are embedded in the blade and connected to the surface through taps. This way of mounting preserves a good blade surface, but implies a dead volume of air which might possibly affect the frequency and phase response of the transducers. However, at the frequencies of interest no noticeable difference with respect to a flush-mounted transducer could be detected during the calibrations.

The entire time-dependent measuring chain is calibrated with a time fluctuating pressure, with the steady-state reference pressure verified with a Betz manometer. After calibration the measurement uncertainty of the entire chain is estimated as ±2% [Schläfli, 1989].

As the pressure transducers are located in the blades, acceleration forces act on them during the blade vibration. The response of these forces is measured during the calibration, and substracted from the response during the data reduction.

The blade motion is measured by an inductive displacement transducer on cascade 1, by means of strain gauges fixed on the spring of the blade suspension on cascades 2 and 3. Either device is dynamically calibrated with respect to a miniature accelerometer fixed at midspan of the blade for this purpose.

The time-dependent data are amplified, low-pass filtered and recorded on an analog tape recorder prior to analysis on a PDP-11/34. Blade vibration signals and the time dependent pressure signals are recorded simultaneously this way.

Unsteady data analysis

The time dependent data reduction technique is based on a Fourier analysis approach. As can be shown, only pressure fluctuations of the blade vibration frequency (first bending mode in the present case) contribute to the aerodynamic work performed on the blade by the unsteady pressures [Carta; 1982]. Therefore only the first eigenfrequency component of the unsteady pressure signal is here of interest for the evaluation of aerodynamic work and damping coefficients.

For evaluation, the data are reproduced at reduced speed to achieve a frequency transformation because of the limited sampling frequency of the Analog/Digital converter. The data are digitized "piecewise" in data frames because of limited storage space in the computer core memory. The data frames (2560 data values per frame) are transferred onto a disk file for further processing. This piecewise processing provides a means of evaluating the quality of the

---

1   ENDEVCO Model 8515-50A. These transducers, rated at 50 psi, have a pressure hysteresis of 0.1% full scale output, a non-linearity of 0.25%, a non-repeatability of 0.1%.

data: each data frame is individually analyzed, yielding a sample amplitude and phase angle for each signal. Typically, ten such samples (A_i, Φ_i) are averaged (Fig. 5), resulting in mean amplitudes and phase angles (A, Φ). The scatter of the sample values around the mean is used to estimate 95%-confidence intervals for the mean, based on the assumption of randomly distributed samples, represented by the circle with radius ΔA. The phase angle interval is defined by $\Delta\Phi = \tan^{-1}(\Delta A/A)$. Large confidence intervals indicate the presence of important random components in the signal.

From the tests in the controlled blade vibration mode unsteady pressures at discrete points on the blade surfaces are obtained during vibrations of the blades. From these unsteady pressures it is then possible to define an unsteady blade surface pressure coefficient $\tilde{c}_p(x,t)$, which can be written with a harmonic assumption:

$$\tilde{c}_p(x,t) = \tilde{c}_p(x)\, e^{i(\omega t + \phi_p)} = \frac{1}{h} \cdot \frac{\tilde{p}(x,t)}{p_{w1} - p_1} \tag{5}$$

where $\tilde{c}_p(x)$ is the amplitude of the pressure fluctuation and $\phi_p(x)$ is the phase lead of the pressure fluctuation with respect to the blade motion.

It should be recognized that the definition of $\tilde{c}_p$ is the conventional one [Carta; 1982], which includes the dynamic pressure $(p_{w1} - p_1)$. The absolute magnitude of $\tilde{c}_p$ depends thus on the level of the dynamic inlet pressure, which in turn depends on the cascade geometry and the inlet flow angle for choked cascades. This is the main reason for the very different scales for unsteady pressure and force coefficients in the cascades discussed below, and must be clearly kept in mind while analyzing $\tilde{c}_p$ for the different examples presented.

Once this pressure coefficient has been obtained, the unsteady aerodynamic force, $\tilde{c}_h(t)$, acting on the blade is calculated as the sum of the discrete pressure responses multiplied with the corresponding blade surface element. For each element the absolute time-dependent pressure is taken as constant, including the leading edge and trailing edge regions.

The unsteady aerodynamic work, $\tilde{c}_{wh}$, due to the aerodynamic forces on the blade during bending vibration, is thereafter determined as the integral, over a period of blade vibration, of the force multiplied by the blade velocity. The unsteady aerodynamic damping is then defined as (for pure bending vibration) [Bölcs and Fransson; 1936]:

$$\Xi = -\frac{\tilde{c}_{wh}}{\pi h^2} = -\tilde{c}_h \sin\phi_h = -\operatorname{Im}(\tilde{c}_h) \tag{6}$$

where $\tilde{c}_h$ is the amplitude of unsteady aerodynamic force and ϕ_h is the phase lead between unsteady aerodynamic force and blade motion.

From this value, the unsteady aerodynamic stability limit $\Xi = 0$, is calculated. If $\Xi > 0$, the flow has a damping effect on the blades, whereas $\Xi < 0$ indicates that the flow gives energy to the blades.

The information of most use for the turbomachine designer is thus the unsteady aerodynamic damping, Ξ. However, in order to understand the details of unsteady aerodynamics it is also necessary to look at the unsteady blade surface pressure distribution $\tilde{c}_p(x,t)$.

The aerodynamic damping Ξ depends on the steady state flow conditions, the reduced frequency k and the interblade phase angle σ. The main parameters of influence for the cascades presented, as the blade vibrating frequency stays constant, can be considered to be the cascade geometry, the interblade phase angle, the outlet flow velocity and the incidence angle.

Decomposition of unsteady data into influence coefficients

The fundamental relationship between the travelling wave formulation and the influence coefficients has been shortly presented above. In the experiment, however, the travelling wave is not realized ideally; there are always slight differences in vibration amplitudes and phase angles between blades in the cascade. In order to account for this, the data reduction procedure has to start from the general formulation (see Crawley [1984]). The motion of the n-th blade in the cascade is

$$h_n(t) = h_n \, e^{i\sigma_n} e^{i\omega t} \tag{7}$$

The unsteady pressure coefficient induced on the zeroth blade is therefore:

$$\tilde{c}_{h,twm}^{0,\sigma}(t) = \sum_{n=-N}^{N} \tilde{c}_{h,ic}^{n,0} \frac{h_n}{h_0} e^{i\omega t} e^{i\sigma_n} \tag{8}$$

Each blade can have a different amplitude and a different phase angle for a given vibration pattern. A set of patterns (e.g. approximate travelling wave modes with diffferent interblade phase angles) is described by the complex matrix-equation of the form:

$$[C] = [H] [L] \tag{9}$$

The vector [C] contains the set of unsteady pressures or forces measured for K different vibration patterns (=interblade phase angles) in the cascade. The vector [L] contains the influence coefficients and the matrix [H] the complex vibration patterns of the 2N+1 different blades in the cascade for the K different vibration patterns:

$$
\begin{bmatrix}
\tilde{c}_{h,twm}^{0,\sigma_1} \\
\tilde{c}_{h,twm}^{0,\sigma_2} \\
\cdots \\
\tilde{c}_{h,twm}^{0,\sigma_K}
\end{bmatrix}
\approx
\begin{bmatrix}
h_{1,-N} & h_{1,-N+1} & \cdots & h_{1,N} \\
h_{2,-N} & h_{2,-N+1} & \cdots & h_{2,N} \\
\cdot & \cdots & \cdots & \cdots \\
h_{K,-N} & h_{K,-N+1} & \cdots & h_{K,N}
\end{bmatrix}
\begin{bmatrix}
\tilde{c}_{h,ic}^{-N,0} \\
\tilde{c}_{h,ic}^{-N+1,0} \\
\cdots \\
\tilde{c}_{h,ic}^{N,0}
\end{bmatrix}
\tag{10}
$$

If the influence coefficients are known, this equation can directly be used to determine the unsteady forces in the cascade for a particular vibration pattern. If, on the contrary, the vibration pattern and the resulting forces are known, as in the experiments, the influence coefficients are determined by the least-square solution:

$$[\bar{L}] = \left[[H]^T [H] \right]^{-1} [H]^T [C] \tag{11}$$

Resolution of this equation requires at least as many independent measurements as there are blades to be considered ($K \geq 2N+1$), but there can be more measurements than blades. The complex matrix-equation can be reduced to a real form by approriate separation of real and imaginary parts at the price of increasing the dimensions of the matrix.

Test results and discussion

To demonstrate the validation of the superposition principle, six typical test conditions, corresponding to sub-, trans- and supersonic outlet flow, are discussed below (Table 2).

Sample case	Cascade	M_{2s}	k
1	I	1.31	0.14
2	II	1.43	0.08
3	II	1.04	0.10
4	III	1.07	0.10
5	II	0.85	0.12
6	III	0.77	0.13

Table 2:   *Test cases presented*

in the travelling wave vibration mode, the entire cascade is excited into vibration for the possible interblade phase angles. In the single blade excitation mode, the instrumented blades and their neighbours (from blade "-4" to blade "+4") are excited separately. In the comparison between the two modes, the travelling wave coefficients are synthesized from the single blade influence coefficients for blades "-4" to blade "+4".

Supersonic outlet flow conditions

Test case 1 with cascade I is an experiment with an outlet flow velocity of $M_{2s}=1.31$ and an upstream flow angle of $\beta_1=20°$. The steady flow conditions are summarized in Fig 6a; the Mach number distribution on the blade shows an expansion and a following recompression near the leading edge, indicating a local flow separation. The continuous expansion of the flow is limited at ca. 80% of the chord by the shock impinging from the neighbour blade. Downstream of the shock the flow is not accelerating any more. For this steady-state operating condition the first three pressure transducers on the suction side are situated in the subsonic flow, and the fourth one just downstream of the sonic transition. The rearmost transducer is situated in the region of the impinging shock ("a" in Fig 6a); an eventual unsteady effect due to the shock should be visible here.

An example for the unsteady blade pressures measured in the travelling wave vibration mode is shown for $\sigma=180°$ in Fig 6b. The most important pressures are generated near the leading edge on the suction side, and they rapidly decay towards the trailing edge. The phase angles are close to the stability limit at $\Phi_p=180°$; the first two pressure transducers indicate a slightly positive aerodynamic damping, with the two following transducers unstable. On the pressure side the pressure fluctuations are considerably smaller and they all induce positive damping.

The aerodynamic damping coefficients as measured in the travelling wave mode and reconstructed from single blade excitation influence coefficients are compared in Fig. 6c. A good agreement between the two methods is observed for both the pressure side and the suction side. The suction side damping has an almost sinusoidal shape, which is an indication for the dominant influence of the direct neighbour blades. On the pressure side this is less obvious, but examination of the influence coefficients in Fig 6d shows a similar dominance of the direct neighbour blades. The significant unsteady interactions extend from the "-2" blade to the "+1" blade; a good correlation in terms of amplitude and phase is observed for influence coefficients with non-zero amplitudes. Coefficients with amplitudes close to zero cannot be expected to agree very well because of the data fluctuations that propagate through the decomposition procedure and affect the small coefficients more severely than the large ones [Schläfli, 1989].

Test case 2 (cascade II) yields similar results: The steady state flow conditions for the example (Fig 7a) show that the shock from the neighbour blade is stronger than compared to cascade I, and it hits the blade in the vicinity of pressure transducer S4. As seen on the unsteady pressure distribution on the blade in Fig 7b, the shock from the neighbour blade affects the unsteady response both in terms of amplitude and phase (transducer S4 at location x/c=0.6). The unsteady pressure amplitudes on the suction side are the most important near the transition from sonic to supersonic flow on the blade; the amplitude sharply drops downstream of this point, but at the shock location the pressure amplitude increases. On the pressure side, the most important response is observed towards the trailing edge, where the flow velocity reaches the speed of sound. An almost constant phase angle distribution ($\Phi_p\sim180°$) is observed for the suction side, with the exception of the shock location, where an important phase shift occurs. On the pressure side, the phase angle smoothly increases along the blade chord. Another effect of the shock is the increased fluctuation of the data, represented by the vertical bars through the symbols.

In this example, the correlation between travelling wave data and single blade predictions is even better than for test case 1, as seen in the comparison of aerodynamic damping coefficients in fig 7c. The almost sinusoidal shape of the suction side damping again indicates that the direct neighbour (the "-1" blade as for cascade I) has the strongest influence on the measuring blade.

Transsonic outlet flow conditions

The first example for transsonic outlet flow conditions is **test case 3** with cascade II. For these close to sonic outlet flow conditions a normal shock is observed near the trailing edge (Fig 8a), and another, weaker one, at about 66% of the blade chord. The rearmost pressure transducer is located in the vicinity of the trailing edge shock. The unsteady pressure distribution for an interblade phase angle of $\sigma=180°$ (Fig 8b) shows that in this case, too, the main interactions are generated in the interblade channel (subsonic flow velocities on the suction side), but the trailing edge shock induces a large fluctuation at transducer S5. The phase angle distribution is similar to the supersonic test case 2 with an important phase shift from the leading edge to the trailing edge.

Again a good correlation between the single blade influence coefficients and the travelling wave data is observed (Fig 8c). Minor discrepancies appear for the suction side damping for interblade phase angles near σ=0°.

Test case 4 is an example from cascade III, which has a flat profile and a large pitch/chord ratio and is very different from cascades I and II. The steady state pressure distribution on the blade (fig 9a) indicates a strong expansion at the leading edge, accompanied by large flow separation. The shock terminating this region does not appear clearly in the pressure distribution, but is visible on shadowgraph flow visualisations not presented here. The shock is heavily smeared in the boundary layer. Fig 9b shows an example for the unsteady blade pressure distribution. On the pressure side, the strongest unsteady response is observed near the leading edge. On the suction side however, the most important responses are observed near the trailing edge downstream of the recompression zone and the shock. Data fluctuations (indicated by the vertical bars through the data symbols) are important for the rearmost pressure transducer, indicating high turbulence levels due to flow separations.

The pressure side phase angles are fairly constant around Φ=0°, whereas on the suction side a jump in the sign of the phase at x/c=0.4 is observed. This location corresponds to the end of the recompression zone of the suction side flow on the profile.

The correlation of the trend between travelling wave data and predicted aerodynamic damping from single blade vibration influence coefficients agrees extremely well (Fig 9c), as in the previous cases. However, somewhat larger discrepancies than previously are noticeable in the absolute values.

Subsonic flow

In **test case 5** (from cascade II) the entire flow field through the cascade is subsonic. A smooth expansion on the suction side over the first 30% of the chord is terminated by an almost constant flow (Fig 10a). The unsteady pressure coefficients in Fig. 10a show a distribution similar to cases 2 and 3 for the pressure side, which is to be expected since the pressure side flow is similar for all outlet flow velocities. The suction side pressure distribution again shows the dominant interaction within the interblade channel; it is quite similar to test case 2.

Again, the correlation between travelling wave data and predicted single blade damping is good (Fig 10b); the shape of the suction side damping curve in this case indicates the relatively important influence of blades more distant than the "+1" and "-1" blade. Note the similarity of the pressure side damping curves with the test cases 2 and 3 (Figs 7c, 8c).

Test case 6 is taken from cascade III, where a supersonic region still exists on the blade suction side near the leading edge, extending to ca 8% of the chord length (Fig 11a). The first pressure transducer is located in this area, all the others in subsonic part of the flow. The unsteady pressures in the example for σ=180° (Fig 11b) are, with the exception of one transducer on the pressure side, almost in opposite phase between pressure and suction surface of the profile; the amplitudes are important near the leading edge. In this case also, the essential features of the reconstructed damping coefficient from single blade influence coefficients are the same as the travelling wave data (Fig 11c).

Conclusions

The superposition principle of unsteady effects in oscillating cascades postulates the equivalence of single vibrating blades with travelling wave vibration modes as regards the resulting unsteady load, i.e.: The unsteady load observed on a cascade vibrating in a travelling wave mode is the sum of the influences of single vibrating blades in the cascade. Attempts to validate this postulate experimentally have been performed by several authors in the past, but without conclusive results as regards the validity in compressible flow regimes. Furthermore most of their work was conducted in linear cascades with their inherent disadvantage of lateral boundaries to the flow, which may invalidate the results.

The work presented above validates the superposition principle of unsteady effects in cascades in the following respects:

- The tests have been performed in an annular cascade. The annular cascade is the only one to be truly pitchwise periodic. Lateral boundaries as in linear test facilities do not exist and therefore cannot influence the experimental results. For this reason the annular set-up is best suited to verify the superposition principle.

- The tests have been conducted with three different cascades (derived from gas and steam turbines at different blade sections), operating at reduced frequencies in the range k=0.08-0.21.

- The tests cover flow conditions with outlet flow velocity varying from subsonic to supersonic.

The results show in all cases that the superposition principle unconditionnally holds for any flow regime, as far as can be established by an experimental investigation. Unsteady blade forces and aerodynamic damping coefficients measured in the travelling vibration mode with all 20 blades vibrating at constant interblade phase angle and constant amplitude are very similar to predictions derived from influence coefficients determined from single vibrating blades.

In the cascades investigated, the coupling effects decay rapidly pitchwise; blade-to-blade interactions between direct neighbor blades are the most important cascade effect. The influences from blades more distant than two to three pitches only marginally affect the global unsteady behaviour of the cascade (stability limit). However, this does not prove that lateral boundaries in linear cascades may not falsify the superposition under certain circumstances.

In the experiments discussed here no evidence of acoustic resonance phenomena as predicted by theoretical models was found. In the annular test facility, as well as in a real turbine, the conditions for the apparition of such phenomena (i.e. homogeneous up- and downstream flow conditions extending to infinity) are not realized. Also, the range of interblade phase angles with potentially superresonant conditions is very small in the upstream flow (i.e. $-8° < \sigma_{ak\ res} < 0°$); in the downstream flow it is somewhat larger (typically $-10° < \sigma_{ak\ res} < 90°$), but the flow inhomogeneity (wakes, shocks) probably prevents such phenomena to develop in a experimentally perceptible manner.

Acknowledgements

References

Bendiksen, O.; Friedmann, P.; 1980
"Coupled Bending-Torsion Flutter in Cascades."
AIAA Journal, Vol. 18, No. 2, February, 1980, pp.194-201
Bloemhof, H.; 1988
"Flutter of Blade Rows with Mistuning and Structural Coupling."
Communication du Laboratoire de thermique appliquée et de turbomachines No. 14, Ecole Polytechnique Fedérale de Lausanne, Lausanne, Switzerland, 1988.
Bölcs, A.; Schläfli, D.; 1987
"Experimental Investigation of the Time-Dependent Flow in a Vibrating Annular Cascade Operating in the Transonic Flow Regime."
Proceedings of the Symposium "Unsteady Aerodynamics of Turbomachines and Propellers", Aachen, West Germany, pp. 245-269, 1987.
Bölcs, A. ; 1983
"A Test Facility for the Investigation of Steady and Unsteady Transonic Flows in Annular Cascades."
ASME paper 83-GT-34, 1983.

Buffum, D.H.; Fleeter S.; 1988
"Investigation of Oscillating Cascade Aerodynamics by an Experimental Influence Coefficient Technique"
AIAA Paper 88-2815, 24th Joint Propulsion Conference, July 11-13, Boston, Massachusetts, 1988

Carstens, V.; 1984
"Theoretical Flutter Investigations on a Plane Cascade in Incompressible Flow."
Proceedings of the Symposium "Unsteady Aerodynamics of Turbomachines and Propellers", Cambridge, United Kingdom, pp. 277-300, 1984.

Carta, F. O.; 1982
"An Experimental Investigation of Gapwise Periodicity and Unsteady Aerodynamic Response in an Oscillating Cascade."
NASA Contractor Report 3513, 1982.

Crawley, E. F.; 1984
"Aeroelastic Formulations for Turbomachines and Propellers."
Proceedings of the Symposium "Unsteady Aerodynamics of Turbomachines and Propellers", Cambridge, United Kingdom, pp. 13-28, 1984.

Davies, M.R.D, Whitehead, D.S..; 1984
"Unsteady Aerodynamic Moment Measurements in a Transsonic Annular Cascade."
Proceedings of the Symposium "Unsteady Aerodynamics of Turbomachines and Propellers", Cambridge, United Kingdom, pp. 487-502, 1984.

Fransson, T. H.; Pandolf, M.; 1986
"Numerical Investigation of Unsteady Subsonic Compressible Flows Through an Oscillating Cascade."
ASME Paper 86-GT-304, 1986.

Gerolymos, G. A.; 1988a
"Periodicity, Superposition and 3D Effects in Supersonic Flutter Aerodynamics."
ASME Paper 88-GT-136, 1988.

Gerolymos, G. A.; 1988b
"Numerical Investigation of the 3D Unsteady Euler Equations for Flutter Analysis of Axial Flow Compressors."
ASME Paper 88-GT-255, 1988.

Hall K. C.; Crawley E. F.; 1983
"Optimal misturning for enhanced aeroelastic stability of transsonic fans."
MIT GTL report n° 176, Cambridge, USA, No. 176,1983.

Hanamura, Y.; Tanaka, H.; Yamaguchi, Y.; 1980
"A Simplified Method to Measure Unsteady Forces Acting on the Vibrating Blades in a Cascade."
Bulletin of the JSME, Vol. 23, No. 180, 1980.

Hoyniak.; Fleeter, S.; 1988
"The Effect of Circumferential Aerodynamic Detuning on Coupled Bending-Torsion Unstalled Supersonic Flutter."
ASME Paper 86-GT-100, 1986.

Kirschner A.; Fosco B.; Muller E.; 1981
"Control of vibration in aeroelastic cascade experiments."
Communication de L'ITA/ EPFL, No. 10, pp. 285-295,1981.

Kobayashi, H.; 1988
"Effect of Shock Wave Movement on Aerodynamic Instability of Annular Cascade Oscillating in Transonic Flow."
ASME Paper 88-GT- 187, 1988.

Kobayashi, H.; 1984
"Unsteady Aerodynamic Force Acting on Controlled-Oscillating Transonic Annular Cascade."
Proceedings of the Symposium "Unsteady Aerodynamics of Turbomachines and Propellers", Cambridge, United Kingdom. pp. 343-359, 1984.

Riffel, R. E.; Rothrock, M. D.; 1980
"Experimental Determination of Unsteady Blade Element Aerodynamics in Cascades."
NASA Contractor Report 159831, DDA EDR 10119, 1980.

Samoloivich, G.; 1967
"Resonance Phenomena in Sub- and Supersonic Flow Through an Aerodynamic Cascade."
Mekhanika Zhidkosti i Gaza, Vol. 2, No. 3, pp. 143-144, 1967.

Servaty, S.; Gallus, H. E.; Kau, H.-P.; 1987
"Computation of Aerodynamic Blade Loads Due to Wake Influence And Aerodynamic Damping of Turbine And Compressor Cascades."
Proceedings of the Symposium "Aeroelasticity in Turbomachines", Aachen, West Germany, pp. 357-386, 1987.

Schläfli, D.; 1989

"Experimentelle Untersuchung der instationären Strömung in oszillierenden Ringgittern."

Ph. D. Thesis, Ecole Polytechnique Fédérale de Lausanne, Lausanne, Switzerland, 1988.

Szechenyi, E. ; 1985

"Fan Blade-Single Blade Instability or Blade to Blade Coupling ?"

ASME paper 85-GT-216, Houston, March 1985.

Széchényi, E.; Cafarelli, I.; Notin, C.; Girault, J. P..; 1984

"A Straight Cascade Wind-Tunnel Study of Fan Blade Flutter in Started Supersonic Flow."

Proceedings of the Symposium "Unsteady Aerodynamics of Turbomachines and Propellers", Cambridge, United Kingdom, pp. 447-458, 1984.

Széchényi, E.; Girault, J. P.; 1983

"An Aeroelastic Testing Technique in a Straight Cascade Wind-Tunnel."

Proceedings of the Symposium "Measuring Techniques in Transonic and Supersonic Cascades and Turbomachines", Aachen, West Germany, pp. 4.1-4.8, 1983.

Széchényi, E.; Finas, R.; 1980

"Aeroelastic Testing in Straight Cascade Wind Tunnel."

Proceedings of the Symposium "Aeroelasticity in Turbomachines", Lausanne, Switzerland, pp. 143-149, 1980

Topp, D. A.; Fleeter, S.; 1988

"Splitter Blades as an Aeroelastic Detuning Mechanism for Unstalled Supersonic Flutter of Turbomachine Rotors."

ASME Paper 86-GT-99, 1986.

Verdon, J. M.; 1987

"The Unsteady Aerodynamic Response to Arbitrary Modes of Blade Motion."

Proceedings of the Symposium "Aeroelasticity in Turbomachines", Aachen, West Germany, pp. 313-334, 1987.

Verdon, J. M.; 1977a

"Further Development in the Aerodynamic Analysis of Unsteady Supersonic Cascades. Part I."

ASME Paper no. 77-GT-44

Verdon, J. M.; 1977b

"Further Development in the Aerodynamic Analysis of Unsteady Supersonic Cascades. Part II."

ASME Paper no. 77-GT-45

Whitehead D. S.; 1987

"Flutter of Turbine Blades."

Proceedings of the Symposium "Aeroelasticity in Turbomachines", Aachen, West Germany, pp. 437-452, 1987.

Fig 1a: Blade numbering scheme in the cascade
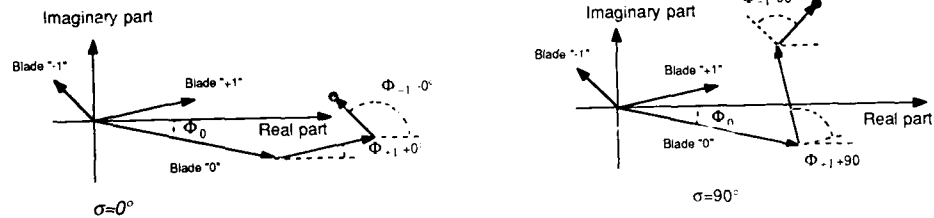
Fig 1b: Superposition of influence coefficients.
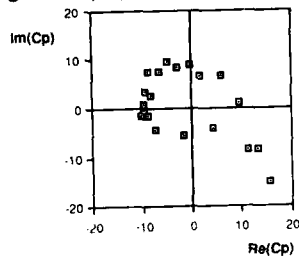
Fig 1c: Example of unsteady blade pressure locus
with influences from several blades

1,2	Inlet valves
3,4	Outer and inner settling chambers
5,6	Outer and inner preswirl guide vanes
7	Test cascade
8	Aerodynamic probes
9	Static wall pressure taps
10	Cylindrical optic for flow visualization
11	Outlet flow collector
12	Outlet valve
->	Boundary layer suction

Fig 2: Annular test facility

Cascade I: Gas turbine cascade, midspan section   Cascade II: Steam turbine cascade, midspan section

Cascade III: Steam turbine cascade, tip section

Fig 3: Model cascades. Dots indicate pressure transducer locations

1 Outer Wall
2 Blade
3 Hub
4 Mass body
5 Exciter coil
6 Impact ring
7 Spring
8 Central body
9 Displacement transducer
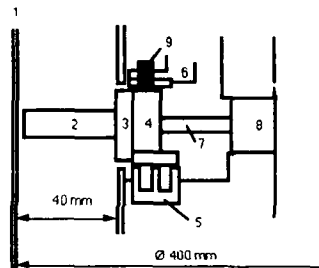
Fig 4a: Schematic view of the blade oscillation system
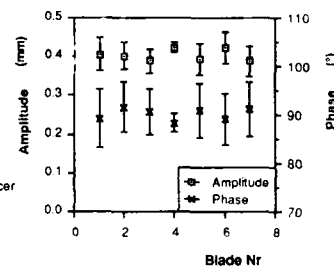
Fig 4b: Blade vibration amplitude and phase fluctuations for travelling wave vibration mode (Cascade I). Bars indicate 95% confidence interval.
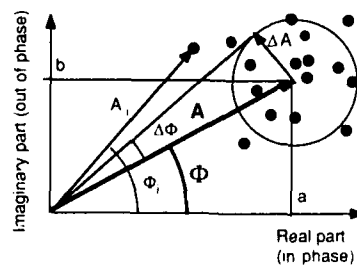
Fig 5: Evaluation of confidence intervals. Each point represents the mean value of a data frame.

reasons for the specific aeroelastic behaviour of a certain cascade are not easily identified. Furthermore results from the "travelling wave" formulation are rather difficult to integrate into the structural analysis of a rotor.

8-10
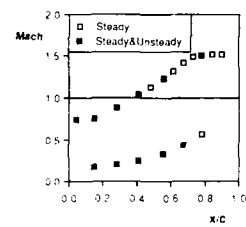
Fig 6a: Cascade I: Steady state flow conditions ($\beta_1 = 20°$, $M_{2is}=1.31$). Unsteady pressure transducer locations marked by closed symbols.
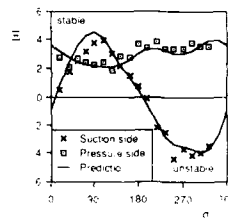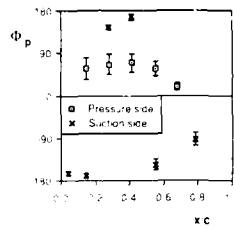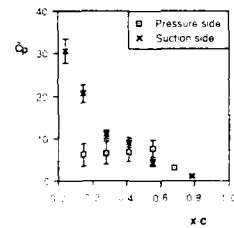
Fig 6b: Cascade I: Unsteady pressure coefficients for interblade phase angle of $\sigma=180°$ ($\beta_1 = 20°$, $M_{2is}=1.31$)

Fig 6c: Cascade I: Experimental aerodynamic damping in the travelling wave vibration mode (symbols) vs. predicted values (solid line) from single blade vibration mode influence coefficients ($\beta_1 = 20°$, $M_{2is}=1.31$)

x	Suction Side Traveling Wave Mode
x	Suction Side Single Blade Excitation
□	Pressure Side Traveling Wave Mode
■	Pressure Side Single Blade Excitation
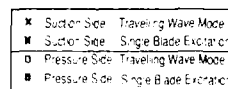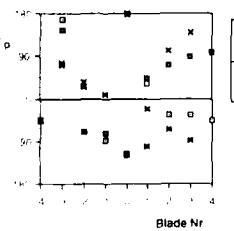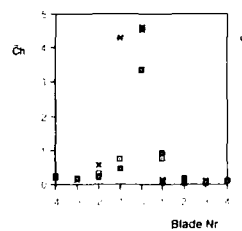
Fig 6d: Cascade I: Force influence cofficients ($\beta_1 = 20°$, $M_{2is}=1.31$)
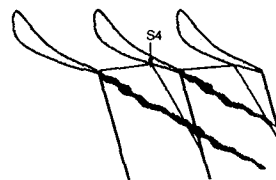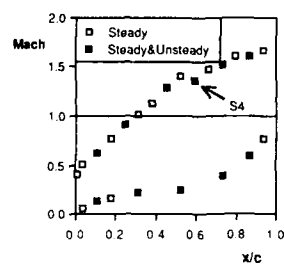
Fig 7a: Cascade II: Steady state flow conditions ($\beta_1=-13°$, $M_{2s}=1.43$). Unsteady pressure transducer locations are marked by closed symbols.
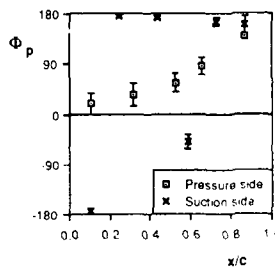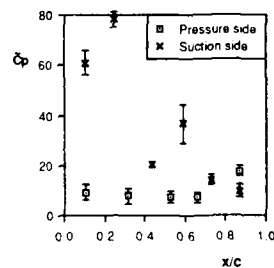
Fig 7b: Cascade II: Unsteady pressure distribution for interblade phase angle $\sigma=180°$ ($\beta_1=-13°$ $M_{2s}=1.43$)
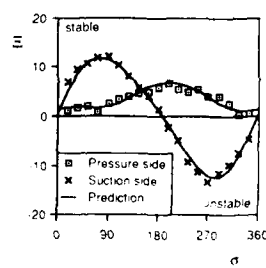
Fig 7c: Cascade II Experimental aerodynamic damping in the travelling wave vibration mode vs predicted values from single blade vibration mode influence coefficients ($\beta_1=-13°$, $M_{2s}=1.43$)
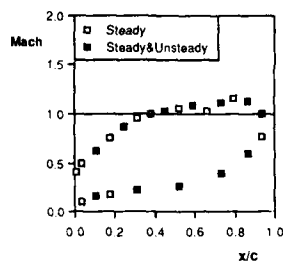
Fig 8a: *Cascade II: Steady state flow conditions ($\beta_1=-21°$, $M_{2s}=1.04$). Unsteady pressure transducer locations are marked by closed symbols*
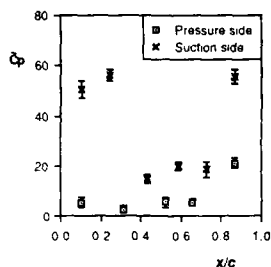
Fig 8b: *Cascade II: Unsteady pressure distribution for an interblade phase angle of $\sigma=180°$ ($\beta_1=-21°$, $M_{2s}=1.04$)*
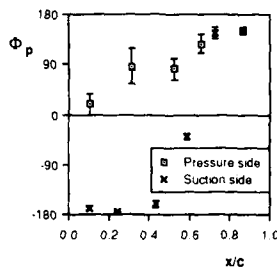
Fig 8c: *Cascade II: Experimental aerodynamic damping in the travelling wave vibration mode vs. predicted values from single blade vibration mode influence coefficients ($\beta_1=-21°$, $M_{2s}=1.04$)*
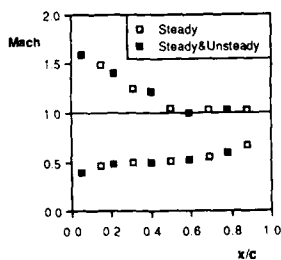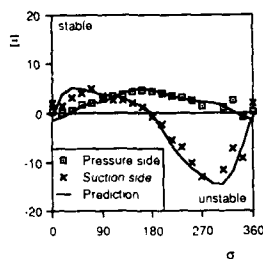
Fig 9a: *Cascade III: Steady state flow conditions ($\beta_1=-69°$, $M_{2s}=1.07$). Unsteady pressure transducer locations marked by closed symbols*
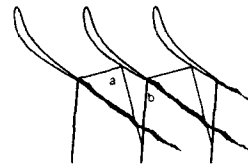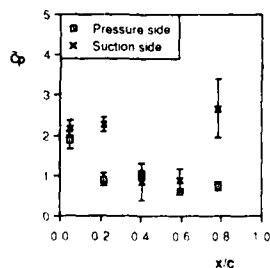

Fig 9b: *Cascade III: Unsteady pressure distribution for an interblade phase angle of $\sigma=180°$ ($\beta_1=-65°$, $M_{2s}=1.07$)*
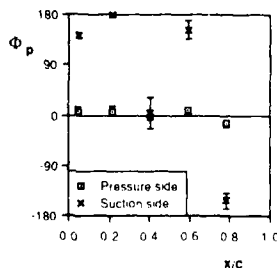
Fig 9c: *Cascade III: Experimental aerodynamic damping in the travelling wave vibration mode and predicted values from single blade vibration mode influence coefficients ($\beta_1=-65°$, $M_{2s}=1.07$)*
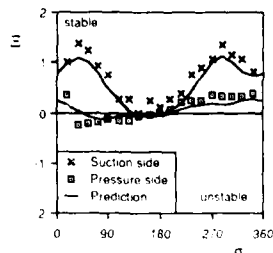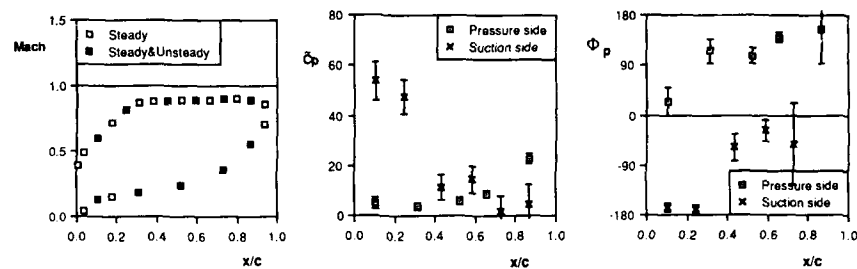
Fig 10a: Cascade II: Steady state flow conditions and unsteady pressure distribution on blade for interblade phase angle σ=180° (β₁ = -15°, M₂s = 0.85)
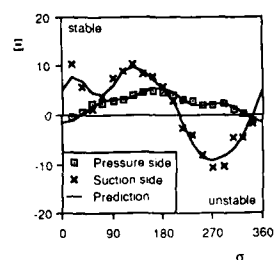
Fig 10b: Cascade II: Experimental aerodynamic damping in the travelling wave vibration mode and predicted values from single blade vibration mode influence coefficients (β₁ = -15°, M₂s = 0.85, σ=180°)

Fig 11a: Cascade III: Steady state flow conditions and unsteady pressure distribution on blade for interblade phase angle σ=180° (β₁=-69°, M₂s=1.07).
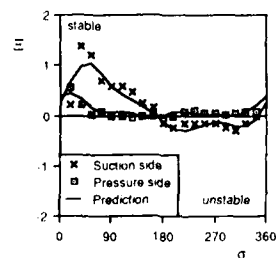
Fig 11c: Cascade III: Experimental aerodynamic damping in the travelling wave vibration mode and predicted values from single blade vibration mode influence coefficients (β₁ = -71°, M₂s = 0.77)

DISCUSSION

M.Guillemier - DRET , France

Quelles sont les limites d'utilisation de la théorie des perturbations par rapport aux amplitudes des vibrations des grilles d'aubes ?

Author's response

The vibration amplitudes in the experiment were in the order of 0.5 percent of the blade chord. Mechanical failure of the cascade is expected for an amplitude of approximately 1.2 percent chord length, therefore the author did not try to explore the limit of validity of the small perturbation theory.

DESIGN GUIDANCE TO MINIMIZE UNSTEADY FORCES IN TURBOMACHINES

R. E. Henderson
Prof. Mechanical Engineering
Applied Research Laboratory
Penn State University
University Park, PA 16802 USA

J. H. Horlock
Vice-Chancellor
The Open University
Walton, Milton Keynes
MK7 6AA UK

SUMMARY

A method is discussed for the development of design charts which provide
guidance in the selection of a stage design loading coefficient and flow
coefficient which minimizes the generation of unsteady forces in a blade row due
to its interaction with the wakes of an upstream blade row. Two configurations
are discussed, (1) the forces on a rotor operating in the wakes of an inlet
stator or guide vane and (2) the forces on a stator downstream of a rotor. An
example demonstrating the generation of a design chart for the first
configuration is presented.

Symbols

b = wake width
c = blade chord
C = fluid velocity relative to casing
C_D = drag coefficient
C_L = unsteady lift coefficient
ℓ = disturbance wavelength
p = pressure
s = spacing
U = blade speed
W = fluid velocity relative to rotor
w = wake velocity defect
w_d = maximum wake velocity defect
x = axial direction
y = pitch direction
α = fluid angle measured from axial direction relative to the casing
β = fluid angle measured from axial direction relative to the rotor
ϕ = flow coefficient
ψ = stage loading coefficient
ξ = stagger angle
ω = reduced frequency

Subscripts

m = mean value between leading and trailing edge
2 = exit of inlet stator, inlet to rotor
3 = exit of rotor blade row, inlet to downstream stator
4 = exit of downstream stator
I = inlet stator
R = rotor
S = downstream stator

INTRODUCTION

Unsteady forces on the blades of axial flow turbomachines can occur due to
potential flow effects arising from the relative movement of neighboring blade
rows (Kemp and Sears, 1953), and due to their interaction with the viscous wakes
arising from blades upstream (Kemp and Sears, 1955), figure 1. Kemp and Sears
derived expressions for the disturbance velocities normal to the blade chord,
and applied the analysis developed by Sears (1941) to calculate the unsteady
lift on the blade.

The analysis by Sears (1941) is for an isolated aerofoil, and has been shown to
be inadequate for closely spaced aerofoils in cascades. Whitehead (1960) and
Smith (1972) have modelled such a cascade using a discrete number of vortices to
represent each aerofoil; Henderson and Daneshyar (1972) have used a continuous
vorticity distribution on the central (or reference) aerofoil and single
vortices on neighboring aerofoils. These authors have derived expressions for
the unsteady lift coefficient as a function of blade stagger angle, space-chord
ratio, intra-blade frequency and reduced frequency.

The cascade analyses provide alternative, improved methods of assessing the
unsteady lift for various turbomachinery stage geometries, as Kemp and Sears did
using the Sears analysis for infinite spacing. However, the application of
these analyses to stage design has not been undertaken in a systematic way, and
that is the purpose of this paper. A method for developing design charts is
demonstrated which permits the minimization of the magnitude of unsteady lift
generated on a blade as a function of the stage design parameters (loading
coefficient and flow coefficient). The viscous wakes from upstream blades are
taken as the cause of the unsteadiness, since the blade row axial spacings used

in practice indicate that the unsteadiness due to viscous effects is
considerably greater than that due to potential flow interaction.
The reduced frequency that appears in the cascade analysis merits discussion.
It is defined as the time required for the flow moving past the blades at mean
relative velocity (W_m) to traverse half the aerofoil chord ($c/2$) divided by the
period of the disturbance past the aerofoil. The circular frequency (1/period)
at which disturbances occur is $2\pi U/\ell$, where U is the velocity at which the
blades moves through a disturbance of wavelength ℓ. The reduced frequency is
then defined as

$$\omega = \frac{\left(\dfrac{c}{2W_m}\right)}{\left(\dfrac{\ell}{2\pi U}\right)} = \frac{\pi U c}{W_m \ell} \ .$$

Whitehead (1959) used an actuator disc analysis to estimate the rotor unsteady
forces at very low values of frequency parameter, $\omega \rightarrow 0$ (chord c being very
small in comparison with disturbances wavelength ℓ) and Horlock, Greitzer and
Henderson (1977) have used semi-actuator disc analysis to study the performance
of closely spaced blades at low frequency parameters. But in practical designs
the first harmonic of the disturbance will have a wavelength roughly equal to
the spacing of the upstream row. With a blade spacing of the same order of
magnitude of the blade chord, and U of the same order of magnitude as W_m, the
reduced frequency will be of the order of magnitude of π. Not only is the use
of the Sears analysis invalid (because of the assumption of infinite spacing),
but also the Whitehead actuator disc analysis for very low frequency parameter
is not applicable for practical cases of a turbomachine stage. The analysis by
Horlock, Greitzer and Henderson (1977) is also limited in application to very
low space-chord ratios.

As a result there is no real alternative to the use of a cascade vortex analysis
for practical design of blade rows with closely spaced blades. Here we will use
one developed by Shen (1980) based on the Henderson/Daneshyar (1972) analysis.
To apply this method to the entire range of compressor geometries would be a
formidable task, so we have restricted the applications to the mean radius
design of a compressor stage with axial inlet flow. We have then considered
cases in which the flow is discharged at different flow angles, including axial
discharge, to a higher static pressure. At the same time we have varied the
flow angle leaving the stator row upstream of the rotor. The calculated
unsteady lift coefficient on a blade is presented as a fraction of the stage
loading coefficient. An alternate presentation could consider the estimation of
the total unsteady axial force on the shaft/hub of a blade row (rotor or
stator), as a fraction of the stage thrust (pressure rise times flow area).

STAGE CONFIGURATIONS CONSIDERED

We have considered two simple stage configurations; (1) an inlet stator, or
guide vane depending on the direction of its fluid discharge, followed by a
rotor and (2) a rotor operating in a uniform inlet flow, no swirl, followed by a
stator with different exit flow angles. Figure 2 shows the velocity triangles
and nomenclature used to describe these configurations.
The ideal stage loading coefficient (ψ) and the stage flow coefficient (ϕ) can
be written in terms of the fluid angles α and β. From the velocity triangles of
Figure 2

$$\tan \beta_3 = \frac{U}{C_x} - \tan \alpha_3$$

so that the flow coefficient becomes

$$\phi = \frac{1}{(\tan \beta_3 + \tan \alpha_3)} = \frac{1}{(\tan \beta_2 + \tan \alpha_2)} \tag{1}$$

The increase in the stagnation pressure through the stage, assuming an ideal,
incompressible flow, is given by

$$\psi = \frac{\Delta P_o}{\rho U^2} = 1 - \phi(\tan \beta_3 + \tan \alpha_2) \tag{2}$$

The first configuration considered (Design A), employs an inlet guide vane
(stator) and a rotor. As an inlet guide vane fluid contra-swirl is provided to
the rotor, $\alpha_2 < 0$, or if swirl is added in the direction of rotor rotation, $\alpha_2 >$
0, the configuration models an inlet stator of a multistage machine. The rotor
is selected to discharge the absolute flow at different angles (α_3) to the axial
direction. Figure 3 shows the relation between ψ, ϕ and α_3 for different values
of α_2.

In the second design considered (Design B) the rotor receives an axial inlet
flow ($\alpha_2 = 0$) and adds tangential momentum. From the velocity triangles at the
mean radius and eq.(1)

$$\phi = \frac{C_z}{U} = \cot \beta_2 \tag{3}$$

The increase in the stagnation pressure for an ideal, incompressible flow is given by eq. (2).

We shall discuss the unsteady flow for the following blade row arrangements:

(i)   Design A in which the inlet guide vane (stator) wakes produce unsteady forces on the downstream rotor blades; and

(ii) Design B in which rotor wakes produce unsteady forces on the downstream stator blades.

DEFINITION OF BLADE WAKES

Kemp and Sears (1955) based their estimates of unsteady forces on the experimental studies of wake flows by Silverstein, Katzoff and Bullivant (1939). They described the "far-field" wake from an aerofoil (figure 4) in terms of three quantities -- the velocity distribution across the wake (w), the wake half-width (b) and center line maximum velocity deficit (w_d). These remain the essential parameters for a description of blade wakes.

In a series of papers, Lakshminarayana and colleagues have provided a comprehensive database of the wakes from aerofoils and lifting blades in cascades, e.g. Raj and Lakshminarayana (1973) and Lakshminarayana and Davino (1980). From this extensive database we have selected the correlation of the latter authors for the maximum velocity defect (w_d) in the wake. Using the inlet stator as the example, figure 4, the maximum velocity defect is written as

$$w_{d_I} = \frac{0.98 \ C_2 \ C_{D_I}}{\left(\dfrac{x'}{c_I} + 0.688 \right)} \tag{4}$$

where C_2 is the free stream velocity at the stator exit, C_{D_I} is the drag coefficient of a single inlet stator blade, and $x' = x \sec \alpha_2$ is measured from the trailing edge along the free stream direction.

Lakshminarayana and Davino (1980) suggest that the variation of the velocity defect across the wake is given by

$$\frac{w}{w_{d_I}} = e^{-0.693 \eta^2} \tag{5}$$

where $\eta = y/L_a$ or y/L_b, and L_a and L_b are distances from the center of the wake on the suction and pressure sides, respectively, to the point where $w = w_{d_I}/2$. No separate correlations for the length scales L_a and L_b are given, but an expression for the wake half-width in the far wake is

$$b_I = (L_a + L_b) = 1.18 \ \frac{s_I}{2} \sqrt{C_{D_I}} \left(\frac{x'}{c_I} + 0.688 \right) \tag{6}$$

where s_I is the blade spacing.

It is possible to express the wake in its various Fourier components, as Kemp and Sears (1955) did for the exponential form of eq.(5). However, their analysis is very complex and based on adding together the blade wakes from neighboring blades (each treated as an isolated aerofoil). On the other hand the Lakshminarayana and Davino (1980) experimental correlations are obtained from direct measurement of annular cascade wakes.

In Appendix A we present a simple Fourier analysis of the variation of the velocity defect across the blade pitch (s) using the expression originally given by Silverstein, et al.,

$$\frac{w}{w_d} = \cos^2 \frac{\pi y}{b} = \frac{1}{2} \left(1 + \cos \frac{\pi y}{b} \right) \tag{7}$$

The resulting Fourier series representation becomes

$$\frac{w}{w_d} = \frac{b}{s} + \sum_{n=1}^{\infty} \frac{\sin \left(\dfrac{2\pi n b}{s} \right)}{n\pi \left(1 - \left[\dfrac{2b}{s} \right]^2 \right)} \cos \frac{2\pi n y}{s} \tag{8}$$

The first harmonic (n=1) has the greatest magnitude and therefore controls the magnitude of the unsteady lift. In Appendix A it is demonstrated that the amplitude of the first harmonic is simply 2b/s for small values of b/s. The

amplitudes of the higher order terms in the series decrease gradually with increasing n. By restricting our considerations to the first Fourier component we will examine the worst case, the highest disturbance velocity. Therefore

$$W_{n-1} = W_d\left(\frac{2b}{s}\right) \tag{9}$$

When the Lakshminarayana and Davino (1980) correlations, eqs. (4) and (6), are used to represent W_d and $2b/s$, it follows that the amplitude of the first harmonic of the inlet stator velocity deficit shown in figure 4 is

$$W_{n-1} = 1.155\ C_{D_I} C_2. \tag{10}$$

Since the data correlations used are for the blade far wake, eq. (10) is for axial blade row spacings of the order of a blade chord or more.

UNSTEADY EFFECTS IN A COMPRESSOR STAGE - GENERAL ANALYSIS

Figure 2 depicts the flow through a three blade row compressor stage. Stations 1, 2, 3, 4 denote entry to the inlet stator, inlet stator exit and rotor inlet, rotor exit and stator inlet, and stator exit, respectively. In practice the consideration of the unsteady flow through a compressor stage during design is usually limited to two blade rows at a time. This is because it is not possible to estimate the effect of an intermediate blade row on the wakes passing through it from an upstream blade row, i.e. the effects of wake chopping and mixing. Therefore either the inlet stator is omitted and a rotor and downstream stator configuration results (Design B) or a guide vane with contra-swirl, or an stator with positive swirl, located upstream of rotor is considered (Design A). The general notation of figure 2 is for both configurations which allows the two design examples to be combined to represent a multistage machine.

We define the flow coefficient as $\phi = C_x/U$ and the ideal stage loading coefficient ψ from eq. (2). For a repeating entry and exit flow, $C_1 = C_4$, the loading coefficient is defined in terms of static pressure rise $\psi = (p_4 - p_1)/\rho U^2$. We consider first the case of a inlet stator and rotor combination (Design A) so that unsteadiness is produced on the rotor ' _ i+ ; interaction with the inlet stator wakes.

The amplitude of the first harmonic of the unsteady rotor lift is given as

$$\tilde{L}_R = \pi \rho W_m c_R W_{n-1} [\tilde{C}_{L_c} \sin \epsilon_R - \tilde{C}_{L_N} \cos \epsilon_R]\ e^{i\nu_R t} \tag{11}$$

where $W_m = C_x \sec \beta_m$ and the mean flow angle defined as

$$\tan \beta_m = \frac{(\tan \beta_2 + \tan \beta_3)}{2} \tag{12}$$

The angle ϵ_R is defined in figure 1. The terms C_{L_c} and C_{L_N} are the unsteady lift response functions for chordwise and normal gusts, respectively. The calculations to be presented later use the analysis by Henderson and Daneshyar (1972) and modified by Shen (1980), to determine the terms C_{L_c} and C_{L_N}. The expression for the velocity deficit entering the rotor is given by eq. (10). We then express the unsteady rotor lift coefficient as a fraction of the stage loading coefficient

$$H_R = \frac{1}{\psi}\left[\frac{\tilde{L}_R}{\frac{1}{2}\rho W_m^2 c_R e^{i\nu_R t}}\right] = \frac{2.31\pi C_{D_I}}{\psi}\ \frac{C_2}{W_m}[C_{L_c} \sin \epsilon_R - C_{L_N} \cos \epsilon_R] \tag{13}$$

With $W_m = C_x \sec \beta_m$, $C_2 = C_x \sec \alpha_2$, and $\psi = (\tan \alpha_3 - \tan \alpha_2)/(\tan \beta_2 + \tan \alpha_2)$, it follows that

$$H_R = 2.31\ \pi\ C_{D_I}\left(\frac{\tan \beta_2 + \tan \alpha_2}{\tan \alpha_3 - \tan \alpha_2}\right)\left(\frac{\cos \beta_m}{\cos \alpha_2}\right)[\tilde{C}_{L_c} \sin \epsilon_R - \tilde{C}_{L_N} \cos \epsilon \ ]. \tag{14}$$

From figure 1, $\epsilon_R = 90 - (\xi_R + \alpha_2)$, where ξ_R is the rotor stagger angle. For zero mean incidence and a circular arc camber line, $\beta_m = \xi_R = \text{atan}[(\beta_2 + \beta_3)/2]$. Hence

$$H_R = 2.31\ \pi\ C_{D_I}\left(\frac{\tan \beta_2 + \tan \alpha_2}{\tan \alpha_3 - \tan \alpha_2}\right)\frac{\cos \beta_m}{\cos \alpha_2}\ [\tilde{C}_{L_c}\cos (\beta_m + \alpha_2) - \tilde{C}_{L_N}\sin (\beta_m + \alpha_2)] \tag{15}$$

The unsteady response of the blades to the upstream wakes is a function of the frequency at which the interaction occurs. For this configuration the reduced frequency is expressed as

$$\omega_R = \frac{\pi c_R}{s_I}(\sin \xi_R + \cos \xi_R \tan \alpha_2) = \frac{\pi c_R}{s_I}(\sin \beta_m + \cos \beta_m \tan \alpha_2) \tag{16}$$

The intra-blade phase angle $r_R = -2\pi s_R/s_I$ relates the spacing of the blade row under consideration and the wavelength of the disturbance, or upstream stator spacing.

A similar analysis can be undertaken for Design B, the rotor and downstream stator which leads to stator unsteadiness from the impingement of rotor wakes. The unsteady stator lift is now

$$L_S = \pi\rho C_m C_S W_{n=1} [\tilde{C}_{L_c} \sin \epsilon_S - C_{L_N} \cos \epsilon_S] \, e^{i\nu_S t} \tag{17}$$

where $C_m = C_x \sec \alpha_m$ and $\tan \alpha_m = (\tan \alpha_3 + \tan \alpha_4)/2$. The disturbance velocity is now given as

$$W_{n=1} = 1.155 \, C_{D_R} \, W_3 \tag{18}$$

where C_{D_R} is the rotor drag coefficient and W_3 the "free stream" velocity relative to the rotor blade exit. The unsteady stator lift coefficient can be expressed as a fraction of stage loading ψ

$$H_S = \frac{1}{\psi} \left[\frac{\tilde{L}_S}{\frac{1}{2}\rho C_m^2 C_s e^{i\nu_S t}} \right] = \frac{2.31\pi C_{D_R}}{\psi} \, \frac{W_3}{C_m} [\tilde{C}_{L_c} \sin \epsilon_S - \tilde{C}_{L_N} \cos \epsilon_S] \tag{19}$$

With $W_3 = C_x \sec \beta_3$, $C_m = C_x \sec \alpha_m$ and $\psi = \tan \alpha_3/\tan \beta_2$ with axial flow at the rotor inlet ($\alpha_2 = 0$), it follows that

$$H_R = 2.31 \, \pi \, C_{D_R} \left(\frac{\tan \beta_2}{\tan \alpha_3}\right)\frac{\cos \alpha_m}{\cos \beta_3} [\tilde{C}_{L_c} \sin \epsilon_S - \tilde{C}_{L_N} \cos \epsilon_S]. \tag{20}$$

From figure 1, $\epsilon_S = 90 - (\xi_S + \beta_3)$. The stator camberline is assumed to be a circular arc and that there is no angle of incidence. This means that the stagger angle is equal to the mean flow angle α_m, so that $\alpha_m = \xi_S = \text{atan}[(\alpha_3 +\alpha_4)/2]$. Hence

$$H_R = 2.31\pi C_{D_R} \left(\frac{\tan \beta_2}{\tan \alpha_3}\right)\frac{\cos \alpha_m}{\cos \beta_3} [\tilde{C}_{L_c} \cos (\alpha_m + \beta_3) - \tilde{C}_{L_N} \sin (\alpha_m + \beta_3)]. \tag{21}$$

The reduced frequency parameter becomes

$$\omega_s = \frac{\pi c_S}{s_R}(\sin \xi_s + \cos \xi_s \tan \beta_3) = \frac{\pi c_S}{s_R} (\sin \alpha_m + \cos \alpha_m \tan \beta_3) \tag{22}$$

and the intra-blade phase angle $r_s = - 2\pi s_s/s_R$.

An alternative presentation of the unsteady response is to relate the unsteady lift force on the blades in a row to the overall total axial steady force on the stage. For both Design A and Design B, the overall total axial steady force on the stage, transmitted through rotating and stationary rows, is

$$F_x = (p_4 - p_1) \, \pi \, (r_t^2 - r_h^2) \tag{23}$$

where r_h, r_t are the hub and tip radii.

The first harmonic of unsteady axial force on a stator blade (Design B) is approximately

$$\tilde{L}_S(r_t - r_h) \sin \xi_S = \pi\rho C_m(r_t -r_h) \, c_S \sin \xi_S \, W_{n=1} [\tilde{C}_{L_c}\sin \epsilon_S - \tilde{C}_{L_N}\cos \epsilon_S] \, e^{i\nu_S t} \tag{24}$$

so that the ratio of blade axial force to stage axial force is

$$R_s = \frac{2.31\pi\rho C_m c_S W_3 \sin \xi_S \, C_{D_R}}{2\pi \, U \, r_m \, (C_{\theta_3} - C_{\theta_2})} \, [\tilde{C}_{L_c} \sin \epsilon_S - \tilde{C}_{L_N} \cos \epsilon_S] \, e^{i\nu_S t} \tag{25}$$

where $r_m = (r_h + r_t)/2$. The axial force on all the stator blades is proportional to

$$[1 + e^{i\nu_s \frac{s_s}{U}} + e^{2i\nu_s \frac{s_s}{U}} + \ldots + e^{i\nu_s(N_s-1) \frac{s_s}{U}}]$$

where $\nu_S = 2\pi \frac{U}{s_R}$, $e^{i\nu_s \frac{s_s}{U}} = e^{i2\pi\mu}$ where $\mu = \frac{s_s}{s_R} = \frac{N_R}{N_s}$.

N_R and N_S are the number of rotor and stator blades, respectively. The term in the square brackets may be summed to give

$$\lambda_s = \left[\frac{1 - e^{i2\pi\mu N_s}}{1 - e^{i2\pi\mu}}\right] = \left[\frac{1 - e^{i2\pi N_R}}{1 - e^{i2\pi \frac{N_R}{N_S}}}\right] \tag{26}$$

Hence

$$R_S = \frac{2.31 \, C_{D_R} C_S}{2r_m} \, \frac{\lambda_s \phi^2}{\psi} \, \frac{\tan \xi_s}{\cos \beta_3} \, [\tilde{C}_{L_c} \cos \, (\xi_S + \beta_3) - \tilde{C}_{L_M} \sin \, (\xi_S + \beta_3)] \tag{27}$$

Similarly it may be shown that for Design A

$$R_R = \frac{2.31 \, C_{D_I} C_R}{2r_m} \, \frac{\lambda_R \phi^2}{\psi} \, \frac{\tan \xi_R}{\cos \alpha_2} \, [\tilde{C}_{L_c} \cos \, (\xi_R + \alpha_2) - \tilde{C}_{L_M} \sin \, (\xi_R + \alpha_2)] \tag{28}$$

where

$$\lambda_R = \left[\frac{1 - e^{i2\pi N_s}}{1 - e^{i2\pi \frac{N_s}{N_R}}} \right] \tag{29}$$

CALCULATION OF UNSTEADY RESPONSE

To provide an indication of the influence of the design parameters on the unsteady response, calculations have been made for Design A configuration. The following stage geometry and operating parameters were selected and calculations performed.

TABLE I - DESIGN A PARAMETERS

Parameter	Value
s_R/c_R	0.5, 0.75, 1.0, 1.5
α_2	-20 deg
α_3	0, 10, 20, 30, 40 deg
$s_I/s_R = N_I/N_R$	0.7

Calculations of H_R have been made for the Design A configuration, inlet stators and rotor, using eq.(13) and for a range of values of ψ and ϕ. The resulting values H_R are presented as a function of ψ for constant values of ϕ and α_3 for each of the selected rotor space-to-chord ratios in figures 5, 6 and 7. These results were then cross plotted to give contours of constant H_R on a plot of ψ versus ϕ, figure 8. These contours indicate the values of ψ and ϕ to be select to minimize the unsteady rotor response for a given value of s_R/c_R.

CONCLUSIONS

The analysis presented is an attempt to define the interaction between two blade rows of an axial flow turbomachine in a manner which permits the selection of design values of ψ and ϕ to minimize the unsteady response of the downstream blade row. Calculations for a configuration of a rotor operating downstream of a set of inlet guide vanes indicate that there are values of ψ and ϕ which result in zero unsteady force on the rotor. While there are many assumptions required to obtain these calculations, it is felt that the results do identify operating conditions leading to minimum unsteady response.

REFERENCES

Henderson, R. E. and Daneshyar, H., "Theoretical Analysis of Fluctuating Lift on the Rotor of an Axial Turbomachine," Aeronautical Research Council R&M 3684 (1972).

Kemp, N. H. and Sears, W. R., "Aerodynamic Interference Between Moving Blade Rows," Journal of Aeronautical Sciences, Vol 20, pp 585-597 (1953).

Kemp, N. H. and Sears, W. R., "The Unsteady Forces Due to Viscous Wakes in a Turbomachine," Journal of Aeronautical Sciences, Vol 22, pp 478-483 (1955).

Lakshminarayana, B. and Davino, R., "Mean Velocity and Decay Characteristics of the Guide Vane and Stator Wake of an Axial Flow Compressor," ASME Journal of Engineering for Power, Vol 102, No. 1 pp. 50-60, (1980).

Raj, R. and Lakshminarayana, B., "Characteristics of the Wake Behind a Cascade of Airfoils," Journal of Fluid Mechanics, Vol. 61, Part 4, pp. 707-730, (1973).

Sears, W. R., "Some Aspects of Non-Stationary Airfoil Theory," Journal of Aeronautical Sciences, Vol 8, pp 104-108 (1941).

Shen, I. C., "Unsteady Pressure Distributions on Airfoils in Cascade," MS Thesis, Department of Mechanical Engineering, Penn State University, University Park, PA (1980).

Silverstein, A., Katzoff, S., and Bullivant, W. K., "Downwash and Wake Behind Plain and Flapped Airfoils," NACA Report No. 651 (1939).

Smith, S. "Discrete Frequency Sound Generation in Axial Flow Turbomachines," Aeronautical Research Council R&M 3709 (1972).

Whitehead, D. S., "Force and Moment Coefficients for Vibrating Aerofoils in Cascade," Aeronautical Research Council R&M 3254 (1960).

Whitehead, D. S., "Vibration of Cascade Blades Treated by Actuator Disc Methods," Proceedings Institute of Mechanical Engineers, Vol 173, No. 21 (1959).

Appendix A: Fourier Analysis of the Wake

Consider the expression given by Silverstein, Katzoff, and Bullivant (1939) for the variation of the wake defect $w = C_{max} - C$ in a direction normal to the wake centerline, y.

$$\frac{w}{w_d} = \frac{1}{2}\left(1 + \cos\frac{\pi y}{b}\right) \tag{A-1}$$

The magnitude of the unsteady lift on a blade is a function of the amplitude of the wake defect which interacts with the blade. Since the theories used to describe this interaction assume that the blade response is harmonic, the wake must be decomposed into a Fourier series and the contributions of the separate harmonics examined. Note that eq. (A-1) describes the wake when $-b < y < b$, but that $w = 0.0$ when $-l = -s/2 < y < -b$ and $b < y < l = s/2$. The Fourier representation of the wake profile becomes

$$\frac{w}{w_d} = a_o + \sum_{n=1}^{\infty} a_n \cos\frac{n\pi y}{b} \tag{A-2}$$

where

$$a_o = \frac{b}{2l} \qquad a_n = \frac{1}{n\pi}\frac{\sin\frac{n\pi b}{l}}{\left(1 - \left[\frac{nb}{l}\right]^2\right)} \tag{A-3}$$

If we assume that the wake fills a certain portion of the blade passage, then we can calculate the Fourier coefficients and examine their relative magnitudes. For example,

	$b/l = 0.25$	$b/l = 0.50$
$a_0 =$	0.1250	0.2500
$a_1 =$	0.2400	0.4240
$a_2 =$	0.2122	0.2500
$a_3 =$	0.1715	0.2550
$a_4 =$	0.1250	0.0
$a_5 =$	0.0800	0.0610

From these calculations we observe:

(1) The magnitude of the first harmonic a_1 is the largest and the higher harmonics decay quite slowly.

(2) For small values of b/l the magnitude of the first harmonic can be approximated as b/l. For example, when $b/l = 1/4$ a value of $a_1 = 0.24$ was calculated demonstrating an error of 4 percent. As b/l decreases so does this error.

We conclude that if we assume the magnitude of the wake defect to be equal to the magnitude of the first harmonic, this represents the case leading to the maximum predicted level of unsteady lift. We will also assume that the $a_1 = b/l$ which gives,

$$w_{n=1} = w_d\frac{b}{l} = 2w_d\frac{b}{s}$$

since l equals $1/2$ of the blade spacing s.
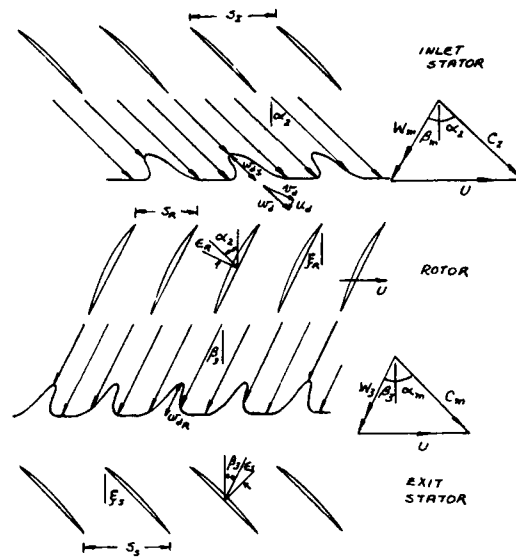
Figure 1 - Blade Row Wake Interaction
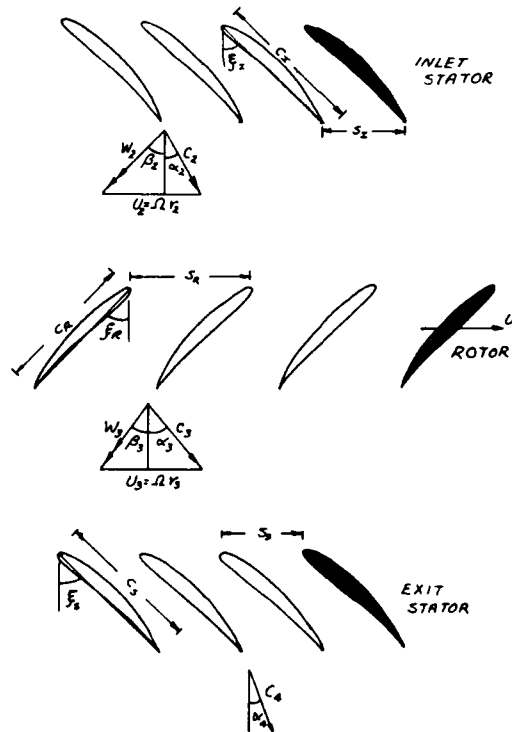
Figure 2 - Stage Velocity Diagrams
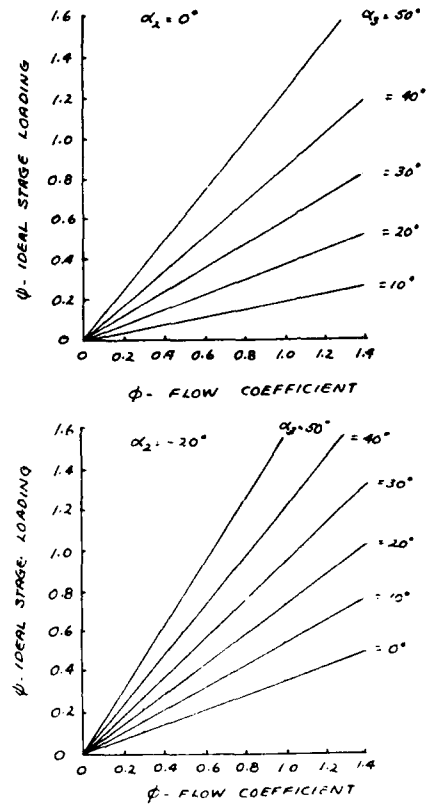
Figure 3 - Ideal Stage Loading versus
Flow Coefficient
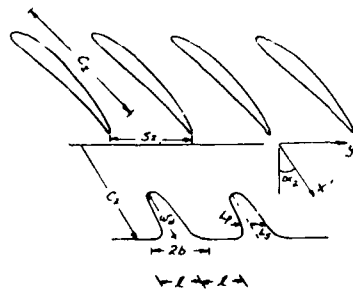
Figure 4 - Inlet Stator Blade Row Wake Definition
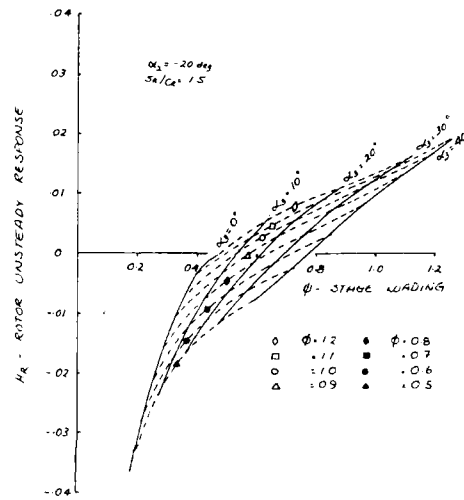
Figure 5 - Rotor Unsteady Response
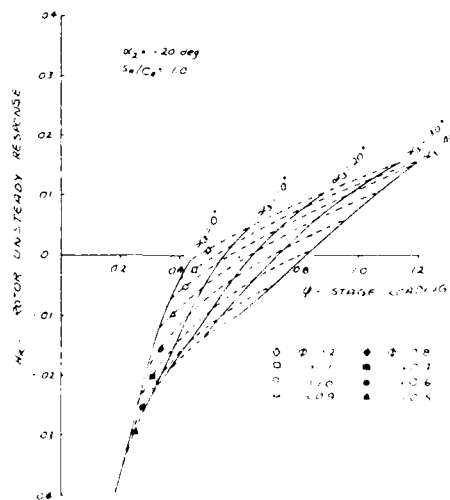
$\alpha_2 = -20$ deg and $s_R/c_R = 1.5$

Figure 6 - Rotor Unsteady Response
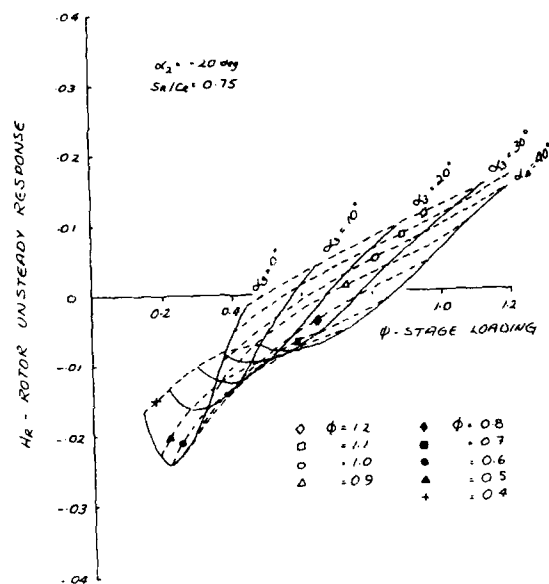
$\alpha_2 = -20$ deg and $s_R/c_R = 1.0$

Figure 7 - Rotor Unsteady Response
α_2 = -20 deg and s_R/c_R = 0.75
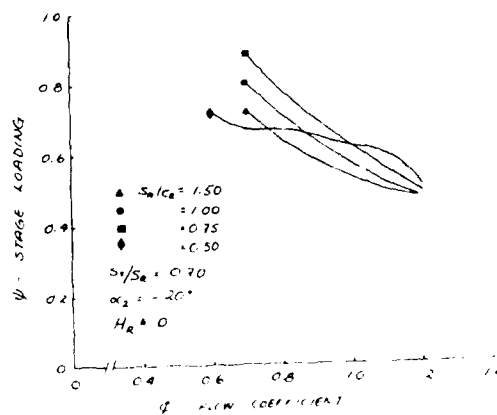
Figure 8 - Contours of H_R = 0.0

DISCUSSION

W. König - University of Darmstadt

The proposed method makes use of experiments carried out by Pr.Lakshminarayana, Penn State University, for measuring the velocity decay and the wake width of rotating compressor blades. Most of these experiments are done in the low speed compressor rig and thereby the question arises, whether the method is applicable on high speed compressors, for example a fan stage?

Author's response :

The calculations presented in Figure 8 of the paper were done assuming incompressible flow within the blade row being analyzed. The wake correlations by Lakshminarayana and Davino were obtained at low Mach numbers and the theory used for the prediction of unsteady forces on the blades assumes an incompressible flow. If wake correlations and an unsteady force predictor are available which include the effects of compressibility, they could be substituted for the ones used in this paper. For instance, Smith (see reference below) describes a flat plate airfoil theory which includes the effects of compressibility. The authors are not aware of a database from which wake correlations have been done for a compressible flow. As a first approximation for high subsonic flows, the Lakshminarayana and Davino correlation could be used with a compressible flow airfoil drag coefficient.

Reference : Smith, S, "Discrete Frequency Sound Generation in Axial Flow Turbomachines" Aeronautical Research Council, Great Britain, R&M 3709, 1972.

Y. N. Chen - Sulzer Brothers Ltd, Switzerland

Figure 8 of the paper shows that the stage loading increases with the decrease in S_R/C_R from 1.5 to 0.75. But curve $S_R/C_R = 0.50$ has a reverse trend compared to the others. It drops steeply in the range of flow coefficients . Would the authors give a physical explanation of this special trend? Kriebel, Seidel and Schwind (1960) showed in their stationary circular cascade that rotating stall occurs earlier at cascades with very small blade spacing due to the shedding of very strong Karman vortices. Is there any relationship between the steep drop mentioned and the early occurrence of rotating stall?

Author's response :

The reason that the curve representing a $s/c = 0.5$ has a different trend than the large values of s/c presented can be attributed to several effects. First the theory by Shen is mathematical limited to $s/c > 0.5$ and stagger angles (60 deg.. Therefore the calculations are near these limits and are starting to reflect numerical inaccuracies. In addition the low value of s/c means that the blade-to-blade interaction is large as the commentator suggests. This can lead to significantly different unsteady response. The theory by Shen is linearized and cannot represent rotating stall.

ETUDE AERODYNAMIQUE DES VIBRATIONS FORCEES DES AUBES
DE STATOR DE COMPRESSEURS AXIAUX

par

H.Joubert et V.Ronchetti
S.N.E.C.M.A.
77550 Moissy Cramayel
France

RESUME

Les aubes de stator des compresseurs axiaux sont soumises à des fluctuations de vitesses liées aux sillages des aubes mobiles les précédant. L'écoulement instationnaire qui résulte de cette intéraction rotor-stator induit des excitations aérodynamiques qui peuvent provoquer une augmentation de la fatigue vibratoire des aubes et mettre en péril l'intégrité du moteur.

Pour étudier ces phénomènes, un code de calcul basé sur la résolution des équations d'Euler 2D a été mis au point. Les fluctuations de conditions amont sont modélisées à l'aide de corrélations établies à partir d'essais. Les pressions instationnaires calculées à l'aide du modèle sont ensuite introduites dans un code de calcul mécanique permettant d'estimer les contraintes dynamiques au sein de la structure de l'aube.

L'influence des grandeurs aérodynamiques telles que les pertes dans la roue mobile et géométriques telles que l'espacement inter roue ou l'influence du nombre d'aubes du stator a été conduite ; et ainsi dès la conception aéromécanique des compresseurs, certains choix de dimensionnement pourront être faits pour minimiser les contraintes sur l'aubage.

AERODYNAMIC STUDY ON FORCED VIBRATIONS ON STATOR ROWS

OF AXIAL COMPRESSORS.

ABSTRACT

Stator vane rows of axial compressors are dependant from velocity fluctuations induced by the wakes of the previous upstream blades row. The unsteady flow resulting from this rotor-stator interaction creates aerodynamic excitations which may initiate vibrating fatigue stress in the vanes and disable the engine.

In order to take into account these phenomena, a numerical model based on two dimensional Euler equations was studied. The upstream conditions fluctuations come from correlations established from wind experimental testing. The unsteady pressures calculated from the model are afterwards introduced in a mechanical model which estimate the dynamic stress inside the vane-structure

The variation of aerodynamic values such as pressure loss in the blade and geometric one such as rotor-stator spacing or fluctuation of the number of the vanes of stator have been studied ; therefore, as soon as the development of aeromechanic design charts of compressor, some sizing choice could be made to minimize the stress on blade assembly.

INTRODUCTION

Afin d'éviter la rupture des aubes de turbomachine par fatigue vibratoire, il importe de prendre en phénomènes aéroélastiques dès le stade de la conception.

Les phénomènes vibratoires pouvant conduire à la rupture des aubes peuvent être scindés en deux catégories : le flottement et les vibrations forcées. Le premier type de vibration est provoqué par une diminution de l'amortissement aérodynamique de l'aube, la force aérodynamique dépend du mouvement vibratoire de la structure (réf. 1 et 2). Le second phénomène est lié à une source extérieure d'excitation tel que le sillage des aubes amont, dans ce cas ci les efforts instationnaires ne dépendent pas du mouvement de l'aube. (figure 1).

Afin de prévoir l'ensemble de ces phénomènes, la SNECMA a développé depuis plusieurs années différents modèles numériques aussi bien aérodynamique que mécanique.

La prévision de l'amortissement aérodynamique en présence de flottement est réalisée à l'aide de codes de calcul basés sur la résolution des équations d'Euler complètes, soit en bidimensionnel soit en tridimensionnel (réf.4).

Les vibrations forcées sont étudiées à l'aide d'une part de forces de réponse mécanique et d'autre laquelle les efforts instationnaires liés à la non axisymétrie de l'écoulement sont obtenus à l'aide d'un code de calcul basé sur la résolution des équations d'Euler. Cette méthode sera appliquée à une étude de compresseurs de compresseurs axiaux.

1 - METHODE DE CALCUL

Hormis dans le cas de la *première roue d'un compresseur*, les aubes de turbomachines ne sont pas alimentées par un écoulement axisymétrique. Ces hétérogénéités d'alimentation sont dues aux sillages des aubages amont qui induisent des efforts instationnaires dont le premier harmonique de la fréquence est égal au produit du nombre d'aubes amont par la vitesse de rotation. Si cette fréquence ou un de ses multiples est proche d'un des modes propres de l'aubage alors celui-ci pourra se mettre à vibrer et si l'amortissement structurel n'est pas assez important une rupture prématurée de l'aubage se produira.

1.1.- Modèle aérodynamique

Bien que les sillages soient d'origine visqueuse, les efforts aérodynamiques qu'ils engendrent peuvent être calculés à l'aide d'un modèle du type fluide parfait (réf [7]).

Les équations d'Euler complètes sont écrites sur une nappe de courant :

Equation de continuité :

$$\frac{\partial \rho b r}{\partial t} + \frac{\partial \rho b r W_m}{\partial m} + \frac{\partial \rho b W_\theta}{\partial \theta} = 0$$

Equation de quantité de mouvement :

$$\frac{\partial \rho b r W_m}{\partial t} + \frac{\partial b r (\rho W_m^2 + p)}{\partial m} + \frac{\partial \rho b W_m W_\theta}{\partial \theta} = p \frac{d b r}{d m} + \rho b (W_\theta + \omega r)^2 \frac{d r}{d m}$$

$$\frac{\partial \rho b r W_\theta}{\partial t} + \frac{\partial \rho b r W_m W_\theta}{\partial m} + \frac{\partial b (\rho W_\theta^2 + p)}{\partial \theta} = -(2 \omega r + W_\theta) b \rho W_m \frac{d r}{d m}$$

Equation d'énergie :

$$\frac{\partial \rho b r E}{\partial t} + \frac{\partial (\rho E + p) b r W_m}{\partial m} + \frac{\partial (\rho E + p) b W_\theta}{\partial \theta} = \rho b r^2 \omega^2 W_m \frac{d r}{d m}$$

Equation d'état :

$$\frac{p}{\rho} = RT$$

Le domaine de calcul est limité à un seul canal interaube, le maillage en H comporte 80 x 15 points (figure n°2).

Le *schéma numérique de résolution* est du type explicite, il fait appel à une formulation du type volumes finis. Il appartient à la classe des schémas de Lax-Wendroff, sa précision est du second ordre en espace et en temps (réf.8)

Afin d'éviter les oscillations numériques en présence de forts gradients, une dissipation numérique du second ordre est ajoutée au schéma numérique (réf.9).

Les conditions aux limites sont traitées à l'aide de la théorie des relations de compatibilité (réf. 10) :

- Sur la frontière amont [AA'] la pression totale, la température totale ainsi que l'angle de l'écoulement sont imposés. Ces grandeurs sont issues d'une modélisation du sillage de la roue amont. La formulation analytique repose sur la théorie de Prandtl, l'ajustement des coefficeints a été réalisé à l'aide de mesures effectuées sur une grille d'aubes de compresseur.

- Sur les frontières amont [AB] et [A'B'] une condition de coupure est imposée. Afin de limiter le domaine de calcul à un seul canal interaube qu'elle que soit la fréquence de l'excitation, la condition de continuité à travers la frontière est réalisée à l'aide d'une hypothèse de périodicité spatio-temporelle (réf.3).

- Sur le profil [BC] et [B'C'] une condition de glissement est imposée.

- Sur les frontières aval [CD] et [C'D'] une condition de sillage associée à une hypothèse de périodicité spatio-temporelle assure la continuité de la pression, de la masse volumique et de la vitesse normale.

- A l'aval, la frontière [DD'], où une condition de non réflexion est imposée.

Après un premier calcul stationnaire, un calcul instationnaire est conduit pendant une quinzaine de périodes. Les pressions instationnaires obtenues sur le profil sont décomposées en série de Fourier. Ce calcul est effectué pour plusieurs coupes et les résultats sont mixés avec une même référence de phase. Les pressions instationnaires en chaque point du redresseur sont alors introduites dans le modèle de réponse mécanique.

1.2. Modèle mécanique

La réponse mécanique de la structure aux excitations aérodynamiques est calculée à l'aide d'une caractérisation modale du redresseur. Cette base modale est calculée à l'aide d'une modélisation éléments finis (SAMCEF).

Un amortissement structurel et aérodynamique est introduit dans le modèle de réponse. Le champ de contrainte en chaque point de la pâle est alors déterminé.

2 - RESULTATS

Une étude paramètrique a été conduite sur un redresseur comportant 120 aubes et soumis à l'excitation de la roue mobile comportant 64 aubes.

L'aubage du redresseur étant encastré en pied et en tête les calculs aérodynamiques ont été réalisés uniquement sur la coupe médiane. Les conditions de fonctionnement stationnaires sont les suivantes :

$$\beta 1 = -22.6°$$
$$MW1 = 0.470$$
$$\beta 2 = -3.9°$$
$$MW2 = 0.435$$

La répartition du nombre de Mach (fig. 3) fait apparaître une survitesse au bord d'attaque intrados du fait d'une incidence négative du profil, en effet le point de fonctionnement pour lequel tous les calculs ont été menés est placé en hors adaptation.

Le sillage du rotor amont induit sur le redresseur une fluctuation de l'angle de l'écoulement amont de l'ordre de + 2° à - 20° par rapport à l'angle moyen (fig.4).

Le module du premier harmonique des pressions instationnaires (fig. 5) présente des niveaux comparables sur l'extrados et l'intrados de l'aube. En revanche les phases (fig. 6) sont assez différertes, le gradient de vitesse stationnaire induit des gradients de la phase des pressions instationnaires. Ainsi les zones au bord d'attaque de l'extrados et de l'intrados présentent des évolutions rapides de phase tandis que sur la partie aval de l'intrados la phase est proche de zéro et n'évolue pas.

Le calcul de la réponse mécanique induite par ces fluctuations de pression instationnaire permet de déterminer la contrainte maximum rencontrée sur l'aubage (fig. 7).

Influence de la distance rotor-stator

Sur la figure n°8 est représentée l'évolution du maximum de contrainte avec la distance du bord de fuite du rotor au bord d'attaque du stator. Lorsque la distance est doublée, la contrainte ne diminue que de 20 %.

Ce paramètre n'apparaît donc pas comme déterminant dans la réponse mécanique de l'aubage.

Influence des pertes de la roue amont

Les pertes de pression totale de la roue mobile amont ont un effet nettement plus marqué sur les contraintes.

Ainsi lorsque celles-ci passent d'une valeur de 7 % à 3,5 % la contrainte diminue de 60 %. La réponse de l'aubage à ces variations de pertes est quasi-linéaire dans le domaine étudié (fig.9).

Cette étude montre l'importance au niveau de la conception de minimiser les pertes non seulement pour l'obtention de performances élevées mais aussi pour assurer la tenue mécanique de certaines roues.

Influence du nombre d'aubes.

Cette étude a été réalisée en modifiant le nombre d'aubes du stator mais en conservant les mêmes aubes, par conséquent le pas relatif et donc la charge stationnaire évolue. La longueur du maillage entre l'amont et le bord d'attaque a été conservée. Le calcul de la réponse mécanique montre qu'il existe un nombre d'aubes optimum de sorte que la contrainte soit minimale (fig. 10).

3 - CONCLUSIONS

L'ensemble des études effectuées sur les interactions inter-roues permettent de mieux comprendre l'influence des sillages sur le comportement mécanique des aubages.

Ces premières études paramètriques ont permis de dégager l'importance de certains choix de dimensionnement.

L'utilisation de ces codes de calcul au niveau de la conception aéromécanique des compresseurs devrait éviter les problèmes de tenue mécanique des aubages. Le développement des futurs moteurs en sera accéléré.

REMERCIEMENTS

7-4

REFERENCES

1/ Lubomsky J.F. "Status of NASA Full-Scale Engine Aeroelasticity Research" AIAA Paper 80-36906- 1980

2/ Lynn E. Snyder and Donald W.Burns "Forced vibration and flutter design methodology" AGARD O GRAPH N°298

3/ Joubert H. "Supersonic Flutter in Axial Flow Compressors" Unsteady Aerodynamics of Turbomachines and Propellers Cambridge, England U.K. 1984.

4/ Gerolymos G. "Numerical integration of the 3D unsteady Euler equations for flutter analysis in axial flow compressors" 33nd ASME Amsterdam, 1988.

5/ Lecordix J.L., Vincent B., Henry R. Mechanical Evaluation of the aeroelastic behaviour of a fan blade 9th ISABE Cincinnati June 1987.

6/ Quiniou H., Etudes théoriques d'Aéroélasticité dans les compresseurs aéronautiques. Bulletin SFM Octobre 1988.

7/ Giles M. "Calculation of unsteady Wake Rotor Interaction" AIAA paper n°87-0006.

8/ Ni R.H. "Multiple Grid scheme for solving the Euler Equations "AIAA Journal, November 1982;

9/ Lerat A., Sides J. "Calcul numérique d'écoulements transsoniques instationnaires" T.P. ONERA n°1977-19.

10/ Viviand H., Veuillot J.P. "Méthodes pseudo-instationnaires pour le calcul d'écoulement transsonique" T.P. ONERA n°1978-4.

Efforts instationnaires

Dynamique de la structure

Exitation forcée
force instationnaire
$\neq$ F (mouvement de l'aube)

C

Amortissement structurel

K

Amortissement aérodynamique
force instationnaire =
F (mouvement de l'aube)

$$\omega = \sqrt{K/M}$$

$$M\ddot{q} + C\dot{q} + Kq = Fa\,\sin\omega t$$
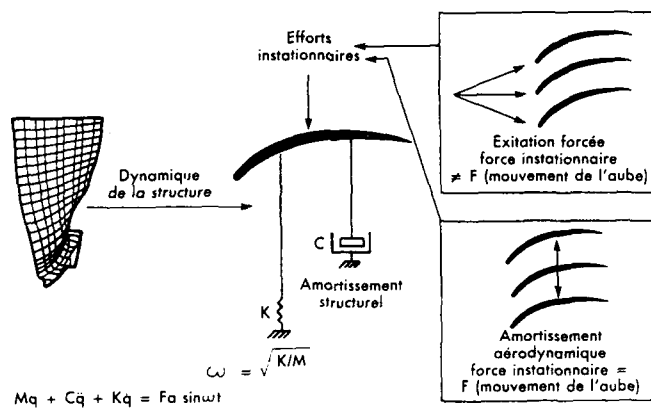
Figure N° 1 : Réponse mécanique aux excitations aérodynamiques
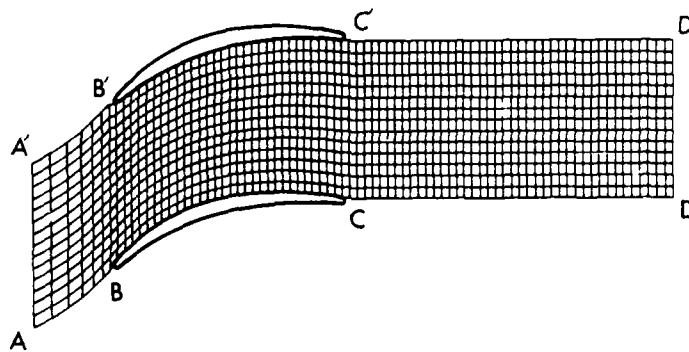
Figure N° 2 : Maillage 80X15 points
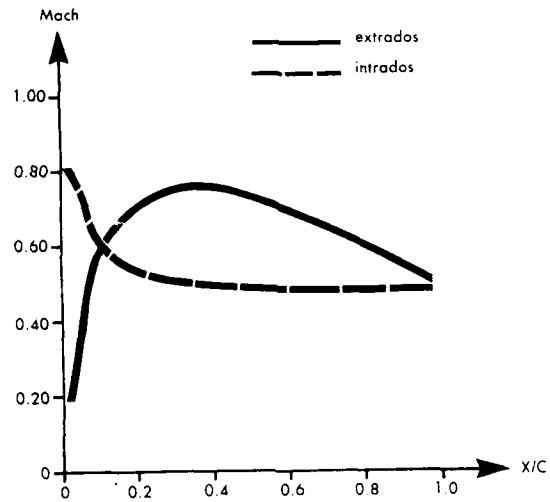
Figure N° 3 : Répartition de nombre de Mach stationnaire
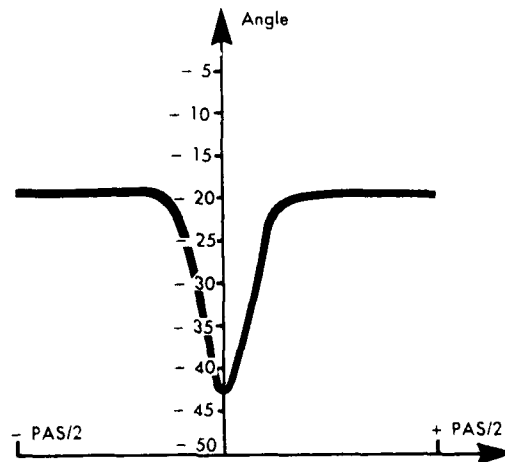
Figure N° 4 · Fluctuation de l'angle amont
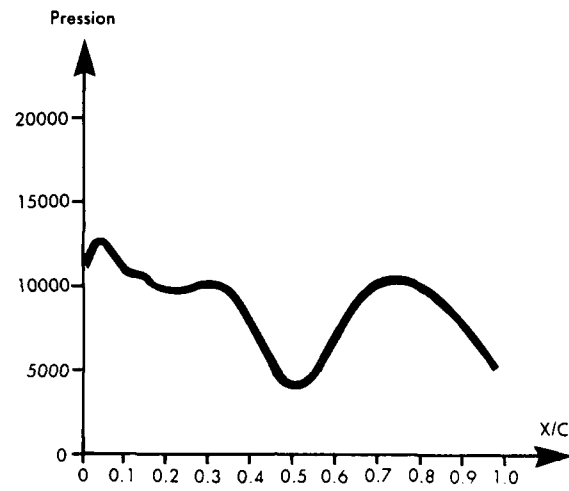
Figure N° 5 a : Extrados

Figure N ⁵ b : Intrauos

Figure N° 5 : Répartition du module du premier harmonique de pression

7-8
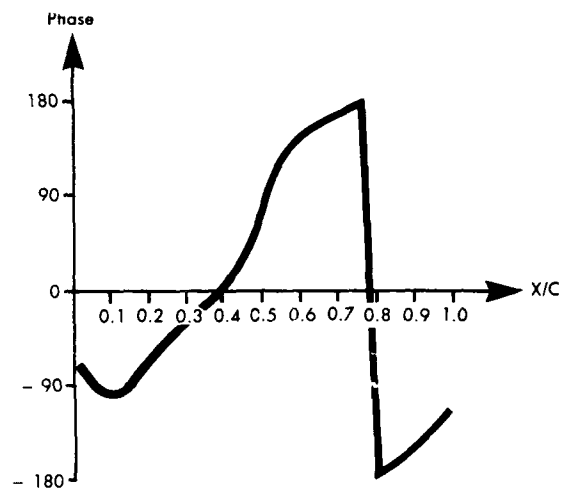
Figure N° 6 a : Extrados
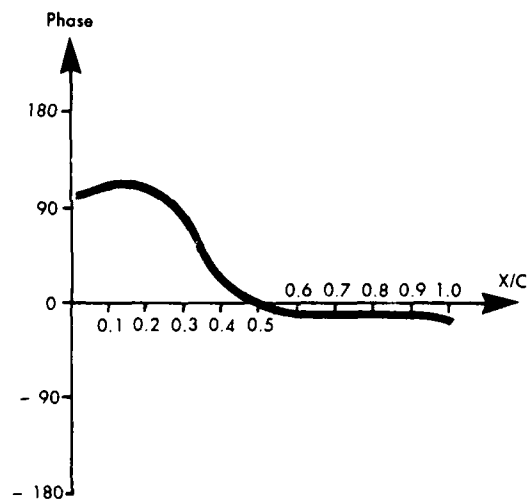
Figure N° 6 b : Intrados

Figure N° 6 : Répartition des phases du premier harmonique de pression
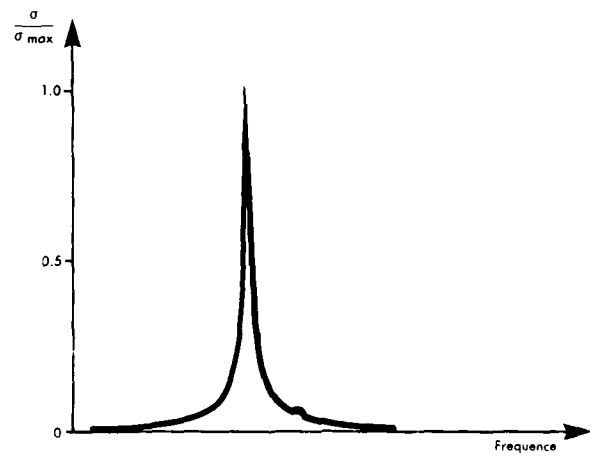
Figure N° 7 : Réponse mécanique de l'aubage
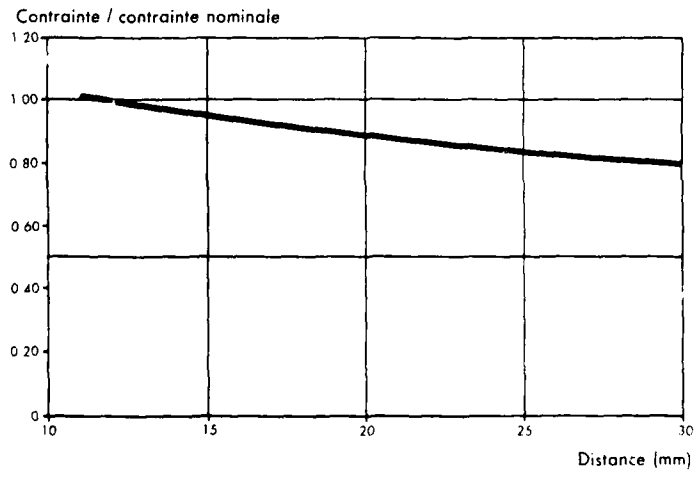
Figure N° 8 : Evolution de la contrainte maximum en fonction de
la distance inter-roue

Contrainte / contrainte nominale
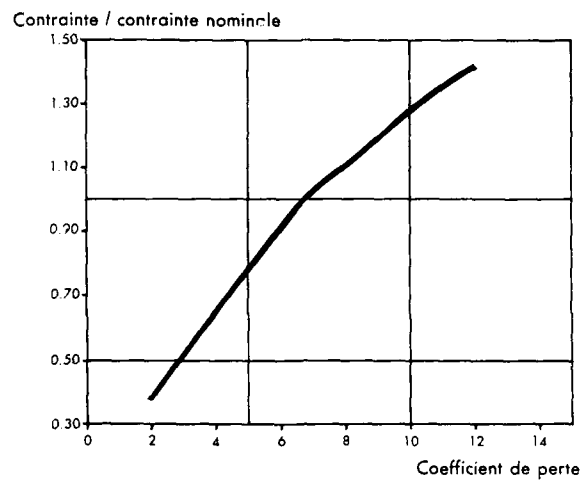
Figure N° 9 : Evolution de la contrainte maximum en fonction du
coefficient de perte de la roue amont

Contrainte / contrainte nominale
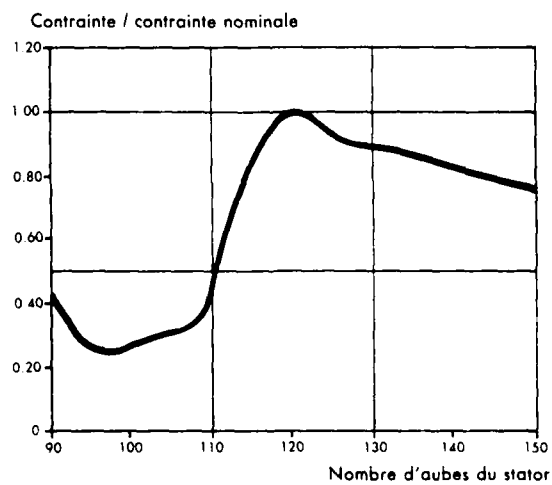
Figure N° 10 : Evolution de la contrainte maximum en fonction du
nombre d'aubes du redresseur

DISCUSSION

A.Klose - M T U Munich, Germany
   (1) In order to calculate vibration amplitudes you have to know the mechanical damping. Do you calculate this mechanical damping or do you use values given by the experience?

Author's respone :
   The mechanical model uses an experimental value for mechanical damping.The aerodynamical damping is obtained by means of an Euler code calculation.

   (2) In paper by Servaty and Gallus, the authors use MacCormack's scheme to solve the Euler equations whereas you use the Lax-Wendroff scheme. Could you give the reasons?

Author's response :
   To solve the Euler code the MacCormack or the Lax-Wendroff schemes are used alternatively. MacCormack is preferred for supersonic flows and Lax-Wendroff for subsonic flows.Furthermore, Lax-Wendroff scheme seems to be stronger in order to take into account high angles of attack. Some comparisons have been made between the two schemes and there is no significant difference.

   (3) Did the authors make any comparison with experiments?

Author's response :
   Up to now, no comparison has been made with experiments.

M.L.G. Oldfield - Oxford University, U.K.
   Can the unsteady prediction code presented predict unsteady separations near the blade leading edge? It is very likely that the strong wakes would cause separations on a real blade.

Author's response :
   The code presented is an inviscid code, so it is impossible to take into account with this method the separation that could take place near the leading edge.

S-1

UNSTEADY BLADE LOADS DUE TO WAKE INFLUENCE

S. Servaty
MTU Motoren- und Turbinen-Union
München GmbH
Dachauer Straße 665
8000 München 50
Germany

and   H.E. Gallus
Institut für Strahlantriebe und
Turboarbeitsmaschinen
RWTH Aachen
Templergraben 55
5100 Aachen
Germany

Summary

An algorithm for calculating unsteady blade forces and moments due to incoming wakes is presented. The mathematical model describes the unsteady two-dimensional flow through compressor and turbine cascades. Only inviscid transport of the wake is considered.

The non-linear Euler-equations in conservative law form are solved by a combined method. MacCormack's explicit predictor-corrector scheme is used at interior points. Time-dependent boundary conditions are formulated by means of a characteristics method.

Fundamental studies and several test cases are presented to check the algorithm. Comparisons with experimental results are discussed as well.

Nomenclature

b	width	t	time, spacing
c	chord length	u	velocity in x-direction
e	energy	U	flow values $(\varrho, \varrho u, \varrho v, e)$
F, G	flux vectors	v	velocity in y-direction
h	depth of the wake	x,y	coordinates
I	unity matrix	ξ,η	coordinates for transformation
J	Jacobian	γ	ratio of specific heats
p	pressure	ϱ	density

Subscripts

a	ambient
D	wake
G	cascade
P	profile
t	total value

Superscripts

n	value at time t
n+1	value at time t + Δt
$\wedge$	value after the transformation
——	result of predictor-step
——	result of corrector-step
$\sim$	fluctuations

Introduction

Design of modern axial-flow turbomachinery bladings has led to highly loaded, slim and comparatively long blades. These blades are more sensitive to flow induced and self excited vibrations. The great number of papers dealing with this subject that have been presented during the last years demonstrates the importance of these problems, see e.g. /1/ and /2/.

This paper presents a method for computing the wake influence on turbomachinery bladings. It is part of a research program that aims at calculating the unsteady blade loads on oscillating cascades due to wake influence and aerodynamic damping. An extensive description of the algorithm used and results for aerodynamic damping are given in a companion paper /3/.

Within this contribution some basic remarks concerning the choice of a suitable numerical method for handling the problem of wake interaction and comparisons with linearized theory are given. Furthermore the influence of the form of the wake prescribed at the inlet on the pressure distribution is shown.

Governing Equations

Although the wakes are generated by viscous forces experimental results show that their transport is mainly an inviscid phenomenon. Therefore the problem of wake interaction may be modelled by the Euler-equations which correctly describe the transport of vorticity and the entropy-production due to shocks:

$$\frac{\partial}{\partial t} U + \frac{\partial}{\partial x} F(U) + \frac{\partial}{\partial y} G(U) = 0 \tag{1}$$

where

$$U = \begin{bmatrix} \varrho \\ m \\ n \\ e \end{bmatrix} \qquad F(U) = \begin{bmatrix} m \\ m^2/\varrho + p \\ mn/\varrho \\ (e+p)\, m/\varrho \end{bmatrix} \qquad G(U) = \begin{bmatrix} n \\ mn/\varrho \\ n^2/\varrho + p \\ (e+p)\, n/\varrho \end{bmatrix}$$

and

$$e = \frac{p}{\gamma-1} + \frac{1}{2} \varrho(u^2 + v^2)$$

This system of four partial differential equations is solved by a combined method using a difference method at interior points and a bicharacteristics method at the boundaries. The physical region (x,y) is mapped onto a computational domain (ξ,η) by means of the numerical transformation of Thompson, Thames and Mastin (4). Subject to this transformation the partial differential equation system (1) can be written (see /5/):

$$\frac{\partial}{\partial t} \hat{U} + \frac{\partial}{\partial \xi} \hat{F} + \frac{\partial}{\partial \eta} \hat{G} = 0 \qquad (2)$$

where

$$\hat{U} = \frac{U}{J} \qquad \hat{F} = \frac{1}{J}\left(U\frac{\partial\xi}{\partial t} + F\frac{\partial\xi}{\partial x} + G\frac{\partial\xi}{\partial y}\right) \qquad \hat{G} = \frac{1}{J}\left(U\frac{\partial\eta}{\partial t} + F\frac{\partial\eta}{\partial x} + G\frac{\partial\eta}{\partial y}\right)$$

with the Jacobian
$$J = \frac{\partial\xi}{\partial x}\cdot\frac{\partial\eta}{\partial y} - \frac{\partial\xi}{\partial y}\cdot\frac{\partial\eta}{\partial x}$$

Choice of a numerical scheme

Several methods may be employed to solve the partial differential equation system (2) numerically. In the following two well-known schemes (an implicit and an explicit one) are briefly described and compared with each other using a simple test case.

Beam, Warming scheme:

A well-known representative for an implicit scheme is the ADI-method of Beam and Warming /6/ presented in 1978. One advantage of the implicit scheme is that a greater time step may be chosen than allowed by the CFL.-criterion /7/ for explicit methods. The stability and usefulness of this scheme has been shown in many applications (e.g. /8/, /9/, /10/, /11/). In the following a brief description is given.

The partial differential equation system (2) is linearized yielding

$$\frac{\partial\hat{U}}{\partial t} + \hat{A}(\hat{U})\frac{\partial\hat{U}}{\partial\xi} + \hat{B}(\hat{U})\frac{\partial\hat{U}}{\partial\eta} = 0$$

with the Jacobians

$$A = \begin{bmatrix} 0 & 1 & 0 & 0 \\ -\frac{1-\gamma}{2}v^2 - \frac{3-\gamma}{2}u^2 & (3-\gamma)u & (1-\gamma)v & \gamma-1 \\ -uv & v & u & 0 \\ -\frac{\gamma eu}{\rho}-(1-\gamma)(u^2+v^2)u & \frac{\gamma e}{\rho}-\frac{\gamma-1}{2}(3u^2+v^2) & (1-\gamma)uv & \gamma u \end{bmatrix}$$

$$B = \begin{bmatrix} 0 & 0 & 1 & 0 \\ -uv & v & u & 0 \\ -\frac{3-\gamma}{2}v^2 - \frac{1-\gamma}{2}u^2 & (1-\gamma)u & (3-\gamma)v & \gamma-1 \\ -\frac{\gamma ev}{\rho}-(1-\gamma)v(u^2+v^2) & (1-\gamma)uv & \frac{\gamma e}{\rho}\frac{\gamma-1}{2}(3v^2+u^2) & \gamma v \end{bmatrix}$$

and

$$\hat{A} = \frac{\partial\hat{F}}{\partial U} = \frac{\partial\xi}{\partial t}I + \frac{\partial\xi}{\partial x}A + \frac{\partial\xi}{\partial y}B$$

$$\hat{B} = \frac{\partial\hat{G}}{\partial\hat{U}} = \frac{\partial\eta}{\partial t}I + \frac{\partial\eta}{\partial x}A + \frac{\partial\eta}{\partial y}B$$

Using the trapezoidal formula and splitting the difference operators into the two coordinate directions results in the following solution scheme:

$$\left(I + \frac{\Delta t}{2} \frac{\partial}{\partial \xi} \hat{A}^n\right) \Delta \hat{U}^{\bullet} = -\Delta t \left(\frac{\partial \hat{F}}{\partial \xi} + \frac{\partial \hat{G}}{\partial \eta}\right)^n$$

$$\left(I + \frac{\Delta t}{2} \frac{\partial}{\partial \eta} \hat{B}^n\right) \Delta \hat{U}^n = \Delta \hat{U}^{\bullet}$$

$$\hat{U}^{n+1} = \hat{U}^n + \Delta \hat{U}^n$$

(For details see /6/ and /8/).

Due to the approximate factorization a third order term is neglected (ref. /12/). This does not disturb the second order accuracy of the scheme but a damping term of higher order has to be added to guarantee the stability of the method.

MacCormack scheme:

The explicit predictor-corrector scheme has been introduced by MacCormack /13/ already in 1969. In the meantime it has been applied to a wide range of problems. Examples for some recent work can be found e.g. in /14/ and /15/. The two steps are:

Predictor-Step:
$$\overline{\hat{U}^{n+1}}_{i,j} = \hat{U}^n_{i,j} - \frac{\Delta t}{\Delta \xi}\left[\hat{F}^n_{i+1-\delta,j} - \hat{F}^n_{i-\delta,j}\right] - \frac{\Delta t}{\Delta \eta}\left[\hat{G}^n_{i,j+1-\epsilon} - \hat{G}^n_{i,j-\epsilon}\right]$$

Corrector-Step:
$$\overline{\hat{U}^{n+1}}_{i,j} = \hat{U}^n_{i,j} - \frac{\Delta t}{\Delta \xi}\left[\overline{\hat{F}^{n+1}}_{i+\delta,j} - \overline{\hat{F}^{n+1}}_{i-1+\delta,j}\right] - \frac{\Delta t}{\Delta \eta}\left[\overline{\hat{G}^{n+1}}_{i,j+\epsilon} - \overline{\hat{G}^{n+1}}_{i,j-1+\epsilon}\right]$$

Averaging yields the value at the new time level n + 1:
$$\hat{U}^{n+1}_{i,j} = \frac{1}{2}\left[\overline{\hat{U}^{n+1}}_{i,j} + \overline{\overline{\hat{U}^{n+1}}}_{i,j}\right]$$

Details of the application of this numerial scheme are described in /3/.

1D-Test case

To compare the two methods outlined above the unsteady flow in a finite duct has been calculated as a first test case (fig. 1). At the upstream boundary total pressure p_t and total temperature T_t are prescribed. The flux variables in the duct are also determined by these stagnation values since the downstream end is closed by a diaphragm. At time $t = 0$ the pressure $p_a < p_t$ is imposed at the right boundary and causes a centered expansion wave propagating upstream. At the left boundary this wave is reflected as a weaker compression wave that moves downstream and reflects in opposite sense from the right boundary. This process of expansion and compression is repeated until a uniform steady flow is reached throughout the duct. This starting process has been calculated using the two methods described above. The result is shown in fig. 2, where each of the two schemes is compared with a characteristics method. The first part shows that both, MacCormack scheme and characteristics method yield a smooth curve reaching the steady state solution.

On the other hand, it is demonstrated in fig. 2 that the Beam-Warming scheme needs an additional damping (here an explicit fourth order term has been added) to achieve a smooth curve without wiggles. Nevertheless, the steady state solution is reached with this scheme as well. (Since for both schemes boundary points are calculated with the characteristics method this example shows also that it is possible to combine such two numerical methods.)

2D-test case

To examine the influence of the numerical damping a simple two-dimensional test case as shown in fig. 3 has been set up, where a velocity distribution in y-direction is prescribed at the left boundary. Starting with the known steady state values for uniform inflow the development of the flow in x-direction is calculated by MacCormack and Beam-Warming scheme. Having reached a converged state the velocity distribution in y-direction is checked at every axial position.

Fig. 4 shows the result: the velocity defect prescribed at the inlet decreases almost linearly when using Beam-Warming algorithm due to the artifical dissipation. Since no additional damping is used with MacCormack scheme the velocity distribution remains nearly constant as it should be for an inviscid calculation.

Boundary conditions

According to the results of the comparison presented above the numerical algorithm for computing the 2-dim., unsteady, subsonic flow uses MacCormack's scheme for calculating the flow variables at the interior points. The boundaries are treated by the bicharacteristics method according to Butler /16/ and Delaney /17/. The application of this algorithm is described in detail in references 11, 18.

Following boundary conditions are prescribed (cf. Fig. 5):

- At the inlet the wake of the preceding cascade is described by a circumferential distribution of flow velocity. A symmetrical distribution according to a gaussian curve in the rotating frame of reference has been assumed. From the given velocity the corresponding distribution of total pressure, total temperature and flow angle is calculated and used as boundary condition at the inlet.

- At the downstream boundary static pressure is assumed known.

- Flow tangency condition is used at the blade profiles.

- Downstream of the blading, the boundaries R5 and R6 are represented by the slipstreams leaving the trailing edge of each blade. This model has been used by Butler /16/, Pandolfi /19/ and other authors. It requires that the pressure and the component of the velocity normal to this line are continuous, whereas the tangential components will show a jump representing the concentrated vorticity.

- The periodic boundaries (R5 and R6) are handled by a special treatment presented by Erdos and Alzner /20/ in 1977. Taking into account that each channel experiences the same states with a constant phase lag the computational domain can be reduced to a single channel. This method has been used in the calculation of oscillating cascades by several authors (e.g. Fransson /21/) and is described in more detail in /3/.

Comparison with linearized theory

To validate the method outlined above a cascade of flat plates is considered. At the inlet boundary a sinusoidal wake is assumed. The amplitude being small enough this configuration (cf. fig. 6) can be analysed using the program LINSUB developed by Whitehead /22/ based upon the theory of Smith /23/.

A comparison between the results of LINSUB and the present method (EULER) are shown in fig. 6. The results of the EULER-method are non-dimensionalized in exactly the same manner as done by LINSUB, using the product of the mean density, the mean speed, and the maximum wake velocity normal to the blade. To be able to compare phase results the wake definitions at the inflow are specified such that the centerline of the wake passes through the blade leading edge at the beginning of the period. The agreement between the results obtained by the linearized theory and by the EULER method are quite well with respect to amplitude as well as phase lag.

As a second example a configuration according to fig. 7 has been calculated. The pitch of the wake being twice the pitch of the cascade ($t_D = 2*t_G$) this example is also a test case for the special periodicity condition. The results of the two methods are compared in fig. 7. Amplitude of differential pressure and phase lag agree fairly well.

Results for a compressor cascade

The results for a flat plate cascade being quite promising the method has been applied to a real compressor cascade. First calculations /24/ indicated that the mesh size had to be refined significantly to get a proper resolution of the wake. Using a computational grid with smaller cell size it was found necessary to add a little amount of numerical damping to the MacCormack scheme for the sake of stability. A fourth order damping term according to Jameson et al. /25/ was introduced. The effect of this damping on the development of the wake is shown in fig. 8 using the previously presented test case (see fig. 3). With a damping factor of $\varepsilon = 10^{-4}$ the wake depth reduces only by 1.5%.

As a first example the effect of a sinusoidal velocity distribution prescribed at the inlet has been calculated. The computed pressure distribution is presented in fig. 9. On the pressure side the amplitude of the dynamic pressure continuously decreases. while on the suction side a varying amplitude is observed with a local minimum at $x/b_p \approx 0.4$ and local maxima at $x/b_p \approx 0.25$ and $x/b_p \approx 0.6$. A 3D-plot of the pressure distribution on suction and pressure side is given in fig. 10. The temporal shift in the pressure signals indicates that the influence of the velocity defect is convected downstream with approximately mean flow velocity.

The pressure amplitudes shown in fig. 11 are due to a gaussian velocity distribution prescribed at the inlet. Compared with fig. 9 (sinusoidal wake prescribed) the pressure amplitudes are larger and a local maximum appears on the pressure side at $x/b_p \approx 0.6$, too. The 3D-plot of the pressure fluctuations in fig. 12 shows the influence of higher harmonics, as expected according to the gaussian velocity distribution.

For the calculations presented above an H-type computational grid with 253x65 points has been used. Compared with a mesh consisting of 76x25 points the calculated dynamic pressure amplitudes are approximately twice as high on the refined grid. Nevertheless, measured pressure fluctuations /26/ are even larger so that further mesh refinement is necessary.

Conclusion

A method for computing wake interaction effects in axial turbomachines is presented. The non-linear Euler-equations describing the two-dimensional, unsteady, compressible, inviscid flow are solved by a combined algorithm. MacCormack's predictor-corrector scheme is used at interior points while boundaries are handled by means of a bicharacteristics method.

Using a simple test case MacCormack's scheme and the ADI scheme of Beam-Warming are compared with each other. Since the explicit method requires less damping the depth of the wake remains nearly constant.

The algorithm is compared with linearized theory for a flat plate cascade. Results are very good and demonstrate the feasibility of the special periodicity condition that is used to restrict the computational domain to one channel even for different cascade and wake pitches.

The calculations for a real compressor cascade indicate the influence of the wake profile prescribed at the inlet boundary. Though a mesh with 253x65 grid points has been used comparison with experimental results shows that further mesh refinement is necessary.

References

/1/   Whitehead, D.S.:
      Proceedings of the 3rd Symposium on Unsteady Aerodynamics of Turbomachines and Propellers, Cambridge (GB), Sept. 1984

/2/   Gallus, H.E., Servaty, S.:
      Proceedings of the 4th Symposium on Unsteady Aerodynamics and Aeroelasticity of Turbomachines and Propellers, Sept. 1987

/3/   Kau, H.-P., Gallus, H.E.:
      Numerical Investigation of Unsteady Flow in Oscillating Turbine and Compressor Cascades
      AGARD Propulsion and Energetics Panel 74th Specialists' Meeting, 1989

/4/   Thompson, J.F., F.C. Thames and C.W. Mastin:
        Boundary-Fitted Curvilinear Coordinate Systems for Solution of Partial Differential Equations of Fields
        Containing Any Number of Arbitrary Two-Dimensional Bodies
        NASA CR-2729, 1977

/5/   Viviand, H.:
        Formes Conservatives des Equations de la Dynamique des Gaz
        La Recherche Aerospatiale, 1974, pp. 65-68

/6/   Warming, R.F., and R.M. Beam:
        On the Construction and Application of Implicit Factored Schemes for Conservation Laws
        SIAM-AMS Proceedings, Vol. 11 (1978)

/7/   Courant, R., Friedrichs, K., Lewy, H.:
        Über die partiellen Differentialgleichungen der mathematischen Physik
        Math. Ann., Vol. 100, 1928, pp. 32-74

/8/   Steger, J.L.:
        Implicit Finite-Difference Simulation of Flow About Arbitrary Two-Dimensional Geometries
        AIAA-Journal, Vol. 16, No. 7, July 1978

/9/   Chaussee, D.S., and T.H. Pulliam:
        Two-Dimensional Inlet Simulation Using a Diagonal Implicit Algorithm
        AIAA-Journal, Vol. 19, No. 2, Feb. 1981

/10/   Steger, J.L., Pulliam, T.H., and Chima, R.V.:
        An Implicit Finite Difference Code for Inviscid and Viscous Cascade Flow
        AIAA-13th Fluid & Plasma Dynamics Conference, AIAA-80-1427, July 1980, Snowmass, Colorado

/11/   Holtmann, H.:
        Ein numerisches Verfahren zur Berechnung der instationären, zweidimensionalen Strömung durch schwingende
        Beschaufelungen axialer Turbomachinen
        Diss. RWTH Aachen, 1984

/12/   Beam, R.M., Warming, R.F.:
        Implicit Numerical Methods for the Compressible Navier Stokes and Euler Equations
        VKI-Lecture Series 1982-04, 1982

/13/   MacCormack, R.W.:
        The Effect of Viscosity in Hypervelocity Impact Cratering
        AIAA-Paper No. 69-354, May 1969

/14/   MacCormack, R.W.:
        Current Status of Numerical Solutions of the Navier Stokes Equations
        AIAA-Paper No. 85-0032, Jan 1985

/15/   Joubert, H.:
        Supersonic Flutter in Axial Flow Compressors
        Proceedings of the 3rd Symposium on Unsteady Aerodynamics of Turbomachines and Propellers
        Cambridge (GB), Sept. 1984

/16/   Butler, D.S.:
        The Numerical Solution of Hyperbolic Systems of Partial Differential Equations in Three Independent Variables
        Proceedings of the Royal Society, Vol. A255 (1960)

/17/   Delaney, R.:
        A Second-Order Method of Characteristics for Two-Dimensional Unsteady Flow with Application to Turbo-
        machinery Cascades
        Ph.D. Thesis, Iowa State University, May 1974

/18/   Holtmann, H., Servaty, S. Gallus, H.E.:
        Computation of the Subsonic Flow Field through Oscillating Compressor and Turbine Cascades
        Proceedings of the 3rd Symposium on Unsteady Aerodynamics of Turbomachines and Propellers, Cambridge
        (GB), Sept. 1984

/19/   Pardolfi, U.:
        Numerical Experiments on Unsteady Flows through Vibrating Cascades, Proceedings of the Symposium on
        Aeroelasticity in Turbomachines, Lausanne, Switzerland, Sept. 1980

/20/   Erdos, J.I., and E. Alzner:
        Numerical Solution of Periodic Transonic Flow Through a Fan Stage
        AIAA-Journal, Vol. 15, No. 11, Nov. 1977

/21/   Fransson, T.H.:
        Numerical Investigation of Unsteady Subsonic Compressible Flow Through an Oscillating Cascade
        Diss. EPFL, Lausanne, 1986

/22/   Whitehead, D.S.:
        Classical Two Dimensional Methods, in AGARD-Manual on Aeroelasticity in Axial-Flow Turbomachines,
        Vol. 1, Unsteady Turbomachinery Aerodynamics, AGARD-AG-298, ed. Platzer, M.F. and Carta, F.O., 1987

/23/   Smith, S.N.:
        Discrete Frequency Sound Generation in Axial Flow Turbomachines
        University Engineering Dept., Cambridge. Report and Memoranda No. 3709, 1972

/24/   Servaty, S., Gallus, H.E., Kau, H.-P.:
Computation of Aerodynamic Blade Loads due to Wake Influence and Aerodynamic Damping of Turbine and
Compressor Cascades
Proceedings of the 4th Symposium on Unsteady Aerodynamics and Aeroelasticity of Turbomachines and
Propellers, Sept. 1987

/25/   Jameson, A., Schmidt, W., Turkel, E.:
Numerical Solutions of the Euler Equations by Finite Volume Methods Using Runge-Kutta Time-Stepping
Schemes
AIAA-Paper 81-1259, June 1981

/26/   Grollius, H.:
Experimentelle Untersuchung von Rotor-Nachlaufdellen und deren Auswirkungen auf die dynamische Be͏ stung
axialer Verdichter- und Turbinengitter
Diss. RWTH Aachen, 1981
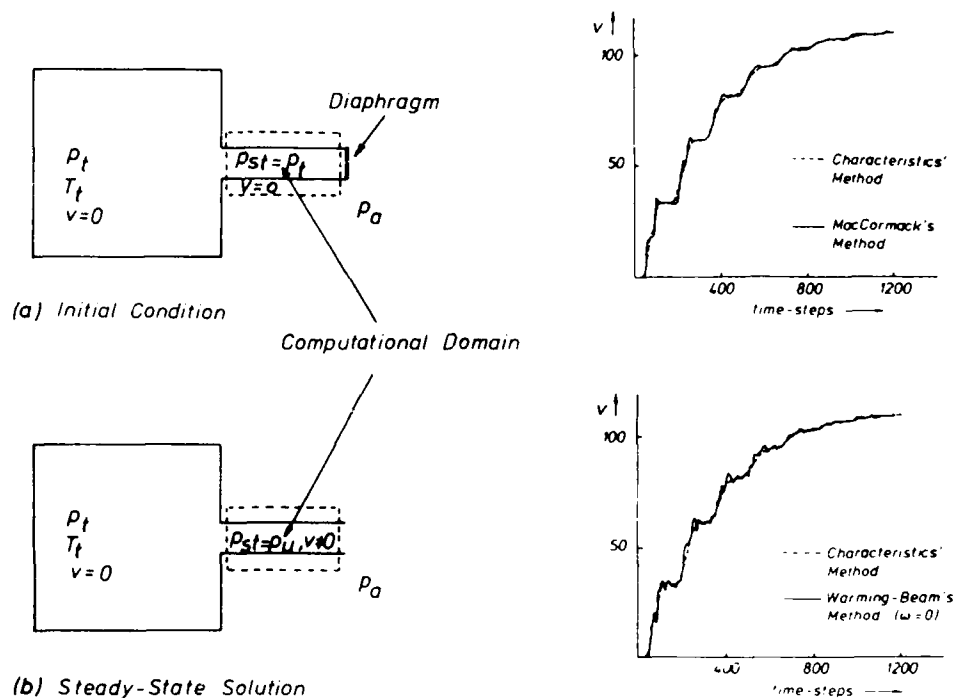
Fig. 1: One-dimensional test case: flow in a duct
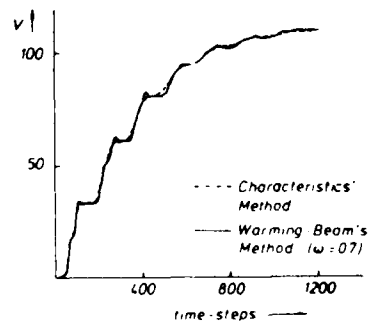
Fig. 2: Velocity distribution for 1D test case during starting process
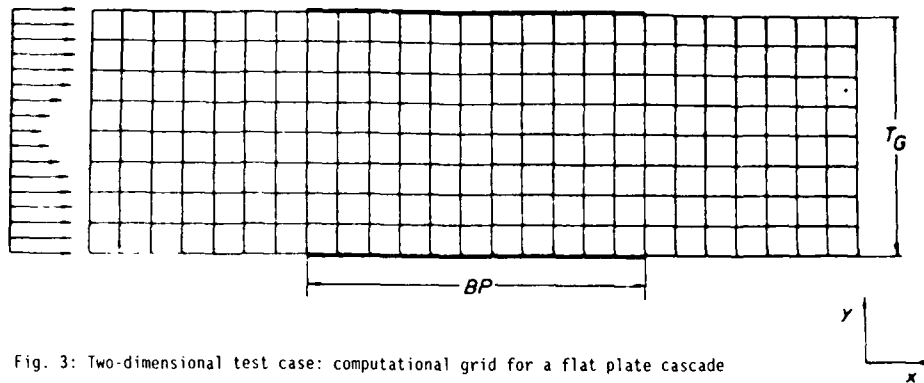
Fig. 3: Two-dimensional test case: computational grid for a flat plate cascade
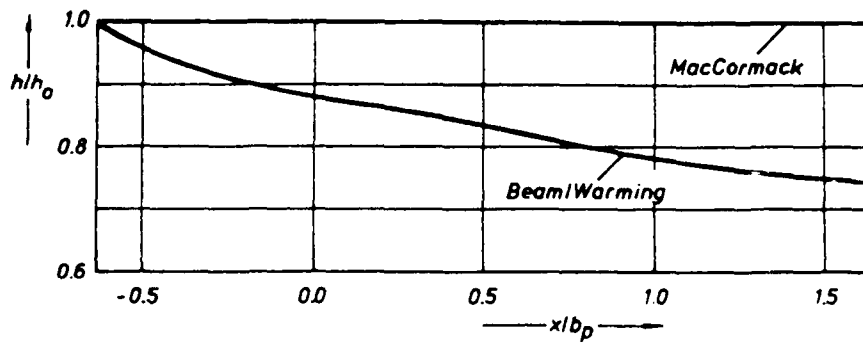
Fig. 4: Comparison of relative wake depths using different numerical methods
(h$_0$: wake depth prescribed at inlet)

R1   - Upstream boundary

R2   - Downstream boundary

R3,R4 - Blade surface

R5,R6 - Slipstream

R7,R8 - Periodical boundary
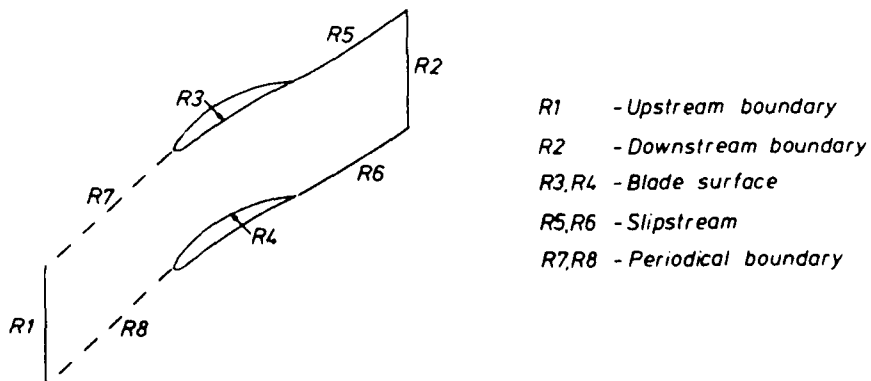
Fig. 5: Computational domain
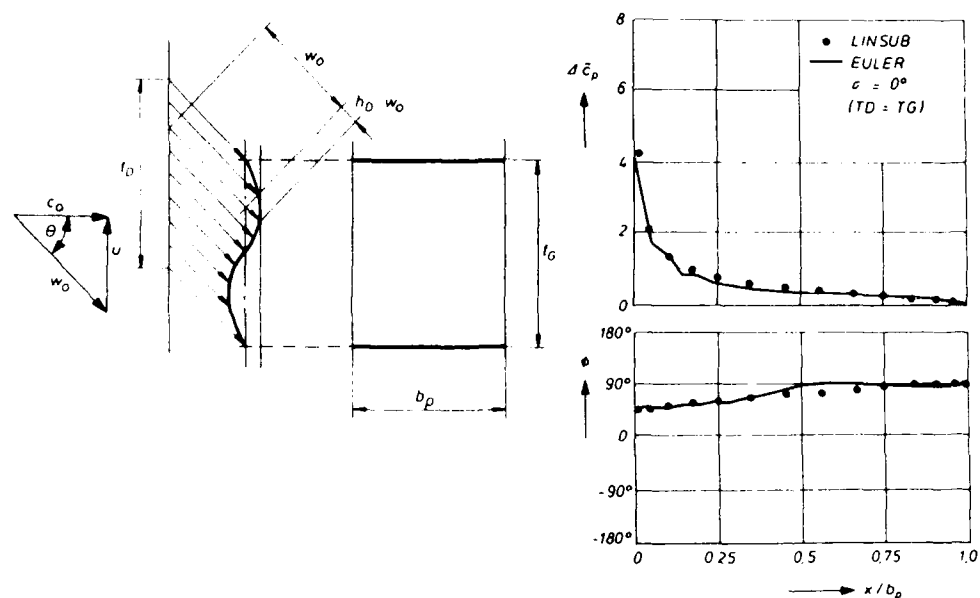
Fig. 6: Comparison of EULER calculation with linearized theory for equal cascade and wake pitch
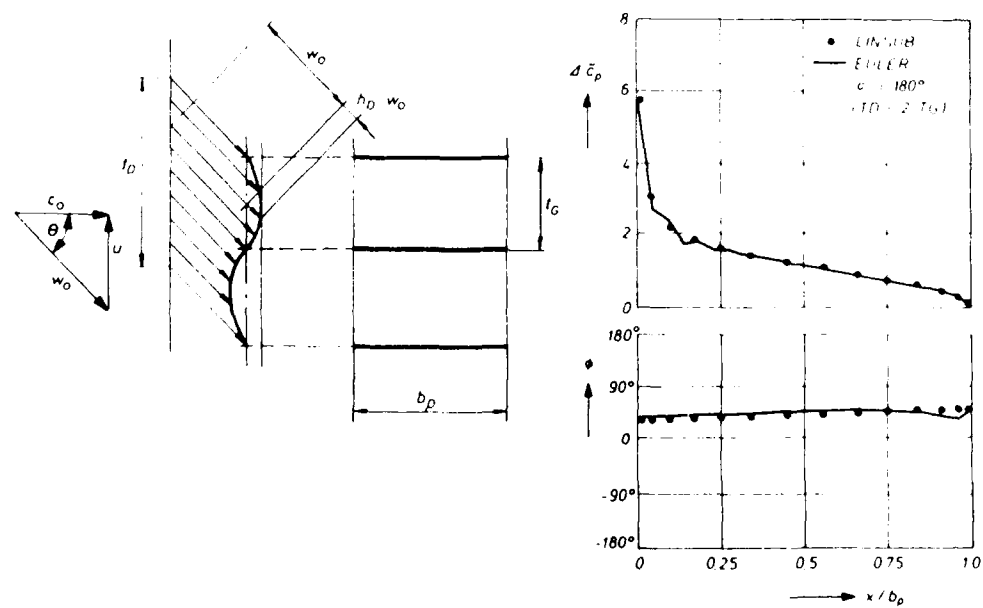
Fig. 7: Comparison of EULER algorithm with linearized theory for wake pitch being twice the cascade pitch
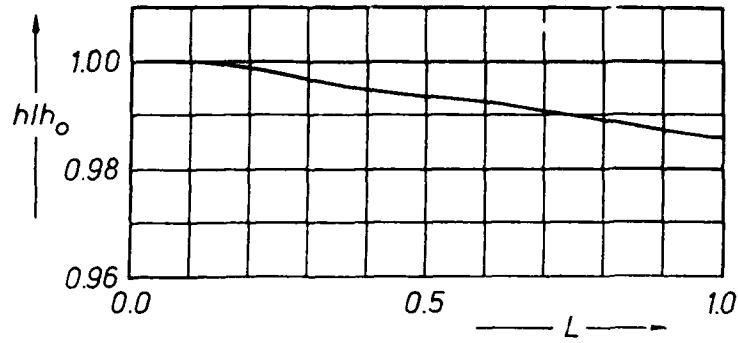
Fig. 8: Influence of artificial damping on wake depth using MacCormack's scheme

$$w(y) = w_o \left[1 + h_D \, \sin \, 2\pi \, \frac{y}{t_D} \right]$$
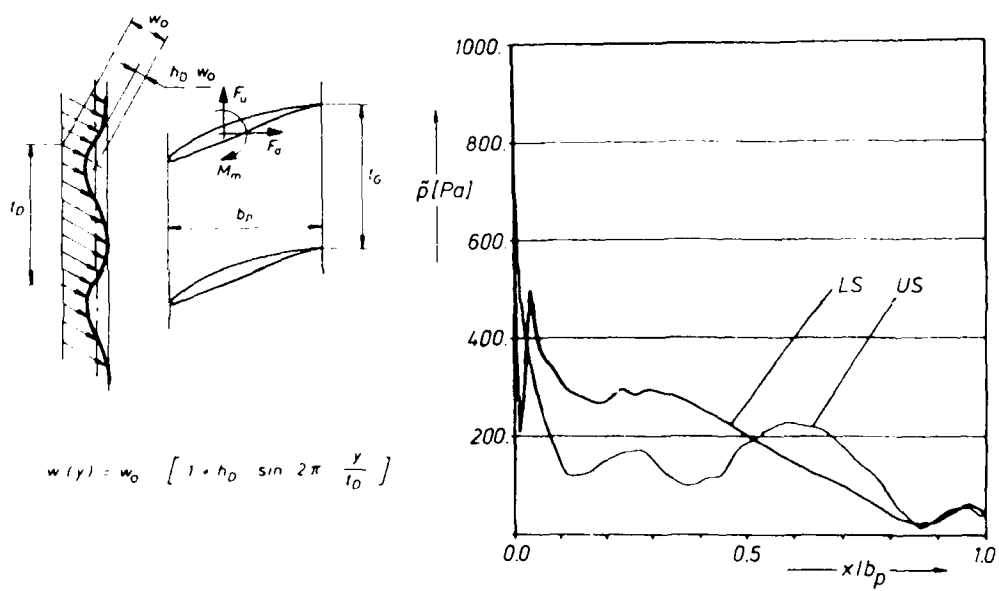
Fig. 9: Amplitudes of pressure fluctuations due to sinusoidal wake ($2*h_D = 0.07$)

SUCTION SIDE

2500

1250

• $\tilde{p}$ [Pa]

-1250

-2500

0.5

x/b_p

0.0

1.0

t/T

2.0

PRESSURE SIDE

2500

1250

• $\tilde{p}$ [Pa]

-1250

-2500

0.5

x/b_p

0.0

1.0

t/T

2.0

Fig. 10: Pressure fluctuations on suction and pressure side due to sinusoidal wake
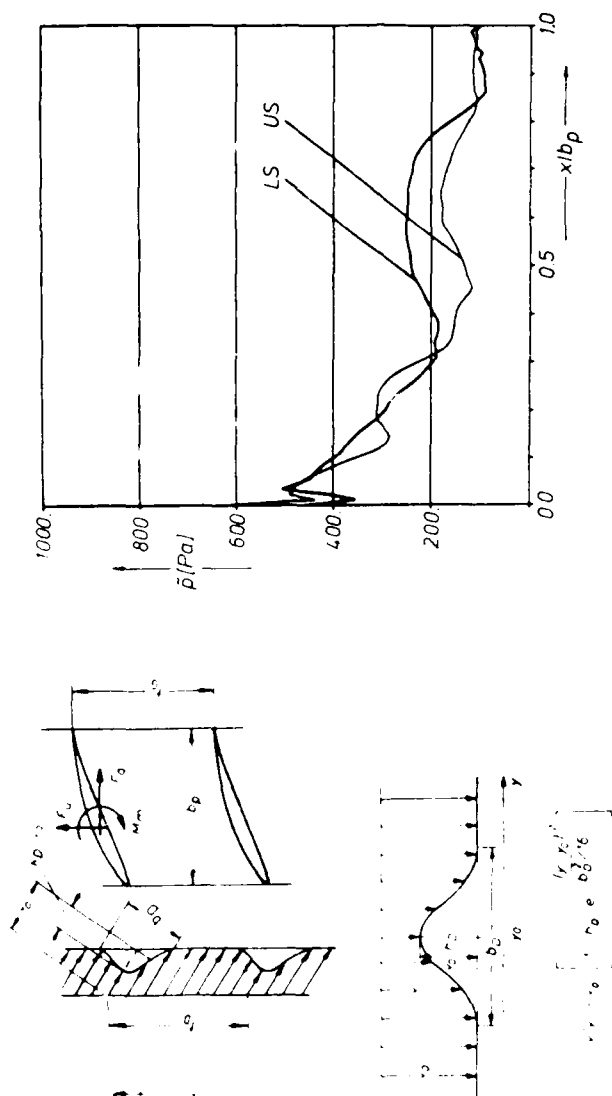
Fig. 11: Amplitudes of pressure fluctuations due to gaussian velocity distribution
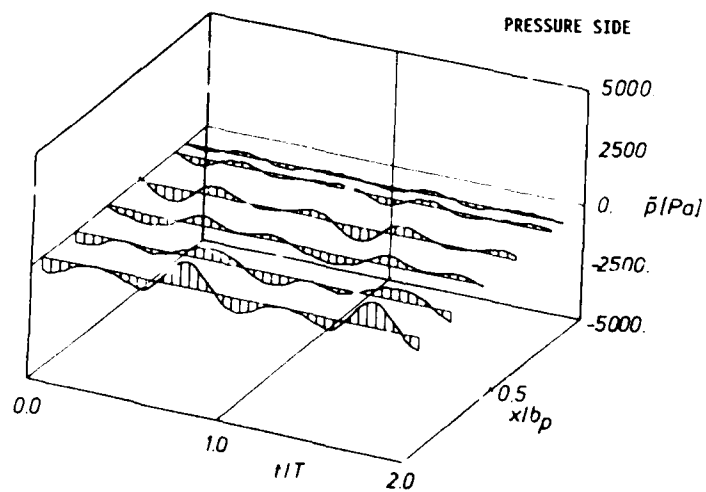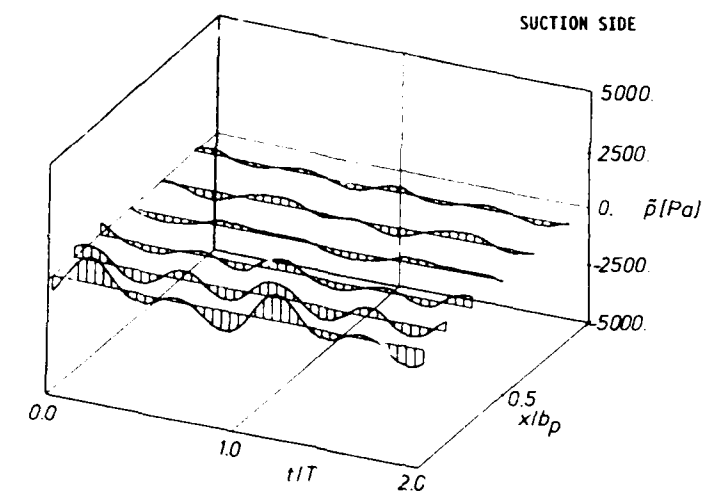
Fig. 12: Pressure fluctuations on suction and pressure side due to a gaussian wake

UNSTEADY AERODYNAMIC PHENOMENA IN A SIMULATED WAKE
AND SHOCK WAVE PASSING EXPERIMENT

A.B. Johnson*	M.J. Rigby*	M.L.G.Oldfield
Schlumberger Cambridge Research,	Rolls Royce plc,	Oxford University
Cambridge, England	Derby, England	Oxford, England

* Formerly at Oxford University

SUMMARY

A detailed study of the propagation of nozzle guide vane trailing edge shock waves and wakes through a turbine rotor passage is presented, using experimental data from a transient cascade tunnel with a rotating bar shock and wake generator. Both unsteady and mean blade surface pressure measurements, together with schlieren flow visualisation were used to unravel the complex sequence of refraction, reflection, and re-reflection of the moving NGV shock waves, together the effects they have on both the unsteady and time averaged blade surface pressures. The effects of the wakes are similarly described. As well as contributing to the fundamental understanding of the inherently unsteady turbine aerodynamics, this paper shows the phenomena which must be predicted by any successful unsteady computational fluid dynamic prediction of the flow.

NOMENCLATURE

c_{ax}	Axial chord (m)	p	Static pressure (Pa)
M	Mach No.	p_o	Total pressure (Pa)
MP	Model point	r	Radius (m)
M_{brel}	Flow Mach No. relative to moving bar	Re	Reynolds number
P	Pressure (Pa)	x	Streamwise direction (m)

INTRODUCTION

With the striving for greater efficiency and performance from modern gas turbine engines the need for a clear understanding of the unsteady processes which occur is increasing. The flow perturbations are intrinsic in the operation of any turbine, they are associated with the periodic chopping of the wakes from an upstream blade row by the next row. With the increasing use of transonic exit flows from stator and rotor passages the importance of the shock wave passing is also becoming more significant. The effect of these perturbations on the aerodynamic performance of the passage, the thermal loading of the blades and the blade profile losses needs to be understood.

Much of the previous work in this field has used unsteady blade surface heat transfer measurements to study moving wakes and shock waves in turbines, either in cascade [1,2,3,4,5,6] or in a rotating turbine. Large rapid surface pressure fluctuations were also seen [3] and it has been shown that these cause correspondingly large fluctuations in heat transfer [10,11].

The present work concentrates on describing in detail the propagation of nozzle guide vane shocks and wakes through the rotor passage as detected by measurements of time resolved and time averaged surface pressures together with flow visualisation using schlieren photography. Analysis of these results reveals a complex sequence of NGV shock wave movements and reflections through the blade passage, and these along with the wake propagation, can be related to features in the measured unsteady pressures.

EXPERIMENTAL CONDITIONS AND METHODS

The tests were carried out in the Oxford Turbomachinery Group [15] Isentropic Light Piston Tunnel (ILPT) [13,14,15] fitted with a linear cascade working section together with an NGV wake and shock wave simulation system [1]. The ILPT is capable of modelling full engine Reynolds No., Mach No. and Gas to Wall temperature ratios. The tunnel is a transient facility and is capable of maintaining constant flow for between 0.3 and 2.0 seconds. The ILPT was fitted with a 6 passage transonic turbine rotor blade cascade (Fig. 1), as used by [5,10,11]. The blade represents the mid-height profile of a transonic HP turbine. The rotor dimensions and test flow conditions, which are the same as would be expected in an engine in terms of Mach number and Reynolds number,but not temperature ratio, are shown in Table 1.
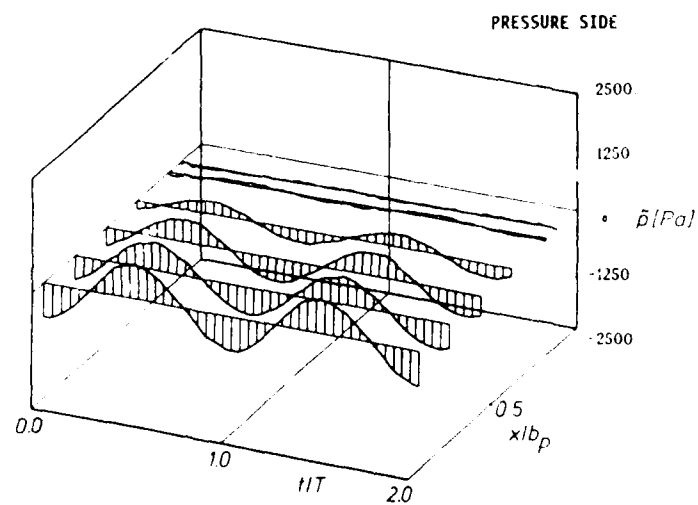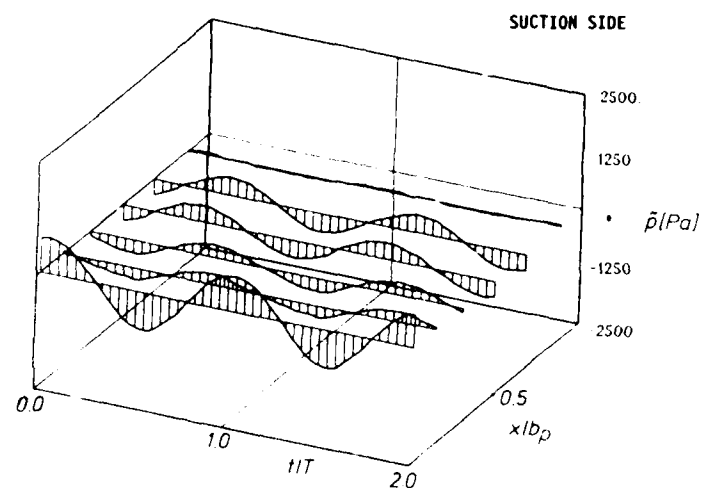
The stationary NGV ring of the HP stage of an engine will produce wakes, and recompression shock waves if it is transonic. These will be convected into the rotating rotor blade row as periodic flow fluctuations. To simulate this phenomenon in the ILPT, the rotor blade cascade remains stationary, while the periodic wakes and shock waves are produced by moving circular cylinders in a parallel plane upstream of the cascade leading edge (Fig. 1). The test configuration is that described in [10,11]. In most of the tests there was no upstream turbulence grid. Two configurations of bar were used:

(a) 16 bars at the NGV pitch to model the engine situation;

(b) 2 bars to give isolated shock and wake passing events.

Table 1   Experimental flow conditions

Inlet Mach number	0.38	Blade inlet span	50.0 mm
Isentropic exit Mach number	1.18	Blade pitch	34.3 mm
Bar relative Mach Number M_{brel}:		Blade chord	41.2 mm
Schlieren tests	1.165	Blade axial chord	34.8 mm
Transonic tests	1.13	Inlet angle	48°
Subsonic test	0.75	Flow Total temperature	290 K
Reynolds number (based on blade	1.0×10^6	Total pressure	170 kPa
chord and isentropic exit conditions)		Bar generator rotational speed	17,000 rpm
Hade angle	10°	Bar diameter	1.6 mm

For the surface pressure measurements, two rotating bar speeds were used: the first simulated a supersonic NGV exit flow with M_{brel} = 1.13 and the second a subsonic exit flow with M_{brel} = 0.75. For the schlieren tests a slightly higher supersonic M_b = 1.165 was used. The wake propagation though the passage has similar characteristics at all three values of M_{brel}.

The bar generated flow field is dependent upon the bar relative Mach number, M_{brel}, which, with the bars mounted radially from a rotating disk, is a function of the radius of the flow generating segment of the bar from the axis of the disk. Consequently the flow perturbations being detected by the blade mounted instrumentation will vary slightly along the span. In these experiments the pressure tappings were distributed across the blade from 30% to 70% of the leading edge span (Fig 2). The nominal M_{brel} of 1.13 varied from 1.08 to 1.18 over this 40% of the span, and consequently the wake angle varied from 74.5° to 77.5°. There is also a small timing shift associated with the spanwise position of the surface mounted instrumentation. Time averaged pressure distributions were measured with two blades, (Fig. 2) with small pressure tappings connected via short flexible tubing to Sensym pressure transducers, type LX-1620D.

As the rotating disk and turbine were mounted on the back of the working section, it was therefore necessary to use a double pass schlieren system.

The unsteady surface pressure measurements were made using three different blade configurations. The first used three Kulite XCQ-060-50D pressure transducers mounted flush with the blade suction surface. These were then transplanted into the pressure surface of another blade for the second series of tests. Tests were carried out with this blade in both the upper and lower blade positions, giving leading edge data for both at the top and bottom of the instrumented passage. Finally a flat pack Kulite LQ9-080-50D was mounted in the pressure surface to measure fluctuations closer to the trailing edge.

The cylindrical pressure transducers, XCQ types, are normally supplied with a protective screen covering the diaphragm, to give it increased durability. The diaphragm has a natural frequency of 600 kHz, but the screening limits the frequency response to about 20 kHz. A single transducer was supplied without the protective screen, but with RTV sprayed onto the diaphragm for protective purposes, this reduced its natural frequency to 150 kHz, but still gave a much better frequency response than the conventional models. The positions of the unscreened transducer are indicated by an • in Fig. 2. The LQ9 transducer was supplied without protective screens but with RTV coatings and had a similar frequency response to the unscreened device.

UNSTEADY WAKE EFFECTS

Time Resolved Surface Pressure Measurements for $M_{brel}=0.75$

Typical raw unfiltered wide bandwidth pressure measurements recorded on the suction surface at MP. P16, x/cax = 0.39 are presented in Fig. 3. The data recorded in the 16 bars configuration tests shows evidence of overlaying of phenomena associated with adjacent bars. The overall effect of the NGV simulation is for the pressure trace to have a regular wave shape, with the same period as that of the bar passing. Examples of this data which have been phase-lock (i.e. ensemble) averaged over 30 cycles are shown in Fig. 4. The data recorded in the two bar configuration tests show evidence of separate identifiable events (Fig. 5). Each trace, which represents one complete period of the bar passing, has been ensemble averaged over four periods for the pressure surface and leading edge measurements and two cycles for the suction surface, with the latter data filtered with a 30 kHz Hamming window filter.

The transducers used in these tests were mounted at different spanwise positions on the blade. This was necessary due to the physical shape of the transducer bodies. The maximum timing variations associated with this spanwise variation in instrumentation position is approximately 20 µs, while the

range of M_{brel} over this radius is from 0.722 to 0.772, this variation will lead to a variation of 7% in the maximum wake velocity deficit and of 14% in the pressure signals associated with it.

A large drop in surface pressure, labelled "A" and "B", in Fig. 5, for the pressure and suction surfaces respectively, can be seen in the data. It is first detected in the instrumented passage at the leading edge of the upper blade. The measured signals indicate that the phenomenon causing the pressure drop moves along the pressure surface towards the trailing edge at less than the local freestream velocity. It is detected on the crown of the suction surface approximately 70 µs after it is first seen on the leading edge of the upper blade. It should be noted that the results for the two surfaces were recorded on different runs so the accuracy of the timing synchronisation is limited by the build to build variation in the mounting of the bar position detector. This makes the synchronisation accurate to only $\pm$ 40 µs. The transducer in the leading edge of the blade and that at MP P16 on the crown of the suction surface are both at mid span on the respective blades so there are no spanwise synchronisation errors. It takes 280 µs for the bar to move through on rotor passage pitch so the phenomenon causing this drop in pressure moves across the passage, even allowing for the maximum synchronisation error, faster than the bar itself, indicating that this is caused by a pressure wave rather than the wake.

A large pressure rise was seen on the suction surface, this is labelled "C" in Fig. 5. It was first detected at the crown of the blade and was seen propagating towards the trailing edge of the blade. There were no pressure transducers mounted on the blade surface between the crown and the leading edge of the blade so its existence could not be tested between these two points. The propagation velocity of the perturbation was approximately M = 0.25, lower than the local freestream velocity, suggesting that it was propagating with the wake. Its appearance on the suction surface is coincident with the expected position of the wake calculated from the timing of the pressure drop at the two leading edge pressure transducers.

There is a small pressure rise which is measured on both surfaces of the passage, labelled "D" in the Fig. 5. The effect is first detected at the leading edge of the upper blade, from where it propagates back along the pressure surface towards the trailing edge and across the passage to the suction surface. Its propagation velocity on both surfaces is well above the local freestream velocity. It is detected on the blade mounted pressure transducers long before the arrival of the wake, careful analysis of the data has shown that it is detected while the bar is still in the slot in the tunnel sidewall.

There is a further rise in pressure detected on the blade surfaces, labelled "E" in Fig. 5. This occurs after the passing of the wake associated effects, first appearing near to the back of the pressure surface. The pressure signature propagates forward along towards the leading edge of this blade then from the crown of the suction surface towards the trailing edge of the lower blade. The propagation of this effect along the suction surface of the passage is at the same time interval relative to the leading edge of the upper blade as the first pressure pulse detected, "D". It appears to be a pressure wave which first contacts the pressure surface near to its trailing edge.

Schlieren Photography Results

There were no schlieren tests carried out with an M_{brel} of 0.75, but the wake propagation identified in the results taken at M_{brel} = 1.165 can be analysed with if careful consideration is given to the differences. The tests carried out with the higher M_{brel} will have a wake that is both narrower and of smaller velocity deficit than one produced by a bar with M_{brel} = 0.75.

The position of the wake in the rotor passage can be identified in the schlieren photographs, as shown in Fig. 7 for the two bar test case. As the wake propagates through the passage, it appears to become narrower on the pressure surface and wider on the suction surface. This is caused by a combination of two effects [17]. Firstly, non uniform passage velocity field slows the flow close to the pressure surface and speeds it up close to the suction surface. Secondly there is the effect known as the "negative jet", where the highly turbulent wake fluid is convected from the pressure surface to the suction surface. In the tests carried out in the 16 bar configuration the wakes from adjacent bars merge together and this makes analysis of wake propagation behaviour from this data impossible.

Wake Propagation and Pressure Wave Effects

The momentum associated with across passage convection of the wake ("negative jet") causes a temporary rise in pressure on the suction surface of the blade and a corresponding drop on the pressure surface. These effects can be seen in the experimental results in Fig. 5. The drop in pressure measured on the pressure surface labelled "A" and the pressure increase on the suction surface labelled "C" is caused by this phenomenon. The results have also indicated that there are various other phenomena which should also be considered. Many of the effects detected with the surface pressure transducers are weak pressure waves or expansions which propagate across the passage and intersect the surfaces. As the waves are only weak then the theory of linear superposition can be applied during the analysis of the pressure

A drop in surface pressure, "B", is measured on the suction surface of the blade. This phenomenon was unexpected. The reduction is caused by an expansion wave which is detected propagating from the leading edge of the cascade. The expansion will travel through the passage at approximately sonic speed relative to the local flow, while the wake will be convected with the flow. So the drop in pressure caused by this expansion and the rise associated with the "negative jet", which are overlayed at MP. P15 (x/cax = 0.28, Fig. 5(f)) will move apart further along the blade. The signal measured at MP. P19 (x/cax = 0.65, Fig. 5(h)) shows that the two effects have separated.

The pressure rise, D, detected on the blades in the figures propagates through the passage very quickly, at a much higher velocity than the wake propagation. It enters the passage at the leading edge of the upper blade, propagating as a pressure wave and appearing to be washed out as it moves across the passage and towards the trailing edge of the lower blade. It is first detected in the passage at the leading edge of the upper blade, 600 μs before the bar synchronisation timing signal, this represents a time before the bar is even level with the upper blade. If the bar was moving at a supersonic velocity relative to the local flow then we would expect to see a bow shock wave in front of it. In this case however the M_{brel} is subsonic, so there will be no bow shock wave, but there will be a weak potential effect travelling upstream of the bar and it is this pressure wave which is detected as the pressure rise in the passage. This effect will not occur in the full engine case, although it will occur in the 16 bar test cases.

The final phenomenon detected in the pressure signals is another rise in surface pressure, labelled "E" in the figures. This is detected on the pressure surface after the large pressure rise associated with the "negative jet" phenomena has been detected on the crown of the suction surface. A pressure wave is formed on the suction surface of the passage by this large rise, it then propagates out from there at sonic velocity relative to the local flow field. It moves across the passage appearing first at the trailing edge of the pressure surface, while the remainder of the wave moves closer to the surface. The surface pressure rise appears to move along the blade very quickly. It will be reflected off the pressure surface back across the passage. Moving at sonic velocity relative to the local flow it will be convected downstream as it crosses the passage, showing similar propagation behaviour to that of first pressure wave, labelled "D". The pressure signal from the wave becomes smaller in amplitude as it propagates across the passage.

The propagation of these pressure waves is similar to the propagation of the unsteady shock waves, described later. All of the pressure waves will be reflected across the passage, but they will also become weaker, so although the waves are there they may not be detected because they are either too weak or their effects are swamped by other pressure effects.

16 Bar Test Results

The analysis carried out so far has been on the two bar data and it must be shown that the same effects occur in the 16 bar tests for the results to apply to the engine case. A programme was written which would overlay the results recorded in the two bar tests with the relevant phase shift, which, assuming superposition of the pressure signals, would predict the 16 bar pressure results from the two bar data. The results of this are shown in Fig.6 and are comparable with the 16 bar results in Fig. 4.

The agreement between the two signals is very good in terms of amplitude, but the higher harmonics are not repeated with the same level of accuracy. The same phenomena can be identified, eg. the sharp spike seen in the suction surface data, but the relative phase of these effects is different. It is thought that this is because of the variation in bar speed between different runs. The time base is stretched so that the relative phase of the bar passing is correct, but in doing this the sonic velocity is changed, so although the phasing of the major changes is correct, the propagation of the sonic waves is incorrect.

UNSTEADY SHOCK WAVE PASSING EFFECTS

Analysis of the NGV trailing edge shock wave propagation through the rotor passage was based on a series of schlieren photographs (M_{brel} = 1.16) and blade surface pressure measurements (M_{brel} = 1.13). The data is presented first, followed by an analysis of the shock wave behavior

Review of Schlieren Data

Typical examples of the schlieren results are shown in Figs. 7, 8 and 9. The 16 bar test data shows the typical overlaying of effects from adjacent bar passing events. In the 2 bar test case the effects from individual bar passing events are almost completely isolated. There are, however, some very weak residual shock waves visible in the lower passage preceding the arrival of the bow shock.

Propagation of a Single Shock Wave Through a Rotor Passage

An understanding of the shock wave propagation was derived from the results of more than 150 schlieren images. A shock wave propagating in a flow field will move at a velocity slightly above the local sonic speed relative to the local flow. Hence, if a plane shock was moving in a uniform flow

field then its shape would remain constant. In a rotor passage, however, the flow field is non uniform so any waves which are moving through the passage will become distorted.

As a shock wave, "a" in Fig. 10, passes the leading edge of a rotor blade it appears to refract around that point forming a tightly curved shock wave "b" which can be seen in Fig. 8. This is due to the high pressure gas from behind the incident shock wave forming a Mach wave as it expands into the low pressure region in the passage which has not seen the incoming wave. The formation and propagation of this Mach wave is almost completely independent of the strength or angle of the incident wave. The shock wave propagation seen in the passage is dominated by these Mach waves, so the results of the shock wave tracking for the bow and recompression shock waves produced by the bar are very similar. The analysis presented here is for a single wave and applies to both bow and recompression waves.

The intersection between the Mach wave and the pressure surface, is initially normal to the blade, producing no reflection. As it moves along the pressure surface towards the trailing edge the wave becomes distorted due to the non uniform passage velocity field with the fluid further away from the wall moving faster than the fluid close to the wall. The wave becomes oblique to the local flow and forms a weak reflected wave at the pressure surface "c" in Fig. 10.2. It is clear in the schlieren photographs (Fig. 9) that this interaction is not a simple reflection as a third wave is formed further behind the reflection.

The original shock wave, moves across the passage to intersect with the suction surface of the lower blade at its crown. The centre of the wave, "d", is reflected off the blade, leaving the end segment, "e", to propagate down to the end of the passage. The intersection of the original incident wave with the blade, "f", continues to move from the crown towards the leading edge of the lower blade, as seen in Fig. 10. As the shock wave moves past the stagnation point and into the next passage, the intersection with the blade surface ceases to form a reflection, leaving only the Mach wave to hit the pressure surface with no reflection. A bifurcation is formed between the original incoming wave and the wave which had been reflected off the suction surface, this is labelled "g" in Fig. 10.1, where it is seen with the incident wave first entering the passage, and can also be seen in Fig. 8 associated with the recompression shock wave.

As the reflected wave, "d", formed off the suction surface moves across the passage it appears to become weaker and distorted, appearing to rotate. Again this is due to the non uniform passage flow field. It initially hits the pressure surface of the upper blade, near to its trailing edge, as labelled "h" in Fig. 10.3. It then propagates across the passage towards the upper surface and out from the leading edge plane, as seen in Fig. 8. As it moves forward there is evidence of a bifurcation in the wave, as labelled "k" in Fig. 10.3. This is the result of the bifurcation, "g", formed around the leading

edge of the blade having been reflected off the suction surface of the blade with the incident wave. The intersection of the reflected wave with the pressure surface, "h", moves forward from the trailing edge as the wave propagates across the passage causing a re-reflected wave to form, as labelled "l" in Fig. 10.4.

This re-reflected wave starts to re-traverse the passage. Its intersection with the pressure surface moves much faster towards the leading edge, in absolute terms, through the low velocity flow than the wave itself towards the suction surface. As the intersection propagates around the leading edge of the blade a tightly curved wave forms around the stagnation point, labelled "m" in Fig. 10.5 and shown in Fig. 8, the end of the wave will start to propagate along the suction surface of the next passage, although by this time the wave will be very weak and hard to identify.

The main re-reflected wave, "l", moves across the passage, almost parallel to the pressure surface, as shown in Fig. 10.5. It hits the suction surface of the lower blade close to the passage shock wave, "p". As the remainder of the wave comes closer to the suction surface the intersection moves forward towards the crown, forming another reflected wave, as labelled "n" in Fig. 10.6. As the intersection approaches the crown the shock wave appears to become stronger. The re-reflected wave moves forward through the passage and out through the leading edge plane, while the next wave propagates back across the passage to intersect with the pressure surface near to the trailing edge once more.

At this point in the shock wave cycle the data available from the schlieren photographs becomes impossible to interpret accurately. This is because the waves have become weaker as they repeatedly crossed the passage. It is clear, however, that the waves continue to be reflected across the passage for a relatively long time after the bar passing event. In the 2 bar tests there is evidence of the shock waves still in the rotor passages when the bow shock wave from the next bar arrives, as shown in Fig. 7(b).

The shock wave propagation within an engine rotor passage will be similar to that seen in these tests. In a full stage, however, when the shock waves propagate out of the leading edge plane of the rotor they will be reflected back into the passage by the suction surface of the upstream NGV [16]. In the cascade tests the weak shock waves propagate out of the leading edge of the cascade and continue upstream into the low velocity flow.

Interaction between Different Shock Waves and the Wake

There are many examples of the shock waves passing through each other. Typically, when the reflected bow shock wave is propagating towards the pressure surface, it crosses over the recompression shock wave, which is being refracted around the leading edge of the upper blade. In all of the cases studied the waves cross with no indication of any interaction. This suggests that they are all weak shock waves. The interaction between the waves and wakes appears to have little effect on either, other than to reduce the definition of the waves in the schlieren images.

Time Resolved Surface Pressure Measurements for $M_{brel} = 1.13$

The surface pressure measurements presented in this section has been either ensemble averaged or filtered using a Hanning filter. Typical 16 bar data are shown in Fig. 12. All show the characteristic overlaying of phenomena. The net effect is a periodic waveform characterised by a number of very steep positive and negative spikes. These spikes are associated with the passing of unsteady shock waves. In the two bar configuration tests, as shown in Fig. 13 the strongest bar associated effects have been isolated although there is again some evidence of residual pressure fluctuations in the passage when the bow shock wave from the next bar arrives. The amplitude of the pressure fluctuations is more than twice that measured in the comparable tests with no rotating bars.

It has been shown [16] that the wake produced by the bar with an M_{brel} of 1.13 is much smaller in terms of width and velocity deficit ratio than the wake produced by the bar with an M_{brel} of 0.75. The maximum velocity deficit ratio for the subsonic tests was approximately 0.3 compared with 0.1 for the supersonic test case. The maximum "negative jet" velocity in the wake for the subsonic test will be M = 0.215, while that for the high speed case will be M = 0.113. There will, therefore, be a surface pressure fluctuation on the blade associated with the wake passing, though it will be approximately $\frac{1}{4}$ of the amplitude of the perturbations detected in the subsonic bar tests. The pressure wave reflected off the suction surface when the "negative jet" impinges there will also exist, as will the reduction in pressure caused by the interaction between the "negative jet" and the accelerating flow in the leading edge plane. The pressure rise detected in the rotor passage before the arrival of the wake will exist in these tests but in the form of a detached bow shock wave and will therefore be larger and steeper than the pressure change seen in the subsonic tests. The measured pressure fluctuations associated with the shock waves are almost an order of magnitude larger than those expected from the wake. It is unlikely, therefore, that the pressure fluctuations associated with the wake will be identifiable.

The position and shape of the recompression shock wave will be independent of M_{brel} and so it will remain parallel to the bar. The maximum synchronisation error associated with the spanwise variation in transducer position will be approximately 10 μs for the recompression shock wave. The position and strength of the bow shock wave is strongly dependent upon the local M_{brel} of the bar. the errors associated with the calculation of the detached bow wave position make it impossible to predict the position of the bow wave with any confidence, although the trend is for it to move closer to the stagnation point as the flow speed increases. The strength of the bow wave will, therefore, vary over the spanwise range of the surface instrumentation. The most accurate indication of the bow wave strength over the range of M_{brel} considered is the static pressure rise across a normal shock wave with that value of upstream Mach number. The range of M_{brel} forming the waves seen by the surface instrumentation is 1.08 - 1.18 (p/p_0 = 1.194 - 1.458. This is a significant range in shock wave strengths and must be considered when analysing the shock wave passing effects on the time resolved pressure signals.

The two large pressure pulses labelled "A" and "B" on the two bar pressure traces, Figs. 13. are the result of the impingement of the bow and recompression shock waves on the blade surface. The effects of the synchronisation errors caused by the spanwise transducer positions is clear in this data, comparing Figs. 13(c) and (d) at MPs P3 and P4 (x/cax = 0.21 and 0.39) respectively on the pressure surface. The latter data is recorded at a point at a radius of 160 mm from the centre of the disk, while the former comes from a point at a radius of 140 mm. In the data the pressure pulse from MP P4 (x/cax = 0.39) is larger in terms of amplitude and closer in terms of time to the pulse associated with the recompression shock wave. The duration of the pulses associated with both waves increases as the waves propagate along the pressure surface.This is due to the splitting of the wave seen in the schlieren results. Both waves become weaker as they propagate through the passage as they are divergent.

On the early part of both surfaces there is a large drop in pressure "C" between the two waves (Figs. 13). This is caused by the expansion fan which exists around the bar. The effect is reduced as the expansion propagates through the passage.

The two waves reflect off the suction surface and re-traverse the passage, impinging onto and being reflected off the blade near to the trailing edge of the pressure surface first, then propagating forward. The pressure pulses associated with this are labelled "D" and "E", Fig. 13. In the data for MP P4 (x/cax = 0.39) the pulse caused by the recompression shock wave "B" and that caused by the ref'ected bow wave "D" lie exactly on top of each other causing a single large pulse.

When the waves impinge on the pressure surface they form a re-reflected wave which is propagated back across the passage to the suction surface. The pulses associated with this impingement are labelled "F" and "G"in Fig. 13. The relative timing of the two waves is such that as the re-reflected recompression wave is impinging upon the suction surface, the bow shock wave which has made one more crossing of the passage and almost merges with it. Also shown in Fig. 13 is a pressure pulse "H". This is due to shock reflections from the endwalls of the tunnel, because of an initial spanwise velocity of the shock waves leaving the rotating bar.

The propagation of the shock waves becomes difficult to analyse later than this point due to the overlaying of the bow and recompression shock wave reflections, together with those reflected off the end wall. It is clear that the waves continue to be reflected across the passage causing surface pressure fluctuations until the arrival of the bow shock wave associated with the next bar.

16 Bar Test Results
The two-bar surface pressure data was again reprocessed to simulate the 16 bar traces. The results of this are shown in Fig. 14 which can be compared with Fig. 12.The agreement between the two sets of data is fairly good, although the amplitude of the high peaks and deep troughs are greater in the superposed 2 bar data. This suggests that there is a weak interaction between the strong shock waves and the expansion fan.

TIME AVERAGED RESULTS
The mean effect of the NGV simulation on the surface pressure can be seen in Fig. 11. Data are presented with no bars, and with 16 bars for two bar relative Mach numbers of 0.75 and 1.13. The total pressure was measured with a Pitot tube mounted downstream of the rotating bars, as this is the total pressure seen by the blades. The static pressure ratio measured on the pressure surface of the blade is independent of the rotating bars at an M_{brel} = 0.75, but shows a slighht reduction at M_{brel} = 1.13. However, the effect on the suction surface is much greater. The static pressure ratio rises, indicating an unloading of the blade. This is due to the "negative jet" effect of the wake contacting the suction surface of the blade. It is very prominent up to an axial chord of 0.6, the region of the throat. After this the two lines diverge slightly, showing slight unloading of the blade. The unloading is greater for M_{brel}= 1.13 than M_{brel}=0.75, because of the greater bar velocity and hence greater transverse wake momentum transfered to the blade.

CONCLUSIONS
Analysis of the isolated wake results at M_{brel} = 0.75 has demonstrated the existence of a various phenomena such as the "negative jet" associated with wake passing. A number of pressure waves which have been shown to propagate across the passage. The first, caused by a pressure wave moving in front of the bar, will exist in the 16 bar tests but not in a full turbine stage. The second is caused by the impingement of the "negative jet", which causes a pressure rise on the suction surface and hence a wave which propagates through the passage. An expansion wave causes a pressure drop on the suction surface before the arrival of the wake. It is the result of an interaction between the wake and the accelerating fluid crossing the leading edge plane of the cascade and is likely to influence the turbine loss characteristics.

Analysis of the data recorded in the two bar configuration tests has highlighted the behaviour of many previously known phenomena and has also demonstrated the existance of new phenomena. It has also been shown that these effects occur in the 16 bar tests and many will occur in a full turbine stage.

The time averaged surface pressure measurements have shown that the NGV simulation has little effect on the pressure surface total to static pressure ratio. On the suction surface, the effect is to increase the surface pressure and reduce the lift on the blade. The effect of the shock waves on the mean surface pressure measurements is to unload the blade.

Propagation of the simulated NGV trailing edge shock waves has been followed in detail from schlieren flow visualisation and pressure measurements, and it has been shown that the complex series of reflections within the blade passage can be related to unsteady blade surface pressure fluctuations. The detail of the shock wave propagation model presented forms a test case for comparison with the results of CFD codes used to model unsteady rotor passage effects.

REFERENCES

1. Doorly, D.J. and Oldfield, M.L.G., "Simulation of Wake Passing in a Stationary Turbine Rotor Cascade" J. Propulsion and Power, Vol. 1, No.4 Jul.-Aug. 1985 pp 316.

2. Doorly, D.J., Oldfield, M.L.G. and Scrivener, C.T.J., "Wake Passing in A Turbine Rotor Cascade", AGARD PEP CP-390, 1985.

3. Doorly, D.J. and Oldfield, M.L.G., "Simulation of the Effects of Shock Wave Passing on a Turbine Rotor Blade", ASME J. Eng. for Gas Turbines and Power, Vol. 107, pp 998-1006, 1985. (85-GT-112)

4. Schultz, D.L., Johnson, A.B., Ashworth, D.A., Rigby, M.J. and LaGraff, J.E., "Wake and Shock Interactions in a Transonic Turbine Stage", AGARD- CP-401 ,1987.

5. Ashworth, D.A., LaGraff, J.E., Schultz, D.L. and Grindrod, K.J., "Unsteady Aerodynamic and Heat Transfer Processes in a Transonic Turbine Stage", ASME J. Eng. for Power, Vol 107, 1985.

6. Doorly, D.J., "Modelling the Unsteady Flow in a Turbine Rotor Passage", ASME J. Eng. for Power, 1988.

7. Guenette, G.R., Epstein, A.H., Giles, M.B., Haimes, R., and Norton, R.J.G., "Full Scale Transonic Turbine Rotor Heat Transfer Measurements", ASME J. Turbomachinery, Vol 111, pp 1-7, 1989.

8. Dunn, M.G., Seymour, P.J., Woodward, S.H., George, W.K. and Chupp, R.E. "Phase-Resolved Heat-Flux Measurements on the Blade of a Full-Scale Rotating Turbine." ASME J. Turbomachinery, Vol 111, pp 8-19, 1989. (88-GT-173).

9. Ainsworth, R.W., Schultz, D.L., Davies, M.R.D., Forth, C.J.P., Hilditch, M.A., Oldfield, M.L.G. and Sheard, A.G., "A Transient Flow Facility for the Study of the Thermofluid-Dynamics of a Full Stage Turbine Under Engine Representative Conditions"., Gas Turbine and Aeroengine Congress, Amsterdam, . ASME Paper No. 88-GT-144, 1988.

10. Johnson, A.B., Rigby, M.J., Oldfield, M.L.G., Ainsworth, R.W. and Oliver, M.J., "Surface Heat Transfer Fluctuations on a Turbine Rotor Blade Due to Upstream Shock Wave Passing", ASME J. Turbomachinery, Vol 111, pp 105-115, 1989. (88-GT-172).

11. Rigby, M.J., Johnson, A.B., Oldfield, M.L.G., and Jones, T.V. "Temperature Scaling of Turbine Blade Transfer with and without Shock Wave Passing." 9th International Symposium on Air Breathing Engines Athens, Sept. 1989.

12. Jones, T.V., Schultz, D.L. and Hendley, A.D., "On the Flow in an Isentropic Light Piston Tunnel", OUEL Report No. 3731, Jan.1973

13. Oldfield, M.L.G., Jones, T.V. and Schultz, D.L., "On-Line Computer for Transient Turbine Cascade Instrumentation", IEEE Transactions on Aerospace and Electronic Systems. Vol. AES 14, No. 5, pp 738-749, Sept. 1978.

14. Schultz, D.L., Jones, T.V., Oldfield, M.L.G. and Daniels, L.C., "A New Transient Cascade Facility for the Measurement of Heat Transfer Rates", AGARD-CP-229 (1978) also OUEL Report, 26 July 1977.

15. Jones, T.V., "Gas Turbine Studies at Oxford 1969 - 1987". ASME-GT-112, 1988.

16. Giles, M.B., "Stator-Rotor Interaction in Transonic Turbines", AIAA/SAE/ASME/ASEE 24th Joint Propulsion Conference, July 1988, Boston, AIAA Paper No. 88-3093.

17. Meyer, R.X., "The Effect of Wakes on the Transient Pressure and Velocity Distributions in Turbomachines", Transactions of ASME, Vol. 80, 1958.
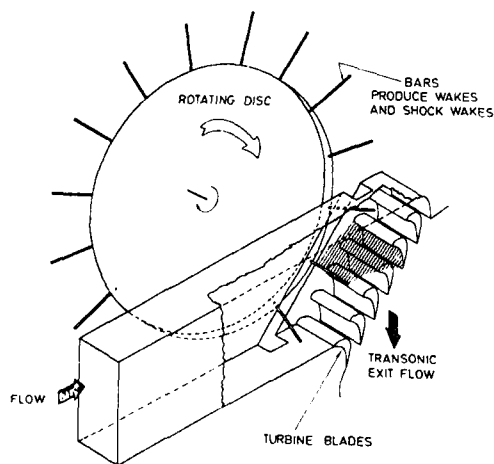
Fig. 1 Rotating disk and bars with linear rotor blade cascade.
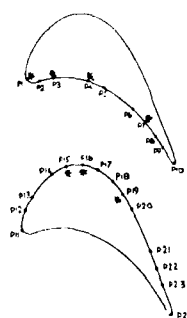
Fig. 2 Position of surface pressure tappings for time averaged pressure measurements also indicating position of spanwise instrumentation plane from centre of the rotating disk. The positions of wide bandwidth surface pressure instrumentation are indicated by a "*".
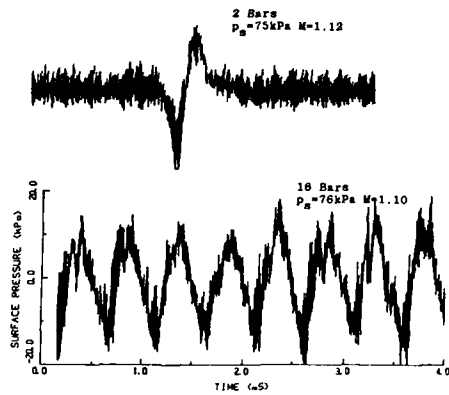
Fig. 3 Raw time resolved surface pressure measurements presented for the 2 bar and 16 bar cases. M_{brel} = 0.75. Suction surface MP P16, x/ca_x = 0.39.
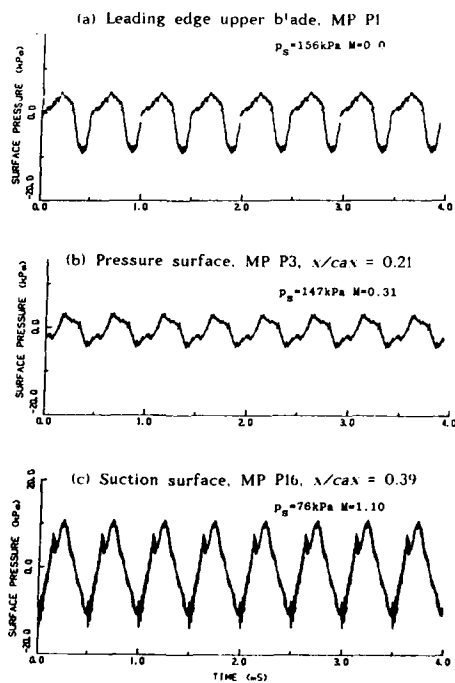
(a) Leading edge upper blade, MP P1

(b) Pressure surface, MP P3, x/ca_x = 0.21

(c) Suction surface, MP P16, x/ca_x = 0.39

Fig. 4 Ensemble averaged time resolved surface pressure measurements for 16 bar, M_{brel} = 0.75.
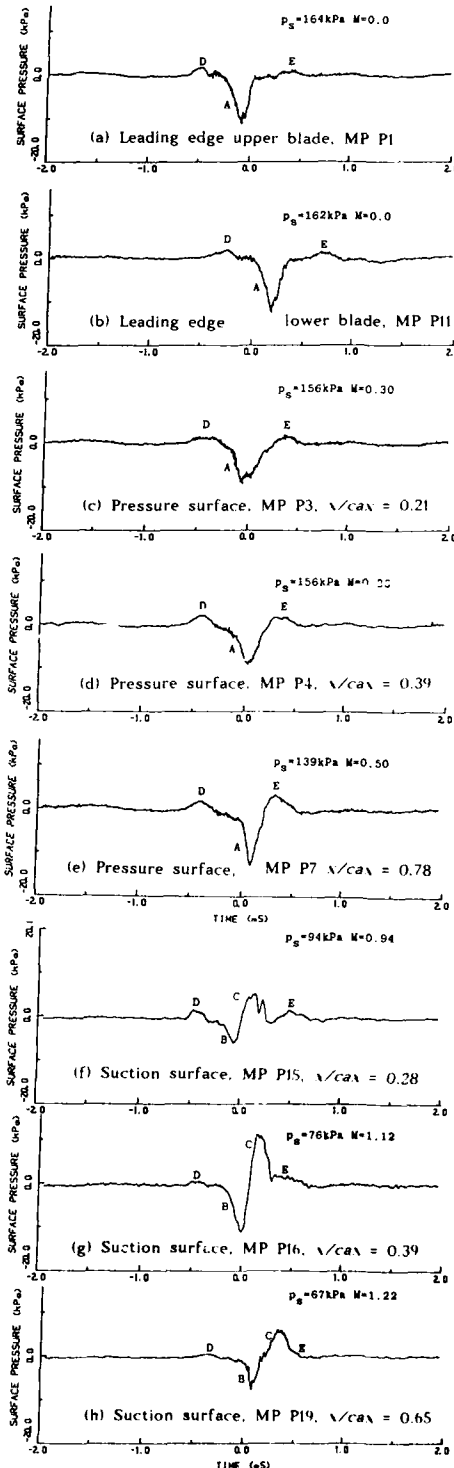
(a) Leading edge upper blade, MP P1

(b) Leading edge lower blade, MP P11

(c) Pressure surface, MP P3, x/ca_x = 0.21

(d) Pressure surface, MP P4, x/ca_x = 0.39

(e) Pressure surface, MP P7 x/ca_x = 0.78

(f) Suction surface, MP P15, x/ca_x = 0.28

(g) Suction surface, MP P16, x/ca_x = 0.39

(h) Suction surface, MP P19, x/ca_x = 0.65

Fig. 5 Ensemble averaged time resolved surface pressure measurements for 2 bar, M_{brel} = 0.75.

Wake

Recompression
Shock Wave

Bar

Bow Shock
Wave

Wake

Recompression
Shock Wave

Bar

Bow Shock
Wave

M_{brel}
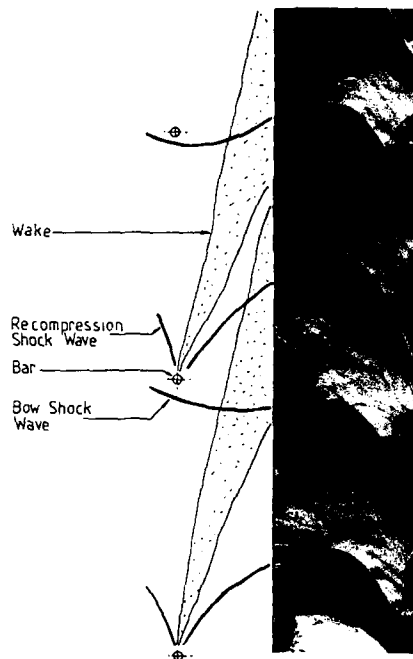
Fig. 7(a) Schlieren photograph recorded in 16 bar configuration. M_{brel} = 1.16, approximate bar positions shown.
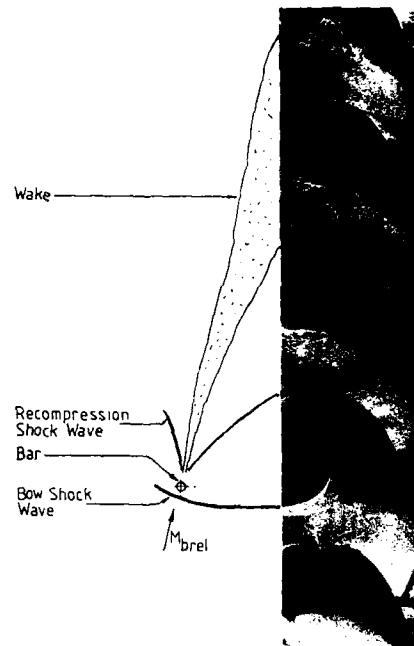
Fig. 7(b) Schlieren photograph recorded in 2 bar configuration. M_{brel} = 1.16, approximate bar position shown.

Bow Shock wave
enters passage

Bow shock wave reflected
off suction surface

Bow shock wave hits pressure
surface, as recompression
wave enters passage, note
Bifurcation

P -reflected bow shock wave
re-traverses passage as
recompression wave hits suction
surface.

Fig. 8 Propagation of shock waves though rotor passage, 2 bars, M_{brel} = 1.16.

Fig. 9 Interaction between shock wave and blade leading edge nucleating vortex and separation bubble, also pressure surface, shock wave interaction. 2 bars. M_{brel} = 1.16.

(a) Leading edge MP P1

(b) Pressure surface MP P3, x/cax = 0.21

(c) Suction surface MP P16, x/cax = 0.39

Fig. 6 Predicted 16 bar time resolved surface pressure measurements, from 2 bar. M_{brel} = 0.75 data.

Fig. 10 Propagation of a single shock wave through the rotor passage.

□ NO BARS
+ 16 BARS M = 8.75
● 16 BARS M = 1.13

FRACTIONAL AXIAL CHORD

Fig. 11 Time averaged surface pressure measurements for no bars and 16 bars. M_{brel} = 0.75 and M_{brel} = 1.13.

(a) Leading edge upper blade, MP P1

(b) Pressure surface, MP P3, x/cax = 0.21

(c) Suction surface, MP P16, x/cax = 0.39

Fig. 12 Ensemble averaged time resolved surface pressure measurements for 16 bar, M_{brel} = 1.13

(a) Leading edge MP P1

(b) Pressure surface MP P3, x/cax = 0.21

(c) Suction surface MP P16, x/cax = 0.21
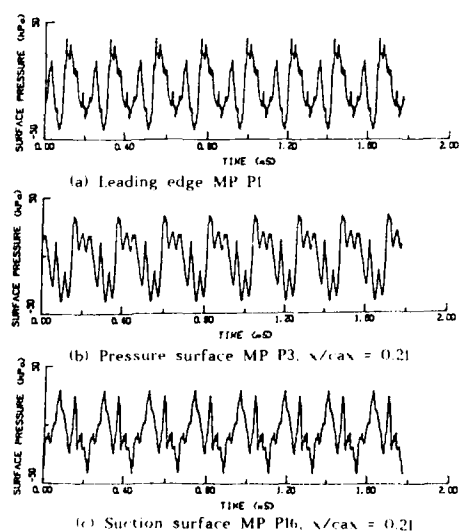
Fig. 14 Predicted 16 bar time resolved surface pressure measurements, from 2 bar. M_{brel} = 1.13

(a) Leading edge upper blade, MP P1

(b) Pressure surface, MP P3, x/cax = 0.21

(c) Pressure surface, MP P4, x/cax = 0.39

(d) Pressure surface, MP P7, x/cax = 0.78

(e) Suction surface, MP P15, x/cax = 0.28

(f) Suction surface, MP P16, x/cax = 0.89

(g) Suction surface, MP P19, x/cax = 0.60
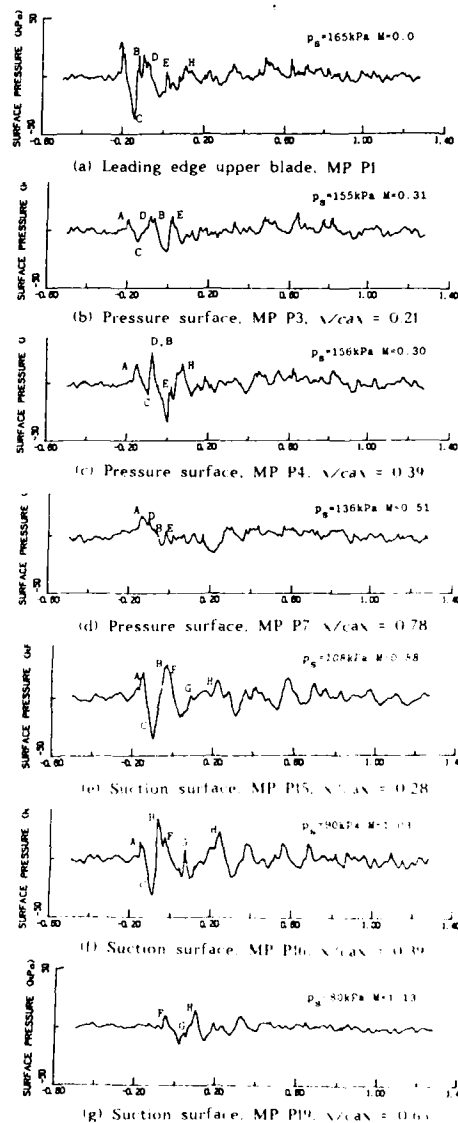
Fig. 13 Ensemble averaged time resolved surface pressure measurements for 2 bar, M_{brel} = 1.13

DISCUSSION

N.A.Ahmed - Cranfield Institute of Technology, U.K.

How repeateable were the results, say e.g. those presented in figure 13? Can the authors give some estimates or a few figures to illustrate them.

Author's response:

The results are very repeateable. The curve in figure 13(f) has been low pass filtered with a 30 KHz bandwith and ensemble averaged in order to remove random pressure fluctuations and highlight the features associated with the periodic band passing. Two wide bandwidth (>100 KHz) raw data are shown in the figure below. In spite of the added random pressure fluctuation and instrumentation noise, the major features due to shock wave passing highlighted in figure 13(f) are easily identified and repeat both cycle- to- cycle and run-to-run. Similar good repeatability has been seen with 16 bars.
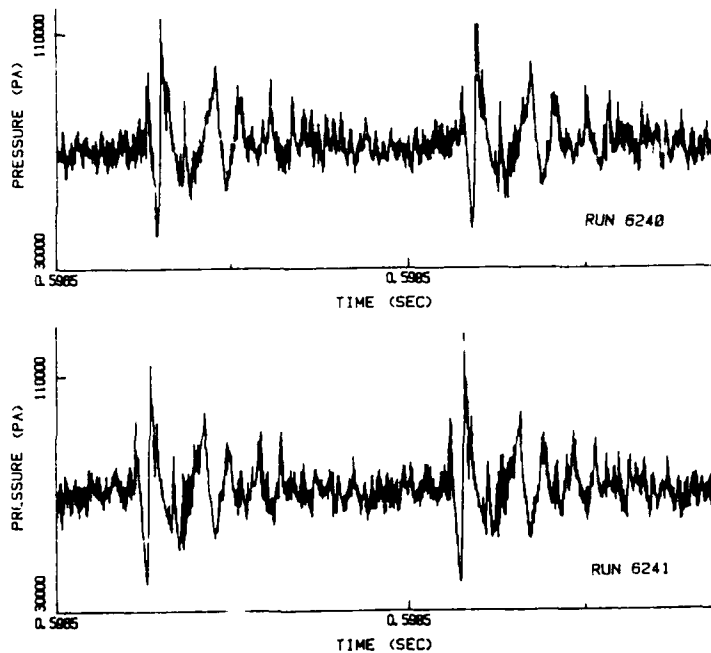
Raw data traces from runs 6240 and 6241 for 2-bars.
M_{brel} = 1.13. Suction surface model point 16. (A pressure scale offset has not been removed).

Gust Response Analysis for Cascades Operating in Nonuniform Mean Flows

Kenneth C. Hall
Research Engineer
Computational & Theoretical Fluid Dynamics

and

Joseph M. Verdon
Manager,
Computational & Theoretical Fluid Dynamics

United Technologies Research Center
East Hartford, Connecticut 06108, U.S.A.

SUMMARY

The linearized unsteady aerodynamic response of a cascade of airfoils subjected to entropic, vortical, and acoustic gusts is analyzed. Field equations for the first-order unsteady perturbation flow are obtained by linearizing the full time-dependent mass, momentum, and energy conservation equations about a nonlinear, isentropic, and irrotational mean or steady flow. A splitting technique is then used to decompose the unsteady velocity field into irrotational and rotational parts leading to field equations for the unsteady entropy, rotational velocity, and irrotational velocity fluctuations that are coupled only sequentially. The entropic and rotational velocity fluctuations can be described in terms of the mean-flow drift and stream functions which can be computed numerically. The irrotational unsteady velocity is described by an inhomogeneous linearized potential equation which contains a source term that depends on the rotational velocity field. This equation is solved via a finite difference technique. Results are presented to indicate the status of the numerical solution procedure and to demonstrate the impact of blade geometry and mean blade loading on the aerodynamic response of cascades to vortical gust excitations. The analysis described herein leads to very efficient predictions of cascade unsteady aerodynamic phenomena making it useful for turbomachinery aeroelastic and aeroacoustic design applications.

1. INTRODUCTION

Destructive forced vibrations can occur in turbomachinery blading when a periodic aerodynamic force, with frequency close to a system natural frequency, acts on the blades in a given row. A primary source of such vibrations is the aerodynamic interactions between adjacent blade rows, of which the two principal types are traditionally referred to as potential flow interaction and wake interaction. The former results from the variations in the velocity potential or pressure field associated with the blades of a given row and their effect on the blades of a neighboring row moving at a different rotational speed. This type of interaction is of serious concern when the axial spacings between neighboring blade rows are small or flow Mach number are high. Wake interaction is the effect of the wakes shed by one or more upstream rows upon the flow through a given blade row. This type of interaction can persist over considerable axial distances.

Until recently, the inviscid unsteady aerodynamic analyses that have been available for turbomachinery aeroelastic applications were based on classical linearized theory (for an informative review see Whitehead [1]). Here the steady and harmonic unsteady departures of the flow variables from a uniform free-stream are regarded as small and of the same order of magnitude, leading to uncoupled linear constant coefficient boundary-value problems for the steady and the complex amplitudes of the unsteady disturbances. Thus, unsteady solutions based on the classical linearization are essentially restricted to cascades of unloaded flat plate blades which operate in an entirely subsonic or an entirely supersonic environment. Very efficient semi-analytic solution procedures have been developed for two-dimensional attached subsonic [2,3,4] and supersonic [5,6,7,8] flows, and have been applied with some success in turbomachinery aeroelastic and aeroacoustic design calculations. It should also be mentioned that extensive efforts have been made to develop three-dimensional unsteady aerodynamic analyses based on the classical linearization for turbomachinery aeroelastic and aeroacoustic applications [9].

Because of the limitations in physical modeling associated with the classical linearization, more general two-dimensional inviscid linearizations have been developed [10,11,12]. These methods account for the effects of important design features such as real blade geometry, mean blade loading and operation at transonic Mach numbers on the unsteady aerodynamic response of a cascade. Here, unsteady disturbances are regarded as small amplitude harmonic fluctuations about a nonuniform steady background flow. The steady flow is determined as a solution of a nonlinear inviscid equation set, and the unsteady flow is governed by a set of linear equations with variable coefficients that depend upon the underlying steady flow. This type of analytical model has received considerable attention in recent years, and we refer the reader to the recent articles by Verdon [13,14] for a detailed description of the theoretical formulation. Useful solution algorithms for the nonlinear steady problem are currently available, and solution methods [15] for linearized unsteady perturbations of isentropic and irrotational steady background flows have reached the stage where it is appropriate to consider them for turbomachinery aeroelastic and aeroacoustic design applications. Unfortunately, for the most part, these have only been developed for blade flutter and acoustic response applications. Recently, Hall and Crawley [12] used the linearized Euler equations to describe the unsteady flow in cascades subjected to wake (entropic and vortical) excitations. The linearized Euler technique, while significantly more efficient than time marching Euler codes, is not as efficient as a linearized analysis based on the isentropic and irrotational mean flow assumptions.

If the flow is subsonic or transonic with weak shocks, then the mean flow is irrotational and isentropic. Under these circumstances, the inviscid conservation equations can be simplified. Goldstein [16,17] expressed the linearized inviscid equations
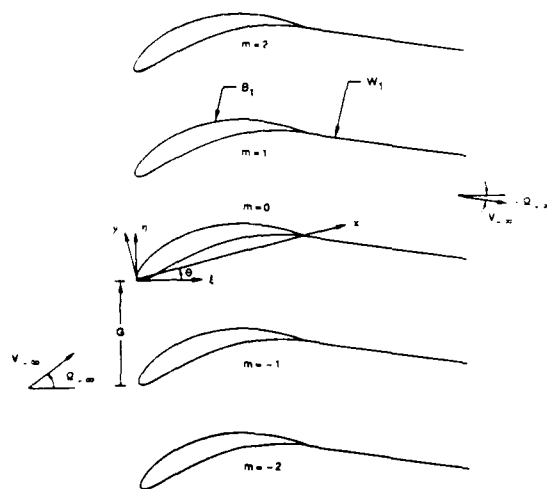
Figure 1: Two-dimensional compressor cascade

in nonconservative form and used a splitting technique to study the behavior of vortical and entropic gusts for flows in which the steady component is both irrotational and isentropic. The unsteady velocity field is split into irrotational and rotational parts leading to linear variable coefficient equations for the entropy, rotational velocity, and velocity potential. These field equations are sequentially coupled so that the entropy transport equation, the rotational velocity transport equation, and the elliptic velocity potential equation can be solved in order. Furthermore, the entropy and rotational velocity can be expressed in closed form. Finally, the unsteady potential is described by an inhomogeneous wave equation in which the source term depends upon the rotational velocity field. The major computational expense is associated with solving the latter equation. Hence, this approach — like the linearized Euler technique — can be used to analyze the gust response problem, but it is nearly as efficient as the potential techniques used for flutter prediction. Furthermore, since the potential equation is essentially the same as that solved using the current unsteady potential codes [10,11], the splitting technique can be incorporated into these existing codes. One drawback of Goldstein's velocity splitting technique is that the rotational velocity is singular along blade and wake surfaces for flows containing stagnation points. Atassi and Grzedzinski [18] have, however, proposed a modification to Goldstein's theory which removes this singularity.

In this paper, an analysis based on Atassi and Grzedzinski's formulation is presented. This analysis has been implemented into an existing computer code LINFLO which can be used to predict the unsteady pressure response of realistic cascade configurations to prescribed external aerodynamic (i.e., incident entropic, vortical and acoustic disturbances) and structural (blade motions) excitations. The analysis is applied herein to a number of cascade configurations, and the results demonstrate that mean loading has a strong effect on the unsteady aerodynamic response to incident vortical excitations.

2. PHYSICAL PROBLEM

We wish to consider the aerodynamic response of a cascade of blades, such as the one shown in Fig. 1, that interacts with wakes or inlet flow distortions. The mean positions of the blade chord lines coincide with the line segments $\eta = \xi \tan \Theta + mG$, $0 \le \xi \le \cos \Theta$, $m = 0, \pm 1, \pm 2, \ldots$, where ξ and η are coordinates in the cascade axial and "circumferential" directions, respectively, m is a blade number index, Θ is the cascade stagger angle, and G is the cascade gap vector which is directed along the η axis with magnitude equal to the blade spacing. In the present discussion all physical quantities are dimensionless. Lengths are scaled with respect to blade chord, time with respect to the ratio of blade chord to upstream free stream speed, density and velocity with respect to upstream free stream density and flow speed, respectively, pressure with respect to the product of the upstream free stream density and the square of the upstream free stream speed, and entropy with respect to the fluid specific heat at constant pressure.

The time dependent or unsteady fluctuations in the flow can arise from one or more of the following sources: blade motions, upstream and/or downstream acoustic disturbances which carry energy toward the blade row, and upstream entropic and vortical disturbances which are convected through the blade row by the mean flow. The foregoing excitations are each assumed to be of small amplitude, i.e., of order ϵ, periodic in time, and to occur at temporal frequency ω. The external aerodynamic excitations are also spatially periodic. In the present investigation, we are primarily concerned with inlet entropic and vortical disturbances. Far upstream of the blade row the entropic and vortical disturbances are of the form

$$s(\mathbf{x},t) = Re\{s_{-\infty} \exp[i(\boldsymbol{\kappa}_{-\infty} \cdot \mathbf{x} + \omega t)]\} \tag{1}$$

and

$$\zeta(\mathbf{x},t) = Re\{\boldsymbol{\zeta}_{-\infty} \exp[i(\boldsymbol{\kappa}_{-\infty} \cdot \mathbf{x} + \omega t)]\} . \tag{2}$$

where $s_{-\infty}$ and $\zeta_{-\infty}$ are the complex amplitudes of incident entropic and vortical fluctuations, $\mathbf{x}$ is a position vector and t is time. We use the symbol $\boldsymbol{\kappa}_{-\infty}$ to denote the wave number of an incident disturbance. Also, the temporal frequency and wave number of an incident entropic or vortical disturbance are related by $\omega = -\boldsymbol{\kappa}_{-\infty} \cdot \mathbf{V}_{-\infty}$, where $\mathbf{V}_{-\infty}$ is the uniform relative inlet velocity.

3. UNSTEADY PERTURBATIONS ABOUT A POTENTIAL MEAN FLOW

While the actual flow through a blade row is extremely complex, i.e., viscous, heat conducting, and three-dimensional, the physics of the gust response problem in axial flow machines is dominated by inviscid effects – at least for attached flows. Hence, we assume that the fluid motion is governed by differential forms of the mass, momentum and energy conservation laws for an inviscid perfect gas (i.e., the Euler equations). For small amplitude excitations, the time-dependent flow can be reguarded as a small perturbation about an underlying nonlinear mean or steady background flow. Thus, for example, we can set

$$\dot{\mathbf{V}}(\mathbf{x},t) = \mathbf{V}(\mathbf{x}) + \dot{\mathbf{v}}(\mathbf{x},t) + \mathcal{O}(\epsilon^2) \tag{3}$$

where $\mathbf{V}$ is the local steady velocity, and $\dot{\mathbf{v}}$ is the local unsteady perturbation velocity.

We assume that the mean flow far upstream of the blade row is at most a small irrotational perturbation from a subsonic uniform flow. In addition, any shocks that might occur are assumed to be of weak to moderate strength and have small curvature. Thus, changes in the entropy and vorticity of a fluid particle as it passes through shocks can be regarded as negligible. Hence, the background flow will be isentropic and irrotational; i.e., $\mathbf{V} = \boldsymbol{\nabla}\Phi$, where Φ is the velocity potential. The field equations that govern the underlying steady flow follow from the mass and momentum conservation laws and the isentropic relations for a perfect gas and are given by

$$\boldsymbol{\nabla} \cdot (\rho \boldsymbol{\nabla} \Phi) = 0 \tag{4}$$

and

$$(M_{-\infty}A)^2 = \rho^{\gamma-1} = (\gamma M^2_{-\infty} P)^{(\gamma-1)/\gamma} = 1 - \frac{\gamma-1}{2} M^2_{-\infty} [(\boldsymbol{\nabla}\Phi)^2 - 1] , \tag{5}$$

where M, A, ρ and P are the local Mach number, speed of sound propagation, density and pressure, respectively, and γ is the specific heat ratio of the fluid. Numerical procedures for determining two-dimensional steady potential flows through cascades have been developed extensively, e.g., see [19,20], particularly for flows with subsonic relative inlet and exit Mach numbers (i.e., $M_{\mp\infty} < 1$).

The field equations that govern the first-order unsteady perturbation of a nonlinear isentropic and irrotational steady flow are determined from the full nonlinear time-dependent mass, momentum and entropy-transport equations and the thermodynamic equation relating the entropy, pressure and density of a perfect gas. After performing some straightforward algebra (see [13,14]), we obtain a system of differential equations for the first-order entropy $(\dot{s})$, velocity $(\dot{\mathbf{v}})$ and pressure $(\dot{p})$, respectively. These equations can be cast in a very convenient form by introducing the Goldstein velocity decomposition [16,17]. Thus, after setting $\dot{\mathbf{v}} = \boldsymbol{\nabla}\dot{\phi} + \dot{\mathbf{v}}_R$ where the unsteady potential fluctuation $\dot{\phi}$ governs the unsteady pressure fluctuation through the relation $\dot{p} = -\rho D\dot{\phi}/Dt$, and $D/Dt = \partial/\partial t + \boldsymbol{\nabla}\Phi \cdot \boldsymbol{\nabla}$ is a mean flow convective derivative operator, we find that the field equations that govern the unsteady flow variables can be written in the form

$$\frac{D\dot{s}}{Dt} = 0 , \tag{6}$$

$$\frac{D}{Dt}(\dot{\mathbf{v}}_R - \dot{s}\boldsymbol{\nabla}\Phi/2) + [(\dot{\mathbf{v}}_R - \dot{s}\boldsymbol{\nabla}\Phi/2) \cdot \boldsymbol{\nabla}]\boldsymbol{\nabla}\Phi = 0 , \tag{7}$$

and

$$\frac{D}{Dt}(A^{-2}\frac{D\dot{\phi}}{Dt}) - \rho^{-1}\boldsymbol{\nabla} \cdot (\rho\boldsymbol{\nabla}\dot{\phi}) = \rho^{-1}\boldsymbol{\nabla} \cdot (\rho\dot{\mathbf{v}}_R) . \tag{8}$$

Several interesting features of these equations are worth noting. First, they are linear and contain variable coefficients that depend upon the mean flow. Second, the equations for $\dot{s}$, $\dot{\mathbf{v}}_R$, and $\dot{\phi}$ are sequentially coupled. Hence, instead of solving a coupled set of four equations, we can solve, in order, a scalar equation for the entropy, a vector equation for the rotational velocity, and a scalar equation for the velocity potential. Finally, a convection equation describes the behavior of the entropy, a modified convection equation describes the rotational velocity, and an inhomogeneous convected wave equation with a source term that depends upon the rotational velocity describes the velocity potential.

This form of the governing equations is very general in that it describes the complete time-dependent first-order perturbation about an isentropic and irrotational mean flow. Most flows of interest in turbomachinery, however, are periodic in time with period T. Hence, the unsteady flow can be represented by a Fourier series in which the fundamental frequency ω is $2\pi/T$. Since the first-order equations are linear, the behavior of each Fourier component can be analyzed individually, then summed together to form the total solution. Thus, without loss in generality, we could analyze the Fourier components term by term, and then sum the results. In this case, the time dependent terms in Eqs. (6)-(8) would be replaced by the individual terms of the Fourier series, e.g., $\dot{\phi}(\mathbf{x},t) \to \dot{\phi}(\mathbf{x})\exp(i\omega t)$, and the convective derivative operator by $D/Dt \to i\omega + \boldsymbol{\nabla}\Phi \cdot \boldsymbol{\nabla}$.

Using the harmonic description of the unsteady flow, the explicit time dependence can be removed from the linearized problem. Equations (6), (7) for the entropy and rotational velocity can be solved over a single extended blade passage region subject to boundary conditions along the upstream far-field boundary. The potential equation, Eq. (8), requires boundary conditions around the entire domain, i.e., the upstream and downstream far-field boundaries, the upstream periodic boundaries, and the airfoil and wake surfaces (see Fig 2).
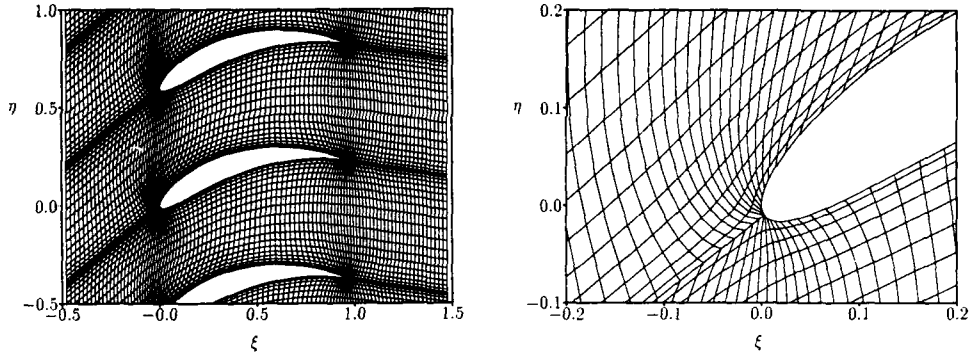
Figure 2: Extended blade-passage solution domain and computational grid.

3.1 Entropy and Rotational Velocity Fluctuations

As demonstrated by Goldstein [16], closed form solutions for the entropy and rotational velocity fluctuations throughout an extended blade-passage region can be determined in terms of the drift (Δ) and stream (Ψ) functions of the steady background flow. The former measures the time required for a fluid particle to traverse the distance between points on a streamline. For the present application we define the drift and stream functions as follows

$$\Delta(\mathbf{x}) = \Delta_0 + \int_{\mathbf{x}_- + (\rho V)_{-\infty}^{-1} \Psi(\mathbf{x}) \mathbf{e}_N}^{\mathbf{x}} V^{-1} d\tau_\Psi \tag{9}$$

and

$$\Psi(\mathbf{x}) = \Psi_0 + \int_{\mathbf{x}_-}^{\mathbf{x}} \bar\rho (\mathbf{e}_z \times \mathbf{V}) \cdot d\tau . \tag{10}$$

In equations (9) and (10), $\mathbf{x}_-$ is the position vector to the point of intersection (ξ_-, η_-) of the reference blade stagnation streamline and the axial line $\xi = \xi_-$. $\mathbf{e}_z$ is a unit vector pointing out from the page. $\mathbf{e}_N = \mathbf{e}_z \times \mathbf{V}_{-\infty}/V_{-\infty}$ is a unit vector normal to the upstream free-stream velocity, $d\tau_\Psi$ is a differential element of arc length along a streamline, and $d\tau$ is a differential vector tangent to the path of integration in (10). The value of Δ at a given point $\mathbf{x}$ is determined by performing the integration in (9) along the streamline that passes through $\mathbf{x}$, whereas $\Psi(\mathbf{x})$ is independent of the path used to evaluate the line integral in (10).

We introduce the vector $\mathbf{X} - \mathbf{V}_\infty t = V_{-\infty}(\Delta - t)\mathbf{e}_T + (\rho V_{-\infty})^{-1}\Psi \mathbf{e}_N$, where $\mathbf{e}_T$ is a unit vector pointing in the direction of the upstream free-stream velocity, and the functions $\Delta - t$ and Ψ are independent material properties (or Lagrangian coordinates) of the steady background flow. Furthermore, we choose the constants Ψ_0 and Δ_0 so that $\mathbf{X} \to \mathbf{x}$, as $\xi \to -\infty$. It follows that any arbitrary scalar or vector function, say $\mathcal{F}$, of $(\mathbf{X} - \mathbf{V}_{-\infty} t)$ is convected without change by the steady background flow and that $\mathcal{F}$ is a function of $\mathbf{x} - \mathbf{V}_{-\infty} t$ far upstream of the blade row, i.e.,

$$\frac{D}{Dt}\mathcal{F}(\mathbf{X} - \mathbf{V}_{-\infty} t) = 0 \quad \text{and} \quad \lim_{\xi \to -\infty} \mathcal{F}[(\mathbf{X} - \mathbf{V}_{-\infty} t)] = \mathcal{F}(\mathbf{x} - \mathbf{V}_{-\infty} t) . \tag{11}$$

The foregoing considerations permit us to write immediately the solution to the entropy transport equation (6) which satisfies the upstream condition (1) as

$$\hat s(\mathbf{x}, t) = \hat s_{-\infty}[(\mathbf{X} - \mathbf{V}_{-\infty} t)] = \text{Re}\{s_{-\infty} \exp[i\boldsymbol{\kappa}_{-\infty} \cdot (\mathbf{X} - \mathbf{V}_{-\infty} t)]\} = \text{Re}\{s(\mathbf{x}) \exp(i\omega t)\} . \tag{12}$$

where $s(\mathbf{x}) = s_{-\infty} \exp(i\boldsymbol{\kappa}_{-\infty} \cdot \mathbf{X})$ is the complex amplitude of the first-order entropy fluctuation.

The rotational velocity fluctuation can also be expressed in terms of the drift and stream functions of the steady background flow and, in this case, the prescribed upstream rotational velocity distribution. For a two-dimensional irrotational steady background flow, the general solution to the rotational velocity transport equation (7) is given by

$$\hat v_R = \nabla \times \mathbf{X} \cdot \mathcal{A}(\mathbf{X} - \mathbf{V}_{-\infty} t) + \frac{\hat s}{2} \nabla \Phi \tag{13}$$

The particular solution to Eq. (7) that satisfies the far upstream condition (2) can be obtained by setting

$$\mathcal{A}(\mathbf{X} - \mathbf{V}_{-\infty} t) = \hat v_{R,-\infty}(\mathbf{X} - \mathbf{V}_{-\infty} t) - \hat s_{-\infty}(\mathbf{X} - \mathbf{V}_{-\infty} t)\mathbf{V}_{-\infty}/2 . \tag{14}$$

where $\hat s_{-\infty}(\mathbf{X} - i V_{-\infty} t)$ is given above and

$$\hat v_{R,-\infty}(\mathbf{X} - \mathbf{V}_{-\infty} t) = \text{Re}\{v_{R,-\infty} \exp[i\boldsymbol{\kappa}_{-\infty} \cdot (\mathbf{X} - \mathbf{V}_{-\infty} t)]\} \tag{15}$$

After combining (12) through (15), we find

$$\check{v}_R(\mathbf{x}, t) = Re\{[\nabla \odot \mathbf{X} \cdot \mathbf{A}_{-\infty} + s_{-\infty}\nabla\Phi/2]\exp[i\boldsymbol{\kappa}_{-\infty} \cdot (\mathbf{X} - \mathbf{V}_{-\infty}t)]\} = \mathbf{v}_R(\mathbf{x})\exp(i\omega t) ,\qquad (16)$$

where $\mathbf{A}_{-\infty} = \mathbf{v}_{R,-\infty} - s_{-\infty}\mathbf{V}_{-\infty}/2$ and $\mathbf{v}_R(\mathbf{x})$ is the complex amplitude of the rotational velocity fluctuation.

3.2 Modification to the Goldstein Velocity Splitting

At this point we have expressed the entropy and rotational velocity fluctuations in terms of the mean flow drift and stream functions. Therefore, these fluctuations and the source term, $\bar{\rho}^{-1}\nabla \cdot (\bar{\rho}\mathbf{v}_R)$, in the unsteady potential equation (8) can be evaluated once the drift and stream functions, and their derivatives, are determined from a solution for the underlying steady flow. However, as pointed out by Goldstein and later by Atassi and Grzedzinski [18], if the background flow has leading-edge stagnation points, the rotational velocity will be singular along blade and wake surfaces. Such behavior is a result of the singular behavior of the drift function, i.e., $\Delta \rightarrow a_0 \ln n$ as $n \rightarrow 0$, where n is the normal distance from the airfoil or wake surface, and a_0 is a constant which describes the behavior of the flow in the vicinity of the stagnation point.

Consider the perturbation velocity

$$\check{\mathbf{v}} = \nabla\check{\phi} + \check{\mathbf{v}}_R .\qquad (17)$$

Atassi and Grzedzinski showed that if one used the velocity decomposition

$$\check{\mathbf{v}} = \left(\nabla\check{\phi} - \nabla\check{\phi}^*\right) + \left(\check{\mathbf{v}}_R + \nabla\check{\phi}^*\right) = \nabla\check{\phi}' + \check{\mathbf{v}}'_R ,\qquad (18)$$

where ϕ^* is a pressure-less or convected potential, i.e., $D\phi^*/Dt = 0$, then $\check{\mathbf{v}}'_R$ satisfies the same transport equation [Eq. (7)] as $\check{\mathbf{v}}_R$. Similarly, $\check{\phi}'$ satisfies the same potential equation [i.e., Eq. (8)] as ϕ. Furthermore, if one chooses ϕ^* carefully, $\check{\mathbf{v}}'_R$ will be regular on the blade and wake surfaces. In particular, if we set

$$\check{\phi}^* = Re\left\{\left[-i\omega^{-1}\mathbf{A}_{-\infty} \cdot \mathbf{V}_{-\infty} + F(Y)\right]\exp[i\boldsymbol{\kappa}_{-\infty} \cdot (\mathbf{X} - \mathbf{V}_{-\infty}t)]\right\} ,\qquad (19)$$

the rotational velocity, $\mathbf{v}'_R$ is given by

$$\check{\mathbf{v}}'_R = Re\left\{\left[\nabla \odot \mathbf{X} \cdot i\boldsymbol{\kappa}_{-\infty}F + \left(c_2 + \frac{\partial F}{\partial Y}\right)\nabla Y + s_{-\infty}\nabla\Phi/2\right]\exp[i\boldsymbol{\kappa}_{-\infty} \cdot (\mathbf{X} - \mathbf{V}_{-\infty}t)]\right\} ,\qquad (20)$$

where $c_2 = -\omega^{-1}V_{-\infty}(\boldsymbol{\kappa}_{-\infty} \times \mathbf{A}_{-\infty}) \cdot \mathbf{e}_z$ and $F(Y)$ is a function which depends upon, among other things, the behavior of the mean flow in the vicinity of a stagnation point. This function is chosen in such a way that the rotational velocity vanishes at blade and wake surfaces. In particular, we set

$$F(Y) = \frac{(\boldsymbol{\kappa}_{-\infty} \times \mathbf{A}_{-\infty}) \cdot \mathbf{e}_z G \cos\Omega_{-\infty}}{2\pi(\omega/V_{-\infty})(1 - ia_0\omega)}\sin\left[\frac{2\pi(Y - Y_0)}{G\cos\Omega_{-\infty}}\right] ,\qquad (21)$$

where Y is $\Psi/(\rho V)_{-\infty}$. This choice of F eliminates the singular behavior of the rotational velocity. Indeed, $\mathbf{v}'_R = 0$ on blade and wake surfaces. However, the perturbation potential source term, $\bar{\rho}^{-1}\nabla \cdot (\rho\mathbf{v}'_R)$, is still singular at these surfaces.

Equations (12) and (20) relate the complex amplitudes of the first-order unsteady entropy and rotational velocity fluctuations to their prescribed amplitudes, $s_{-\infty}$ and $\mathbf{v}_{R,-\infty}$, and wave number, $\boldsymbol{\kappa}_{-\infty}$, at inlet and to the velocity, drift function and stream function of the steady background flow. Note that $\mathbf{v}'_R$ depends upon Δ and Ψ and the first partial derivative of these functions. Therefore, the unsteady vorticity, $\nabla \times \mathbf{v}'_R$, and the source term, $\bar{\rho}^{-1}(\nabla \cdot \rho\mathbf{v}'_R)$ depend also upon the second partial derivatives of the mean-flow drift and stream functions. Thus, an accurate solution for the nonlinear steady background flow is a critical prerequisite to properly determining the unsteady effects associated with inlet entropic and vortical excitations.

4. NUMERICAL SOLUTION PROCEDURE

The theoretical foundation for the present linearized analysis has been outlined. We will proceed to discuss the procedures used to determine the complex amplitudes of the unsteady entropy, s, rotational velocity, $\mathbf{v}'_R$, and source term, $\bar{\rho}^{-1}\nabla \cdot (\rho\mathbf{v}'_R)$. The finite-difference numerical model used to solve the boundary-value problem for the complex amplitude of the unsteady potential, ϕ', has been described in previous work. Since the only changes required for the gust problem are those needed to accomodate the source term in the field equation (8) and rotational velocity effects in the far-field boundary conditions, we will not repeat the description here, but simply refer the reader to Refs. [11,21,22] for the details.

4.1 Generation of Streamline Grid

In the previous section, it was shown that the unsteady entropy and rotational velocity can be expressed in terms of the drift and stream functions, Δ and Ψ, of the steady background flow. For this reason it is convenient to use an H-grid in which one set of mesh lines are the streamlines of the steady background flow for the numerical evaluation of these unsteady flow variables. The first step in the grid generation process is to specify the grid point locations on the boundary of the physical solution domain, i.e., the single extended blade-passage region of finite extent shown in Fig. 2. The boundaries of this region are the suction and pressure surfaces of the blades, the upstream and downstream axial lines $\xi = \xi_{\mp}$ and the upstream and downstream stagnation streamlines. The stagnation streamlines locations are determined from the solution for the nonlinear steady background flow.

The locations of the stagnation streamlines are found by particle tracing, i.e., by integrating the equation

$$\frac{\partial \mathbf{x}}{\partial \tau} = \mathbf{V} \tag{22}$$

using a variable-step, fifth-order, Runge-Kutta algorithm [23], from the leading and trailing edges of a blade to the far upstream $(\xi = \xi_-)$ and far downstream $(\xi = \xi_+)$ boundaries. The location of the leading-edge stagnation point is determined by curve fitting the blade profile and the steady potential distribution along the blade using cubic splines. The stagnation point is defined as the point on this curve at which the steady potential has a minimum value, and is found by bisection. After integrating Eq. (22) from the leading-edge stagnation and the trailing-edge points to the far-field boundaries, the calculated points on the stagnation streamlines a-e curve fit using cubic splines.

Once the boundaries of the H-grid have been determined, the locations of the interior points are found using an elliptic grid generation technique similar to that developed by Thompson et al. [24]. An elliptic grid generator offers the advantages that relatively smooth grids can be determined and grids for complicated flow geometries, such as those associated with cascades of thick, highly cambered blades, are easy to generate. Following Thompson et al., the grid lines are described by the partial differential equations

$$\nabla^2 \Xi = P \tag{23}$$

and

$$\nabla^2 \mathcal{H} = Q . \tag{24}$$

The "axial" and "streamwise" grid lines correspond to lines of constant Ξ and $\mathcal{H}$, respectively. The functions P and Q can be used to control the spacing and orthogonality of the grid lines. In this investigation, however, we have chosen the function Q so that $\mathcal{H}$ is the stream function Ψ of the irrotational steady background flow, i.e., $Q = \mathbf{V} \times \nabla \bar{\rho}$.

Rather than solve Eqs. (23) and (24) for Ξ and Ψ as functions of ξ and η, we invert these equations to determine ξ and η as functions of Ξ and Ψ. It can be shown that

$$\alpha \frac{\partial^2 \xi}{\partial \Xi^2} - 2\beta \frac{\partial^2 \xi}{\partial \Xi \partial \Psi} + \gamma \frac{\partial^2 \xi}{\partial \Psi^2} = -D^2 \left(P \frac{\partial \xi}{\partial \Xi} + Q \frac{\partial \xi}{\partial \Psi} \right) \tag{25}$$

and

$$\alpha \frac{\partial^2 \eta}{\partial \Xi^2} - 2\beta \frac{\partial^2 \eta}{\partial \Xi \partial \Psi} + \gamma \frac{\partial^2 \eta}{\partial \Psi^2} = -D^2 \left(P \frac{\partial \eta}{\partial \Xi} + Q \frac{\partial \eta}{\partial \Psi} \right) , \tag{26}$$

where D is the determinant of the Jacobian of the independent variable transformation, $(\xi, \eta) \leftrightarrow (\Xi, \Psi)$, i.e.,

$$D = \frac{\partial \xi}{\partial \Xi} \frac{\partial \eta}{\partial \Psi} - \frac{\partial \xi}{\partial \Psi} \frac{\partial \eta}{\partial \Xi} , \tag{27}$$

and the coefficients α, β, and γ are given by

$$\alpha = \left(\frac{\partial \xi}{\partial \Psi} \right)^2 + \left(\frac{\partial \eta}{\partial \Psi} \right)^2, \quad \beta = \frac{\partial \xi}{\partial \Xi} \frac{\partial \xi}{\partial \Psi} + \frac{\partial \eta}{\partial \Xi} \frac{\partial \eta}{\partial \Psi}, \quad \gamma = \left(\frac{\partial \xi}{\partial \Xi} \right)^2 + \left(\frac{\partial \eta}{\partial \Xi} \right)^2 . \tag{28}$$

The nonlinear partial differential equations (25) and (26) are solved numerically over a rectangular region in Ξ, Ψ-space subject to Dirichlet conditions on ξ and η at the boundary. The values of ξ and η along the boundary of the rectangular domain are defined by their values at the prescribed points along the boundary of the extended blade-passage domain. Because the Ξ, Ψ-grid is rectangular, difference approximations are easy to construct. In the present investigation, nonconstant transformed grid spacings are used to control the spacings in the physical plane. For example, by choosing appropriate values of $\Delta \Xi_i$ and $\Delta \Psi_j$, the streamwise and axial grid lines can be packed near blade and wake surfaces and near the leading and trailing edges of the blades, respectively.

The difference equations for ξ and η are solved using a successive line over-relaxation procedure in which the coefficients α, β and γ, and the terms on the right-hand-sides of Eqs. (25) and (26) are lagged, i.e., they are computed just prior to each line over-relaxation. Also, because the function Q is fairly expensive to compute, and because it is fairly insensitive to small changes in ξ and η, this function is updated only every tenth iteration.

A typical grid generated for a compressor cascade operating at an inlet Mach number of 0.3 and an inlet flow angle of 40.0 deg is shown in Fig. 2. The blades are thick and highly cambered, and the cascade has a gap-to-chord ratio, G, of 0.6 and a stagger angle Θ of 15 deg. The steady flow, which is determined using the analysis of Ref. [19] is used to generate the stagnation streamlines and to determine the function Q in Eqs. (25) and (26). For the grid shown in Fig. 2, the function P has been set equal to 0. Note the clustering of streamlines near the blade and wake surfaces and axial lines in the vicinity of the blade leading and trailing edges, which is achieved by employing nonconstant rectangular grid spacings, $\Delta \Xi_i$ and $\Delta \Psi_j$, in the transformed plane.

4.2 Drift Function

Because a streamline mesh is used, the drift function can be evaluated by straightforward numerical integration of Eq. (9). The procedure is simply to specify the drift function along the far upstream boundary $\xi = \xi_-$, and then to evaluate this function along each streamline using the second-order difference approximation

$$\Delta_{i+1,j} = \Delta_{i,j} + \frac{\tau_{i+1,j} - \tau_{i,j}}{0.5 \left(|\mathbf{V}_{i+1,j}| + |\mathbf{V}_{i,j}| \right)} \tag{29}$$

Since the reciprocal of the steady flow speed, V^{-1}, appears in the denominator of the integrand in Eq. (9), the drift function will be singular at flow stagnation points. Hence, for a blade having a blunt leading edge this function will be singular along the entire surface of each blade and its wake.
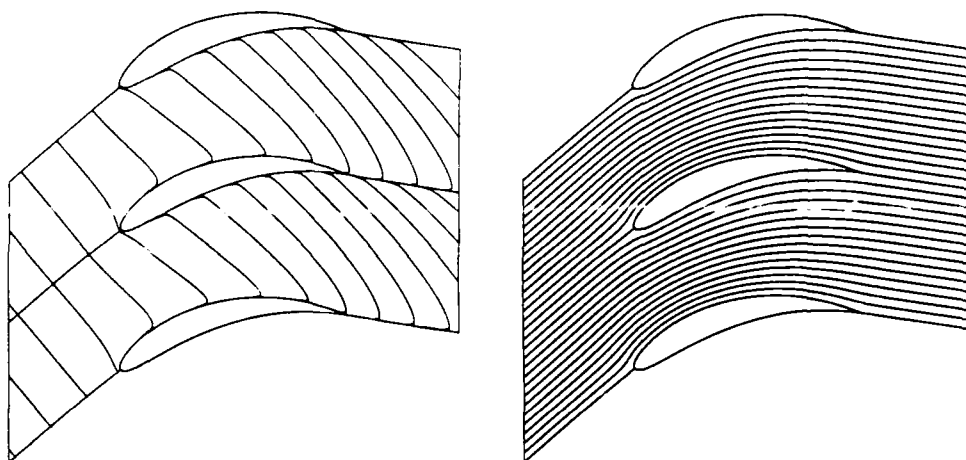
Figure 3: Drift and stream contours for two-dimensional steady cascade flow.

The calculated drift and stream function contours for the the compressor cascade of Fig. 2 are shown in Fig. 3. Note that the drift function contours are orthogonal to the streamlines far upstream of the blade row. This is not a requirement, but it does simplify certain parts of the formulation. Note also the singular behavior indicated by the drift function contours near the blade and wake surfaces.

The derivatives of the drift and stream functions at a given grid point are determined using the finite difference operators developed by Caspar and Verdon [21]. Because the drift function is singular along blade and wake surfaces, one sided difference approximations are used to evaluate its derivatives at the nodes on the first streamlines away from theses surfaces. The derivatives of the drift function at blade and wake surfaces are singular, but are not required to evaluate v_R' and $\rho^{-1}\nabla \cdot (\rho v_R')$ on these surfaces or in the field.

As noted previously, a numerical resolution of the linear, variable-coefficient, unsteady, boundary-value problem that governs the velocity potential is required over a single extended blade-passage region of finite extent. The field equation, Eq. (8), must be solved in continuous regions of the flow subject to boundary or jump conditions which are imposed at the mean positions of the blade, wake and shock surfaces. Also, the unsteady near-field numerical solution must be matched to far-field analytical solutions (see [25]) at finite axial distances ($\xi = \xi_\mp$) upstream and downstream from the blade row. The numerical procedures for determining ϕ' are described in Refs. [11,21,22].

5. NUMERICAL RESULTS

Unsteady aerodynamic response predictions are given below to demonstrate important features of the foregoing linearized analysis. We will consider flat-plate cascades and cascades consisting of blades that are constructed by superposing the thickness distribution of a NACA four-digit series airfoil on a circular arc camber line. For the latter, H_T is the blade thickness and H_C is the height of the circular-arc camber line at the blade midchord. The flows to be considered here are entirely subsonic. The steady background flows have been determined using the methods of Ref. [19]. In each case a Kutta condition has been applied at blade trailing edges and therefore, only inlet uniform flow information, e.g., $M_{-\infty}$ and $\Omega_{-\infty}$, must be specified for the steady calculation. First-harmonic unsteady solutions were determined on an H-type mesh (see Fig. 2) consisting of 120 "axial" lines and 30 mean-flow streamlines. The grid lines were "packed" near the blade and wake surfaces and near the blade edges, respectively.

We will first apply the analysis to flat-plate cascades in which the blade mean positions are aligned with the inlet free-stream flow direction, i.e., $\Theta = \Omega_{-\infty}$, to compare present response predictions with those based on Smith's [1] classical linearized analysis. We will then consider cascades of uncambered NACA airfoils to study the effects of blade thickness on the unsteady aerodynamic response to an incident vortical gust. Finally, we will examine the response of a more realistic cascade configuration, a compressor exit guide vane (EGV) consisting of thick, highly cambered blades ($H_T = 0.12$, $H_C = 0.13$).

We are primarily interested in linearized unsteady flows excited by vortical gusts, such as those that arise, for example, from wakes off the blades of an adjacent upstream blade row. If the "circumferential" spacing between the blades in the adjacent upstream row is G_{EXC} and if these blades move at velocity $V_{EXC}e_\eta$ relative to the blade row under consideration, then the interblade phase angle (i.e., the difference in the phase of a disturbance from one blade to the next) and temporal frequency of the fundamental or blade passing vortical excitation are $\sigma = \kappa_{\eta,-\infty}G = -2\pi G/G_{EXC}$ and $\omega = -\kappa_{\eta,-\infty}V_{EXC} = \sigma G^{-1}V_{EXC}$, where $\kappa_{\eta,-\infty} = -2\pi/G_{EXC}$ is the circumferential wave number of the excitation. For the present study, we will choose $\sigma = -2\pi$, $\omega = 5$ and $v_g = (1,0)$ to describe a "standard" vortical gust. Here, v_g is the complex amplitude of the gust velocity component normal to the inlet free-stream flow direction at the point $(x,y) = (0,0)$. Note that v_g is the amplitude at the leading edge of the reference blade that would exist if the incident gust was convected through the blade row, without distortion, by the uniform inlet flow.
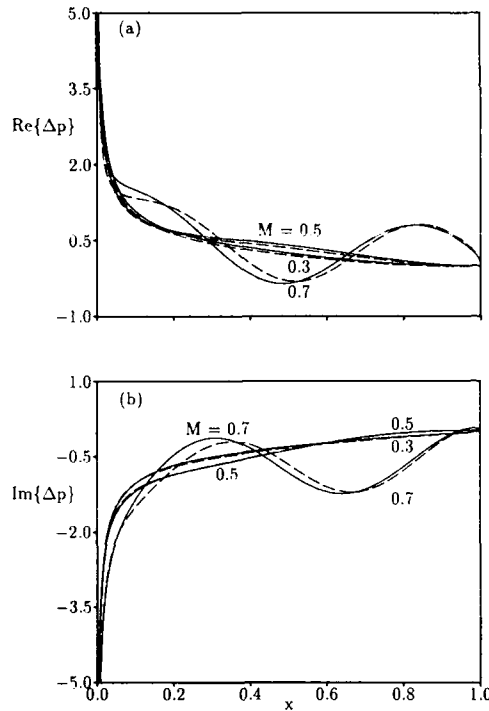
Figure 4: Effect of Mach number on the unsteady pressure-difference response of a flat-plate cascade with $\Omega = \Theta = 45$ deg and $G = 1$ subjected to an incident vortical gust with $v_g = (1,0)$, $\omega = 5$ and $\sigma = -2\pi$: (a) in-phase component (real part) of Δp, (b) out-of-phase component (imaginary part); $- - -$ Smith analysis [4], ———— present analysis.
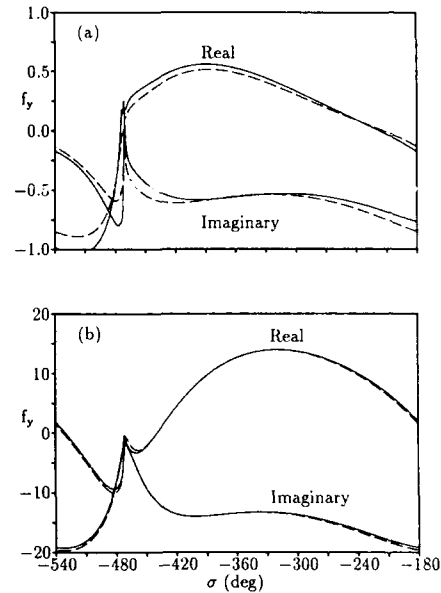
Figure 5: Unsteady lift versus interblade phase angle for a flat-plate cascade with $M = 0.3$, $\Omega = \Theta = 45$ deg and $G = 1$: (a) unsteady lift due to incident vortical gusts with $v_g = (1,0)$ and $\omega = 5$; (b) unsteady lift due to blade bending vibrations with $h_y = (1,0)$ and $\omega = 5$; $- - -$ Smith analysis [4], ———— present analysis.

5.1 Flat-Plate Cascade

The example flat-plate cascade has a stagger angle, Θ, of 45 deg and a blade spacing, G, of 1.0 and operates at three different inlet Mach numbers, i.e., $M_{-\infty} = 0.3$, 0.5 and 0.7. In each case the inlet flow angle, $\Omega_{-\infty}$, is 45 deg and vortical excitations with $v_g = (1,0)$ and $\omega = 5$ are imposed far upstream of the blade row. Predicted unsteady pressure-difference distributions acting on the reference ($m = 0$) blade for the standard vortical excitation at $\sigma = -2\pi$ are shown in Fig. 4, where the solid and dashed curves represent the results of the present and of Smith's analysis, respectively. Recall that in the present analysis the unsteady potential equation contains the source term $\bar{\rho}^{-1}\nabla \cdot (\bar{\rho}v_R')$ and $\nabla\phi' \cdot n = 0$ on blade and wake surfaces, whereas in the classical linearization the potential equation is homogeneous, and the normal component of the irrotational velocity must cancel the normal component of the gust velocity at blade surfaces. The results in Fig. 4 show that the two analyses yield pressure-difference predictions that are in very good agreement for $M_{-\infty} = 0.3$ and $M_{-\infty} = 0.5$, but the agreement is not quite so satisfactory for $M_{-\infty} = 0.7$. We suspect that the differences at $M_{-\infty} = 0.7$ occur because the computational grid used in the present numerical calculation was not dense enough to resolve the high wave number acoustic response phenomena that are associated with high subsonic Mach numbers and high excitation frequencies. Therefore, such differences should disappear if a mesh of sufficient density is employed in the numerical calculation.

The unsteady lift responses at the reference blade of the flat-plate cascade operating at $M_{-\infty} = 0.5$ to prescribed vortical excitations with $v_g = (1,0)$ and $\omega = 5$ and to prescribed blade translations, $h_y \exp(i\omega t)$, normal to the blade chord with $h_y = (1,0)$ and $\omega = 5$ are plotted versus interblade phase angle in Fig. 5. The excitations occur over interblade phase range extending from -540 deg (-3π) to -180 deg $(-\pi)$. Abrupt changes in the lift response curves occur at $\sigma = -473.8$ deg (-2.62π) and -471.1 deg (-2.63π). The excitations at these interblade phase angles produce resonant acoustic response disturbances in the far field. The lift responses to the vortical excitations predicted by the numerical and semi-analytic solution procedures are in good agreement; however, this agreement is not nearly as good as that between the lift responses to the blade translational excitations, suggesting that the present numerical analysis still requires some improvements so that the source term, $\bar{\rho}^{-1}\nabla \cdot (\bar{\rho}v_R')$, can be evaluated more accurately.
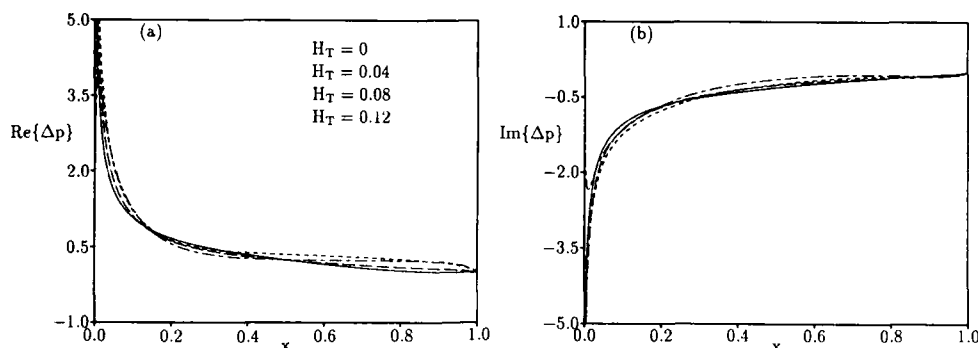
Figure 6: Effect of blade thickness on the unsteady pressure-difference response of NACA 00XX cascades with $M_{-\infty} = 0.3$, $\Omega_{-\infty} = 45$ deg, $\Theta = 45$ deg and $G = 1$ subjected to an incident vortical gust with $v_g = (1,0)$, $\omega = 5$, and $\sigma = -2\pi$: (a) and (b) as in Fig. 4.

5.2 Effects of Blade Thickness

We proceed to evaluate the present analysis by applying it to a family of cascade configurations. Here $\Theta = 45$ deg, $G = 1$, the blades are uncambered ($H_C = 0$), but the blade thickness varies from $H_T = 0$ to $H_T = 0.12$. These cascades operate at an inlet Mach number of 0.3 and an inlet flow angle of 45 deg, and are subjected to the standard vortical gust excitation at $v_g = (1,0)$, $\omega = 5$ and $\sigma = -2\pi$.

This cascade family has been studied to indicate the effects of blade thickness on the unsteady aerodynamic response to a vortical gust excitation. It should be noted that although the blades are uncambered and their chord lines are aligned with the inlet flow direction, i.e., $\Theta = \Omega_{-\infty}$, there is a small mean or steady lift force acting on the blades for $H_T \neq 0$. This force increases in magnitude, from 0 for $H_T = 0$ to 0.062 for $H_T = 0.12$, with increasing blade thickness. The exit Mach numbers (M_{∞}) vary from 0.3 for $H_T = 0$ to 0.314 for $H_T = 0.12$, and the exit flow angles (Ω_{∞}) from $45°$ to $47.22°$. The unsteady pressure-difference distributions along the reference blades of the cascades with $H_T = 0$, 0.04, 0.08 and 0.12 are shown in Fig. 6. These results indicate that blade thickness has only a limited impact on the aerodynamic response to a vortical excitation. Indeed, the pressure-difference response for the cascade of 2% thick blades (not shown) closely resembles that for the flat-plate ($H_T = 0$) cascade. This result provides an important check on the present analysis, indicating that the mathematical difficulties associated with mean flow stagnation at blade leading edges have been successfully overcome.

5.3 Exit Guide Vane

We turn now to a more realistic configuration, i.e., we consider the compressor exit guide vane (EGV) which consists of thick, $H_T = 0.12$, highly cambered, $H_C = 0.13$, modified NACA four digit airfoils. The EGV has a stagger angle of 15 deg, a blade spacing of 0.6 and operates at a prescribed inlet Mach number and inlet flow angle of 0.3 and 40 deg, respectively. The calculated exit Mach number, exit flow angle and mean lift force, F_y, acting on each blade are 0.226, -7.4 deg and 0.36, respectively. Steady Mach number contours and Mach number distributions along the blade surface for this configuration are depicted in Fig. 7.

We will examine the unsteady pressure response of this cascade to incident vortical excitations and compare it to that for a corresponding flat-plate cascade with $\Theta = \Omega_{-\infty} = 40$ deg, $G = 0.6$ and $M_{-\infty} = 0.3$. Note that since the blade mean positions are aligned with the inlet flow, the local steady Mach number, M, and flow angle, Ω, are constant for the flat-plate configuration. Contours of the real part of the complex amplitude of the unsteady vorticity and pressure for unsteady flows through the EGV and the corresponding flat-plate cascade are shown in Figures 8 and 9, respectively. Here, the unsteady flows are excited by the standard vortical gust. The prescribed gust is severely distorted as it is convected by the nonuniform mean flow through the EGV blade row. In contrast, this same gust is convected without distortion by the uniform mean flow through the flat-plate blade row. Also, since the vorticity is convected at different mean velocities along the upper and lower surfaces of the EGV blades, it is discontinuous across their wakes. Finally, the contours depicted in Fig. 9 indicate that the unsteady pressure behaviors associated with the EGV and flat-plate cascades are similar far upstream, but differ substantially in the vicinity of the blade surfaces and downstream of the blade row.

The pressure-difference responses along the reference blade of the EGV and flat-plate cascades to the standard vortical excitation at $v_g = (1,0)$, $\omega = 5$ and $\sigma = -2\pi$ are shown in Fig. 10. The unsteady lift forces acting on the reference blades of the two cascades are plotted versus interblade phase angle for vortical excitations at $v_g = (1,0)$, $\omega = 5$ and $-3\pi \leq \sigma \leq -\pi$ in Fig. 11. The excitations at $\sigma = -404.2$ deg and -293.9 deg produce resonant acoustic response disturbances far upstream and far downstream of the flat-plate cascade and far upstream of the EGV; those at $\sigma = -414.3$ deg and -308.8 deg produce such response disturbances far downstream of the EGV. The results in Figures 10 and 11 indicate, to some extent, the relative importance of nonuniform mean flow phenomena on the local and global unsteady aerodynamic response at a blade surface for cascades subjected to incident vortical excitations. It should be noted that the unsteady lift acts in the direction of the positive y-axis (see Fig. 1), and this is inclined at different angles relative to the axial flow direction for the EGV ($\Theta = 15$ deg) and
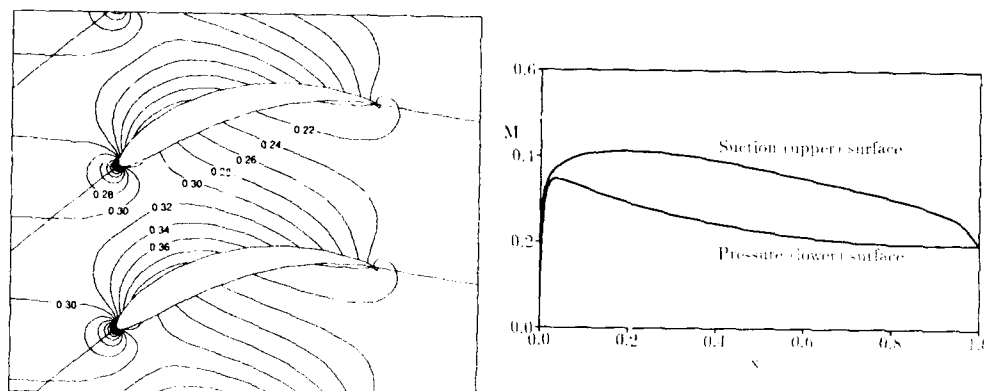
Figure 7: Mach number contours and blade surface Mach number distributions for a steady flow with $M_{-\infty} = 0.3$ and $\Omega_{-\infty} = 10$ deg through the EGV cascade ($\Theta = 15$ deg, $G = 0.6$, $H_T = 0.12$ and $H_C = 0.13$).
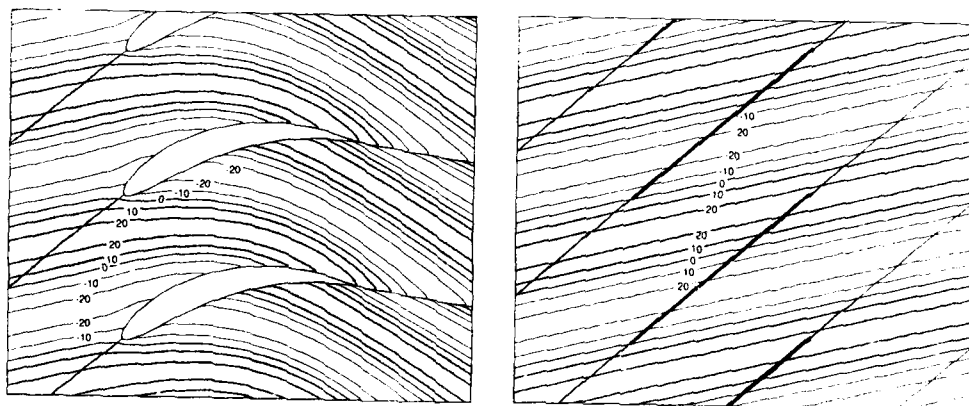
Figure 8: Contours of the real part of the unsteady vorticity for the EGV and the corresponding flat-plate ($M = 0.3$, $\Omega = \Theta = 10$ deg, $G = 0.6$) cascades subjected to an incident vortical gust with $v_g = (1, 0)$, $\omega = 5$ and $\sigma = -2\pi$.

Figure 9: Contours of the in-phase unsteady pressure for the EGV and the corresponding flat-plate cascades subjected to an incident vortical gust with $v_g = (1, 0)$, $\omega = 5$ and $\sigma = -2\pi$.

Figure 10: Unsteady pressure-difference response for the EGV and corresponding flat-plate cascades subjected to an incident vortical gust with $v_g = (1,0)$, $\omega = 5$ and $\sigma = -2\pi$: (a) in-phase component (real part); (b) out-of-phase component (imaginary part); $---$ flat-plate cascade, $\longrightarrow$ EGV cascade.
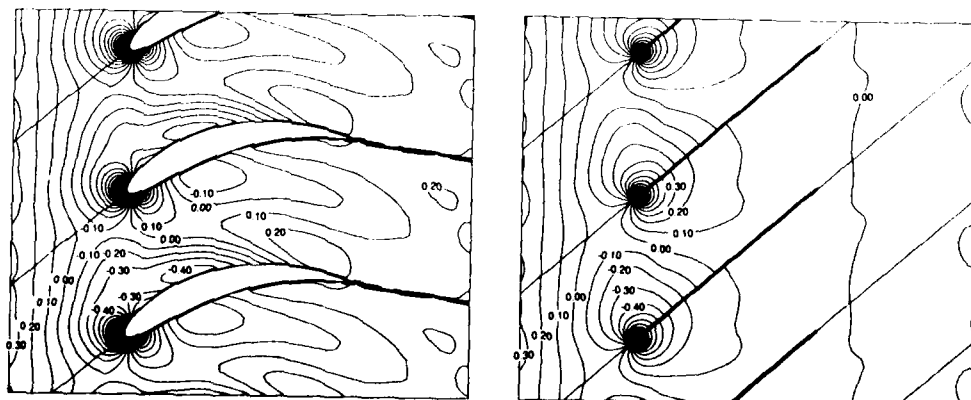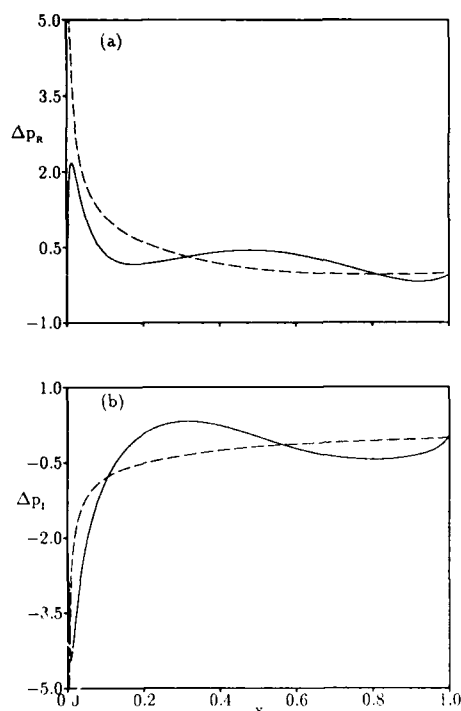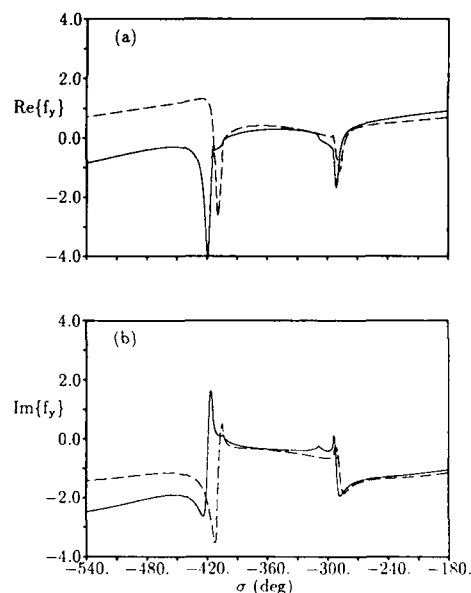
Figure 11: Unsteady lift versus interblade phase angle for the EGV and corresponding flat-plate cascade subjected to incident vortical gusts with $v_g = (1,0)$ and $\omega = 5$: (a), (b). $---$ and $\longrightarrow$ as in Fig. 10.

flat-plate ($\Theta = 40$ deg) cascades. Also, the flat-plate pressure-difference distributions in Fig. 10 are in very good agreement with the corresponding results of Smith's analysis. Finally, the flat-plate lift distributions in Fig. 11 are in good agreement with Smith's results, except for interblade phase angles lying in the range -540 deg $< \sigma < -404.2$ deg, where the out-of-phase lift responses, i.e., $\mathrm{Im}(f_y)$, predicted by the two analyses are similar qualitatively but show small quantitative differences.

6. CONCLUDING REMARKS

A method for predicting the linearized unsteady aerodynamic response of a cascade of airfoils to external aerodynamic excitations has been presented. The unsteady flow is regarded as a small perturbation of a nonuniform isentropic and irrotational steady background flow. Goldstein's splitting, [16,17], along with a recent modification introduced by Atassi and Grzedzinski [18] are used to decompose the linearized unsteady velocity into irrotational and rotational parts leading to equations for the linearized unsteady entropy, rotational velocity, and velocity potential which are coupled only sequentially. The entropic and rotational velocity fluctuations are described in terms of the mean-flow drift and stream functions, and the potential fluctuation is governed by an inhomogeneous convected wave equation in which the source term depends on the rotational velocity field. In this paper the analytical and numerical techniques used to determine the linearized unsteady flow have been outlined and demonstrated through a series of numerical examples.

The results obtained using the present analysis were found to be in very good agreement with the results of Smith's [4] analysis for flat-plate cascades operating at low ($M = 0.3$) and moderate ($M = 0.5$) Mach numbers, but the agreement for flat-plates operating at high subsonic Mach number ($M = 0.7$) was not satisfactory. It appears that the grid used in the numerical calculation was not adequate for resolving the high wave number acoustic response phenomena that is associated with high steady-flow Mach numbers and high excitation frequencies. Results for the cascades of symmetric NACA 00XX airfoils show reasonable trends with varying blade thickness, and indicate that blade thickness has only a limited impact on the response of a cascade to incident vortical gusts. The blade thickness study also indicates that the present analysis overcomes the mathematical difficulties associated with unsteady vortical perturbations of potential mean flows containing leading edge stagnation points.

More detailed gust response predictions have been presented for a compressor exit guide vane (EGV), including contours of vorticity and pressure that illustrate the manner in which a vortical gust is distorted as it is convected, by the mean flow, through a blade row and the unsteady pressure response that is excited by the interaction of this gust with the blade row. These numerical results serve to demonstrate the capabilities of the present analysis for predicting the unsteady pressure response of cascades operating under high mean load conditions.

The analysis described in this paper leads to very efficient predictions of the aerodynamic response of realistic cascade configurations to unsteady aerodynamic excitations. Therefore this analysis should be useful in turbomachinery aeroelastic and aeroacoustic design investigations. Improvements are still needed to resolve high wave number acoustic response phenomena and to accurately calculate the source term over broad ranges of reduced frequencies and interblade phase angles. Also, in future work the composite-mesh solution capability of Ref. [22] should be incorporated into the present gust analysis so that entropic and vortical excitations of transonic flows with weak shocks can be analyzed.

References

[1] D. S. Whitehead, "Classical Two Dimensional Methods," *AGARD Manual on Aeroelasticity in Axial-Flow Turbomachines*, Vol. 1, *Unsteady Turbomachinery Aerodynamics*, M. F. Platzer and F. O. Carta, editors, AGARD-AG-298, March 1987, Chapter III.

[2] D. S. Whitehead, "Vibration and Sound Generation in a Cascade of Flat Plates in Subsonic Flow," Cambridge Univ. Engineering Department, Cambridge, UK, CUED/A Turbo/TR 15, 1970.

[3] S. Kaji and T. Okazaki, "Propagation of Sound Waves Through a Blade Row, II. Analysis Based on the Acceleration Potential Method," *Journal of Sound and Vibration*, Vol. 11(3), March 1970, pp. 355-375.

[4] S. N. Smith, "Discrete Frequency Sound Generation in Axial Flow Turbomachines," British Aeronautical Research Council, London, UK, Reports and Memoranda 3709, 1971.

[5] J. M. Verdon, "Further Developments in the Aerodynamic Analysis of Unsteady Supersonic Cascades, I. The Unsteady Pressure Field, II. Aerodynamic Response Predictions," *Trans. ASME, A: Journal of Engineering for Power*, Vol. 99(4), October 1977, pp. 509-525.

[6] T. Nagashima and D. S. Whitehead, "Linearized Supersonic Unsteady Flow in Cascades," British Aeronautical Research Council, London, UK, Reports and Memoranda 3811, 1978.

[7] J. J. Adamczyk and M. E. Goldstein, "Unsteady Flow in a Supersonic Cascade with Subsonic Leading Edge Locus," *AIAA Journal*, Vol. 16(12), December 1978, pp. 1248-1254.

[8] R. H. Ni, "A Rational Analysis of Periodic Flow Perturbation in Supersonic Two-dimensional Cascade," *Trans. ASME, A: Journal of Engineering for Power*, Vol. 101(3), July 1979, pp. 431-439.

[9] M. Namba, "Three Dimensional Flows," *AGARD Manual on Aeroelasticity in Axial-Flow Turbomachines*, Vol. 1, *Unsteady Turbomachinery Aerodynamics*, M. F. Platzer and F. O. Carta, editors, AGARD-AG-298, March 1987, Chapter IV.

[10] D. S. Whitehead, "The Calculation of Steady and Unsteady Transonic Flow in Cascades," Cambridge Univ. Engineering Department, Cambridge, UK, CUED/A Turbo/TR 118, 1982.

[11] J. M. Verdon and J. R. Caspar, "A Linearized Unsteady Aerodynamic Analysis for Transonic Cascades," *Journal of Fluid Mechanics*, Vol. 149, December 1984, pp. 403-429.

[12] K. C. Hall and E. F. Crawley, "Calculation of Unsteady Flows in Turbomachinery Using the Linearized Euler Equations," *AIAA Journal*, Vol. 27(6), June 1989, pp. 777-787.

[13] J. M. Verdon, "Linearized Unsteady Aerodynamic Theory," *AGARD Manual on Aeroelasticity in Axial-Flow Turbomachines*, Vol. 1, *Unsteady Turbomachinery Aerodynamics*, M. F. Platzer and F. O. Carta, editors, AGARD-AG-298, March 1987, Chapter II.

[14] J. M. Verdon, "Unsteady Aerodynamics for Turbomachinery Aeroelastic Applications," *Unsteady Transonic Aerodynamics, Progress in Astronautics and Aeronautics*, D. Nixon, editor, *Progress in Astronautics and Aeronautics*, Vol. 119, AIAA, New York, 1989.

[15] E. Acton and S. G. Newton, "Numerical Methods for Unsteady Transonic Flow," *AGARD Manual on Aeroelasticity in Axial-Flow Turbomachines*, Vol. 1, *Unsteady Turbomachinery Aerodynamics*, M. F. Platzer and F. O. Carta, editors, AGARD-AG-298, March 1987, Chapter VI.

[16] M. E. Goldstein, "Unsteady Vortical and Entropic Distortions of Potential Flows Round Arbitrary Obstacles," *Journal of Fluid Mechanics*, Vol. 89, December 1978, pp. 433-468, Part 3.

[17] M. E. Goldstein, "Turbulence Generated by the Interaction of Entropy Fluctuations with Non-uniform Mean Flows," *Journal of Fluid Mechanics*, Vol. 93, July 1979, pp. 209-224, Part 2.

[18] H. M. Atassi and J. Grzedzinski, Unsteady disturbances of streaming motions around bodies, to be published in the *Journal of Fluid Mechanics*, 1989.

[19] J. R. Caspar, "Unconditionally Stable Calculation of Transonic Potential Flow Through Cascades Using an Adaptive Mesh for Shock Capture," *Trans. ASME. A: Journal of Engineering for Power*, Vol. 105(3), July 1983, pp. 504–513.

[20] D. S. Whitehead and S. G. Newton, "A Finite Element Method for the Solution of Two-Dimensional Transonic Flows in Cascades," *International Journal for Numerical Methods in Fluids*, Vol. 5, February 1985, pp. 115–132.

[21] J. R. Caspar and J. M. Verdon, "Numerical Treatment of Unsteady Subsonic Flow Past an Oscillating Cascade," *AIAA Journal*, Vol. 19(12), December 1981, pp. 1531–1539.

[22] J. M. Verdon and W. J. Usab, Jr., "Advances in the Numerical analysis of Linearized Unsteady Cascade Flows," Department of the Air Force, Air Force Systems Command, U.S. Air Force Report AFWAL-TR-8° -2055, August 1988. UTRC Report R88-957685–1.

[23] W. H. Press, B.P. Flannery, S. A. Teukolsky, and W. T. Vetterling, *Numerical Recipes: The Art of Scientific Computing*, Cambridge University Press, Cambridge, England, 1986, pp. 550–560.

[24] J. F. Thompson, F. C. Thames, and W. Mastin, "A Code for Numerical Generation of Boundary-Fitted Curvilinear Coordinate Systems on Fields Containing any Number of Arbitrary Two-Dimensional Bodies," *Journal of Computational Physics*, Vol. 24(3), 1977, pp. 274–302.

[25] J. M. Verdon, "The Unsteady Flow in the Far Field of an Isolated Blade Row," *Journal of Fluids and Structures*, Vol. 3(2), March 1989, pp. 123–149.

Acknowledgements

NUMERICAL PREDICTION OF AXIAL TURBINE STAGE AERODYNAMICS

H. V. McConnaughey and
L. W. Griffin
NASA George C. Marshall Space Flight Center
ED32 Computational Fluid Dynamics Branch
Marshall Space Flight Center, Alabama 35812
U.S.A.

SUMMARY

A preliminary assessment is made of two NASA-developed unsteady turbine stage computer codes. The methodology and previous partial validation of the codes are briefly outlined. Application of these codes to a Space Shuttle main engine turbine for two sets of operating conditions is then described. Steady and unsteady, two and three-dimensional results are presented, compared, and discussed. These results include time-mean and instantaneous airfoil pressure distributions and pressure fluctuations, streamlines on the airfoil surfaces and endwalls, and relative total pressure contours at different axial locations in the rotor passage. Although not available at the time this writing, experimental data for one of the operating conditions simulated is forthcoming and will be used to assess the accuracy of the unsteady as well as the steady predictions presented here. Issues related to code usage and resource requirements of the two codes are also discussed.

INTRODUCTION

Improvements in the performance and durability of turbomachines is desired of future engines, especially in the rocket propulsion arena where the operating environment can be hostile. The goal of increased payload capability drives the requirements of low weight and high combustion chamber pressure. These, in turn, severely limit the engine size (and thus turbine diameter and airfoil aspect ratio) and impose high turbine temperatures, pressures, and rotor speeds. Additionally, the rapid start-up and shut-down processes subject the turbine to severe transient loads. Consequently, rocket engine turbines experience an unsteady environment which is extreme, both during transient and steady-s ate operation, and the turbine flowfield is highly three-dimensional. The unsteadiness and three-dimensional nature of the flow significantly compromise the turbine's durability and performance. Were the turbine designer better able to characterize and analyze these unsteady and three-dimensional effects, he could better compensate for them in the design of turbines for future rocket propulsion systems to yield enhanced durability and performance.

The aim of this paper is to present an independent, preliminary assessment of analytical tools which have become available during the past few years for the analysis of unsteady, three-dimensional turbine stage flowfields. The tools, which are computational fluid dynamics codes, are not sufficiently advanced to accurately analyze many of the adverse conditions experienced by rocket engine turbomachinery. They do offer promise, however, in the analysis of nominal operation and associated unsteady (periodic) loading, flow angle variations, and high-cycle fatigue. This information alone is of interest and benefit to the designer. In addition, unsteady turbine stage codes may become very useful in enhancing one's understanding of the physics of unsteady flows in turbomachines and the effect of various nonuniformities or geometry variations on these unsteady flows.

Examples of such turbine-stage codes which are in the public domain and which have already been partially validated by the code developers are described in references 1-4 To date, validation efforts have focused on comparison of time-averaged numerical results with time-mean experimental data reported in references 5 and 6. Additional code validation and assessment is desirable, however. In particular, the accuracy of time-resolved predictions should be evaluated, and the suitability for rocket propulsion applications should be assessed. Such is the aim of the work reported here.

Specifically, the two-dimensional code reported in reference 1 and a three-dimensional code derived from that reported in reference 4 are used to analyze flows in the high pressure fuel turbopump (HPFTP) turbine of the Space Shuttle main engine (SSME). Two different sets of operating conditions have been analyzed to date: those corresponding to SSME 100% power level (FPL) operation and those corresponding to nominal rig conditions for two full-scale HPFTP turbine test articles. The time-resolved and time-mean rig data will not be measured until late 1989 or early 1990, thus the results presented here constitute true predictions. Because the data is not available at the time of this writing, the accuracy of the SSME analyses cannot be well evaluated. Computed results are compared with each other, however, and the code performance, efficiency, ease of use, computational resources, and other issues associated with the two codes used in this study are discussed here. These codes represent different solution methodologies and philosophies of approach and have distinct advantages and disadvantages. These are discussed along with the numerical results.

METHODOLOGY AND PREVIOUS VALIDATION

The two codes used in the present study are ROTOR1, developed by M. M. Rai (ref. 1) and FDNS3D developed by Y. S. Chen (ref. 7). The methodology upon which each code is based is thoroughly described in the cited references, thus details of the solution procedures are omitted in the present discussion. An overview of the two approaches is provided, however.

The code ROTOR1 is an axial turbine stage code which solves the unsteady, thin-layer, compressible Navier-Stokes equations in two space dimensions. It features a factored, iterative, implicit solution algorithm, first-order accuracy in time, and a third-order accurate upwind differencing scheme. The Baldwin-Lomax turbulence model is applied down to the solid wall, thus requiring resolution of the viscous sublayer. The laminar viscosity is calculated based on Sutherland's law.

A system of four grids are used to discretize the domain: a very fine (151 X 51) O-grid surrounds each airfoil and is overlaid on a coarser (66 X 71) H-grid as shown in figure 1. The two H-grids are patched together at a common interface and the rotor H-grid slides by the stator H-grid in time to simulate rotor-stator passage. All viscous terms are neglected in the H-grids. The turbine stage is assumed to have an equal number of stator vanes and rotor blades in order to impose periodicity across one pitch. To correct for the incorrect blockage which this assumption would otherwise entail, the rotor blade is scaled up by a factor of NR/NS, where NR is the number of rotor blades and NS is the number of stator vanes in the stage. At the inlet, Riemann invariant R_1 and the entropy are held fixed, the flow angle is fixed at zero, and the Riemann invariant R_2 is extrapolated from the interior. The static pressure is fixed at the exit and the exit values of all other variables are extrapolated. Periodicity is imposed at the upper and lower H-grid boundaries. The no-slip condition, zero normal pressure gradient, and an adiabatic wall are imposed along the airfoil surfaces. Conservative patch boundary conditions are applied at the zonal interface between the H-grids, and interpolation is used to couple each O-grid solution to its companion H-grid solution.
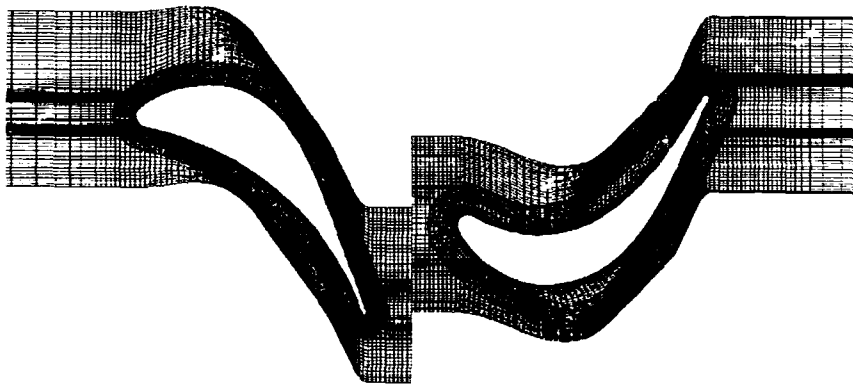

Figure 1. ROTOR1 grid

The code FDNS3D is a general three-dimensional code which employs a pressure-based solution algorithm, a first or second-order, time-centered time marching scheme, and a spatial discretization procedure involving second-order central differencing plus variable order (usually third-order) upwind dissipation. It solves the unsteady Reynolds averaged Navier-Stokes equations and is capable of simulating incompressible or compressible, steady or unsteady flows. For turbulent flows, a two equation k-ε turbulence model (either the standard or the extended, high Reynolds number [ref. 8] version, is coupled with the standard wall function approach and eddy viscosity turbulence concept. The laminar viscosity calculation assumes a power law relation between viscosity and temperature

For unsteady turbine stage analysis, a multiple zone approach is taken in which an H-grid surrounding the rotor blade slides past a stationary stator H-grid and the stationary rotor shroud. The two H-grids overlap by one cell but are discontinuous at their interface. Because the wall function approach is followed, rather than boundary-layer resolution, a fine grid system may not be required. For the H'FTP calculations to be reported here, the grid used was very coarse (71 X 33 X 31) as shown in figure 2. At the interface between the two H-grids, simple interpolation is implemented to communicate solution information between the zones. Periodicity is imposed at the upper and lower (midchannel) boundaries which, like the ROTOR1 simulations, incorrectly assumes a one stator vane to one rotor blade correspondence. Again, the rotor blade size is

increased to account for the correct blockage. At the inlet boundary, density,
temperature, and velocity are held fixed at a constant value. At the exit boundary, all
variables are extrapolated such that mass conservation is enforced. This nonreflective
boundary condition allows any pressure waves generated to escape the flowfield. A
prescribed exit pressure boundary condition can also be implemented, but this was not done
for the present study. The solid wall boundary conditions are the no-slip and zero
pressure gradient conditions, and the wall temperature is fixed at 90% of the freestream
value. Boundary conditions and interface interpolation are implemented implicitly.
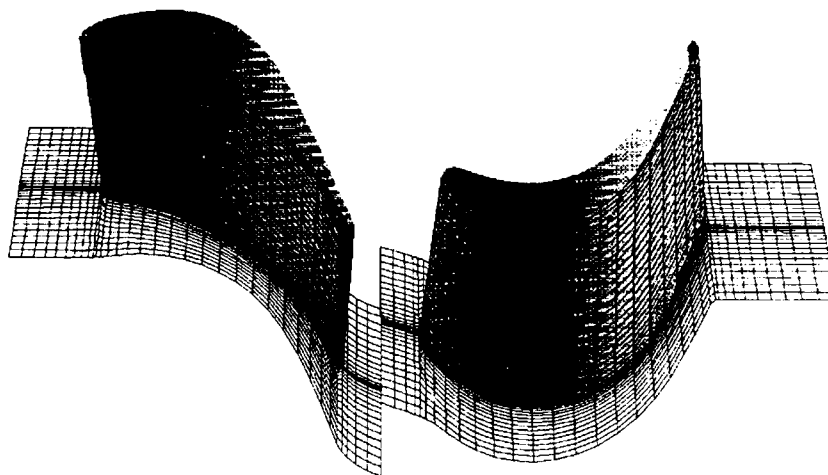

Figure 2. FDNS3D grid

Both codes and/or their derivatives have been partially validated by comparison of
numerical predictions with experimental data reported in references 5 and 6. In
particular, predictions by the ROTOR series of codes (references 1-3, 9) have been compared
with measured time-mean stator and rotor pressure distributions at 2%, 50%, and 89% or 98%
span. Excellent agreement with the experimental data was exhibited except for the case of
the rotor suction surface at the hub. Computed and measured amplitudes of the pressure
fluctuations on the airfoils at the same spanwise locations were also compared to assess
the time accuracy of the calculations. The agreement was fairly good in most cases.
Errors were attributed to the incorrect blade/vane ratio assumed and to the reflective exit
boundary condition. In addition, very good agreement was achieved between predicted
limiting streamlines and experimental visualization of flow on the airfoil surfaces and
between fine grid (ref. 9) predictions and measurements of total pressure contours in the
stator and rotor exit planes. The ROTOR codes have thus far been shown to yield high
accuracy, high resolution results. The computer time required to obtain a periodic
solution in three dimensions is reportedly exorbitant, however, which precludes the routine
application of this series of codes.

A precursor of the FDNS3D code has also been partially validated for turbine stage
predictions against the data in reference 5. This work, reported in reference 4, compares
results of a two-dimensional, arbitrary blade/vane count simulation to the time-mean
airfoil pressure distributions and pressure amplitudes reported by Dring (ref. 5). The
numerical results are comparable to the ROTOR2 (ref. 2) results, i.e. time-mean predictions
exhibit excellent agreement with the data while the agreement between measured and
predicted pressure amplitudes is fair. Three-dimensional turbine stage predictions using
FDNS3D have not yet been calibrated by comparison with experimental data. This will be
done when the HPFTP rig data becomes available.

Because the ROTOR codes and the FDNS3D precursor codes have performed well and
comparably for Dring's experimental configuration, it is reasonable to expect that they
would produce similar and accurate time-averaged numerical results for the cases run in the
present study. These cases are described in the following section.

APPLICATION CONFIGURATIONS

The HPFTP turbine is a two-stage turbine with a mean diameter of 25 cm (10 in), 41 first-stage vanes and 63 first-stage blades with average airfoil chord and span of less than 2.5 cm (1 in), and FPL power output of 56 MW (75,000 hp). At 109% power level (ref. 18 Sept., 1985 engine power-balance), the turbine rotates at 36,600 rpm and is driven by a gaseous hydrogen and steam mixture which enters the turbine at approximately 1050 K (1900°R), 3750 N/cm² (5440 lbf/in²), and 70 kg/s (154 lbm/s). The inlet Mach number is .13 and the Reynolds number per 2.5 cm (1 in) based on inlet velocity is 3.3 X 10⁶. This is one of the operation points for which numerical results will be presented.

The second set of operating conditions numerically simulated in the present study corresponds to the nominal test conditions for two full-scale HPFTP turbine test articles. One will be tested in a blow-down air facility at NASA Marshall Space Flight Center (MSFC), and will produce performance and time-mean aerodynamic data. The second test article will be tested in a shock tunnel facility at the Calspan University of Buffalo Research Center (CUBRC). The latter test series will generate time-resolved as well as time-mean aerodynamic and heat transfer data. Both series of tests are expected to begin in the next six months and both will use as its reference test condition the 104% SSME power level (ref. 27 April, 1987 engine power-balance), which is the current SSME flight power level. This corresponds to a power output of 49 MW (65,400 hp), inlet temperature of 1012 K (1830°R), inlet pressure of 3578 N/cm² (5190 psi), and flowrate of 68 kg/s (149 lbm/s). The inlet Mach number is .14. Air equivalent conditions will be tested, but the Reynolds number will not be matched in the case of the MSFC tests due to facility limitations. CUBRC will test at both the MSFC Reynolds number (8 X 10⁵) and the SSME Reynolds number (3.4 X 10⁶). The MSFC case is that simulated in the second set of calculations performed for this study.

In actuality, the conditions simulated by the calculations reported here and by the experiments to be performed are not true to the real HPFTP operating environment. The already severe environment is exacerbated by rotor eccentricity, leakage flow at the platform seals, radially and circumferentially nonuniform inlet profiles generated by the upstream fuel preburner, and a circumferential pressure gradient at the turbine exit caused by the asymmetric manifold located downstream. It is hoped that current unsteady turbine analysis codes will eventually evolve to the point of being able to analyze the effects of such nonuniformities on the flowfield characteristics.

RESULTS AND DISCUSSION

Aerodynamic results for the HPFTP first stage are now presented for the two sets of nominal operating conditions just described. The SSME FPL case is presented first and ROTOR1 results are emphasized. For the MSFC rig conditions which follow the FPL case, the FDNS3D simulation is highlighted. In all cases, the time-averaged pressure coefficients are defined as

$$C_p(x) = \frac{p(x) - p_{Tro}}{1/2 \rho_o W_o^2} , \qquad (1)$$

where p is the time-averaged pressure, and ρ_o and W_o represent averages of density and relative velocity across one midspan pitch at the stator or rotor inlet, p_{Tro} is the midspan relative total pressure at the stator or rotor inlet and x is the axial distance from the airfoil leading edge. The pressure amplitudes are defined as

$$C_p(x) = \frac{p_{max}(x) - p_{min}(x)}{1/2 \rho_o W_o^2} . \qquad (2)$$

SSME FPL OPERATION

The time-averaged pressure coefficients at the midspan of the HPFTP first stator and first rotor are plotted in Figures 3 and 4 for two different cases. One corresponds to the prediction obtained using the standard laminar viscosity model found in ROTOR1, i.e. Sutherland's law with constants appropriate for air. As pointed out in reference 10, Sutherland's law is not valid for the HPFTP turbine gas mixture for any choice of the Sutherland's constant. Consequently, we have incorporated real gas properties into ROTOR1 for more correct analysis of rocket engine turbines. Predictions using the real gas properties to approximate the laminar viscosity are seen as the dashed curves in figures 3 and 4, while those obtained using Sutherland's law are represented by solid curves. Virtually no differences are seen between the pressure coefficients obtained using the two different laminar viscosity calculations. A very significant effect has been seen, however, in a parallel investigation of HPFTP turbine heat transfer using ROTOR1. Consequently, the Sutherland's law is no longer used at MSFC for analysis of turbines operating in gases other than air. Sutherland's law for air is a very common model for approximating laminar viscosity in turbulent flow calculations of all kinds. The analyst should be aware that this may be a very inappropriate model for any rocket propulsion analysis involving other than purely aerodynamic effects and that its use may significantly contaminate numerical results.
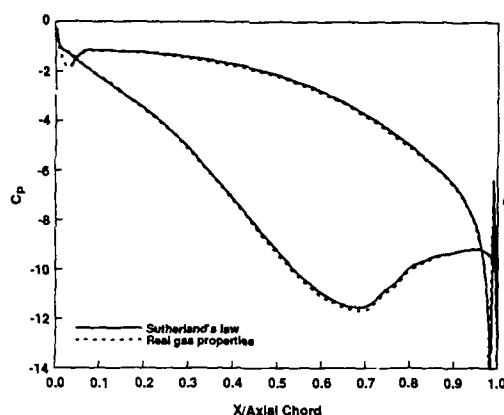
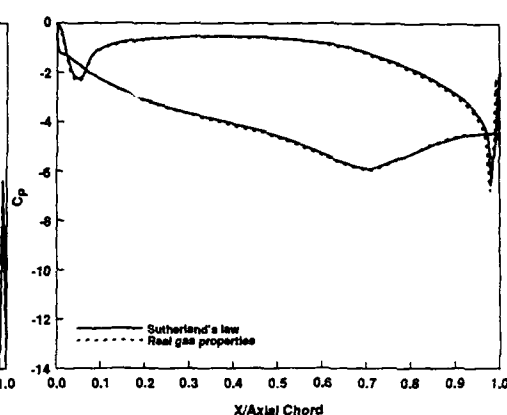Figure 3. Stator midspan pressure distribution

Figure 4. Rotor midspan pressure distribution

Instantaneous stator-wake/rotor relative positions and associated instantaneous stator and rotor airfoil pressure fluctuations are shown in figures 5 and 6. These illustrate the variation in time of the loading experienced by each airfoil due to rotor-stator interaction. The profile shapes are seen to vary significantly from one time to the next, and the amplitudes of the fluctuations are most pronounced on the rotor, as is to be expected. The unsteady pressure fluctuations have been animated to allow viewing of a nearly continuous variation in time of the airfoil loadings. Disturbances caused by stator wake passage are seen to travel down the rotor blade in an indulant manner. Quantitative information about the fluctuating airfoil loads is of importance to the structural dynamicist in assessing the dynamic response of the rotor to vane wake passage. In addition, unsteady loadings are required by the stress analyst when transient blade stress analyses are performed. It is thus important to validate, or at least calibrate, the accuracy of these instantaneous predictions. That will be accomplished when the CUBRC data becomes available.
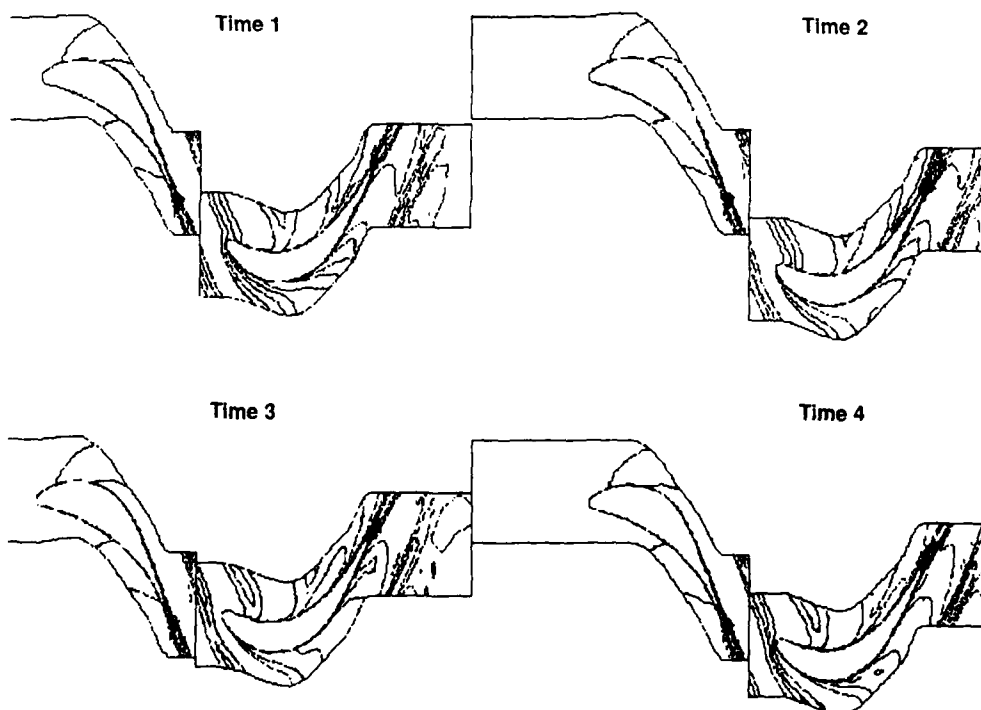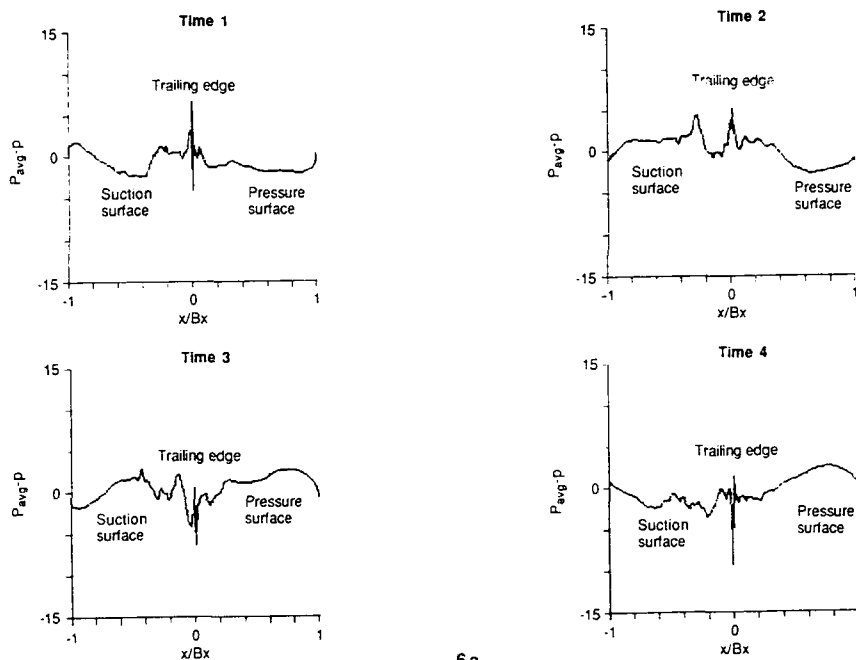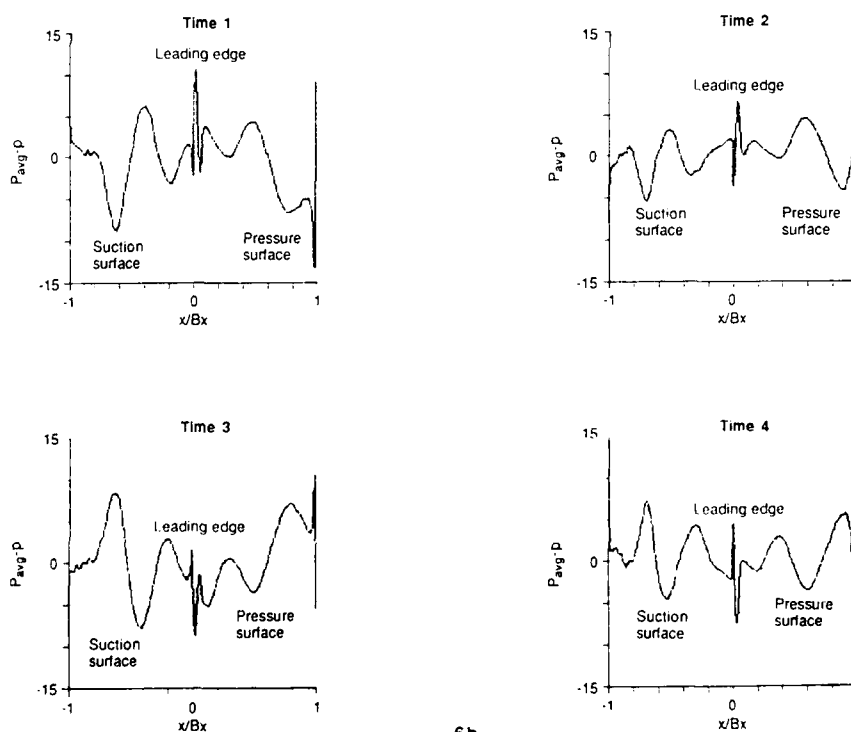

Figure 5: Entropy contours showing stator-wake/rotor relative location
at four equally spaced times within one ROTOR1 cycle.

6a.

6b.

Figure 6: Instantaneous stator (a) and rotor (b) pressure fluctuations (in lbf/in²) at the four times illustrated in figure 5.

Predictions obtained for SSME FPL operation using a predecessor of the FDNS3D code have been reported by the code developer in reference 4. Side-by-side comparisons of the midspan FDNS3D results cannot be made with figures 3 and 4, however, because a different engine power-balance reference and a different nondimensionalization were used in reference 4. The FDNS3D profile shapes appear to be nearly identical to the ROTOR1 profile shapes, however, with one set being merely scaled relative to the other.

MSFC RIG TEST CONDITION

Time-averaged pressure coefficients and fluctuating pressures predicted by FDNS3D are shown as the solid curves in Figures 7 and 8 for three spanwise locations of the HPFTP turbine first stage airfoils operating at the nominal MSFC test condition described in the previous section. Little spanwise variation in the stator pressure distribution is reflected by figure 7, however, the rotor profiles vary considerably from hub to tip. The net force on the rotor hub is small while the tip is highly loaded. The high pressure on the rotor hub suction surface is presumably due to the impingment of the leading edge vortex and the associated radial outflow which it causes. This is further discussed in connection with figure 9. The low pressure region at the tip of the rotor suction surface at approximately 60% chord corresponds to the minimum pressure region of the rotor tip vortex. The dashed lines in figure 7 correspond to the ROTOR1 prediction for the stator and rotor midspan. The latter 25% of the stator suction surface and the entire rotor surface are predicted to have somewhat different pressure distributions than indicated by FDNS3D. The likely explanation for this is the difference in exit boundary conditions. The nonreflective exit boundary condition used in the FDNS3D calculation does not fix the exit pressure. At convergence, the pressure ratio across the stage was .845 in contrast to the value of .808 resulting from imposition of a pressure ratio of .80 in the ROTOR1 calculation. (A pressure ratio of .80 is indicated by the mean diameter velocity vector diagram for this operating condition). Also, the relative Mach number at the rotor inlet calculated by FDNS3D was .167, whereas ROTOR1 predicted a value of .185. To assess the role of the exit boundary condition in these discrepancies, the FDNS3D calculation will be redone with a fixed pressure ratio of .80 imposed. Ultimately, the data obtained in the rig test will indicate the correct airfoil loading. The discrepancy between FDNS3D and ROTOR1 predictions is puzzling in light of the very similar predictions the two codes produced for the test configuration of reference 5. This shows the importance of considering more than one database in validating the accuracy of a given code.

The pressure amplitudes on the stator and rotor hub, midspan, and tip as predicted by FDNS3D are shown in figure 8. The lack of smoothness in the curves is a result of the very coarse grid. Little fluctuation is seen on the stator except at the trailing edge and at approximately 80% axial chord on the suction surface, but the amplitude of the fluctuations is small. On the rotor, more substantial fluctuations are seen at the leading edge and especially at the tip due to the tip leakage flow and tip vortex.

The three-dimensional nature of the flow is clearly depicted in figure 9 which shows particle traces in the fluid near the solid surfaces. Although the stator pressure surface flow apears to be essentially two-dimensional, the suction surface streamlines show evidence of a strong secondary flow at the tip over the last third of the vane. No hub vortex is indicated by the vane or hub streamlines, however. It is likely that the grid is too coarse to detect the weaker horseshoe vortex which is expected at the hub. The rotor endwall flow traces do indicate the formation of a horseshoe vortex at the rotor leading edge, on the other hand, causing a strong passage vortex which impinges on the suction surface. This passage vortex is seen to induce strong radial flow on the suction surface and extends to over 60% span at the trailing edge. A significant tip vortex is also formed on the rotor and the radial flow toward the tip due to the relative eddy (ref. 11) is also distinctly seen on the pressure surface. The nature of the surface flow represented by the streamlines in figure 9 is common to all of the instantaneous flow solutions observed indicating that this is an essentially steady-state behavior.

The unsteady nature of the overall turbine stage flow is manifested in figures 10 and 11. Figure 10 shows entropy contours for flow in the midspan plane of the stage at four instants of time. The changing position of the rotor relative to the stator can been seen, and the interaction between the rotor and stator wake is evident. Corresponding to these four time "slices" and relative midspan rotor-stator positions are plots in figure 11 of relative total pressure in the rotor passage at three axial locations. The vertical lines in the four plots of figure 10 show the position of these axial locations.
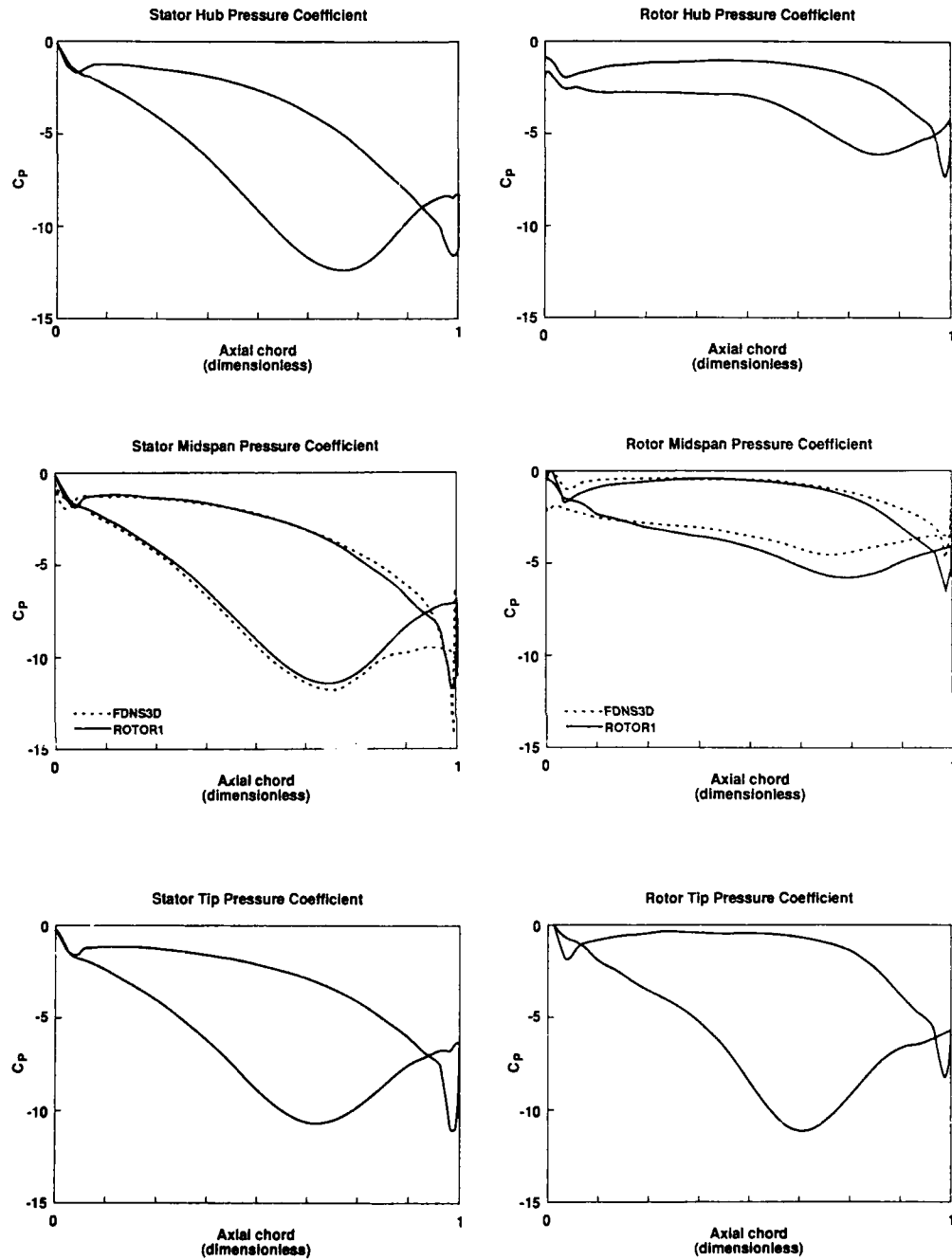
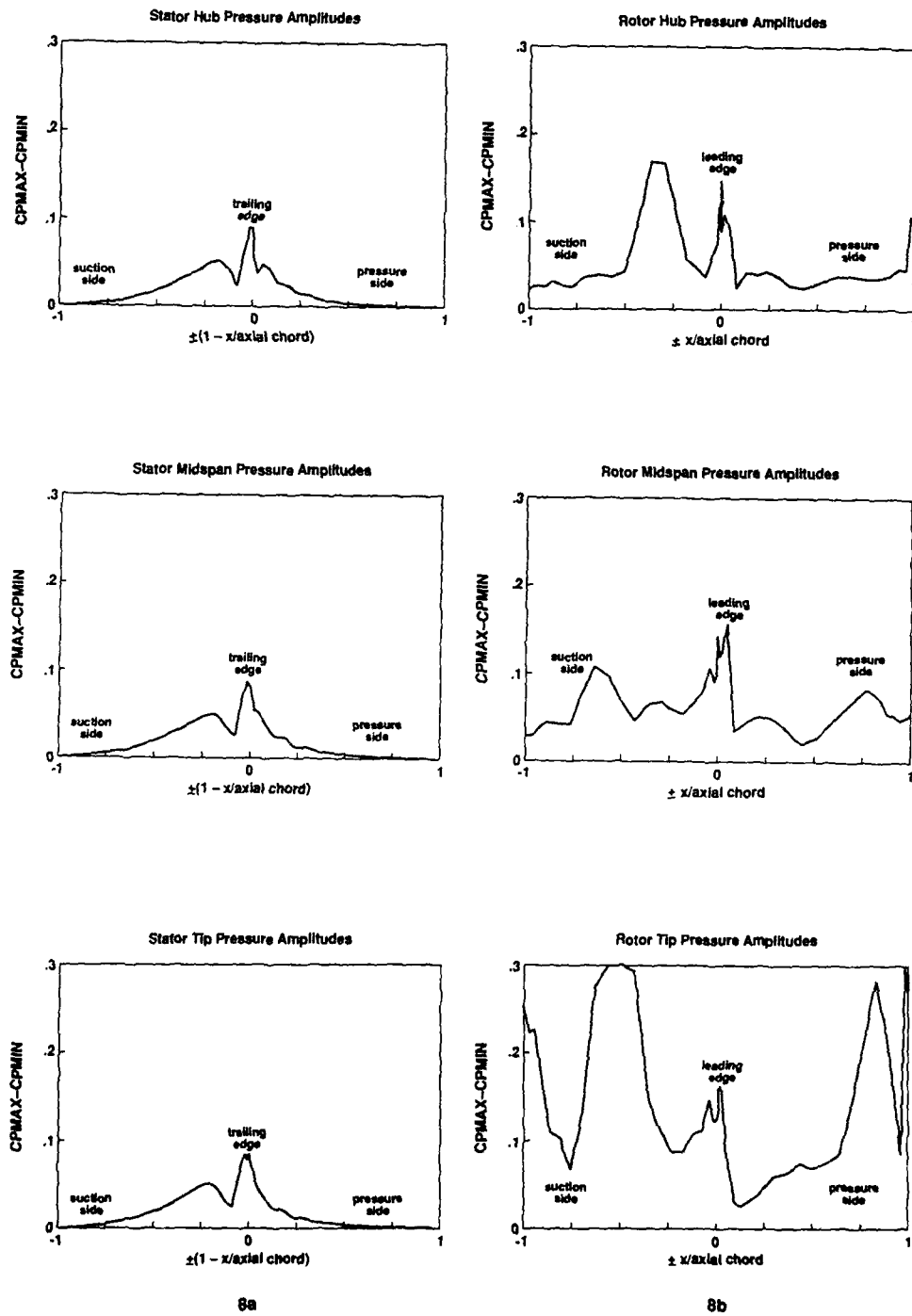**Figure 7: Time–averaged pressure coefficients at stator (a) and rotor (b) hub, midspan, and tip.**

Figure 8: Pressure amplitudes at stator (a) and rotor (b) hub, midspan, and tip.

Stator Suction Surface   **Stator Pressure Surface**   **Stator Hub**

Rotor Suction Surface   **Rotor Pressure Surface**   **Rotor Hub**
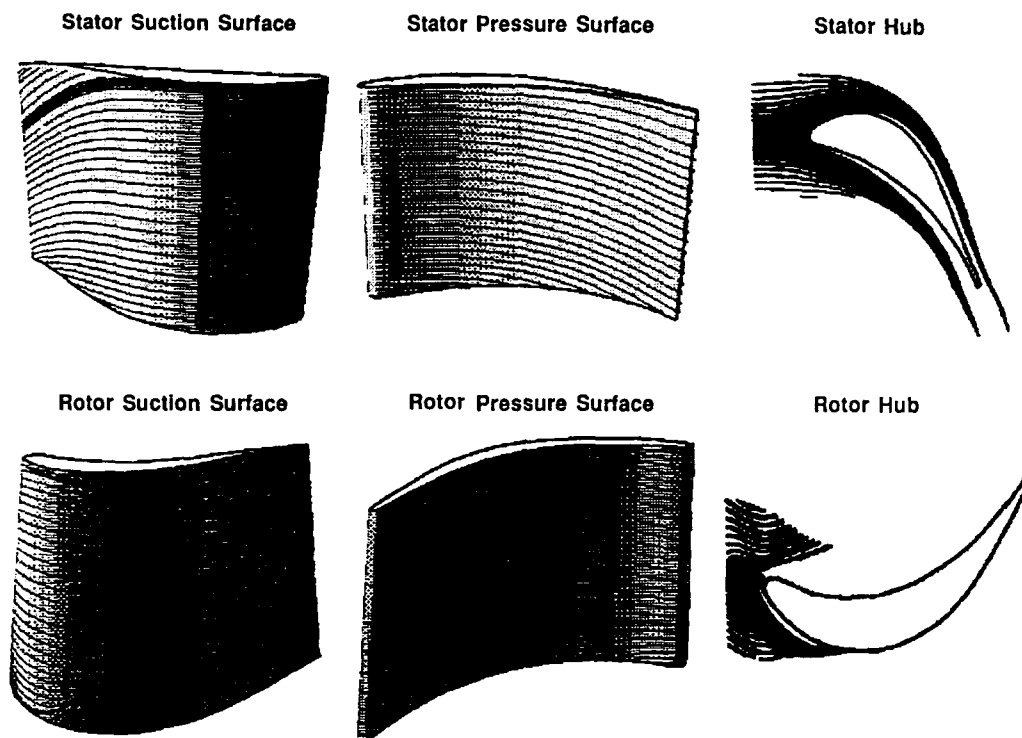

Figure 9. Particle traces on airfoil surfaces and hub endwalls.

The rotor passage depicted in figures 11a-c is oriented with hub at the base, tip endwall at the top, and the rotor rotates to the right. Thus in figures 11b, the rotor suction surface is to the left and pressure surface is to the right. The axial position shown in figure 11a is located just upstream of the rotor leading edge, and the relative total pressure contours in this plane clearly show the periodic nature of the inlet profile experienced by the rotor. The stator wake seen in figure 11a is at the rotor leading edge at time 1, moves toward the center of the passage at time 2, is in the center of the plane at time 3, and moves back toward the suction surface at time 4. This is entirely consistent with figure 10. Figure 11a also shows the passage vortex which was generated at the stator tip endwall, as discussed earlier in connection with figure 9, to enter between rotor blades at time 1, and to be at the rotor leading edge at time 3.   The plane in figure 11b is located downstream of the rotor leading edge at approximately 15% chord. In this portion of the rotor passage, the stator wake appears inclined toward the tip of the suction surface and the passage vortex is correspondingly skewed. At time 1, the stator wake is approximately centered on the hub but is approaching the suction surface near the tip. At time 2, the wake is on the suction surface at the top of the blade enabling the oncoming passage vortex to flow through the passage relatively freely and thus to fill the upper passage. Just after the wake of the next stator impinges on the pressure side (time 3), the oncoming vortex from the next stator passage enters the plane and the former passage vortex moves toward the suction side. The continuation of this progression is seen at time 4. For the plane just downstream of the rotor trailing edge (figure 11c), the relative total pressure contours become more steady. The strong tip leakage vortex occupies the upper one-third of the span and two-thirds of the pitch and has the smallest relative total pressure. The rotor wake and associated low total pressure region fills most of the right side of the plane. The passage vortex is squeezed between consecutive rotor wakes and occupies the left side of the plane below the tip leakage vortex.

Time 1

plane c

plane b

plane a

Time 2

Time 3

Time 4
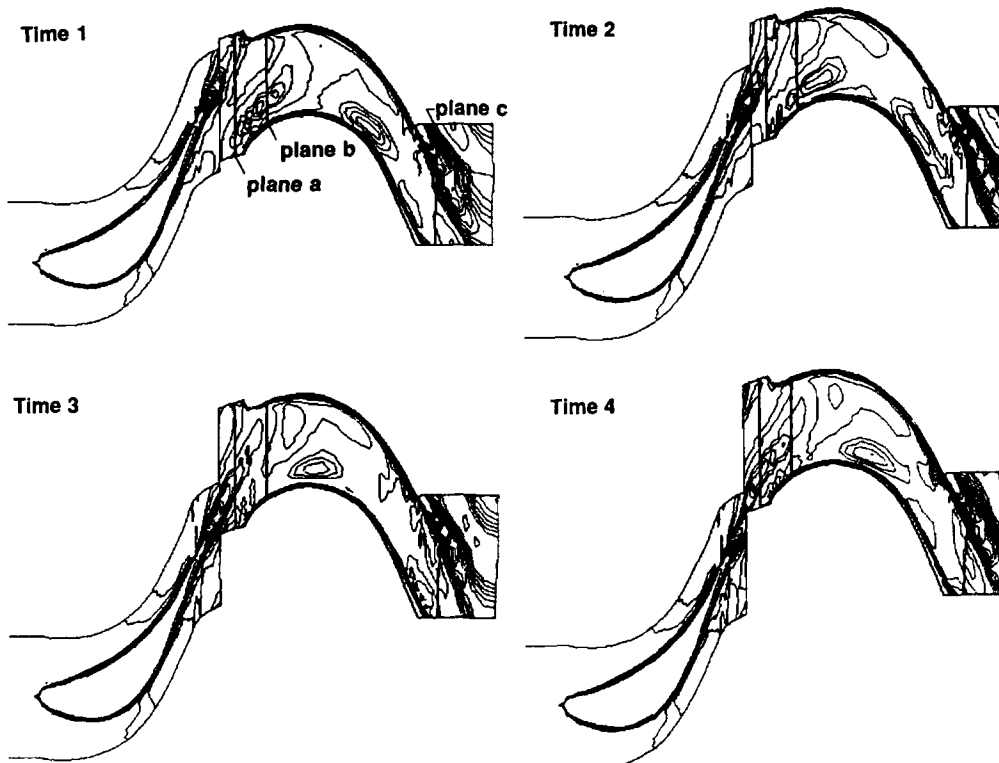
Figure 10. Entropy contours showing midspan stator wake/rotor relative
location at four different times within one cycle.

Time 1   Tip

Time 2   Tip

Hub

Hub

Time 3   Tip

Time 4   Tip

Hub

Hub

11a
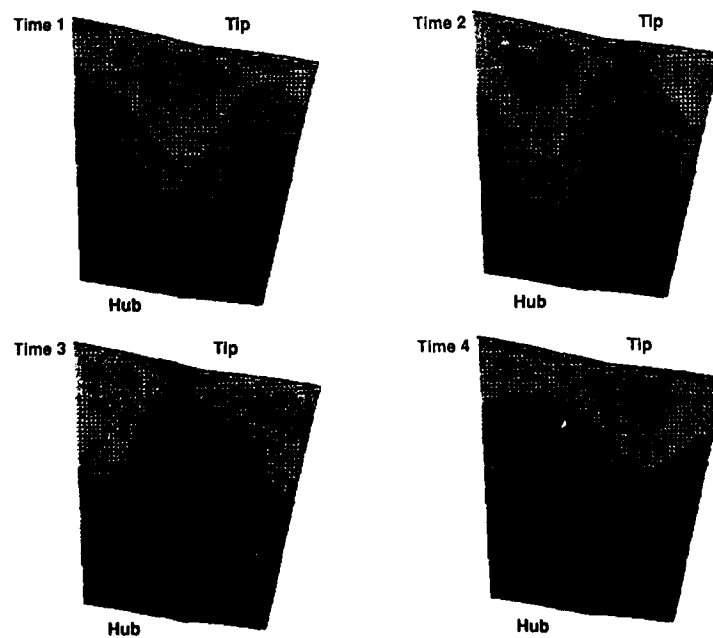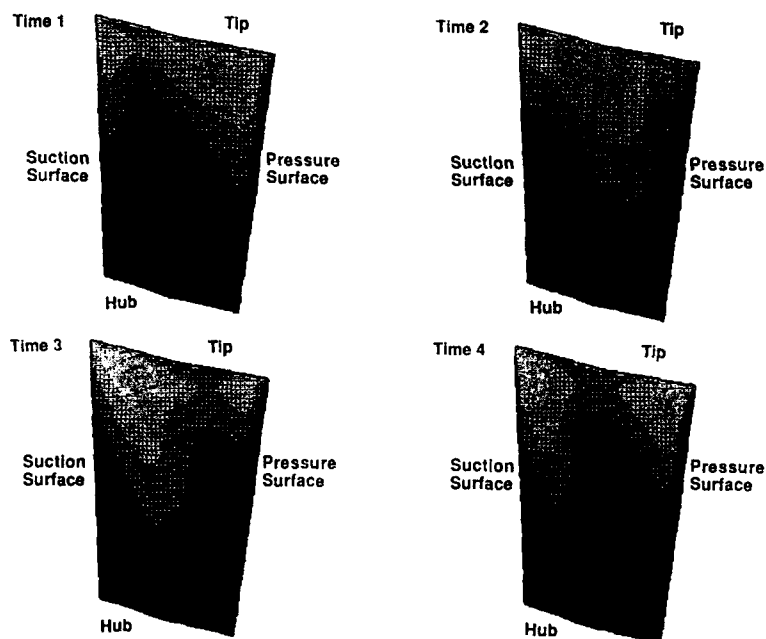
11b
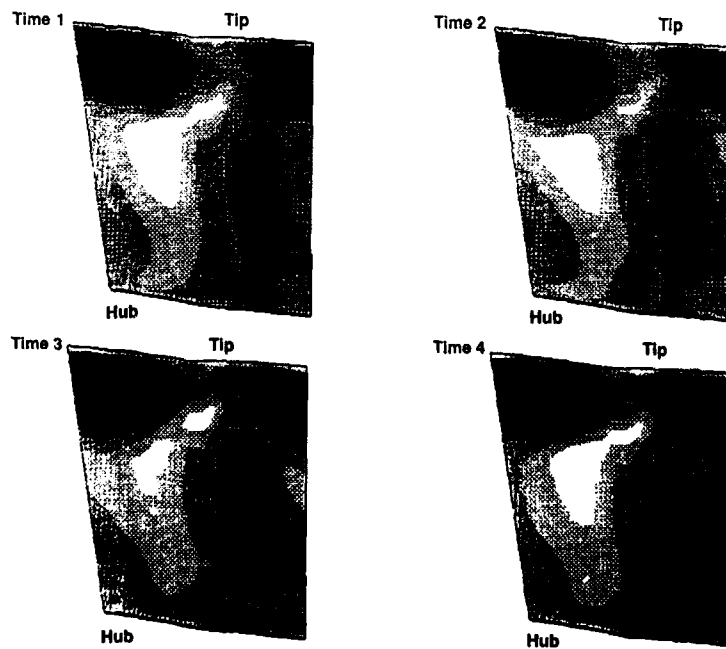
11c

Figure 11. Relative total pressure contours at 4 times shown in figure 10 at axial locations: (a) just upstream of rotor leading edge (b) in rotor passage at 15% chord (c) at rotor exit. Dark shade indicates lowest relative total pressure

Further graphical interrogation of the numerical solution can shed additional light on the behavior of the unsteady three-dimensional flow through the turbine stage. Although the solution has not yet been quantitatively validated via comparison with data, the nature of the flow as depicted in figures 7-11 is reasonable. The characteristics of the flow are seen to be remarkably similar (qualitatively) to the experimental results presented in reference 6. Forthcoming data from MSFC and CUBRC, which will enable true verification or calibration of the unsteady predictions of both the FDNS3D and ROTOR1 codes, will include time-resolved and/or time-mean airfoil pressures at 10%, 50%, and 90% span, endwall pressure distributions, and exit-plane total pressure, total temperature, and flow angle distributions (spanwise and blade-to-blade).

CODE USAGE AND RESOURCE REQUIREMENTS

Both codes are relatively easy to use and to read. FDNS3D contains approximately 5,000 lines of FORTRAN while ROTOR1 contains 3180 lines; both of these counts include comment lines and exclude grid generators. FDNS3D is conveniently run from an input file, whereas the ROTOR1 source code must be modified for each different application. Both codes require the user to process and interpret output files containing airfoil pressure information to assess "convergence," i.e. the attainment of perodicity in time. ROTOR1 conveniently provides time-averaged, maximum and minimum (over one cycle) values at each airfoil node while FDNS3D provides instantaneous values of pressure. Both codes are fairly robust, but ROTOR1 must be "soft-started," i.e. the rotor must be brought up to full rotational speed gradually if starting from freestream conditions. Also, very small time steps (e.g., 2000 steps/cycle) are required by ROTOR1 during the first several cycles when starting from freestream conditions. ROTOR1 has one intrinsic deficiency associated with its nonreflective inlet boundary condition. Because the dependent flow variables are not fixed there, they tend to reach values at the attainment of periodicity in time which are different than the freestream values assumed at the outset of the calculation. Thus the rotor speed must be adjusted and additional cycles run to again reach time-periodicity. The inlet values attained at "convergence" must again be examined and this iterative process must be repeated until the flow coefficient based on the final inlet values is equal to the required flow coefficient. This can significantly add to the computer time required to obtain the final solution. The FDNS3D code, on the other hand, is seen to yield potentially erroneous exit pressures when run with its nonreflective boundary condition.

For the calculations simulating the nominal MSFC rig condition, ROTOR1 was found to require .00013 sec per grid point per time step on a CRAY X-MP computer. Two hundred time steps per cycle were used and 5 cycles were required to attain periodicity in time for the first iteration on flow coefficient starting from a "good" initial flowfield solution (the final FPL solution). A total of 3 iterations on flow coefficient were required. In all, 15 cycles were required to obtain the final two-dimensional solution corresponding to 3 CPU hours. For the SSME FPL case, 25 cycles starting from freestream values and 9 CPU hours were needed. In both cases, 2,100,000 words of core memory plus 400,000 words of SSD (solid-state storage device) were used. The MSFC rig calculation using FDNS3D used .0003 sec per grid point per time step, 200 time steps per cycle, and five cycles to reach periodicity in time when starting from an initial flowfield corresponding to a turbulent, steady turbine stage flowfield with a stationary rotor grid and slip at the interface between H-grids. (This was provided by Y. S. Chen.) The five unsteady cycles required six CPU hours and the initial flowfield generation consumed 2 CPU hours for a total of 8 hours to obtain the final time-periodic solution in three space dimensions. Forty-nine words of core memory per grid point were required.

SUMMARY AND CONCLUSIONS

The unsteady turbine stage codes ROTOR1 and FDNS3D have been applied to the first stage of the SSME HPFTP turbine for two sets of operating conditions. Time-resolved and/or time-averaged experimental data will soon be taken which will correspond directly to one of the operating conditions simulated here. This data will be used to calibrate the accuracy of the calculations performed in this study.

The ROTOR1 code has previously been seen to yield high-resolution, smooth solutions which offer the promise of high accuracy and resolution of fine scale flow phenomena. The associated requirement of fine spatial resolution carries with it the penalty of large computer time requirements, however. The code is useful for providing unsteady midspan airfoil loadings and for characterizing unsteady features of the turbine stage flowfield.

The FDNS3D code has not yet been validated for three-dimensional turbine stage predictions, and this study should provide some code calibration when coupled with forthcoming rig data. Numerical predictions for the MSFC rig conditions appear reasonable, however. Results admittedly lack smoothness, in some ways, due to the coarse spatial resolution of the grid used. Nevertheless, important flow features are revealed and at relatively low computer and manhour requirements. This code has the potential of being a useful analysis tool which can be used in a quick-turnaround manner to provide unsteady flow information to the turbine designer and analyst. Care must be taken, however, to carefully assess its accuracy and understand its limitations before it is used to influence hardware design.

REFERENCES

1. Rai, M. M., "Navier-Stokes Simulations of Rotor-Stator Interaction Using Patched and Overlaid Grids," *Journal of Propulsion and Power*, Vol. 3, No. 5, 1987, pp. 387-396.

2. Rai, M. M., and Madavan, N. K., "Multi-Airfoil Navier-Stokes Simulations of Turbine Rotor-Stator Interaction," American Institute of Aeronautics and Astronautics Paper No. 88-0361, 1988.

3. Rai, M. M., "Three-Dimensional Navier-Stokes Simulations of Turbine Rotor-Stator Interaction," Journal of Propulsion and Power, Vol. 5, No. 3, 1989, pp. 305-319.

4. Chen, Y. S., "3-D Stator-Rotor Interaction of the SSME," American Institute of Aeronautics and Astronautics Paper No. 88-3095, 1988.

5. Dring, R. P., et al, "The Effects of Inlet Turbulence and Rotor/Stator Interactions on the Aerodynamics and Heat Transfer of a Large-Scale Rotating Turbine Model," NASA Contractor Report 4079, 1986.

6. Joslyn, H. D. and Dring, R. P., "Three Dimensional Flow and Temperature Profile Attenuation in an Axial Flow Turbine," United Technologies Research Center Report R89-957334-1, 1989.

7. Chen, Y. S., "Compressible and Incompressible Flow Computations with a Pressure Based Method," American Institute of Aeronautics and Astronautics Paper No. 89-0286, 1989.

8. Chen, Y. S. and Kim, S. W., "Computation of Turbulent Flows Using an Extended k-ϵ Turbulence Closure Model," NASA Contractor Report CR-179204, 1987.

9. Madavan, N. K. et al, "Grid Refinement Studies of Turbine Rotor-Stator Interaction," American Institute of Aeronautics and Astronautics Paper No. 89-0325, 1989.

10. Griffin, L. W. and McConnaughey, H. V., "Prediction of the Aerodynamic Environment and Heat Transfer for Rotor-Stator Configurations," American Society of Mechanical Engineers Paper No. 89-GT-89, 1989.

11. Dring, R. P. and Joslyn, H. D., "The Relative Eddy in Axial Turbine Rotor Passages," American Society of Mechanical Engineers Paper No. 83-GT-22, 1983.

ACKNOWLEDGEMENTS

DISCUSSION

B.H.Becker - Siemens AG, W.Germany
Both codes presented handle the one-to-one situation, but experiments have different number of rotor and stator blades.
How do the authors handle this situation?

Author's response :
Actually there is some discrepancy between test results and calculations. However, 2-d calculations have been made with the correct number of blades and for the time averaged solution the difference is not substantial. For unsteady amplitude there may be some difference, but not enough to disregard what the code brought already.

M.Cambier - ONERA, France
(1) Did the authors have any difficulties in the 2-d code in the wake, at the interface region between the region where the 'O' grid is used for the Navier-Stokes equations and the one where the 'H' grid is used for the Euler equations.

Author's response :
The main problem is loosing definition of the wake when one goes from one grid to the other. The wake is diluted in essence, but from the viewpoint of the mathematics, interpolation is easy.

(2) Can the author state the number of meshpoints used in the tip clearance region, for the 3-d code.

Author's response :
There were only 3 grid lines in the tip clearance region.

SIMULATION NUMERIQUE DES ECOULEMENTS TRIDIMENSIONNELS ET INSTATIONNAIRES DANS LES TURBOMACHINES

par Antoine FOURMAUX, Gilles BILLONNET, Alain LE MEUR et Alain LESAIN

OFFICE NATIONAL D'ETUDES ET DE RECHERCHES AEROSPATIALES
29, avenue de la Division Leclerc
92320 CHATILLON (FRANCE)

RESUME

Dans l'étude aérodynamique des turbomachines, la simulation numérique des écoulements occupe une place grandissante. Ces écoulements de fluide visqueux et compressibles sont tridimensionnels et instationnaires : ils sont donc régis par les équations de Navier-Stokes complètes.

Toutefois, les méthodes numériques résolvant ces équations sont, pour le moment, d'utilisation limitée et seules des applications des méthodes "Euler" sont présentées dans cet article. Après un bref rappel des phénomènes physiques et de la méthode numérique utilisée, les conditions sur les frontières du domaine de calcul sont décrites. L'accent est mis sur les hypothèses simplificatrices permettant le calcul d'un étage complet. Les exemples présentés concernent des simulations d'écoulements instationnaires dans un étage de turbine et dans une tuyère supersonique.

NUMERICAL SIMULATION OF THREE-DIMENSIONAL UNSTEADY FLOWS
IN TURBOMACHINES

ABSTRACT

For the aerodynamic study of turbomachinery, the numerical flow-simulation takes a larger and larger place. These viscous and compressible fluid flows are three-dimensional and unsteady : so they are governed by the full Navier-Stokes equations.

Nevertheless, the use of numerical methods solving these equations is limited at the present time, and only applications of "Euler" methods are presented in this paper. After a short description of the physical phenomena and of the numerical method used, the conditions on the calculation domain boundaries are described. The simplifying assumptions wich allow the complete stage computation, are emphasized. The examples presented concern unsteady flow simulations in a turbine stage and in a supersonic nozzle.

Notations

$\vec{V}$: vecteur vitesse avec :

$\vec{V_3}$: composante axiale

$\vec{V_\lambda}$: composante radiale

$\vec{V_\theta}$: composante azimutale

$\vec{V_m} = \vec{V_3} + \vec{V_\lambda}$: composante méridienne

$\beta = (\vec{V_m}, \vec{V})$: angle de l'écoulement par rapport au plan méridien

$$\left(V_m = V \cos\beta \quad , \quad V_\theta = V \sin\beta \right)$$

$\varphi = (\vec{V_3}, \vec{V_m})$: angle méridien

$$\left(V_3 = V_m \cos\varphi \quad , \quad V_r = V_m \sin\varphi \right)$$

1. INTRODUCTION

Cet article est destiné à présenter les différentes possibilités de simulation numérique des écoulements compressibles dans les turbomachines. D'une façon générale, ces écoulements sont tridimensionnels, visqueux et instationnaires. Ils sont donc régis par les équations de Navier-Stokes complètes. Les différentes approches actuellement utilisées dépendent du degré des simplifications admises dans ces équations selon l'analyse physique des phénomènes réels. La première partie de cet article est précisément consacrée à une brève description des aspects 3D, visqueux et instationnaires ainsi qu'à la présentation des hypothèses actuellement retenues dans les programmes de calcul. Ensuite, divers résultats obtenus sur des configurations variées permettront d'apprécier les capacités des différents codes développés à l'ONERA pour la simulation numérique des écoulements dans les turbomachines.

2. ASPECTS VISQUEUX, TRIDIMENSIONNELS ET INSTATIONNAIRES

L'analyse numérique des phénomènes visqueux nécessite des méthodes "Navier-Stokes", qui font actuellement l'objet d'un effort important de développement et de validation, notamment en ce qui concerne la modélisation de la turbulence. Ces méthodes sont néanmoins lourdes et coûteuses d'emploi, comparativement aux méthodes "Euler" ou méthodes de "fluide parfait". Lorsque les effets visqueux sont estimés peu importants, l'approche "Euler" est utilisée avec profit : elle permet de mener rapidement et à moindre coût des calculs où les effets tridimensionnels et/ou instationnaires sont prioritaires. Notons qu'à l'ONERA en particulier, un modèle simple de simulation des effets visqueux, intégré aux méthodes "Euler", permet d'améliorer notablement la qualité des résultats obtenus.

L'aspect tridimensionnel se traduit par le gauchissement des surfaces de courant à la traversée d'un canal interaube, et seuls des calculs 3D peuvent restituer ce phénomène. Toutefois les calculs 2,5D (calculs aube-à-aube sur une surface de courant axi-symétrique) ou 2D sont encore d'une grande utilité pour de nombreux problèmes : conception et optimisation d'aubages (méthodes Euler), études particulières de base, etc...

Quant aux phénomènes instationnaires, il importe de définir clairement le cadre de leur étude. Un écoulement stationnaire dans une turbomachine est très particulier : seul le cas d'une roue isolée considérée dans son repère relatif avec des conditions amont et aval constantes dans le temps correspond à un régime stationnaire. Par comparaison, l'écoulement dans un étage, avec des conditions d'entrée et de sortie analogues à celles d'une roue isolée, bien qu'étant instationnaire, possède un caractère permanent, globalement stationnaire : on pourra définir des valeurs moyennes dans le temps de même nature que les valeurs stationnaires. Le problème est très différent quand il s'agit de suivre, au cours du temps, l'évolution d'un phénomène transitoire (amorçage d'une tuyère par exemple). On reviendra sur ce point dans la suite de l'article.

3. METHODES DE CALCUL

Nous allons dans ce paragraphe décrire très rapidement les méthodes de calcul utilisées pour obtenir les résultats présentés dans cet article.

Les équations d'Euler (équations de continuité, de quantité de mouvement et d'énergie) sont directement discrétisées dans l'espace physique.

Dans le cas tridimensionnel, le repère choisi est un repère cylindrique (R, θ, z), tandis que dans le cas 2.5D, il s'agit du repère (m, θ).

Les équations discrétisées sont résolues à l'aide d'un schéma numérique du type prédicteur-correcteur de Mac Cormack, capable de calculer les écoulements compressibles avec ondes de choc.

Le traitement des conditions aux limites du domaine (ou des sous-domaines) de calcul utilise la théorie des relations caractéristiques, ou relations de compatibilité.

Les détails sur ces techniques numériques pourront être trouvés en [1], [2], [3].

Il est évident que la qualité des simulations numériques dépend grandement des conditions appliquées aux frontières du domaine de calcul. Le paragraphe suivant, qui rappelle parfois des concepts élémentaires, est consacré à ce point important.

4. NATURE DES PHENOMENES ET SIMULATION NUMERIQUE

4.1. Frontières amont et aval du domaine de calcul

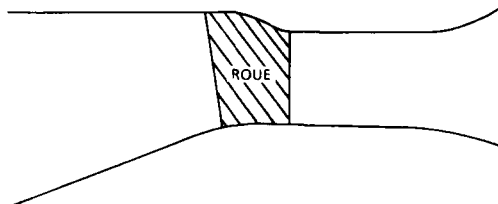Considérons l'exemple simple d'une roue isolée de turbomachine (fig. 1).

Fig. 1 - Roue isolée en veine réelle.

La simulation numérique de l'écoulement implique avant tout le choix d'un domaine de calcul englobant la roue et une partie de la veine à l'amont et à l'aval.

Ce domaine possède à l'évidence deux types de frontières :

- les frontières "solides" (carters, aubes) sur lesquelles sera appliquée une condition d'adhérence ou de glissement,

- des frontières "fluides" externes à l'amont et à l'aval, sur lesquelles les conditions limites appliquées devront être en accord au mieux avec la nature de l'écoulement réel. En général, ces conditions sont aérodynamiquement assez simples, car il n'est pas possible de déterminer avec sureté des conditions plus complexes dépendant du rayon ou de l'azimut, voire du temps. Quelques précautions s'imposent alors quant au choix de l'emplacement de ces frontières.

    - frontière amont,
Lorsque la vitesse débitante est subsonique, il est usuel d'imposer deux grandeurs d'arrêt (pression et température) et deux grandeurs statiques (en 3D) : nombre de Mach, ou angle β de l'écoulement ou vitesse tangentielle, et angle méridien φ . Si, par exemple, la condition amont impose $\beta = 0$, $\varphi = 0$ (écoulement axial dans le repère absolu), la frontière doit être suffisamment éloignée de la roue pour que l'influence amont de cette dernière soit négligeable ; de plus il est nécessaire que la veine soit à rayon constant au voisinage de la frontière (écoulement par nappes concentriques, $\varphi = 0$).

    - frontière aval,
Le problème est tout à fait similaire lorsque l'on impose une condition de pression constante suivant l'azimut et le temps, mais variable en fonction du rayon suivant un équilibre radial simple.

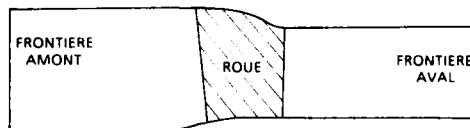Le domaine de calcul, en vue méridienne, prend l'allure représentée fig. 2.

Fig. 2 - Roue isolée - domaine de calcul.

D'après ce qui précède, on entrevoit que certains calculs seront, par principe, délicats à mener en roue isolée, en particulier ceux concernant une roue alimentée par un écoulement avec prérotation ($\beta \neq 0$). C'est le cas, par exemple, d'une roue mobile de turbine ou d'un redresseur d'étage de compresseur. La condition amont devra en effet restituer une évolution radiale moyenne de la prérotation, connue (ou souhaitée) juste devant la roue.

La difficulté de trouver une telle condition amont a été à l'origine des calculs en étage présentés dans la suite de cet article.

4.2. Partage du domaine de calcul en sous-domaines

4.2.1 Roue isolée

Pour le calcul de l'écoulement stationnaire dans une roue isolée, le domaine se réduit à un canal interaube (fig. 3). On voit apparaître d'autres frontières fluides, à travers lesquelles la continuité azimutale de l'écoulement est assurée grâce à la périodicité spatiale.

Ces domaines pourront être divisés en sous-domaines, en vue d'améliorer la qualité des résultats (maillages H, O, C...).
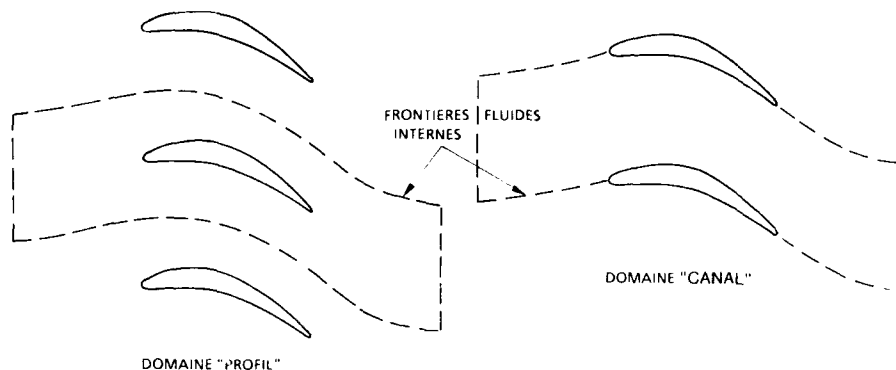
FRONTIERES | FLUIDES
INTERNES

DOMAINE "CANAL"

DOMAINE "PROFIL"

Fig. 3 - Domaine de calcul pour un canal.

4.2.2. Etage :

L'approche précédente n'est plus valable pour le calcul de l'écoulement dans un étage composé de deux roues dont les nombres d'aubes sont différents. Bien que chaque roue présente encore une périodicité géométrique, l'écoulement y est instationnaire et non périodique d'un canal à l'autre.

Pour des raisons pratiques, le domaine de calcul sera formé de plusieurs sous-domaines (type "profil" ou "canal"). Outre les frontières fluides internes entre deux canaux adjacents, apparaissent les frontières fluides internes entre les deux roues (fig. 4).
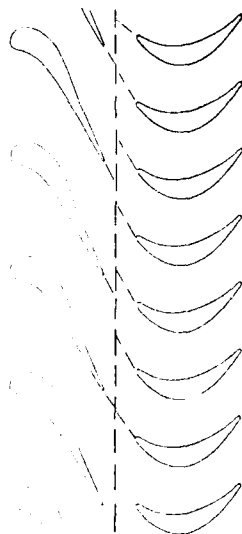

Fig. 4 - Domaine de calcul pour un etage

Si le domaine de calcul inclut tous les canaux de chaque roue, c'est-à-dire si le calcul est mené sur l'étage complet, les conditions limites sur les frontières internes est traduite par la continuité azimutale (à la place de la périodicité spatiale en roue isolée) et la continuité axialo-radiale.

Dans cette hypothèse, la taille-mémoire d'ordinateur et le temps de calcul seraient très importants, et même inacceptables. C'est pourquoi diverses techniques ont été proposées, ayant comme but commun de réduire la taille du domaine de calcul à des proportions compatibles avec les capacités des calculateurs actuellement disponibles.

4.3. Techniques de réduction du domaine de calcul

Dans leur majorité, ces techniques visent à retrouver une périodicité spatiale de l'écoulement sur un nombre réduit de canaux de chaque roue [4], [5].

Certaines font appel à un changement d'échelle des profils permettant de retrouver la périodicité géométrique et donc la périodicité aérodynamique. Ce type d'approche, justifiable en écoulement bidimensionnel, parait néanmoins délicat à mettre en oeuvre sur des machines tridimensionnelles où les carters subissent de fortes variations du rayon (machines axialo-radiales notamment).

D'autres mettent en jeu diverses moyennes azimutales, effectuées coupe par coupe, ce qui a pour conséquence de masquer certains effets tridimensionnels, en particulier la variation azimutale de l'angle (pente méridienne de l'écoulement) à l'entrée de chaque roue.

On peut également citer des voies sensiblement différentes :

- utilisation des propriétés de déphasage espace-temps pour l'établissement de conditions limites instationnaires périodiques [6],

- passage des coordonnées physiques à des coordonnées de calcul dans lesquelles l'écoulement est spatialement périodique [7].

La technique développée à l'ONERA [8] permet de contourner certains des obstacles évoqués ci-dessus. Elle va être rapidement décrite dans les lignes qui suivent.

On considère un étage comportant N_1 aubes dans la roue amont et N_2 dans la roue aval. On choisit tout d'abord deux entiers K_1 et K_2 aussi petits que possible, mais tels que les rapports K_1/K_2 et N_1/N_2 soient voisins. K_1 et K_2 représentent les nombres de canaux effectivement calculés respectivement dans la roue amont et la roue aval.

Les extensions azimutales de chaque groupe de canaux sont :

- pour la roue 1 $e_1 = K_1 \, p_1 = K_1 \times 2\pi/N_1$

- pour la roue 2 $e_2 = K_2 \, p_2 = K_2 \times 2\pi/N_2$

On définit alors une extension moyenne par :

$$e_c = 1/2 \ (e_1 + e_2)$$

ainsi que :

$$\lambda_1 = e_c/e_1 \qquad \lambda_2 = e_c/e_2 \qquad \left(\frac{\lambda_1}{\lambda_2} = \frac{e_2}{e_1} = \frac{N_1}{N_2} \times \frac{K_2}{K_1} \right)$$

Les quantités λ_1 et λ_2 servent, au cours du calcul, à dilater ou contracter les gradients azimutaux à l'interface des deux roues de façon à les rapporter à l'extension circonférentielle commune e_c, à travers laquelle on assure la continuité axialo-radiale. Par ce biais il est alors possible d'appliquer la condition de périodicité spatiale sur les frontières hautes et basses de chaque groupe de canaux.

Quelques remarques :

- comme on le voit, il s'agit seulement d'un traitement aux frontières de continuité (frontières fluides internes) du domaine de calcul. En particulier, il est important de noter que les géométries réelles des canaux ne sont pas affectées, et que n'importe quel type de machine peut être pris en compte,

- les approximations induites sont d'autant plus faibles que K_1/K_2 est proche de N_1/N_2 : la solution est d'ailleurs exacte si $K_1/K_2 = N_1/N_2$,

- il est aisé de démontrer que les valeurs moyennes (dans le temps) de grandeurs globales comme le débit ou la charge sur les roues sont indépendantes du choix des nombres K_1 et K_2,

- cette technique peut être étendue à un nombre de roues supérieur à 2 par

$$e_c = \frac{1}{n} \sum_{i=1}^{n} K_i * p_i \qquad \lambda_i = e_c/e_i$$

Les résultats de calcul présentés ultérieurement porteront sur la validation de cette technique sur une coupe d'étage de turbine transsonique et sur son application à un étage 3D.

4.4. Simulation des écoulements transitoires

Ce genre de simulation peut concerner les phénomènes physiques suivants :

- évolution au cours du temps des conditions amont et/ou aval
- variation de la vitesse de rotation.

Lorsque ces changements sont très rapides, ils peuvent induire des efforts importants (analogues à des chocs), éventuellement dommageables pour les structures de la machine.

D'un point de vue numérique, les méthodes utilisées pour les régimes stationnaires ou permanents s'appliquent aux régimes transitoires, après quelques modifications minimes.

Du point de vue informatique, les choses sont différentes : une solution convergée (3D, régime stationnaire en roue isolée ou permanent en étage) est obtenue en quelques millisecondes de temps réel, à raison de 5000 à 8000 itérations par milliseconde. Pour un maillage de l'ordre de 40 000 points, ceci représente environ 3h de CRAY XMP.18. La description d'un phénomène transitoire sur 1 seconde nécessiterait 200 à 250 fois plus de temps, soit quelques 30 jours C.P.U. ! On conçoit que ce genre de calcul soit limité aux écoulements bidimensionnels dont la phase transitoire est extrêmement brève.

5. VISUALISATION DES RESULTATS DE CALCUL

Lorsque l'on effectue des calculs instationnaires, on pense naturellement à visualiser certains résultats sous forme d'un film d'animation, ce qui permet de mieux percevoir l'évolution des phénomènes au cours du temps.

Pour cela il est intéressant de disposer de logiciels simples, peu coûteux en temps de calcul et surtout qui puissent être totalement intégrés au programme principal.

C'est en fonction de ces quelques contraintes qu'a été développé un procédé de création d'images de synthèse pour la visualisation de champs divers sur des surfaces gauches définies dans l'espace 3D telles l'extrados et l'intrados d'une aube de turbomachine.

Ceci se déroule en deux étapes. La première est celle de la création d'une matrice numérique 2D dont chaque élément sera ultérieurement associé à un pixel (point) de l'image sur l'ecran de visualisation. La surface à représenter est décomposée en facettes triangulaires élémentaires projetées sur le plan image, et un simple test sur la distance permet l'élimination des zones cachées. Les matrices ainsi créées sont stockées pour, dans une seconde étape, être visualisées sur un écran graphique, et servir à la réalisation de courts films d'animation.

6. RESULTATS NUMERIQUES

6.1. Coupe d'étage de turbine

Des calculs 2,5D ont été menés sur une coupe de pied d'étage de turbine transsonique dans le but de valider la technique proposée ci-dessus (traitement des conditions-limites sur les frontières fluides internes, associé à la réduction du domaine de calcul).

Le distributeur comprend $N_1 = 31$ aubes, et la roue $N_2 = 53$, soit un rapport $N_1/N_2 = 0,585$.

Les différents cas envisagés sont les suivants :

Cas 1.1 $K_1 = 1$, $K_2 = 1$ ($K_1/K_2 = 1$)
Cas 1.2 $K_1 = 1$, $K_2 = 2$ ($K_1/K_2 = 0.5$)
Cas 3.5 $K_1 = 3$, $K_2 = 5$ ($K_1/K_2 = 0.6$)
Cas exact par utilisation des propriétés de déphasage espace-temps, grâce à une technique proche de celle décrite en réf. [6].

Dans cet étage de turbine, un écoulement supersonique est amorcé dans le distributeur, donnant à l'aval de celui-ci un système d'ondes de choc et de détente, et provoquant donc des gradients azimutaux des grandeurs aérodynamiques. Si l'on passe du repère fixe au repère tournant, la roue se voit donc attaquée par un écoulement subsonique non uniforme. Les fluctuations les plus importantes sont celles de l'angle relatif d'entrée (amplitude de l'ordre de 20°). Tout ceci induit dans l'écoulement des effets instationnaires non négligeables, nettement plus accentués pour la roue mobile que pour le distributeur [8]. Ils sont mis en évidence par exemple sur l'évolution au cours du temps de la répartition de la pression statique sur une aube du rotor (pression rapportée à la pression génératrice de l'écoulement amont) (fig. 5). L'intervalle couvert (période) correspond au franchissement d'un pas du distributeur ; ce résultat concerne le calcul exact (cas n° 4).
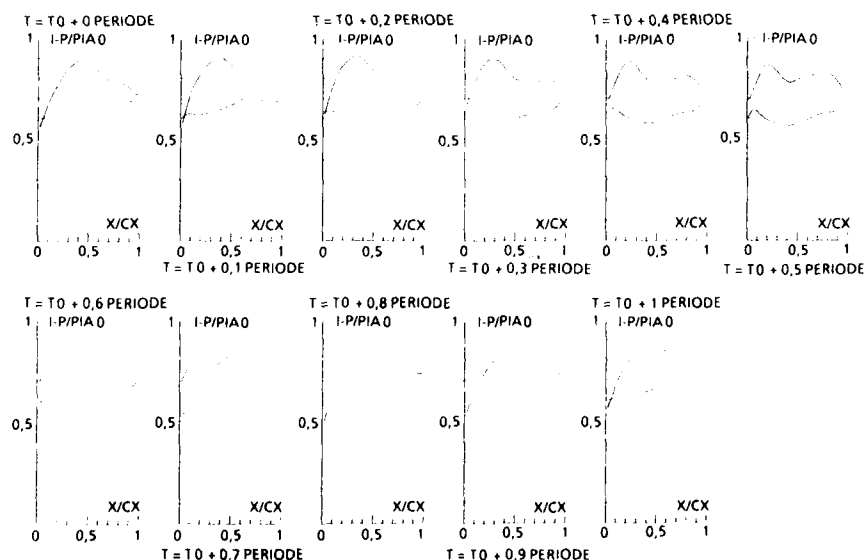

Fig 5 - Evolution au cours du temps de la pression statique sur une aube du rotor

Une analyse comparative poussée des quatre configurations de calcul a été effectuée pour mieux cerner les différences existant de l'une à l'autre. On a examiné notamment les évolutions au cours du temps de grandeurs intégrées (charge des profils, débit) ou de grandeurs locales, moyennées ou non en espace (angles et vitesses en repères relatif et absolu) ainsi que les moyennes en temps de différentes quantités.

En particulier, l'observation de l'évolution temporelle du débit dans un canal de la roue mobile (fig. 6) permet de formuler les deux remarques suivantes :

a) Le cas 1.1 est très différent des autres car la périodicité y a été forcée d'un canal à l'autre : il n'est donc pas possible d'avoir, à un instant donné, des débits différents dans des canaux voisins, alors que, dans la réalité, le fluide entrant dans la roue mobile a la faculté de se répartir inéga- lement dans les canaux, donnant ainsi des fluctuations nettement plus importantes (fig. 6d).

b) Si l'on examine les cas intermédiaires, on note des différences quasi-insignifiantes entre le cas 3.5 (fig. 6c) par rapport au cas exact pris comme référence. Les différences sont plus marquées, mais restent raisonnables pour le cas 1.2 (fig. 6b).

Pouvoir répartir inégalement le débit entre plusieurs canaux semble donc être un élément-clé important dès lors que l'écoulement présente azimutalement une non uniformité significative. Dans le cas précis de l'étage de turbine présenté, l'approximation 1-1 apparaît insuffisante, alors que l'approxi- mation 1-2, nettement plus proche du cas réel, représente un bon compromis entre le coût d'un calcul et, la qualité des résultats qu'elle fournit. Elle a d'ailleurs été utilisée pour l'étage 3D présenté maintenant.
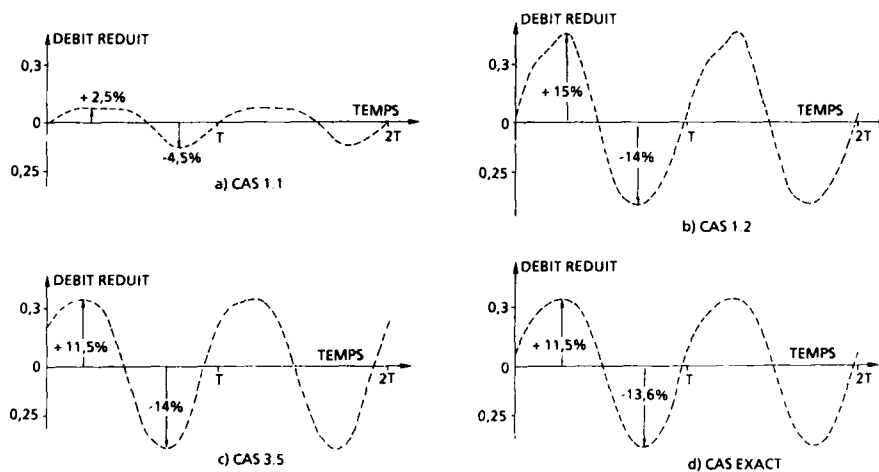

Fig. 6 - Débit à l'entrée d'un canal de la roue mobile

6.2. Etage 3D de turbine

Il s'agit de l'étage correspondant à la coupe décrite ci-dessus. Les nombres d'aubes sont donc 31 et 53. Précisons les principales caractéristiques de fonctionnement :

taux de détente sans pertes	τ = 3,25
taux de détente avec pertes	τ' = 3,48
pression génératrice amont	P_{iao} = 11,08 10^5 Pa
température génératrice amont	T_{iao} = 1250 K
rapport des chaleurs spécifiques	γ = 1,31
chaleur spécifique à pression constante	C_p = 1182 J/kg/K
coefficient de frottement	C_f = 0,0025.

Les maillages utilisés sont présentés sur la fig. 7 ; l'ensemble comporte environ 44000 points. Avec ces maillages, le régime permanent est atteint après 12000 à 15000 itérations (temps CPU sur CRAY de l'ordre de 3h).

Cet étage a fait l'objet de deux séries de calcul [9, 10], la première en fluide parfait, la seconde avec simulation des effets visqueux par introduction d'un frottement pariétal. Les deux calculs présentés ici correspondent à la même chute d'enthalpie (ce qui explique que les taux de détente soient différents).

MAILLAGES AUBE A AUBE

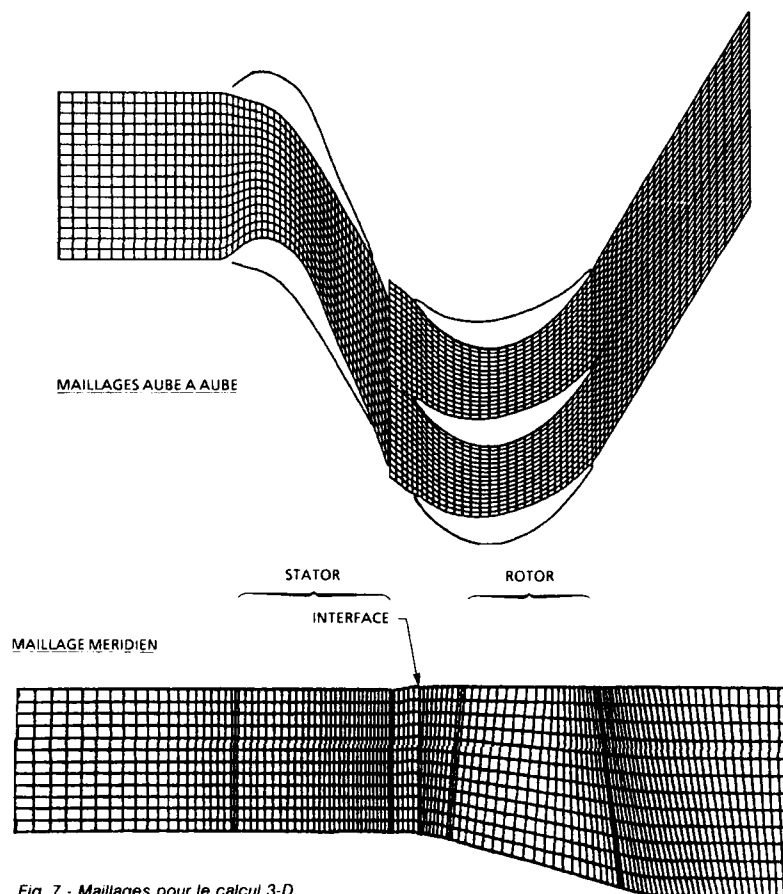STATOR   ROTOR

INTERFACE

MAILLAGE MERIDIEN

Fig. 7 - Maillages pour le calcul 3-D.

       Dans la partie amont du distributeur, l'effet de la simulation des pertes est pratiquement inexistant. Dans la partie aval, ainsi que dans la roue mobile, deux points sont à signaler :

1) Introduire un frottement provoque une diminution de la section de passage disponible : en écoulement supersonique la vitesse atteint un niveau moins élevé, avec le contraire en écoulement subsonique. Ceci est observé sur l'extrados du distributeur.

2) La vitesse et la direction de l'écoulement de sortie du stator sont modifiées, ce qui entraîne un changement notable de la vitesse et de l'angle relatif à l'entrée de la roue mobile (fig. 8) : dans cette roue, les effets visqueux simulés contribuent à augmenter le niveau moyen de la pression sur l'extrados près du bord d'attaque. Il y a aussi transformation de l'évolution dans le temps du débit dans le rotor (fig. 9) : avec pertes, l'amplitude est un peu accrue à l'entrée, mais diminuée à la sortie.

β_{rel}

- 40°

COUPE DE TETE

0°

TEMPS

β_{rel}

-60°

COUP DE PIED

-20°

SANS PERTE   AVEC PERTES
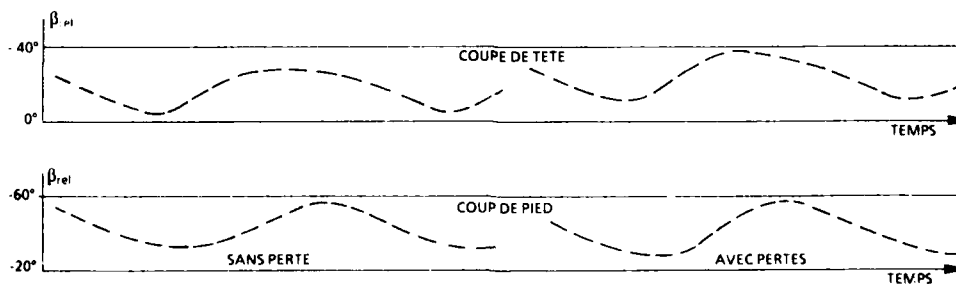
TEMPS

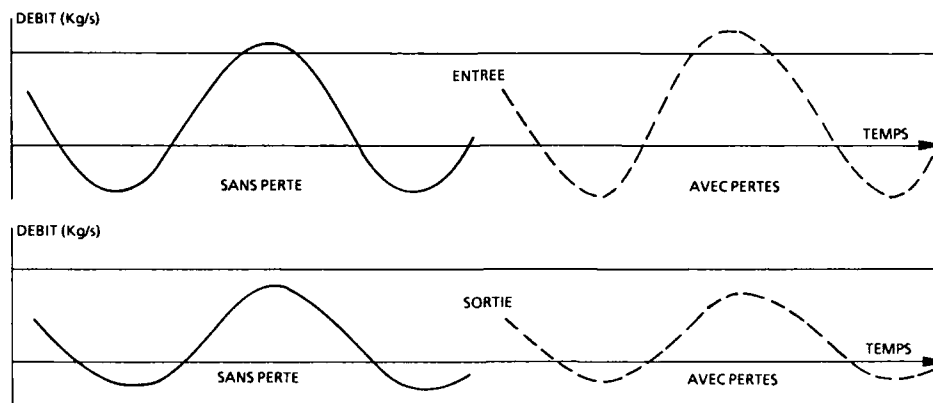Fig. 8 - Angle relatif devant un bord d'attaque du rotor en fonction du temps.

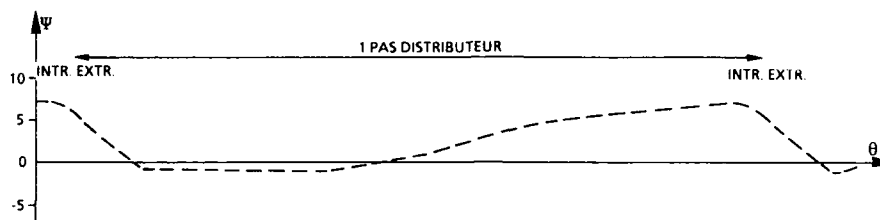Fig. 9 - Débit dans un canal de la roue mobile en fonction du temps.

Fig. 10 - Angle méridien à l'interface (coupe moyenne).

Les effets tridimensionnels présents dans cet étage peuvent traverser l'interface entre les deux roues grâce au traitement proposé pour les conditions-limites. Ils sont traduits par l'évolution azimutale de l'angle φ, montrée pour un instant arbitraire (fig. 10).

6.3. Amorçage d'une tuyère bidimensionnelle

La phase d'amorçage d'une tuyère est caractérisée par une variation rapide du taux de détente (pression statique aval rapportée à la pression d'arrêt amont). On peut obtenir ceci de plusieurs façons :

- soit par variation de la pression d'arrêt amont, la pression aval étant maintenue constante,

- soit par variation de la pression statique aval, la pression d'arrêt amont ne changeant pas,

- soit par variation simultanée des deux pressions.

Il est évident que la phase transitoire ne sera pas la même suivant le choix de la variation du taux de détente. Pour l'exemple présenté, (fig. 11), on a retenu la seconde possibilité [10]. L'écoulement initial est stationnaire, à basse vitesse sauf dans la région du col où il y a une onde de choc droite de faible intensité. Au fur et à mesure de l'amorçage, cette onde se propage dans le divergent, se transforme en onde de choc oblique d'intensité décroissante. En fin d'amorçage l'écoulement redevient stationnaire après la stabilisation de la pression aval.

Ces résultats montrent qu'il existe des ondes de choc d'intensité non négligeable : la validité de l'approche "Euler" pourrait être remise en cause quant à sa signification physique. Il n'en reste pas moins que cette approche permet une première compréhension des phénomènes réels.

On notera enfin que la solution obtenue dépend étroitement des conditions-limites (amont et aval) parfois difficiles à évaluer avec sureté dans la réalité.
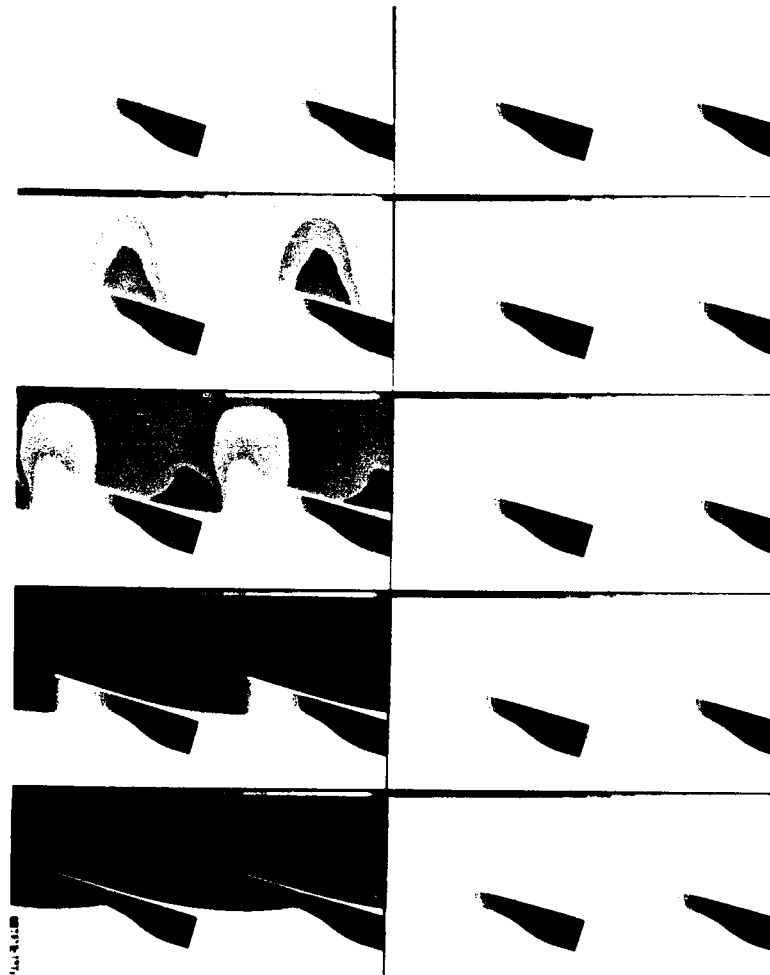
Fig. 11 - Amorçage d'une tuyère supersonique (champs des isobares).

Fig. 12 - Etage 3-D de turbine transsonique (isobares).

7. CONCLUSION

Dans cet article, l'accent a été mis sur l'importance des conditions-limites dans la simulation numérique de l'écoulement dans des éléments de turbomachines.

Actuellement, on est toujours conduit, selon le but recherché, à privilégier certains aspects de l'écoulement, et donc à en négliger d'autres ; il convient alors naturellement de ne pas oublier que les résultats de calculs sont fonction des hypothèses simplificatrices adoptées.

En dépit de ces hypothèses, l'utilisation des méthodes de calcul s'avère être d'une grande utilité pour l'analyse et la compréhension des écoulements compressibles de turbomachines. En effet, ces méthodes mettent en évidence les aspects tridimensionnels instationnaires et visqueux des écoulements, parfois mal connus sur le plan expérimental.

On notera enfin que les méthodes "Euler" seront sans doute encore largement exploitées dans les années à venir, car les méthodes "Navier Stokes", qui commencent à être opérationnelles, restent très coûteuses.

REFERENCES

[1]   SOVRANO, R.,
        "Calcul de l'Ecoulement Transsonique dans un Compresseur Centrifuge par une Méthode Pseudo-Instationnaire",
        AGARD/PEP "Centrifugal Compressors, Flow Phenomena and Performance", Bruxelles, 1980,
        T.P. ONERA n° 1980-42.

[2]   VIVIAND, H. et VEUILLOT J.P.
        "Méthodes Pseudo Instationnaires pour le Calcul d'Ecoulements Transsoniques",
        Publication ONERA, n° 1978-4.

[3]   VEUILLOT, J.P. and MEAUZÉ, G.
        "A 3-D Euler Method for Internal Transonic Flows Computation with a Multi-Domain Approach",
        AGARD PEP L.S. 140
        ONERA T.P. n° 1985-41.

[4]   RAI, M.M.,
        "Navier Stokes Simulations of Rotor-stator Interaction Using Patched and Overlaid Grids"
        AIAA Paper 85-1519, 1985.

[5]   CHEN, Y.S.
        "3-D Stator-Rotor Interaction of the SSME"
        AIAA Paper 88-3095, 1988.

[6]   ERDOS, J.I., and ALZNER, E.
        "Computation of Unsteady Transonic Flows Through Rotating and Stationary Cascades",
        NASA CR-2900, 1977.

[7]   GILES, M.B.,
        "Stator-Rotor Interaction in a Transonic turbine",
        AIAA Paper 88-3093, 1988.

[8]   FOURMAUX, A. and LE MEUR, A.
        "Computation of Unsteady Phenomena in Transonic Turbines and Compressors",
        4th Symposium on Unsteady Aerodynamics and Aeroelasticity of Turbomachines and Propellers,
        AACHEN, 1987.

[9]   LE MEUR, A.
        "Three-Dimensional Unsteady Flow Computation in a Transonic Axial Turbine Stage",
        AIAA 26th Aerospace Sciences Meeting,
        RENO, 1988.

[10]   REVUE FRANÇAISE DE MECANIQUE n° 1988-4.

DISCUSSION

A.Uçer -O D T U, Turkey
    (1) The downstream condition used by the authors is the non-reflection condition. What is the upstream condition.

Author's response :
    At the upstream boundary the total pressure, the total temperature and one static condition, e.g. the flow angle, are imposed.

    (2) Is the 3-d code taking into account losses and how is it managed?

Author's response :
    A conventional friction coefficient is imposed on the walls whenever the flow does not separate, and constant pressure when the flow separates.

            Oxford University, u.K.
    There is a general comment to be made from the viewpoint of the experimentalists:

    it would be useful to have calculation results presented as curves duplicating test results. For example a plot of unsteady pressures on the blade surface can be directly compared to tes results, whereas pressures inside the passage cannot be compared to test results.

Author's response :
    There is certainly a lack of experimental results and theoreticians and experimentalists should reach an agreement how to present results in order to allow comparison between computation and tests.

H.Joubert, SNECMA Villaroche, France

    Pourquoi les auteurs n'utilisent-ils pas une condition de périodicité spatio-temporelle pour diminuer le domaine de calcul ?

Réponse de l'auteur :

    Le cas bi-dimensionnel 31/53 aubes a été fait dans ces conditions. Lorsque le nombre d'étages devient plus important, cela est pratiquement impossible.

DEVELOPMENT OF A MASS AVERAGING TEMPERATURE PROBE
by
S.C. Cook[1], R.L. Elder[2]

1. Rolls Royce plc,
   PO Box 31, Derby, UK

2. Cranfield Institute of Technology,
   Cranfield, Bedford, UK

SUMMARY

In research and development testing of axial flow fan and compressor rigs the overall performance can normally be determined to a satisfactory accuracy using conventional methods. It is known, however, that conventional slow response instrumentation does not respond correctly to the highly unsteady flows encountered between blade rows in high speed turbomachines. Consequently measurements made in these areas, in an attempt to "split the loss" of the machine, typically lead to gross errors in stage, or blade element, performance assessments. A novel slow response temperature sensor, the Reverse-Kiel probe, has been created by employing a judicious shield design in an attempt to allow the probe to indicate the correct mass-weighted temperature of such unsteady turbomachinery flows.

The mass-weighted Reverse-Kiel temperature probe has been developed using some simple arguments supported by flow visualisation and computational modelling. The predicted best probe designs were evaluated and confirmed on the purpose built 'Blade-Wake' rig. The optimum probe has been built as a standard rig probe and now is undergoing preliminary test studies.

LIST OF SYMBOLS

C   Absolute flow velocity
d   Probe inlet hole diameter
K   Constant
κ Kinetic energy of turbulence
$\dot{m}$ Mass flux per unit area entering probe shield
$\dot{M}$ Mass flux per unit area of flow (external to probe)
Mn Mach number of flow
Re Reynolds number
Rf Recovery factor
t   Time
T   Absolute temperature
Tp Probe indicated temperature
Ts Calibration tunnel static temperature
Tt Calibration tunnel total temperature
U   Rotor blade speed
V   Relative flow velocity

SUBSCRIPTS

a   Axial component
R   Rotor relative
O   Total quantity
1   Rotor inlet
2   Rotor exit

GREEK SYMBOLS

ε Rate of turbulence dissipation
θ Flow incidence angle relative to rig axis
ρ Fluid density
τ Period of pulsatile flow

1.   INTRODUCTION

The advanced measurement technique detailed in this report has been developed to aid compressor research and development. Compressor rig testing is carried out to determine the compressor characteristics over a range of speeds and flow conditions. A schematic of a typical compressor test facility is shown in Figure 1. Upstream of the test unit or compressor the inlet mass flow, pressure and temperature are measured to the required accuracy. Downstream of the compressor the outlet temperature and pressure are measured. It is then a simple matter to derive the isentropic (or polytropic) efficiency of the unit. A multistage compressor (6 to 10 stages) will typically produce a temperature rise of 250 K to 550 K. However a single stage compressor typically produces only a temperature rise of 50 K. It has been found that when a small temperature rise is to be measured on a rig it is more accurate to derive work input using a shaft torquemeter (Reference 1) rather than make the measurement directly with a thermocouple system. A non-contacting shaft torquemeter, such as the highly accurate phase-shift transducer (Reference 2) yields net torque after corrections are made for rig bearing losses and windage, and shaft modulus variation with temperature. From the net shaft torque and inlet mass flow function the temperature rise through the compressor can be calculated. The inherent high accuracy of the torque measuring devices leads to a more accurate determination of temperature rise than could be obtained from a direct temperature measurement (in the case of small temperature rises).

Hence the overall efficiency of a compressor can be determined to a satisfactory accuracy but a major problem occurs when attempts are made to make efficiency measurement between blade rows. This is required on a single stage machine, such as a model fan, to provide a thorough analysis of the individual performances of the fan and the by-pass outlet guide vanes. Additionally the radial distribution of loss (or efficiency) is required in order to assess the elemental performance of the fan blade which usually has large changes of stagger and camber over the blade span. In a multistage compressor rig, detailed knowledge is required of the performance of each of the stages (and individual blade rows). It is found that conventional, slow response pressure and temperature probes do not respond correctly to the highly unsteady flows encountered between blade rows in high speed turbomachinery and the resultant efficiency derived from these measurements can be grossly in error. Consequently, compressor research and development is hampered by the poor accuracy of conventional measurement techniques which do not permit the compressor engineer to resolve the areas of deficiency along a blade span or between blade rows. This leads directly to longer and more costly compressor development paths.

The interstage instrumentation limitations arise because a steady state measurement approach has been adopted without an appreciation of the effect of the unsteady flow on the input to the instrumentation. The interstage flow is highly complex comprising unsteady rotating and stationary wakes, the residuals of passage vortices etc. This paper concerns itself with the development of an interstage measurement technique which yields encouraging improvements in performance assessments. The technique is required to be low cost, rugged enough for routine testing and be preferably simple to manufacture, operate, record and analyse. The target measurement accuracy for radial distribution of efficiency over a blade span, or individual blade efficiency within a multistage compressor is $\pm 0.5\%$ of a point in efficiency.

The temperature required to yield accurate efficiency measurements in turbomachinery is the mass-averaged temperature. In a pulsatile flow of period τ this equates to:

$$\bar{T}_{MA} = \frac{\int_t^{t+\tau} \dot{M}.T.\, dt}{\int_t^{t+\tau} \dot{M}.\, dt} \tag{1}$$

and in conditions of fluctuating density and axial velocity is found not to be equal to the time-averaged temperature, which is given by:

$$\bar{T} = \frac{1}{\tau} \int_t^{t+\tau} T.\, dt \tag{2}$$

Simple velocity triangles are drawn in Figure 2 for a compressor rotor. The flow associated with the wake is arbitrarily taken to have 40% reduction of rotor relative velocity compared to the free stream or jet flow. The rotor relative angle of the wake and jet flows are assumed to be equal. Consequently the absolute angle of the wake flow increases over that of the jet flow. There is, however, only a minimal increase in the speed of the wake flow over the jet flow. Most importantly, it can readily be seen that the whirl velocity (and therefore temperature rise via Euler) is increased in the wake and the axial velocity is reduced in the wake. Hence in order to obtain the correct mass averaged temperature in a pulsatile flow field, oscillating between jet and wake flows, it is necessary that the hot wake flow is weighted by it's correspondingly low axial velocity and not by it's relatively high absolute velocity. This presents the instrumentation engineer with a difficult task.

In this study a slow response temperature sensor (type K thermocouple) has been combined with a judicious shield design in an attempt to permit the probe to respond correctly in unsteady flows. In particular, the design intent has been to produce a temperature probe which indicates the correct mass-averaged temperature of the unsteady flows.

2. REVIEW OF PREVIOUS WORK

PREVIOUS ROLLS-ROYCE/CRANFIELD STUDIES

In recognition of the requirement to make sensible (close to rotor) temperature measurements, Cranfield and Rolls-Royce undertook a study to identify the error mechanism and to produce a new design of probe which was demonstrably better. Much of the work carried out has already been reported as Reference 3 but additional work was undertaken with modified temperature probes which led to the discovery of a new probe type with an apparently significantly improved response in unsteady flows. The following precis of the work leads onto the previously unreported new probe type.

The Cranfield study began by considering the velocity triangles at hub, mid-height and tip for a typical fan. Convective heat transfer from cylindrical sensors (hot wires) and spherical sensors (thermocouple beads) was considered. Internal conduction effects and sensor shielding was also modelled. By assuming the pulsatile flow to be an alternation of jet and wake flows at variable mark-space ratios it was shown that an error would indeed exist between the temperature a sensor would indicate and the mass averaged temperature. The magnitude of the error was shown to be a function of the relative convective heat transfer coefficients of the jet and wake, the axial velocities and densities of the jet and wake flows, the proportion of the blade pitch that the wake occupies and the flow sampling characteristics of the probe itself. In practise, however, it would be highly unlikely that such details would be known about the probe and flow (permitting the error to be defined). Therefore the use of the model, beyond identifying the salient parameters, is restricted to estimating likely measured errors based on reasonable estimates of the above parameters.

The model was used to estimate errors that a shielded and unshielded (bare thermocouple bead) probe would experience when exposed to the hub, mid-height and tip velocity triangles in a typical fan. In general it was confirmed that due to the large difference between the time averaged flow temperature and

the mass averaged flow temperature, significant errors (relative to the mass averaged temperature) would be expected from the shielded probe, with a marginal improvement if an unshielded probe was used. In all cases the largest errors were seen at the fan tip.

Having produced a model which showed that the largest errors were associated with fan tip conditions, a rig (Blade-Wake rig) which simulated the gross flow difference, at representative frequencies, was developed. The rig was calibrated with a constant current anemometer to measure the dynamic temperature profile, and calibrated using a constant temperature anemometer to record the dynamic velocity profile. The rig was found to generate a wake of some 40% of the blade pitch which was approximately 25 K hotter than the jet flow. Various industry standard design probes (Reference 4) were exposed to the flow on the blade wake rig and their response recorded. As expected the largest errors were seen close to the rotor trailing edge; at a downstream distance equal to 0.125 rotor chord, an open bead read 7.5 K high, a Kiel shrouded probe read 6.5 K to 11 K high (depending on bleed hole area), a Cobra probe fitted with a thermocouple read 5 K high and a cylindrical probe indicated 6 K high. However at one rotor chord downstream all the probes indicated a temperature in close agreement with the mass averaged temperature.

It was suspected by Agnew (co-author of Reference 3) that a probe with a ma. .ed yaw sensitivity would be less influenced by wake (off angle) flow and using information in Reference 4, concerning angular sensitivity of pneumatic probes, coupled with an empirical approach, he developed the "Reverse-Kiel" probe. A number of Reverse-Kiel probes were built with varying inlet diameters and applied to the Blade Wake rig. The datum design, illustrated in Figure 3, seemed to be excellent showing negligible error at only 0.25 rotor chord downstream of the rotor. It was then discovered that the correlation between probe performance and probe design was not straightforward and that an understanding of the probe was largely based on intuition and experimental evidence rathe. than detailed analysis. Consequently it was decided to initiate a further programme of study to appreciate how the Reverse-Kiel probe tended to respond to the flow mass averaged temperature and to determine how to further improve the response of the probe.

3. DEVELOPMENT OF A MASS-AVERAGING (REVERSE-KIEL) TEMPERATURE PROBE

The nature of the flow within the shield of the original (datum) Reverse-Kiel probe has been studied using both, flow visualisation and computational studies. The flow visualisation was carried out on large scale perspex models of the probe head, using smoke wire, and a novel hot wire method. These techniques revealed the internal flow structure. In parallel with the flow visualisation, a 3D finite difference numerical technique was used to model the probe and the flow which was used to assess a number of the probe geometries investigated during the flow visualisat.cn s udies. Subsequently the flow predictions were confirmed by the flow visualisation results. A theory is then proposed to explain how the Reverse-Kiel temperature probe tends to indicate the desired flow mass-averaged temperature. A parametric variation study on the original (datum Reve.se-Kiel probe design was carried out by combining the quantitative data from the numerical model with the developed theory to predict the probe optimum design which was tested on the purpose built Blade-Wake rig.

CONSIDERATION OF FLOW FIELDS IN GEOMETRICALLY SIMILAR ENVIRONMENTS

The geometry of the Reverse-Kiel probe and its orientation relative to the incident flo. suggests that a jet like flow will be internally generated through the small inlet orifice of the probe. Knowledge of the jet flow (or its resultant) within the shield is therefore required in order to appreciate why the thermocouple junction in the Reverse-Kiel probe tends to indicate a mass averaged temperature and how the jet flow can be controlled to improve and stabilise the probe response.

A review of literature on axisymmetric jets revealed that this classical problem of turbulent mixing has largely been the subject of semi-empirical theories. Reference 5 gives a number of simple engineering expressions for the general case of a turbulent jet issuing into parallel moving air streams, and it is a trivial matter to reduce these expressions to the limiting case of a jet issuing into a stationary fluid However an important difference which exists between the jet cases reported above and the internal flow in the Reverse-Kiel Probe is the presence and proximity of the internal walls of the shroud relative to the flow issuing through the inlet orifice. In effect the situation equates to a sudden enlargement of cross sectional area of 1:64. The internal geometry and small inlet orifice of the Reverse-Kiel Probe is not unlike the rooms, and associated ventilation holes, studied in Reference 6. The study of mean flow fields within gas turbine axisymmetric combustors is also of relevance to the Reverse-Kiel Probe because of the similarity of internal geometries and possibly internal flows (e.g. reference 7).

The studies of axisymmetric jets, ventilating into rooms and combustion chamber flows can be expected to be of limited use in fully understanding the internal flow generated within the Reverse-Kiel Probes as none of the flow situations or geometries exactly match that in the Reverse-Kiel Probe where the flow n.u the probe is certainly not fully developed and where a large sudden expansion takes place into an open ended cavity of length less than 2.5 cavity diameters. The work reported above has, however, been helpful in establishing an initial assessment of the flow process.

FLOW VISUALISATION STUDIES

The successful use of flow visualisat on technioes in combustion chamber flows encouraged exploration of the possibility of performing similar studies for the Reverse-Kiel probe geometry. A variety of combustion chamber flows had been modelled but each inlet flow was fixed and remained steady. The flow onto a Reverse-Kiel probe in a compressor is neither fixed nor steady, with varying conditions of speed, incidence, temperature, heat transfer, turbulence etc. in the wake and free stream. Consideration of the probe size, flow velocity and flow periodicity, however, suggest an improved understanding of the problem could be obtained using a quasi-steady model for the following reasons. Consider the datum Reverse-Kiel probe geometry (Figure 3) and the application of such a probe to a typical research compressor downstream of the rotor with absolute speed of 250 m/s and blade passing frequency of 8 kHz. In this case the flow is periodic repeating every 125 μs and the flow transit period through the probe is 15 μs. Hence it is proposed that the flow through the probe can be approximated to a quasi-steady flow switching between states (this is clearly an assumption requiring justification).

Flow visualisation through a "full-size" model of the Reverse-Kiel probe was considered to be impracticable due to the miniature dimensions of the probe. Consequently a larger scale model was constructed to give a reasonable seeding and viewing volume. Various flow visualisation techniques were

considered to determine the external, but more importantly the internal flow (Reference 8). The most promising and convenient technique for flow visualisation of this particular geometry and flow appeared to be smoke (vaporised oil) flow visualisation (Reference 9). With the working fluid (air) being the same for the probe and model cases, dynamic similarity dictates that a scaled-up model would need to be tested in a corresponding air velocity. Consequently the datum probe geometry when exposed to a flow of 200 m/s was simulated by a 50 times size model (conveniently giving an inlet diameter of 9 mm) in a 4 m/s flow.

Consequently a 50 times size perspex model of the probe shield was constructed and run on a purpose built smoke flow visualisation tunnel at the Transport Technology Department at Loughborough University. Smoke filaments were generated by a 30 element smoke rake positioned in the contraction area upstream of the tunnel working section. The model shield could be yawed relative to the incident flow. Figure 4 is an example of the results obtained from the Loughborough tunnel. The datum probe geometry is shown at an incidence of 60° to the tunnel flow. The flow external to the perspex model is clearly visible, with acceleration around, and separation from, the perspex model. A single smoke filament enters the model and remains essentially axisymmetric (relative to the model) throughout its length. This characteristic was seen to persist over a wide yaw range ($\pm$ 75°). Generally the Loughborough tunnel was quick and easy to use and provided a useful Reynolds number range (based on inlet plate diameter) up to 1800. Unfortunately the tunnel provided only details of the flow external to the shield but nothing on the internal flow structure (except along the shield centre line).

An alternative facility, within Rolls-Royce, was used to study flows internal to the probe at a more useful Reynolds number range of 1800 < Re < 3000. The method chosen to visualise the internal flow in the same model was the smoke-wire technique (References 10 and 11). Three pairs of bosses were fixed into the model to allow fine wires to be fixed horizontally across an internal diameter within the shield. The wire was coated with a suitable oil (such as Shell "Ondina") so that small beads of oil form along the length of the wire. The wire is suddenly heated (electrically) causing smoke filaments to originate from each bead. Provided the Reynolds number (based upon wire diameter) does not exceed approximately 20, the flow around the wire does not break down into a laminar vortex sheet and reasonable smoke filaments are produced. The fixed wire positions were at axial distances of 2d, 8d and 12.5d downstream of the inlet orifice (diameter d), with the 12.5d position corresponding to the axial location of the thermocouple bead within the actual probe. The wires were spring loaded to maintain a diametral orientation without sagging at temperature.

An alternative utilisation of the wires fitted for smoke flow visualisation is the novel hot wire visualisation technique (developed as part of this programme). By continuously operating the wires at elevated temperatures (through resistive heating) to glow red (greater than 600°C) the convective heat transfer over the wire length could be qualatatively judged by looking for grey (cooler) lengths of wire corresponding to higher convective heat transfer and thus higher velocities. In particular this technique was found to be very useful in defining the width, at each wire location, of the relatively high velocity jet flow.

Results from the flow visualisation of the datum geometry model at 15° incidence on the Rolls-Royce tunnel are included as Figure 5a (smoke flow visualisation) and Figure 5b (hot wire visualisation). At this 2d position the central jet flow is evident with recirculation regions either side of the jet. Figures 6a and 6b show similar results for the 12.5d sensor position at a model incidence of 30°. A clear asymmetry of the jet within the probe is evident with both flow visualisation techniques.

The use of flow visualisation techniques in conjunction with a large scale perspex model of the Reverse-Kiel probe has facilitated a good appreciation of the detailed flow structure expected within the actual Reverse-Kiel probe. The smoke flow visualisation studies at Loughborough University indicated that there appeared to be surprisingly little difference in probe centre-line internal flow over the range of model geometries tested, and over a wide range of flow incidences. The complimentary flow visualisation studies carried out at Rolls-Royce (using smoke wire and the novel hot wire flow visualisation techniques) revealed the detailed internal flows. It was found that although a jet-like structure was maintained to large angles of incidence, there was a clear jet asymmetry within the shield of the model probe. These observations of the detailed internal flow serve as a means of qualitative validation of numerical models.

3D FINITE DIFFERENCE NUMERICAL MODELLING OF FLOWS

In parallel with the flow visualisation studies it was also decided to numerically model the Reverse-Kiel probe geometry and associated flows. It was hoped that numerical modelling would enable a faster, more efficient, more detailed parametric study of the probe geometry than could be achieved using physical models with smoke flow visualisation. The Rolls-Royce Predictions of Aerodynamics and Combustor Emissions (PACE) suite of programmes was identified as being able to model the three dimensional, steady, elliptic, isothermal, turbulent flows associated with the Reverse-Kiel probe. PACE takes the continuity equation and the three momentum equations or Navier-Stokes equations, and solves these four simultaneous partial differential equations to yield pressure and the three components of velocity. The pressure field must be chosen in such a way that the solutions of the momentum equations (in which the gradient of the pressure appears) yield a velocity field which also satisfies continuity. This is achieved by using an iterative technique, incorporating pressure and velocity corrections at each step, until both the continuity and momentum equations are satisfied simultaneously. This scheme is based on that discussed in Reference 12. A grid distribution, or mesh, is defined over the flow domain to be solved for. A finite difference scheme is used to replace the partial differentials in the flow equations with ratios of finite differences. PACE uses the k-ε turbulence model (Reference 13) to represent time averaged turbulence effects.

The initial flow geometries modelled using PACE were very simple (2 dimensional) but the model was progressively extended until a 3 dimensional model, suitable for the intended parametric design variation, was developed. The final version of the 3 dimensional model was based on a suitable mesh for the datum Reverse-Kiel probe, but had sufficient resolution to be a reasonable mesh for a useful variation of inlet hole diameter, inlet plate thickness, shield length and shield wall thickness (ie. outlet hole diameter). The mesh size was 30 axial lines x 27 radial lines x 17 circumferential lines. This gave a resolution of 5 axial lines and 5 radial lines through the inlet hole of the datum Reverse-Kiel probe.

The flow predictions for the datum geometry at zero incidence were compared to earlier two dimensional flow predictions and found to be in good agreement. Additionally, the spread of the internal jet flow was measured and found to be in reasonable agreement with jet spread angles noted with axisymmetric jets, ventilation flows and combustion chamber flows. The hot wire flow visualisation studies also fully supported the numerical predictions. Figures 7 and 8 show PACE predictions for an axial velocity of 200 m/s with a flow incidence of 45° onto the datum geometry. Flow is seen to enter the solution domain along the left hand side and bottom boundaries and exit the flow domain along the right hand side and upper boundaries. The presence of the centre line blockages, simulating the datum probe geometry, is seen to distort the flow field local to the probe geometry, but far downstream of the probe the flow field is relatively undisturbed. Figure 8 is a windowed down version of Figure 7, to allow closer examination o the flow within the shield. Flow enters the probe through the inlet orifice and issues as a jet into the probe shield. However the internal jet is actually slightly offset (relative to the probe centre lin axis) tending to turn back on the external flow direction. This characteristic was also present in the results of the experimental modelling (Figure 6). Hence the PACE computations for incident flow onto the datum Reverse-Kiel geometry correctly predicted the asymmetrical nature of the jet within the probe shield, and it was concluded that the 3D PACE model could be used to examine parametric design variations to the datum probe geometry.

4. CAVITY AVERAGED TEMPERATURE THEORY AND PARAMETRIC VARIATION

With a suitable model available for the parametric variation study, some criterion was sought by which to judge various designs. To this end it was proposed that the thermocouple bead responds to the average temperature of the flow within the shield, "the cavity averaged temperature" determined by evaluating the energy flow into the shield over a complete cycle as follows:-

$$\bar{T}_{RK} = \frac{\int_t^{t+\tau} \dot{m}T \, dt}{\int_t^{t+\tau} \dot{m} \, dt} \tag{3}$$

where $\dot{m}$ is the flow per unit area entering the cavity, Figure 9.

Now the true mass averaged temperature of the flow (equation 1) is:-

$$\bar{T}_{ma} = \frac{\int_t^{t+\tau} \dot{M}T \, dt}{\int_t^{t+\tau} \dot{M} \, dt} \tag{1}$$

and $\dot{M}$ is the external mass flow per unit area. Therefore, it is reasonable to expect the Reverse Kiel probe to provide the correct result only if $\dot{m}$ is proportional to $\dot{M}$.

That is, the correct result can be expected only if the mass flow entering the cavity is at all times proportional to the external velocity and the cosine of its incidence onto the probe, (for constant density flows).

i.e. $\dot{m} = K C \cos \theta$ (where K is a constant)

A shield design which satisfies Equation (4), over a given range of flows, will input the correctly weighted mass flux into the shield. Thus the cavity averaged temperature will equal the mass averaged temperature over the given range of flows. This criterion can be used to evaluate Reverse-Kiel probe designs.

The main PACE solver was specified to include a calculation, based on flow information from the last iteration step, of the convected inlet mass flux through the inlet orifice of the shield being modelled. The parametric design variation encompassed 14 configurations and for each simulated probe geometry it was considered that a minimum of 3 flow angles (0°, 30° and 60°) were required to establish how close the particular design was to satisfying Equation (4). A constant value of absolute velocity of 250 m/s was chosen for the three flow angles as this required a variation in the axial velocity component, and therefore mass flow, as the flow angle varied.

A selection of results from PACE of the parametric design study are shown in Figure 10. If the characteristics of a probe are to satisfy Equation (4), then the non-dimensional inlet mass flow function will be seen to vary with the cosine of the incident flow angle. Hence Figure 10 includes a curve representing this ideal characteristic as a reference. Figure 10(a) indicates the effect on probe performance of varying the inlet hole diameter for an otherwise datum probe design. Results are shown for inlet diameters of 0.2 mm (datum), 0.3 mm, 0.5 mm, 0.9 mm and 1.5 mm. The 0.2 mm diameter inlet represents the practical minimum for an aerodynamic probe not to suffer from "clogging" with airborne contaminants. The datum probe is seen to have the worst response of the probes with the 0.5 mm and 0.9 mm inlet diameters very closely following the desired cosine response. At 60° incidence, the predicted order of inlet diameter improving probe response is 0.2 mm, 0.3 mm, 1.5 mm, 0.9 mm and 0.5. Figure 10(b) indicates the effect on probe performance of varying the inlet hole diameter for a probe with a shield length of 2.5 mm. Results are shown for inlet diameters of 0.2 mm (datum), 0.5 mm and 0.9 mm. Comparing Figures 10(a) and (b) it is clear that reducing the shield length for a given inlet diameter increases the angular sensitivity of the resultant probe. The results shown indicate that the short probes with the 0.5 mm and 0.9 mm inlet holes are actually over-sensitive to incidence angle relative to the desired cosine response.

It was recognised that a more complete analysis of total convected mass flux would be achieved by considering the flow at the exit of the probe, across the outlet hole diameter. However preliminary analysis had shown that the inlet mass flux greatly exceeded the reverse mass flux at the probe exit for all but the extreme flow angles ie. greater than 60°. Also the magnitude of the reverse mass flux relative to the inlet mass flux reduced with increasing inlet diameter (the direction of the parametric variation).

In conclusion to the parametric design variation and subsequent analysis based on the cavity averaged temperature theory, PACE predictions (tempered by practicalities) included a marginal improvement in the datum probe response when fitted with a thinner inlet plate or a shorter overall shield length. No advantage was predicted for reducing the exit hole diameter and the level of turbulence specified for the PACE solutions was found to have a minimal effect on the predicted results. However the main design feature governing probe response was predicted to be the inlet hole diameter with the optimum inlet hole diameter, for an otherwise datum probe, being 0.5 mm or 0.9 mm (the original Cranfield study did not include any probes of a greater inlet diameter than 0.3 mm. Probes with inlet hole diameters of 0.5 mm or 0.9 mm coupled with short (2.5 mm) length shields were predicted to be overly sensititve to incidence. As a result of these numerical predictions, test thermocouple probes were manufactured as a modular kit for application on the Blade-Wake rig to examine both their response and the cavity averaged temperature theory predictions and subsequently to select the optimum probe to be built as a rig standard instrument.

5. BLADE-WAKE RIG TESTING

As a result of the development of the slow response, mass averaging, Reverse-Kiel temperature probe, test thermocouple probes were manufactured and applied to the Blade-Wake rig. The Blade-Wake rig, shown in Figure 11 and fully described in Reference 3, was a free running axial flow air turbine with 37 blades (25.4 mm axial chord, 12.7 mm height) running at a design speed of 8,000 r.p.m. To generate a wide, energetic wake the turbine blade trailing edges were blunt and occupied some 33% of the blade pitch. The blade loading was light, comprising only of windage and bearing losses. Fourteen configurations (see Table 1) of Reverse-Kiel temperature probe were applied to the Blade-Wake rig at 0.125, 0.25, 0.375, 0.5, 0.75, 1.0, 2.0 and 3.0 rotor axial chord lengths downstream of the rotor (trailing edge). At each axial position the test probe temperature relative to a downstream reference probe temperature (the "error") was noted. In recognition that the reference probe and the test probes will not necessarily have the same recovery characteristics, the collated results are corrected by taking the "error" at any given axial location and deducting from it the "error" at a distance of 5 axial chords downstream. In this way the reference probe characteristics are eliminated from the results, with the test probe performance being compared to itself at a far downstream position.

With all probes tested, the greatest errors were seen close to rotor trailing edge and these reduced to zero (ie. probe temperature equal to flow mass meaned temperature) as the flow became more ordered with advancing distance from the rotor. It was found that the error associated with probes having the datum inlet hole diameter (0.2 mm) was independent of inlet hole length (over the tested 4:1 range). It was also noted that the general trend was that reducing the shield length marginally improved probe performance. The main design feature which controlled probe performance was the inlet hole diameter. Results are shown in Figure 12(a) which includes results from the bare wire thermocouple probe (H). It is noteworthy that the earlier work had included a full flow survey at three radial heights with hot wire anemometry. Significant radial variations were noted at rotor exit and the characteristic of certain probes at certain axial locations indicated a temperature less than the apparent mass meaned temperature which was attributed to radial fluid migration. Of the probes tested during this study, 1F had the largest inlet diameter, which samples some 12% (in the radial direction) of the rig annulus, and was therefore most susceptible to radial fluid migration confusing equi-radial flow analysis. Figure 12(b) shows the performance of the short length shield probes of differing inlet hole diameters. The bare wire thermocouple probe was again included as a reference. At 0.125, 0.25 and 0.375 rotor axial chord, probe 2D (0.9 mm diameter inlet hole) was consistently more accurate than the other probes. From 0.5 rotor axial chord onwards there was again little difference between the probes. Also, as before, the larger inlet diameter probes, tend to indicate a slightly lower than correct mass averaged temperature until beyond 0.5 rotor axial chord.

The probe configurations tested as 1E and 2E require some explanation. Having proposed the Cavity Averaged Temperature theory as the mechanism for the success of the Reverse-Kiel class of probe, it is apparent that the convected inlet mass flux, rather than any consideration of an internal jet flow, is the key feature to be be considered. A more uniform inlet distribution of convected mass flux might be achieved if more than one inlet orifice was employed. The modelling limitations of PACE prohibited investigation of multi-hole inlet plates, but it was a simple matter to make up probes 1E and 2E with a central 0.2 mm diameter hole and 8 x 0.2 mm diameter holes equi-spaced on a pitch circle diameter of 1 mm. Based on inlet areas, this is equivalent to a single central 0.6 mm diameter inlet hole. The performance of the standard length probe 1E is shown in Figure 12(c), as the probe indicated error versus axial downstream distance. The responses of probes 1D (0.9 mm diameter) and 1G (0.5 mm diameter) are also included. The cumulative inlet area of the E-series probe response is seen to lie between the G-series and D-series probes. It appears that the response of the probe is closely governed by the inlet areas and that the form of that area (single or multi-hole) is not critical to the performance of the probe. This, of course, is not inconsistent with the Cavity Averaged Temperature theory.

The probe which indicated the least error on the Blade-Wake rig was 2D. At 0.25 and 0.375 rotor axial chord the probe error was 0.5 K and 0.2 K respectively. At these same positions the datum Reverse-Kiel probe, 1A, indicated errors of 1.6 K and 0.9 K respectively. The bare bead (unshielded) thermocouple, probe H, was seen to indicate 3 K and 1.2 K error at these distances. Hence probe 2D was demonstrated to reduce the error by a factor of six over a bare bead thermocouple and reduce the error by a factor of three to four over the datum Reverse-Kiel probe. Therefore probe 2D was selected as the basis for the rig standard Reverse-Kiel probe and manufactured accordingly.

A comment on the predictive accuracies of PACE is also relevant here. Using the Cavity Averaged Temperature theory in conjunction with PACE it was predicted that

(a) a marginal improvement in probe response could be achieved by shortening the probe shield,

(b) a marginal improvement could also be achieved by using a thinner inlet plate and

(c) a major improvement could be made by using a 0.5 mm or 0.9 mm diameter inlet hole (the predicted order of increasing probe accuracy being 0.2 mm, 0.3 mm, 1.5 mm, 0.9 mm, 0.5 mm).

As a result of testing on the Blade-Wake rig it was found that

i) a marginal improvement in probe response was achieved by shortening the probe shield,

ii) no discernible difference was observed in varying the inlet plate thickness and

iii) a major improvement was made by using an 0.9 mm diameter inlet hole (the measured order of increasing probe accuracy being 0.2mm, 0.5 mm, 1.5 mm, 0.9 mm).

It is concluded that the analysis of PACE data using the Cavity Averaged Temperature theory has been very successful in identifying the changes in probe design necessary to optimise probe performance.

6. AERODYNAMIC CALIBRATION DATA

An aerodynamic recovery factor calibration was carried out on the rig standard Reverse-Kiel probe in a wind tunnel of known flow.

$$\text{Recovery Factor, } Rf = \frac{Tp - Ts}{Tt - Ts} \qquad (5)$$

It was found that the recovery factor for this probe tended to be low (~ 0.75) and its yaw sensitivity influenced by the precise position of the bead within the sensor. This provides users of the probe with a problem at high Mach numbers where the recovery correction can be significant.

7. FAN AND COMPRESSOR RIG TESTING

To date only limited testing has been undertaken but where it has been applied, integrated mass averaged temperatures derived using the Reverse Kiel Probe have agreed with torquemeter readings better than those obtained using conventional combination probes. Of the very few results, however, some have been confusing and have not been as encouraging as the Blade Wake measurements but further testing is to be undertaken shortly.

8. CONCLUSIONS AND RECOMMENDATIONS

A slow response temperature sensor has been combined with a judicious shield design in an attempt to permit the probe to respond correctly in a variety of unsteady turbomachinery flows ie. to indicate the correct mass-weighted temperature of flows.

8.1 The mass-weighted Reverse-Kiel temperature probe has been developed using ideas from flow fields in similar geometries, flow visualisation studies (which included the development of the new technique of hot wire visualisation) and computational fluid dynamics modelling. A parametric variation on the probe design was assessed using the proposed cavity averaged temperature theory which considered the inlet mass flux characteristics associated with each design. The predicted best designs were manufactured and tested on the purpose built Blade-Wake rig.

8.2 The testing on the Blade-Wake rig largely confirmed the numerical predictions and the performance of the optimum probe was quantified. At close to rotor trailing edge positions (ie. 0.25 to 0.375 rotor axial chord downstream) the optimum probe was demonstrated to reduce the error by a factor of six over a bare bead thermocouple and reduce the error by a factor of three to four over the datum Reverse-Kiel probe. The optimum probe was therefore selected as the basis for a rig standard Reverse-Kiel probe.

8.3 It is inconvenient, and potentially a source of error, for the Reverse-Kiel temperature probe recovery characteristics to be so low.

In conclusion, it is felt that a significant advance has been achieved towards the goal of measuring interstage temperature using a comparatively 'low technology' probe and its wider use in research fan and compressor rigs is anticipated.

REFERENCES

1. Fleegar, D.W. et al.   Aerodynamic Measurements in Turbomachines.
                             AGARD-AG-207, Section 2, 1975

2. Allan, J.   Instrumentation Problems in Small Gas Turbine Engines.
                             AIAA-8301293.

3. Agnew, B. et al.   An Investigation of the Response of Temperature Sensing Probes to an
                             Unsteady Flow Field. ASME
                             85-GT-223.

4. Bryer D.W. et al.   Pressure Probe Methods for Determining Wind Speed and Flow Direction.
                             National Physical Laboratory, HMSO 1971.

5. Bradbury, L.J.S.   Simple Expressions for the Spread of Turbulent Jets. Aero. Quart. Vol.
                             18, May 1967, pp 132-142.

6. Linke, W.   Aspects of Jet Ventilation.
                             Kaltetechnik-Klimatisierung, Vol. 18, No. 3, 1966, pp 122-126.

7. Rhode, D.L.   Mean Flowfield in Axisymmetric Combustor Geometries with Swirl. AIAA
                             Journal Vol. 21, No. 4, 1983 pp 593-600.

8. Merzkirch, W.   Flow Visualisation. Academic Press, Inc. 1974.

9. Mueller, T.J.   On the Historical Development of Apparatus and Techniques for Smoke
                              Visualisation of Subsonic and Supersonic Flows. AIAA 80-0420, 1980.

10. Batill, S.M. et al.   Visualisation of Transition in the Flow over an Airfoil Using the
                              Smoke-Wire Technique. AIAA 80-0421R, 1980.

11. Sieverding, C.H. et al.   The Use of Coloured Smoke to Visualise Secondary Flows in a Turbine -
                              Blade Cascade. J. Fluid Mech. (1983), vol 134 pp 85-89.

12. Patankar, S.V. et al.   A Calculation Procedure for Heat, Mass and Momentum Transfer in
                              Three-Dimensional Parabolic Flows. Int. J. Heat Mass Transfer, Vol. 15 pp
                              1787 - 1806, 1972.

13. Jones, W.P. et al.   The Prediction of Laminarisation with a Two-Equation Model of Turbulence.
                              Int. J. Heat Mass Transfer, vol. 15, pp 301-315, 1972.

Probe Designation	Inlet Plate		Shield Length in mm
	Hole Diameter in mm	Hole Length in mm	
1A	0.2	0.25	3.4
2A	0.2	0.25	2.25
1B	0.2	0.125	3.4
2B	0.2	0.125	2.25
1C	0.2	0.5	3.4
2C	0.2	0.5	2.25
1D	0.9	0.25	3.4
2D	0.9	0.25	2.25
1E *	9 x 0.2	0.25	3.4
2E *	9 x 0.2	0.25	2.25
1F	1.5	-	3.4
2F	1.5	-	2.25
1G	0.5	0.25	3.4
2G	0.5	0.25	2.25

* 8 holes were drilled of 0.2mm diameter on a PCD of 1mm, in
addition to a central hole of 0.2mm diameter.

A bare wire thermocouple (unshielded) was also tested and is
designated Probe H.

TABLE 1   DESIGNATION OF THERMOCOUPLE PROBE CONFIGURATIONS
          AS TESTED ON THE BLADE-WAKE RIG

AIR FILTERS

SMOOTHING
BAFFLES

TO ATMOSPHERE
(VIA SILENCER)

INLET THROTTLE

SURGE TANK

OUTLET
THROTTLE

TEST
UNIT

OUTLET
COLLECTOR

PRIME
MOVER

AIRMETER

GEARBOX

TORQUEMETER

DISTRIBUTOR
PIPE

RETURN BLEED PIPE

METERING ORIFICE

CONTROL THROTTLE
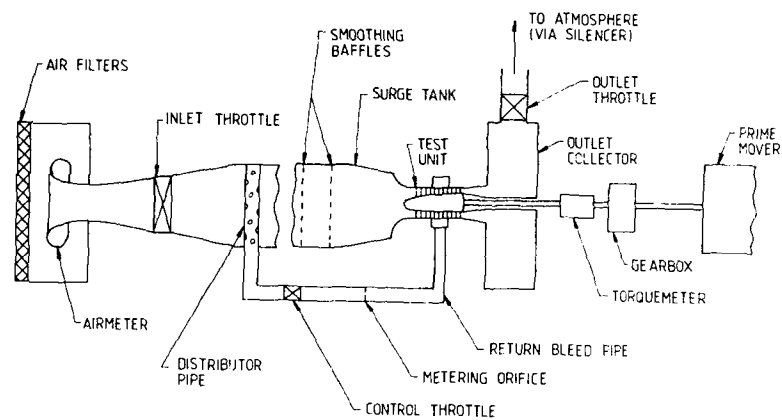
FIGURE 1   SCHEMATIC OF TYPICAL COMPRESSOR TEST FACILITY

SCC APRIL 1989

ROTOR VELOCITY , U

RELATIVE
VELOCITY , Vr

ABSOLUTE
WAKE
VELOCITY

WAKE AXIAL VELOCITY

FREESTREAM AXIAL VELOCITY

ABSOLUTE
FREESTREAM
VELOCITY

Vr

U
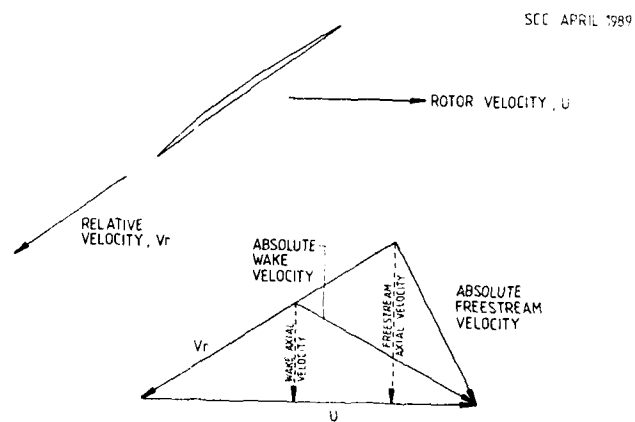
FIGURE 2   TYPICAL FAN EXIT VELOCITY TRIANGLE (TIP)

VIEW ON FRONT

SECTION THRU' PROBE

VIEW ON REAR
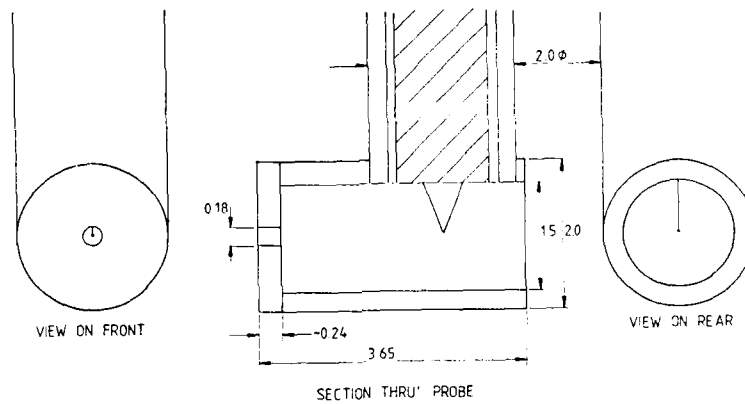
FIGURE 3. DESIGN DETAILS OF THE DATUM REVERSE - KIEL PROBE
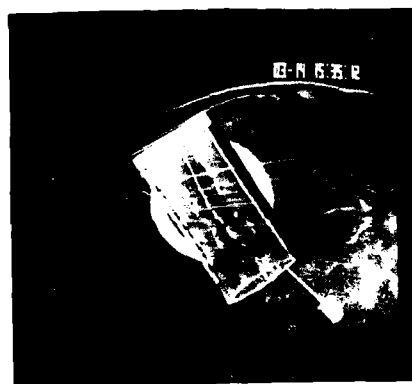
Figure 4   Smoke Visualisation of Flow in the model
at 60° Incidence (Loughborough Facility)
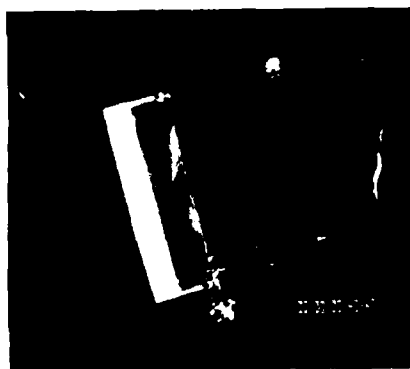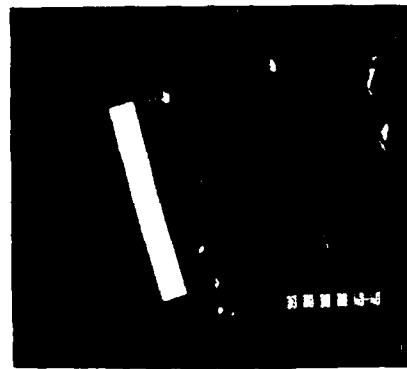
(a)   (b)

Figure 5   Smoke wire (a) and Hot Wire (b) Visualisation
of Flow in the model at 15° Incidence (Hucknall
Facility)

(a)   (b)

Figure 6   Smoke Wire (a) and Hot Wire (b) Visualisation
            of Flow in the model at 30° Incidence (Hucknall
            Facility)

Figure 8   PACE model of the Flow within the Probe
            (Incidence 45°)

Figure 7   PACE model of the flow in the Far Field
            (Incidence 45°)
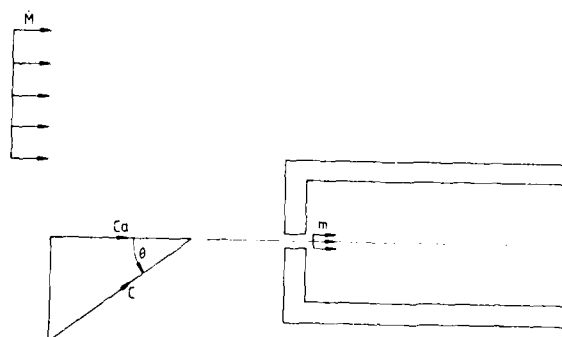
FIGURE 9   DIAGRAMATIC REPRESENTATION OF REVERSE-KIEL PROBE
            IN A FLOW
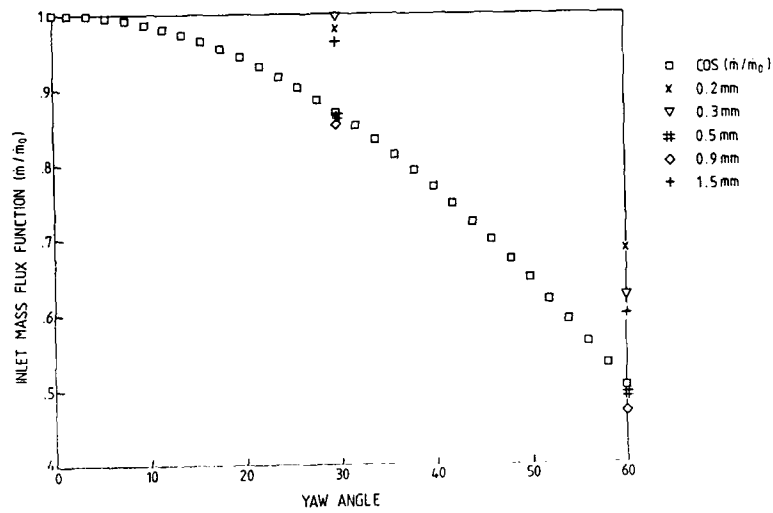
FIGURE 10a. VARIATION IN PROBE INLET MASS FLUX FUNCTION
DIFFERENT DIAMETER INLET ORIFII (DATUM PROBE)
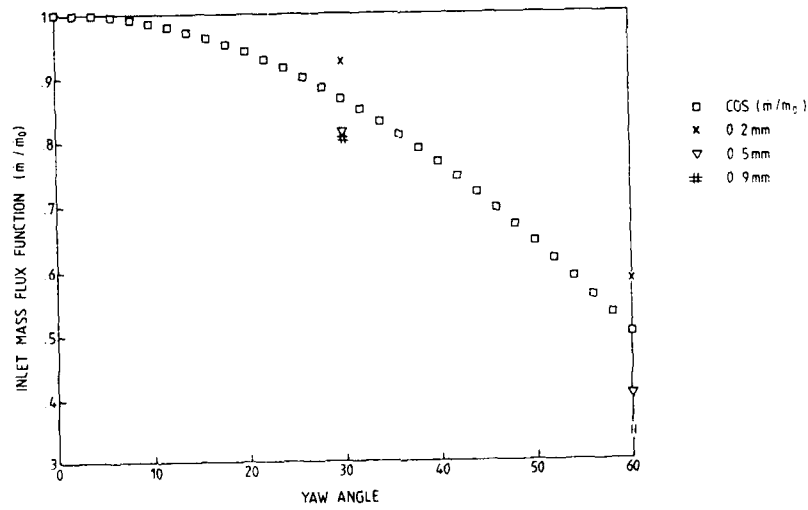
FIGURE 10b VARIATION IN PROBE INLET MASS FLUX FUNCTION
DIFFERENT DIAMETER INLET ORIFII (SHORT PROBE)
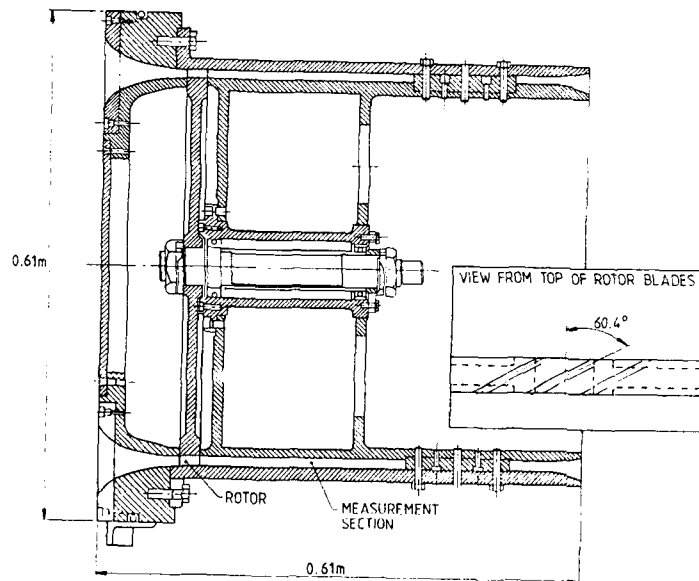
FIGURE 11 BLADE WAKE RIG
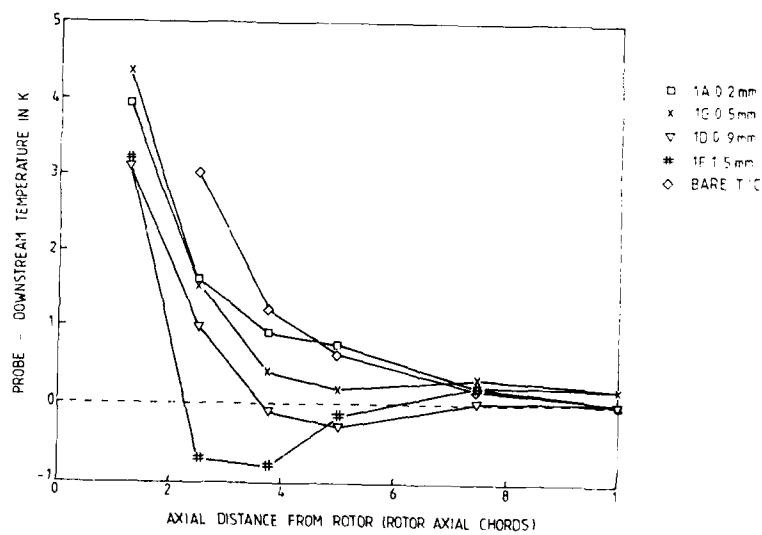
FIGURE 12(a) PROBE ERROR ON BLADE - WAKE RIG
DIFFERENT DIAMETER INLET ORIFII (DATUM PROBE)

13-14
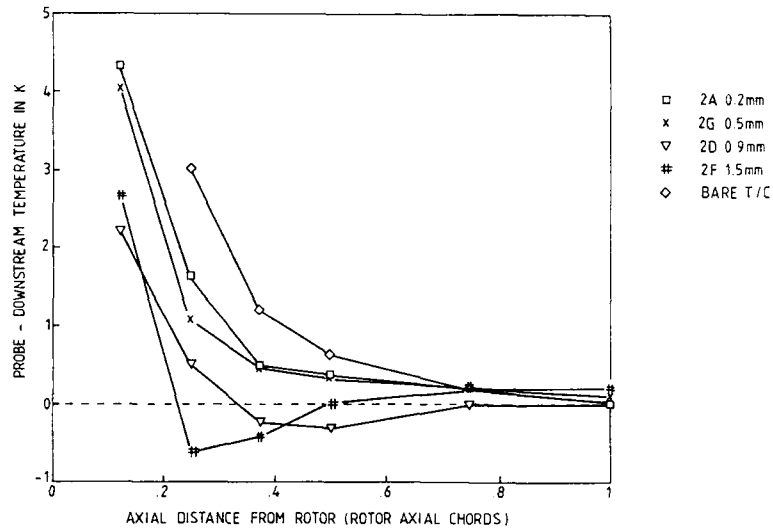
FIGURE 12(b) PROBE ERROR ON BLADE - WAKE RIG
DIFFERENT DIAMETER INLET ORIFII (SHORT PROBE)
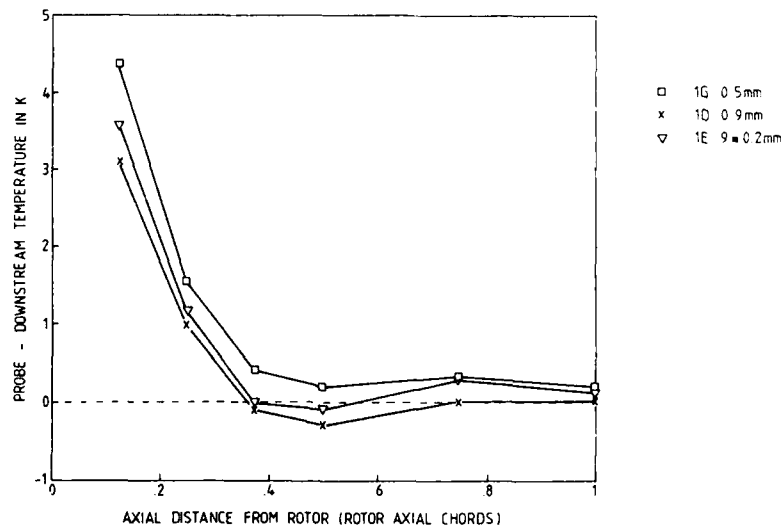
FIGURE 12(c) PROBE ERROR ON BLADE - WAKE RIG
DIFFERENT DIAMETER INLET ORIFII (DATUM PROBE)

BLADE ROW INTERACTION EFFECTS ON COMPRESSOR MEASUREMENTS

by
A.H. Epstein
M.B. Giles
T. Shang
Gas Turbine Laboratory
Massachusetts Institute of Technology
Cambridge, MA 02139 USA
and
A.K. Sehra
Textron Lycoming
Stratford, CT 06497 USA

SUMMARY

The influence of a downstream stator row on the measurement of compressor rotor performance has been examined using a CFD code backed by laser anemometry data on a transonic fan stage. The upstream potential influence of the stator causes unsteady circulation about the rotor blades which is a function of the rotor circumferential position. This, in turn, results in a non-uniform circumferential pattern of time averaged temperature and pressure in the stationary frame. An analytical theory relating the temperature and pressure variations to the circulation perturbation is presented and shown to give good agreement with the numerical calculations. The results of a parametric study show that the magnitude of this effect is a strong function of rotor-stator blade row spacing and relative blade counts. The effects range from negligible for large spacings typical of high bypass ratio fans to several percent of the stage pressure and temperature rise for closely spaced blade rows typical of high compressors. Because the temperature and pressure perturbations are in spatial phase,.the net effect on measured rotor efficiency is negligible so long as the pressure and temperature measurements are made in the same location relative to the stators. If they are not, errors of $\pm 1.5\%$ can result. The effects of axial position and stator loading are shown to be relatively small.

INTRODUCTION

Aerodynamic performance measurements are the most basic of turbomachinery tools, required for research, design verification, and development. By performance we refer to measurements of average temperature and pressure made of the machine inflow and outflow as well as between the blade rows, used to deduce the turbomachine work and efficiency. It has long been recognized that the interpretation of these measurements is far from straightforward.

Because these turbomachine flow fields are spatially nonuniform and highly unsteady, questions concerned with averaging have received considerable attention. These concerns have started at the probe inlet (how do conventional pitot type probes behave in unsteady flow fields [1]) and continue through to measurement interpretation (which averaging technique -- time, mass, stream thrust, etc. -- most closely represents the thermodynamic quantities of interest [2]). Here, we are concerned with questions of spatial uniformity and spatial averaging.

The best agreements between aerodynamic and shaft torque-based efficiency measurements are generally found when the aerodynamic measurements are made far downstream of the turbomachine in a region of uniform flow. In this case, the fluid mechanics of mixing have homogenized the flow, effectively spatially averaging the temperature and pressure (and incurring a mixing loss in the process, of course). Often, such preferred probe placement is not possible. The probes may be embedded within the blade rows and often, to reduce blockage, within the stators themselves. This is especially true in cases in which the rotor performance is required, in multistage machines when individual stage behavior must be measured, and in small machines in which instrumentation placement is extremely constrained by blockage and access problems.

Any stationary intra-turbomachine instrumentation placement is dependent on the presumption that the flow is uniform in the pitchwise direction to the degree that it is adequately sampled by relatively few rakes mounted about the circumference. For stator leading edge mounted probes in compressors, for example, the flow is presumed to be completely azimuthally uniform since only one pitchwise position relative to the stators (e.g. the stator leading edge) is sampled. We know that the flow is not uniform in the case of multistage machines in which upstream stators clearly introduce azimuthal variation. Circumferential traversing of probes and rakes solves this problem but is often not done (especially in compressors) due to access, blockage, or cost considerations. The goal of the work described herein was to examine the importance of probe placement to the measurement of aerodynamic performance in high speed compressors, and then generate guidelines for probe placement and/or data "correction". This is very much work in progress but we feel that the results to date are of general interest.

The methodology adopted was to employ a multiblade row, unsteady two-dimensional computational fluid mechanics (CFD) calculation as the basic tool and compare measurements at various locations as calculated by the code with the true mass averaged performance of the compressor. The basic fidelity of the calculation was assessed by comparison of the CFD results with laser anemometer measurements where available. The following sections describe the calculational procedure, the compressor examined, the code verification, the calculated spatial variation of aerodynamic performance, a discussion of fluid mechanic mechanisms generating the variations, and the implications and recommendations for the accuracy of performance measurements.

CALCULATIONAL PROCEDURE

The basic tool for this study was a two-dimensional, multiblade row, unsteady, computational fluid mechanics code known as UNSFLO. UNSFLO uses Ni's explicit Lax-Wendroff method to solve the unsteady Euler equations on an unstructured grid of quadrilateral cells. A time-inclined computation plane facilitates the calculation of stages with unequal rotor-stator numbers, greatly reducing the computation time required. For the calculations presented here, approximately 16,000 grid points were used. The computations were done for either one rotor and one stator passage or two rotor and three stator passages, depending on the relative blade row count. The time tilting then serves to adjust the calculation to the desired blade row pitch ratio. More details on the solution method can be found in [3] and [4].

Approximately 10,000 iterations were required for an initial steady state solution with approximately an equal number required to achieve unsteady periodicity (this was approximately 30 blade passing periods). A typical solution time was approximately 10 hours on a three processor Alliant FX/8 computer, or 6 hours on a Stellar, or 90 hours on a DEC μVAX-III (all three machines were used at different times).

The work described herein uses an inviscid version of the code. Further calculations using the viscous version are underway and will be reported at a later date. A specific advantage of UNSFLO for this investigation is that it permits essentially arbitrary rotor-stator pitches (blade counts) while incurring little computational overhead. This greatly facilitates parametric examination of the importance of stage design parameters on measurement accuracy.

COMPRESSOR DESCRIPTION

The compressor chosen for this study is a 1.68 pressure ratio, low aspect ratio, single-stage transonic fan stage designed at the NASA Lewis Research Center in the mid 1970's [5]. Known as stage 67, this 0.5 meter diameter machine was selected primarily because of the large amount of experimental data -- including laser anemometry [6], [7], and time resolved intrastage flow measurements [8] -- which are in the public domain. Also, there is a considerable number of 2-D, 3-D, inviscid, and viscous calculations published on this geometry [9], [10]. The flow path is shown in Figure 1. Calculations were done only for the 2-D streamsurface indicated, which is slightly outboard of the sonic radius. This position was selected because of the availability of both laser anemometer and high response probe data at that location as well as a detailed, unsteady 2-D viscous solution [10].
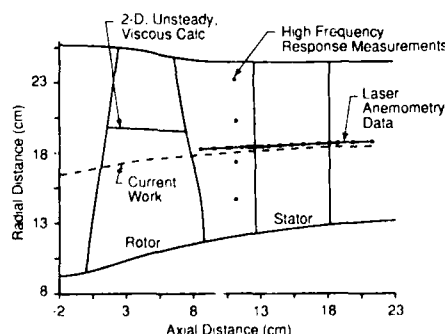

Fig. 1: Flow path of NASA LeRC stage 67 showing streamline used in this study
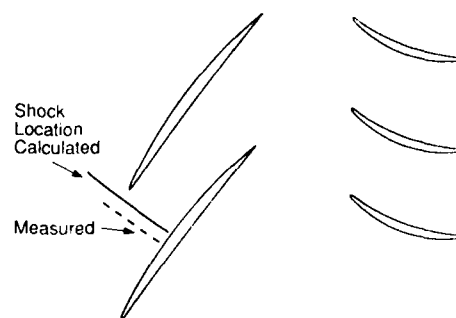

Fig. 2: Comparison of measured and calculated shock positions

VERIFICATION OF CFD CALCULATION

Although UNSFLO had been shown to give quite good results with turbines, it had not been previously used for high speed compressors. Therefore, it was thought important to establish the fidelity of the calculation by comparison with data. Also, the influence of the inviscid flow assumption had to be assessed. Table 1 compares the calculated and measured values of specific flow (mass flow per unit area), and the stage pressure and temperature ratio at the stage exit along the selected streamline at the design point conditions. These are quite close for an inviscid calculation. At this condition, there is a small discrepancy between the axial location of the calculated and measured (by laser anemometry [6]) shock wave positions shown in Figure 2. This can be explained by a small difference in rotor blade incidence angle and the absence of boundary layer blockage in a design with small choke margin.

TABLE 1
Comparison of Calculated and Measured Performance
Along a 2-D Streamtube Near Midspan

	CFD	Measured
Mass Flow (ρU)	280.1	276.8
P_{t3}/P_{t0}	1.609	1.634
T_{t3}/T_{t0}	1.153	1.160

The circumferential variation in the time averaged total temperature as calculated with the Euler turbine equation from the circumferential velocity change at an axial station between the rotor and stator is shown in Figure 3 for both the laser anemometer data and the CFD calculation. Although the absolute levels differ by a small amount, the level of circumferential variation in temperature is quite well predicted. The experimental and predicted pitchwise variation in axial velocity perturbation also agree well (Fig. 4).

We conclude from comparisons including those above that the inviscid CFD calculation is capturing the essential features of the flow field, giving an adequate picture of the spatial distribution of the compressor flow.
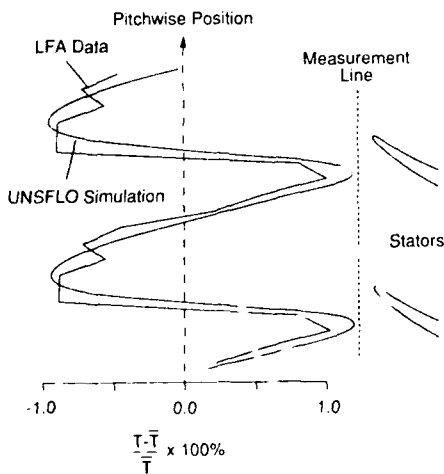
Fig. 3: Comparison of measured and calculated time-averaged temperature estimated with Euler's turbine equation from the tangential velocity, as a function of pitchwise location. T is the local temperature, $\bar{T}$ the pitchwise averaged temperature.
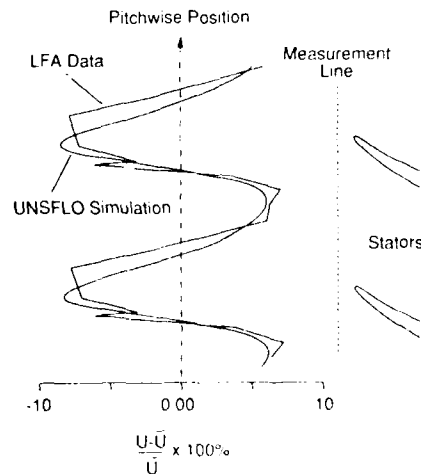
Fig. 4: As in Fig. 3, but comparison of the time averaged axial velocity distribution: U is the local axial velocity; $\bar{U}$ the pitchwise averaged velocity.
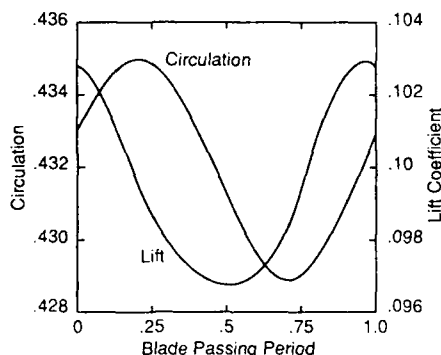
Fig. 5: Time variation of rotor blade circulation
and lift as a function of blade passing period
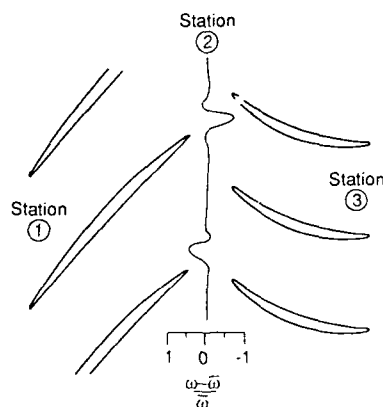(time required to traverse one stator pitch)

Fig. 6: Pitchwise vorticity distribution at one instant
in time illustrating the magnitude of the shed
vorticity perturbation. ω, compared to the
time averaged vorticity, ω

CALCULATIONAL RESULTS

The Euler temperature measurements and calculations of Figure 3 show a significant variation in the flowfield temperature with pitchwise position, about $\pm1\%$ ($6°K$). Before looking in more detail at probe placement effects, let us try to understand why the flowfield in the compressor behaves in this manner -- what causes flow variations on the order of the stator spacing? An obvious answer is the upstream influence of the potential field of the stator on the rotor aerodynamics. Indeed, this can be seen in the variation of rotor blade circulation and lift with pitchwise position (Figure 5). The change in circulation results in the shedding of vorticity downstream of the rotor (Figure 6). In addition, the change in lift and back pressure moves the passage shock wave, varying its strength and thus the entropy it produces. This is the only explicit source of loss in this inviscid calculation. Since the work done by the rotor blade varies with position, the temperature and pressure fields will vary as well.

VORTEX SHEET ANALYSIS OF THE TIME AVERAGED SPATIAL FLOW VARIATION

Given the variation in rotor blade circulation induced by the potential field of the downstream stators, we can calculate the spatial variation in the time averaged flow field analytically as well as numerically. Horlock [11] calculated the stagnation pressure variation due to the circulation change for an incompressible flow using a continuous vortex sheet model, assuming the distribution to be sinusoidal (i.e. considering only the first spatial harmonic). Here, we attack the problem somewhat differently, permitting arbitrary spatial variation and generalizing the analysis to enthalpy variation, so that compressible flow may be analyzed.

In the absolute, stator frame of reference, the flow can be modelled as a sequence of propagating vortex sheets passing through an otherwise irrotational flow field. Since the unsteady circulation around the rotor blades is phase-locked to the stator motion relative to the rotors, in the absolute frame the flow field is periodic in time, with the period being equal to the rotor blade passing period. Thus, at a fixed point in the absolute frame, the vortex sheets which pass by always have the same strength. It is this fact which causes the time-averaged stagnation enthalpy to be spatially non-uniform.

The starting point for the analysis is Crocco's theorem in the absolute (stator) frame of reference:

$$T \nabla S + \vec{u} \times \vec{\omega} = \nabla H_0 + \frac{\partial \vec{u}}{\partial t}$$
(1)

with T, the temperature; S, the enthalpy; u, the velocity vector; ω the vorticity; and H_0, the stagnation enthalpy.

Assuming that the flow is isentropic and irrotational, <u>except</u> for the passing unsteady vortex sheets shed by the rotors due to their varying circulation, time-averaging gives

$$\nabla \overline{H_0} = \overline{\vec{u} \times \vec{\omega}} \tag{2}$$

where the sole contribution to the time average $\overline{\vec{u} \times \vec{\omega}}$ comes from the passing vortex sheets.

Defining $\vec{u}_\omega(x,y)$ to be the local velocity $\vec{u}(x,y,t)$ at the time t at which the vortex sheet passes the point (x,y), y being the tangential direction, it follows that

$$\vec{u}_\omega \cdot \nabla \overline{H_0} = 0 \tag{3}$$

and hence $\overline{H_0}$ is constant along pathlines generated by vortex sheet elements.

Given this result for the "convection" of $\overline{H_0}$, it is now sufficient to find the variation of $\overline{H_0}$ in the circumferential y-direction, at the x-location corresponding to the rotor's trailing edge.

With a suitable choice of origin, the position of the trailing edge of one particular rotor blade is given by $(x,y) = (0,Vt)$, where V is the rotor wheel speed. Near the trailing edge, the vorticity distribution is given by a delta function in a coordinate system which is rotated to be normal to the vortex sheet.

$$\omega(x,y,t) = -\gamma \delta \left((y-Vt)\cos \alpha - x \sin \alpha\right) \tag{4}$$

α is the rotor-relative flow angle at the trailing edge, and γ is the strength of the vortex sheet shed at the trailing edge of the rotor which varies as the rotor moves, and so is a function of the position of the trailing edge. Kelvin's theorem (which is valid for an isentropic compressible fluid) gives the following relationship between $\gamma(y)$ and $\Gamma(y)$, the circulation around the rotor which is also a function of y, the position of the trailing edge.

$$U_\gamma = -\frac{d\Gamma}{dt} = -V \frac{d\Gamma}{dy} \tag{5}$$

In the above equation, U is the magnitude of the rotor-relative velocity at the trailing edge, averaged over the two sides of the trailing edge. With these pieces, and defining τ to be the blade passing period, it is now possible to calculate the variation of $\overline{H_0}$ in the y-direction.

$$\begin{aligned}
\frac{\partial \overline{H_0}}{\partial y} &= -\overline{u\omega} \\[6pt]
&= -U \cos \alpha \frac{1}{\tau} \int_0^\tau \omega \, dt \\[6pt]
&= -\frac{U\gamma}{\tau V} \\[6pt]
&= -\frac{1}{\tau} \frac{d\Gamma}{dy}
\end{aligned} \tag{6}$$

Integrating this equation produces the final, simple relationship between the perturbation in the time-averaged stagnation enthalpy H_0' and the perturbation in the circulation Γ'.

$$H_0' = \frac{\Gamma'}{\tau} \tag{7}$$

This analysis, of course, does not tell us what the circulation perturbation is; that would require considerably more work.

We can, however, take the circulation perturbation from the numerical analysis (Fig. 5), and use that to predict the spatial variation in stagnation enthalpy. This is compared to the numerically calculated variation and to that predicted using Horlock's method [11] in Figure 7. The close agreement among the three is primarily a consistency check between the analytical and numerical methods, lending credence to both. It also shows that, at least for this geometry, the spatial variation in circulation is essentially sinusoidal and that those phenomena modelled numerically but not analytically -- shock wave effects, for example -- are not important here.
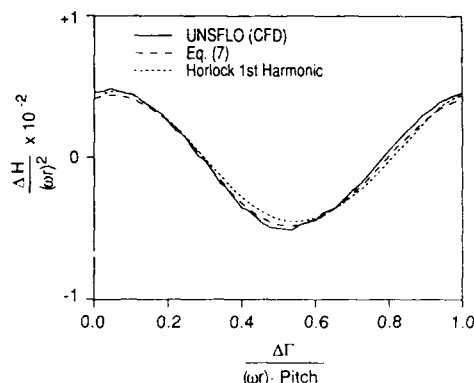
Fig. 7: Pitchwise enthalpy distribution as calculated by the CFD code UNSFLO, Eq. (7), and using Horlock's methods [11]

PARAMETRIC EXAMINATION OF THE INFLUENCE OF DESIGN VARIABLES

If the pitchwise flowfield variation is primarily due to the potential field of the stators, we would expect that the magnitude of this effect to vary with stage design parameters -- in particular, with the axial distance between the rotor and stator (the gap) and the relative spacing between adjacent stator blades compared to the spacing between rotor blades (the pitch ratio). The rotor-stator gap should be important since the potential influence of the stators should die out exponentially upstream of the stators. Thus, increasing the gap should decrease the pitchwise flowfield variations. Similarly, increasing the pitch ratio (the number of stator blades relative to the number of rotor blades) should decrease the pitchwise flow variation since in the limit of an infinite number of stators, the time averaged pitchwise flowfield must be uniform.

We infer from the above that it is important to parametrically examine the influence of these effects, especially since, depending upon the application, there are very large variations in rotor-stator gap and pitch ratios. Gaps can vary from as low as 10% of rotor chord in high compressors to 400% in high bypass ratio fans. Also, the gaps are, in general, not fixed but can vary with radius due to blade sweep. Similarly, rotor-stator pitch ratios can vary from 2 to 0.1 (a few large struts about the circumference). The stage studied has a design gap of 0.78 (axial distance between rotor trailing edge and the stator leading edge divided by the rotor axial chord) and a pitch ratio of 1.45 (rotor pitch divided by stator pitch). The relatively large gap had been
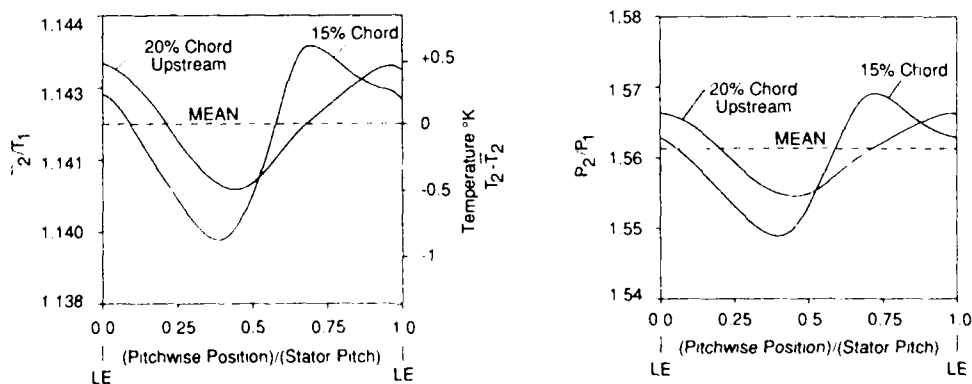

Fig. 8: Pitchwise distribution of time averaged stage temperature and pressure ratio at two axial locations (as percentage of stator axial chord). The rotor-stator gap is 0.2 and the rotor-stator pitch ratio is 1.45.

selected to facilitate detailed intra-stage measurements. Because the UNSFLO CFD code readily accepts essentially arbitrary pitch ratios, it was straightforward to parametrically vary the gap and pitch ratio of the calculations (the stator pitch was varied, the rotor pitch held constant -- essentially stator blades were added or deleted).

The calculated pitchwise variations in the time averaged rotor temperature and pressure ratio for a gap of 0.2 and pitch ratio of 1.45 are shown in Figure 8 for measurement simulated at two axial stations upstream of the stator leading edge, 15 and 20 percent of the stator axial chord. There are several important observations to make here. The first is that the pitchwise variation in flow quantities is quite substantial, so these are not negligible effects. The second is that the pitchwise distribution of temperature and pressure are more sensitive to the axial measurement location than is the magnitude of the variation. The third observation is that the pressure and temperature variations are in phase with each other and of similar magnitude. For this reason, we will only present the results for temperature ratio from here on. Both area and mass averages were calculated but differed by less than 0.002% for these flows so that only area averages are presented.

The pitchwise variation in the time averaged total temperature between the rotor and stator is shown in Figure 9 as a function of rotor-stator pitch ratio for a fixed gap of 0.2 for two axial measurement stations immediately behind the rotor and 10% of stator chord upstream of the stator leading edge. The temperature is plotted as the local deviation from the pitchwise mean (the time averaged local temperature, T_2, minus the pitchwise average of the time averaged total temperature, $\overline{T}_2$) normalized by the mean rotor temperature rise ($\overline{T}_2$ minus the average rotor inlet total temperature, $\overline{T}_1$). Note that the magnitude of the pitchwise temperature variation changes from quite small at large pitch ratios (2) to quite large at pitch ratios approaching 1. The difference in distance between the rotor and stator in the three cases implies a difference in convection times from the rotor trailing edge to the stators, thus the relative phase shift seen in the near stator leading edge plots. The variation with rotor-stator gap for the same two axial stations is shown in Figure 10 for a fixed pitch ratio of 1.45. Note here that, at the gaps typical of fans (0.75-4), the effects are small; but at the closer spacing typical to compressors, the spatial variation becomes significant.

The above plots reflect the pitchwise nonuniformity of the time averaged flowfield. They also illustrate that the flow is nonuniform in the axial direction as well. While the variation with pitchwise position is larger than that for axial position, the axial variation is not negligible.
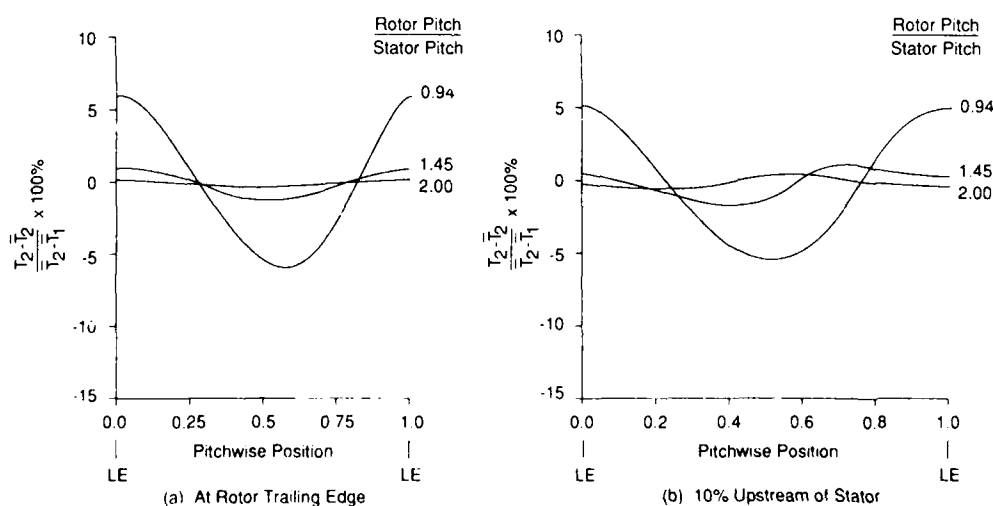

Fig. 9: The effect of rotor-stator pitch ratio (number of rotors/number of stators) on the normalized, time averaged temperature rise as would be measured at different pitchwise positions
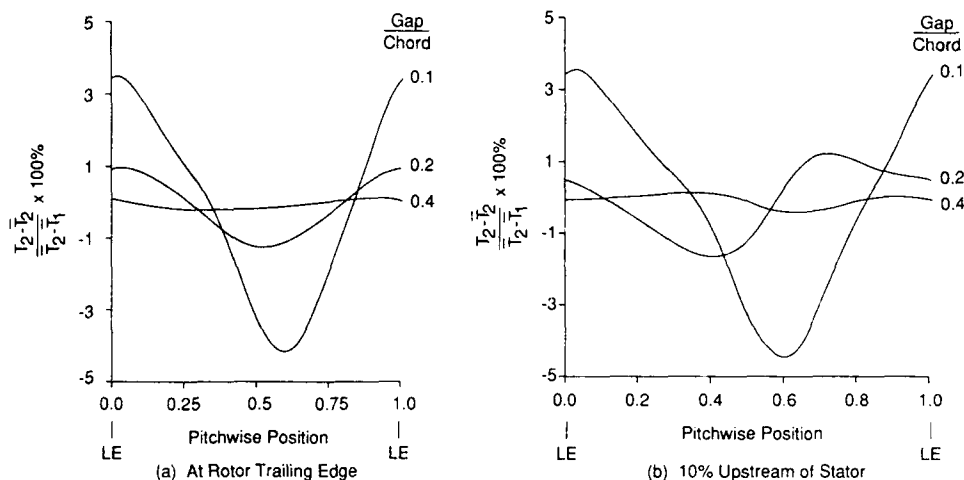
Fig. 10: The effects of rotor-stator spacing (gap) on the normalized, time averaged rotor temperature rise as would be measured at different pitchwise positions

EFFECTS ON MEASURED EFFICIENCY

A primary measure of compressor performance is adiabatic efficiency, which can be calculated from the measured total temperature and pressure. The efficiency calculated from the time averaged temperature and pressure at each pitchwise location in Figure 8 is plotted in Figure 11 as the efficiency perturbation - the local efficiency, η, minus the pitchwise mean, $\bar{\eta}$. Here, we see that the variation of efficiency with pitchwise location is very small, although the variations of pressure and temperature are not. The reason for this is that the pitchwise flow variations result predominantly from the variation in rotor blade lift and work as the rotor blades pass through the potential field of the stator blades. This variation in work is performed at essentially constant efficiency (at least in this inviscid calculation) so that the pitchwise variation in temperature and pressure are in phase, as can be seen in Figure 8.

It is very important to note that small efficiency variations seen in Figure 11 are based on the presumption that the pressure and temperature are measured in exactly the same pitchwise location. This is not necessarily the case in all measurement programs. The result of arbitrary pitchwise location of the temperature and pressure probes relative to each other and the stator leading edges at one axial location is shown in Figure 12 as contours of local adiabatic efficient error (the local value minus the average). The variation for the worst case (one probe in mid passage, the other at the stator leading edge) is 3%, a significant error. We conclude from this that it is extremely important to locate pressure and temperature instrumentation at the same pitchwise locations relative to the stator blades to avoid this type of sampling errors.
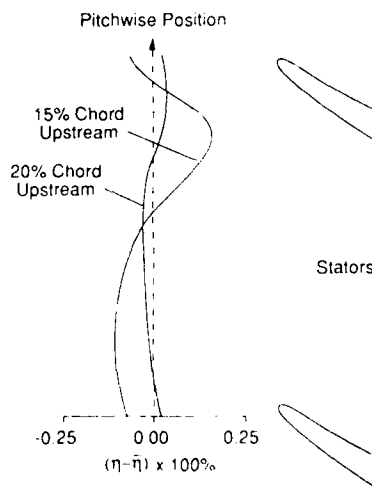
Fig. 11: Adiabatic efficiency deviation from the pitchwise mean for the flow in Fig. 6 at two axial stations upstream of the stator leading edge

MEASUREMENTS NEAR THE STATOR LEADING EDGE PLANE

Instrumentation on multistage compressors is most commonly done by cantilevering probes from the stator leading edge, in order to minimize blockage. Fortunately, this will also minimize the sampling errors in efficiency measurement by ensuring that the probes are placed at the same relative pitchwise location, as mentioned above.

We wished to examine whether small changes in axial probe position near the stator leading edge plane would influence accuracy (in other words, does the length of the pitot tube cantilever matter). In this inviscid calculation, the leading edge flows are not resolved in sufficient detail to permit an accurate assessment in that region. Therefore, the flow near midpassage was examined. Figure 13 shows the deviation in measured efficiency for small changes in the probe axial location. The effects are essentially negligible.

INFLUENCE OF STATOR LOADING

The influence of stator loading on the blade row interactions was examined by generating a family of similar airfoils with differing camber. The results are illustrated in Figure 14, which shows a relatively small influence on rotor exit temperature distribution for a ±8 degree change in stator turning.

TIME UNSTEADY FLOW

So far, we have examined only the time averaged flow field. The time resolved flow is, of course, influenced by the blade row interaction as well. The spatial distribution of the time average is a reflection of the variation of the time resolved rotor exit flow field with instantaneous pitchwise position. This is illustrated in Figure 15, which shows the instantaneous temperature ratio at two pitchwise positions upstream at the same axial station in the rotor stator gap. Note that the waveform shape changes as well as the mean level. This may introduce a small error in pitot type probes [1].

CONCLUSIONS

The work to date has concentrated on examining the influence of rotor-stator interactions on the measurement of compressor rotor performance. The results can be summarized as follows:

1. The upstream potential field of the stators results in unsteady lift on the upstream rotor blade.
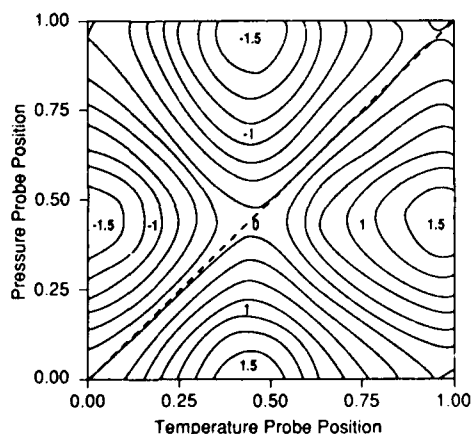
Fig. 12: Error in efficiency (deviation from the average efficiency) as a function of the locations of the temperature and pressure probes relative to each other and the stators. --- line of similar placement.
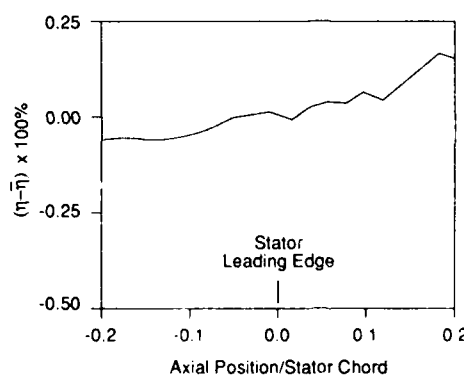
Fig. 13: Variation in apparent efficiency measurement with probe axial position near stator midpassage
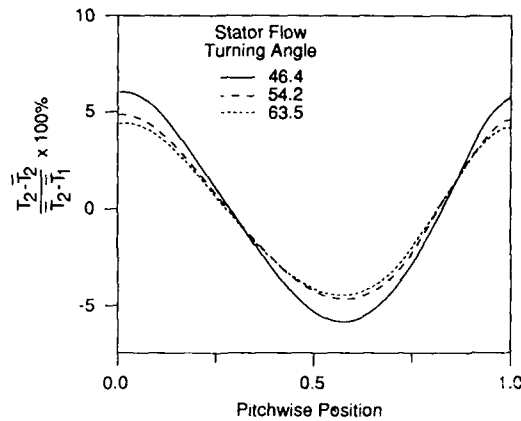
Fig. 14: Influence of stator loading on rotor
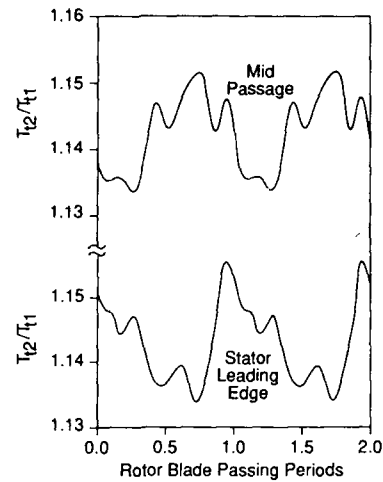outflow pitchwise temperature
distribution

Fig. 15: Instantaneous total temperature as would
be measured at two pitchwise locations at
mid rotor-stator gap

2. The unsteady rotor lift results in circumferential or pitchwise nonuniformity of the rotor exit time averaged
flow field.

3. The magnitude of the pitchwise nonuniformity is strongly dependent on the rotor stator spacing and the
relative number of rotor and stator blades.

4. At blade row spacings typical of high bypass ratio turbofans, the nonuniformity is negligible.

5. At blade row spacings typical of compressors, the flow nonuniformity can be substantial, ±2-3% of the stage
average temperature or pressure rise (about 1.5°C for the stage studied).

6. Although the temperature and pressure nonuniformity is large, the adiabatic efficiency is nearly uniform
since the temperature and pressure variations are in phase.

7. Stator leading edge temperature and pressure instrumentation will, therefore, read about 1% high but the
resultant efficiency will be within 0.2% of the true pitchwise average.

8. Placing temperature and pressure instrumentation at different relative circumferential positions can result in
large efficiency errors, ±1.5% for the stage studied.

This is very much a report on work in progress. A viscous version of the CFD code is now being run
and other geometries will be examined. An experimental verification of these conclusions is being planned.

REFERENCES

1. Weyer, H., "The Determination of Time-Weighted Average Pressures in Strongly Fluctuating Flows,
Especially in Turbomachines," ESRO TT-161, May 1975.

2. Pianko, M., Wazelt, F., "Suitable Averaging Techniques in Nonuniform Internal Flows," AGARD-AR-
182.

3. Giles, M.B., "Calculation of Unsteady Wake/Rotor Interaction," J. of Prop. and Power, Vol. 4, No. 4,
July/August 1988, pp. 356-362.

4. Giles, M.B., "Stator/Rotor Interaction in a Transonic Turbine," AIAA Paper 88-3093, July 1988.

5. Urasek, D.C., Gorell, W.T., Cunnan, W.S., "Performance of Two-Stage Fan Having Low-Aspect-Ratio, First-Stage Rotor Blading," NASA TP-1493, August 1979.

6. Strazisar, A.J., Powell, J.A., "Laser Anemometer Measurements in a Transonic Axial Flow Compressor," *J. of Eng. for Power*, Vol. 103, No. 2, April 1981, pp. 430-437.

7. Hathaway, M.D., Private Communication, 1988.

8. Gertz, J.B., "Unsteady Design-Point Flow Phenomena in Transonic Compressors," Ph.D. Thesis, MIT, 1985.

9. Wood, J.R., Strazisar, A.J., Simonyi, P.S., "Shock Structure in a Transonic Fan Using Laser Anemometry," AGARD CP-401, September 1986.

10. Owen, P.R., "Computational Simulation of Unsteady Flow in an Transonic Compressor Rotor," M.S. Thesis, MIT, 1986.

11. Horlock, J.H., Daneshyar, H., "Stagnation Pressure Changes in Unsteady Flow," *Aero. Quarterly*, Vol. XXII, August 1971, pp. 207-224.

ACKNOWLEDGEMENTS

DISCUSSION

Ph.Ramette - SEP, France
The paper is based on inviscid flow calculations using the Euler equations.Has the viscous version of the code been already tested and will it modify the conclusions?

Author's response :
First results from the viscous version of the multiblade row code UNSFO are just arriving. It is expected that the trends remain the same, although the magnitudes may increase somewhat. Also the conclusion that the efficiency remains almost constant accross the stator gap if the temperature and pressure probes are co-located may change when viscous losses are present.

S.C.P.Cook - Rolls-Royce, Derby, U.K.
Could the authors comment on the magnitude of errors, seen typically in measuring efficiency by their industrial sponsor, i.e. are the errors seen of the same order of magnitude or greater than the predictions presented in the paper?

Author's response :
Measurement discrepancies on the order of 5°K have been observed in the rear stages of high pressure compressors. This is higher than the numbers presented in this paper but, of course, the geometries are different and so one would expect the flows to be somewhat different as well.

Comments by H.B.Weyer - DLR Cologne, Germany
The paper demonstrates two sources of major errors when performing measurements downstream of rotors. There is, however, a third error often neglected, which derives from the local throttling of immerged probes.

HIGH-RESOLUTION EULER COMPUTATIONS OF UNSTEADY TRANSONIC FLOWS IN CASCADES

F. Bassi*, C. Osnaghi**, M. Savini***

*   Universita' di Catania, Istituto di Macchine, via A. Doria 6, 95125 Catania, Italia
**   Politecnico di Milano, Dipartimento di Energetica, piazza Leonardo da Vinci 32, 20133 Milano, Italia
***   CNR/CNPM, viale F. Baracca 69, 20068 Peschiera Borromeo (Mi), Italia

SUMMARY

A two-dimensional finite volume TVD Euler solver, suited to handle time-dependent transonic flow fields in turbomachinery components, is here presented and used togheter with a method of characteristics (using a shock fitting technique) and with an explicit central-difference finite volume code in order to investigate unsteady flow fields. Special care is given to the accurate treatment of boundary conditions, both of solid-wall and far-field type. The method is used to compute two unsteady flow problems which have features of transonic internal flows of practical importance in the analysis of turbomachinery components. The problems are the unsteady flow in a transonic nozzle with oscillating back pressure and the transonic flow in a rotor blade row with translating disturbancies at the inflow boundary simulating the wakes shed by a preceding stator blade row. In the first problem the influence of oscillation frequency upon the flow field is investigated with the three methods so as to obtain some indications of the relative accuracies of the schemes and a better understanding of the physical phenomena occurring.

INTRODUCTION

The numerical solution of unsteady fluid dynamics in turbomachinery is gaining more and more interest in view of a better permormance prediction and a correct mechanical design of the most stressed components. Actually the most dangerous and least known stresses on turbomachinery bladings are mainly due to pulsating forces and to.aeroelastic instability phenomena. The experimental investigation in this field often encounters great difficulties to properly account for differences in shape, amplitude and frequency in a wind tunnel, as well as to manage the complexities and costs of experimental measurements in rotating machines. For these reasons in the last thirty years analytical and semi-analytical methods were developed to predict the aerodynamic loadings in presence of periodic disturbances. Informations obtained in this way proved to be very valuable and easy to extend in the frequency domain, but are limited to simple geometric configurations, small deflections, and incompressible flows. As these limitations are unacceptable in many turbomachinery flows, a great work has been devoted to the extension of analytical and numericai approaches; limiting ourselves to consider inviscid fluid dynamics, that nevertheless includes a large class of unsteady phenomena, one can trace back the following basic steps of the research:
. extension of analytical and semi-analitycal methods to strong deflections, thicknesses, and to subsonic, transonic and supersonic flows.
. linear potential numf l solutions.
. small perturbations ·   ential and Euler) harmonic solutions superimposed on non-linear steady Euler ones.
. numerical solutions of unsteady Euler equations.
Obviously all these different approaches vary greatly in the complexity of the physical models as well as in the computational times required; depending on the problem examined, even the old simplest methods can still provide useful informations about the influence of the flow unsteadiness on the blade characteristics. In particular, the small perturbation Euler solutions of Ni [6] and Hall [7] represent an important improvement since they allow to treat transonic problems characterized by the presence of slip lines and shock waves; this is especially worth in turbomachines, where many unsteady aerodynamic instances depend on chocking and/or shock wave motion. However there are restrictive conditions on amplitude and frequency of a disturbance located at some boundary for the linearization to be valid throughout the domain. Perhaphs the most striking example of the inherent non-linearity of the transonic regime is an oscillating shock wave: the fluid interested by this motion experiences finite variations no matter how small is the cause of the motion. Hall overcame this difficulty [7] separating the domain with discontinuities (shocks) whose motion can be linearized and explicitly accounted for (shock-fitting). Yet is clear that a transonic flow field in presence of high gradients, and hence great distortions in the propagation of waves, is highly non linear and an harmonic analysis is often not permissible with perturbations at the boundary of the order of a few percent. If one turns to the solution of the full Euler equations, one must be aware that the numerical scheme strongly influences the propagation of disturbances, both in phase and amplitude. So it is useful to test different methods against each other; especially those based on the correct physical signal propagation. In some situations the comparison is illuminating and emphasizes the crucial need, in turbomachinery applications, for a rigorous formulation of boundary conditions.

THEORETICAL APPROACH AND NUMERICAL METHODS

The basis of the present flow analysis are the unsteady Euler equations. As previously seen, these equations can be used to model with a good approximation several unsteady phenomena in turbomachinery blade rows. Using the non-linear Euler equations one is not restricted to consider small unsteadiness amplitudes and flows periodic in time; the counterparts of these advantages are the increased computational difficulty and cost of

the numerical solution. In this section the TVD (Total Variation Diminishing) method is presented in some detail togheter with a brief description of the unsteady method of characteristics used in the first unsteady problem. The TVD scheme applies to the two-dimensional Euler equations in conservation form; in a Cartesian coordinate system (x,y) they can be written as

$$\frac{\partial}{\partial t}\int_V W\,dV + \oint_{\partial V}\left(fn_x + gn_y\right)dS = 0 \qquad (1)$$

where

$$W = [\rho, \rho u, \rho v, \rho E]^T$$

$$f = \left[\rho u, \rho u^2 + p, \rho uv, \rho uH\right]^T$$

$$g = \left[\rho v, \rho vu, \rho v^2 + p, \rho vH\right]^T$$

$$p = (\gamma - 1)\rho e$$

$$E = e + \frac{1}{2}\left(u^2 + v^2\right)$$

$$H = E + \frac{p}{\rho}$$

and n_x, n_y are the components of the unit vector normal to the surface, fixed in space, that encloses the volume V. The relation among pressure, density and internal energy assumes that the fluid is an ideal gas with constant specific heats of ratio equal to γ.

Euler equations in conservation form admit weak solutions, i.e. solutions with discontinuities: if one uses an appropriate numerical scheme to discretize eqn. (1), discontinuities in transonic and supersonic flows can be automatically captured and followed in their movement; however this appealing feature of the conservative formulation has some drawbacks that will be addressed below. The Euler equations in integral form lead almost naturally to a finite volume discretization which has the advantage to fit well complex body geometries, thus simplifying the treatment of solid wall boundary conditions; however, the grid must be sufficiently smooth and not too skewed so as not to deteriorate the accuracy of the numerical scheme. Looking at the Euler equations from another point of view, it can be shown that different wave fields, with different directions and velocities of propagation, combine themselves to give the solution: thus it is important, especially if dealing with unsteady flows, that the numerical approximation to eqn. (1) properly accounts for signals propagation; in a finite volume formulation this can be obtained with a suitable definition of the numerical fluxes at cell interfaces. The TVD formulation used in the present work tries to satisfy both the requirements of conservation and of correct signal propagation by using a conservative "upwind" discretization: globally the method can be included in the family of the so-called MUSCL (Monotonic Upstream-centered Schemes for Conservation Laws) type schemes which have been originally proposed by B. van Leer [17,18], and further developed in its various parts by other authors.

The semi-discretization of eqn. (1) for the cell i,j gives

$$\frac{d\hat{W}_{i,j}}{dt} + \left(\hat{F}_{i+\frac{1}{2},j} - \hat{F}_{i-\frac{1}{2},j}\right) + \left(\hat{F}_{i,j+\frac{1}{2}} - \hat{F}_{i,j-\frac{1}{2}}\right) = 0 \qquad (2)$$

where $W_{i,j}$ is the product of the average cell value W times the volume V of the cell and the various $\hat{F}$ represent the numerical fluxes normal to the cell faces. The numerical fluxes at cell interfaces are calculated with the following procedure which combines the requirements of accuracy and upwinding. In the following we use the index m for both i or j and omit the other index. At every cell interface $m+1/2$ two sets of variables $W^+_{m+1/2}$ and $W^-_{m+1/2}$ are defined just to the right and to the left of the cell interface. These values are used to set up a local Riemann problem, the solution of which gives the contribution to the fluxes associated with right and left travelling waves. In the present work the Roe's approximate Riemann solver [16] is employed: first one finds the eigenvalues and the right and left eigenvectors of the Jacobian matrix of $F_{m+1/2}$ in the state between $W^+_{m+1/2}$ and $W^-_{m+1/2}$ defined by Roe's averaging; defining by $u_{m+1/2}$ and $v_{m+1/2}$ the velocity components normal and tangential to the face $m+1/2$, i.e.

$$\bar{u}_{m+\frac{1}{2}} = \left(un_x + vn_y\right)_{m+\frac{1}{2}}$$

$$\bar{v}_{m+\frac{1}{2}} = \left(vn_x - un_y\right)_{m+\frac{1}{2}}$$

one obtains

$$a^l_{m+\frac{1}{2}} = (\bar{u} \mp c)_{m+\frac{1}{2}} \qquad\qquad l = 1,3$$

$$a^{l}_{m+\frac{1}{2}} = \bar{u}_{m+\frac{1}{2}} \qquad\qquad l = 2,4$$

and

$$R_{m+\frac{1}{2}} = \begin{pmatrix} \dfrac{1}{c} & \dfrac{1}{c} & \dfrac{1}{c} & \dfrac{1}{c} \\[2mm] \dfrac{u}{c} - n_x & \dfrac{u}{c} + n_y & \dfrac{u}{c} + n_x & \dfrac{u}{c} - n_y \\[2mm] \dfrac{v}{c} - n_y & \dfrac{v}{c} - n_x & \dfrac{v}{c} + n_y & \dfrac{v}{c} + n_x \\[2mm] \dfrac{H}{c} - \bar{u} & \dfrac{q^2}{2c} - \bar{v} & \dfrac{H}{c} + \bar{u} & \dfrac{q^2}{2c} + \bar{v} \end{pmatrix}_{m+\frac{1}{2}} \tag{3}$$

$$L_{m+\frac{1}{2}} = \begin{pmatrix} \dfrac{\chi}{c}\dfrac{q^2}{2} + \bar{u} & -n_x - \dfrac{\chi}{c}u & -n_y - \dfrac{\chi}{c}v & \dfrac{\chi}{c} \\[2mm] -\dfrac{\chi}{c}\dfrac{q^2}{2} + \bar{v} + c & n_y + \dfrac{\chi}{c}u & -n_x + \dfrac{\chi}{c}v & -\dfrac{\chi}{c} \\[2mm] \dfrac{\chi}{c}\dfrac{q^2}{2} - \bar{u} & n_x - \dfrac{\chi}{c}u & n_y - \dfrac{\chi}{c}v & \dfrac{\chi}{c} \\[2mm] -\dfrac{\chi}{c}\dfrac{q^2}{2} - \bar{v} + c & -n_y + \dfrac{\chi}{c}u & n_x + \dfrac{\chi}{c}v & -\dfrac{\chi}{c} \end{pmatrix}_{m+\frac{1}{2}} \tag{4}$$

where $\chi = (\gamma-1)/2$. The numerical flux $\widehat{F}_{m+1/2}$ is then given by

$$\hat{F}_{m+\frac{1}{2}} = \left[F(W^-) + \sum_{l=1}^{4} a^{l-} a^l R^l \right]_{m+\frac{1}{2}}$$

$$= \left[F(W^+) - \sum_{l=1}^{4} a^{l+} a^l R^l \right]_{m+\frac{1}{2}} \tag{5}$$

where a^{l-} and a^{l+} are, respectively, the negative and positive projections of the eigenvalues on the normal to the face and α^l is defined as

$$\alpha^{l}_{m+\frac{1}{2}} = \left[L^l (W^+ - W^-) \right]_{m+\frac{1}{2}}$$

Eqn. (3) states that the numerical flux is given by the left (right) flux plus (minus) the changes in the flux due to the wave fields which have negative (positive) eigenvalues. The accuracy of the scheme depends on the definition of the W^+ and W^- values, which are interpolated from the values in the neighboring cells taking care to properly limit the gradients in order to satisfy the TVD constraint. Interpolation is defined, field by field, by the following relations:

$$\alpha^{l}_{m+\frac{1}{2}} = L^l_m (W_{m+1} - W_m)$$

$$\alpha^{l}_{m-\frac{1}{2}} = L^l_m (W_m - W_{m-1})$$

where the matrix L is evaluated in the cell centroid. The differences in characteristic variables are properly limited in such a way that no new maxima or minima are introduced in the reconstruction. The limited differences are defined using the so-called minmod function, i.e.

$$\tilde{\alpha}^{l}_{m+\frac{1}{2}} = \text{minmod}\left(\alpha^{l}_{m+\frac{1}{2}}, b\,\alpha^{l}_{m-\frac{1}{2}} \right)$$

$$\tilde{\alpha}^{l}_{m-\frac{1}{2}} = \text{minmod}\left(\alpha^{l}_{m-\frac{1}{2}}, b\,\alpha^{l}_{m+\frac{1}{2}} \right)$$

$$b = \frac{3-k}{1-k}$$

where the parameter k defines schemes of varying accuracy; in the one-dimensional case with uniform mesh spacing and without any limiting, the value $k = 1/3$ results in a third order upwind-biased scheme, the choices $k = -1$ and $k = 0$ define, respectively, the second order fully upwind and the second order Fromm scheme. Reckoning the importance of reducing the dispersion errors, here was adopted $k = 1/3$. The minmod function is defined as $minmod(x,y) = sign(x)max\{0,min[|x|,ysign(x)]\}$ and is 0 if x and y have opposite signs; as a consequence the scheme, second order or third order accurate in regions of smooth flow, becomes first order accurate at points of maxima and minima: this is the principal drawback of the TVD limiter formulation, which introduces significant errors where the gradients change sign.

The values $W^{+}_{m+1/2}$ and $W^{-}_{m+1/2}$ are finally given by

$$W^{-}_{m+\frac{1}{2}} = W_m + \frac{1}{4}\sum_{l=1}^{4}\left[(1+k)\tilde{\alpha}^{l}_{n+\frac{1}{2}} + (1-k)\tilde{\alpha}^{l}_{m-\frac{1}{2}}\right]R^{l}_{m}$$

$$W^{+}_{m-\frac{1}{2}} = W_m - \frac{1}{4}\sum_{l=1}^{4}\left[(1+k)\tilde{\alpha}^{l}_{m-\frac{1}{2}} + (1-k)\tilde{\alpha}^{l}_{m+\frac{1}{2}}\right]R^{l}_{m}$$

The finite volume discretization described above allows to calculate the residual in each cell; from eqn. (2) the unknowns can be marched in time by a proper time discretization. In this work a simple explicit two stage Runge-Kutta algorithm has been used:

$$W^{*}_{m} = W^{n}_{m} - \frac{\Delta t}{V_m}R\left(W^{n}_{m}\right)$$

$$W^{n+1}_{m} = W^{n}_{m} - \frac{1}{2}\frac{\Delta t}{V_m}\left[R\left(W^{n}_{m}\right) + R\left(W^{*}_{m}\right)\right]$$

Boundary conditions

In turbomachinery applications one usually finds four types of boundary conditions, namely: solid wall, periodicity, inflow, outflow.

Solid wall boundary conditions

An accurate treatment of solid wall boundary points is crucial especially for inviscid flows, because most of the spurious entropy productions of conservative schemes arise at solid surfaces. In the TVD scheme a node-centered finite volume discretization has been used and hence the boundary points lie just on the boundary, on the outer edge of a half control volume. At the boundary points the updating of unknowns is based on the theory of characteristics: the compatibility relations in the direction normal to the wall are found by multiplying the matrix (4) of left eigenvectors by the system of eqn. (1). The boundary condition is implemented substituting the row of L associated with the incoming eigenvalue with the tangency condition. The discretized form of the compatibility relations can be written as

$$L^{n}_{1}\left[\Delta W + \frac{\Delta t}{V}R\left(W^{n}\right)\right] = 0 \qquad (6)$$

where in the matrix L_1 the row corresponding to the incoming eigenvalue is set to zero; ΔW expresses the variation of the unknowns over the time step and $R(W^n)$ are the residuals. The residuals have a contribution from the balance of fluxes along the boundary (performed as for the interior points) and a contribution from the balance of fluxes in the transversal direction (at the wall containing only the pressure term). The system of eqn. (6) is completed with the tangency condition, i.e.

$$\Delta(\rho u)n_x + \Delta(\rho v)n_y = 0 \qquad (7)$$

The system of eqn. (6) and (7) can thus be solved for

$$\Delta W = \left(L^{n}_{2}\right)^{-1}\left[-L^{n}_{1}\frac{\Delta t}{V}R\left(W^{n}\right)\right] \qquad (8)$$

where the matrix L_2 is equal to L_1 except for the null row substituted with that deduced from eqn. (7). The described procedure is applied both in the predictor and in the corrector step of time integration.

Periodicity boundary conditions

If grid points are periodic in tangential direction and if any eventual unsteadiness along the inflow and outflow boundary is periodic over the pitch, the periodicity conditions are trivial to implement. The treatment of disturbancies with period different than the pitch is more difficult because one must introduce periodicity conditions lagged in time or perform the calculations over a group of blades; an original alternative, proposed by M. Giles, is to tilt in time the computational plane (see Ref. [11]).

Inflow and outflow boundary conditions

A correct and accurate implementation of inflow and outflow b.c.'s is extremely important both in steady and unsteady calculations; in the former case one is interested not to introduce spurious reflections that slow down convergence and alter significantly the interior flow field (forcing one to keep the boundaries off the blades), in the latter one wants to assign b.c.'s which allow to specify the evolution in time of some variables and which interact correctly with the interior of the computational domain. The theory of characteristics, with different degrees of approximation, can be used to specify both the number and the type of b.c.'s. As for the solid wall b.c.'s, the TVD method updates inflow and outflow boundary points finding the local compatibility relations and substituting the relations associated with the incoming eigenvalues with the boundary conditions. If non-reflecting b.c.'s are desired, one must set the values of the characteristic variables associated with the incoming eigenvalues. This is not a trivial task even in a one-dimensional problem because one ten wants to impose a variable that is not a characteristic one (for example the pressure at the outflow boundary); in two dimensions this is harder since one has to find the boundary distribution of characteristic variables whi h in turn depends on the inner solution and which satisfies user specified boundary values in an average sense. The non-reflecting b.c.'s here implemented follow closely the theory developed by M. Giles: the complete description can be found in Ref. [10-11]. Briefly, Giles' approach is based upon a characteristic analysis of the linearized Euler equations; the main feature is that the b.c.'s are truly two-dimensional. In the steady case the changes over a time step of the incoming characteristic variables are given by an average change, determined to satisfy a number of specified average quantities (flow angle, total enthalpy and entropy at inflow, pressure at outflow), plus a distribution of local changes. The spatial harmonics of the local changes in the incoming characteristics are related to the outgoing ones through the non-reflecting boundary conditions. The unsteady b.c.'s must prescribe unsteady incoming disturbances and must be transparent to outgoing waves. The first function is accomplished by defining appropriate models of the sources of unsteadiness (for example wakes, weak shocks, potential disturbances): note that these models specify variations over the time step of all the four conservative variables, however the actual changes in the outgoing characteristic variables depend upon the difference between computed and prescribed values. The non-reflecting condition leads to a set of first-order partial differential equations along the boundary.

The method of characteristics (CHAR) used in this work is presented in detail in Ref. [15], where it is applied to different problems (concerning nozzles, airfoils and turbomachinery blade rows). Essentially it solves the two-dimensional unsteady Euler equations in non-conservative form, where the energy equation is substituted with the conservation of entropy along the path line. The set of equations is hyperbolic in time and hence can be reduced to a set of compatibility equations along special bicharacteristic lines lying on the Mach cone and along the path line. The numerical solution at each node of the computational grid is obtained starting from the solution at the previous time level, where the variables at the intersections of the bicharacteristics are evaluated by means of a bi-parabolic interpolation. All the numerical interpolations are performed by accurately preserving the physical domain of dependence for the Riemann variables. If discontinuities are detected, they are explicitly introduced as slip-lines or shock waves. The characteristics define the flow field on both sides of the discontinuities and the proper explicit relatios (e.g. the Rankine-Hugoniot relations) complete the solution giving the speed and the geometry of the discontinuity surfaces. The detection and the geometrical definition of the shocks are very complicated and at present the method can not treat intricate shock patterns.

RESULTS AND DISCUSSION

Before presenting and discussing the results of the unsteady computations, an example of a steady flow calculation is given, showing the effectiveness of the solid wall and of the far field b.c.'s implemented in the TVD scheme. For this purpose, the staggered wedge cascade shown in Fig. 1 (an AGARD test case proposed by J. Denton) has been chosen since it has an analytical solution and presents some flow features difficult to be accurately solved by a numerical method, namely: shock reflection and cancellation, small total pressure losses, strong trailing edge shock crossing the outflow boundary. Fig. 2 (isobar lines and total pressure distribution along the blade) shows that no reflection originates at the outflow boundary and that the total pressure loss is rather close to the analytical result. The improvement of these results with respect to those shown in Figs. 3 and 4, obtained with the well known Jameson's Adaptive Dissipation (AD) method (Ref. [14]) and with a previous version of the TVD scheme, is striking: in the AD method the far field b.c.'s are based on a one-dimensional characteristic approach and the pressure at solid walls is found by using the normal momentum equation; in the previous TVD version the far field was treated as in the AD method and the pressure at solid walls was determined by solving a local one-dimensional Riemann problem. The shortcomings experienced with the TVD method concern the high number of operations per time step and the slow convergence rate to the steady state (this behaviour is ascribed by some authors to the influence of high frequency errors introduced by the flux limiters). The conclusion that stems from this steady test case is that the TVD method is very accurate (even not so fast and easy to implement) and represents an improvement over more commonly used schemes.

The use of numerical methods in unsteady computations is rather delicate and requires special attention to the accuracy, dissipation and dispersion properties of the schemes in order to discriminate between numerical and

physical aspects in the numerical solution. In the first unsteady flow problem considered in this work three different methods, namely the TVD, CHAR, and AD methods, have been used to perform a comparative study; the aim was twofold:

. to get some hints of the numerical errors peculiar to each method by comparing the results obtained with the different schemes;

. to gain some insight into the physical aspects of the propagation of unsteady perturbations in transonic regime.

The problem considered is the transonic unsteady flow in a nozzle with a shock wave in the divergent part subject to a back pressure oscillat.. e sinusoidally in time; the pressure oscillation amplitude was set to 7% of the steady value and the influence of the perturbation frequency f (oscillations per second) upon the computed flow field was examined spanning the following values of reduced frequency: 1/3, 1, 3, where the reduced frequency f_r is defined as

$$f_r = f \frac{L}{C_{2is}}$$

where L is the nozzle length and C_{2is} is the outlet speed of sound based on the isentropic outlet conditions. Fig. 5 shows the 60x20 computational grid, algebraically generated and endowed with good properties of smoothness and orthogonality; in this Figure are also indicated the steady shock positions for the maximum, average, and minimum outlet pressure (corresponding to isentropic Mach numbers of 0.565, 0.65, 0.727) and the points on the axis where the pressure was recorded during the unsteady computations. The isoMach lines of Fig. 6 show how the starting solution ($M_{2is} = 0.65$) was computed by the TVD and CHAR methods: it is noteworthy that despite the conceptual difference between the two methods the solutions are almost identical. The unsteady behaviour was examined looking at a global parameter (the integral of nozzle wall pressure) and at the local pressure in the aforementioned points; in all cases the unsteady computations were continued until the periodicity of the solution was satisfactory: note that in the following graphs the cycle count refers to the last three complete periods of oscillation. As regards the integral of wall pressure represented in Fig. 7, it is evident a general trend: rising the frequency of the disturbance increases the phase lag and reduces the amplitude of the response, i.e. the unsteady flow deviates more from a quasi-steady solution. Analogous results, not reported here, are obtained with the other two methods: however, the AD method shows a more pronounced difference between the results at the highest frequency and those at lower frequencies. From a careful examination of Fig. 7 it can be argued that a non-linear behaviour develops rising the frequency: this feature is more clear in Figg. 9 and 10 where the pressure evolution at the stations on the axis is represented. At the lowest frequency the pressure varies harmonically at all stations but the one affected by the shock motion, whilst at the highest frequency the pressure oscillation is far from being sinusoidal. In this latter case the shock moves quite a short   (see Fig. 8 where the shock displacement has been normalized over the length of the nozzle divergent portion): this suggests the observation that a little shock displacement is not necessarily associated with a linear behaviour of the flow field. From Figg 11 and 12 it appears that for $f_r = 1/3$ the behaviour is quite similar for the three methods (apart from the shock region); on the other hand the results of Fig. 13 for $f_r = 3$ outline a marked phase difference between the CHAR and TVD methods and a very great phase and amplitude difference between the AD and the other two methods. In order to investigate these aspects more closely, the calculations for $f_r = 3$ have been repeated on a refined 180x30 computational grid; Fig. 14 shows that the results of the three methods are now in much better agreement but all strongly non-linear. The comparison between coarse and fine mesh results allows to draw the following conclusions:

. the AD method suffers from relevant errors in the amplitude and phase propagation of a high frequency disturbance; in this respect the TVD and CHAR methods perform much better showing only a bit noisy solution.

. the non-linear behaviour of the flow field depends on the amplitude and on the frequency of the imposed oscillation: in fact, due to the non-linear character of the Euler equations, sinusoidal disturbances with very small amplitude but sufficiently high frequency may develop into waves which conserve the small amplitude but that are no longer sinusoidal. This means that a criterion to distinguish between linear and non-linear wave propagation should take into account the amplitude of the assigned disturbance as well as its time derivative.

The second unsteady problem considered in this work is the simulation of wakes shed by a stator row and entering the inflow boundary of the following rotor row. The wake is modeled in the stator frame of reference where it is supposed to be isobaric and isoenthalpic and to have an assigned velocity defect: the assumed velocity profile has a maximum velocity defect of 20% and its thickness is 20% of the pitch. In the rotor frame of reference the wake is moving in tangential direction with a velocity equal to twice the isentropic outlet sound speed; this exagerate velocity has been chosen to test the numerical accuracy of the method in a severe situation. At present the code, based on the TVD method, can treat unsteady disturbances periodic over the rotor pitch; moreover, it must be stressed that we successfully implemented only the one dimensional non-reflecting unsteady b.c.s described in Ref. [11]. The turbine blade is the widely tested [19] VKI gas turbine rotor section. Fig. 15 shows the 128x32 computational grid and the isobar and isoMach contours of the steady solution for $M_{2,s} = 1.21$. The mesh was generated with an algebraic zonal approach which guarantees a rather uniform mesh spacing with skewed cells limited to a small portion of the computational domain: these properties are important to get a uniform level of accuracy in unsteady computations. As in the staggered wedge case, the shock resolution is excellent (nearly two mesh points), no reflection is visible, even for this close enough downstream boundary, and it is evident the interaction between the shock and the wake generated by the numerical dissipation at the trailing edge. Not reported here, there is also very good agreement between the calculated and the experimental pressure distribution on the blade surface.

The unsteady computations were started from the steady solution and a periodic solution was established after ten cycles of the inlet disturbance (each cycle corresponding roughly to 760 time steps). Fig. 16 shows the history of the tangential force experienced by the blade; it is interesting to note that the tangential force oscillates

around a mean value that is somewhat lower than the steady value. In Fig. 17 are reported the contours of relative total pressure difference between the steady and the actual values, i.e. $(p_{t,\text{steady}}-p_t)/p_{t1,\text{steady}}$; the interval contour is 0.005. The wakes deform passing trough the channel due to faster flow near the suction side. The unsteady velocity vector plot of Fig. 18, obtained by subtracting the steady solution from the actual one, shows the "negative jet" behaviour of the wake and the vortices that are generated on the two sides of the wake segment inside the blade channel. These vortices are not so evident as in the example reported in Ref. [13]; this is due to the fact that the wakes follow each other in a rapid sequence and the leading vortex of a new wake segment entering the blade channel tends to attenuate the lagging vortex generated by the preceding wake segment. A calculation with a more resonable tangential velocity of the wakes should give a clearer picture of the vortices inside the blade channel. A final observation about Fig. 18 is that the arrows around the trailing edge shock are meaningless and are caused by a slight unsteady shock motion.

All the computations presented in this section were performed on a HP835 computer, characterized by a CPU speed of 14 Mips.

CONCLUSIONS

The TVD method presented in this work has proven to be accurate both for steady and unsteady Euler computations of internal flows. The addressed cases confirmed the importance to precisely treat the solid-wall and far-field boundaries. The first unsteady problem investigated allowed to emphasize two interesting topics: the numerical properties of different schemes and the physical influence of the frequency of an imposed disturbance. It can be concluded that in the analysis of unsteady phenomena are more advisable schemes that account for the correct propagation of waves, and that in some transonic high-frequency oscillating flows the non-linearities play an essential role. The second unsteady problem examined showed the practical interest of such computations in turbomachinery applications, even without tackling the more complex issue of the stator-rotor interaction. Further investigation is needed to properly implement the two-dimensional far-field unsteady boundary conditions.

REFERENCES

[1]   Whitehead, D.S., "The Calculation of Steady and Unsteady Transonic Flow in Cascades", Univ. of Cambridge, Dept. of Engg., Report CUED/A-Turbo/TR 118, 1982.

[2]   Verdon, J.M., "Unsteady Aerodynamics for Turbomachinery Aeroelastic Applications", UTRC Report R86-151774-1, 1986.

[3]   Verdon, J.M., Caspar J.R., "A Linearized Unsteady Aerodynamic Analysis for Transonic Flows", Journal of Fluid Mechanics, vol. 149, December 1984.

[4]   Ni, R.H., "A Rational Analysis of Periodic Flow Perturbation in Supersonic Two-Dimensional Cascade", ASME Journal of Engineering for Power, vol. 101, July 1979.

[5]   Erdos, J.I., Alzner, E., "Computation of Unsteady Transonic Flows Through Rotating and Stationary Cascades", NASA CR-2900, December 1977.

[6]   Ni, R.H., Sisto, F. "Numerical Computation of Nonstationary Aerodynamics of Flat Plate Cascades in Compressible Flow", ASME Journal of Engineering for Power, vol. 101, April 1976.

[7]   Hall, K.C., Crawley, E.F., "Calculation of Unsteady Flows in Turbomachinery Using the Linearized Euler Equations", AIAA Journal, vol. 27 no 6, 1989.

[8]   Rai, M.M., Chaussee, D.S., "New Implicit Boundary Procedures - Theory and Applications", AIAA Journal, vol. 22 no 8, 1984.

[9]   Chakravarthy, S.R., "The Versatility and Reliability of Euler Solvers Based on High-Accuracy TVD Formulations", AIAA paper no 86-0243, 1986.

[10]   Giles, M.B., "Non-Reflecting Boundary Conditions for the Euler Equations", Technical Report TR-88-1, MIT Computational Fluid Dynamics Laboratory, 1988.

[11]   Giles, M.B., "UNSFLO: A Numerical Method for Unsteady Inviscid Flow in Turbomachinery", Technical Report 195, MIT Gas Turbine Laboratory, 1988.

[12]   Giles, M.B., "Calculations of Unsteady Wake/Rotor Interaction", AIAA Journal of Propulsion and Power, vol. 4 no 4, 1988.

[13]   Hodson, H.P., "An Inviscid Blade-to-Blade Prediction of a Wake-Generated Unsteady Flow", ASME paper 84-GT-43, 1984.

[14]   Jameson, A., Schimdt, W., Turkel, E., "Numerical Solutions of the Euler Equations by Finite Volume Methods Using Runge-Kutta Time-Stepping Schemes", AIAA paper no. 81-1259, 1981.

[15]   Osnaghi, C., "Explicit Evaluation of Discontinuities in 2-D Unsteady Flows Solved by the Method of Characteristics", 11th ICNMFD, Lecture Notes in Physics, vol. 323, Springer Verlag, 1989.

[16]   Roe, P.L., "Approximate Riemann Solvers, Parameter Vectors, and Difference Schemes", Journal of Computational Physics, vol. 43, 1981.

[17]   Van Leer, B., "Towards the Ultimate Conservative Difference Scheme: IV. A New Appoach to Numerical Convection", Journal of Computational Physics, vol. 23, 1977.

[18]   Van Leer, B., "Towards the Ultimate Conservative Difference Scheme: V. A Second-Order Sequel to Godunov's Method", Journal of Computational Physics, vol. 32, 1979.

[19]   Sieverding, K., "Experimental Data on Two Transonic Turbine Blade Sections and Comparison with Various Theoretical Methods", VKI Lecture Series 73-59, 1973.
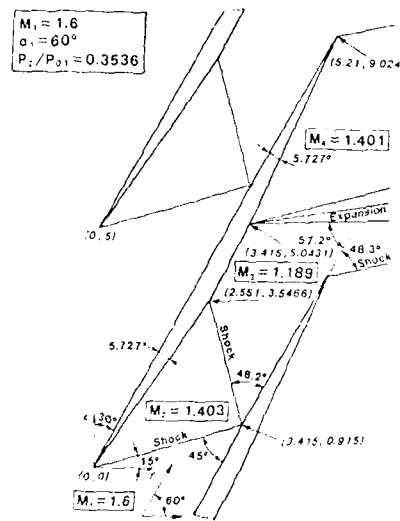
$M_1 \approx 1.6$
$\alpha_1 = 60°$
$P_2/P_{01} \approx 0.3536$

(5.21, 9.024)

$M_4 \approx 1.401$
5.727°

Expansion

57.2°
(3.415, 5.0431)
48.3°
Shock

$M_3 = 1.189$
(2.551, 3.5466)

5.727°

Shock

48.2°

$M_2 = 1.403$

(0, 5)

1.20°
Shock
15°
45°
(3.415, 0.915)

(0, 0)

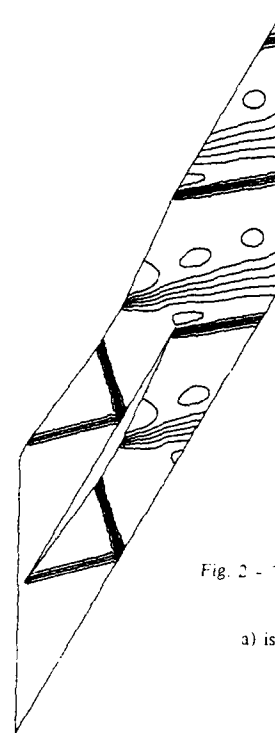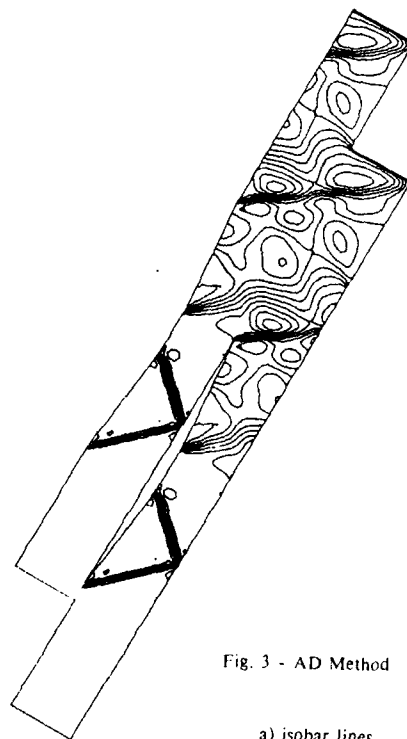$M_1 = 1.6$
60°

Fig. 1 - Supersonic wedge cascade

Fig. 2 - TVD Method
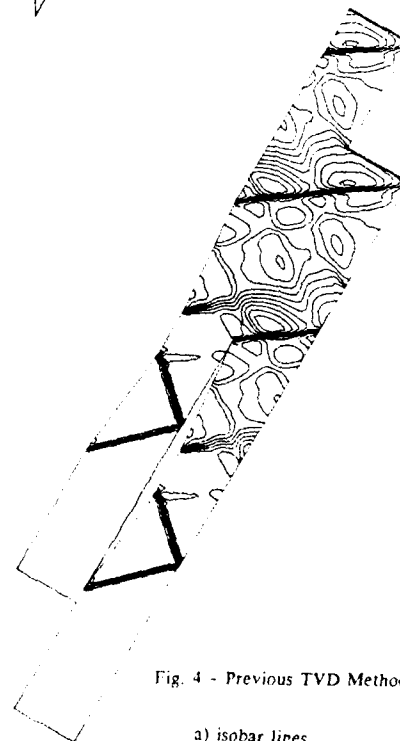
a) isobar lines

Fig. 3 - AD Method

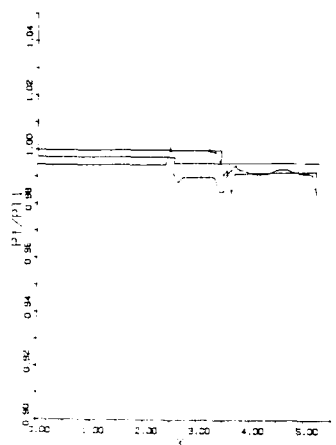a) isobar lines

Fig. 4 - Previous TVD Method

a) isobar lines

Fig. 2 - TVD Method   Fig. 3 - AD Method   Fig. 4 - Previous TVD Method

b) total pressure along the blade   b) total pressure along the blade   b) total pressure along the blade
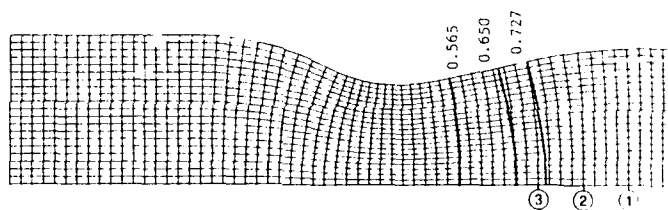
Fig. 5 - Transonic nozzle
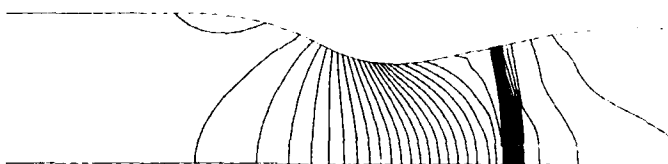
a) TVD Method
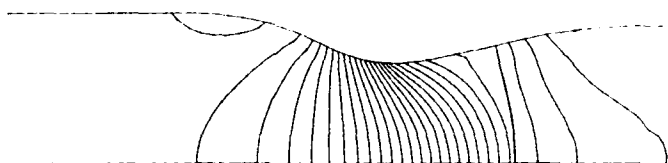
b) CHAR Method

Fig. 6 - IsoMach lines

INTEGRAL OF WALL PRESSURE - TVD METHOD

Fig. 7

SHOCK DISPLACEMENT - CHAR METHOD

Fig. 8

TVD METHOD - RED.FREQ. = 1/3

Fig. 9

TVD METHOD - RED.FREQ. = 3

Fig. 10

STATION n. 2 - RED.FREQ. = 1/3

Fig. 11

STATION n. 3 - RED.FREQ. = 1/3

Fig. 12

STATION n. 3 - RED.FREQ. = 3

Fig. 13

STATION n. 3 - RED.FREQ. = 3

Fig. 14
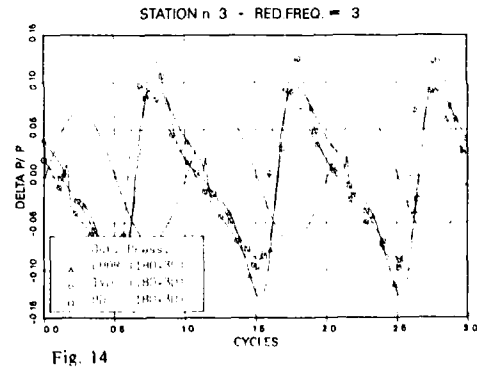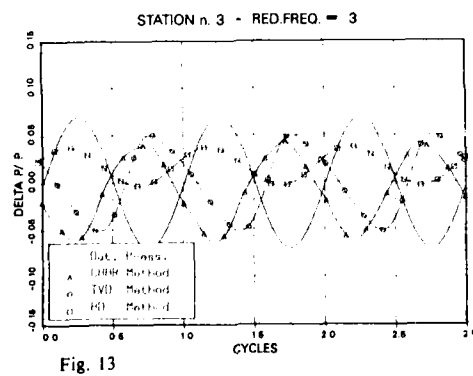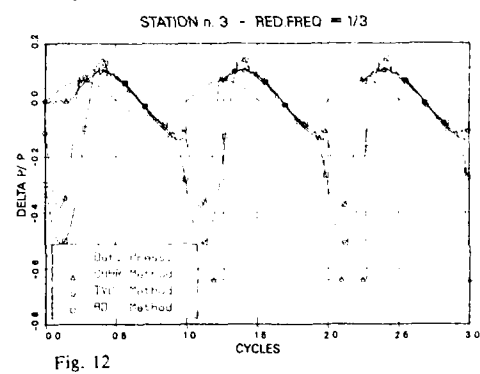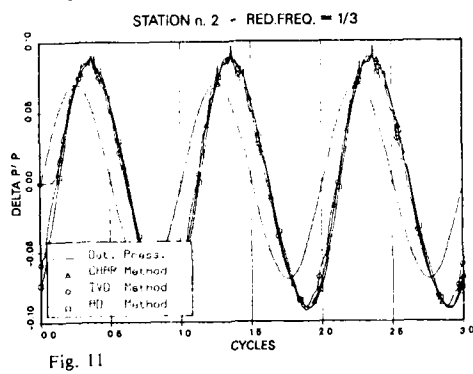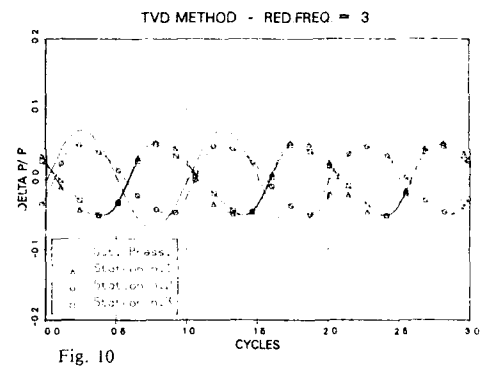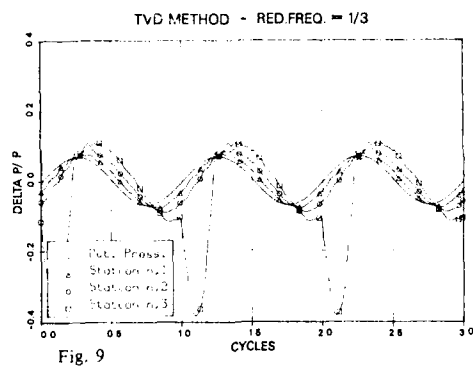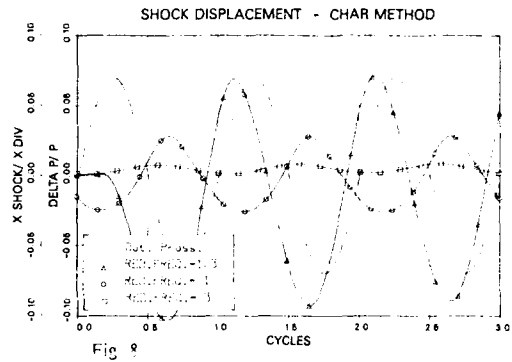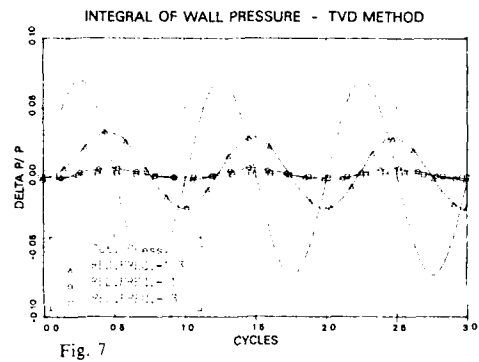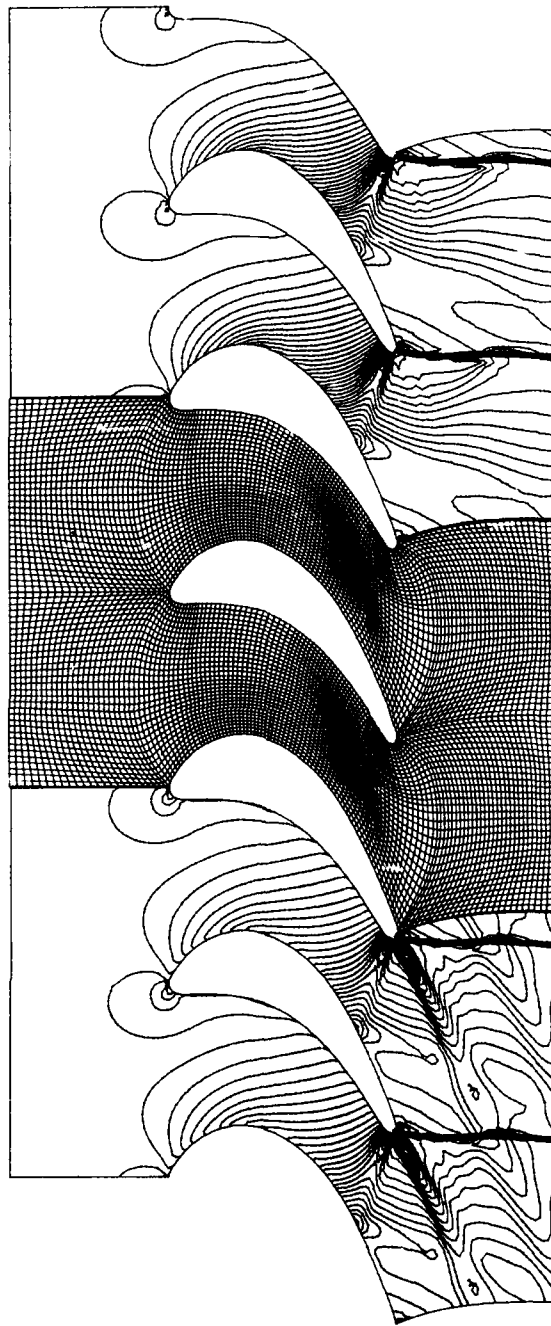
Fig. 15 - Isobars, computational grid and isoMach lines for $M_{2is} = 1.21$

HIGH FREQUENCY WAKE AT INLET
RELATIVE CHANGE IN TANGENTIAL FORCE
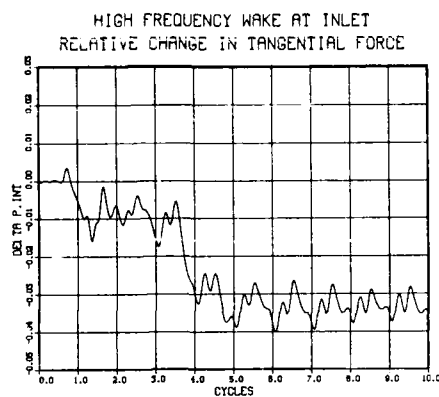
Fig. 16
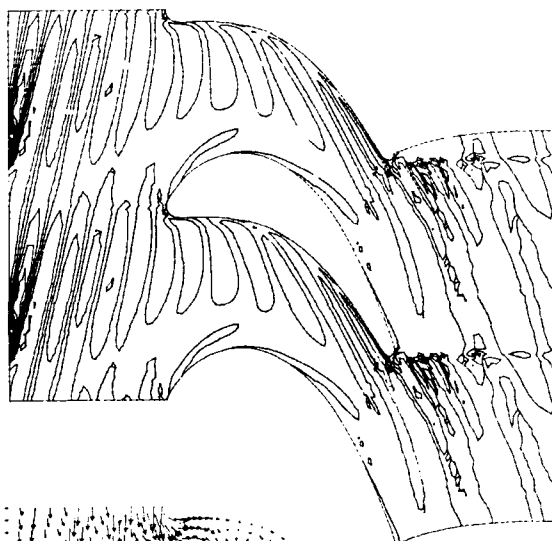
Fig. 17 - Iso-deficit of total pressure
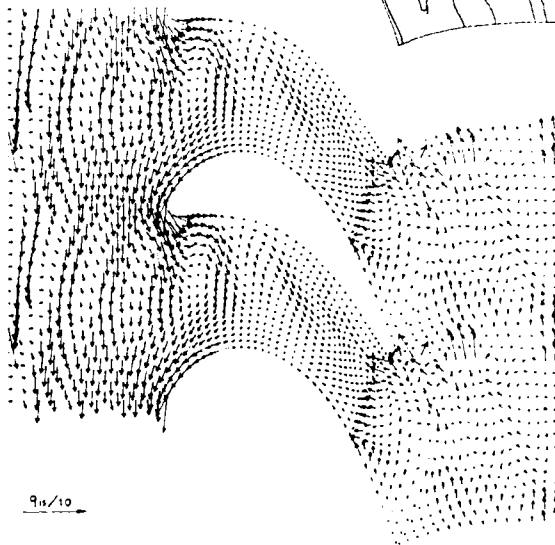
Fig. 18 - Unsteady velocity vectors

ASYMPTOTIC ANALYSIS OF TRANSONIC FLOW THROUGH OSCILLATING CASCADES

Dr. Franz Koller
Prof. Dr. Alfred Kluwick
Technische Universität Wien
Institut für Strömungslehre und
Wärmeübertragung
Wiedner Hauptstraße 7
A-1040 Wien, Austria

Summary

The plane flow of a perfect gas through an oscillating cascade at a Mach number close to one is analyzed using matched asymptotic expansions. In the case of steady flow the field quantities in the regions between airfoils are governed by equations for one-dimensional flow in a first approximation if thickness, camber and angle of incidence of the blades are small. Moreover, for a particular range of these parameters the velocity disturbances satisfy linear equations ahead of and behind the cascade. The same property is shown to hold in the case of unsteady flow provided the reduced frequency and the amplitudes of the oscillations are small compared to unity. Furthermore, the effects of the sizes of the various parameters on the flow field are discussed. Surface pressures are calculated for cascades of flat plate and double circular arc airfoils.

1 Introduction

Rapid progress in the design of turbomachines has made transonic flow through parts of the compressor or turbine stages a normal feature. At the same time, it has substantially increased the need to study unsteady flow effects. Some of these can be described, sufficiently accurate for engineering purposes, by means of the equations of inviscid flow [11]. This applies for instance to the passage of sound waves, which are introduced into the flow ahead of or behind the blades of a stage and unstalied forced or self-excited oscillations (flutter) of the blades. These three phenomena can be approximated by the same mathematical model, however. The following considerations, therefore, are restricted to plane, inviscid, unsteady flow through a cascade of airfoils. Before turning to the mathematical approach adopted in this study it is useful first to outline briefly the methods which have been applied so far. Details can be found in [11] and [14] and in the references cited therein.
Linearization of the governing equations leads to the complete decoupling of the effects due to airfoil shape and airfoil motion. Accordingly, the unsteady problem reduces to that for the flow through a cascade of flat plates at zero mean angle of incidence. As shown by Lin et al [8] and Landahl [7], linearization of the governing equations of unsteady transonic flow is possible, if the unsteady effects take place sufficiently fast i. e. if the frequency is sufficiently high. Unsteady transonic cascade flows have been studied in this limit by Surampudi and Adamczyk [12].
However, the interaction between steady and unsteady contributions to the flow field is significant for the prediction of unsteady phenomena in many cases of practical importance. These interaction effects are retained to some extent if time linearization of the governing equations is carried out. To this end it is assumed that the unsteady disturbances of the field quantities are small compared to the quantities characterizing the steady flow field governed by nonlinear equations. As in the case of purely linear theory, the unsteady perturbations satisfy linear differential equations. The coefficients entering these equations vary with the spatial coordinates, however [14].
One of the important features of transonic flows is the occurrence of different length scales associated with the variation of the field quantities in longitudinal and lateral direction i. e. the distance in the direction of the flow required for the change of a field quantity by a certain amount is much less than the distance in lateral direction required for the same change. This suggests that singular perturbation theory may be useful to obtain approximate solutions for transonic flow through cascades. As shown by Messiter and Adamson [9] for the case of steady transonic flow, application of the method of matched asymptotic expansions leads to a decomposition of the flow field into several subregions which can be studied separately. Apart from the substantial simplification of the original problem a much deeper insight into the physical phenomena involved is gained in this way. Specifically, Messiter and Adamson [9] found that the field quantities in regions between airfoils are governed by equations for one-dimensional flow in a first approximation if thickness, camber and angle of incidence of the blades are small. Moreover, for a particular range of these parameters the velocity perturbations satisfy linear equations ahead of and behind the cascade. Based on these investigations and the studies of Messiter and Adamson [10] dealing with unsteady channel flow, a small perturbation theory for the treatment of unsteady transonic flow through oscillating cascades will be developed. As it will turn out, the decomposition of the flow field into several subregions holding in case of steady flow only applies if the frequency of the oscillation is sufficiently low. However, results from the investigation of unsteady channel flow indicate that interesting phenomena, such as motion

of shocks through the whole channel and formation of shocks in the channel region occur in this parameter range.

2 Problem formulation

We consider disturbances caused by an oscillating two-dimensional cascade which is placed into a uniform stream slightly below or above the speed of sound, Fig.1. The flow medium is a perfect gas with constant ratio γ of the specific heats. It will be assumed that the thickness δ, the camber δ_c, the amplitude $\tilde{\delta}_b$ of the plunging motion nondimensional with the chord length $\tilde{c}$, the angle of incidence α and the amplitude $\tilde{\alpha}_p$ of the pitching motion are small compared to one. Since viscous effects are neglected and shock waves are weak, the field quantities can be expressed in terms of the velocity potential $\tilde{\Phi}$ to the order considered.
Introducing the nondimensional variables

$$x = \frac{\tilde{x}}{\tilde{c}} \, , \; y = \frac{\tilde{y}}{\tilde{c}} \, , \; \tau = \tilde{\omega}\tilde{t} \, , \; u = \frac{\tilde{u}}{\tilde{a}^*} \, , \; v = \frac{\tilde{v}}{\tilde{a}^*} \, , \; \Phi = \frac{\tilde{\Phi}}{\tilde{a}^*\tilde{c}} \, , \; k = \frac{\tilde{\omega}\tilde{c}}{\tilde{a}^*} \, , \qquad (1)$$

where $(\tilde{x}, \tilde{y})$, $\tilde{t}$, $(\tilde{u}, \tilde{v})$, $\tilde{a}^*$, $\tilde{\omega}$ and k denote Cartesian coordinates, the time, the velocity components, the critical speed of sound, a characteristic frequency and the reduced frequency, respectively, the gasdynamic equation can be written in the form

$$k^2\Phi_{\tau\tau} + grad\,\Phi\,grad\left[2k\Phi_\tau + \frac{1}{2}(grad\,\Phi)^2\right] - a^2\Delta\Phi = 0 \, . \qquad (2)$$

Here the speed of sound is given by

$$a^2 = (\gamma - 1)\left[\frac{\gamma+1}{2(\gamma-1)} - k\Phi_\tau - \frac{1}{2}(grad\,\Phi)^2\right] \qquad (3)$$

The boundary conditions at the blade surface $y=h^*(x,\tau)$ requires, (Fig.1)

$$\Phi_y(x, h^*, \tau) = k\frac{\partial h^*(x, \tau)}{\partial \tau} + \Phi_x(x, h^*, \tau)\frac{\partial h^*(x, \tau)}{\partial x} \qquad (4)$$

Vortex sheets caused by the time dependence of the circulation around blades are assumed to emanate from the trailing edges. Hence, the difference of the pressure disturbances between the upper and lower surface of a blade vanishes as the trailing edge is approached and the velocities remain finite (unsteady Kutta condition, see e. g. [3]). Furthermore, appropriate jump relations across moving shocks [5] and the radiation condition [4], pp418, have to be satisfied. The jump relation across vortex sheets is found to be

$$\left[\left[k\Phi_\tau + \frac{1}{2}\left(grad\,\Phi\right)^2\right]\right] = 0 \, . \qquad (5)$$

We consider the two-dimensional cascade to be an idealization of a three-dimensional stage. Hence, the flow field is assumed to repeat itself in $\tilde{x}$-direction after N_b blades of the rotor or stator, (Fig.1). Since the spatial period can be smaller, however, it is defined by an effective number of blades N_θ.
Using the definition of the reduced frequency (1) and choosing $\tilde{c}=0.1m$ for the chord length and $\tilde{a}^*=300m/sec$ for the critical speed of sound yields $k=0.4$-2.1 for vibrations of the airfoils with natural frequencies of 200 to 1000Hz [1], pp236, and $k=0.2$ for the passage of sound waves with a frequency of 100 Hz through the cascade. The periodic pressure changes associated with the relative motion of the rotor and stator cascades are equivalent to $k=9.4$ based on a circumferential velocity of 450m/sec, a blade spacing of $\tilde{b}=0.1m$ and transonic relative-velocities in the stages.

In the following and throughout the the rest of the paper we shall consider uniform flow with a free stream Mach number M_∞ slightly below or above one which is perturbed by a cascade of thin airfoils performing oscillations of small amplitude. As a consequence, parameters small compared to one represent the difference between the speed of sound and the velocity of the free stream and the magnitudes of all other disturbances. Hence, the velocity potential $\tilde{\Phi}$ can be written in the form

$$\Phi = x + \varphi \, . \qquad (6)$$

With the exception of small regions centered at the leading and trailing edges of the blades the derivatives $|\varphi_x|$, $|\varphi_y|$ and $|\varphi_\tau|$ of the disturbance potential φ are small compared to one.
Inserting eq.(6) into Eqs.(2) to (5) yields the approximation

$$k^2 \varphi_{\tau\tau} + 2k\varphi_{x\tau} + (\gamma + 1)\varphi_x \varphi_{xx} - \varphi_{yy} + \ldots = 0 \qquad (7)$$

to the gasdynamic equation. The boundary conditions reduce to

$$\varphi_y(x, h^*_{u,l}, \tau) = k\left[\delta_b \frac{dg_b(\tau)}{d\tau} - (x - x_p)\hat{\alpha}_1 g_p(\tau)\right] + (1 + \varphi_x)\left[-\hat{\alpha}_1 g_p(\tau) + \delta \frac{df_{u,l}(x)}{dx}\right] + \cdots \quad (8)$$

$$h^*_{u,l} = \delta_b g_b(\tau) - (x - x_p)\hat{\alpha}_1 g_p(\tau) + \delta f_{u,l}(x) + \cdots$$

Indices u, l are used to characterize the upper or the lower surface of an airfoil. The time dependent functions $g_b(\tau)$ and $g_p(\tau)$ describe the plunging and the pitching motions of the airfoils. The jump relation across vortex sheets simplifies to

$$[[k\varphi_\tau + \varphi_x + \frac{1}{2}|grad\,\varphi|^2]] = 0 \qquad (9)$$

The jump relations across shocks have to be transformed accordingly, but will not be needed in the following.

3 Flow field structure for low reduced frequency

To simplify the discussion of the asymptotic flow structure it is useful first to specify the relative orders of magnitude of the relevant perturbation parameters $|1-M_\infty^2|$, δ, $\hat{\alpha}_p$ and δ_b. To this end the modified perturbation potential φ^+ accounting for the different orders of magnitude of the velocity disturbances and the different length scales in the various subregions is defined in the form

$$\varphi(x, y, \tau) = \mu^+ \varphi^+(x^+, y^+, \tau) + o(\mu^+) \qquad (10)$$

where

$$x^+ = \beta_1^+ x, \quad y^+ = \beta_2^+ y, \quad \mu^+ \ll 1.$$

The parameters β_1^+, β_2^+ and μ^+ have to be chosen such that $\varphi_{x^+}^+$, $\varphi_{y^+}^+$ and φ_τ^+ are O(1) in the region under consideration. Inserting eq.(10) into eq.(7) yields

$$\mu^+ k^2 \varphi_{\tau\tau}^+ + \mu^+ \beta_1^+ 2k\varphi_{x^+\tau}^+ + \mu^{+2}\beta_1^{+3}(\gamma+1)\varphi_{x^+}^+ \varphi_{x^+x^+}^+ - \mu^+ \beta_2^{+2}\varphi_{y^+y^+}^+ = 0 \qquad (11)$$

Without loss of generality the boundary condition (8) and the jump relation across vortex sheets (9) can be written as

$$\mu^+ \beta_2^+ \varphi_{y^+}^+(x^+, h^*_{u,l}, \tau) = k\delta G^+(x^+, \tau) - \hat{\alpha}_p g_p(\tau) + \delta\beta_1^+ \frac{df_{u,l}(x^+, \beta_1^+)}{dx^+} \qquad (12)$$

$$k[[\varphi_\tau^+]] + [[\beta_1^+\varphi_{x^+}^+ + \cdots]] = 0 . \qquad (13)$$

where

$$\hat{\alpha}_p \quad k\hat{\alpha}_1 \quad \delta .$$

As indicated by eq.(12), the locations of the pivots of the airfoils have no first order influence on their unsteady aerodynamic response to the pitching motion if $k \ll 1$. The representation of the perturbation potential φ^+ given by eq.(10) is appropriate for the discussion of the channel region but has to be modified according to

$$\varphi(x, y, \tau) = \frac{(M_\infty^{*2} - 1)}{\beta_1^+} x^+ + \mu^+ \varphi^+(x^+, y^+, \tau) + o(\mu^+) . \qquad (14)$$

in the flow regions upstream and downstream of the cascade. M_∞^* denotes the Mach number of the free stream based on the critical speed of sound. As pointed out earlier, it is one of the aims of the present study to identify ranges of the perturbation parameters such that the flow outside the channel region is governed by linear equations. The requirement that the transonic similarity parameter $\chi = (1-M_\infty^2)/[(\gamma+1)\delta M_\infty^2]^{2/3}$ is large compared to one then yields immediately

$$\delta^{2/3} \ll |1 - M_\infty^2| . \qquad (15)$$

Of course, the characteristic streamwise length scales in the channel regions and
outside the channel are O(1). It will be assumed that the distance between the blades is
comparable with the chord length. As a consequence, the lateral length scale in the
channel region is O(1) too, while it is $O(|1-M_\infty^{*2}|^{-1/2})$ in the regions upstream and down-
stream of the channel region. Furthermore, the v-component of the velocity is of the
same order of magnitude in the whole flow field. Hence, the u-disturbances in the regi-
ons between the blades are much larger than those elsewhere. This indicates that addi-
tional regions centered at the leading and trailing edges of the blades, where the u-
perturbations change their orders of magnitude, have to be included to obtain the
complete flow structure. Since the lateral length scale in these transition regions is
O(1) the streamwise length scale is much smaller and $O(|1-M_\infty^{*2}|^{1/2})$. Finally, a more
detailed analysis indicates that the regions upstream and downstream of the transition
layers have to be devided into near and far fields.
Inspection of the jump relation (9) holding across the vortex sheets emanating from the
trailing edges of the blades shows that

$$\ldots \quad O\left(\ldots\right) \ldots$$

Here μ characterizes the amplitude of the unsteady velocity perturbations in the channel
region, eq.(10). Since the vortices forming the vortex sheets are convected downstream
approximately with the free stream velocity the appropriate length scale in the
streamwise direction entering the equation for the perturbations caused by these sheets
is O(1/k).
The different scalings of the coordinates and the field quantities outlined so far can
be formulated most simply if the parameters β_1^+, β_2^+ and μ^+ holding in the various
subregions of the flow field are expressed in terms of one reference parameter which
will be chosen as

$$\ldots \quad 1 \quad M_\infty^{*} \quad \ldots$$

Owing to the condition (15) the flow in the far field regions is governed by linear
equations. Imposing the additional requirement that the field quantities in the regions
between the blades satisfy the equations for one-dimensional unsteady flow one obtains

$$\ldots \quad O\left(\ldots\right) \ldots$$

Insertion of expansions (10), (14) and appropriate generalizations holding in the tran-
sition layers into the governing equations (e. g. (11), (12), (13) for the channel flow
region etc.) taking into account eqs.(15) and (16) finally leads to the sets of parame-
ters β_1^+, β_2^+ and μ^+ listed in table 1.

region	β_1^+	β_2^+	μ^+	
channel	1	1		
entrance, exit		1		
near field	1	1		
far field				
pressure waves	1			
vortex sheets		1		

Table 1: Coordinate stretchings and orders of magnitude of the velocity disturbances in
the various regions of the asymptotic flow structure.

It should be noted that these results remain unchanged if the governing equations
holding in the channel region are further simplified as summarized in table 2.

δ	δ	k	flow characterisation for the channel region
$O(\varepsilon^{+2})$	$O(\varepsilon^{+2})$	$O(\varepsilon^{+})$	nonlinear
$O(\varepsilon^{+2})$	$o(\varepsilon^{+2})$	$O(\varepsilon^{+})$	time-linearization
$O(\varepsilon^{+2})$	$O(\varepsilon^{+2})$	$o(\varepsilon^{+})$	quasisteady
$o(\varepsilon^{+2})$	$o(\varepsilon^{+2})$	$O(\varepsilon^{+})$	linear

Table 2: Properties of the flow inside the channel region for various parameter ranges.
δ.....thickness or angle of incidence
δ ....amplitude of the pitching oscillation $\tilde\alpha_p$ or $k\tilde\delta_b$ of the plunging oscillation.

Following Messiter and Adamson the perturbation parameter ε is defined as

$$ h \quad h \quad O(\cdot) $$

The asymptotic expansions of the field quantities holding in the various regions of the flow field are found to proceed in powers of $\varepsilon^{1/2}$ and powers of $\varepsilon^{1/2}$ multiplied by $\ln\varepsilon$ [6]. In passing we mention that the description of the flow in terms of these expansions requires, in addition, the introduction of suitably chosen coordinate systems which reflect the geometric properties of the flow structure, Fig.1. A more detailed description of these coordinate systems is given in [6] and [9].
Finally, two consequences of the choice of the reference quantities and the assumptions leading to the results discussed in this section should be pointed out. First, using the airfoil chord as the reference length requires the effective period of the cascade $N_e d$ to be $O(1)$. Second, due to cumulative effects associated with the description of wave propagation phenomena by linear differential equations the far field solutions are not uniformly valid at large distances from the cascade. Preliminary considerations indicate that the range of validity of the asymptotic theory in its present form can be extended in both cases using the method of multiple scales. However, detailed calculations have not been carried out so far.

4 Time linearization for cascades of flat plate and double circular arc airfoils performing pitching oscillations

The upper and lower surfaces of the blades are given in the form

$$ \cdots $$

It is assumed that the blades of the cascade perform harmonic pitching oscillatons about their mid chord points with equal phase shift σ between adjacent blades. The angle of incidence of the cascade in steady flow is chosen such that there is no flow around the leading edges. As a consequence, the solution to the transonic small disturbance equation governing the flow in the entrance and exit regions reduces to that of uniform flow [9]. So far, the case of shock-free flow in the channel region has been studied. Work dealing with the effects of shock waves on the flow in these regions is in progress. Finally, the following discussion of the flow properties will be restricted to the leading order terms of the asymptotic expansions for the field quantities which exhibit the same frequency as the pitching motion. Owing to the nonlinearity of the governing equations terms depending on multiples of the driving frequency occur if higher order.
According to the results listed in table 2 the concept of time linearization applies if $\alpha\,O(\varepsilon^2)$, $\delta\,O(\varepsilon^2)$, $k\,O(\varepsilon)$ and $\tilde{a}_p\,O(\varepsilon^{1/2})$. Introducing the expansions of the velocity potential for the various regions into the governing equation (7), the boundary condition (8) and, if necessary, the jump relation across vortex sheets (9) yields the steady and unsteady problems for these regions. Since the steady problems have been discussed extensively in [9] it suffices to concentrate on the calculation of the unsteady disturbances.

Channel region

The first unsteady terms of the expansion for the perturbation potential are governed by inhomogeneous wave equations with coefficients depending on the leading order steady velocity distribution. Since the speed of downstream propagating waves is infinite in terms of the scaled time, solutions to this equations depending on the spatial coordinates describe upstream propagating waves. Exploiting the fact that field quantities are harmonic functions of time finally leads to a set of ordinary differential equations.

Entrance region

Even upstream propagating waves pass the entrance region in a time interval which is asymptotically small. Similar to [9], solutions to Laplace's equation governing the first order unsteady perturbation potential can be found using a Schwarz-Christoffel mapping. As in case of steady flow source eigensolutions [13], pp52, have to be added to this solution. The Poisson equation governing the higher order terms can be solved using the complex characteristics of Laplace's equation. The first order velocity disturbance is found to contain the well known leading edge singularity. To remove this nonuniformity it would be necessary to consider an additional asymptotic expansion holding in small neighborhoods of the leading edges.

Exit region

Solutions to the equations for the terms of the expansions of the perturbation potential
can be obtained in a similar manner as in case of the corresponding problems for the
entrance region. Since the Kutta condition has to be satisfied, there is no flow around
the trailing edges of the blades, however

Near and far field ahead of the cascade

Matching of solutions valid in the near fields and that valid in the far field yields
the boundary condition for the homogeneous wave equation governing the first order
unsteady potential in the far field. A solution can be derived from that of the classical linear wave equation for subsonic flow (see e.g. [4], pp418). Source singularities
representing the flow around the leading edges, have to be taken into account. Solving
the wave equation using the method of separation of variables yields the condition for
acoustic resonance

$$ \ldots $$

in agreement with the results given by Boles and Fransson [12].

Near and far field behind the cascade

Solutions can be found in a similar manner as in case of the corresponding problems for
the regions ahead of the cascade. Since the Kutta condition is satisfied there is no
flow around the trailing edges.

The solutions holding in the various subregions discussed so far contain a number of
arbitrary constants and functions which have to be determined by matching. Owing to the
Kutta condition the solutions valid in the near fields and that valid in the far field
behind the cascade are completely specified and thus serve as the starting point of the
matching procedure.
Starting from the far field solution behind the cascade the exit, channel, entrance and
the far field solution ahead of the cascade are determined. Composite solutions can be
constructed in various ways to yield smooth distributions of the field quantities at the
upper and the lower surface of the blades. The following procedure was applied to obtain
the pressure/velocity distributions presented in this paper. A composite solution for
the upper side valid in the interval 0<x<d was found by adding the corresponding
solutions holding in the relevant entrance and near field subregions (i.e. 1, region 2,
4, 7) and subtracting the common parts. Similarly, a composite solution for the interval
d<x<1 was constructed using the entrance, the channel and the exit solutions. The same
procedures yielded composite solutions for the intervals 0<x<d and d<x<1 at the
lower blade surface. For small but finite values of the perturbation parameter ε, however, the composite solutions calculated at x=0, x=d, x=1-d and x=1 do not agree with
the corresponding entrance and exit solutions. Hence, small jumps in the pressure/velocity distributions occur at these points.

5 Results

The evaluation of the analytical results was carried out at equally spaced points in the
intervals 0<x<d, d<x<1 for the upper blade surface and 0<x<1-d, 1-d<x<1 for the lower
blade surface. Cubic splines were used for interpolation and calculation of the
difference between the values of the pressure coefficient

$$ \ldots $$

at the upper and lower surface of the blades [6].
Pressure distributions for the case of steady flow are depicted in fig.2, results for
the superimposed unsteady pressure perturbations are summarized in figures 3 to 10.
As expected, the magnitudes of the unsteady pressure distributions at the blade surface
strongly depend on the distance between the airfoils both for the flat plate and the
double circular arc cascades. The phase lag between airfoil oscillation and unsteady response is seen to increase substantially with frequency. Furthermore, the reduction of
the distance between the airfoils increases the influence of the steady velocity disturbances on the unsteady response. This effect diminishes rapidly as the distance increases (Figs.5 to 10) due to the small thickness of the airfoils.
Unfortunately, experimental data fitting the parameter range covered by the asymptotic
theory in its present form seem not to be available. However, some numerical results
which satisfy the basic assumptions of this theory at least approximately have been
obtained by Verdon [15]. Numerical and analytical results for 1-d=0.707, k=0.022,
depicted in fig.11, are in good agreement despite the fact that the channel region is
rather short compared to the blade length in this case. Results for the distribution of

the unsteady pressure disturbances caused by oscillations with a relatively large value
of the reduced frequency k=0.23 are displayed in Fig.12 and still satisfactory agr ent
between numerical and analytical predictions is observed. Deviations occur in the ase
lag between the oscillation of the ate and its aerodynamic response. This effect is
probably a consequence of the simplification of the flow properties in the entrance and
exit subregions where the asymptotic theory predicts an infinite wave propagation speed.

6 Concluding remarks

It has been shown that asymptotic methods can be applied successfully to study the flow
through lightly loaded, oscillating cascades at transonic conditions.

In its present form the theory outlined in this paper applies to purely subsonic flows.
However, only minor modifications are necessary to include also the case of slightly su-
personic flow. Further generalizations which should be considered concern the case of
airfoils of more general shapes at arbitrary angles of incidence and moving shock waves.
This would substantially widen the applicability of the method to engineering problems.
The developement of a theory to investigate the case of steady and unsteady disturbances
being of the same order of magnitude also seems to be possible as indicated by the
results obtained for channel flows of this type [10].

References

[1] BOLCS, A., SUTER, P.: Transsonische Turbomaschinen, G. Braun, Karlsruhe, 1986.

[2] BOLCS, A., FRANSSON, T.H.: Aeroelasticity in turbomachines -- comparison of theore
    tical and experimental results, EPFL Lausanne, 1986.

[3] CRIGHTON, D.J.: The Kutta condition in unsteady flow, Ann. Rev. Fluid Mech $\underline{17}$
    (1985), pp 411-445.

[4] FUNG, Y.C.: The Theory of Aeroelasticity, Wiley & Sons, New York, 1955.

[5] KLUWICK, A.: Zur Ausbreitung schwacher Stöße in dreidimensionalen instationaren
    Stromungen, ZAMM $\underline{51}$ (1971), pp 225-232.

[6] KOLLER, F.: Schallnahe, instationare Stromung durch Flugelgitter,
    Dissertation, TU Wien, Institut fur Stromungslehre und Warmeubertragung, 1989.

[7] LANDAHL, M.: Unsteady Transonic Flow, Pergamon Press Ltd, Oxford, 1961.

[8] LIN, C.C., REISSNER, E., TSIEN, H.S.: On two-dimensional nonsteady motion of a
    slender body in a compressible fluid, J.Math.Phys. $\underline{27}$ (1948), pp 220-231.

[9] MESSITER, A.F., ADAMSON, T.C. JR.: Transonic small disturbance theory for lightly
    loaded cascades, AIAA J $\underline{19}$, No 8 (1981), pp 1047-1054.

[10] MESSITER, A.F., ADAMSON, T.C. JR: Forced oscillations of transonic channel and
    inlet flows with shock waves, AIAA J. $\underline{22}$, No 11 (1984), pp 1590-1599.

[11] PLATZER, M.F.: Unsteady flows in turbomachines - a review of current developments,
    AGARD CP 227 (1977).

[12] SURAMPUDI, S.P., ADAMCZYK, J.J.: Unsteady transonic flow over cascade blades, AIAA
    J. $\underline{24}$, No 2 (1986), pp 293-302.

[13] VAN DYKE, M.: Perturbation Methods in Fluid Mechanics, Parabolic Press, Stanford
    1975.

[14] VERDON, J.M. and CASPAR, J.R.: A linearized unsteady aerodynamic analysis for tran-
    sonic cascades, J. Fluid Mech. $\underline{149}$ (1984), pp 403-429.

[15] VERDON, J.M.: Unsteady aerodynamics of blade rows, Paper presented at the Tenth
    U.S. National Congress of Applied Mechanics, June 16 - 20, 1986.

Acknowledgement
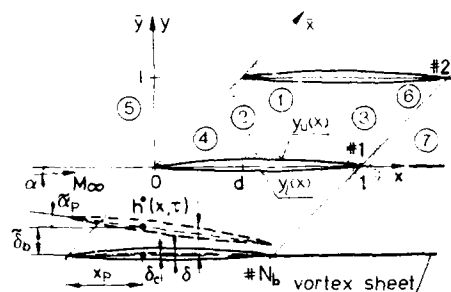
Fig 1 Two-dimensional cascade - main vortex structure of
the flow field.
1 ... channel region.
2,3 ... entrance, exit regions.
4,6 ... near fields.
5,7 ... far fields.

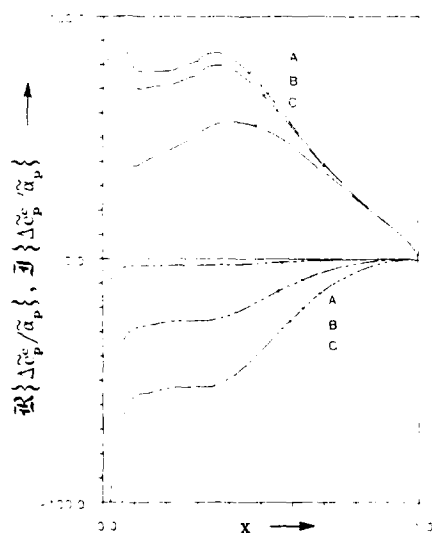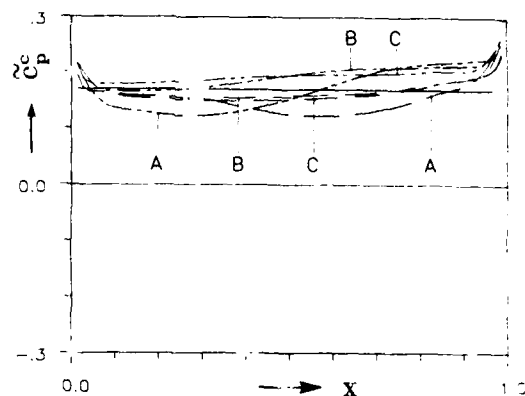Fig 2 Steady pressure coefficient at the surfaces of the
plate and double circular airfoil in a cascade with
$l = d$, $M_\infty = 0.9$, $\tau = 0.0035$, $\sigma = 0.02$. α
is chosen such that there is no flow around the
leading edge
Flat plate ——— upper, ——— lower side
D.c.a. airf. ——— upper, ——— lower side
A $l = 0.3$, B $l = 0.5$, C $l = 0.707$

Fig 3 Influence of the oscillation frequency k on the real
and the imaginary part of the unsteady pressure
difference between the upper and the lower surfa-
ces of double circular arc airfoil in a cascade with
$l = d = 0.3$, $M_\infty = 0.9$, $\tau = 0.0035$, $\sigma = 0.02$
α is chosen such that there is no flow around the
leading edge, $\tau = 180$, $\sigma = 0.0016$
——— real part, ——— imaginary part
A $k = 0.0092$, B $k = 0.092$, C $k = 0.23$
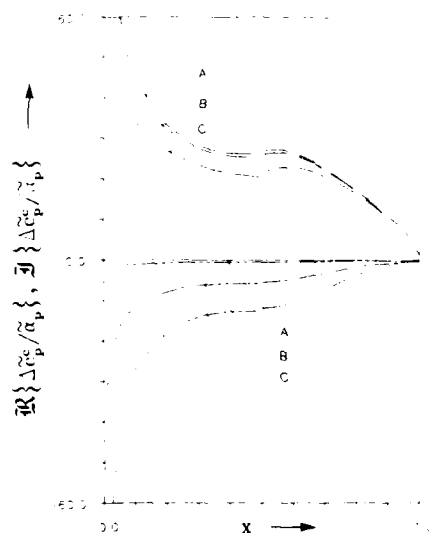
Fig 4 Influence of the oscillation frequency k on the real
and the imaginary part of the unsteady pressure
difference between the upper and the lower surfa-
ces of double circular arc airfoil in a cascade with
$l = d = 0.5$, $M_\infty = 0.9$, $\tau = 0.0035$, $\sigma = 0.02$
α is chosen such that there is no flow around the
leading edge, $\tau = 180$, $\sigma = 0.0016$
——— real part, ——— imaginary part
A $k = 0.0092$, B $k = 0.092$, C $k = 0.23$
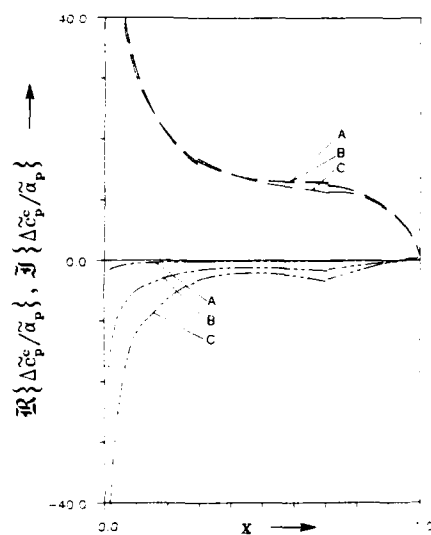
Fig.5: Influence of the oscillation frequency k on the real and the imaginary part of the unsteady pressure difference between the upper and the lower surfaces of double circular arc airfoils in a cascade with $l = d = 0.707$, $M_\infty = 0.9$, $\delta_d = 0.0035$, $\delta_s = 0.002$, α is chosen such that there is no flow around the leading edge, $\sigma = 180^\circ$, $\alpha_p = 0.0016$.
— — — real part, - - - - - imaginary part;
A: $k = 0.0092$, B: $k = 0.092$, C: $k = 0.23$.

Fig.6: Influence of the distance l between the airfoils on the real and the imaginary part of the unsteady pressure difference between the upper and the lower surfaces of double circular arc airfoils in a cascade with $l = d$, $M_\infty = 0.9$, $\delta_d = 0.0035$, $\delta_s = 0.002$, α is chosen such that there is no flow around the leading edge, $k = 0.092$, $\sigma = 180^\circ$, $\alpha_p = 0.0016$.
— — — real part, - - - - - imaginary part.
A: $l = 0.3$, B: $l = 0.5$, C: $l = 0.707$.
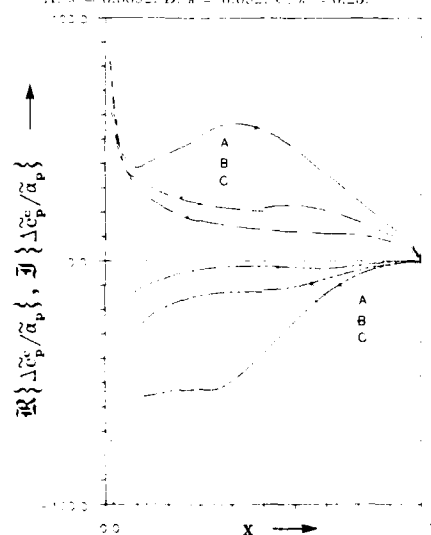
Fig.7: Influence of the distance l between the airfoils on the real and the imaginary part of the unsteady pressure difference between the upper and the lower surfaces of double circular arc airfoils in a cascade with $l = d$, $M_\infty = 0.9$, $\delta_d = 0.0035$, $\delta_s = 0.002$, α is chosen such that there is no flow around the leading edge, $k = 0.23$, $\sigma = 180^\circ$, $\alpha_p = 0.0016$.
— — — real part, - - - - - imaginary part.
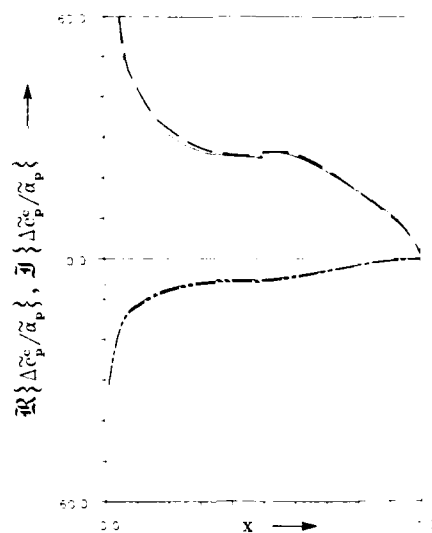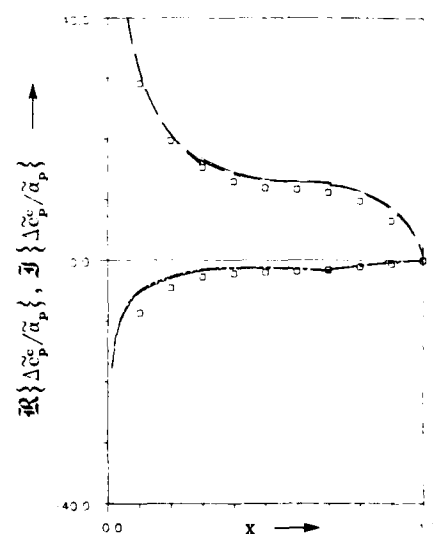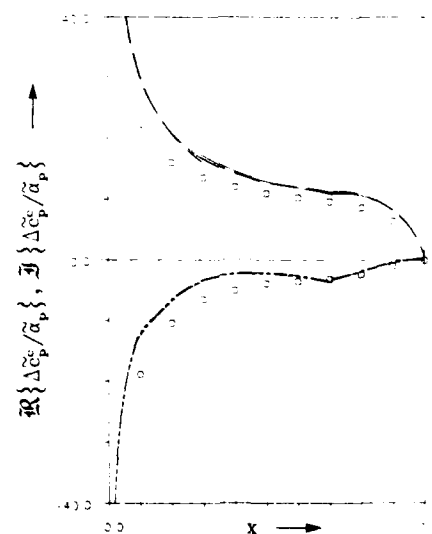A: $l = 0.3$, B: $l = 0.5$, C: $l = 0.707$.
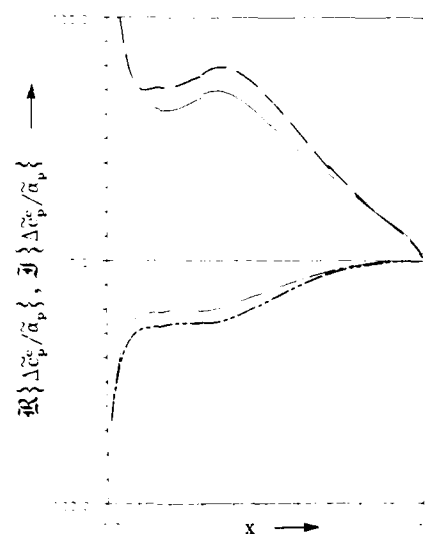
Fig.8: Real and imaginary part of the unsteady pressure difference at the surfaces of flat plate and double circular arc airfoils in cascades with $l = d = 0.3$, $M_\infty = 0.9$, $\delta_d = 0.0035$, $\delta_s = 0.002$, α is chosen such that there is no flow around the leading edge, $k = 0.092$, $\sigma = 180^\circ$, $\alpha_p = 0.0016$.
Flat plate — — real, - - - - - imaginary part.
D.c.a. airf. — — real, - - - - - imag. part.
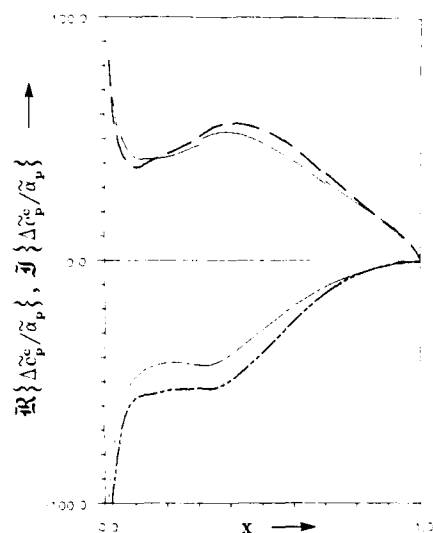
Fig.9: Real and imaginary part of the unsteady pressure difference at the surfaces of flat plate and double circular airfoils in cascades with $l = d = 0.3$, $M_\infty = 0.9$, $\delta_d = 0.0035$, $\delta_s = 0.002$, α is chosen such that there is no flow around the leading edge, $k = 0.23$, $\sigma = 180°$, $\tilde\alpha_p = 0.0016$.
Flat plate: — real, ···· imaginary part.
D.c.a. airf.: —·— real, ··—·· imag. part.

Fig.10: Real and imaginary part of the unsteady pressure difference at the surfaces of flat plate and double circular airfoils in cascades with $l = d = 0.5$, $M_\infty = 0.9$, $\delta_d = 0.0035$, $\delta_s = 0.002$, α is chosen such that there is no flow around the leading edge, $k = 0.092$, $\sigma = 180°$, $\tilde\alpha_p = 0.0016$.
Flat plate: real, imaginary part.
D.c.a. airf.: real, imag. part.

Fig.11: Real and imaginary part of the unsteady pressure difference at the surfaces of flat plate and double circular airfoils in cascades with $l = d = 0.707$, $M_\infty = 0.9$, $\delta_d = 0.0035$, $\delta_s = 0.002$, α is chosen such that there is no flow around the leading edge, $k = 0.092$, $\sigma = 180°$, $\tilde\alpha_p = 0.0016$.
Flat plate: —·— real, ···· imaginary part.
□ numerical results [15];
D.c.a. airf.: —·— real, ··—·· imag. part.

Fig.12: Real and imaginary part of the unsteady pressure difference at the surfaces of flat plate and double circular airfoils in cascades with $l = d = 0.707$, $M_\infty = 0.9$, $\delta_d = 0.0035$, $\delta_s = 0.002$, α is chosen such that there is no flow around the leading edge, $k = 0.23$, $\sigma = 180°$, $\tilde\alpha_p = 0.0016$.
Flat plate: —·— real, imaginary part.
□ numerical results [15].
D.c.a. airf.: —·— real, imag. part

EXPERIMENTS ON THE UNSTEADY FLOW IN A SUPERSONIC COMPRESSOR STAGE

W. Elmendorf

G.K. Kauke

K.D. Broichhausen

Institut für Strahlantriebe
und Turboarbeitsmaschinen
RWTH Aachen
Templergraben 55
5100 Aachen
Fed. Rep. of Germany

KHD Luftfahrttechnik GmbH
Hohemarkstraße 60-70
6370 Oberursel
Fed. Rep. of Germany

MTU München GmbH
Dachauer Str. 665
8000 München 50
Fed. Rep. of Germany

Summary

The intensity of unsteadiness in compressors strongly depends on the flow velocity and the overall pressure ratio. Thus investigations of the unsteady effects in case of supersonic flow are of great importance with regard to performance and reliability. For that purpose the unsteady flow in a supersonic compressor stage was studied in a series of experiments at the Technical University Aachen.
A review on the specially developed measuring techniques including flow visualization and the design of miniaturized semiconductor probes is given. The main features of unsteady supersonic flow in the compressor are discussed by means of characteristic experimental results.

Nomenclature

c	absolute velocity		α	absolute flow angle
Ma	Mach number		α_{max}	range of yaw angle
n/n_0	speed ratio			calibration
p	pressure		β	relative flow angle
T_p	blade passing period		κ	ratio of specific
U	voltage			heats
w	relative velocity			

Subscripts			Superscripts	
abs	absolute		$-$	time averaged value
ax	axial		$\sim$	fluctuating value
L	left		$\wedge$	behind the shock
R	right			
rel	relative			
t	total			

1. Introduction

The aerodynamic and mechanical performance of highly loaded trans- and supersonic compressors is influenced to a great extent by unsteady effects (stall and surge, flutter, excitation by blade row interaction). Referring to subsonic flow the latter subject is discussed in numerous papers, summarized for example in /1/.
For transonic and supersonic flow in compressors the data base is limited. The principles of unsteady blade row interaction at supersonic flow velocities for the first time have been investigated by the method of characteristics in /2/ for the example of flat plate cascades. The unsteady upstream effects in front of cascades are studied in /3/ by theory and experiment.

First data on the complex unsteady blade row interaction for transonic/supersonic flow in a real compressor stage are achieved by measuring the unsteady wall pressure distribution /4,5/, by optical techniques /6,7,8/, and by semiconductor probe traverses /9,10/. A theoretical approach of viscous unsteady transonic cascade flow is given in /11/. On the basis of these results the blade row interaction in transonic and supersonic compressors can be characterized as shown in Fig. 1:

- In case of supersonic relative or absolute flow velocities in the gap between the blade rows in addition to viscous effects also gasdynamic effects (shocks/expansion waves) yield unsteady blade row interaction.
- Regarding gasdynamic effects the axial Mach number is decisive for the transport of disturbances.
- For axial subsonic flow and supersonic relative (rotor) respectively absolute (stator) velocities the suction side part of the front waves and the pressure side part of the trailing edge shock system result in an unsteady influence on the neighbouring blade row.
- If the axial Mach number is supersonic, the upstream impact vanishes. In downstream direction both the suction and the pressure side trailing edge waves of the rotor interfere with the downstream stator.
- Generally the viscous effects are concentrated in the wakes of the blading, causing heavy unsteady fluctuations of the inlet shock system of the downstream blade row.

-        In addition the self excited oscillation of shock waves caused by their interaction with boundary layers and/or wakes can influence also the bow shock system and thus generate unsteady upstream effects with a frequency different from blade passing harmonics.

The present paper will give additional data and their interpretation on the unsteady effects in case of axial subsonic/supersonic relative flow in front of rotors and in case of axial subsonic respectively supersonic flow in stators.

2. Techniques of Measurement

The investigations of unsteady rotor and stator flow are performed in a compressor test rig run with an air-freon-mixture /12,13/. In the supersonic flow the visualization of density gradients is possible by means of schlieren-photography. The whole set-up of the optical arrangement applied in the test rig is shown in Fig. 2. By using a cylindrical optical system and a reflecting, polished hub the flow field in the stator is visualized. For the investigation of unsteady flow effects a stroboscopic light with a flash duration of few nanoseconds is used. The flash frequency is triggered by the rotor blades. An additional time-delay-unit allows phase angle variations, i.e. a definition of fixed relative positions between rotor and stator blading.
The main requirement for the acquisition of unsteady flow data are high response pressure transducers. The eigenfrequency of the applied semiconductor transducers (Kulite XCQ-050, XCQ-093, LQL-062 and LQL-080) is about 125 to 250 KHz. Thus, the pressure fluctuations induced by the rotor blade frequency of f_{max} = 4.2 KHz can be determined with a sufficient accuracy. In order to avoid possible errors because of the offset drift due to temperature influence, only the fluctuating part of the semiconductor signal is measured. The fluctuation quantities then are superimposed to the pneumatically measured time averaged data. The pressure transducers are implemented in the casing and in the blade surface of several stator blades (Fig. 3). Thus, the determination of pressure fluctuations is possible along the casing and the pressure and suction side of the profiles.

To perform measurements of flow angle and pressure fluctuations in the supersonic flow behind the rotor two probes have been developed. Previous investigations /14/ in case of low supersonic Mach numbers and big yaw angles showed strong interactions between the detaching stem shock and the probe head for probes with a cranked stem. This would cause an abrupt change of the probes' characteristics. To avoid this, the applied probes have been designed with a wedge type pick-up-head, Fig. 4. Pneumatic pressure taps on the lateral side of the wedge allow to adjust the probes with respect to the time mean flow. Pressure fluctuations are measured by Kulite XCQL- and LQL-transducers.

The calibration of the probes was carried out in a closed calibration channel. To increase or decrease the pressure level an additional air-compressor and a vacuum-pump are connected to the closed loop. Supersonic Mach numbers in the test section can be generated by exchangeable Laval-nozzles. Calibration tests with variation of Mach number and pressure level were performed in air and an air-freon-mixture. Due to differences of the concentration of the air-freon-mixture in calibration and compressor tests the influence of the ratio of specific heats has to be considered. Therefore, the probes' characteristics are determined directly by a theoretical description of the supersonic flow around the wedge /15/.

In the case of the total pressure probe the assumption of a normal shock in front of the total pressure tube is made. A comparison of total pressure losses calculated with basic equations for the normal shock on the one hand and measured data on the other hand shows good agreement, Fig. 5. The total pressure behind the shock remains constant over a range of $\pm$ 20° yaw angle variation.
Regarding the wedge probe for static pressure and yaw angle measurement different flow conditions have to be distinguished, depending on the direction of the flow vector (Fig. 6). Assuming the flow direction behind the shock is parallel to the wedge surface the flow turning angle β is defined as follows:

left: $\beta = \beta_{wedge} + \alpha$

right: $\beta = \beta_{wedge} - \alpha$ (β_{wedge} = 15°)

Then a division into three domains is possible (Fig. 6):

I β < 0   Prandtl-Meyer-Expansion

II   0 < β < β_{max} attached shock

III β_{max} < β < 90°   detached shock

Configurations I and II can be calculated with basic equations of supersonic aerodynamics. The third domain is approached by considering the extreme point β = 90°. For β = 90° the assumption of a normal shock is made, i.e. the pressure registered by the transducer is interpreted as the total pressure behind a normal shock. A cubic spline interpolation based on data points from configurations I and II and the extreme point β = 90° is utilized for the description of the yaw angle characteristic. Fig. 7 gives a comparison of this approach to the experimental results in air. The agreement is quite

good, the average error in yaw angle is less than 0.5°. In general, the approach gets more accurate for high Mach numbers.

The described procedure allows the calculation of the probe's characteristic for any ratio of specific heats. For the mixture of air and freon ($\kappa = 1.15$) the correspondance between calibration data and the theoretical approach was investigated in the same way. The agreement between experiment and theory is as good as was shown for the measurements in air, so the developed approach seems suitable for the description of the wedge probes' characteristic in the flow behind the supersonic rotor.

The signals of the yaw angle probe are caused by pressure and angle fluctuations. A pressure change is registered by both transducers equally independent of the angle position. According to this an alternation of the flow angle results in opposite changes of the transducer signals. To evaluate measured data the following separation of the signal into pressure-dependent and angle-dependent components is applied:

$$U_{L,R} \ (p,\alpha) = f_{p-L,R} \ (p(t)) + f_{\alpha-L,R} \ (\alpha(t))$$

$f_{p-L,R}$ only depends on pressure and is given by the static pressure calibration of the transducers:

$$U = -\frac{K_0}{K_1} + \frac{1}{K_1} p \qquad a_{0-L,R} = -(\frac{K_0}{K_1})_{L,R} \qquad a_{1-L,R} = (\frac{1}{K_1})_{L,R}$$

$$f_{p-L,R}(p(t)) = a_{0-L,R} + a_{1-L,R} \ p(t)$$

$f_{\alpha-L,R}$ is known by the yaw angle characteristic calculated in the described manner. To simplify the computation the angle characteristic is reduced to a linear function in the environment of the measured data point.

$$f_{\alpha-L,R} \ (\alpha(t)) = b_{0-L,R} + b_{1-L,R} \ \alpha(t)$$

As measurements are only carried out with respect to the time mean flow, the first coefficient vanishes. To avoid errors due to the zero offset of the transducers, only the fluctuating parts of the voltage are registered during the measurements:

$$U_{L,R} \ (\tilde{p}, \ \tilde{\alpha}) = \tilde{U}_{L,R} = a_{1-L,R} \ \tilde{p} + b_{1-L,R} \ \tilde{\alpha}$$

By linear combinations

$$\tilde{U}_L \pm \tilde{U}_R = (a_{1L} \pm a_{1R}) \ \tilde{p} + (b_{1L} \pm b_{1R}) \ \tilde{\alpha}$$

the fluctuation quantities of static pressure and flow angle are derived:

$$\tilde{p} = \frac{b_{1L} \ \tilde{U}_R - b_{1R} \ \tilde{U}_L}{a_{1R} \ b_{1L} - a_{1L} \ b_{1R}} \qquad \tilde{\alpha} = \frac{a_{1R} \ \tilde{U}_L - a_{1L} \ \tilde{U}_R}{a_{1R} \ b_{1L} - a_{1L} \ b_{1R}}$$

The resulting time dependent values are superimposed on the time averaged data. As the characteristics of both probes depend on the above calculated pressure and Mach number, the procedure is carried out as an iteration until a certain error margin is reached. The consideration of the ratio of specific heats which depends on the measured concentration in the closed freon cycle is included in this procedure.

3. Quasisteady upstream effects of rotors

A survey on the general flow pattern under discussion gives Fig. 8, showing the wall pressure distribution (superposition of the pneumatic pressure measurements and semiconductor data) upstream and in passage of the supersonic rotor. The upstream axial flow obviously is subsonic. Thus the front waves moving with the rotor in circumferential direction result in an unsteady pressure disturbance of the inlet flow.

The strong 3D-nature of this quasisteady pressure field upstream of a supersonic rotor is shown by the isobars of the unsteady portion of local static pressure in Fig. 9. These data are acquired by traverses with semiconductor probes about half a pitch upstream of the rotor. The decay of this quasisteady disturbances of the inlet flow was studied at midspan. A summary of these data is given in Fig. 10. For different axial positions at midspan in front of the supersonic rotor the amplitude of the local pressure pulsation is plotted. The rotor speed is chosen as an additional parameter. The following main features can be stated:

- The pulsations induced by the rotor front waves, as expected, decay hyperbolically in axial direction for $n/n_0 > 0.75$.
- If the rotor speed becomes lower the intensity of the pressure disturbances remains more severe moving upstream from the rotor.

- For a fixed axial position the amplitude grows reducing the rotor speed. Thus the reduction in relative Mach number and resulting drop in front wave pressure ratio is overcompensated by the detachment of the leading edge shock system and *accordingly bigger shock angles. The* most intensive fluctuations are generated at 75% speed where the relative velocities are slightly supersonic and the front waves detach remarkably from the leading edge.
- The shock induced quasisteady upstream effects for equal axial position are an order of magnitude higher than subsonic upstream interference (e.g. $n/n_0 = 0.38$).

The intensity and the losses of bow shocks are commonly modelled by 2D-approximations accounting for leading edge thickness and deviation of the stagnation streamline /16,17/. As the upstream effects of supersonic/transonic rotors are quasisteady, these models can also be applied to determine the upstream decay of pressure pulsation induced by the rotor. Comparing, however, the results with the measured data (Fig. 11) the bow shock pressure ratio computed by the 2D-method proves to be too low. Only if the 3D-nature of the bow shock (see Fig. 9) and especially the influence of the passage flow and the back pressure respectively is taken into account, i.e. a 3D or quasi 3D-computation of the whole rotor is carried out /18/, the predicted quasisteady pressure rise in the front waves meets the experimental data.

4. Experimental results of unsteady measurements behind the rotor

Rotor exit flow

As shown in Fig. 1 the interacting phenomena are reinforced considerably by trailing edge shock and expansion waves in case of supersonic exit Mach numbers. In more detail, the flow configuration in the rotor exit is clarified by means of the flow pattern in Fig. 12. In the investigated supersonic impulse-type rotor the relative flow is accelerated from inlet to exit /12/. So the trailing edge shock formation is found as in trans- and supersonic turbine cascades.

The location of the shocks results from measured fluctuating quantities downstream of the rotor. A result of these measurements is shown in Fig. 13. The distribution of the alternating static pressure in the midspan of the divergent annulus is presented. The influence of the pressure side trailing edge shock is recognizable by steep gradients. An analysis of the point of time at which the shock-induced gradients of unsteady pressure are registered (see marks in Fig. 13a) leads to the quasisteady location of the pressure side trailing edge shock (Fig. 13b). In comparison with this the suction side shocks cause small pressure gradients which are more difficult to recognize. One reason is the diminishing shock strength due to the expansion waves of the neighbouring rotor blade.

A more detailed investigation of the shock induced gradients takes place by studying the alternating parts of unsteady pressures and Mach numbers in the rotor exit at measuring position 7. In Fig. 14a the fluctuating quantities versus time related to the blade passing period of time are represented. The marks on the non-dimensional time axis indicate the position of a rotor blade.

Due to the direction of the suction side shocks the probes register first the state after the shock and then, with increasing time, the state in front of the shock. Therefore, a transient increase of the unsteady total pressure and simultaneously a reduction in amplitude of the unsteady static pressure indicates the influence of the suction side trailing edge shocks. Owing to the different geometry, the pressure side trailing edge shock causes negative gradients in case of total pressure and positive ones in case of static pressure. In Fig. 14a the zones influenced by the pressure side and the suction side trailing edge shock are indicated with "SS" and "PS".

Within the wake region, a sharp separation of the interacting boundary layer-, expansion- and shock-effects is not possible. Reference values for the shock-induced changes of the alternating pressure amplitude can be derived from the shock equations. The estimated increase of static pressure across the pressure side shock is corresponding very well with the measured gradients.

Within the wake region, a deceleration of the flow down to sonic and subsonic Mach numbers is registered. Simultaneously, local minima of the unsteady total and static pressure occur. Especially, the axial Mach number becomes subsonic. Outside of the wake region the loss of total pressure declines, the flow expands up to high supersonic Mach numbers as the angle of absolute flow increases and the angle of relative flow decreases. This can be described as a periodically unsteady starting process of the axial flow component. In order to emphasize this Fig. 14b shows the unsteady velocity triangles resulting from measured values at the numbered positions of a rotor pitch.

Unsteady stator flow

The rotor-produced inhomogeneities discussed above lead to periodical alternations of the flow quantities in the stator. To analyse these unsteady flow effects a spark-stroboscopic-schlierentechnique as well as semiconductor transducers mounted in the surface of the stator blades are applied. In the following the results of these investigations are discussed.

The photographs of the stator flow taken at design speed show the transport of the wake flow and the pulsating shock systems (Fig. 15). By means of a different phase shift of the spark release relative to the rotor blade trigger a comparison of the same stator channels in different photographs provides information about the time-dependent changes of the flow field.

In the entrance region of the stator the suction side trailing edge shocks of the rotor are marked. Because of that a geometrical assignment of the trailing edges of the rotor to the illustrated stator blades is possible. One can see that the suction side leading edge shocks of the stator are erased within the influential sphere of the wake (picture A, channel 2; B,2; D,3; E,1; E,4). Due to the higher degree of turbulence, the wake flow is recognizable within the stator channels in the more coarse structure areas on the schlieren-photographs. The transient transport of the wake flow is recognizable in channel 2 and 3 by succeeding comparison of the pictures A to E. Near the pressure side the zones of higher turbulence exist longer than near the suction side (B,2; C,2). With exception of the entrance region of the stator, the influence of the dissipative wake flow along the suction side is limited at a small sphere near the surface of the profile (E). In this area, the transport takes place in strongly accelerated flow so that with time increase, the wake flow is accelerated.

In the range of the undisturbed main flow, the suction side leading edge shocks are located within the entrance of the stator. The turning of the supersonic flow along the pressure side is caused by single shocks which are focussed in the area of the leading edge of the second blade row. Under the influence of the strong gradients in the wake flow, the shock systems are pulsating (pressure side channel 2 and 4).

Fig. 16 shows the quantitative consequences of the inhomogeneous flow in the stator inlet on the alternating profile pressure distribution. The wake induced turning of the absolute velocity vector in circumferential direction causes simultaneously occuring pressure alternations ("W") on both sides of the stator profiles at the position of the first pressure transducers (PS1 and SS1). The compression at the pressure side results in a positive gradient and the expansion around the suction side in a negative gradient of the unsteady pressure. The wake-induced increase of the pressure side shock strength and the decrease of the suction side shock strength causes a reinforcement of the pressure amplitudes. The wake-induced reduction of the absolute velocity causes pressure changes of the same amount and same gradient on the pressure and suction side of the profile. The pressure fluctuations with the same gradients on both sides of the stator blades ("S") are caused by the interactions of the trailing edge shocks of the rotor blades with the stator front shocks.

Due to inhomogeneous flow of the rotor blades the shock systems in the whole stator are stimulated to oscillations. These shock pulsations are reinforcing the unsteady pressure fluctuations in the flow field. As a result in the area of supersonic turning and in the pressure side channel between the first and the second row of the stator, the registered magnitude of the alternating pressure is clearly higher than the registered pressure changings on the suction side. This is a consequence of the steep gradients in the wake flow which are concentrated near the pressure side of the stator blades as seen in the schlieren-pictures (Fig. 15).

In subsonic flow, on both sides of the surface of the profile, the registered maximum amplitudes of the alternating pressure are nearly of the same amount (Fig. 17). With increasing Mach numbers, the unsteady pressure fluctuations grow and reach maximum values at design speed and supersonic axial Mach numbers. In the entrance region of the profiles the range of pressure fluctuations increases due to the high incidence angles.

As a result of the increasing intensity of unsteady pressure pulsations (with increasing Mach numbers) the relation between the fluctuating and mean-time values of the alternating profile-load-components increases, too. With higher supersonic Mach numbers, the maximum range of variation of the dynamic blade-load reaches the order of magnitude of the time-mean values /19/.

5. Conclusion

The main features of unsteady supersonic flow in a compressor have been discussed. In case of a supersonic relative flow the upstream effects have a strong 3D-structure. The maximum of rotor-induced upstream pressure fluctuations is found for transonic relative flows.

The downstream unsteady pressure gradients are reinforced considerably by the trailing edge shocks of the supersonic rotor. Within the wake region the axial Mach number at design speed becomes subsonic by simultaneously increasing relative flow angles and decreasing absolute flow angles. Over the whole blade-passing period a periodically unsteady starting process of the axial flow takes place. By means of schlieren-photographs the interactions of rotor trailing edge shocks and wake flow with the leading edge shocks of the stator is shown. Within the stator, the transport of the wake flow is visible. The main part of the wake flow is located near the pressure side of the stator blades. Especially in these regions the wake-induced shock oscillations reinforce the amplitude of the unsteady pressure. Along the suction side the registered pressure fluctuations are lower.

References

/1/ Gallus, H.E.: "Unsteady Aerodynamic Measurements on Rotors", AGARD AG-298, Vol. 1

/2/ Rhyming, I.: "Axiale Rückwirkung von Überschallschaufelgittern", ZAMM 37 (1957), Nr. 11/12, pp. 370 - 385

/3/ Favrat, D., Suter, P.: "Interaction of the Rotor Blade Shock Waves in Supersonic Compressors with Upstream Stator Vanes", ASME-Paper 77-GT-13, 1977

/4/ Weyer, H.B., Hungenberg, H.G.: "Analysis of Unsteady Flow in a Transonic Compressor by Means of High-Response Pressure Measuring Techniques", Unsteady Phenomena in Turbomachinery, AGARD CP-177, 1975

/5/ Gallus, H.E.: "Results of Measurements of the Unsteady Flow in Axial Subsonic and Supersonic Compressor Stages", Unsteady Phenomena in Turbomachinery, AGARD CP-177, 1975

/6/ Gallus, H.E., Bohn, D., Broichhausen, K.D.: "Measurement of Quasi-Steady and Unsteady Flow Effects in a Supersonic Compressor Stage", ASME J. Eng. Power, Vol. 99, No. 4, 1977

/7/ Dunker, R. et al.: "Redesign and Performance Analysis of a Transonic Compressor Stator and Equivalent Plane Cascades with Subsonic Controlled Diffusion Airfoils", ASME J. Eng. Power, Vol. 106, 1984, pp. 279 - 288

/8/ Hathaway, M.D. et al.: "Measurements of the Unsteady Flow Field within the Stator Row of a Transonic Axial Flow Fan, Part II: Results and Discussion", ASME Paper No. 87-GT-227, 1987

/9/ Broichhausen, K.D., Gallus, H.E.: "Analysis of the Supersonic Unsteady Compressor Flow by Means of Semiconductor Probes and Visualization Techniques", Proceedings of Symposium on Measuring Techniques in Transonic and Supersonic Flow in Cascades and Turbomachines, RD/L/N 166/79, 1979

/10/ Hathaway, M.D. et al.: "Rotor Wake Characteristics of a Transonic Axial Flow Fan", AIAA Journal, Vol. 24, No. 11, 1986

/11/ Scott, J.N., Hankey, W.L., jr.: "Navier-Stokes Solution of Unsteady Flow in a Compressor Rotor", ASME Paper No. 86-GT-226, 1986

/12/ Simon, H.: "Anwendung verschiedener Berechnungsverfahren zur Auslegung eines Überschallverdichter-Laufrades und dessen experimentelle Untersuchung", Diss. RWTH Aachen, 1973

/13/ Bohn, D.: "Untersuchung zweier verschiedener Überschallverdichterstufen unter besonderer Berücksichtigung der Wechselwirkungen zwischen Lauf- und Leitrad", Diss. RWTH Aachen, 1977

/14/ Broichhausen, K.D., Kauke, G.K., Shi, Zhi-da: "Some aspects of semiconductor probe development", Proceedings of Symposium on Measuring Techniques in Transonic and Supersonic Flow in Cascades and Turbomachines, Aachen, 1983

/15/ Elmendorf, W., Kauke, G.K.: "Semiconductor Wedge Probes for Unsteady Flow Measurement", Proceedings of Symposium on Measuring Techniques for Transonic and Supersonic Flow in Cascades and Turbomachines, Oxford, 1988

/16/ Moeckel, W.E.: "Approximate Method for Predicting Form and Location of Detached Shock Waves on Cones and Spheres", NACA TN 2000, 1950

/17/ Miller, G.R., Lewis, G.W., Hartmann, M.J.: "Shock Losses in Transonic Compressor Blade Rows", ASME J. Eng. Power, 1961

/18/ Broichhausen, K.D., Gallus, H.E.: "Theoretical and Experimental Analysis of the Flow through Supersonic Compressor Rotors", AIAA Journal, Vol. 20, No. 8, 1982

/19/ Kauke, G.K.: "Untersuchungen zur Nachlaufwechselwirkung im Tandemleitrad einer axialen Überschallverdichterstufe", Diss. RWTH Aachen, 1986
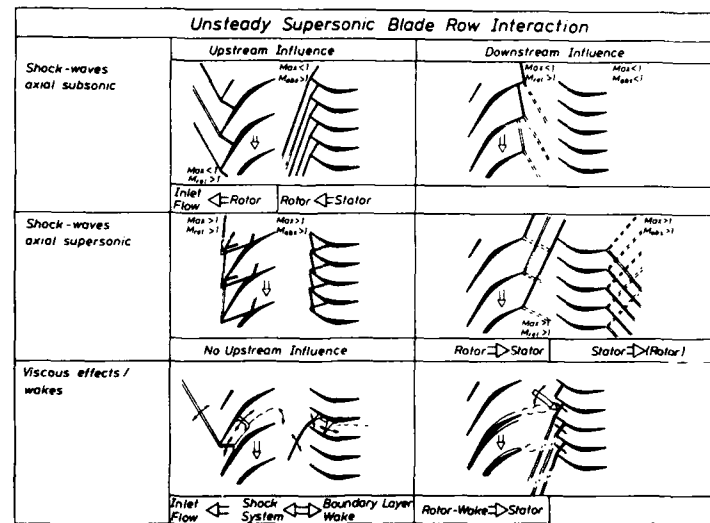
Fig. 1: Blade row interaction in transonic
and supersonic compressors
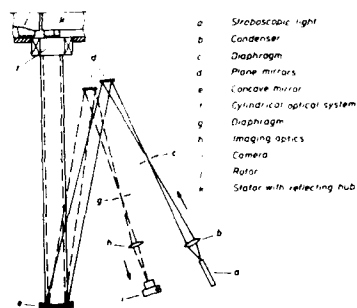
Fig. 2: Set-Up of schlierenoptical
arrangement

a Stroboscopic light
b Condenser
c Diaphragm
d Plane mirrors
e Concave mirror
f Cylindrical optical system
g Diaphragm
h Imaging optics
i Camera
j Rotor
k Stator with reflecting hub

Fig. 3: High response pressure
transducers mounted in the
blade surface
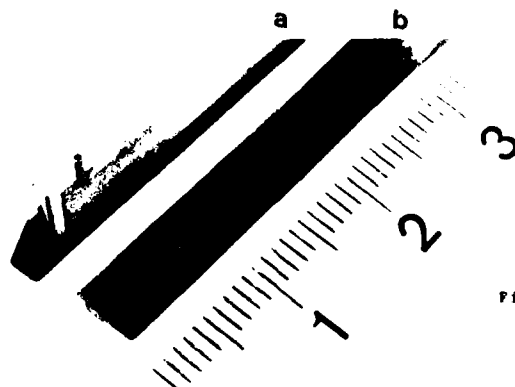
Fig. 4: Semiconductor wedge probes
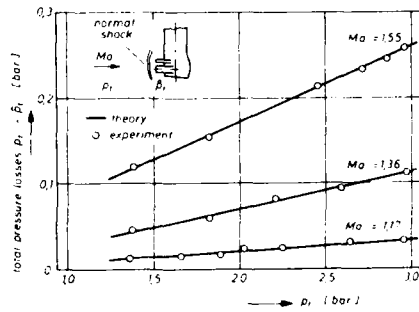a) total pressure probe
b) probe for static pressure and
yaw angle measurement

Fig. 5: Comparison of total
pressure losses
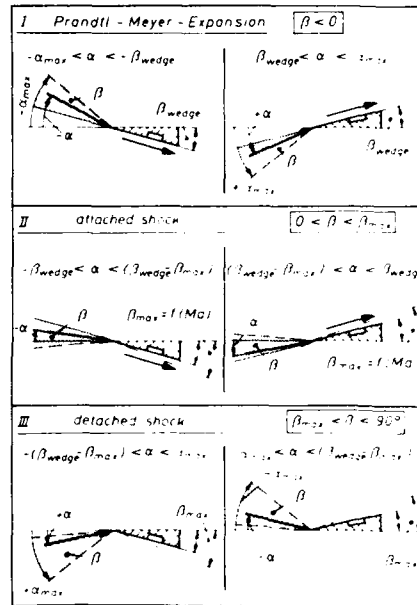
Fig. 6: Flow conditions around
the wedge
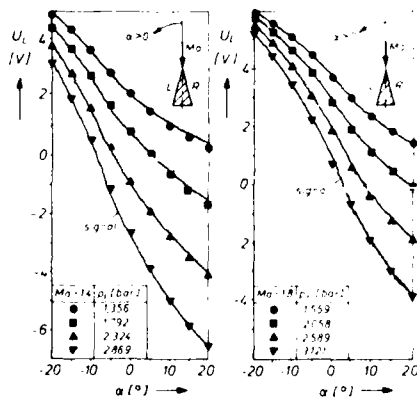
Fig. 7: Comparison of experimental data
and theoretical approach

Fig. 8: Unsteady wall pressure
distribution
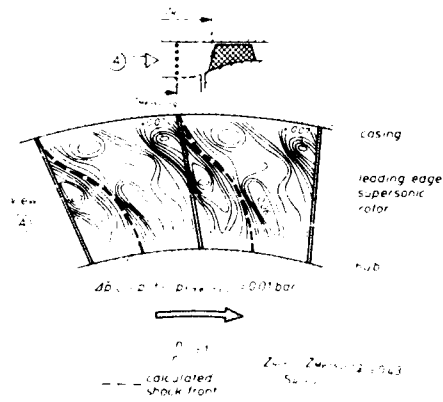
Fig. 9: Unsteady pressure field
upstream of the supersonic
rotor
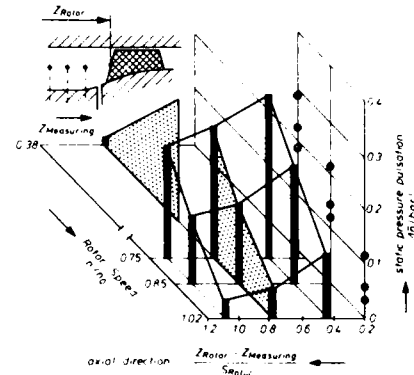
Fig. 10: Amplitudes of pressure pulsation
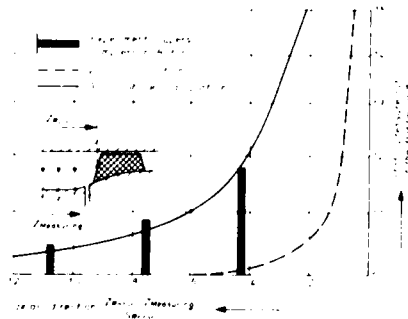
Fig. 11: Comparison of theoretical
and experimental results
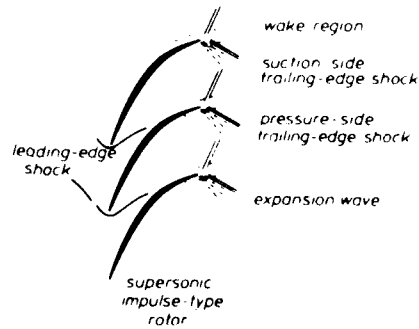
Fig. 12: Flow pattern of the trailing
edge shocks and expansion waves
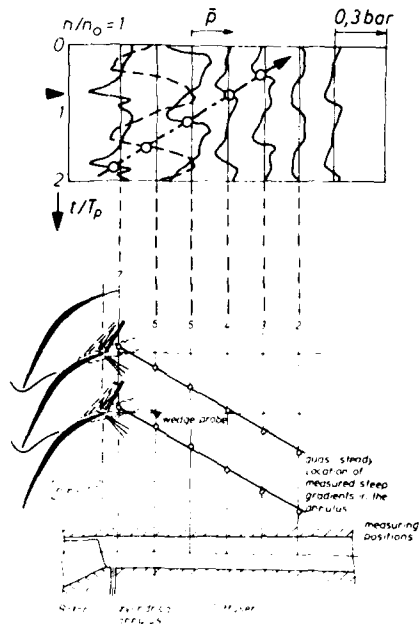
Fig. 13a: Unsteady static pressure
pulsations downstream of
the rotor

Fig. 13b: Location of trailing-edge
shocks downstream of
the rotor
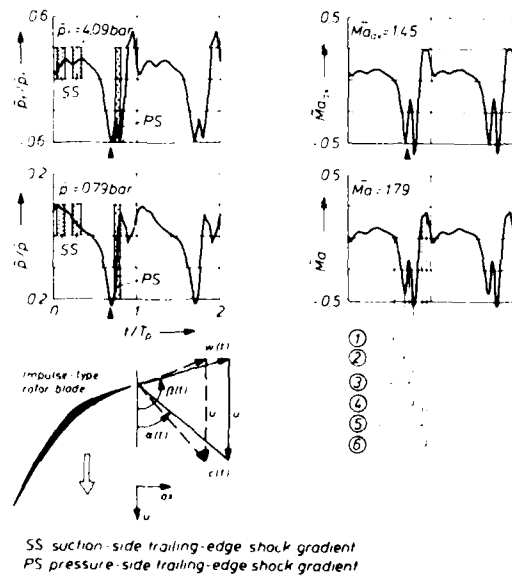
Fig. 14a: Fluctuating part of the
unsteady flow properties

SS suction-side trailing-edge shock gradient
PS pressure-side trailing-edge shock gradient

Fig. 14b: Unsteady velocity triangles
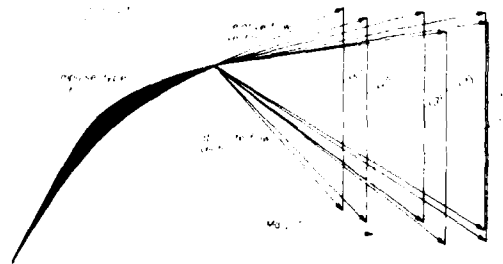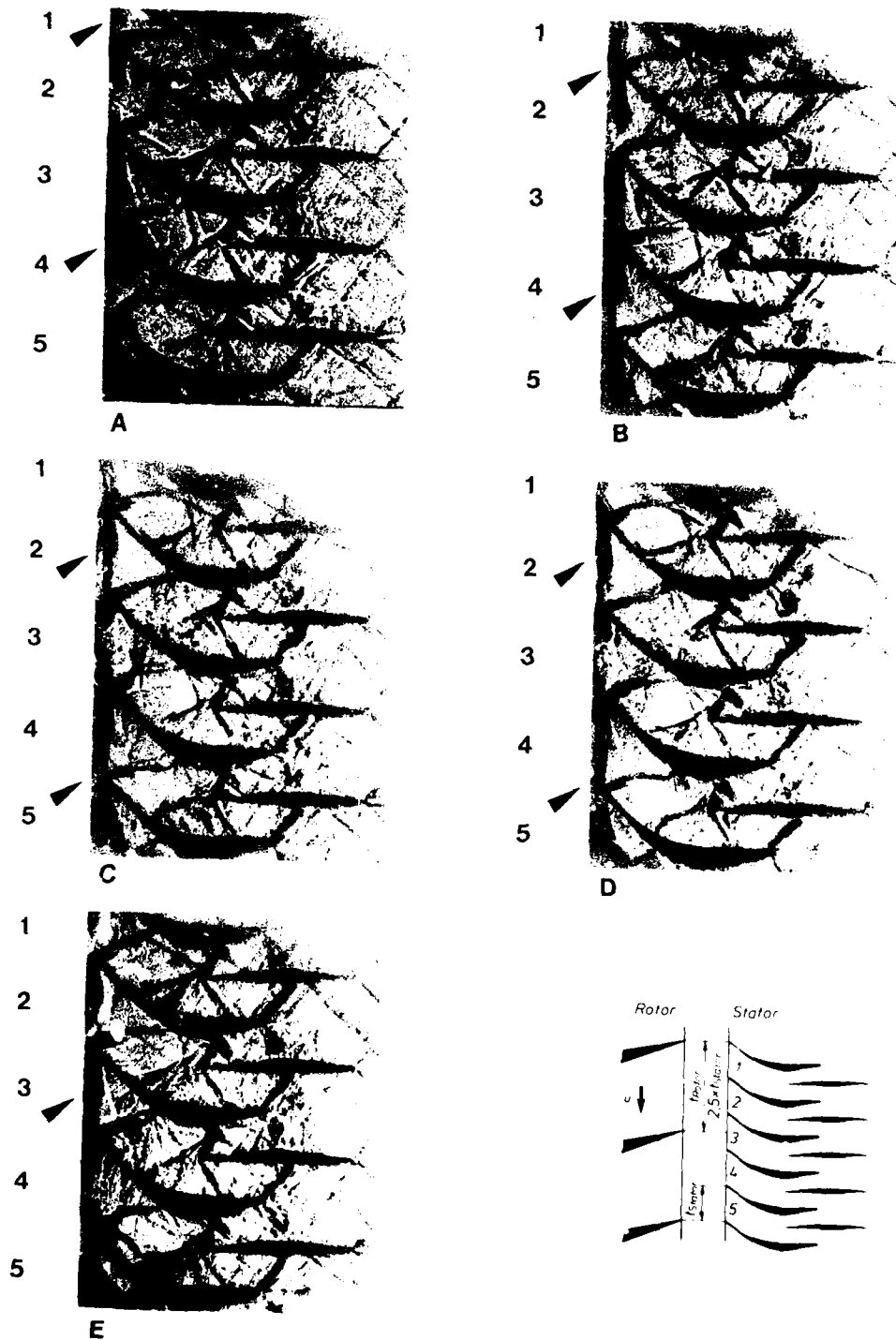
Fig. 15: Spark-Schlieren-Photographs of the
unsteady stator flow at different
rotor positions
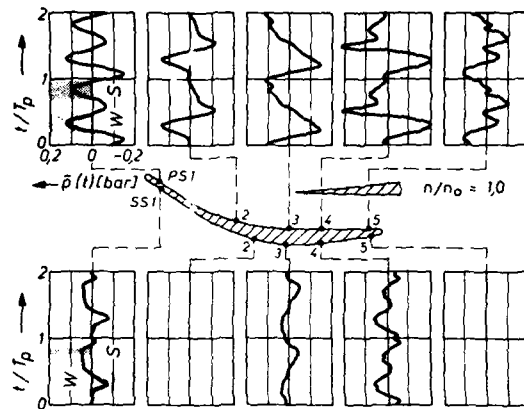
Fig. 16: Blade surface pressure fluctuations
at design speed

n/n_0	PS	SS	Ma	Ma_{ax}
1,00	●	○	>1	>1
0,83	■	□	>1	<1
0,41	▲	△	<1	<1
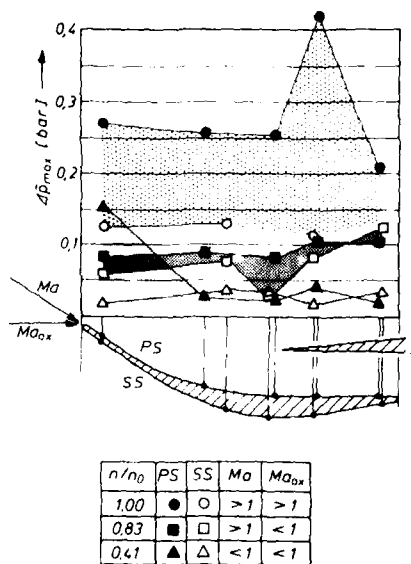
Fig. 17: Maximum range of alternating pressure

DISCUSSION

H.J. Lichtfuss, MTU, Germany

The paper shows a total pressure probe for supersonic flow and the calibration curves obtained in a calibration tunnel. Within this figure the agreement is good between measured and calibrated normal shock pressure rises. The real problem within a compressor comes from the fact that the local Mach Number is not known and the measured static pressure has to be used, which is usually of more doubt.

Author's response :

The comparison of the total pressure losses across a normal shock in front of the wedge probe results from measurements in a calibration channel, where Mach Number, total pressure and static pressure were well known.

In case of the measurements in the compressor, the information concerning the Mach Number results from the measured pressures of the second wedge probe. Thus, both probes have to be used simultaneously. More details are given in the reference.

Reference : W.Elmendorf - "Semiconductor Wedge Probes for Unsteady Flow Measurements" in Symposium on measuring techniques for transonic and supersonic flow - Oxford 1988

S.C.P. Cook - Rolls-Royce, U.K.

Question concerning the calibration of the semiconductor wedge probes: could the author state on the effect of pitch on the wedge probe calibrations and to what extent, if any, it can be believed that the actual compressor test results will have been influenced by this.

Author's response :

Due to the wedge type pick-up-head opf the probes, there is only little influence of the pitch angle in the supersonic flow. This was verified by several calibration tests. Consequently, the pitch influence on the compressor test results was neglected.

K.R.Garwood - U.K.

Could the authors state wether in the data presented for the rotor exit traverse, the stator vanes were in the correct axial pitching relative to the rotor, or had they been removed.

Author's response :

Actually the stator vanes have been removed, the measurements of the Rotor exit Flow were carried out without the stator.

MODELLING UNSTEADY TRANSITION AND ITS EFFECTS ON PROFILE LOSS

by

H.P.Hodson
Department of Engineering
Whittle Laboratory
Madingley Road
Cambridge CB3 0DY
United Kingdom

ABSTRACT

This paper considers the effects of wake interactions on the transition processes of turbomachine blade boundary layers. A simple model of unsteady transition is proposed which is then used to identify a relationship between a new reduced frequency parameter and the profile loss of a blade row which is subjected to unsteady inflow. The value of this new parameter is also used to identify the nature of the boundary layer development on the blade surfaces. The influence of other parameters on the transition process is also discussed. The model is then extended to deal with the more general case. The validity of the models is demonstrated by a comparison with a correlation of the effects of wake-generated unsteadiness on profile loss which was originally proposed by Speidel. The effects of unsteady inflow on four idealized turbine blades are considered.

NOMENCLATURE

C_x	Axial chord of current blade row	γ	Time averaged intermittency factor
p	Pitch of upstream blade row		(0=laminar; 1=turbulent)
r	Mean Radius	θ	Boundary layer momentum thickness
Re_θ	Reynolds number based on local momentum	ϕ	Flow coefficient
	thickness and free-stream velocity	ω	Radian Frequency = $2\pi/T$
s	Surface Distance	ϖ	Reduced Frequency Parameter
T	Wake Passing Period		
t	Time	*Subscripts*	
t^*	Dimensionless Time = t/T	ft	Fully Turbulent (see text)
U_b	Mean Blade Speed	l	Laminar, End of attached laminar flow
V	Free-Stream Velocity	le	Leading Edge
Y	Profile Loss Coefficient	m	End of unsteady transition zone
		max	Maximum Value of
α	Angle of trajectory of leading edge of	t	Turbulent, Start of turbulent flow
	transition zone in s-t diagrams	te	Trailing Edge
β	Angle of trajectory of trailing edge of	tr	Transition
	transition zone in s-t diagrams	x	Axial

1. INTRODUCTION

It is known that in axial-flow turbomachines the efficiency of the mid-span blade-sections can be significantly different to that of equivalent cascades which operate with steady inflow (e.g. Lopatitskii et al., 1969). It is only recently, however, that the details of the unsteady flow have received much attention.

The relative motion of adjacent blade rows in axial turbomachines gives rise to a variety of unsteady interactions. The potential influence of a blade extends both upstream and downstream. Wakes convect only downstream of the blades and their rate of decay is much less than that of the potential influence (Dring et al., 1982). In low aspect ratio machines, the secondary flow vortices also cause unsteadiness in succeeding blade rows (Binder, 1985). In transonic turbines, further interactions arise as the direct result of the impingement of the trailing shock waves on the downstream blade row (e.g., Doorly and Oldfield, 1985). Despite the increased awareness of the importance of unsteady flows very few publications (e.g. Speidel, 1957, Hodson, 1983, Tanaka, 1984, Hodson and Addison, 1988, Binder et al., 1988 and Sharma et al., 1988) have concerned themselves with the effect of unsteady flows on the overall performance of axial machines.

Wake interactions are present in all turbomachine stages. The present paper is specifically concerned with wake interactions and their effect on profile loss. A simple model of unsteady transition is presented. This is used to explain the effects of periodic unsteadiness on the profile loss of turbomachine blade rows and to highlight the most important aspects. The model is then extended to deal with the more general case. Comparisons are made between results obtained using the model and available experimental data.

2. PREVIOUS RESEARCH INTO UNSTEADY BOUNDARY LAYER DEVELOPMENT

The majority of research concerned with the impact of wake interactions on blade surface boundary layers (e.g. Walker, 1974, Hodson, 1984, Doorly, 1987, Dong 1988) has concluded that the most significant effect of the interaction is the periodic forcing of transition of the boundary layers. It is this forcing that is responsible for the changes in profile loss.

Distance-time diagrams are often used to illustrate how the state of a boundary layer varies with time over the blade surface. Fig. 1 is a distance-time diagram based on those presented by Pfeil et al. (1982), Doorly (1985), LaGraff et al. (1988), Hodson and Addison (1988), Dong (1988) Addison and Hodson (1989a) and Addison and Dong (1989) who investigated the effects of wakes on the transition process. The abscissa is the non-dimensional surface distance (s/s_{max}) while the ordinate is the non-dimensional time ($t^*=t/T$) where T represents the wake passing period. In such diagrams, a line parallel to the distance axis represents instantaneous propagation while a line parallel to the time axis indicates a stationary phenomenon. The hatched area represents the turbulent flow.

In fig. 1 the first occurrence of transition from laminar to turbulent flow which marks the creation of the turbulent patch begins not at the leading edge but at a short distance beyond the point at which the response of the boundary layer to large disturbances in the free-stream first becomes unstable (Addison and Hodson, 1989a and 1989b). Currently available data suggest that transition does not begin until the momentum thickness-based Reynolds number Re_θ exceeds a value of approximately 163, which is consistent with the known behaviour of laminar boundary layers undergoing natural transition (e.g. Abu-Ghannan and Shaw, 1980). Having formed, the turbulent patch begins to grow as is convects along the blade surface. As a consequence, the front of the turbulent patch propagates at a velocity which is of similar magnitude to that of the free-stream while the rear propagates at a speed which is much less than that of the leading edge but still in the downstream direction. Eventually, the leading edge of one patch catches up with and then merges with the trailing edge of the preceding patch thus forming a turbulent boundary layer. In several respects, these turbulent patches are equivalent to the individual turbulent spots which form during natural transition.

Table 1 lists the available data concerning propagation rates. The first six cases are concerned with the formation of individual turbulent spots. The table shows that in the majority of cases, the trailing edge of a turbulent patch or individual spot propagates at approximately half the free-stream velocity and that the quoted values vary very little. In contrast, the propagation rates of the leading edge differ considerably.

In the cascade simulations and turbomachine tests which are listed in Table 1, the leading edge propagation rate usually appears to be equal to or greater than that of the free-stream. Addison and Hodson (1989a) explain that this is because although transition is most likely to occur near the centre-line of the wake, where the turbulence is greatest, the undisturbed (i.e. laminar) part of the

Authors/Configuration/Reynolds Number/Cause of transition	V_{le}/V (Apparent)	V_{te}/V (Apparent)
Schubauer and Klebanoff, Flat Plate, Spark	0.88	0.5
Wygnanski et al., Flat Plate, Spark	0.89	0.5
Obremski and Fejer, Flat Plate, Oscillating external flow	0.88	0.58
Houdeville et al., Flat Plate, Oscillating external flow	0.89	0.48
Pfeil et al., Flat Plate, Accelerating flow, Wakes	0.75 - 0.9	0.54
Hodson et al., Single Stage Turbine rotor, Re=3.5x10^5, Individual turbulent spots	~1.0	~0.5
Doorly and Oldfield, Turbine rotor cascade, Wakes, Re=2x10^6, Ensemble averaged data	≥1.0	0.5
LaGraff et al., Turbine rotor cascade, Wakes, Re=9x10^5, Ensemble averaged data	~1.0	0.5
Addison and Hodson, Single Stage Turbine rotor, Re=3x10^5, Ensemble averaged data	·1.0	0.3
Dong, Supercrit. Compressor cascade, Re=3x10^5, Wakes, Ensemble averaged data	0.76	0.56
Addison and Dong, Supercrit. Compressor cascade, Re≈1.5x10^5, Wakes, Ensemble averaged data	>1.0	~0.5

Table 1 Comparison of Propagation Rates for Leading and Trailing Edges of Turbulent Patches in Transitional Boundary Layers

boundary layer continues to develop so that it becomes capable of undergoing transition at the lower levels of free-stream turbulence which are to be found away from the centre-line of the wakes. Simultaneously, the wake itself travels at a speed approximately equal to that of the free-stream and therefore at a faster rate than the leading edge of a conventional spot (e.g. Schubauer and Klebanoff, 1955). Thus, further spots can form ahead of the zone of influence of the single initial spot. Because the formation of spots is a stochastic process and the transition data are usually ensemble averaged, the above effects combine to produce an apparent propagation rate of the leading edges which is at least equal to the free-stream velocity. Though not necessarily a true propagation rate, the term will continue to be used for convenience. The extent to which this apparent propagation rate can exceed the free-stream velocity is dependent on the wake characteristics and Reynolds number (Addison and Hodson, 1989b). It is also more appropriate to refer to these periodically intermittent regions as transitional rather than turbulent. In the case of the trailing edge of the transitional patches, the effects mentioned above tend to cancel so that the propagation rate indicated by the ensemble averaged data corresponds more closely to that associated with the rear of a single spot.

In order to be able to predict the effect of unsteady inflow on the profile loss of compressor or turbine blade rows, it is necessary to make an estimate (in the absence of a model) of the time dependent "intermittent" state of the blade surface boundary layers. Ideally, the formation and growth rates of the individual turbulent spots which make up the transitional patches should be employed. Unfortunately, published data is not in form which allows an estimate of these parameters to be made. However, the state of the boundary layers is also related to the information presented in s-t diagrams and the analyses presented below rely on appropriate choices for the apparent leading and trailing edge propagation rates of the turbulent patches. Specifying these propagation rates is equivalent to specifying a certain combination of the average formation and growth rates of the individual turbulent spots.

3. A SIMPLE MODEL OF UNSTEADY BOUNDARY LAYER TRANSITION AND DEVELOPMENT

The results of Speidel (1957) suggest that the profile loss of a blade row is dependent on a reduced frequency which defines the character of the wake-generated unsteady flow in relation to the development of the blade surface boundary layers. The simplest model of unsteady wake-induced boundary layer transition will be used to explain why this is so.

Figs 1 and 2 are idealized surface distance-time diagrams which illustrate two possible modes of boundary layer transition. In the case of steady flow, natural transition or laminar separation takes place at a distance s_l from the leading edge. In the unsteady case, transition begins at a distance s_t from the leading edge where a turbulent and not a transitional patch begins to develop. The boundary layer state is assumed to be either laminar or turbulent. It is never intermediate between the two and transition occurs in a step-wise fashion. Thus, the hatched areas represent the turbulent flow. Fig. 1 refers to the case where the turbulent (i.e. not transitional) patches generated by successive wakes merge at a surface location s_m (points M) which is upstream of the location of steady state transition s_l. Fig. 2 corresponds to the situation when only part of the wake passing cycle contains a moving transition "point". In either case, attached laminar flow may persist up to the trailing edge when operating with stationary inflow (i.e., $s_l=s_{max}$).

The transition process will be assumed to be quasi-steady. Justification for the quasi-steady assumption may be found in the discussion by Addison and Hodson (1989b). They argued that the most important time-scales with regards to unsteady transition were those associated with the time it takes for the free-stream turbulence to diffuse into the boundary layer and the periodic time of the wake passing, which will generally be much greater than the diffusion time so that the process may be regarded as quasi-steady. Since values for the conventional forms of the reduced frequency parameter will therefore convey little or no information about the unsteady transition process, an alternative definition is required.

The coalescence of turbulent patches formed by successive wakes is related to the rate at which they grow as they move across the blade surface and the time interval between them. A new reduced frequency is therefore defined by the equation

$$\varpi = \omega \int_{s_t}^{s_l} \frac{ds}{V} \qquad (1a)$$

where ω is the frequency of the disturbances and V is the free-stream velocity. Since, in the present simplified analysis, the latter will be assumed to be constant and equal to the average value over the surface between the points s_t and s_l, eqn (1a) becomes

$$\varpi = \omega \frac{s_l - s_t}{V} \qquad (1b)$$

The reduced frequency as defined above represents the ratio of convection to periodic time-scales and relates specifically to the unsteady transition zone of the blade surface in question.

For the purposes of this simple model, it will also be assumed that the leading edge of a turbulent patch advances at the same rate as the free-stream (lines AA in fig. 1 and fig. 2) while the trailing edge lags, convecting at a rate which is one half of the free-stream velocity. Therefore, the slope of the trailing edge of each patch is twice that of the leading edge in the distance-time diagrams, i.e.

$$2 \tan \alpha = \tan \beta \qquad (2)$$

The above assumptions are equivalent to specifying a linear variation of a time-averaged intermittency function γ between the locations s_t (γ=0) and s_m (γ=1) in the case of fig. 1 and between the locations s_t (γ=0) and s_l (γ<1) with a step change to fully turbulent flow (γ=1) at s_l, in the case of fig. 2. None of the above assumptions are strictly necessary; they are made in order to simplify the analysis. The assumption of constant free-stream velocity is based on the premise that the unsteady transition zone will not occupy a large proportion of the surface length. Dring et al. (1982), Hodson (1983), Ashworth et al. (1985) have all shown that unsteady transition of this type occupied no more than 40 percent of the surface length at typical reduced frequencies in axial turbines.

For transition of the type shown in fig. 1, trigonometric considerations lead to the result that the physical length of the unsteady transition zone ($s_m - s_t$) is given by

$$1 + \tan \alpha \left[\frac{s_m - s_t}{s_{max}} \right] = \tan \beta \left[\frac{s_m - s_t}{s_{max}} \right] \tag{3}$$

so that by eqn. (2)

$$\left[\frac{s_m - s_t}{s_{max}} \right] = \frac{1}{\tan \alpha} \tag{4}$$

where

$$\tan \alpha = \frac{\omega}{2\pi} \frac{s_1 - s_t}{V} \frac{s_{max}}{s_1 - s_t} = \frac{\varpi}{2\pi} \frac{s_{max}}{s_1 - s_t} \tag{5}$$

Fig. 3 shows the results of a series of boundary layer calculations in which the laminar-turbulent transition point s_{tr} was varied from the leading to the trailing edge of a flat plate. The flat plate had a constant free-stream velocity. The ordinate in fig. 3 is the increase in profile loss above the laminar value ($Y-Y_l$) expressed as a fraction of the maximum possible change, the latter being the difference between the fully turbulent (Y_t) and fully laminar (Y_l) values. The results show that for the case of zero pressure gradient, the increment in loss varies almost linearly with the amount of surface ($s_{max} - s_{tr}$) that is covered by turbulent flow. Therefore, it will be assumed that the profile loss varies linearly with the extra amount of blade surface which is, on average, covered by turbulent flow. Evaluating the area under the curve of fig. 3 reveals that, in the case of a transition point which slowly and cyclically moves back and forth between the leading and trailing edges of the flat plate in, say, a sawtooth fashion, the above assumption leads to an error in the average additional profile loss which is equal to 4 percent of the maximum change (Y_t-Y_l).

When transition follows the pattern shown in fig. 1, the above assumptions lead to the result that the profile loss associated with the blade surface in question is equal to the average of the values which correspond to transition at the points T and M, whence

$$Y = \tfrac{1}{2} (Y_t + Y_m) \tag{6}$$

Furthermore, if transition occurs at s_1 in the absence of wakes or free-stream turbulence, then

$$Y_m = Y_t + (Y_1 - Y_t) \left[\frac{s_m - s_t}{s_1 - s_t} \right] \tag{7}$$

or

$$Y = \tfrac{1}{2} \left[2Y_t + (Y_1 - Y_t) \left\{ \frac{s_m - s_t}{s_1 - s_t} \right\} \right] \tag{8}$$

which on substitution from eqn. (2) can be rearranged to give

$$\frac{Y - Y_1}{Y_t - Y_1} = 1 - \frac{1}{2} \frac{2\pi}{\varpi} \tag{9}$$

The left-hand side of eqn. (9) represents the fractional increase in loss above the steady state value. It approaches unity when the reduced frequency becomes very large.

In circumstances which give rise to transition of the type indicated in fig. 2 and using the same assumptions as above, the profile loss coefficient is given by

$$Y = \tfrac{1}{2} (Y_1 + Y_t) (1 - \Delta t^*) + Y_1 \Delta t^* \tag{10}$$

where Δt^* represents the fraction of the wake passing cycle for which laminar flow persists at the trailing edge of the attached laminar region ($s=s_1$). Here, trigonometry and the above mentioned assumptions result in

$$(1 - \Delta t^*) = \left[\frac{s_1 - s_t}{s_{max}} \right] \tan \alpha \tag{11}$$

which, on substitution into and rearrangement of eqn. (10), gives

$$\frac{Y - Y_1}{Y_t - Y_1} = \frac{1}{2} \frac{\varpi}{2\pi} \tag{12}$$

Eqn. (9) and eqn. (12) are identical when the turbulent patches converge either at the steady state transition point ($s_m=s_1$) or at the trailing edge ($s_m=s_{max}$). This equality corresponds to the special case

$$\frac{\varpi}{2\pi} = 1 \tag{13}$$

while eqn. (12) is valid for lower values of the reduced frequency ($\varpi/2\pi \leq 1$) and eqn. (9) for higher values ($\varpi/2\pi \geq 1$). Thus,

$$\frac{Y - Y_1}{Y_t - Y_1} = \begin{cases} 1 - \frac{1}{2} \frac{2\pi}{\varpi} & : \quad \frac{\varpi}{2\pi} \geq 1 \\ \\ \frac{1}{2} \frac{\varpi}{2\pi} & : \quad \frac{\varpi}{2\pi} \leq 1 \end{cases} \tag{14}$$

where ϖ is defined by eqn. (1b).

4. SPEIDEL'S UNSTEADY PROFILE LOSS CORRELATION: A COMPARISON WITH THE SIMPLE MODEL

The generalized effects of wake-generated unsteadiness on the time-averaged profile loss of a turbine blade row have been considered by Speidel (1951,1952,1953 and 1957). A symmetrical aerofoil was tested either in a free-stream or in two different but symmetrical convergent ducts in order to create typical turbine blade surface velocity distributions. The measured distributions are presented in fig. 4. Simulated wakes from an upstream blade row were generated using a steel wire aligned with the span-wise direction 0.15 chord lengths ahead of the aerofoil. The wire had a diameter of 0.02 chord lengths; above this diameter, the profile loss of the aerofoil was shown to be independent of the size of the wire. Unsteady inflow was created by oscillating the wire in the pitch-wise direction. The amplitude of the oscillations was sufficient to ensure that the increase in profile loss was also independent of the amplitude. Since it is the turbulence in the wake that is largely responsible for the transition of the boundary layers, it is therefore unlikely that the experiment was compromised by the use of an oscillating wire. Indeed, the symmetry of the entire test configuration meant that the time-mean response of each surface of the aerofoil to the wakes was identical and that it was sufficient to measure the effects of the oscillating wire on the loss within the wake flow. The results obtained by Speidel, therefore, may be used to validate the proposed models.

Speidel found that the profile loss depended on a reduced frequency parameter which characterized the unsteady flow. He defined the reduced frequency parameter by the equation

$$\varpi_{Speidel} = \omega \frac{s_1}{V} \tag{15}$$

where s_1 is the distance along the surface from the leading edge to the end of attached laminar flow when the inflow is undisturbed, V is the average surface velocity over that length and ω is the disturbance frequency of the wakes.

Speidel expressed the fractional increase in loss as the difference between the actual profile loss Y and that with steady inflow Y_1, expressed as a fraction of the difference between a maximum value Y_{ft} and the steady state low turbulence value Y_1. He correlated this against the reduced frequency parameter $\varpi_{Speidel}$ so that the general form of the correlation

$$\frac{Y - Y_1}{Y_{ft} - Y_1} = f\left(\varpi_{Speidel}\right) \tag{16}$$

is similar to that of eqn. (14). The value of Y_{ft} in eqn. (16), which Speidel claimed was the value for fully turbulent flow, was deduced from measurements made with the wire positioned on the axis of the tunnel so that the wake continuously affected both surfaces of the aerofoil. In practice, it is unlikely that turbulent spots could have been sustained within the boundary layer close to the leading edge. However, the chord-based Reynolds numbers associated with Speidel's experiments are typically in the range from 1.6 to 3.7x10^{6} and calculations show that $Re_\theta \approx 163$ when $s/s_{max} \approx 0.05$ so that the stability point for large free-stream disturbances will be very close to the leading edge. Thus, it is not unreasonable to assume that wake induced transition effectively commences at the leading edge (i.e., $s_t \ll s_1$) so that

$$\varpi \approx \varpi_{Speidel} \tag{17}$$

and

$$Y_t \approx Y_{ft} \tag{18}$$

Thus, eqn. (14) represents a more general form of Speidel's correlation.

Fig. 5 shows Speidel's correlation together with eqn. (14) and some additional data. As the reduced frequency increases from zero, the profile loss increases (in practice, it may sometimes decrease) from the undisturbed level and asymptotically approaches a limit equal to that obtained with steady turbulent flow over the surface from s_t to s_{max}. It should be noted that in some cases, the numerator and denominator of the ordinates are produced by the subtraction of very similar numbers so that some scatter of the data is inevitable. The reduced frequencies of the majority of turbomachine blade rows will lie in the range from 0.5 to 1.0. Given the simplicity of the model proposed above and the accuracy of the experimental data, the agreement between the data and eqn. (14) is very satisfactory.

The success of the simple model in predicting the observed trends is essentially due to the recognition that the nature of the time-dependent unsteady transition, as illustrated by the s-t diagrams, dominates the generation of the additional loss. Fig. 5 confirms the significance of the reduced frequency parameter ϖ in relation to the generation of profile loss. This is because the quantity $\varpi/2\pi$ represents the ratio of the time it takes for a wake to convect across the transition zone ($s_t - s_1$) at the free-stream velocity V to the periodic time of the disturbance ($\omega/2\pi$). The agreement between the data and eqn. (14) shows that suitable choices have been generally made for the propagation rates of the leading ($V_{le}=V$) and trailing edges ($V_{te}=\frac{1}{2}V$) of the turbulent spots, the data of the present author being the major exception as will be discussed below. It is sufficient to assume that the state of the boundary layer is either laminar or turbulent.

The significance of the parameter $\varpi/2\pi$ extends beyond that indicated by eqn. (14) since its magnitude can be used to predict the unsteady nature of the blade surface boundary layers. For example, laminar separation is unlikely to occur if $\varpi/2\pi \geq 1$ (see fig. 1) and in this case, the value of $\varpi/2\pi$ dictates the length of the unsteady transition zone (see eqn. (2)). Likewise, if $\varpi/2\pi \leq 1$ (see fig. 2), then should laminar separation be predicted when the flow is steady, it is most probable that it will occur in the presence of unsteady flow. In this case, the value of $\varpi/2\pi$ determines the fraction Δt^* of the wake-passing period for which the laminar flow exists at the distance s_1/s_{max} from the leading edge (see eqn (11)). In a multistage axial flow turbine, Binder et al. (1988), Dong (1988) and Addison and Dong (1989) have observed the periodic formation and decay of laminar separations in the presence of wake interactions. If $\varpi/2\pi \ll 1$, the profile loss may be satisfactorily determined from steady state measurements or predictions.

5. THE DATA OF YURINSKIY AND SHESTACHENKO

The effects of wake-generated unsteady flow on profile loss have also been reported by Yurinskiy and Shestachenko (1974), who rotated a spoked wheel of radial, circular bars in front of a linear cascade of impulse blades. They investigated the effects of changing the axial distance between the bars and the cascade over a range of flow coefficients. The changes in axial distance resulted in differing wake strengths. The test rig was similar in principle to the later construction of Doorly and Oldfield (1985).

It is not possible to add their data to the correlation of fig. 5 because the asymptotic value Y_t is unknown. Instead, their data have been plotted in fig. 6. The abscissa is the ratio of the bar speed U_b to the isentropic expansion velocity V_{is} which, on substitution of the values quoted by the authors, is approximately one half of the ratio $\varpi/2\pi$ (i.e., $U_b/V_{is}=\frac{1}{2}\varpi/2\pi$) when $s_t=0$. Fig. 6 shows that for the range of U_b/V_{is} investigated and a given axial spacing, the additional loss due to the unsteadiness increases linearly. This is consistent with eqn. (14) when $\varpi/2\pi \leq 1$.

Unfortunately, fig. 6 also shows that the additional loss is also dependent on the axial gap between the rotating bars and the impulse cascade. The variation in gap is very large. This fact becomes particularly evident when it is noted that the inlet flow angle will be of the order of 70° (the actual value is not given). Therefore, the character of the inflow will vary from discrete wakes at the smallest gap to a virtually uniform flow, albeit with turbulence, at the largest gap. Transition correlations (e.g. Abu-Ghannan and Shaw, 1980) indicate that the critical value of the Reynolds number based on the momentum thickness of the boundary layer Re_θ is a strong function

of the free-stream turbulence level when the level is of the order of a few percent. Therefore, the effect of these changes will be to alter the position s_t at which transition first occurs. The variation of loss with axial gap, which amounts to a factor of two at a given value of U_b/V_{is} suggests a change in the maximum available transition length (s_l-s_t) of the same magnitude (see eqn. (14) for example) which is not unreasonable. These results therefore support the case that it is inadequate to assume that transition begins immediately the wakes touch the blade surface or, indeed, when Re_θ reaches a value of 163.

6. THE EFFECT OF A FINITE WAKE THICKNESS

The simple model presented above is based upon the premise that transition is periodically initiated at a point which corresponds to the centre-line of the wake. In practice, the profile of turbulence within a wake is such that near the centre-line, the intensity is relatively constant. If the wake is relatively thin, this is not important. When the wake width is large however, as it might be in L.P. turbines if gross separation of the suction surface boundary layers were to occur, it is possible that transition will not be initiated at a point in time and space but, in effect, at a point in space over a finite period in time. The length of this period, when expressed as a proportion of the periodic time, is denoted by the quantity Δw^* as shown by fig. 7. The s-t diagrams of Addison and Hodson (1989a) contain more than a suggestion of such a phenomenon.

Following the same lines as the simple analysis presented above, it can be shown that

$$\frac{Y - Y_l}{Y_t - Y_l} = \begin{cases} 1 - \frac{1}{2}\frac{2\pi}{\omega}(1 - \Delta w^*)^2 \; ; & \frac{\omega}{2\pi} \geq 1 - \Delta w^* \\[4mm] \frac{1}{2}\frac{\omega}{2\pi} + \Delta w^* \quad ; & \frac{\omega}{2\pi} \leq 1 - \Delta w^* \end{cases} \tag{19}$$

which reduces to eqn. (14) when $\Delta w^*=0$.

Eqn. (19) is plotted in fig. 8. It shows that at low reduced frequencies, the fractional increase in profile loss is equal to Δw^*, the effect being reduced when the frequency exceeds the value given by

$$\frac{\omega}{2\pi} = 1 - \Delta w^* \tag{20}$$

which also corresponds to the frequency at which the individual patches caused by successive wakes merge at the point where attached laminar flow would otherwise cease. The relationship (eqn. (20)) is plotted as a dashed line in fig. 8 and shows that the reduced frequency at which this occurs reduces in proportion to the wake thickness. Typical values of Δw^* are, as yet, unavailable but given the success of the simple correlation, they may generally be expected to be small at least at the higher Reynolds numbers found in turbomachines.

7. THE EFFECT OF A NON-UNIFORM FREE-STREAM VELOCITY: A MORE EXACT MODEL

So far, it has been assumed that the free-stream velocity is equal to the mean value over the maximum possible extent of the unsteady transition zone (i.e., $s_t \leq s \leq s_l$). In practice, the velocity may not be constant over this distance so that the turbulent wedges shown in figs. 1 and 2 are no longer bounded by straight lines. Fig. 11 shows one such example. Nor is it correct to use the form of the reduced frequency given in Eqn. (1b); the more general definition (i.e., Eqn. (1a)) will be employed below.

It has already been noted that in Speidel's experiments, turbulent flow is unlikely to have been sustained near the leading edge and that the earliest transition could have occurred would have been near $s/s_{max}=0.05$, where $Re_\theta \approx 163$. If it is assumed that this location represents the distance s_t and that s_l is equal to the values given by Speidel (1953), the data of fig. 5 can be replotted against the reduced frequency parameter as defined by Eqn. (1a) to produce the correlation shown in fig. 9. The data of Pfeil and Herbst (1979) ($s_t/s_{max}=0.14$, $s_l/s_{max}=1.0$) and the present author ($s_t/s_{max}=0.54$, $s_l/s_{max}=0.8$) are also shown. The differences between the positions of the data points in the two figures are very small, which helps to explain the success of Speidel's original correlation.

A non-uniform velocity distribution will also result in a growth rate of the laminar and turbulent boundary layers which is different to that on a flat plate in a zero pressure gradient. Fig. 10 shows the effect of changing the transition point upon the fractional increase in profile loss of the *kanal II* and *freistrahl* aerofoils. The calculations were carried out at the highest Reynolds number tested and the transition point was varied over the range shown in the figure. Unlike the case of the flat plate, the loss no longer varies linearly with the location of transition, particularly for the *kanal II* aerofoil. The results for the turbine rotor suction surface of the present author ($s_t/s_{max}=0.54$, $s_l/s_{max}=0.8$) are also shown in fig. 10. Like the *freistrahl* aerofoil, there is less variation in the free-stream velocity in this case so that the variation of loss is nearly linear. Thus, the assumption that the additional loss produced by the wake interaction is proportional to the additional area of the blade which is on average covered by turbulent flow appears to be valid for the turbine rotor and the *freistrahl* aerofoil but not for the *kanal II* aerofoil.

In order to examine the significance of a non-uniform velocity distribution, the velocities measured by Speidel (fig. 4) were used as input data to two calculation methods. The first part of each method consisted of a time-marching calculation which traced the development of adjacent turbulent patches in s-t space and so determined their shape. The time-marching calculation produces s-t diagrams such as that of fig. 11. Thus, it is possible to determine the relative proportion of time for which a boundary layer is turbulent at a given location in space, which is in effect the intermittency γ, or where and when transition begins for a parcel of boundary layer fluid which leaves the leading edge at a given time with a specified convection rate.

7.1 A strip calculation method

In the first series of calculations, the s-t space was divided into small strips of equal width in time Δt running from the leading to the trailing edge of the blade. The width Δt was sufficiently small that the final solution was independent of the size of the strip. For each strip, it was assumed that the development of the boundary layer was quasi-steady and that the rate of convection of information (the mean propagation rate) was $0.72V$, though the precise value is of little significance. Thus, a series of steady state boundary layer calculations (Cebeci and Carr, 1978) were performed for each strip using the information on boundary layer state derived from the s-t diagrams. The mean integral thicknesses of the boundary layer during its development beyond the start of unsteady transition were then determined by averaging the results obtained for all the strips.

The results obtained by this method are shown by the dotted and chain-dotted lines in fig. 9. The line for the *kanal II* aerofoil (Re = 3.6×10^6) shows that it should be significantly more sensitive to unsteady inflow than the *freistrahl* aerofoil which has a flat-topped pressure distribution. This is consistent with the trends exhibited by the experimental data though the prediction indicates a higher level of sensitivity than the data admits to. This discrepancy is not understood although the margin of error in the experimental data relating to the *kanal II* aerofoil is known to be typically of the order $\frac{1}{2}(Y_t-Y_l)$: much greater than for the other two of Speidel's test cases. Nevertheless, the model and data suggest that a correlation based solely upon the reduced frequency parameter, while indicating the general trends, is not sufficient for an accurate prediction of the effects of unsteady inflow when there is a very large variation in the free-stream velocity over the potential transition zone. Under these circumstances, it is necessary to take account of the non-linear relationship which exists between the profile loss and the location of transition. It will be shown below that the effect of a varying free-stream velocity on the shape of the turbulent patches in the s-t diagrams (i.e. the intermittency) is much less important.

In the case of the experiments conducted by Pfeil and Herbst and by Hodson, transition occurs in a region of essentially constant velocity so that the profile loss varies almost linearly with the location of the transition point along the surface over the potential transition zone. Therefore, the data of Pfeil and Herbst agree particularly well with the model. However, the model significantly underestimates the effect of unsteady inflow on the turbine rotor of the present author, a result which can be attributed to the very rapid spread of the turbulent patches (see below).

7.2 An average intermittency model

The s-t diagrams, using the same assumptions as above, may be used to specify the time-averaged intermittency of the blade surface boundary layers. The boundary layer calculation employs a differential method using an eddy viscosity derived from mixing length arguments. For a given height within the boundary layer, the eddy viscosity was determined according to the relationship

$$\epsilon_{eff} = \epsilon_{laminar} + \gamma \epsilon_{turbulent} \tag{21}$$

where γ is the intermittency determined from the s-t diagrams.

A calculation was performed for the *kanal II* aerofoil, again at a Reynolds number of 3.6×10^6. This test case was chosen again since, of those investigated, it exhibits the greatest deviation from the 'wetted area' assumption. The reduced frequency chosen corresponds to that of fig. 11. The corresponding variation of intermittency is plotted in fig. 12. It has a value of zero before the start of transition and unity after transition is complete. Over the unsteady transition zone, the variation of γ is virtually linear so that the effect of having a non-uniform free-stream velocity over the transition zone is slight.

Table 2 compares the losses predicted by the 'strip' and 'average-intermittency' models. The difference amounts to only approximately 16 percent of the fractional increase in the predicted loss.

Calculation method	$\dfrac{Y - Y_l}{Y_t - Y_l}$
Strip method	0.54
Average-intermittency method	0.63

Table 2: Comparison of predicted losses for the kanal II aerofoil for $\omega/2\pi = 0.7$

A question remains as to which of the above two methods is more appropriate. At most low reduced frequencies (say, $\omega \leq 1.0$) when, for example, separated flow or natural transition may persist for relatively long periods of time between the wakes, the quasi-steady method is clearly more applicable. The average-intermittency method denies the very existence of unsteady flow. However, at high reduced frequencies, the time-scales for turbulent diffusion will be greater than those of the wake-passing (Addison and Hodson, 1989b) so that the average-intermittency method may well be more appropriate.

8. THE INFLUENCE OF THE FORMATION AND GROWTH RATES OF THE TURBULENT SPOTS

So far, the unsteady transition process has been assumed to be periodic, with a single turbulent patch forming at a distance soon after the response of the boundary layer to large disturbances becomes unstable. The leading edge of the wedges has been assumed to propagate with the wake in the free-stream. Fig. 13 is based upon a figure presented by Addison and Hodson (1989a), who showed that the above may not always be the case; several turbulent spots may form underneath the footprint of a single wake and as a consequence, the apparent rate of propagation may be so great as to appear negative (see Table 1). The data in fig. 13 were obtained on the suction surface of a turbine rotor blade using surface mounted hot-film gauges which were calibrated for the measurement of wall shear stress. The figure shows the development of the phase-locked random unsteadiness. It indicates that turbulent flow begins near $s/s_{max}=0.45$ which is soon after $Re_\theta=163$. The latest occurrence of transition is limited by a possible laminar separation at $s/s_{max}=0.8$. The free-stream velocity is relatively constant over the specified transition zone so that the variation of loss with transition location is almost linear (see Fig. 10)

To illustrate the importance of using the correct value of the (apparent) leading edge propagation rate, the strip calculation method was applied to the profile of Hodson (and of Addison and Hodson), a variety of leading and trailing edge propagation rates being chosen. For the purpose of the calculation, due regard was given to the fact that the experimental data is ensemble averaged and that as a result, the start of transition at $0.45s_{max}$ as indicated by fig. 13 does not represent the start of fully turbulent flow within the wedges formed on the s-t diagram. Therefore, transition from fully laminar to fully turbulent flow was specified as beginning at $s_t/s_{max}=0.54$ rather than at $0.45s_{max}$.

Fig. 14 shows the results of the predictions, the information being presented in the same way as in fig. 9. For the purpose of plotting the experimental data point, the maximum and minimum values of the trailing edge momentum thicknesses are those given by the predictions. Fig. 14 shows that the increase in profile loss is a strong function of the apparent leading edge propagation rate which is in reality, a combination of the spot formation rate and the propagation rate of the individual spots. The solid line drawn over the s-t diagram of fig. 13 shows the start of transition employed by the calculation with the turbine operating at the condition corresponding to the measurements. The agreement between the prediction, based upon the measured propagation rates ($V_{le}=1.0V$; $V_{te}=0.3V$), and the measured trailing edge momentum thickness is also encouraging, although the measured value is higher than that predicted. A comparison was also made between the predictions of the strip and average intermittency methods for the turbine rotor of Hodson. The maximum difference in the integral thicknesses of the boundary layers predicted by the two methods at any point on the blade surface was insignificant.

The surface distributions of the integral parameters of the suction surface boundary layer are also available for the above test case (Hodson, 1983). Fig. 15 shows the measured variation of the momentum thickness θ and shape factor H ($=\delta^*/\theta$). The measured values for a laminar flow cascade of equivalent geometry to the turbine rotor (Hodson, 1983) are also shown. The data show that in the turbine rotor, the measured momentum thicknesses and shape factor are, respectively, higher than and lower than the cascade values. Addison and Hodson (1989a) argue that these differences suggest that the boundary layer ahead of transition is not fully laminar. Thus, an underprediction of the measured loss might be expected using the models so far described.

The average intermittency (Eqn. (21)) model was modified to take account of the facts noted above. The s-t diagram of fig. 13 was again used as a basis for the predictions but with the simple alteration that the average intermittency γ was not allowed to be lower than 0.1. The resulting surface variations of the integral parameters which correspond to the operating point of the turbine are plotted in Fig. 15. The agreement between the predictions and measured data is self evident, the further increase in trailing edge momentum thickness due to the change representing 7 percent of the predicted value. It is also noted that although the average intermittency varies almost linearly with surface distance, the shape factor falls more rapidly during the earlier stages of transition than towards the end suggesting that care must be taken when using the shape factor to represent the "state" of the boundary layer.

9. AN EXAMINATION OF FORWARD AND AFT-LOADED TURBINE BLADES

In this section, the effects of unsteadiness upon two sets of idealized turbine blades are considered at a Reynolds number of 3×10^5. The profiles have not been optimized in any way, their distributions being chosen so as to permit a simple comparison of differing design philosophies

The velocity distributions corresponding to the suction surfaces of the four profiles are shown in fig. 16. Peak suction on the

forward-loaded profiles 30L and 30H occurs at s/s$_{max}$ = 0.3 while it is found at s/s$_{max}$ = 0.5 on the aft-loaded profiles 50L and 50H. Profiles 30L and 50L have attached laminar flow over their entire surface length when the inflow is steady. They are relatively lightly loaded, the lift as defined by the line integral

$$\Gamma = \frac{1}{s_{max}} \int_0^{s_{max}} \frac{V}{V_2} ds$$
(22)

being equal to 0.925. Profiles 30H and 50H have a higher loading (Γ=0.975). As a result, laminar separation occurs at s/s$_{max}$ = 0.8 on profile 50H in the absence of wakes. For the sake of simplicity, transition in the absence of unsteady inflow was specified at this location. Laminar separation will not occur in the case of profile 30H. The location of the start of transition (Re$_\theta$=163) is also indicated in fig. 16.

The strip calculation method described above was used to calculate the trailing edge momentum thickness for each of the four profiles over a range of frequencies. Two different leading edge propagation rates (V$_{le}$=1.0V, V$_{le}$=∞) were investigated. Since the variation in velocity over the potential transition zone is relatively small, the four profiles appear to be equally sensitive to unsteady inflow when the results are plotted in a manner similar to previous figures. However, this disguises the fact that the upper (Y$_t$) and lower (Y$_l$) limits of the profile loss and the lengths of the transition zones (s$_l$ - s$_t$) of the four profiles exhibit differences. Thus, the data is presented as in fig. 17, where the abscissa represents the ratio of the convection time over the entire surface to the periodic time while the ordinate is the predicted trailing edge momentum thickness per unit lift. Usually, the abscissa will have a value in the range from 0.5 to 2.0. The loss typically rises by 50 percent over this range.

Fig. 17 shows that the forward-loaded profiles 30L and 30H respectively present a lower time-averaged profile loss than the aft loaded profiles 50L and 50H at the lower frequencies. At the highest frequencies, the opposite is true. The change-over point for the more highly loaded profiles occurs at a much higher frequency. This is because profile 50H has a higher profile loss in the absence of wakes and because it is much less susceptible to unsteady inflow since it has a shorter surface length over which unsteady transition can occur. The change-over point occurs at lower frequencies for higher values of V$_{le}$ (i.e. when rate of formation and growth of the turbulent spots is higher).

If a turbine stage has significantly more rotor than stator blades, the stator blades will tend to lie to the right of the above mentioned change-over point and the rotors to the left. In such cases, the results of fig. 17 suggest that the stator blades should be aft-loaded and that rotors should be forward-loaded. However, if laminar separation can be avoided in between the wakes, the differences between the aft- and forward-loaded profiles is relatively small. In situations where the design constraints dictate that laminar separation will occur whatever the loading philosophy, the relative insensitivity of these profiles to incoming wakes suggests that steady flow calculations may well be sufficient. This might explain the relative success of some highly loaded L.P. turbine designs.

10. FURTHER DISCUSSION

This paper has attempted to present, by modelling, the most important features of wake-induced boundary layer transition. It has been shown that a new form of the reduced frequency parameter (eqn. (1)) can be used to characterize the boundary layer development and the additional profile loss associated with the unsteady transition, providing that a reasonable estimate is made of the rate of growth and the formation of the turbulent spots during transition. A linear variation (or nearly linear in the case of non-uniform free-stream velocities) of the time-averaged intermittency over the unsteady transition zone (s$_t$≤s≤s$_l$) has been found to be adequate for the present purposes. In practice, of course, the formation of spots within the so-called transitional patches is a stochastic process so that transition appears on the s-t diagrams to be gradual rather than instantaneous when ensemble averaged over many cycles (see fig. 13). Similarly, natural transition to turbulent flow which occurs between the wakes at low reduced frequencies is also gradual. Nevertheless, the assumption that transition is step-wise in fashion also appears to be sufficient for the present purposes.

The models presented successfully predict the influence of wakes upon high Reynolds number blade profiles. This is because there is much less uncertainty over the growth rates of the turbulent patches (see Table 1). With reference to the last point, Addison and Hodson (1989b) have suggested that it is only at relatively low Reynolds numbers (Re~3x10^5) that significant differences exist between the idealized processes of fig. 1 or fig. 2 and the true process. It is also important to recognize that transition does not necessarily commence close to the leading edge and that the wakes may be sufficiently broad so as to affect the shape of the s-t diagrams, particularly at these low Reynolds numbers. Though a start of transition criterion has been suggested (Re$_\theta$=163), evidence of later transition has also been presented. The success of all the analyses provides further evidence to suggest that the process of wake-induced transition can be considered to be quasi-steady at representative reduced frequencies.

The effects of wake-generated unsteadiness on the profile loss of a turbine blade were considered recently by Sharma et al. (1988) who also replotted and added to the earlier correlation of Speidel (1957). Sharma et al. chose to re-define the reduced frequency parameter as

$$f_{Sharma} = \frac{\omega}{2\pi} \frac{C_x}{V_x} = \frac{U_b}{p} \frac{C_x}{V_x} = \frac{1}{\phi} \frac{C_x}{p}$$
(23)

which represents the ratio of the convection time of the wakes through the blade row (C$_x$/V$_x$) to the wake passing period (ω/2π). Presumably, this form was chosen because it is a simple function of the flow coefficient (ϕ=V$_x$/U$_b$) and the geometry. The above definition differs from that proposed by the present author (eqn. (1)) and by Speidel (eqn. (15)) and so does not admit to the possibility that it is the ratio of the time it takes for a wake to convect across the transition zone (s$_l$ - s$_t$) at the free-stream velocity V to the periodic time of the disturbance (ω/2π) which determines the transition process. Attention should be paid to the flow on each blade surface before the effect of wake-generated unsteady flow can be modeled.

In their current forms, the present models and the correlation are of limited use to the turbine designer during the initial stages of the design process. This is because the exact nature of the geometry (s$_{max}$) and the limits for boundary layer transition (s$_t$ and s$_l$) are unknown until a design nears completion. However, manufacturers of specific turbines tend to design within relatively narrow constraints so that relationships can be established, for example, between the chord and surface lengths and between, say, the Reynolds number and the distances s$_t$/s$_{max}$ and s$_l$/s$_{max}$. This approach, rather than using a form of the reduced frequency such as that proposed by Sharma et al., is to be preferred since the physical process of unsteady transition is embodied within the parameter ω/2π. Once a design nears completion, the location of first point of instability s$_t$ can be determined, for example, by use of transition correlations; the undisturbed transition length s$_l$ may be found and it is no longer necessary to assume a constant free-stream velocity.

Though much of the above discussion has concerned itself with the effects of wake-interactions on the profile loss of turbine blades, compressors are not excluded from the model but there is little available evidence to confirm this (e.g. Tanaka, 1984, Dong, 1988). Likewise, the influence of wake-induced transition of the time-averaged heat transfer characteristics of turbine blades might readily be modelled though in such circumstances, the assumption that transition occurs in a step-wise fashion will probably result in local errors.

11. CONCLUSIONS

A simple model of unsteady transition has been proposed. It has been used to identify a relationship between a new form of the reduced frequency parameter and the profile loss of a blade row which is subjected to unsteady inflow. The value of this new parameter not only determines the effect upon the profile loss but also the nature of the unsteady transition process. It describes, for example, whether forced transition ends before the location of either natural transition or laminar separation and the length of the resulting unsteady transition zone. The model is shown to be consistent with experimental observations. It successfully explains the correlation by Speidel of effects of wake-generated unsteadiness on the profile loss of turbine blade rows.

Extensions to the simple model show that the formation and growth rates of the turbulent spots have a major influence on the susceptibility of a profile to unsteady inflow and that further information is required regarding these matters and the stability of laminar boundary layers in the presence of unsteady, turbulent wake flows. The transition process may be considered to be quasi-steady and adequately represented by a step change in boundary layer state.

A simple investigation of four idealized turbine blade surface velocity distributions showed that, for a given loading, aft-loaded blades are to be preferred at the higher blade passing frequencies and that forward loaded profiles are more suitable at the lower frequencies encountered in typical turbomachines. In the case of the more lightly loaded profiles, for which laminar separation was not predicted under steady flow conditions, the benefits of changing the loading distribution were slight. When the distance between the first possible occurrence of transition and the start of steady transition, whether via laminar separation or not, is small, then the profile will be relatively insensitive to unsteady inflow.

12. ACKNOWLEDGEMENT

13. REFERENCES

Abu-Ghannan, B.J. and Shaw, R., "Natural transition of boundary layers - the effects of turbulence, pressure gradient and flow history," J. Mech. Eng. Sci., Vol. 22, No. 5, 1980, pp 213-228

Addison, J.S. and Hodson, H.P. "Unsteady Transition in an Axial Flow Turbine - Part 1, Measurements on the Turbine Rotor," ASME paper No. 89-GT-289, June 1989, 1989a

Addison, J.S. and Hodson, H.P. "Unsteady Transition in an Axial Flow Turbine - Part 2, Cascade Measurements and Modelling," ASME paper No. 89-GT-290, June 1989, 1989b

Ashworth, D.A., LaGraff, J.E., Schultz, D.L., and Grindrod, K.J., "Unsteady Aerodynamic and Heat Transfer Processes in a Transonic Turbine Stage," ASME Paper 85-GT-128, 1985.

Binder, A., "Turbulence Production Due to Secondary Vortex Cutting in a Turbine Rotor," ASME Journal of Engineering for Gas Turbines and Power, Vol 107, October 1985, pp 1039-1046.

Binder, A., Schroeder, Th., Hourmouziadis, J., "Turbulence measurements in a multistage low-pressure turbine," ASME paper No. 88-GT-79, 1988.

Dong, Y., "Boundary Layers on Compressor Blades," PhD Thesis, Cambridge University, April 1988.

Doorly, D.J. and Oldfield, M.L.G., "Simulation of the effects of shock wave passing on a turbine rotor blade," ASME paper No. 85-GT-112, 1985

Dring, R.P., Joslyn, H.D., Hardin, L.W., and Wagner, J.H., "Turbine Rotor-Stator Interaction," ASME paper 82-GT-3, 1982

Hodson, H.P., "Boundary Layer and Loss Measurements on the Rotor of an Axial Flow Turbine," ASME Jnl. of Engineering for Gas Turbines and Power, Vol. 106, April 1984.

Hodson, H.P., "The Development of Unsteady Boundary Layers on the Rotor of an Axial-Flow Turbine," AGARD conf. on Viscous Effects in Turbomachines, AGARD CP-351, Copenhagen, June 1983.

Hodson, H.P. et al., unpublished data.

Hodson, H.P. and Addison, J.S., "Wake-Boundary Layer Interactions in an Axial-Flow Turbine at Off-Design Conditions," ASME Paper 88-GT-233.

LaGraff, J.E., Ashworth, D.A., and Schultz, D.L., "Measurement and Modelling of the Gas Turbine Blade Transition Process as Disturbed by Wakes," ASME Paper 88-GT-232, 1988.

Lopatitskii, A.O., et al., "Energy Losses in the Transient State of an Incident Flow on the Moving Blades of Turbine Stages," Teploenergetika, Vol. 17, No. 10, 1970, pp. 21-23.

Obremski, H.J. and Fejer, A.A., "Transition in Oscillating Boundary Layer Flows," Journal of Fluid Mechanics , Vol 29, pp 93-111.

Pfeil, H., and Herbst, R., "Transition Procedure of Instationary Boundary Layers," ASME Paper 79-GT-128, 1979.

Pfeil, H., Herbst, R. and Schroeder, T., "Investigation of Laminar-Turbulent transition of boundary layers disturbed by wakes," ASME paper No. 82-GT-124, 1982

Schubauer, G.B., and Klebanoff, P.S., "Contributions on the Mechanics of Boundary Layer Transition," NACA TN 3489 (1955) and NACA Rep. 1289 (1956)

Sharma, O.P., Renaud, E., Butler, T.L., Milsaps, K, Dring, R.P. and Joslyn, H.D. "Rotor-stator interaction in multi-stage axial-flow turbines", AIAA paper No. AIAA-88-3013, presented at AIAA/ASME/SAE/ASEE 24th Joint Prop. Conf., Boston Ma., July 1988.

Speidel, L., "Untersuchungen über die Verwendung von Laminarprofilen in einer Reaktionsturbine", Bericht 51/5, Institut für Strömungsmechanik der Technischen Hochschule Braunschweig, 1951

Speidel, L., "Untersuchungen über die Verwendung von Laminarprofilen in einer Reaktionsturbine", Bericht 52/11, Institut für Strömungsmechanik der Technischen Hochschule Braunschweig, 1952

Speidel, L., "Untersuchungen über die Verwendung von Laminarprofilen in einer Reaktionsturbine", Bericht 53/14, Institut für Strömungsmechanik der Technischen Hochschule Braunschweig, 1953

Speidel, L., "Beeinflussung der laminaren Grezschicht durch periodische Strörungen der Zuströmung," Z. Flugwiss. 5, Vol. 9, 1957.

Tanaka, S., "Influence of a Periodical Fluctuation on a Profile Loss of a Cascade - Part 1, Determination of the Total Pressure Loss Coefficient," Bulletin of JSME, Vol. 27, No. 226, Apr. 1984, pp. 660-666.

Walker, G.J., "The Unsteady Nature of Boundary Layer Transition on an Axial-Flow Compressor Blade," ASME Paper 74-GT-135.

Wygnanski, I., Sokolov, M., and Friedman, D., "On a Turbulent Spot in a Laminar Boundary Layer,", J.F.M., Vol. 78, Pt. 4, 1976, pp. 785-819

Yurinskiy, V.T., and Shestachenko, I.,Ya., "Losses in an Impulse Turbine Cascade in an Unsteady Flow," Fluid Mechanics-Soviet Research, Vol. 3, No. 1, Jan 1974, pp. 22-27.
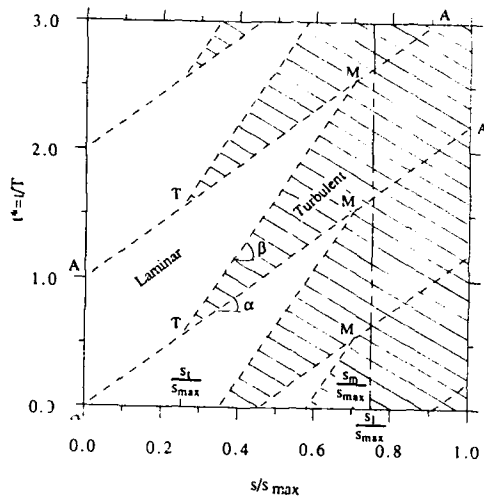
Fig. 1 Schematic distance-time diagram of boundary layer states showing end of forced transition before natural transition (assuming constant free-stream velocity)
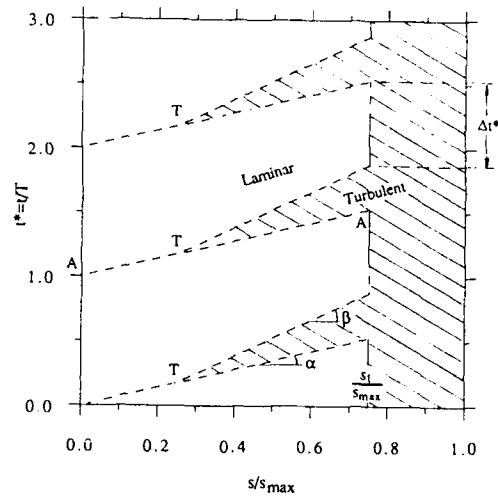

Fig. 2 Schematic distance-time diagram of boundary layer states showing combined forced and natural transition (assuming constant free-stream velocity)
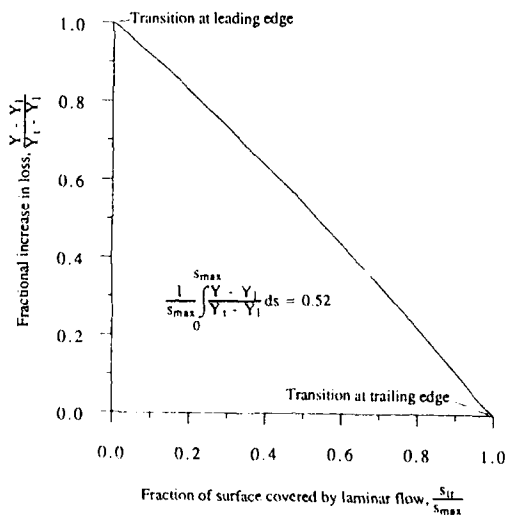

$$\frac{1}{s_{max}} \int_0^{s_{max}} \frac{Y - Y_l}{Y_t - Y_l} \, ds = 0.52$$

Fig. 3 Effect of transition location on profile loss of a flat plate with zero pressure gradient
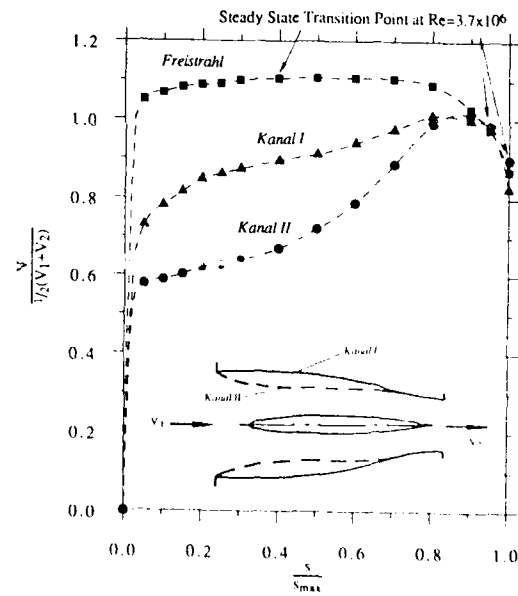
Fig. 4 Velocity distributions corresponding to Speidel's test cases
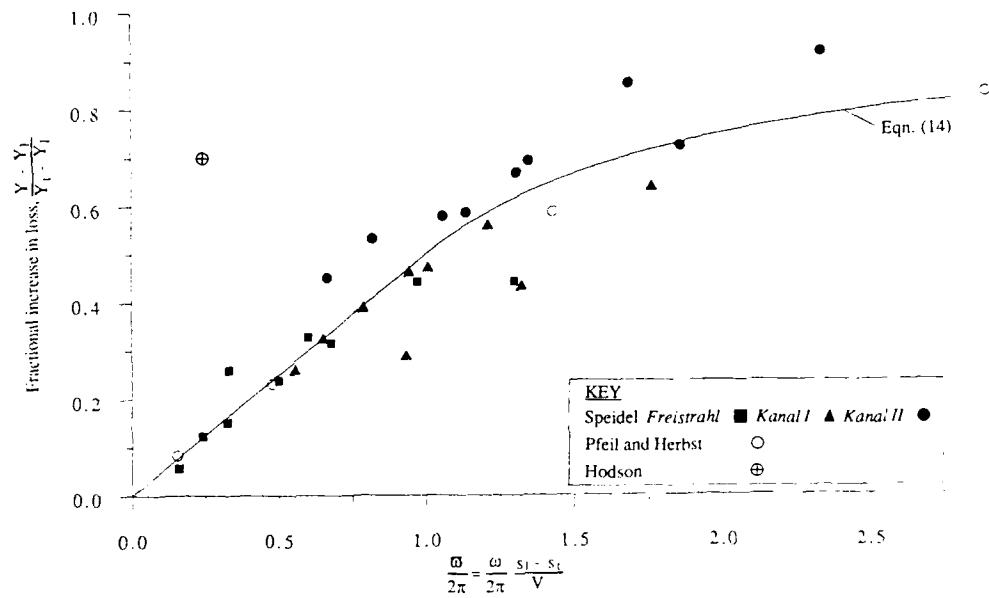
Fig. 5 Correlation after Speidel of effects of unsteadiness on profile
loss showing comparison of simple model and experimental
data
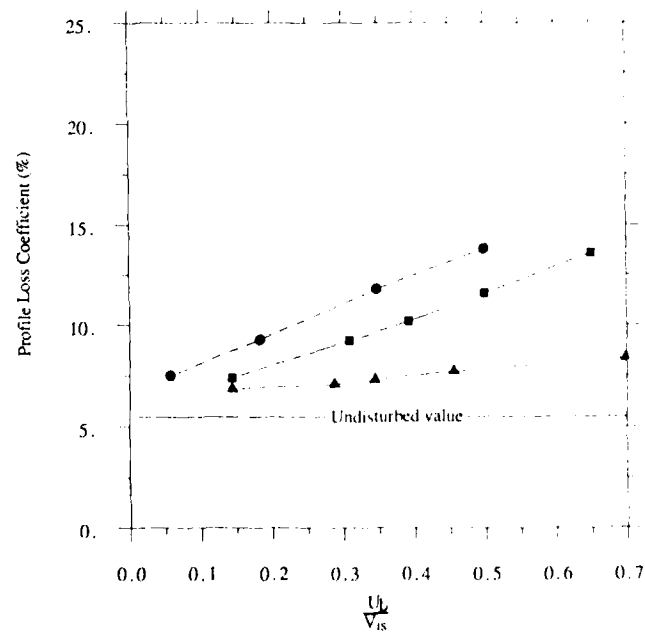
Fig. 6 Effect of wake passing frequency, axial spacing and wake
intensity on profile loss (after Yurinskiy and Shestachenko),
blade chord = 30mm, bar diameter = 1.5mm. ● axial gap =
$^1/_6$ Chord; ■ axial gap = $^2/_5$ Chord; ▲ axial gap = $^1/_2$ Chord.
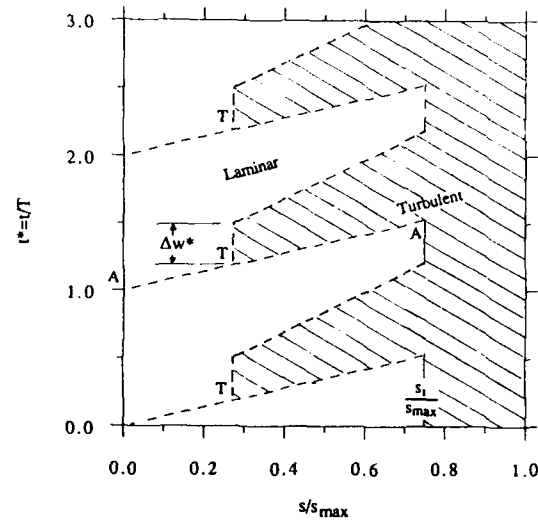
Fig. 7 Schematic distance-time diagram of boundary layer states showing combined forced and natural transition, with forced transition being initiated by a wake of width Δw^* (assuming constant free-stream velocity)
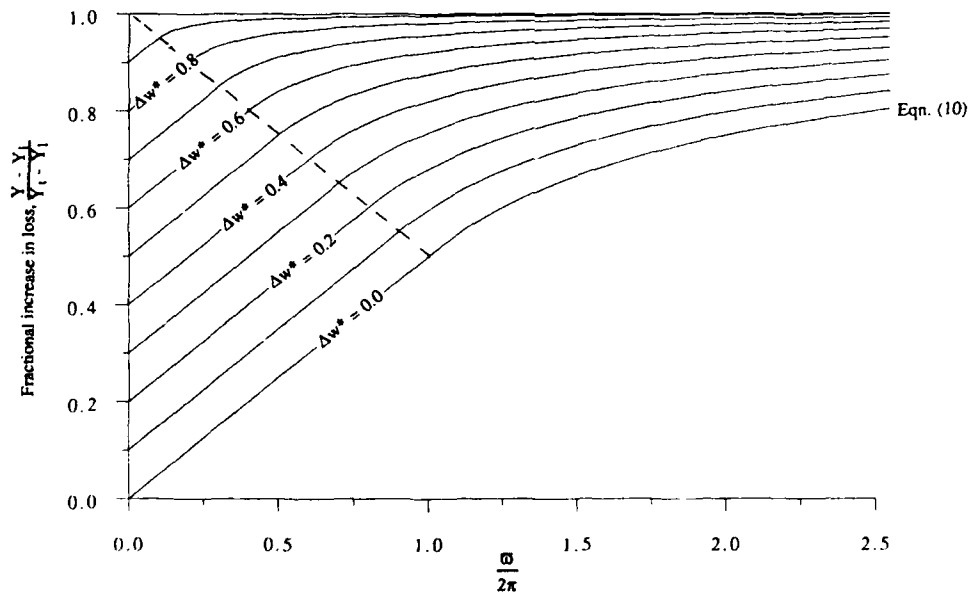
Fig. 8 Prediction, from eqn. (19), of effect of unsteadiness on profile loss showing effect of wakes of finite width width Δw^* (see also fig. 5)
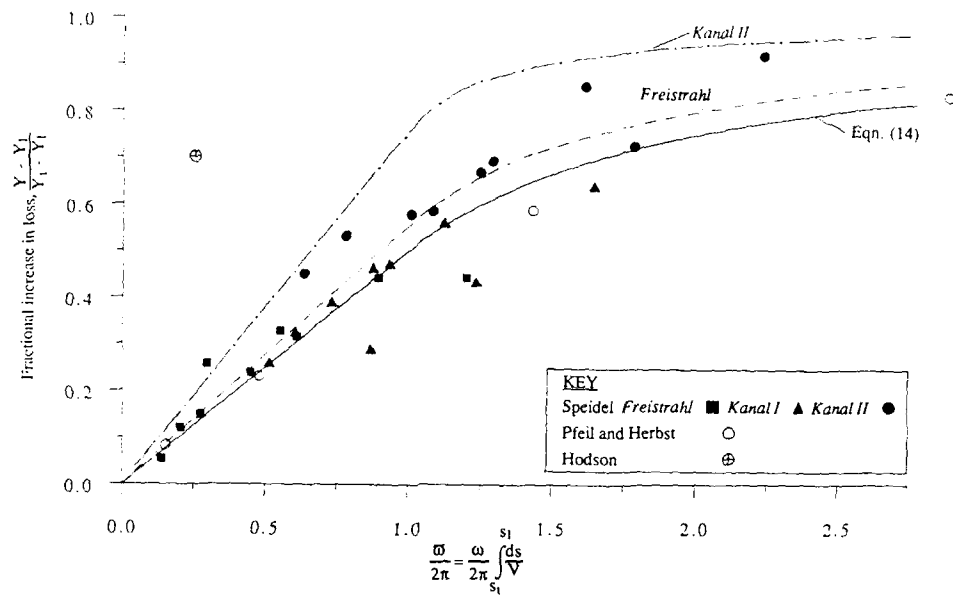
Fig. 9 Re-correlation of the effects of unsteadiness on profile loss
showing comparison of models and experimental data (see
also fig. 5)
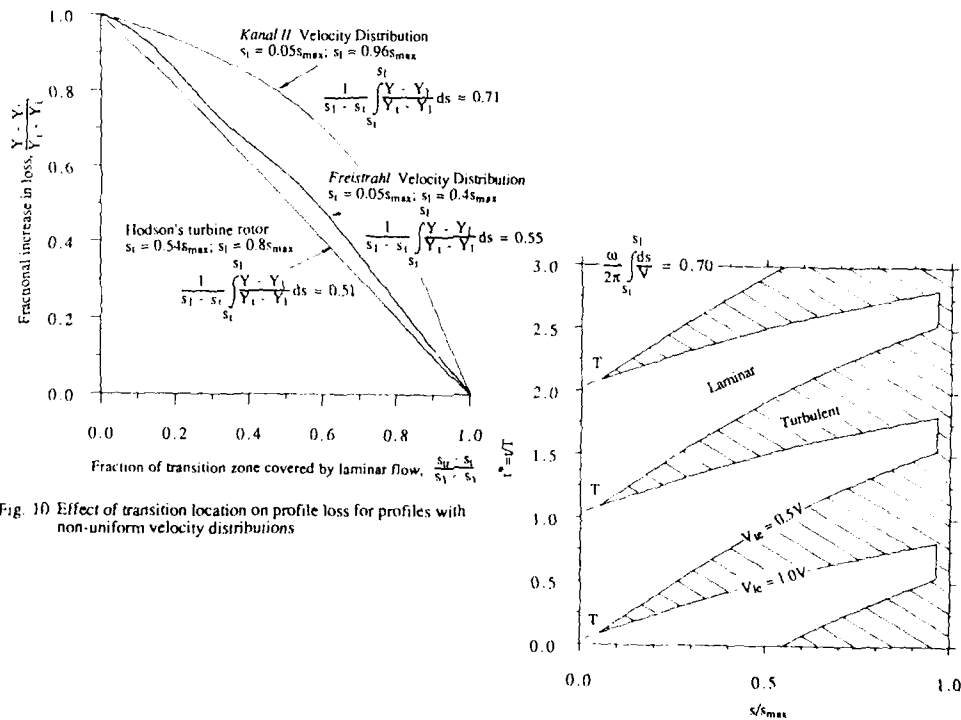
Fig. 10 Effect of transition location on profile loss for profiles with
non-uniform velocity distributions

Fig. 11 Distance-time diagram of boundary layer states showing
effect of non-uniform velocity distribution for Speidel's
Kanal II aerofoil
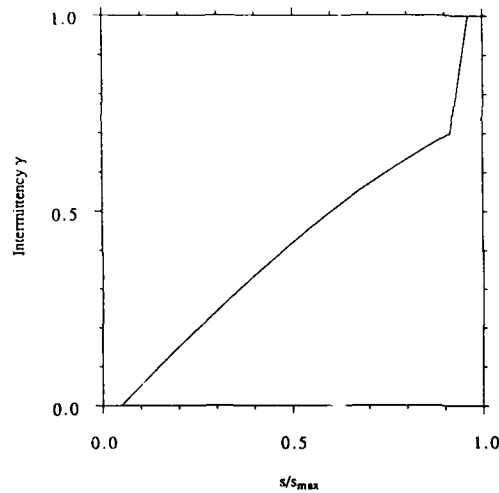
Fig. 12 Variation of time-averaged intermittency function based on results of Fig. 11 for Speidel's *kanal II* test case
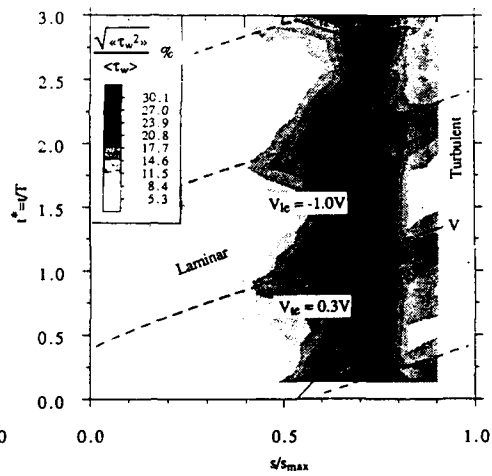
Fig. 13 Distance-time diagram of suction surface random unsteadiness deriv d from hot-film data acquired in axial flow turbine rotor (Addison and Hodson, 1989a):
«τ_w^2» = ensemble variance,
<τ_w> = ensemble mean of wall shear stress

$$\frac{\varpi}{2\pi} = \frac{\omega}{2\pi} \int_{s_1}^{s_1} \frac{ds}{V}$$
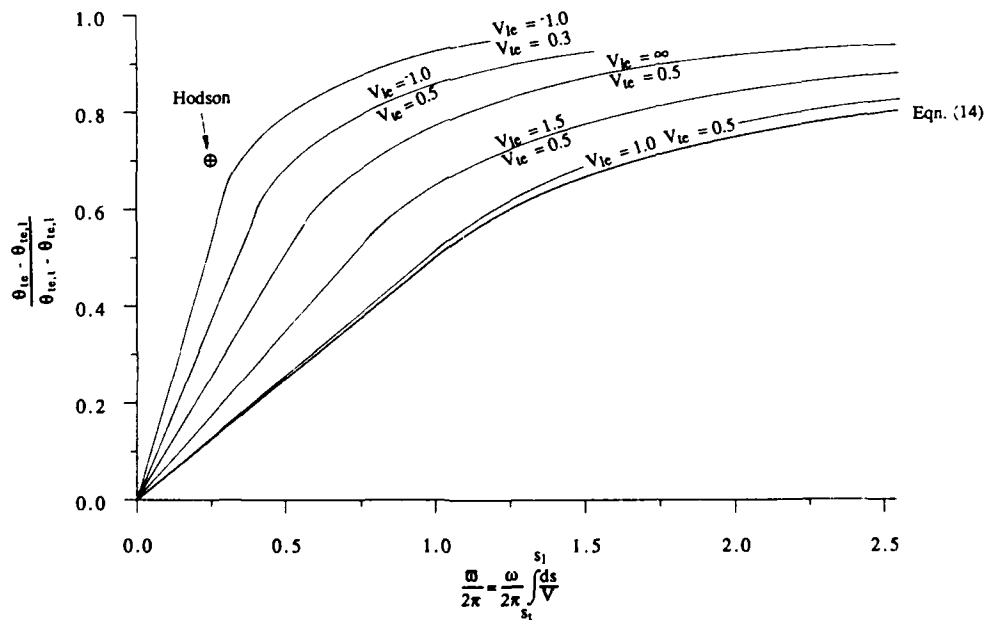
Fig. 14 Prediction of effect of spot leading and trailing edge propagation rates (V_{le} and V_{te}) on profile loss of Hodson's turbine rotor
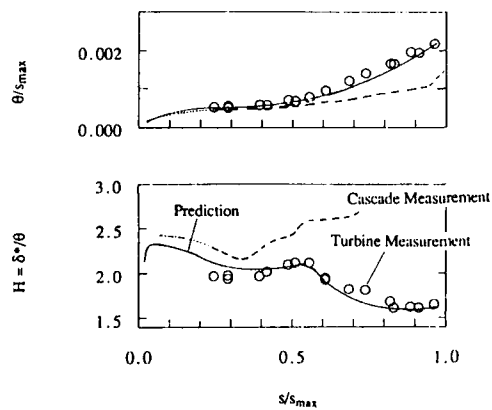
Fig. 15 Predicted and measured suction surface boundary layer
development for the turbine rotor of Hodson
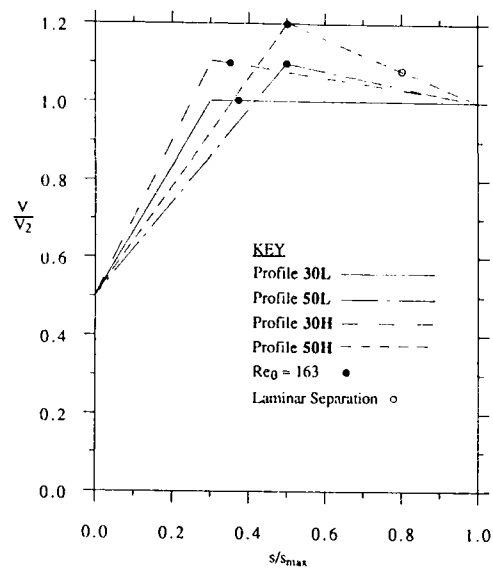
Fig. 16 Idealized velocity distributions for turbine suction surfaces
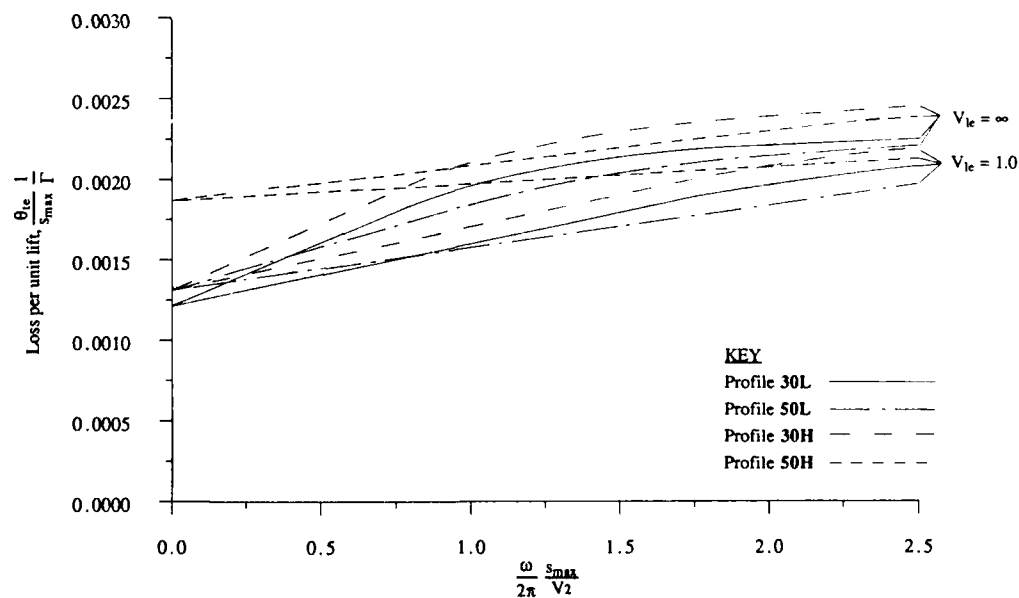
Fig. 17 Effect of unsteadiness on loss of idealized turbine suction
surfaces

DISCUSSION

M.L.G. Oldfield, Oxford University, UK

Have you considered modifying your simple model to take into
account the effects of a finite wake width ? This would make
the initial transition width greater and increase the losses
further. Your data shows a "blunt" start to transition,
which would confirm this.

Authors' response :

The paper does discuss this aspect of unsteady transition.
Equ (19) and fig. 8 reveal that at low reduced frequencies,
the additional profile loss increases in proportion to the
initial width of the wake while at high reduced frequencies
this effect is reduced. With reference to our own data, the
"blunt start" to transition does appear to exist but as
section 8 shows, this is of little relevance. This is because
the "start" represents the earliest detected occurrence of a
turbulent spot and not the location where, on a more rational
basis, transition is sufficiently well underway during each
wake passing cycle that the profile loss is affected.

H.D. Schulz, RWTH Aachen, Germany

To apply your model, one needs to know first where the flow
commences forced transition (due to the wakes) and secondly,
at low reduced frequency, where the flow in between wakes
undergoes natural transition. Do you have any suitable
correlations for that ?

Author's response :

The experimental test data on the unsteady loss correlation style
plots can only appear because the start of forced and natural
transition are either known or easily inferred. In general,
this will not be the case and, as the question suggests,
additional data in, say, the form of a correlation is
required. At the Whittle Laboratory, we have already had some
success at predicting the start of unsteady transition using
steady flow correlations (see Addison and Hodson, 1989b) but
the question of spot formation growth rates still remains
unanswered. In the present paper, I have attempted to
illustrate the importance of the various aspects of unsteady
steady transition rather than make time predictions.

L. Leboeuf, ECL, France

How do you compute the starting location and length of transition
region ?

Author's response:

The model presented assumes that transition occurs in a step-
wise manner so that the "transition length" can simply be
determined from the s-t diagrams. In practice, the change of
state is gradual but the simplifying assumption does not appear
to affect the overall result.

Time-dependent Measurements on Vibrating Annular Turbine Cascades Under Various Steady State Conditions

A. Bölcs, T. H. Fransson, D. Schläfli

Ecole Polytechnique Fédérale de Lausanne

Lausanne, Switzerland

Abstract

Two-dimensional sections of three turbine blades have been investigated experimentally in an non-rotating annular cascade facility with respect to its steady-state and unsteady aerodynamic characteristics. The sections are representative for the near tip sections of the blades where the nominal flow conditions are subsonic at inlet and near sonic or supersonic at the outlet. Emphasis has been put on the time dependent aerodynamic coupling effects between the neighbour blades.

Unsteady experimental data have been obtained with the blades vibrating both in the "travelling wave" mode as well as with "single blade excitation". Decomposition of the experimental data, obtained in the "travelling wave mode", into local (along the blade surfaces) and integrated unsteady aerodynamic influence coefficients indicates that the largest aerodynamic excitation comes from the suction surface leading edge region and, in some cases, from the pressure surface trailing edge region for all three cascades.

The unsteady aerodynamic influence coefficients indicate that for sub- and supersonic outlet flow velocities, all three blade-geometries are self-damped (i.e. a single vibrating blade has a damping influence on itself), but an instability may arise because of the aerodynamic coupling effects between, essentially, the reference blade and its immediate suction side neighbour and, to a lesser extent, its pressure side neighbour. For transonic outlet flow velocities however, a clear destabilizing effect of the (for this flow regime) almost normal shock on the blade itself appears, constituting an excitation mechanism leading eventually to single blade flutter.

Nomenclature

Symbol	Explanation		Dimension
A	Blade amplitude		[mm or deg]
B_n	Blade number "n"		[-]
c	Blade chord length		[mm]
$\tilde{c}_h$	Unsteady force coefficient in direction of bending vibration mode	$\tilde{c}_h = \sum_i \tilde{c}_{pi} \, \Delta\,(x/c)_i$	[-]
$\tilde{c}_p$	Unsteady perturbation pressure coefficient	$\tilde{c}_p\,(x,t) = \frac{1}{h}\,\frac{\tilde{p}(x,t)}{p_{w1}\text{-}p_1}$	[-]
$\tilde{c}_p'$	Modified unsteady perturbation pressure coefficient	$\tilde{c}_p'\,(x,t) = \frac{1}{h}\,\frac{\tilde{p}(x,t)}{p_{w1}}$	[-]
$\tilde{c}_{p,ps}^{n,m}$	Unsteady pressure side pressure coefficient generated on blade "m" by vibration of blade "n"		[-]
$\tilde{c}_{p,ss}^{n,m}$	Unsteady suction side pressure coefficient generated on blade "m" by vibration of blade "n"		[-]
c_w	Aerodynamic work coefficient per cycle of blade vibration mode		[-]
D_i	Pressure transducer number "i" on blade pressure surface		[-]
f	Blade vibration frequency		[Hz]
h	Dimensionless (with chord) bending vibration amplitude		[-]

k	Reduced frequency	$k = \dfrac{\omega\ c}{2\ w_1}$	[-]
M	Mach Number		[-]
p	Time-averaged pressure		[mbar]
$\tilde{p}$	Unsteady perturbation pressure		[mbar]
S_i	Pressure transducer number "i" on blade suction surface		[-]
t	Time		[sec]
w	flow velocity		[ms^{-1}]
x	chordwise coordinate		[m]
y	normal to chord coordinate		[m]
β	Flow angle		[deg]
γ	Stagger angle		[deg]
δ	Blade vibration direction		[deg]
$\Delta\ (x/c)_i$	Normalized blade surface element projected into the normal to vibration direction		[-]
ω	Natural frequency of the blades		[s^{-1}]
σ	Interblade phase angle. Positive when blade "n+1" leads blade "n"		[deg]
φ	Phase angle. Positive when perturbation quantity leads blade "n"		[deg]
Ξ	Aerodynamic damping coefficient		[-]

Subscript

h	Bending motion
loc	local value
ls	Blade lower surface (=suction surface)
ps	Blade pressure surface
s	Isentropic
ss	Blade suction surface
us	Blade upper surface (=pressure surface)
1	Upstream flow conditions
2	Downstream flow conditions

Introduction

The last rotor stages of modern turbines have blade rows with high aspect ratios and relatively low natural frequencies, especially when unshrouded. Such blade rows may be subject to self-excited flutter vibrations, in particular in the transonic flow region, where normal shock waves on the blade can constitute a powerful excitation mechanism. As the power per machine unit is increasing, such operating conditions are often realized, and it is therefore important to predict the aeroelastic stability of bladings working in the transsonic flow domain.

At present several theoretical models to predict the unsteady dynamic forces on vibrating turbomachine blades show acceptable results with respect to the flutter stability limits for blades operating at low an medium subsonic flow velocities. However, their validity has not yet been clearly established for high subsonic and transsonic flow regimes [Bölcs and Fransson, 1986]. For a safe design of turbomachine blades it is therefore still necessary to perform experimental aercelastic investigations. Instrumentation and testing on full scale or model machines are difficult and expensive [see e.g. Barton and Halliwell, 1987]. For this reason tests are often performed in annular [Kobayashi, 1984;1988; Bölcs and Schläfli, 1987] or linear test facilities [Buffum and Fleeter, 1988; Széchényi et al, 1984; Carta, 1982].

Linear cascades allow easy flow measurements with good flow visualizations at reasonable costs, but have also disadvantages such as the necessity of tailboards to establish a flow periodicity within the cascade. Especially at transsonic flow velocities tailboards influence the flow field. In the annular test facility, on the other hand, flow measurements in the transonic flow regime are easy since, without any special precautions, the flow periodicity is self-regulated in the cascade. The disadvantage of the annular cascade is the higher cost and a more difficult set-up and interpretation of Schlieren and other flow visualizations.

The annular arrangement is of importance for unsteady measurements because of the true circumferential steady and unsteady flow periodicity; the unsteady pressure waves propagate circumferentially without interruption. This is not the case in linear cascades with tailboards, whose influence on the time-dependent experimental results is a priori unpredictable. On the other hand, recent experimental and numerical results in annular cascades indicate that in practical cases considering only 7-9 blades (out of 20 in the annular cascade) is sufficient to determine correctly the essential features of the unsteady behaviour of the cascade [Bölcs et al, 1989; Gerolymos, 1988; Buffum and Fleeter, 1988].

The objective of the present study is to examine the steady-state and unsteady aerodynamics through three different vibrating turbine cascades for sub-, trans- and supersonic outlet flow conditions.

The steady-state and unsteady blade surface pressures of the annular non-rotating turbine casacades operating under these conditions are studied, with the blades at rest or oscillating in the "travelling wave" vibration mode in the first bending direction, respectively.

Annular test facility and data reduction

The tests on the cascades presented were performed in the non-rotating annular cascade tunnel at the Swiss Federal Institut of Technology, Lausanne [Bölcs, 1983]. The flow in this wind tunnel is created in the radial-axial annular nozzle shown in Fig. 1. The velocity and flow angle profiles in the test section are obtained by the regulation of the two separate inlet valves ("1" and "2" in Fig. 1) and the two independent inlet guide vanes ("5" and "6").

The velocity profile in the inlet section can furthermore be influenced by two separate boundary layer suctions immediately downstream of the preswirl vanes. Four independent suctions just up- and downstream of the test cascade can act on the velocity profile as well as on the boundary layer on the outer and inner tunnel walls.

As the annular cascade is "closed" circumferentially, the up-and downstream flow periodicity will not be disturbed by lateral boundaries as in a linear test facility, and the inlet and outlet flow conditions adjust themselves in relation to the pressure ratio.

The flow conditions are measured with two aerodynamic probes ("8") which can traverse the channel height. Measurement in the circumferential direction is achieved by rotating the cascade in small steps, while the probe remains fixed. Pressure taps ("10") are located on the inner and outer walls in order to determine the periodicity and the static pressure in the flow field. The test facility is also equipped with Schlieren optic ("9") and laser holography for flow visualization.

The compressed air for the test facility is produced by a continuously running four stage radial compressor which has a maximum mass flow rate of 10 kg/s and a maximum pressure ratio of 3.5. The suction of the wall boundary layers can be performed with a second compressor (2 kg/s, pressure ratio 8).

Unsteady flow experiments with vibrating blades can be performed in two ways in the annular cascade test facility at the EPF-Lausanne [Schläfli, 1989]. In the first way all the blades are vibrated in the travelling wave mode, and in the second one only one blade is oscillated at the time. Summation of the effects of the single vibrating blades yields the information for the travelling wave mode. Schläfli [1989] has shown that both measuring techniques give similar unsteady aerodynamic results.

For the tests presented here the data were obtained in the travelling wave formulation, and thereafter reduced into influence coefficients. Both the steady state and time dependent data acquisitions, as well as the data reduction procedure for the time dependent results in the travelling wave mode have been reported earlier (for example by [Bölcs and Schläfli, 1987]) and are thus not described here.

Model Cascades

The three annular cascades presented here consist of 20 prismatic blades each. The model test blades have a tip diameter of 0.4 m, a hub diameter of 0.32 m and a blade height of 0.0395 m with a tip-clearance of 0.5 mm (see Fig. 2 and Table 1 for cascade geometries). The nominal flow conditions of the sections under investigation are also given in Table 1. All three cascades have blades equipped with steady-state and time-dependent instrumentation. As the present

study treats the unsteady aspects of the cascades, only the time-dependent instrumentation is represented in Fig. 2. The pressure transducers employed are mounted directly in the vibrating blades. Details about the mounting of the pressure transducers and the data acquisition accuracy is given by Bölcs et al [1989] and is thus not repeated here.

Each blade is elastically suspended on a spring-mass system (Bölcs and Schläfli [1984]), designed to reproduce the first three eigenfrequencies, as well as the vibration direction of the first bending mode, as determined from the real blading in the turbine for the corresponding section.

The blades are forced into an organized vibration mode by means of electromagnetic exciters and the vibration is measured by inductive displacement transducers or strain gauges on the spring (Bölcs and Schläfli [1984]). The electromagnetic system can exert a limited force on the blade. The blade vibration amplitude and phase angle are therefore not rigorously constant in time and between the blades, but subject to small fluctuations that depend on the mechanical properties of the cascade (such as coupling between the blades) and the vibration mode selected, as well as non periodic flow perturbations (see for example Schläfli [1989]).

Machine type		Cascade I Gas turbine	Cascade II Steam turbine	Cascade III Steam turbine
Stagger angle	(°)	49.0	56.6	73.4
Blade chord	(mm)	78.5	74.4	52.8
Profile thickness/chord length	(%)	10	17	5.2
Pitch/chord ratio	(-)	0. 72	0.74	1.07
Nominal upstream Mach number M_1	(-)	0.34	0. 31	0.40
Nominal inlet flow angle β_1	(°)	10	-44	-62
Nominal downstream Mach number	(-)	0.95	0.90	1.34
Nominal outlet flow angle β_2	(°)	-58	-72	-71
Vibration direction δ	(°)	90	61	43
Vibration frequency (1st bending)	(Hz)	210-230	140-150	220-230
Reduced frequency	(-)	0.14-0.21	0.08-0.13	0.08-0.17
Pressure transducers on suction side		6	6	5
Pressure transducers on pressure side		5	5	5

Table 1: Cascade data

Results and discussions

The results presented have been selected as representative for the three cascades under different steady-state operating conditions. The presentation of the results relies heavily on the influence coefficient concept as discussed by Bölcs et al, [1989].

The unsteady force coefficients presented below are the result of a sum of the unsteady pressure coefficients, weighed with the blade surface element associated to the particular pressure. Obviously, for rapidly chordwise changing pressure coefficient amplitudes and phase angles, the so determined force coefficient is not very accurate for the limited number of pressures measured on the blade. Nevertheless, it is representative for the global effetcs observed and perfectly suitable for the comparison between and classification of the different experimental results.

Cascade 1

Aerodynamic damping

The aerodynamic damping coefficient as presented in fig 3 resumes the unsteady behaviour of cascade 1 as a function of the outlet flow velocity. The pressure side is stable for most of the cases over the entire interblade phase angle range with a maximum stability in the range σ=180°-270° and a minimum from σ=0°-18°. The damping coefficient is a smooth function for some tests, but shows some scatter for others; the origin of this scatter is uncertain. On the suction side, the damping curve is roughly sine wave shaped, centered at different Ξ-levels depending on the outlet flow velocity: For supersonic flow (M_{2s}=1.31) it is centered approximately at the stability limit resulting in an unstable interblade phase angle range 200° < σ

< 360°. For lower flow velocities (M_{2s}=1.19, 1.06) the damping curve is shifted towards more stable values and the unstable interblade phase angle range decreases. For near-sonic outlet flow however, a radical change in the shape of the damping is observed: The suction side becomes unstable over the entire interblade phase angle range. It becomes sufficiently unstable indeed to outweigh the positive damping generated on the pressure side: the blade is aerodynamically unstable regardless of the interblade phase angle. Examination of the influence coefficients below shows that this behaviour is caused by the normal shock on the suction side itself, causing a single-blade instability. The scatter of the data compared to the other cases is larger, which is attributed to a large random component of the shock motion superposed on the harmonic component.

For subsonic outlet flow conditions, the cascade behaves in a manner similar to the supersonic case: The pressure side is stable over the entire interblade phase angle range, and the suction side shows an instability around $\sigma \approx -90°$. A certain discrepancy is observed for two experiments at M_{2s}=0.93, where only the inlet flow angle and vibration frequency are slightly different ($\bullet$: f=234Hz, β_1=12°, $\blacktriangle$: f=210 Hz, β_1=15°). In the latter case a larger damping is observed. The reason for this is the pressure side influence coefficient phase angles for blade "0", which are closer to Φ_p=90° and yield therefore a larger stability margin. On the suction side differences in the amplitude and phase angles are observed in the rear part of the profile, leading to the different stability. There are no obvious reasons for these discrepancies.

From the aerodynamic damping curves the following conclusion can be drawn: the unsteady behaviour of the cascade for sub- and supersonic outlet flow is, in terms of aerodynamic damping, very similar; a different behaviour is observed for transsonic flow, where the generalized instability of the suction side over the whole interblade phase angle range is observed.

Influence coefficients

The differences related to the outlet flow velocity occur mainly on the suction side, wherefore pressure side data are not presented here.

An example for supersonic flow shows that the relevant interactions occur between blade "0" and "-1" (fig 4). At the leading edge, an influence from more distant blades, propagating in the upstream flow, is observed. Towards the trailing edge, the amplitude of the interactions decreases rapidly. An effect of the impact of the trailing edge shock from blade "-1" on blade "0" is observed at x/c=0.64 (symbol "$\blacktriangle$"). For transsonic flow, however (fig 5), a difference is observed towards the trailing edge: The normal shock situated in the proximity of the rearmost pressure transducer symbol generates a large pressure amplitude depending on the vibration of the blade at which it is attached, blade "0" (symbol "$\times$"). Influences from the other blades are relatively small, but even the "+1" neighbour blade (symbol "$\blacksquare$") generates a perceptible effect near the trailing edge.

The imaginary part of the "0"-blade pressure influence coefficient indicates whether a blade generates a exciting or damping effect on itself. This eigen-stability is summarized in Fig 6: For super- and transsonic outlet flow velocities, a small unstable zone is observed between 20% and 50% of the blade chord. It is compensated by the stable zones near the leading edge and in the rear part of the profile. In the transsonic case however, the phase angle of the pressure induced by the shock motion (symbol "+", rearmost position) results in an important negative damping: integration of the local damping coefficients into the self-damping of the entire profile yields a negative value; the shock motion causes a single blade flutter instability, which is independent of aeroelastic coupling effects. For subsonic flow, a behaviour globally similar to the supersonic case is observed, but the data are considerably more scattered. It is interesting to note that for decreasing outlet Mach number, the suction side becomes slightly unstable.

Cascade 2

Aerodynamic Damping

The unsteady behaviour of cascade 2 in terms of aerodynamic damping is summarized in Figs 7 and 8. In a similar manner to cascade 1, the pressure side is stable for most of the operating conditions; in some cases a slight instability occurs for interblade phase angles close to σ=0°. On the suction side however, a considerable influence of the downstream Mach number is observed: For M_{2s}=1.42, the damping is a sine-wave shaped curve, centered quite accurately at the stability limit Ξ=0. For decreasing outlet flow velocity, the damping curve conserves is sine-wave shape, but is shifted towards positive values (M_{2s}=1.26, M_{2s}=1.13) as for cascade 1: This means that the eigen-stability of the blade increases while the coupling effects remain similar. For outlet flow velocities close to sonic, the damping curve is shifted towards negative values; at the same time the amplitude of the curve decreases, which indicates weaker coupling effects. The mean value of the curve, which indicates directly the eigen-stability of the blade, is negative for this case. As shown by the local eigendamping along the blade chord in fig 9a, this effect is caused by the shock on the suction side, much the same way as for cascade 1.

For subsonic outlet Mach numbers, the pressure side damping in fig 8 is the same as for supersonic flow; differences are noticeable on the suction side: For $M_{2s}=0.85$, $M_{2s}=0.86$ a "hole" in the damping coefficient curve appears for $\sigma=54°$, which disappears for higher and lower outlet flow velocities. It is due to the effect of the more distant "-2" and "-3" blades which change in relative intensity and phase angle, resulting in different superposed global effects.

The influence of the steady state flow conditions in the cascade on the local eigendamping on the profile is shown in fig 9. The stabilizing effects of the shocks at $M_{2s}=1.42$, $M_{2s}=1.13$ in contrast with the destabilizing effect of the normal shock at $M_{2s}=1.04$ is clearly visible.

Influence of the inlet flow angle:

The steady state inlet flow velocity depends directly on the flow angle, thus affecting the scale of the conventional unsteady pressure coefficient definition. Therefore an alternate form of the unsteady pressure coefficient $(\tilde{c}_p)$ independent of the inlet flow velocity is used to compare results with different inlet flow angles. A difference of almost 30° in the inlet flow angle influences the steady state blade Mach number distribution (fig 10a) on the first 20% of the blade chord on the suction side and on about 80% on the pressure side. The unsteady behaviour however only marginally depends on the inlet flow angle (fig 10b and c). For the close to axial inlet flow angle of $\beta_1=-12°$ a less smooth rise of the unsteady pressure towards the trailing edge is observed on the pressure side than for $\beta_1=-45°$. The phase angles show the same trend, with a more pronounced scatter for $\beta_1=-45°$. On the suction side, for the close to axial flow the expansion at the leading edge is stronger and the unsteady pressure amplitude larger than for $\beta_1 -45°$, as well as the (for this cascade) typical drop of the unsteady pressure observed aft of the throat location and the chordwise phase angle variation. In conclusion, a difference of more than 30° of the inlet flow angle leads only to some quantitative discrepancies, but not to a qualitatively different behaviour of the cascade. This is to be expected, since the steady-state flow through the cascade is almost the same.

Interblade Channel effects

Examination of the pressure influence coefficients shows also how the important interactions are generated across the blade passage. The example in fig 11 illustrates this in the following way: If we imagine that only blade "B2" is vibrating, then blade "B1" will see a pressure induced by its pressure side neighbour "+1", while for blade "B3" the same blade "B2" will be suction side neighbour "-1". Therefore the pressure side interblade channel is described by the coefficients $\tilde{c}_{p,ps}^{0,0}$ (symbol "■") for the vibrating blade itself and $\tilde{c}_{p,ss}^{-1,0}$ (symbol "●") for its neighbour "B3". The suction side interblade channel is described by the coefficients $\tilde{c}_{p,ss}^{0,0}$ (symbol "×") for the blade itself and $\tilde{c}_{p,ps}^{+1,0}$ (symbol "✱") for blade "B1". It is readily seen that the suction side loads induced have phase angles close to 0° and 180° near the throat location (at about 30% cord), which means that they behave in an almost quasi-steady manner. As regards the pressure side effects, a change of sign along the chord is observed: From almost in-phase at the leading edge, it changes to opposite-phase towards the trailing edge. Pressure and suction side pressures across the channel throat are almost in opposite phase as schematically represented below.

Cascade 3

Cascade 3 is non-overlapping, to the difference of cascades 1 and 2. The inlet flow angle of the cascade has a large influence on the pressure side steady state pressure distribution on the blade (see fig 12a), while the suction side pressure distributions are almost identical despite of a 21° difference of the inlet flow angle. A strong expansion at the leading edge is followed by a shock and recompression extending over more than 50% of the blade chord. This is due to a flow separation at the leading edge for both cases. Schlieren flow visualizations show a normal shock which can be identified from the blade surface pressures. The unsteady pressure distributions (fig 12b) are different in both cases especially on the suction side despite of the similarity of the steady state pressures. On the pressure side, for $\beta_1=-65°$, the largest unsteady pressure is generated at the leading edge and the phase angle varies smoothly from the leading to the trailing edge. For $\beta_1=-44°$ the unsteady pressure increases from the leading edge to the trailing edge. The phase angle near the leading edge is in opposite phase with respect to the former case, but amplitudes and phase angles tend to similar values towards the trailing edge. On the suction side, large discrepancies are observed: Amplitudes and phase angles differ much in the first half of the profile and tend to somewhat similar values in the aft part of the profile. The essential difference is observed in the (modified) aerodynamic damping which shows that the cascade is stable or neutral for $\beta_1=-65°$, but unstable for $\beta_1=-44°$ over the whole interblade phase angle range. As for cascades 1 and 2, the damping curve is centered at a negative value, which means that the suction side is intrinsically unstable due to single blade flutter, depending on the inlet flow angle.

For subsonic flow an aerodynamic damping as shown in fig 13 is obtained. The pressure side is close to neutral over almost the entire interblade phase angle range, whereas the suction side is slightly unstable between $180°<\sigma<360°$. On the suction side a peak in the damping is observed for an interblade phase angle $\sigma=54°$ which is close to the theoretical downstream resonance phase angle. The pressure influence coefficients show that the important interactions are generated near the leading edge between blades "0" and "-1", both for the pressure and suction side. Influences from the other blades are considerably smaller with the exception of blade "+1", which generates a noticeable effect towards the trailing edge, closest to the source of the perturbation.

Acoustic resonances

One topic that still stirs controversy is the question of the acoustic resonances. The axial propagation conditions of unsteady perturbations are called "subresonant" (or "cut-off") when perturbations decay axially and "superresonant" (or "cut-on") when perturbations propagate undamped. The limit between the two cases is called the "acoustic resonance" and corresponds to perturbations propagating undamped circumferentially. In theoretical predictions, the resonance results in a discontinuity of e.g. the unsteady blade load as a function of the interblade phase angle (see for example [Verdon, 1987]). Resonance effects have been experimentally observed in a test rig with long ducts [Smith, 1972], but none of the experimental results from oscillating cascades to the authors' knowledge exhibits evidence of these resonance effects.

In the experiments presented above, the axial length of undisturbed flow is relatively short (in the order of 6 to 8 blade chords downstream, 3 blade chords upstream). This may be too small for a reliably perceptible resonance effect to develop, and the possibility of reflections from up- and downstream is uncertain. However, this corresponds more to the real operating conditions of a turbine than infinite undisturbed up- and downstream flow. On the other hand, theoretical predictions for cascade 2 show a very narrow interblade phase angle region where definite resonance effects would occur, and their detection would probably be difficult in the cascade experiment.

Conclusions

The unsteady behaviour of different types of turbine cascades have been investigated in an annular cascade test facility. The investigations concentrated on the influence of the interblade phase angle for the unsteady parameters and the outlet flow velocity for the steady state flow, the effect of the inlet flow angle being studied only briefly and partly.

The following conclusions are drawn from the experiments:

•   For all cascades the relevant interactions are observed between direct neighbour blades. Their most important intensity is localized in the overlapping part of the cascade (where present), in the "interblade duct". Influences from more distant blades have to propagate in the up- and downstream flow field and are considerably weaker.

•   For supersonic flow, the oblique shock waves in the cascade flow have a stabilizing influence, which is more or less pronounced according to the flow velocity and the cascade geometry.

•   For transsonic outlet flow conditions an instability appears (which may depend on the inlet flow angle), which is caused by the normal shock on the suction side of the profile of turbine blades. The inherent instability of a normal shock acts with a positive feedback on the blade vibration and presents a single-blade flutter mechanism: It is independent of the vibration of neighbour blades and cannot be fought by measures such as mistuning of the blade row. This phenomenon is to be expected on compressor blades also.

•   The inlet flow angle has little influence on the unsteady behaviour of overlapping turbine cascades with well defined interblade channels. It has a large influence on cascades with tip-section profiles, which may be stable for small and unstable for large incidence flow angles.

Acknowledgements

References

Barton, H.A.; Halliwell, D.G.; 1987
"Detailed On-Blade Measurements on a Transonic Fan in Unstalled Supersonic Flutter"
Proceedings of the 4th International Symposium on Unsteady Aerodynamics and Aeroelasticity in Turbomachines and Propellers - Aachen, RFA - 1987

Bölcs, A.; 1983
"A Test Facility for the Investigation of Steady and Unsteady Transonic Flows in Annular Cascades."
ASME Paper 83-GT 34, 1983

Bölcs, A.; Fransson, T. H.; Schläfli, D.; 1989
"Aerodynamic Superposition Principle in Vibrating Turbine Cascades"
AGARD Propulsion and Energetics Panel No. 74A, Conference Proceedings, 1989

Bölcs, A.; Schläfli, D.; 1987
"Experimental Investigation of the Time-Dependent Flow in a Vibrating Annular Cascade Operating in the Transonic Flow Regime"
Proceedings of the 4th International Symposium on Unsteady Aerodynamics and Aeroelasticity in Turbomachines and Propellers - Aachen, RFA - 1987

Bölcs, A.; Fransson, T.; 1986
"Aeroelasticity in Turbomachines: Comparison of Theoretical and Experimental Cascade Results"
Communication N°13 du Laboratoire de Thermique Appliquée et de Turbomachines de ."Ecole Polytechnique Fédérale de Lausanne,Switzerland

Bölcs, A.; Schläfli, D.; 1984
"Flutter Phenomena in a Transonic Turbine Cascade."
Proceedings of the Symposium "Unsteady Aerodynamics of Turbomachines and Propellers", Cambridge, United Kingdom, pp. 411-426, 1984.

Buffum, D. H.; Fleeter, S.; 1988
"Investigation of Oscillating Cascade Aerodynamics by an Experimental Influence Coefficient Technique."
AIAA Paper 88-2815, 24th Joint Propulsion Conference, July 11-13, Boston, Massachusetts, 1988.

Carta, F. O.; 1982
"An Experimental Investigation of Gapwise Periodicity and Unsteady Aerodynamic Response in an Oscillating Cascade."
NASA Contractor Report 3513, 1982.

Gerolymos, G. A.; 1988a
"Periodicity, Superposition and 3D Effects in Supersonic Flutter Aerodynamics."
ASME Paper 88-GT-136, 1988.

Gerolymos, G. A.; 1988b
"Numerical Investigation of the 3D Unsteady Euler Equations for Flutter Analysis of Axial Flow Compressors."
ASME Paper 88-GT-255, 1988.

Kobayashi, H.; 1988
"Effect of Shock Wave Movement on Aerodynamic Instability of Annular Cascade Oscillating in Transonic Flow."
ASME Paper 88-GT- 187, 1988.

Kobayashi, H., 1984

"Unsteady Aerodynamic Force Acting on Controlled-Oscillating Transonic Annular Cascade."

Proceedings of the Symposium "Unsteady Aerodynamics of Turbomachines and Propellers", Cambridge, United Kingdom, pp. 343-359, 1984.

Schläfli, D.; 1989

"Experimentelle Untersuchung der instationären Strömung in oszillierenden Ringgittern."

Ph. D. Thesis, Ecole Polytechnique Fédérale de Lausanne, Lausanne, Switzerland, 1989.

Smith , S.N .; 1972

"Discrete Frequency and Soung Generation in Axial Flow Turbomachines."

ARC Reports and Memoranda No 3079, March 1972

Széchényi, E.; Cafarelli, I.; Notin, C.; Girault, J. P.; 1984

"A Straight Cascade Wind-Tunnel Study of Fan Blade Flutter in Started Supersonic Flow."

Proceedings of the Third International Symposium on Unsteady Aerodynamics of Turbomachines and Propellers. Cambridge, UK, September 1984, pp. 447-458.

Verdon, J. M.; 1987

"The Unsteady Aerodynamic Response to Arbitrary Modes of Blade Motion."

Proceedings of the Symposium "Aeroelasticity in Turbomachines", Aachen, West Germany, pp. 313-334, 1987.

Whitehead D. S.; 1987

"Flutter of Turbine Blades."

Proceedings of the Symposium "Aeroelasticity in Turbomachines", Aachen, West Germany, pp. 437-452, 1987.

1,2	Inlet valves	9	Cylindrical optic for flow visualization
3,4	Outer and inner settling chamber	10	Static wall pressure taps
5,6	Outer and inner preswirl vanes	11	Outlet flow collector
7	Test cascade	12	Outlet valve
8	Aerodynamic probes up- and downstream	->	Boundary layer suction
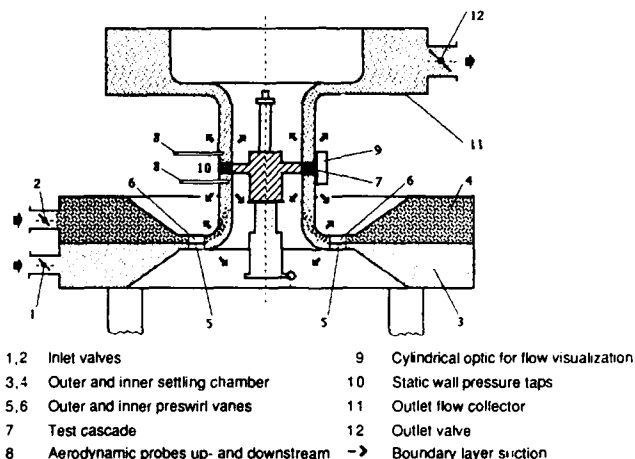
Fig. 1: Schematic view of the annular test facility at the EPF-Lausanne.

a: Cascade 1: Gas turbine cascade, midspan section

b: Cascade 2: Steam turbine cascade, midspan section

c: Cascade 3:   Steam turbine cascade, tip section
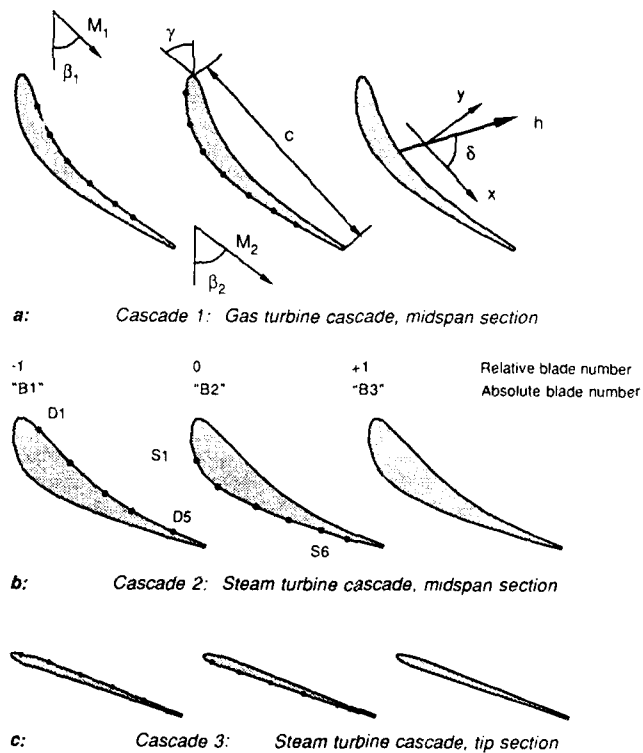
Fig. 2:   Cascade geometries and locations of pressure transducers
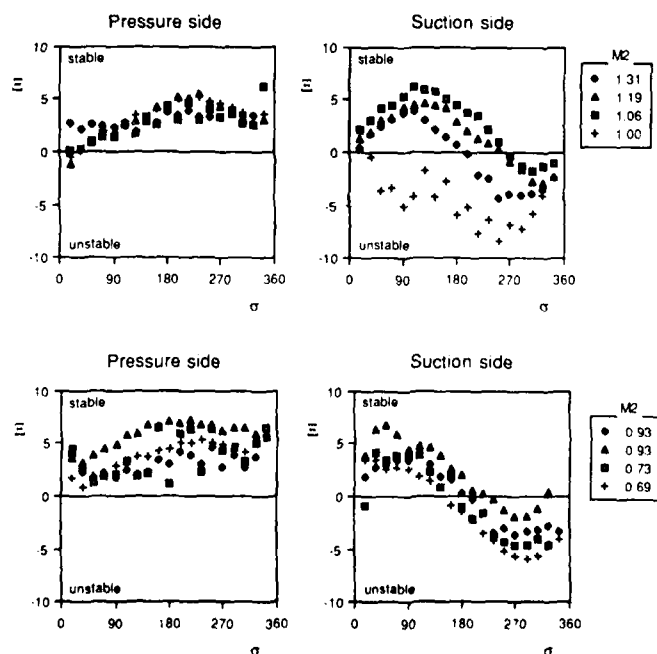
Fig. 3:   Cascade 1: Aerodynamic Damping coefficients for various outlet flow velocities

Fig. 11 Distance-time diagram of boundary layer states showing
effect of non-uniform velocity distribution for Spe..del's
Kanal II aerofoil
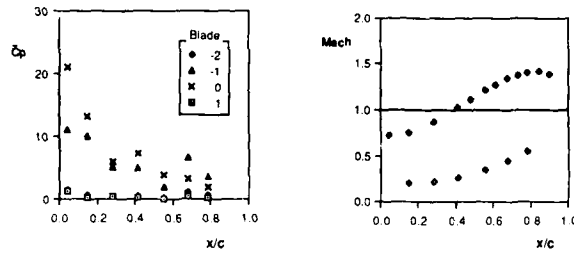
Fig 4: Cascade 1: Pressure influence coefficients (suction side) for supersonic outlet flow ($\beta_1 = 14°$, $M_{2s} = 1.19$) with corresponding steady state Mach number distribution on the profile
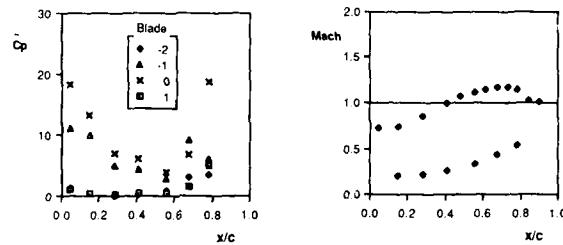
Fig 5: Cascade 1: Pressure influence coefficients (suction side) for transsonic outlet flow ($\beta_1 = 15°$, $M_{2s} = 1.0$) with corresponding steady state Mach number distribution on the profile
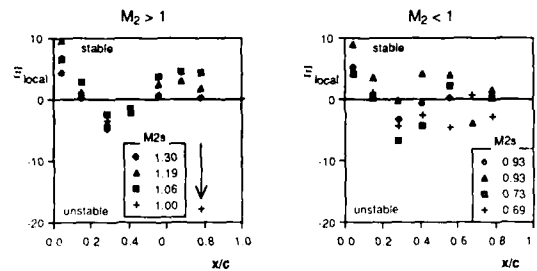
Fig 6: Cascade 1: Local eigendamping as a function of outlet flow velocity
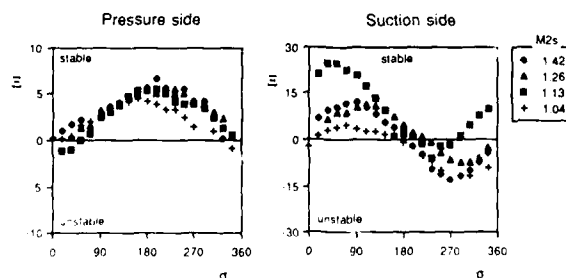
Fig 7: Cascade 2 Aerodynamic Damping for supersonic and transsonic outlet flow velocity

19-12

Pressure side   Suction side
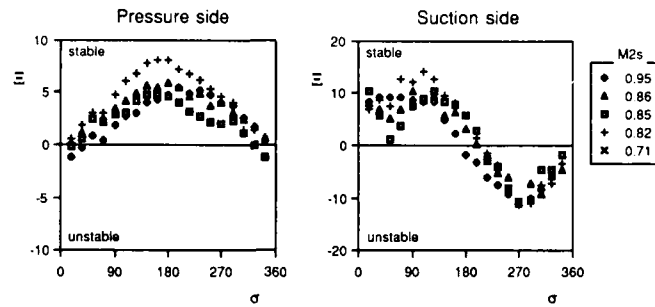
Fig 8:   Cascade 2: Aerodynamic damping for subsonic outlet flow

a) M_{2s}=1.43   b) M_{2s}=1.13

Suction side

c) M_{2s}=1.04
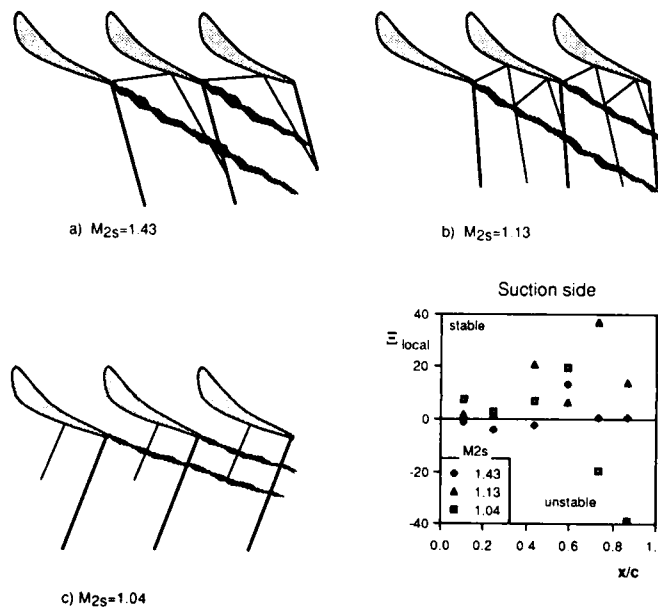
Fig 9:   Cascade 2: Shock patterns in the cascade for different outlet flow
          velocities and local selfdamping on the profile
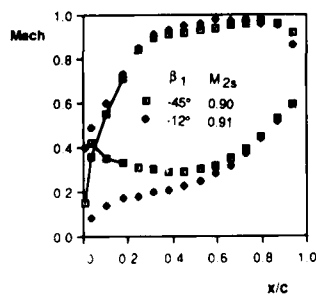
Fig 10a: Cascade 2: Steady state Mach   Fig 10b: Cascade 2: Modified unsteady pressure coefficients on the
          number distribution on the blade   pressure side as a function of β_1 ($M_{2s} = 0.83...0.91$, $\sigma = -90°$)
          for different inlet flow angles
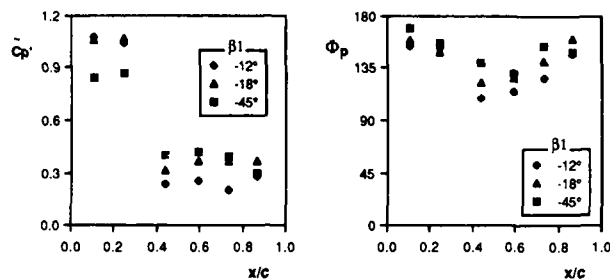
Fig 10c: Cascade 2: Modified unsteady pressure coefficient on the suction side as a function of β_1 $(M_{2s} = 0.83...0.91, \sigma = -90°)$
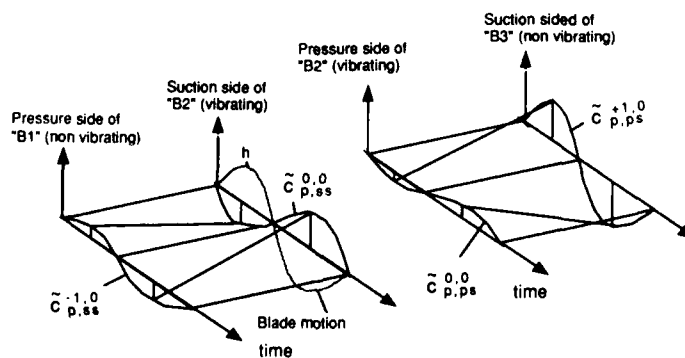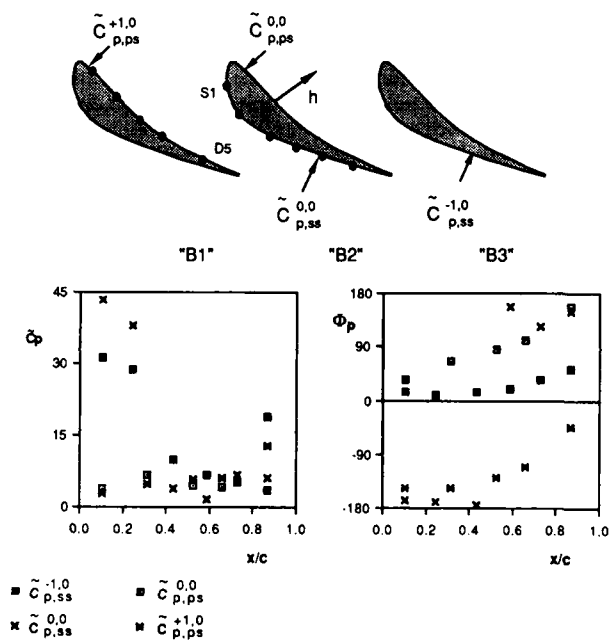
Fig 11: Cascade 2: Interblade channel effects across cascade throat (between pressure transducers D5 and S2) for subsonic flow $(M_{2s}=0.82)$
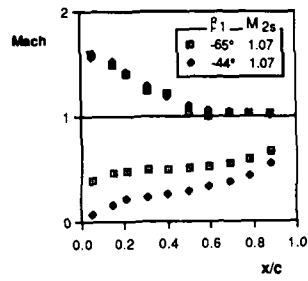
Fig 12a: Cascade 3: Steady state Mach number on the blade for different inlet flow angles (M2s=1.07)
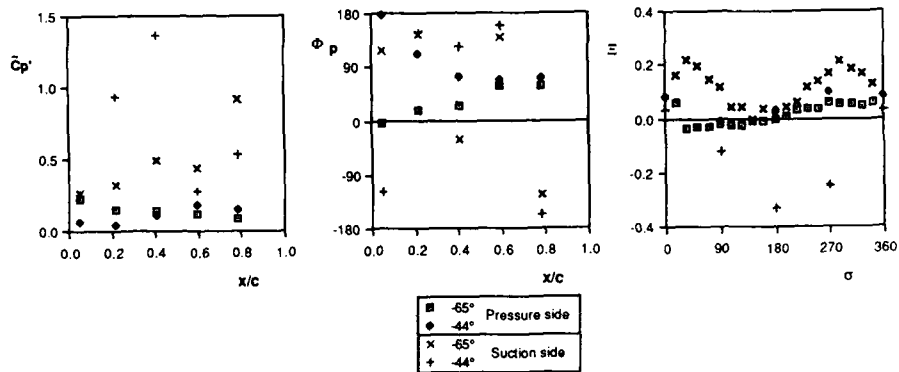
Fig 12b: Cascade 3: Unsteady pressure distribution for σ=-90° and aerodynamic damping for different inlet flow angles (M₂ₛ=1.07)
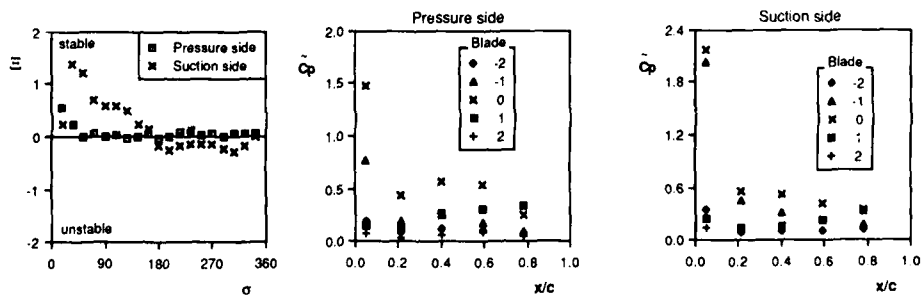
Fig 13: Cascade 3: Aerodynamic damping and pressure influence coefficients for subsonic outlet flow (β₁=-69°, M₂ₛ=0.77)

EXPERIMENTAL INVESTIGATION OF THE INFLUENCE OF ROTOR WAKES ON THE

DEVELOPMENT OF THE PROFILE BOUNDARY LAYER AND THE PERFORMANCE

OF AN ANNULAR COMPRESSOR CASCADE

Dipl.-Ing. H.D. Schulz
Prof. Dr.-Ing. H.E. Gallus

Institut für Strahlantriebe
und Turboarbeitsmaschinen
RWTH Aachen
Templergraben 55
5100 Aachen, W.-Germany

SUMMARY

The development of the profile boundary layers, particularly the locii of transition and separation, largely depend on the turbulence level of the free-stream and the wake flow effects.
For comparison, a detailed survey of the profile boundary layers in an annular compressor cascade has been carried out first at a steady, uniform incoming flow and secondly with a rotor upstream. The rotor incorporates cylindrical spokes causing periodic wakes and thus a higher overall turbulence level of the flow. Its impact on the profile boundary layer history and the performance of the compressor cascade will be discussed.

NOMENCLATURE

BPf	blade passing frequency		U	anemometer output voltage
c	blade chord		U_o	anemometer output voltage
C	absolute flow velocity			at zero flow
Cp	pressure coefficient		W	relative velocity
	$Cp = (P_{1oc}-P_{c\,\bullet\bullet})/(P_{t\,2}-P_{c\,\bullet\bullet})$		W	wake
E	rate of heat transfer		x	axial direction
ET	end of transition		y	circumferential direction
F	free-stream		z	spanwise direction
i	incidence		α	flow angle measured from
H	blade height			axial direction
L	blade surface length		δ	boundary layer thickness
LSB	laminar separation bubble		δ_2	momentum thickness
Ma	Mach number			
P	pressure			
PS	pressure side			$\delta_2 = \int_0^{\delta} (1-c/c)(c/c)\,dy$
r	radius			
r_N	leading edge radius			
r_H	trailing edge radius		ε	turning angle
$Re_{\bullet\bullet}$	non steady Reynolds number		λ	stagger angle
s	blade spacing		ρ	density
S	center of gravity		τ	shear stress
SS	suction side		$\bar{\omega}$	circumferentially mass-
ST	start of transition			averaged loss coefficient
t	blade thickness			$\bar{\omega} = (\bar{P}_{t\,2}-\bar{P}_{t\,3})/(\bar{P}_{t\,2}-\bar{P}_2)$
T	blade passing period		Ω	vorticity
TS	location of turbulent boundary layer separation			
Tu	turbulence level Tu = C_{RMS}/C			
U	rotational velocity			

Subscripts

0	design flow angle		( )	mass-averaged
2	upstream of the cascade			(circumferential)
3	downstream of the cascade		( )	time-averaged
loc	local		(—)	averaged over the entire
•	blade midspan height			passage
RMS	root mean square		(~)	periodical fluctuation
s	static			
sec	secondary			
t	total			
w	blade surface			
w	wake			
•	free-stream			

Superscripts

1) INTRODUCTION

The recent trend towards closer blade row spacing in turbomachinery, especially in aircraft engines, amplifies the considerable unsteadiness in the flow field. Most of the present analysis and design of aircraft engines are based on steady aerodynamics, even though it is known that the close proximity of rotating and stationary blade rows and the resulting unsteady flow can have a profound effect upon the performance of turbomachines (Hodson /1/).

The unsteady flow associated with blade row interaction has a major influence on blade boundary layers, transition, turbulence intensities, corner separation, blade pressures and the performance of a blade row. The most significant effect is thought to be the periodic forcing of the transition of the blade surface boundary layers and the influence this has upon the aerodynamic and thermodynamic performance of the blade row (references /1,2,3/). The presence of the wake above the blade surfaces causes the formation of a turbulent patch within an otherwise laminar boundary layer. The leading edge of this patch travels with the leading edge of the wake at approximately the free-stream velocity. The rear of the patch travels more slowly, at a rate which is more typical of that observed at the rear of turbulent spots formed by natural transition (Pfeil et al. /2/). Due to the differing leading and trailing velocities, the patches merge and form a turbulent boundary layer. It was found that while the turbulence in the wake always provokes an earlier start of transition, the transition length might increase due to becalmed regions in between wakes where no turbulent spot can arise (Pfeil et al. /2/). Hence, depending on wake spacing, the transition process might be completed downstream or ahead of the would-be position of the end of natural transition, and up to now little is known about the transition behaviour on compressor blades in rotating machines.

The performance of a turbomachine is governed to a large extent by the boundary layers developing in a blade row, and the influence of unsteady flow upon performance is still not understood, especially at off-design operation and at low aspect ratio bladings, where three-dimensional effects and corner separation might influence the blade boundary layer even at midspan (Schulz and Gallus /4/). The present paper is concerned with the mechanism and relevance of wake interactions in an annular compressor cascade. It describes an investigation of the blade boundary layers and the performance of the cascade at steady incoming flow and in the presence of rotor-stator interaction. A simple configuration was chosen to generate viscous wake interaction with negligible potential flow interaction. A rotating row of cylinders was placed upstream of the cascade, and measurements were taken at almost identical inlet incidence and other inflow conditions as those in the steady case (with the rotor being removed). Data is aquired at four different incidences and only representative results are given in this paper.

2) EXPERIMENTAL DETAILS

Research Test Rig and Inlet Conditions

The experiments were performed in the annular cascade shown in Fig. 1. A turbocompressor set provides a continuous airflow to the test rig. The swirl angle of the flow is varied by means of 48 adjustable inlet guide vanes (IGV (5)). Angular momentum is conserved while the flow passes through a channel contraction to level out the wakes of the IGV. The test cascade (8) consists of 24 untwisted blades, mounted on the hub (tip clearance 0.8 percent of blade height), with a hub to tip ratio of 0.75 and a tip diameter of 428 mm. The aspect ratio is 0.86 and the solidity at midspan is 0.78. The blade profiles are radially stacked at their center of gravity and the blade metal angles at inlet and exit are 44° and 15°, respectively (measured from axial); other geometric parameters are shown in Fig. 2.
Two sets of tests have been performed. One with a steady and uniform incoming flow, where the rotor (labeled (7) in Fig. 1) has been removed. In the other set of measurements, rotor-stator viscous wake interaction was generated by a rotor with cylinders (simulating blades) located at 57 percent of chord or 7 diameters of the cylinder upstream of the cascade. The rotor incorporates 24 rods with a diameter of 5.3 mm. The rotational speed was kept constant for all investigations at 3000 RpM. Fig. 2 shows the geometry of the cascade. All dimensions are in millimeters and the velocity triangle is drawn for an inlet angle of α_2 49.2°. Rotating cylinders were chosen to achieve nearly identical inlet conditions as those in the case without rotor, at constant rotational speed of the rotor but different inlet angles. This could not have been achieved with a rotor incorporating blades.

The inlet angle and velocity distribution are shown in Fig. 3. These were taken at 5 percent chord upstream. The points of operation are identified by the time averaged yaw angle α_2 measured at midspan. The incidence angle is almost identical for both cases, with and without rotor. Even though the velocity profile differs slightly on the hub wall, the boundary layer thickness is almost identical in both cases, as shown in Fig. 4. The phase-lock averaged velocity at cascade inlet has been measured with a hot-wire probe. Fig. 5 shows the variation of the total velocity, the turbulence intensity and the incidence variation with time in the absolute frame of reference for an inlet angle of α_2 49.2° at midspan. Also indicated is the time averaged incidence angle i. Velocity defects $\Delta C/C$ of 15 percent and incidence changes from Δi -2° to Δi +8° were observed at α_2 49.2°. The maximum turbulence intensity (inside the wake) was

13 percent and the mean turbulence intensity was 7 percent, which is much higher compared to 1.2 percent turbulence intensity measured in the no-rotor case.

Measurement Techniques

Flow Visualization. The flows on the blade and hub surface have been visualized using dye injection, oil film and titanium-dioxide. Dye injection and oil film techniques have been described in detail by Schulz and Gallus /4/. All flow visualization studies have been filmed in motion with a video camera equipment.

Five-Hole Probe Measurements. Detailed radial and circumferential measurements were carried out with a five-hole probe at the cascade exit plane (35 percent of chord downstream of the blade trailing edge). The probe head diameter is 2.6 mm and the uncertainty of the measurements was about $\pm$ 2 percent in Cp-values and $\pm$ 1 degree in flow angle. Due to the high flow angle variation in the exit plane (plane 3), here the probe had to be yawed at every measuring position. Measurements were taken at 22 radial and 21 circumferential positions. A description of the probe and its calibration is given by Bohn and Simon /5/.

Surface Mounted Hot-Film Anemometers. The development of the stator suction and pressure surface boundary layers was investigated using an array of DANTEC surface mounted constant temperature hot-film anemometers. Since the blades of the compressor cascade are untwisted, the multi element gauge was mounted on an elongated blade, which can be traversed radially to move the sensors to different spanwise positions. There are 21 sensors placed along the blade suction side and 14 along the pressure side (Fig. 6).

The similarity between the velocity and temperature profiles, the latter generated by the hot-film anemometer, leads to a relationship between the rate of heat transfer to the fluid (E) and the wall shear stress of the form

$$E^2 - A^2 = k \ \tau_w^{1.3} \tag{1}$$

where the constant A represents the heat lost to the substrate /6/. Since the calibration of an array would have been both difficult and extremely time consuming, it was decided to adopt a similar procedure to that described in reference /7/. It is assumed that the constant A in the above equation can be approximated by the bridge voltage measured under zero flow conditions U_0. Furthermore, reducing the data to the form of (U^2/U_0^2-1) should suppress the effects of different values of the constant of proportionality k, given the assumption that the rates of heat transfer to the air and substrate are similar functions of the same variables. In practice, a further simplification was introduced whereby the data acquired were in the form of voltages.

Hot-Wire Measurements. The suction side boundary layers have been measured using a hot-wire probe. Since the boundary layers are very thin, only a single wire probe could be used. Thus the probe can only sense the value of the total velocity, and the flow direction could not be determined. The hot wire probe incorporates an additional prong which causes the traversing unit to stop if the prong touches the blade, thus positioning the probe at exactly 0.15 mm away from the surface. As described in more detail by Schulz and Gallus /4/, care has to be exercised in obtaining accurate data from a hot-wire probe in a highly turbulent flow. In general, the time averaged flow velocity will be measured too high and the velocity fluctuation too small, if the local turbulence level exceeds 30 percent (Dengel and Vagt /8/). This is particularly valid for separated flows in the presence of backflow vents. Hence measurements in these regions should be viewed as qualitative. When turbulence level is below 20 percent and the radial velocity is small (like in the midspan region of the passage), the error in total velocity is about $\pm$ 2 percent.

Data Analysis and Processing

The use of phase-lock averaging to process periodic data out of raw signals obtained in rotating machinery is a well established technique requiring little further explanation. The data from the high response hot-film and hot-wire anemometers were acquired and recorded in digital form via an analog-digital converter with a sampling rate of 89 kHz. The system was operated in the external trigger mode so that data could be synchronized with the rotor. Two hundred samples were taken along one cylinder passage and averaged 128 times (N = 128). Also real time data were stored to derive turbulent quantities (RMS-values). All data were processed to physical units after the tests.

The ensemble averaged, time averaged and RMS-values are defined as follows:

$$\bar{u}(t) = \frac{1}{N} \sum_{n=1}^{N} u(n,t) \tag{2} \qquad \bar{u} = \frac{1}{T} \int_{t=0}^{T} \frac{1}{N} \sum_{n=1}^{N} u(n,t) \tag{3}$$

$$u_{RMS}(t) = \sqrt{\frac{1}{N} \sum_{n=1}^{N} (u(n,t) - \bar{u}(t))^2} \tag{4} \qquad Tu(t) = u_{RMS}(t) / \bar{u}(t) \tag{5}$$

where U is a function of x/c and represents instantaneous values, phase-locked to a constant angular position (t/T) of the rotor. The analog digital converter used has a 12 bit resolution. The accuracy in conversion therefore is 0.024 percent of the measured value. Lakshminarayana and Poncet /9/ derived a relation for the random error occurring in an ensemble averaging data reduction process, which includes the turbulence intensity and the number of ensemble averages (N). The error in the present tests is estimated to be 1.4 percent in mean pressure and in mean velocity data.

3) RESULTS AND DISCUSSION

Surface Flow Visualization

The oil film method has been applied to the blade suction surface to detect regions of separated flow qualitatively. A comparison of the surface flow on the blade suction side with and without the rotor is shown in Fig. 7 for all incidences under investigation.
Three major changes can be observed. First, the three-dimensional laminar separation bubble (LSB), found in the case without the rotor, disappears at all incidences at the suction and the pressure side (not shown here). Because of its elimination, the flow along the blade becomes more two-dimensional upstream of the turbulent separation in the rotor case. Secondly, the regions of turbulent separated flow in the vicinity of the end walls decrease in the rotor case, especially at smaller inlet angles (or blade loading). Third, the midspan boundary layer seems to separate earlier at the trailing edge in the rotor case.

The disappearance of the laminar separation bubble with free-stream turbulence levels higher than 3 percent has also been observed by Hoheisel and Kiock /10/ in turbine cascades. In their investigation the location of boundary layer transition was weakly dependent on the turbulence level, even though prediction of Dunham /11/ showed a much higher influence.
Walker /12/ points out that the periodic disturbances, arising from the passage of rotor wakes have a major influence on the transition process, but they will only have an effect on the location of the transition point when their scale is large compared with the boundary layer instability length or if their amplitude is high. However, an earlier transition of the suction surface boundary layer due to the rotor wakes would account for the here observed turbulent separation of the boundary layer near midspan. The effect the rotor wakes have on the transition process will be discussed in more detail with the results from the hot-film measurements.

Fig. 8 shows streamlines at the hub and the blade suction side, with and without rotor, at $\alpha_2 = 44.2°$. It can be seen that due to the presence of the rotor, not only on the blade but even more significantly on the wall, the separated region is reduced. This might partly result from the different hub boundary layers at the cascade inlet (Fig. 4). The well known formula given by Squire and Winter /13/ may be applied for discussion.

$$\Omega_{...} = -2\varepsilon \partial C / \partial z \tag{6}$$

Since for the rotor case $\partial C / \partial z$ is smaller inside the hub boundary layer but larger right at the wall, the secondary flow could be different with respect to the no-rotor case. This would influence the migration of low momentum fluid towards the hub suction side corner region and hence the corner separation. Since Fig. 8 shows no evidence of diminished secondary flow on the hub, it is felt that the flow oscillation and the increase in turbulence level due to the rotor are responsible for the reduced corner stall.
Measurements by Takei and Masuda /14/ in a two-dimensional diffuser revealed that an enforced velocity oscillation significantly reduces the extent of a separated region. The oscillation enhances the formation of vortical structures in the separated shear layer and thus reenergizes the retarded flow near the wall. In their investigation Takei and Masuda could relate the reduction in separated flow directly to the amplitude of the velocity fluctuation.
It has been observed by Castro and Haque /15/ that an increase in free-stream turbulence level has a favourite effect on a turbulent boundary layer, which is close to separation. The high free-stream turbulence causes more random fluctuation and hence more entrainment at the edge of the boundary layer. This does increase the wall shear stress and postpones the separation.
It is not clear from the experiments described in this paper if the higher random or the periodic fluctuations of the flow is responsible for the decrease in corner stall. It is intended to repeat these tests without rotor but with grids giving the same mean free-stream turbulence as the rotor (about 7 percent (compare Fig. 5)).

Determination of the Blade Boundary Layer Transition Behaviour

Hot-Film Measurements at Steady Incoming Flow. Fig. 9 shows the normalized random fluctuation of the surface mounted hot-films versus chord and inlet angle for the no-rotor case. Indicated with a bar is the laminar separation bubble (LSB) found in the oil flow visualization (Fig. 7). The location of the bubble corresponds with a sharp increase in random fluctuation. This is due to the high turbulent spot production rate inside the laminar separation bubble, where the flow undergoes transition and then reattaches turbulent downstream.
This can be seen more clearly from the real-time traces shown in Fig. 10. The left hand

side set of traces is taken at an inlet angle of α_2 = 44.2° on the blade suction side. At x/L = 0.295 the trace shows spikes arising from turbulent spots in an otherwise laminar boundary layer. These spots coalesce and at x/L = 0.432 the signal reveals the high random fluctuation of an intermittant boundary layer. This corresponds with the local peak in the RMS-distribution in Fig. 9. At x/L = 0.523 the boundary layer is already reattached and nearly fully turbulent, but still showing some downwards spikes indicating laminar intermittancy. At x/L = 0.614 the transition process is completed and the flow fully turbulent. Further downstream the turbulence level increases again (Fig. 9), which is due to the development of the turbulent boundary layer under an adverse pressure gradient. When the flow commences turbulent detachment at the trailing edge (compare Fig. 7), the RMS-values exceed the ones found inside the laminar separation bubble, but the point where the flow leaves the blade surface cannot be identified clearly.

On the blade suction side the laminar separation bubble and hence the transition region moves upstream with increasing inlet angle (Figs. 7 and 9). This is brought about by the increased loading and the earlier onset of diffusion at higher angles of attack.
At steady incoming flow the effect of incidence upon the transition process on a blade row is primarily related to the extent to which the velocity (or pressure) distribution is modified by a change of incidence. Fig. 11 presents predicted midspan Mach number distributions, obtained using the method of Lücking /16/, for a range of angles of attack. Even though this inviscid calculation does not take into account the blockage caused by the separated corner regions, it does predict the loading of the suction surface and the unloading of the pressure surface boundary layer with increasing inlet angle.
On the pressure surface the laminar separation bubble moves downstream with increased loading, and at inlet angles above 49° it disappears (Fig. 7). The hot film measurements though show, that the pressure surface boundary layer undergoes natural transition, which is clear from the local maximum in the RMS-distribution (Fig. 9) and the real-time traces (Fig. 10, right hand side column). Due to limitation of the multi sensor probe the last hot-film sensor on the pressure side is mounted at x/L - 0.667, and it can be seen that the boundary layer is still kept transitional at this location by the moderate diffusion of the flow at these incidences (Fig. 11).

Hot-Film Measurements with Cylinder Rotor. The oscillation of a flow and its turbulence level have a significant effect on the transition process of the blade boundary layers. In oscillating flow, the manner in which transition occured was found to depend on the value of the "non steady Reynolds number" (Miller and Fejer /17/)

$$Re_{ns} = L \cdot \Delta U / 2\pi \nu \qquad (7)$$

in which the characteristic length, L = $2\pi U_o/\omega$, is the distance traveled by a fluid particle in the free-stream during one cycle of the imposed oscillation, and the characteristic velocity ΔU, is the amplitude of the oscillation. When Re_{ns} exceeds a certain value, transition begins with turbulent bursts appearing periodically at the frequency of the free-stream oscillation. For zero pressure gradient this value is about 26.000, but Walker /12/ observed that in adverse pressure gradient $Re_{ns,crit}$ can be as low as 1000. In the experiments described in this paper, the value of Re_{ns} was about 6.600, and the turbulent bursts where exspected to occur periodically with blade passing frequency (BPf).
Fig. 12 presents real-time traces of the hot-film signals along the blade suction surface at an inlet angle of α_2 = 44.2°. Also shown are the RMS-values and the Cp-distribution versus chord. At the leading edge (x/L = 0.023) the lower wall shear stress caused by the velocity deficit in the cylinder wake is clearly visible, but already at x/L = 0.114 one can see turbulent spikes occuring with BPf. The sequence of the real time traces in Fig. 12 is very much alike the one of the transitional boundary layer shown in Fig. 10, except that the turbulent spikes do not appear randomly but with BPf. Beyond x/L = 0.705 there is no periodicity recognizable, but only random fluctuations, which are much higher than those without rotor (compare Fig. 10).
The ensemble averaged signals in Fig. 13 give valueable information about the physical phenomena occuring in the transient suction surface boundary layer. The normalized difference in voltage $\tilde{U}$ - $\bar{U}$ is a measure for the periodical and U_{RMS} for the random fluctuation of the wall shear stress time averaged at a particularly rotor position. As already discussed in Fig. 12, the velocity defect inside the cylinder wakes (W) cause a lower wall shear stress at the leading edge (x/L = 0.023). The random fluctuation (U_{RMS}) of the wall shear stress are high when a rotor wake is passing due to turbulent velocities inside the wakes. They are nearly zero in the free-stream between two wakes (F), an indication of an otherwise laminar boundary layer at the leading edge.
At x/L = 0.114 the trace of the periodic fluctuation seems to be inverted compared to the one at the leading edge. Turbulent spot production underneath the wake gives rise to higher wall shear stresses when a rotor wake is passing and hence an increase in U. Since there is a large content of randomness in this process, U_{RMS} is also high at these time intervals (W). The near-zero values of the RMS-traces indicate the extent (in time) of the quiescent state.
Turbulence and intermittancy grow as the turbulent patches move downstream (x/L - 0.205). As the flow develops further on the suction surface, natural transition occurs in the free-stream between two wakes (F), so that at 38.6 percent chord, the RMS-values no longer approach zero for any part of the wake passing cycle, and the periodic variation of the ensembled signal shows large fluctuation.
At x/L = 0.477 transition is nearly completed underneath the wake (W), but in the free-stream (F) the flow is still in a transient state, and intermittantly occuring laminar flow causes a drop in U. In a transitional boundary layer the change of state results

in a change of heat transfer rate from the hot-film which is much greater than the fluctuations observed in turbulent boundary layers. This is made clear by the RMS-value distribution at this location, which also reveals that the laminar flow must occur randomly at these time intervals.
At 70.5 percent chord the transition process is completed and for a.m. reasons the mean RMS-values and the periodic fluctuation are much less than in the transient boundary layer.

By evaluating the hot-film traces along the blade suction and pressure side in the above described manner, the start and the end of the transition process could be determined for all points of operation under investigation, i.e. for different blade loadings. Fig. 14 presents a summary of all boundary layer investigations described in this paper.
In the case without rotor the transition process occurs via a laminar separation bubble (LSB) which moves upstream on the blade suction side and downstream on the pressure side with increasing inlet angle. At higher loading the pressure surface boundary layer undergoes natural transition due to the nearly constant static pressures at these points of operation (Fig. 11).
With rotor, the laminar separation bubble disappears and transition starts (ST) shortly downstream the leading edge nearly independent of blade loading. Turbulent spots are produced underneath the wake forcing the boundary layer to commence transition ahead of the location seen in the steady case. The transition length though differs on the blade suction and pressure side due to different local pressure gradients and wake decay. The transition length on the suction side is greater, and the end of transition (ET) is further downstream than in the steady case. This is brought about by becalmed regions in between wakes (Pfeil et al. /2/) and the stabilization of the flow which occurs during the accelerating phase of the velocity fluctuation caused by the rotor wake passage. This has also been observed by Walker /12/.
In an extensive investigation of the unsteady pressure- and flow field along the blade surface (Schulz et al. /19/), it was found that on the pressure surface the wakes decay much more rapid than on the suction surface. Hence this stabilizing effect is reduced, and on the pressure surface the transition process is completed ahead of the position in the steady case.

The location where turbulent separation (TS) occurs on the blade surfaces has been determined by the results from the surface mounted hot-films, the flow visualization and the hot wire measurements described in the next section. No turbulent separation occurs on the blade pressure surface at any loading and in neither case with and without rotor. At steady incoming flow the suction surface boundary layer at midspan commences turbulent separation at the trailing edge for inlet angles α_2 greater than 49°. This is brought about by the hub corner stall which extends up to and even beyond midspan at these blade loadings (Fig. 7).
With rotor, turbulent separation was found at the trailing edge at all incidences (Fig. 7). This is a result of the early transition and the subsequent development of the turbulent boundary layer. Even though the high free-stream turbulence in the presence of the rotor has a favourable effect on boundary layers near separation, the reattached turbulent boundary layer in the steady case can withstand the adverse pressure gradient more successfully. The effect of the hub corner stall, however reduced, is felt at the high inlet angles also in the case with rotor (Fig. 14).

Predictions of the blade surface boundary layer development have been made using an integral method described by Truckenbrodt /20/ and Scholz /21/. Criteria by Dunham /11/ and Scholz /21/ are used to predict boundary layer transition and turbulent separation, respectively. The Mach number distribution from the inviscid flow calculation (Fig. 11) and the measured static pressure distribution were used as input data. The predicted locations of transition (dashed and dotted lines) and turbulent separation (dashed lines) are indicated in Fig. 14. For the no-rotor case the code gives an accurate prediction of the location of transition and the transition behaviour (laminar separation bubble) on the blade surfaces. When using the calculated Mach number distribution as input, it also predicts turbulent separation, however too far upstream for $\alpha_2 < 49°$ and too far downstream for $\alpha_2 > 49°$. It should be noted that the boundary layer equations, because there is no upstream influence, tend to predict early separation in regions of very rapid diffusion. It also cannot account for the three-dimensional effects which occur at the high inlet angles.
In the rotor case the predicted location of turbulent separation remains unchanged since the criterion /21/ does not account for different turbulence level. The criteria for boundary layer transition /11/ however does, and the predicted location moves upstream. This criteria is based upon correlations of steady flow effects. However, given that it is the turbulence in the wakes which appears to cause transition, the use of steady flow correlations might be justified.

Hot-Wire Measurements

The passage flow as well as the blade boundary layers have been measured using a single wire hot-wire probe. Hot-wire anemometry is a well known technique to survey boundary layers, and it has been established /7/ that it can detect separated flow as well as boundary layer transition reliably. The boundary layer measurements have been reported in more detail in earlier papers, i.e. for the steady case (Schulz and Gallus /4/) and for the rotor case references /18/ and /19/. The development of the midspan momentum thickness δ_2 along the blade suction surface for both the rotor and the no-rotor case are compared in Fig. 15. At the first 40 percent of chord the boundary layer is very thin and accurate measurements are difficult. The hump between 40 percent and 55

percent of chord, due to the laminar separation bubble in the steady case, has disappeared in the presence of the rotor. At about 75 percent of chord, the subsequent development of the turbulent boundary layer after the early start of transition with rotor results in a higher momentum thickness. It is assumed that this will give higher profile losses despite the disappearance of the laminar separation bubble.

Loss Measurements

While the previously discussed measurements were mainly concerned with the development of the midspan boundary layer, the loss measurements consider profile and endwall losses. Emphasis is placed upon to evaluate the effects, rotor-stator interactions have upon the overall performance of a compressor blade row. To achieve this objective, detailed flow field measurements in the exit plane of the cascade with pneumatic five-hole probes have been performed. Contour plots of the total pressure loss at the cascade exit plane are shown in Fig. 16. The loss coefficient is defined as the difference between the local stagnation pressure and the inlet stagnation pressure at midspan, normalized by the midspan dynamic head at inlet. The contour plots taken in the presence of the rotor are compared with measurements at steady incoming flow. Due to the rotor, there is a slight positive total pressure gradient towards the casing at the cascade inlet. The region of zero loss, therefore, seems to be more confined in the upper part of the passage.

Several observations can be made by comparing the loss contours for the two cases shown in Fig. 16: The flow field near the tip, including separation and tip clearance flow, remains nearly unchanged. The maximum losses as well as the extent of losses in the hub-blade suction side corner are reduced for the rotor case. As observed in the flow visualization (Fig. 7 and Fig. 8), the corner separation is reduced due to rotor-stator interaction effects, i.e. flow oscillation and high free-stream turbulence level, and this has a major effect on the loss development along the hub endwall. The blade wake is more distinguishable in the case with rotor. As already discussed in Fig. 15, the early onset of transition and the subsequent development of the turbulent boundary layer produces higher momentum thicknesses at the blade trailing edge. This has a major effect on the profile losses which increase despite the disappearance of the laminar separation bubble.

The variation of the mass-averaged loss coefficient at midspan and the overall loss coefficient with incidence are shown in Fig. 17. As exspected the midspan losses increase in the presence of the rotor, except at the high loading where the hub corner stall extends beyond midspan. This increase is about 30 percent, which is in agreement with investigations by Zil'berman et al. /22/, Cyrus /23/ and Evans /24/. The overall losses ($\overline{\omega}$) decrease as much as 40 percent due to the decreased hub corner stall, except at the negative incidence, where the separation is small for both cases (Fig. 7). Higher profile losses and lower endwall losses result in nearly the same values of $\overline{\omega}$ as in the case without rotor. These results suggest that rotor-stator interaction can be benificial for the overall performance of a compressor blade row, but this depends on blade loading and blade aspect ratio. While in high pressure stages the endwall losses govern most of the loss production, the number one loss source in front stages are profile losses. Rotor-stator interaction, therefore, might generate opposite effects in high pressure and low pressure stages.

4) CONCLUSIONS

The influence of rotor-stator interaction on the development of the blade surface boundary layers, endwall corner separation and on the losses of an annular compressor cascade have been evaluated.
At all angles of attack under investigation, the laminar separation bubbles observed at steady and uniform incoming flow have disappeared due to the presence of the rotor. This results in decreased three-dimensionality in the flow field on the blade upstream of turbulent separation.
The formation of turbulent spots underneath a rotor wake force transition to start periodically upstream of the location it was observed at steady incoming flow. The subsequent development of the turbulent boundary layer results in higher momentum thicknesses at the trailing edge.
The transition length is a function of blade passing frequency, turbulence level, local pressure gradient and wake depth. The transition length increases on the suction side, compared with the steady case, due to the stabilization of the flow, which occurs during the accelerating phase of the velocity fluctuation caused by the rotor wake passage. In the rotor case, the end of transition was therefore found further downstream even though the onset of transition has moved towards the leading edge. On the pressure surface the wakes decay much more rapid than on the suction surface, and this stabilizing effect is reduced. In the presence of the rotor, the transition process on the pressure surface starts and is also completed ahead of the positions found in the ste ly case.
With the rotor upstream, the hub corner stall and hence the losses near the hub have significantly decreased. This is mostly due to the wakes and the high turbulence level and partly due to the absence of the laminar separation bubble. It is not caused by the change in the hub wall boundary layer at the cascade inlet since the flow visualization on the hub does not show any change in secondary flow, which might influence the separated region.
Even though the losses at midspan increase up to 30 percent due to the early onset of transition and the unsteady boundary layer, the overall losses for the entire passage decrease by nearly 40 percent (depending on incidence). This is primarily caused by

decreased corner separation. The profile losses increase and the endwall losses decrease. Therefore blade loading and blade aspect ratio are important parameters when evaluating the effect of rotor-stator interaction.

5) REFERENCES

/1/ Hodson, H.P.: "Boundary Layer and Loss Measurements on the Rotor of an Axial-Flow Turbine", ASME Jnl. of Engineering for Gas Turbines and Power, Vol. 106, April 1984

/2/ Pfeil, H., Herbst, R., Schroder, T.: "Investigation of Laminar-Turbulent Transition of Boundary Layers Disturbed by Wakes", ASME Paper No. 82-GT-124, 1982

/3/ Hodson, H.P., Addison, J.S.: "Wake Boundary Layer Interaction in an Axial-Flow Turbine Rotor at Off-Design Conditions", ASME Paper No. 88-GT-233, 1988

/4/ Schulz, H.D., Gallus, H.E.: "Experimental Investigations of the Three-Dimensional Flow in an Annular Compressor Cascade", Jnl. of Turbomachinery, Vol. 110, 1988, pp. 467

/5/ Bohn, D., Simon, H.: "Mehrparametrige Approximation der Eichräume und Eichflächen von Unterschall- bzw. Überschall-5-Loch-Sonden", ATM Meßtechnische Praxis, Lieferung 470, 1975

/6/ Bellhouse, B.J., Schultz, D.L.: "Determination of Mean and Dynamic Skin Friction, Separation and Transition in Low Speed Flow with a Thin-Film Heated Element", Jnl. Fluid Mech., Vol. 24, No. 2, 1966

/7/ Hodson, H.P.: "Boundary Layer Transition and Separation Near the Leading Edge of a High Speed Turbine Blade", ASME Jnl. Engineering for Gas Turbines and Power, Vol. 107, January 1985

/8/ Dengel, P., Vagt, J.D.: "A Comparison Between Hot-Wire and Pulsed-Wire Measurements in Turbulent Flows", Proceedings 4th Turbulent Shear Flow Conference, Karlsruhe, 1983

/9/ Lakshminarayana, B., Poncet, A.: "A Method of Measuring Three-Dimensional Rotating Wakes Behind Turbomachinery Rotors", Jnl. of Fluids Engineering, 1974, pp. 87-91

/10/ Hoheisel, H., Kiock, R., Lichtfuss, H.J., Fottner, L.: "Influence of Free-Stream Turbulence and Blade Pressure Gradient on Boundary Layer and Loss Behavior of Turbine Cascades", ASME Jnl. of Turbomachinery, Vol. 109, 1987, pp. 210-219

/11/ Dunham, J.: "Prediction of Boundary Layer Transition on Turbomachinery Blades", AGARDograph No. 164, 1972, pp. 55-71

/12/ Walker, G.J.: "The Unsteady Nature of Boundary Layer Transition on an Axial-Flow Compressor Blade", ASME Paper No. 74-GT-135

/13/ Squire, H.B., Winter, K.G.: "The Secondary Flow in a Cascade of Airfoils in a Nonuniform Stream", Jnl. of the Aero. Science 1951, pp. 271-277

/14/ Takei, N., Masuda, S.: "Acoustic Control of Turbulent Separation in a Two-Dimensional Diffuser", Second European Turbulence Conference, 1988

/15/ Castro, I.P., Haque, A.: "The Structure of a Shear Layer Bounding a Separation Region - Part II: Effects of Free-Stream Turbulence", Jnl. of Fluid Mech., Vol. 192, 1988

/16/ Lücking, P.: "Numerische Berechnung der dreidimensionalen reibungsfreien und reibungsbehafteten Strömung durch Turbomaschinen", Ph.D. Thesis, Rheinisch-Westfälische Technische Hochschule, Aachen, 1982

/17/ Miller, J.A., Fejer, A.A.: "Transition Phenomena in Oscillating Boundary Layer Flows", Jnl. of Fluid Mech., Vol. 18, 1964, pp. 438-449

/18/ Schulz, H.D., Gallus, H.E., Lakshminarayana, B.: "Three-Dimensional Separated Flow Field in the Endwall Region of an Annular Compressor Cascade in the Presence of Rotor-Stator Interaction - Part I: Quasi-Steady Flow Field and Comparison with Steady-State Data", ASME Paper No. 89-GT-76, 1989

/19/ Schulz, H.D., Gallus, H.E., Lakshminarayana, B.: "Three-Dimensional Separated Flow Field in the Endwall Region of an Annular Compressor Cascade in the Presence of Rotor-Stator Interaction - Part II: Unsteady Flow and Pressure Field", ASME Paper No. 89-GT-77, 1989

/20/ Truckenbrodt, E.: "Ein Quadraturverfahren zur Berechnung der laminaren und turbulenten Reibungsschicht bei ebener und rotationssymmetrischer Strömung", Ingenieur-Archiv, Vol. 4, 1952

/21/ Scholz, N.: "Ergänzungen zum Grenzschichtquadraturverfahren von E. Truckenbrodt", Ingenieur-Archiv, Band 24, 1960

/22/ Zil'berman, A.S., Lopatitski, A.O., Nakman, Y.V., Vol'fson, I.M.: "Additional Energy Losses due to Periodic Non-Steadiness of the Flow in the Moving Blades of Turbine Stages", Teploenergetika, Vol. 20, 1973

/23/ Cyrus, V.: "The Effect of the Inlet Velocity Profile in the Three-Dimensional Flow in a Rear Axial Compressor Stage", ASME Paper No. 88-GT-46

/24/ Evans, R.L.: "Boundary Layer Development on an Axial-Flow Compressor Stator Blade", ASME Paper No. 77-GT-11

6) ACKNOWLEDGEMENTS

7) FIGURES
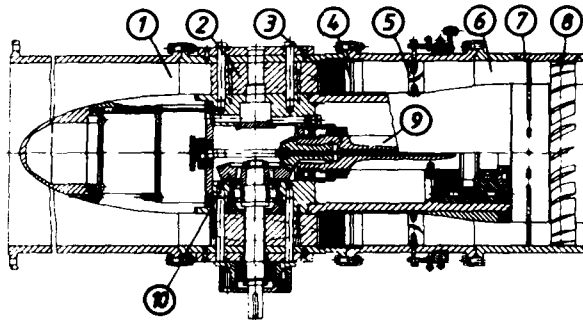
Fig. 1: Test facility with IGV (5), cylinder rotor (7)
and measuring cascade (8)
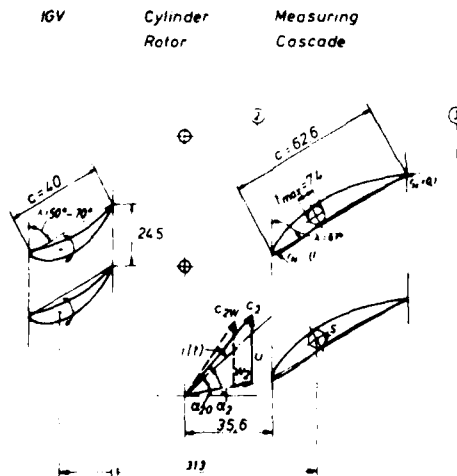
Fig. 2: Cascade geometry at mid-span
(units in mm)
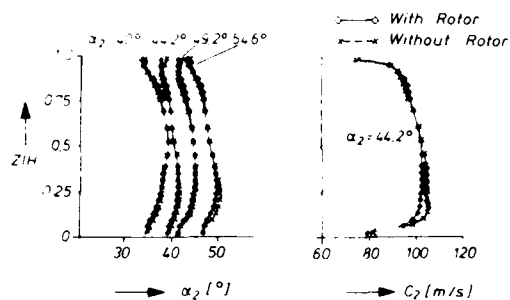
Fig. 3: Inlet angles α_2 (measured from the axial direction) and velocity distribution at cascade inlet
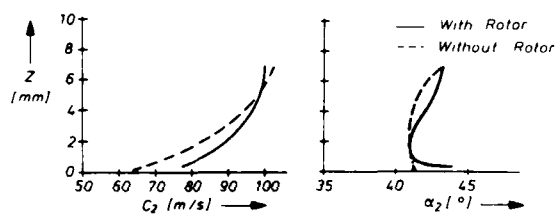
Fig. 4: Hub wall boundary layers at the cascade inlet
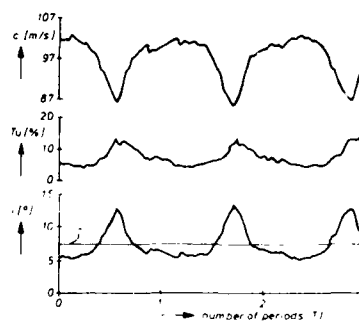
Fig. 5: Phase-lock averaged velocity (c), turbulence level (Tu) and incidence (i)
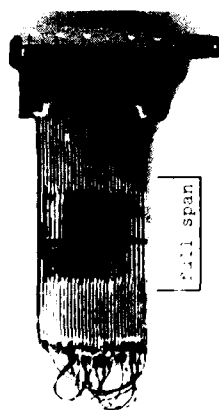
Suction Side   Pressure Side
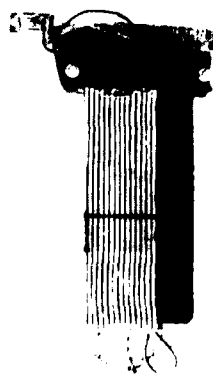
Fig. 6: Elongated blade instrumented with hot-film gauges on about the suction and pressure side
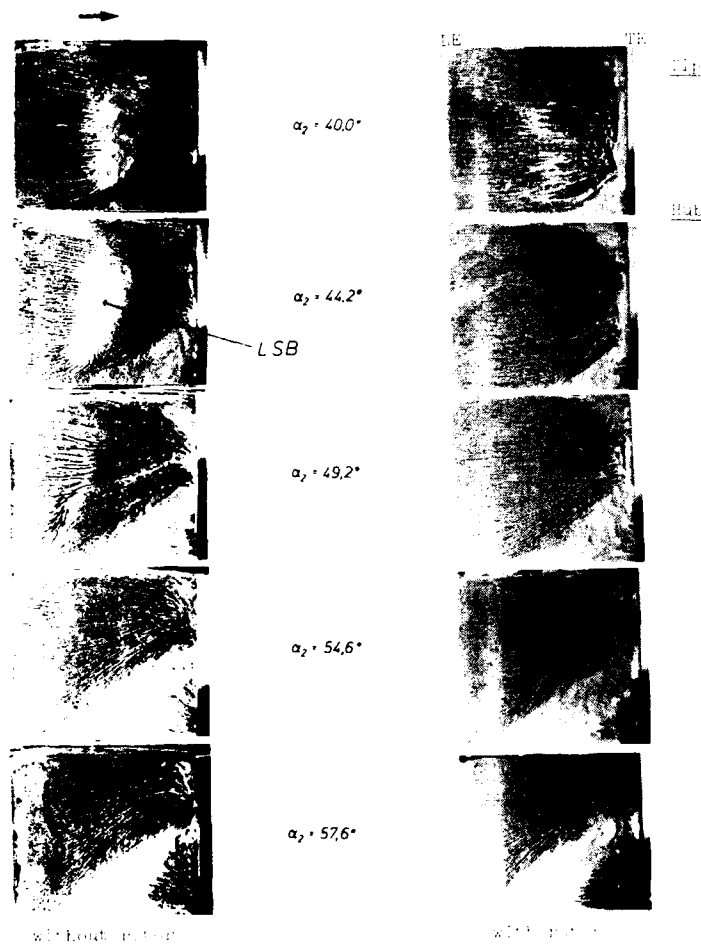
$\alpha_2 = 40.0°$

$\alpha_2 = 44.2°$

L SB

$\alpha_2 = 49.2°$

$\alpha_2 = 54.6°$

$\alpha_2 = 57.6°$

without rotor

with rotor

Fig. 7: oil flow visualization on the blade suction side

without rotor

with rotor

Fig. 8: oil flow visualization on the suction side
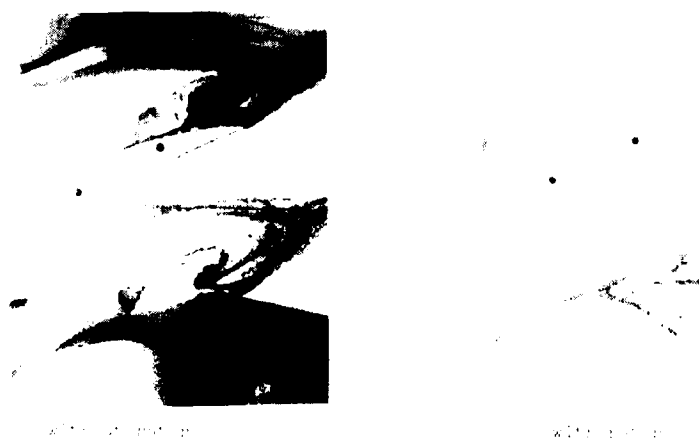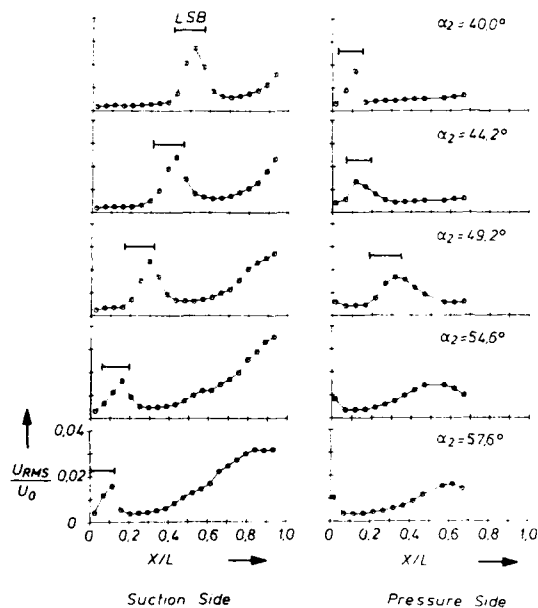
Fig. 9: Random fluctuation of the hot-film
signals versus chord at midspan
(steady case)
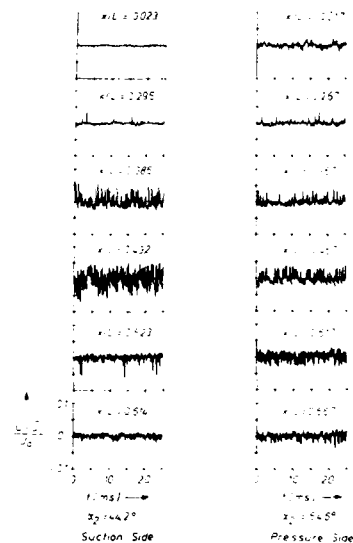
Fig. 10: Real-time traces of the
hot-film signals at
midspan (steady case)
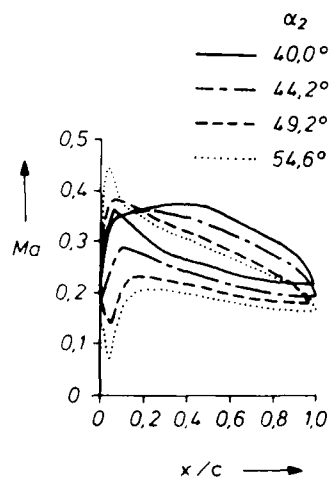
Fig. 11: Evolution of predicted
midspan isentropic
Mach number distribu-
tion with incidence
angle

Fig. 12: Unsteady results at midspan with varying
incidence
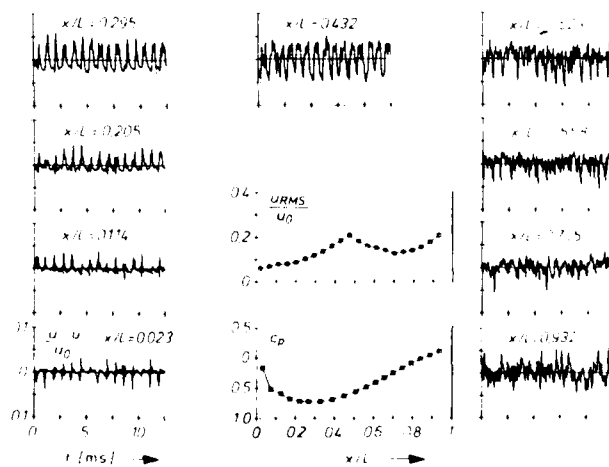
Fig. 13: Hot-film results at
         midspan (with rotor,
         $\alpha_2 = 44.2°$)

$x/L = 0.023$ $x/L = 0.068$ $x/L = 0.114$

$x/L = 0.205$ $x/L = 0.386$ $x/L = 0.477$

$x/L = 0.523$ $x/L = 0.705$ $x/L = 0.932$

$\frac{\tilde{U}-\bar{U}}{U_o}$

$\frac{U_{RMS}}{U_o}$

$t\,[ms]$

$W \triangleq Wake$

$F \triangleq Freestream\ in\ between\ Wakes$

Suction Side

Pressure Side

Fig. 14: Midspan blade boundary
         layer history with and
         without rotor

Without Rotor   With Rotor
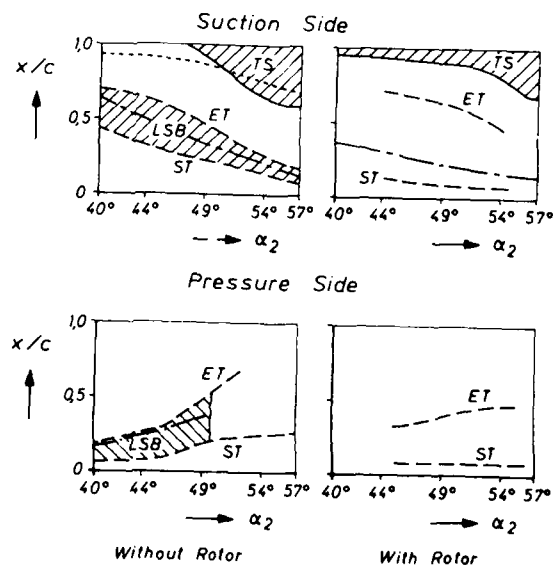
ST   Start of Transition   — · — predicted Transition
ET   End of Transition   ········· predicted Separation
TS   Turbulent Separation
LSB   Laminar Separation Bubble

21-14
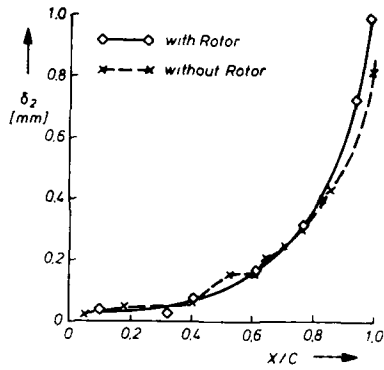
Fig. 15: Comparison of midspan momentum
thickness with and without rotor

$$\omega = (\bar{P}_{t2m} - P_{t3})/(\bar{P}_{t2} - \bar{P}_{s2})_m$$
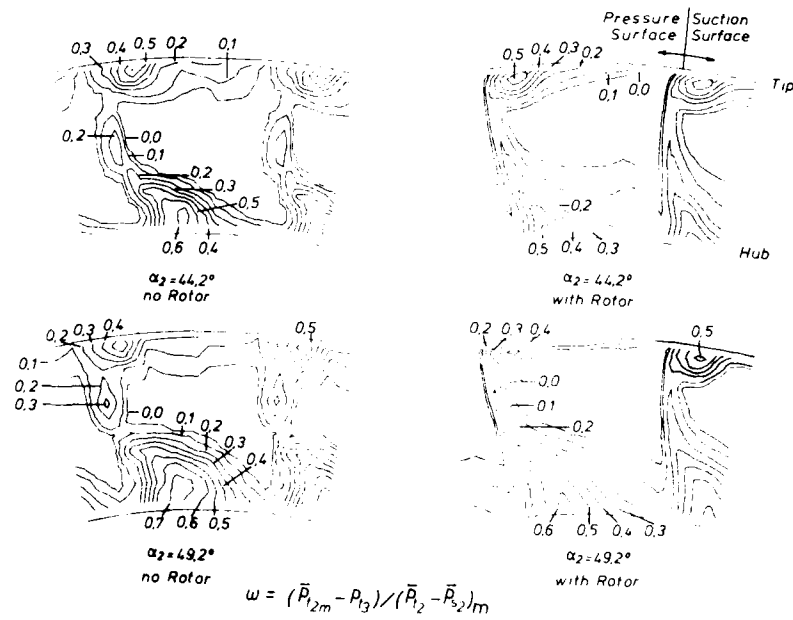
Fig. 16: Cascade exit loss contours
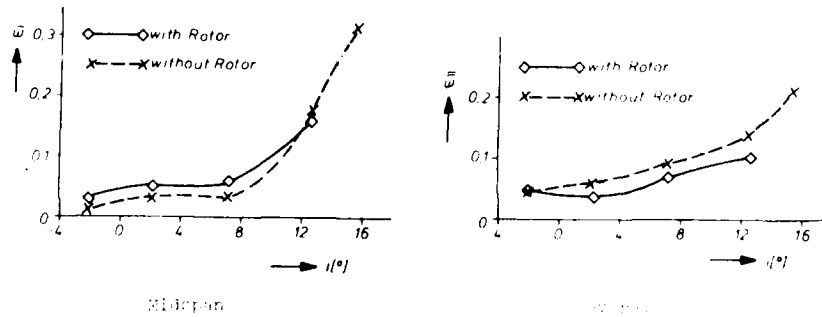
Midspan

Fig. 17: Midspan and overall losses versus incidence

DISCUSSION

F.Leboeuf, Ecole Centrale de Lyon, France
How does the velocity angle change in the vicinity of the hub, in presence of a rotor and how could the decrease of the corner stall be connected to the increase of upstream secondary vorticity.

Author's response
This is a very crucial question, and as being pointed out in the paper, an enormous effort was put into trying to establish the same inlet conditions with and without a rotor upstream of the test section. As shown on fig 3 and fig 4, this has been achieved to a very reasonable degree of accuracy. The inlet boundary layer thickness is the same in both cases, and the slight difference in boundary layer profile are confined to the region close to the hub.

These differences, though, do not have any effect on the secondary flow inside the passage (as shown on fig 8 of the paper) and therefore it is felt that the decrease in corner stall can be directly related to the increase of turbulence level and the flow oscillation induced by the rotor .

J.Chauvin - LEMFI,France
Using the author's experimental data that were communicated in advance, a 3-D steady flow method has been used for the study of the mid-span region. Qualitatively, the disappearence of the laminar bubble and the increase of the turbulent separation zone was shown by these calculations.Using information from unsteady flat plate measurements (Michel, ONERA,France) the modification of the transition zone on the suction side of the blades could also been explained.

Author's response
It is very encouraging that these experimental data have been compared to the results of a numerical code. It is also very encouraging that the code shows the same trends. In order to give additional input to modeling transition in the presence of wakes, the data will be analyzed in even more detail.

S.C.P.Cook - Rolls-Royce, Derby, U.K.
Regarding the hot film sensor results, was any attempt made to analyse the data in the frequency domain?

Author's response :
This analysis was made, the results are on file and available to everyone who is interested in it, although these results are not published.

Fast Fourier transformation was applied to the hot-film signals and the blade passing frequency as well as the Tollmien-Schlichting instabilities, inherent to the flow, could be traced. Analysis of the data is not finished yet and some more work will be done with respect to the physical reasoning of the prolongated transition region on the suction side of the blades, in the case with rotor.

METHODS FOR MAKING UNSTEADY AERODYNAMIC PRESSURE
MEASURMENTS IN A ROTATING TURBINE STAGE

R.W. Ainsworth, J.L. Allen and A.J. Dietz
Department of Engineering Science
Oxford University
Parks Road
Oxford
OX1 3PJ
UK

ABSTRACT

A new method for obtaining detailed unsteady pressure measurements in a rotating turbine stage is described. The novelty of the technique is based on the use of miniature semiconductor pressure sensors attached directly to the surface where the measurement is required, permitting simultaneously a high surface density of instrumentation together with a high frequency response.

In reviewing typical semi-conductor transducer behaviour, attention is drawn to some of the traditional constraints encountered with these devices. In describing the development of the new technology employed here, the methods used to circumvent these traditional constraints are outlined.

1. INTRODUCTION AND BACKGROUND

In the continuing strive towards obtaining experimental data at conditions resembling as closely as possible those found in the high pressure turbine section of modern gas turbines, there is a corresponding need to increase the sophistication of the enabling instrumentation. In the area of heat transfer and pressure field measurement, there is currently great interest in fully three dimensional rotating unsteady experiments conducted at engine values of the relevant important non-dimensional groups. Globally, and currently, there are three research groups conducting transient experiements capable of these measurements: those at Calspan (Dunn et al [1,2,3,4]), those at MIT (Epstein Guenette et al [5,6,7]), and those in Oxford (Ainsworth et al [8,9]). It is in relation to the latter experiments that the developments in unsteady pressure measurement described in this paper are apposite.

Here, the aim of the experiment is to further the understanding of the physics of the flow in a three dimensional geometry under rotating conditions, as well as providing highly detailed heat transfer and pressure field information for comparison with CFD calculations of the flow (so called code validation). The choice of blade profile in this project has the advantage of allowing comparison with the earlier two dimensional unsteady data of Doorly [10,11,12,13], being the three dimensional blade profile from which this profile was defined (at mid-height). In addition, considerable further aerodynamic studies have been conducted on it in two dimensional cascade [14]. In Doorly's work, the unsteady nature of the nozzle guide vane wake rotor blade interaction was represented by using a rotating bar wake generator ahead of a cascade of stationary rotor blades. A major aim of the Oxford rotor experiment will be to investigate the validity of the two dimensional bar wake unsteady simulation, in determining behaviour in an essentially three dimensional environment.

The conditions and mode of operation of the new rotor facility are of paramount importance in discussing the high surface density - high frequency response pressure sensors which have been developed. In essence [8] an Isentropic Light Piston tunnel (Figure 1) is used to compress air, to a pre-determined pressure and temperature level. Prior to this compression process, the rotating turbine assembly (Figure 2) is accelerated from rest to a speed of 6000 r.p.m. using an air motor, and at the selected instant, the compressed air is allowed to pass through the turbine, further accelerating it through the design point (table 1), to an ultimate speed of 9000 r.p.m. (see Figure 3). An important feature of the experiment is to acquire data at the 'correct' incidence, and within a tolerance of 1° of incidence, nozzle guide vane-rotor blade events may be captured at a sampling rate of 200 kHz, in the time available with 4Kbytes of memory per channel.In terms of static pressure field instrumentation on the rotor blades themselves, the project called for one hundred measurement sensors to be mounted in as high a spatial density as possible, and capable of producing accurate data under the conditions of operation. The device chosen in this application was the piezo-resistive semi-conductor pressure sensor, a sensor well capable of meeting frequency response and with the newly developed technology, spatial density targets, but traditionally exhibiting some disadvantages too. These considerations are discussed in the next section.

2. PROPOSED INSTRUMENTATION

2.1 Method of Implementation

The project started by identifying an available commercial transducer which came closest to meeting the specifications in terms of size, construction, frequency response,and base-strain sensitivity. This was found to be the Kulite LQ-047 microline flat pack series transducer, specifically designed for turbine blade mounting, in terms of thin section (0.635mm), low sensitivity to radial acceleration (.00004 %FS/g for a 25psi transducer) and high frequency response (>200 kHz). It was subsequently realised that if the semi-conductor chip itself could be mounted directly onto the blade surface itself, with no accompanying mounting shim and minature printed circuit board for lead-outs, a considerable increase in sensor surface density could be achieved, and transducers could be mounted in thinner sections of the blade.

The proposed method was as follows:

Pockets for the sensor were firstly machined in a bare turbine blade, and the blade was subsequently coated with a vitreous enamel. The F300 Agemaspark spark erosion machine was capable of eroding holes as small as 75µm with an accuracy of reproduction of up to ± 10µm depending on the range selected and a best surface finish of 0.3µm. The enamel coating was applied as a viscous liquid slip (frit materials plus mill additions), ground to a specific fineness and suspended in water. The coating was approximately 50µm thick and was dried in a warm cabinet to 120°C for 30 minutes. After drying the coating was fired at 940°C for 15 minutes followed by air drying. Application of the wiring and a second coating of enamel followed. Finally the leads were exposed and the sensors were installed and connected by Kulite (Figure 4).

In looking at a physical and an electrical model of the sensor (Figure 5), the sensing element itself is constructed by firstly micro-machining grooves into a 125µm thick silicon diaphragm and attaching it to a strain isolating pillar, with a vacuum filled cavity between the active part of the diaphragm and the pillar. P type piezo-resistive elements are formed over the grooves by diffusing an impurity element into the silicon through a photolithographic mask. All materials exhibit a piezo-resistive effect, a change in electrical resistivity with applied stress, and in a semi-conductor this effect can be very large. For a semi-conductor the resistivity ρ is inversely proportional to the product of the number of charge charries N_i and their average mobility μ_{ave}, $\rho = 1/(eN_i\mu_{ave})$. The effect of an applied stress is to change both the number of carriers and their average mobility. Subsequently, as pressure is applied, the thinnest part of the diaphragm deflects (where the piezo-resistive elements are located), and by connecting the resistors in a Wheatstone bridge network, the change in balance of the bridge due to change in values of the resistors can be monitored as a changing output voltage when a constant excitation voltage is applied.

This is the basis of operation, but there are a few more sophisticated features which have to come in to play to make a semi-conductor sensor an accurate transducer for aerodynamic purposes. The resistances are arranged on the diaphragm such that on each half of the bridge, one gauge is in tension and the other in compression as the diaphragm deflects, maintaining a linear output from the sensor over a wide range of deflections. A major constraint in operation would lie in the temperature sensitive nature of the piezo-resistive elements, if nothing were done about it. For a semiconductor device, each resistive element can be considered to have a TCR (temperature coefficient of resistance) and a TCGF (temperature coefficient of gauge factor). If no temperature effects were present, one

would expect a certain change in electrical output for a given pressure change (the gauge factor being change in resistance per mechanical strain). However, with the temperature effects indicated above occurring, not only will the balance point of the bridge shift with temperature but the overall gauge sensitivity will change too. This is normally compensated for by the addition of a span and null shift compensating resistors (Figure 6) but in the case of the new 'chip-on' technology outlined here, this would add a lot of external components and an alterative means of compensation was sought. It was realised that by measuring bridge output voltage and bridge current consumed as both functions of temperature and pressure, the gauge TCRs and TCGFs could be established. Subsequently with the sensor in use, by monitoring both current input and voltage output, the transducer output could be software corrected to allow for any temperature sensitive effects

There was some choice of available semi-conductor sensors from Kulite, ranging from under 1mm square to 1.5mm square. Ultimately the chosen element (Figure 7) was 1.2mm square.

2.2 Mechanical Constraints

A primary consideration in determining whether the proposed method of mounting bare chips directly onto a turbine blade would work or not lay in checking the retention of the aerodynamic profile of the blade when the vitreous enamel was applied. In fact, this was found to be good (Figure 8). After installation of the pressure sensor, the blade profile was restored by adding a layer of a silastomer over the chip surface, producing a surface flush with the rest of the blade. Any deleterious effects on transducer frequency response would have to be evaluated (section 3.3). Additional mechanical constraints lay in the level of centrifugal acceleration which would be experienced by the sensor diaphragm which was calculated as 20000g at 8400 r.p.m (tangential acceleration was negligible in comparison), and the level of stress in the blade, resulting in base strain on the sensor base. As part of his research programme on the mechanical design of the Oxford rotor facility, Sheard [15] conducted a finite element analysis of the blade at design conditions (Figure 9) and calculated that the levels of base strain would be of order 200 $\mu\varepsilon$ at the blade mid-height section.

2.3 Programme of Testing

Whilst the initial examination of the proposed technique looked promising, it had high-lighted the need for an experimental programme of work to investigate the operating envelope under which this technology could be used. Specifically, the effects of base strain sensitivity, centrifugal acceleration or g sensitivity, frequency response, temperature sensitivity and calibration stability were all phenomena to be investigated. The results shown below are the first preliminary results to be given.

3. SEMI-CONDUCTOR TRANSDUCER PERFORMANCE

The test programme consisted of four main experiments conducted in separate facilities using specially constructed test specimens. The first experiment made use of a purpose built calibration facility in which all the specimens could be tested. One such specimen (Figure 10) was built for base strain sensitivity calibration in a tensile testing machine, with 10 transducers of three differing types attached. Twelve other sensors were mounted on three separate discs for g sensitivity tests in a spinning rig. A number of specimens, such as the one shown in Figure 11, were constructed for work on wiring location, insulation and the chip mounting technique. Further specimens were aimed at experiments conducted in a shock tube to determine the frequency response of the sensors and any degrading effects of adding silastomers over the diaphragm surface. The four main experiments and associated facilities are outlined below.

3.1 Calibration

3.1.1 Aim. The aim of the calibration tests is to characterize the temperature response of the transducer in a form which will allow active temperature compensation during the digital processing of pressure measurement results. If the pressure response of the transducer is linear, with a unique slope and intercept at each temperature, its temperature response will be fully described by the temperature sensitivity of these two variables. The sensitivity of the slope is known as Span Sensitivity or sometimes as the Temperature Coefficient of Gauge Factor and the sensitivity of the intercept is known as the Null Shift. An accurate measurement of the transducer's bridge temperature will also be required for the active compensation technique. This can be done by measuring the voltage drop across a sense resistor in series with the bridge. The temperature sensitivity of this sense resistor voltage drop is a measure of the Temperature Coefficient of Resistance (T.C.R.) of the chip.

3.1.2. Calibration Facility. A computer controlled calibration facility was constructed to permit precision testing of the transducers over a wide range of pressures and temperatures (Figure 12). The heart of the rig, lay in the use of a Druck DPI 501 digital pressure controller linked to a pressure vessel inside an environmental chamber. The DPI 501 , controlled by an IBM PC AT through an IEEE interface, could control pressure to an accuracy of $\pm.007\%$ FS, the sensing element being a large vibrating cylinder pressure transducer manufactured by Schlumberger. The environmental chamber (Unilab Thermoduct) is also controlled by a digital interface, and can cycle between $- 70^{\circ}$ C and $+ 250^{\circ}$ C. Up to ten transducers at a time can be mounted in the test chamber and their outputs monitored on HP 3478A digital voltmeters, again capable of being controlled and read down the IEEE interface.

The procedure used in obtaining the three required calibration results outlined above may be illustrated by following the calibration of a sample transducer. The voltage drop across the sense resistor (V_{sense}) and the transducer output voltage (V_{out}) were measured over the transducer's rated pressure range (0 to FSD) over a range of temperatures from -50 $^{\circ}$ C to 100°C. The transducer was stabilized at each temperature and then calibrated over a minimum of two cycles, from 0 to FSD and back, with at least 6 pressures between. At each pressure, 6 measurements were taken at 30 second intervals to check that the voltages were stable. A plot of the calibration of the sample transducer is given in Figure 13a showing the output voltage over a pressure range for a number of temperatures. A similar plot for the calibration of the transducer's sense resistor voltage (Vsense) is given in Figure 13b.

3.1.3 Vsense It can be seen from Figure 14b that Vsense is relatively insensitive to pressure. Hence an average value may be calculated at each temperature. A plot of this is given in Figure 14 and by using a least squares line fit the intercept γ_{vs} and slope β_{vs} may be determined. From these measurements the TCR may be calculated using the equation:

$$T.C.R. = \frac{-V_{in} \ \beta_{vs} \ R_S}{\gamma_{vs}^2 \ R_{BR}} \times 100 \ \%$$

where V_{in} is the 10V input voltage, Rs the value of the sensing resistor and R_{BR} the resistance accross the transducer at a reference temperature, nominally 15°C For the transducer under consideration , the T.C.R. was calculated as 17.8 $\%/100^{\circ}$C and most of the transducers measured showed T.C.R's of this order. The linearity of the Vsense plot and its insensitivity to pressure changes show that the measurement of the voltage across a sense resistor is a feasible way of recording bridge temperature.

3.1.4 Span Sensitivity. The span sensitivity may be expressed as a change in the Full Scale Deflection with temperature i.e., % FSD/100°C , with 15°C again being the reference temperature. The use of a sense resistor with a transducer powered by a constant voltage source will reduce the span sensitivity of the transducer providing its T.C.R. is less than its initial span sensitivity [16]. The sense resistor acts as a voltage divider, increasing the bridge voltage as the bridge resistance increases with temperature, compensating for the decreasing span sensitivity. With the transducers tested, a sense resistor which matched the bridge resistance was found to give good results. Any temperature sensitivity still remaining in the span may then be removed in the active compensation. For the sample transducer, the compensation sensitivity was -6.8 %FSD/100ºC (Figure 15). The line fit gives reasonable correlation and a parabolic fit would give even better results in the software compensation, removing most of the systematic temperature sensitivity.

3.1.5 Null Shift. The sense resistor has no passive compensating effect on the null shift and rather than introducing further parallel resistors , active software compensation was chosen The plot of null shift with temperature for the sample transducer is given in Figure 16. The linearity of the plot shows that the null shift should be easily compensated.

3.2 Base Strain Sensitivity

The tensile specimen was constructed using the same technique that was to be applied to the blades The specimen was manufactured from Inco 718, machined with pockets to take the transducers and coated with vitreous enamel in the usual way. The specimen was mounted in a Instron tensile testing machine and tested to a base strain of 800 $\mu\varepsilon$ with 200 $\mu\varepsilon$ being the expected strain level on the blade midheight section at design rotational speed (Section 2.2). A plot of the tensile test results for one chip, aligned in the tensile specimen with its strain sensitive elements parallel to the load giving a worst case result, is shown in Figure 17. Two load cycles were performed with the specimen being reversed in the clamps for the second cycle to cancel any bending moment introduced by misalignment of the grips. The base strain sensitivity calculated from this plot is -.00164 %FS/$\mu\varepsilon$.

3.3 Frequency Response

In order to make detailed measurements of the static pressure field during the valid data acquisition window, a frequency response flat to > 100kHz was desirable. Tests were set up in a shock tube in order to determine the response of the transducer to a step input.
The transducers were mounted in two positions:

a) A side-port to avoid damage to the silicon diaphragm caused by impact damage from the nylon bursting diaphragm.

b) An end-port where a greater likelihood of damage was possible.

The problem with position a) was that of the finite time taken to traverse the silicon diaphragm and the corresponding degradation of step input. In practice, little difference was observed between the two mounting positions, and transducers with (Figure 19) and without silastomer (Figure 18) covering their diaphragms were tested. Results of the time response, which clearly show the diaphragm natural *frequency*, and *by transposing to the frequency domain*, of the power spectral density (Figure 20) showed that the amount of silastomer used was having a small effect on the useable frequency range.

3.4 Performance Under Rotating Conditions

A *spinning rig* (Figure 21) was used to evaluate the performance of the sensors under rotating conditions. Up to four sensors could be mounted on a small circular disc (Figure 22) which could itself be fitted into a large diameter spinning disc. The spinning disc was rotated by an air motor under computer control, with signals being extracted from the rotating frame using a slip-ring. The whole assembly was housed in a pressure chamber, permitting variation of pressure from 500Pa to 350 kPa. For the initial tests, no signal conditioning was used. The output from the transducers was taken straight through the slipring and recorded by a CIL 6380 A/D convertor. A sample plot of the transducer output over the speed range from 0 to the design speed of 8000 rpm at 500 Pa is given in Figure 23. This is again a worst case result with the strain sensitive elements aligned in the radial direction, The plot is linear and so rotational effects will be able to be included in the active software compensation. A plot comparing the transducer signal under rotation to the stationary signal is given in Figure 24. There is no rotational induced noise in the signal.

4. CONCLUSION

A method for mounting semi-conductor sensors directly onto a turbine blade surface has been outlined. The potential advantage in the technique lies in increasing the spatial density of measurement points whilst retaining the benefits of high frequency response that these small semi-conductor devices possess. The first preliminary measured performance of these devices indicate that they can be used with reliability and confidence, though many more tests will be required to complete the programme. Other potential applications beyond blade static pressure measurement are currently under investigation including the use of this technology to construct wedge and pyramid two and three dimensional aerodynamic probes.

Turbine operating point

Specific Speed	$(\frac{\dot{}}{\sqrt{T_0}})$	4.36 rpm K$^{\frac{1}{2}}$
Mass Flow Number	$(\frac{\dot{m}\sqrt{T_0}}{P_0})$	7.04×10^{-4} ms K$^{\frac{1}{2}}$
Reynolds Number	(NGV exit, axial chord)	2.7×10^6
Mach Number	(NGV exit mid-height)	0.946

Tunnel Operating Parameters

Tunnel Parameters	Temperature Ratio T_R/T_w		
	1.0	1.3	1.5
Initial Tube Pressure	5.55 Bar	3.1 Bar	2.25 Bar
Initial Tube Temperature	288 K	288 K	288 K
Final Tube Pressure	5.55 Bar	7.77 Bar	9.29 Bar
Final Tube Temperature	288 K	374 K	432 K
Blade Relative Total Temperature	253 K	328 K	379 K
Blade Relative Temperature Ratio	0.877	1.14	1.32
Run Time	0.412 s	0.189 s	0.121 s
Turbine Output Power	1.41 MW	2.24 MW	2.88 MW
Turbine Speed Change (during a run)	4315 rpm	2750 rpm	2139 rpm
Turbine Design Speed	7397 rpm	8434 rpm	9060 rpm

Table 1

5. ACKNOWLEDGEMENTS

6. REFERENCES

[1] DUNN, M.G.,
Heat Flux Measurements for the Rotor a Full Stage Turbine: Part 1, Time Average Results. ASME Paper No. 86-GT-77

[2] DUNN, M.G., RAE, W.J. and HOLT, J.L.,
Measurement and Analysis of Heat Flux Data in a Turbine Stage. Journal of Engineering for Gas Turbines and Power, pp 229 - 240, Vol. 106, January 1984

[3] DUNN, M.G., GEORGE, W.K., RAE, W.J., WOODWARD, S.H., MOELLER, J.C., and SEYMOR . P.J.,
Heat Flux Measurements for the Rotor of a Full Stage Turbine. Journal of Turbomachinery pp 287 - 293, Vol. 108, 1986

[4] DUNN, M.G., SEYMOR . P.J., WOODWARD, S.H., GEORGE, W.J. and CHUPP, R.E.
Phase Resolved Heat Flux Measurements on the blade of a Full-scale Rotating Turbine. Journal of Turbomachinery, pp 8 - 19, Vol. III, January 1989.

[5] EPSTEIN . A.H., GUENETTE., G.R. and NORTON . R.J.G,
The MIT Blowdown Turbine Facility. ASME Paper 84-GT-116

[6] EPSTEIN, A.H., GUENETTE, G.R., NORTON, R.J.G. and CAO YUZHANG,
High Frequency Response Heat Flux Gauge for Metal Blading. AGARD CP-390, Bergen, Norway, 1985

[7] GUENETTE, G.R., EPSTEIN, A.H., GILES, M.B., HAINES, R. and NORTON, R.J.G,
Fully Sealed Transonic Turbine Rotor Heat Transfer Measurements Journal of Turbomachinery, pp 1-7, Vol. III, January 1989

[8] AINSWORTH, R.W., SCHULZ, D.L., DAVIES, M.R.D., FORTH, C.P.J., HILDITCH, M.A., OLDFIELL M and SHEARD, A.G.
A Transient Flow Facility for the Study of the Thermofluid-Dynamics of a Full Stage Turbine Under Engine Representative Conditions. ASME Paper 88-GT-144

[9] AINSWORTH, R.W., ALLEN, J.L., DAVIES, M.R.D., DOORLY, J.-, FORTH, C.J.P., HILDITCH, N OLDFIELD, M.L.G. and SHEARD, A.G.
Developments in Instrumentation and Processing for Transient Heat Transfer Measurement in a Full Stage Model Turbine. Journal of Turbomachinery pp 20-27, Vol. III, January 1989

[10] DOORLY, D.J.,
A Study of the Effect of Wake-Passing on Turbine Blades. D.Phil Thesis, Oxford University, 1984

[11] DOORLY, D.J. and OLDFIELD, M.L.G.,
Simulation of Wake Passing in a Stationary Turbine Rotor Cascade. Journal of Propulsion, pp 316-318 Vol 4, July 1985

[12] DOORLY,D.J., and OLDFIELD, M.L.G.
Simulation of the Effects of Shock Wave Passing on a Turbine Rotor Blade. Journal of Engineering for Gas Turbines and Power, pp 998-1006, vol 107, October 1985

[13] DOORLY, D.J., OLDFIELD, M.L.G. and SCRIVENER, C.T.J.,
Wake Passing in a Turbine Rotor Cascade. AGARD CP-390, Bergen, Norway 1985

[14] KING,P.,
D.Phil Thesis, University of Oxford, 1987.

[15] SHEARD,A.G.,
D.Phil Thesis, University of Oxford, 1989.

[16] Kulite Semiconductor Strain Gauge Manual, Leonia, New Jersey, USA, 1988

Internal diam of pump tube 24" 0.61 m
Length of pump tube 18' 5.49 m
Driver cylinder pressure 2000 psig 13.79 MPa
Max pressure in pump tube 500 psig 3.45 MPa
Max pressure in dump tank 70 psia 0.48 MPa
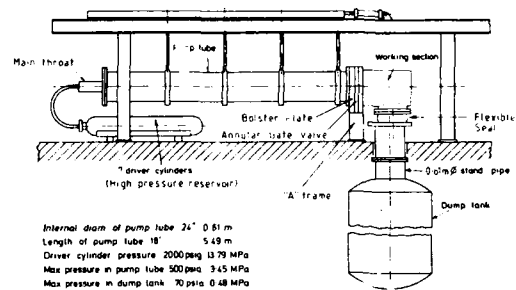
FIG. 1. General Arrangement of the O.U.E.L. Transient Turbine Facility
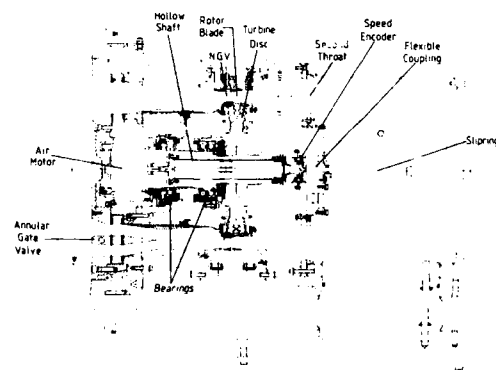
FIG. 2 O.U.E.L. Turbine Module

$$T_R(abs) = \frac{T_o(abs)}{T_{blade}}$$

$$T_R(rel) = \frac{T_o(rel)}{T_{blade}}$$
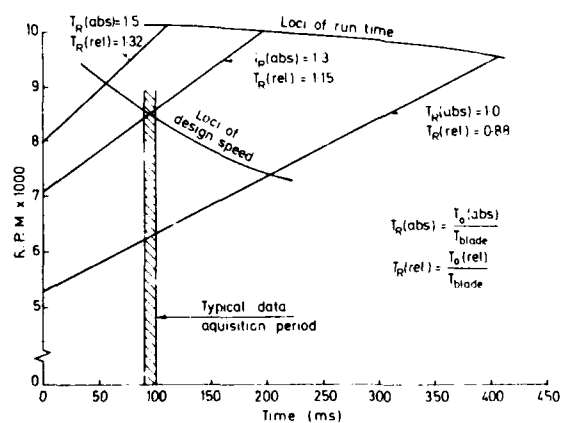
FIG. 3 Speed Characteristics of the O.U.E.L. Turbine At Various Temperature Ratios

FIG. 4. Schematic Diagram of Chip Mounting

FIG. 5. Chip Electrical Model and Schematic (from 1 1)

FIG. 6. Chip Electrical Compensation

FIG. 7. Chip Photograph
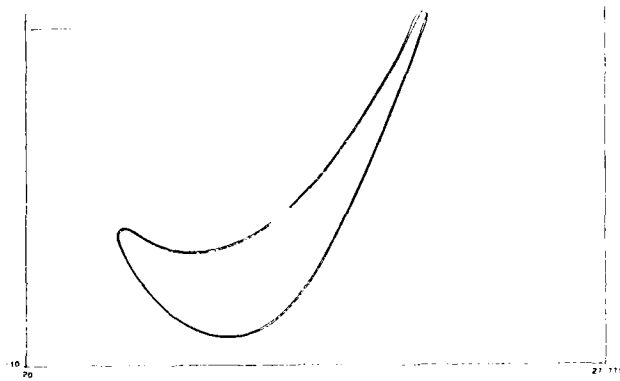
FIG. 8. Measured Blade Profile Before and After Enamelling
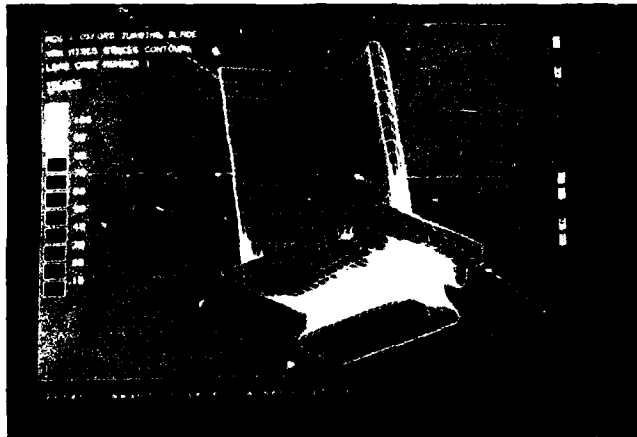
FIG 9. Finite Element Model Showing Blade Stress Profile

FIG. 10 10 Chip Tensile Test Specimen
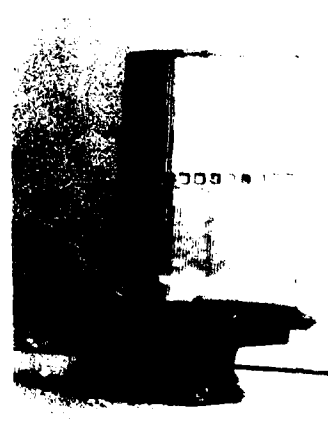
FIG. 11 15 Chip Blade Model with Photo Etched Leads

...
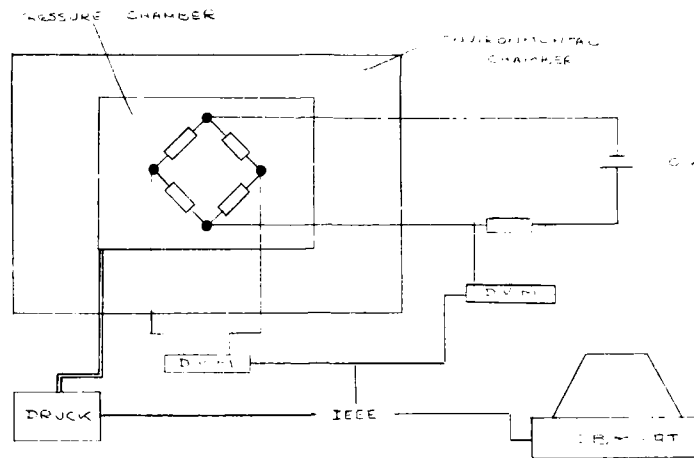
FIG 12   Schematic of Calibration Station
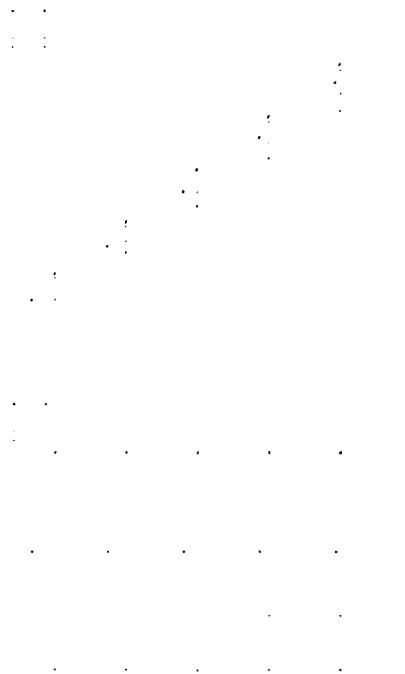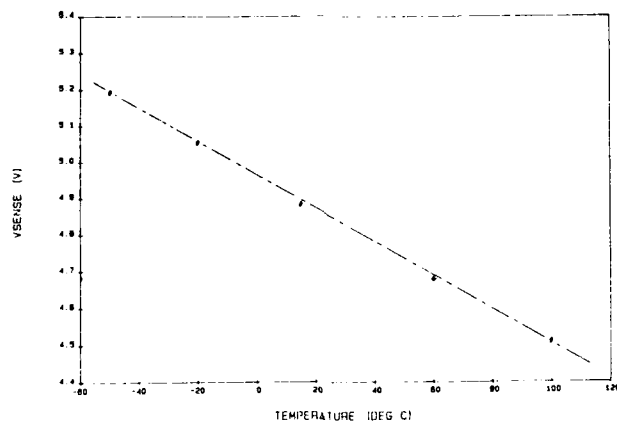
FIG 14 Sense Resistor Voltage Drop Temperature Sensitivity
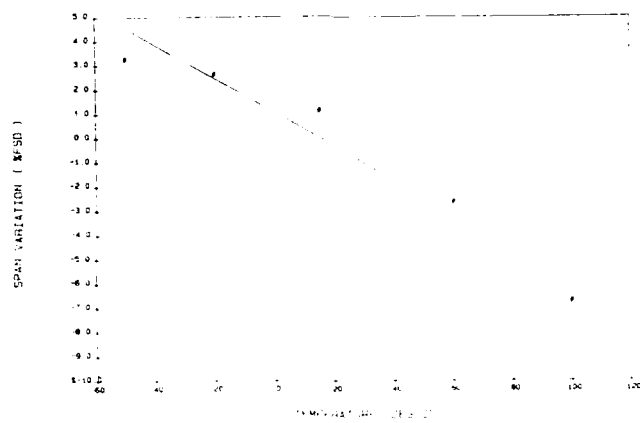
FIG 15 Span Temperature Sensitivity
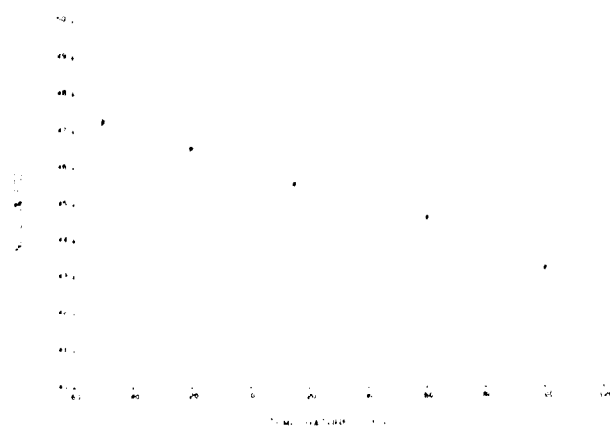
FIG 16 Zero Temperature Sensitivity

FIG. 17 Base Strain Sensitivity
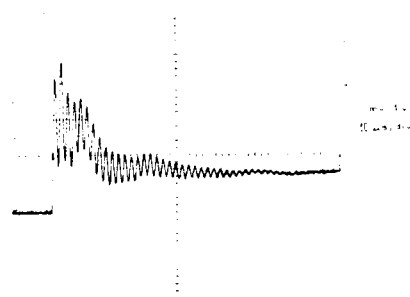
FIG. 18 The Output from a Silicon Diaphragm
with No Silastomer Present
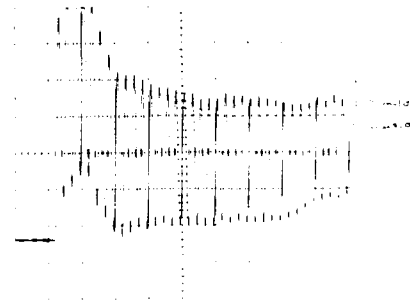
FIG. 29 The Output from a Silicon Diaphragm
with Silastomer Present

FIG. 30 Power Spectral Density for Diaphragm
with Silastomer Present

SAFETY SHEAR.   WEAK-LINK

AIR MOTOR

DISC

IN-SHAFT ELECTRONICS
DRUM

BEARING

HELICAL FLEXI-COUPLING
ALSO WEAK-LINK

24 CHANNEL SLIP-RING

SIGNAL AND POWER
CABLE TO SLIP-RING

SOLID STEEL BASE PLATE
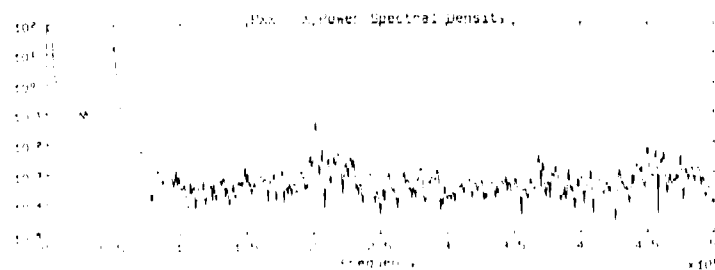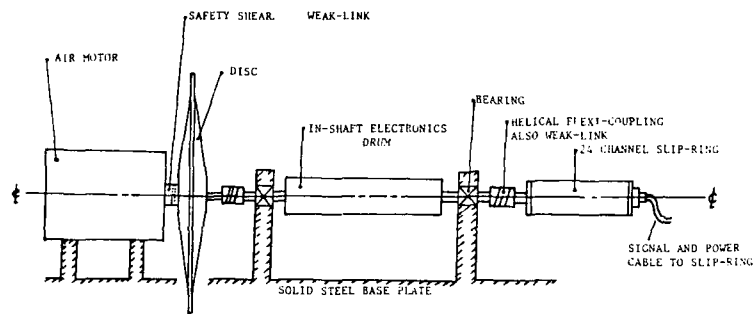
FIG. 21   Schematic of O.U.E.L. Spinning Rig
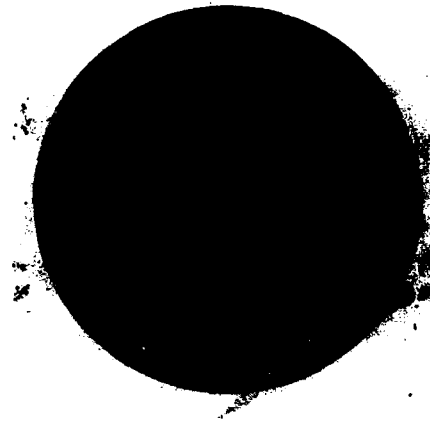
FIG. 22   Photograph of specimen with 4 chips
for mounting in the spinning rig
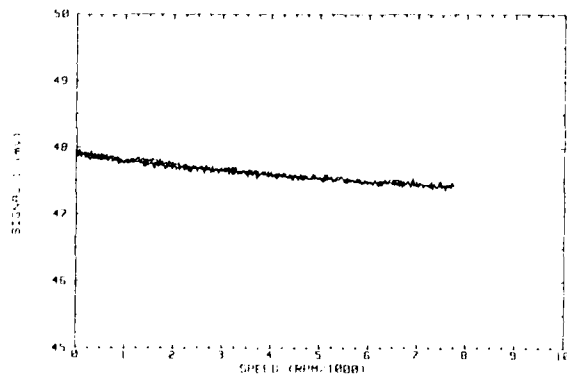
FIG. 23   Transducer output versus speed
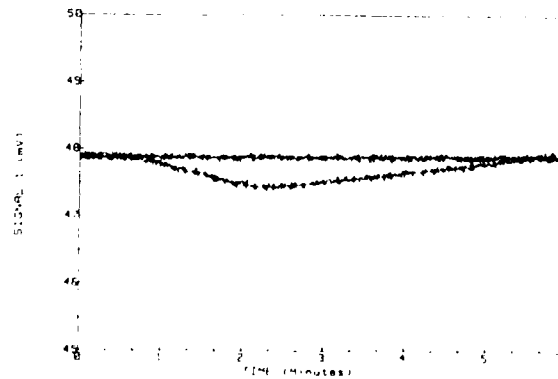
FIG. 24   Transducer output with and without rotation

DISCUSSION

B.H.Becker, Siemens AG, Germany

When the airflow starts, the blade begin to vibrate. How can the effects of accelerating forces and pressure forces induced by blade vibration be identified?

Author's response :

No calibration of transverse acceleration (perpendicular to the diaphragm) effects were conducted. the blade tested was a low aspect ratio, solid blade and therefore very stiff. Hence the transverse acceleration of the chip is expected to be very small. Results from a finite analysis of the dynamics of the blade confirm this assumption. However, the method can be extended to less stiff blades and acceleration forces could be accounted for, if required.

A suggested method for determining the effect of vibration would be to record the output from two chips located close to eachother on a single blade with one chip having been rendered insensitive to pressure (taped over). The variation in the two signals would then give an estimate of the vibration effects.

Th Schröder, MTU, Munich, Germany

The pressure transducers presented are a very promising tool for the investigation of unsteady boundary layer phenomena. There are two important questions in order to determine the possibility of using this sensor on a real test rig:

(1) What is the maximum possible environmental temperature for the sensors?

Author's response:

The sensors have been tested up to temperatures of 100°. This is not a maximum limit however and the sensors themselves are rated to a maximum temperature of 240 °C. Further high temperature tests are programmed in order to investigate the performance of the sensors over a greater range of temperatures. Further development is currently underway at Kulite on a sensor capable of temperatures over twice their current maximum.

(2) Is it possible to run these sensors in compressor or turbine rigs under long time (say several hours) of operation?

Author's response :

The transducer mounting technique has been demonstrated on both compressor and turbine sample blades with success. The only limitation on long term operation would be the drift in the calibration and this would have to be checked.

Semiconductor transducers have been successfully used for testing periods over 100 hours. There is no reason why the technique presented in the paper would not perform similarly.

R.J.Hansen - Office of Naval Research, USA

What is the actual active area of the pressure measurement transducer.

Author's response :

The active area of the transducer is approximately 80% of the chip's surface area. This percentage will depend on the diaphragm design, including the edge clamping and etch patterns and as such will vary from chip to chip. The actual chip sizes having been tested vary from 1 mm square to 1.5 mm square.

W.O'Brien, Virginia Polytechnic Institute, U.S.A.

The experimental results presented correspond to isothermal conditions. Could tests be made in a rapidly varying temperature environment ?

Author's response :

The testing up to date has concerned equilibrium temperature changes of the chip and blade. The effect of a rapidly varying temperature environment will depend on the heat transfer and resulting temperature of the chip itself. This will be moderated by the silastomer covering the chip and the thermal inertia of the chip itself.

MEASUREMENT OF VELOCITY PROFILES AND REYNOLDS STRESSES
ON AN OSCILLATING AIRFOIL

by

J. DE RUYCK, B. HAZARIKA, C.HIRSCH

Dept. of Fluid Mechanics
Vrije Universiteit Brussel
Pleinlaan 2, 1050 Brussels
Belgium

ABSTRACT

This work describes the flow around a sinusoidally oscillating NACA 0012 airfoil in presence of leading edge separation bubble and with leading edge stall, including laminar-turbulent transition.

The airfoil oscillates about an axis at 25% chord from the leading edge, with a nominal reduced frequency of 0.3 and Reynolds number of 300,000. The experiments are made at 4° to 14°, 5° to 15°, 6° to 16° and 8° to 18° angle of attack, covering flow conditions from no stall to full leading edge stall. It is found that the most probable cause of leading edge stall is due to the leading edge separation bubble burst and it occurs as soon as the static stall limit is exceeded. The leading edge stall is not due to the rapid upstream movement of the trailing edge separation.

The velocity vectors and the Reynolds stress tensors are measured using a slanted rotating single sensor hot-wire. The complete suction side boundary layer profile and the near wake is surveyed at 5° to 15° oscillation where no interaction is observed between the leading edge and the trailing edge flows, and at 8° to 18° in full stall conditions.

INTRODUCTION

Rapid advancees in the capacity of computers and the development of numerical methods to solve the full Navier-Stokes equations have pushed the computation of unsteady flows far ahead of the existing experimental data, with which the computed results could be validated. Most of the previous experiments on unsteady flow past airfoils were either of a qualitative nature (flow-visualization) or were aimed at finding the overall effect of the flow such as pressure coefficient, pitching moment coefficient, normal force coefficient etc.

Extensive measurements of mean velocity vectors and Reynolds stress tensors in the 2-dimensional unsteady boundary layer over an oscillating airfoil and in the wake behind the airfoil were carried out by De Ruyck and Hirsch [1-6], using a slanted single sensor hot-wire. The method has been quite successful in mapping the flow in the investigated region, giving a clear picture of the flow, including flow reversal and vortex formation. These experiments were conducted using an NACA 0012 airfoil with a tripping wire to promote transition of the boundary layer. The present experiments are the extensions of these measurements. They were conducted without tripping wire, to take a closer look at the formation of the leading edge separation bubble and the events leading to the turbulent separation downstream of the bubble. The measurements near the trailing edge and in the wake of the airfoil were conducted with and without tripping wire. These experiments throw new light on the Unsteady Kutta Condition for airfoil operating under stalled condition.

PREVIOUS WORK

A number of excellent reviews were published by various authors on the subject of unsteady flows [7,8,9]. The general picture which emerges from these reviews is that further investigations are required in

(i) measurements of the mean and the turbulent quantities in unsteady flows for validation of analytical methods.
(ii) the extent and duration of the leading edge separation bubble.
(iii) the extent of trailing edge separation and the effect of the leading edge separation bubble on the trailing edge separation.
(iv) the effect of the separation bubble and leading edge stall on the unsteady Kutta condition.

EXPERIMENTAL TECHNIQUES AND APPARATUS

The experiments were conducted in an open-circuit blow-down wind tunnel in the Department of Fluid Mechanics of VUB, Brussels. The test-section is 1m x 2m, and the tests were conducted at the nominal wind speed of 11.32 m/s and the free stream turbulence intensity less than 0.2 %. The test model consists of an airfoil and two end plates (figure 1). The airfoil is a NACA 0012 airfoil section with 60.4 cm chord and 94 cm span. The lower end plate is used as a platform to mount the traverse mechanism. The reduced frequency and the Reynolds number based on the chord of the airfoil and the nominal wind speed were 0.309 and 300,000 respectively. The profile shape near the leading edge was accurately measured close to the mid span. The largest deviation of the profile from the standard NACA 0012 profile was found to be less than 0.01% chord.

A 45° slanted single sensor hot-wire is used for all the velocity and turbulence measurements (DANTEC 5 micron gold plated hot-wire type 55P02). The periodic sampling was triggered by a pressure transducer for the cases where a sharp change of wall pressure signal was available (during test cases when leading edge stall occurs). The triggering of the periodic sampling was accomplished by an optical device when the

pressure signal was erratic or insufficient.

Detection of separation bubble and leading edge stall :

Since the separation bubble exists in a very thin region close to the solid surface and the effect of unsteady flow is to make it thinner [10], the rotating single slanted hot-wire technique could not be used to investigate the separation bubble. A combined analysis of pressure signals and fixed hot-wire signals was used to identify the duration for which a station was in the separation region. The signals contain 542 data points per period, and are ensemble averaged over 100 periods.

Figure 2 shows a sample of ensemble averaged traces, with the corresponding rms values over approximately 2 cycles of oscillation. These rms values of pressure and hot wire signal are used to detect the transition and the high turbulence areas. Since the normal velocities are very small close to the wall, the averaged single wire signal can be used to estimate the velocity. Although the flow direction cannot be determined without ambiguity, these signals allow to determine the reversed flow areas and the data on figure 2 can be interpreted as follows.

The period between A and B is a significantly laminar flow period with fluctuations in the hot-wire signal less than the resolution of the acquisition. The fluctuation in the pressure in this region is due to drift in the transducer. At time B, the transition to turbulence crosses the measuring station, while moving upstream. In reality the transition is already upstream of it at time B, since the wire is 1.5 mm away from the wall. Indeed, slightly ahead of B, a dip in the mean wall pressure signal (pt,m) is observed, with a small peak in the pressure rms (pt,f). From all the experiments, these dips appear to correspond with the passage of a transition or separation point. From B to C, the transition point moves further upstream, the boundary layer is growing (decreasing velocity, increasing turbulence). At point C there is an important drop in the ensemble averaged hot-wire output to point D, accompanied by: (i) slight increase in the rms value of hot-wire signal, (ii) a large reduction in the ensemble averaged pressure signal and most important of all (iii) sudden increase in the pressure rms. The application of the high turbulence correction of De Ruyck [6] yields a velocity quite close to zero at point D. The increase in the output between point C and D indicates flow reversal (as will appear from the overall results, the flow is completely separated in the leading edge region, from D to F). During this period the fluctuations remain high in the hot wire signal and small in the averaged pressure signal. During the period between E and F, after correcting for high turbulence the mean velocity was found to be negligibly small (same order of magnitude as the turbulence, smaller than the turbulence in some cases). During this period the pressure rms is about the half of the peak value.

The increase in the rms values between F and G is attributed to the cycle to cycle variation, since the reattachment time was observed not to be perfectly periodic. Since the rate of change of velocity is large at this time, about 10% to 50% of the measured turbulence is due to the cycle to cycle variation of events. At other times this effect is negligible.

Figure 3 shows clearly the detection of a separation bubble at 5° to 15° angle of attack, at 3.5% chord from the leading edge. The traces are taken at different distances from the wall. At the distance 1 mm from the surface of the airfoil, during the period A to B a laminar flow is observed. The hot-wire signal suddenly reduces during the period from B to C accompanied by an increase in the rms value. After turbulence correction, the velocity at C yields a value close to zero. This indicates that the separation point has crossed the position of the sensor and moved upstream of it. The sensor remains in the separated region from C to D where the backflow velocity first increases then falls to the near zero velocity value. Between D and E the velocity sharply increases and rms value reduces to zero, indicating that the separation point has moved downstream of the sensor. The output at 1.5 mm from the surface is similar to that at 1 mm in many respect. A laminar portion from F to G, sharp drop during G to H and a sharp increase in velocity between I to J. However, between H and I the flow is turbulent and the velocity is near zero, during this time the sensor is in the free shear layer formed on the top of the reverse flow region. At 2.5 mm away from the surface only a slight reduction in the mean velocity along with increase in turbulence was observed near the point L. This indicates that the sensor during this time was at the outer edge of the shear layer. A near perfect sinusoidal variation of the output is observed at the position 3.5 mm away from the airfoil surface. slight turbulence which appears near M is probably caused by the cycle to cycle variation of the separation. In conclusion, the two dips in the lowest signal correspond to flow reversals, revealing the presence of the bubble with a thickness of approximately 1.5 mm.

Velocities and Reynolds stresses :

The 2D velocities and Reynolds stresses are measured with a single rotating slanted hot wire. This technique is presented in [2,4] and it allows experiments in 2D reversed high turbulent flows. Ensemble averages were made with 542 samples per period and 100 periods and 48 rotational positions. The low number of periods is compensated by the high amount of samples per periods which allows some local time averaging. The ensemble averaging is done in real time, reducing considerably the required amount of mass storage.

Accuracy :

The resolution in the chordwise position was 0.5 mm (0.08% chord). The resolution in the transverse position was better than 0.08 mm (0.013% chord). However, the amplitude of vibration of the probe was found to be 0.1 mm by using a piezo-electric accelerometer fixed near the tip of the probe holder.

Instantaneous cooling velocities are measured with an accuracy of about 1.3% of the nominal wind speed. Compensations for temperature changes and wire foouling are introduced by taking reference measurements during the experiments.

The scatter on the results for unstalled conditions is in general very small (less than 1% on all the results). In stalled conditions, important scatter is observed, in particular on the turbulent shear stress. In this region the random error on ensemble averaged velocity varies between 1% and 5%, scatter on

normal stress profiles varies between 2% to 10% and for the turbulent shear stress the maximum scatter exceeds 15%. The systematic error for the measurements of the stresses in high turbulent conditions (above 10%) is increased by linearizations during the processing of the data. These errors are estimated at 5 to 10%, and to 1 to 2% in unstalled conditions.

At reattachment, slight cycle to cycle changes are observed. Due to the strong velocity changes at reattachment, the error introduced in the corresponding turbulence quantities due to the cycle to cycle variation is quite important (more then 50% increase in turbulence). At present no way is found to correct the data for this problem.

LEADING EDGE MEASUREMENTS

The results obtained at the leading edge are shown on figures 4 to 13 The data are represented in a time-space domain on figures 4 and 5 (chordwise direction), and as instantaneous boundary layer data on figure 6 to 13.

Time-space contour plots :

Figures 4 and 5 show isovelocity lines and isoturbulence lines in a space-phase angle (or time) domain. Two series of results are shown : results at a fixed distance of 1.5 mm from the wall and increasing angles af incidence (figures 4) and results at a fixed incidence 5° to 15° and different distances from the wall (figure 5). In all cases, eventual flow reversals have been detected and considered in the representation of the data. Returned flow areas are left blank for contrast, indicating the bubble area. The laminar regions correspond with the blank in the turbulence plots.

The events that occur on a plane parallel to the airfoil surface at 1.5 mm and 4° to 4° oscillation are shown in figures 4.a. At 4% chord a very low speed area (below 0.1 of the outer speed) and a small reversed flow area were observed for a part of the oscillating period when the angle of incidence was above 10°. Peak values of turbulence (>25%) were observed at 5% chord around maximum incidence which is just downstream of the low speed area. As will be observed below, a larger reversed flow area is present closer to the wall (the separation bubble) and the dark area in figure 4.a represents the duration and the extent of the shear layer above that separation bubble. Experiments at closer distances are necessary, preferably with sensors on the surface, to determine the exact separation and reattachment positions. It can be argued that th separation bubble extends from about 2% to 5% chord at the maximum incidence in this case. The turbulence reaches a maximum around or just before the reattachment point and above the bubble. This is in accordance with observations in [15]. The pressure rms values reach a maximum inside the separated area (figure 1,[12,13]). Downstream of the separation bubble, on this plane, the velocity increases up to 9% chord due to the recovering boundary layer. Downstream of this position (9% chord) the velocity gradually reduces indicating decelerating flow and boundary layer growth. After the lowest angle of attack (indicating a mild phase lag of about 10°) the transition occurs much more downstream, at positions up to 20% distance from the leading edge, and nothing indicates the presence of separation bubbles. A high turbulence (>15%) appears in the transition area around 15% chord at 9° incidence.

Figure 4.b shows the events at 5° to 15° oscillation, in many respect these figures are similar to the ones at 4° to 14° with one striking difference - a sudden enlargement of the low velocity region downstream of the bubble immediately after the maximum incidence. This indicates the onset of a bubble burst which can trigger the leading edge separation. Turbulence peaks are observed at the same time and place. It is also an onset of asymmetry in the non-stalled results where in general no significant phase lag is observed near leading edge. The burst onset clearly occurs at decreasing angle of attack and it is probable that it would burst completely if the angle of attack was kept above 14° to 15°, which is around the static stall angle. The laminar region in this case extends to about 15% chord distance at the lowest angle of incidence, in this case also the appearance of the high turbulence area near 15% chord was noticed around 9° incidence.

At higher angles of attack (6° to 16°, figure 4.c) a reversed flow region extending to all the measurement stations appears. This phenomenon appears near the 5% chord immediately after the airfoil crosses 16° incidence. The reverse flow is not seen upstream of 5% chord at 1.5 mm from the surface, but it is clear that nearer to the airfoil the reverse flow region will be found even upstream of 2% chord. The reversed flow region then rapidly spreads in both upstream and downstream directions from 5% chord position. From the figures 4.a and 4.b, the presence of a bubble around 4% chord can be assumed, this bubble eventually bursts into leading edge separation. Hence, the leading edge separation is not due to interactions with the trailing edge separation, in contradiction to observations from [14,15]. It can be seen that the slopes of the lines dividing the reverse flow from the forward flow region are positive downstream of 5% chord (4.c). The dividing lines on the left side of the figures downstream of 5% chord is the reattachment line. Therefore, the reattachment point rapidly moves downstream as phase angle increases and cause leading edge separation. Only a negative slope on this line will indicate rapid movement upstream of a downstream separation point, which was not the case. The higgh turbulence areas (>25%) in this case appears in the separated region and during the reattachment. The portion of the leading edge that remains laminar again becomes largest slightly after the minimum incidence. The laminar portion reduces to 13% chord for 6° to 16° (4.c) and to 10% for 8° to 18° (not shown). The high turbulence (>15%) areas around 15% chord are again evident around 9° incidence.

Figure 5 shows the results of measurements at various distances from the airfoil surface a. 5° to 15° oscillation. At 1 mm distance (5.a) more than 2% of the chord (ahead of 3% up to 5%) shows a reversed flow. At 1.5 mm distance the region appears as a low forward velocity region (5.b) but at 2.5 mm only a sharp velocity gradient is observed (5.c). From the turbulence plots, it appears that the highest turbulence occurs in the free shear layer above the separation bubble.

The highest turbulence intensity encountered at 4° to 14° and 5° to 15° incidence cases were 36% of the nominal velocity. If the value of the turbulence intensity is expressed as a fraction of the highest

velocity encountered for the particular case, this value reduces to less than 20% and is comparable to the values reviewed in [11]. As discussed earlier, the high values observed for the cases with complete flow reversal (more than 45% of the nominal velocity) are partly due to the contribution of cycle to cycle variations at reattachment.

In conclusion it seems that the leading edge stall is triggered by the burst of the leading edge bubble, after which the complete flow pattern is changed. When periodic stall is present, the separation starts not at the leading edge, but at about 4% chord distance from it, with rapid propagation in both directions. The reattachment occurs through a rapid downstream motion of the separation point. In the absence of separation bubble, the location of the area of transition to turbulence varies considerably with incidence. The use of sensors on the surface can indicate the exact location and the movement of the transition point. The present results are further analysed below, in conjunction with experiments over the whole airfoil.

Instantaneous data :

On figures 6 to 13 instantaneous data at the leading edge are shown at some relevant times (out of the 181 available ones). The velocities and turbulence intensities obtained with the fixed wire are shown in (d) and (e) respectively. The figures (f) and (g) show the corresponding chordwise turbulence intensity and Reynolds shear stresses as they are obtained from the rotating hot wire. The minimum distance from the wall is 2 mm for the rotating wire, which is outside of the bubble.

The series of figures starts at increasing angle of attack, when the transition is found around 13% chord from leading edge (figures 6d, 6f). As the angle of attack increases, a low speed area can be observed close to the wall near 12% chord from the leading edge (figure 7e). A high turbulence level in the shear layer above this low velocity region is observed (figures 7f, 7g). The decrease in velocity in the inner layer could not be reached by the rotating wire. There may be a bubble close to the wall, as discussed in the previous section. The low speed area disappears and another one appears around 5% chord from 9° angle of attack (figure 8). At 10° (figure 9) this low speed area is increasing, with a very thin but highly turbulent shear layer above it. Unfortunately the rotating wire reaches only the outer part of this layer and only a small portion of the corresponding stress is observed. The increasing incidence makes the separation bubble thicker and it was possible to detect the turbulent quantities by the rotating wire in more of the upstream stations. At 9° incidence (figure 8) the fixed wire measurement shows 10% turbulence near 7% chord, the rotating wire measurement also shows an increase in turbulence intensity and Reynolds shear at the station near 8% chordwise position. This upstream movement of the transition point near the leading edge (d, f and g) is evident in all the figures starting from 6 to 13, after which the transition point gradually moves downstream. At 10° incidence (figure 9) small values of Reynolds shear stress are measured at 5.7% chord position. Around the same incidence the fixed wire at 1 mm from the surface at 4% chord shows the presence of the leading edge separation bubble (figure 4a). Therefore, the rotating wire is measuring the turbulence quantities in the free shear layer when it is just becoming turbulent.

A rapid increase in Reynolds shear stress as well as chordwise turbulence intensity with the increasing incidence at 5.7% chord could be observed till maximum incidence time (figures 9, 10 and 11). The Reynolds shear stress at the stations downstream of 10% chord for the same figures does not increase considerably. However, growth of the turbulent layer is evident in all the stations downstream of 5% chord. This growth can be attributed to the large coherent structures present at the reattachment of the separation bubble. The large values of Reynolds shear stress are the effect of the large velocity gradients in the free shear layer over the separation bubble. When the incidence decreases from the maximum value of 15° a tendency towards bubble burst was observed (figure 5). In the corresponding figure (figure 11, between 5% to 10% chord) the rotating wire detects a decrease of all the turbulent quantities towards the wall. This region roughly coincides with the elongated low speed portion in figure 5b. The Reynolds shear stress measured at 5.7% chord nearest to the surface (2 mm) even shows a negative value (figure 11g, note that the values plotted are minus the Reynolds stresses). The situation at this point is very close to separation (bubble bursting). The negative Reynolds st ses observed from the rotating wire data, would indicate a negative turbulence production : although   reliability of this result is poor in such extreme situations, it is systematically observed at separation in the earlier experiments of De Ruyck and Hirsch [5,6] and it may be an indication of stall onset. At this time it can be seen that the trailing edge flow is separated up to about 60% chord, which is too far to cause the leading edge bubble to burst, hence the leading edge stall onset is not affected by trailing edge separation in this particular case. Further decrease in incidence below 13° reduces this tendency of bubble bursting and typical transition behaviour is again observed (figures 12 and 13). Apart from slight phase lag, the reducing angle of incidence brings about the same series of events in the reverse of what was seen during thee increasing incidence. The turbulent boundary layer becomes thinner, the turbulent quantities gradually reduce in value and become zero station after station starting with 5.7% chord station. At the lowest incidence (5°) the turbulent transition can be seen only at stations downstream of 15% chord (not shown).

BOUNDARY LAYER AND WAKE FLOW

Experiments with the rotating wire has been made at 5° to 15° angle of attack, without tripping wire, including leading edge and near wake. In addition to the experiments of De Ruyck and Hirsch [5,6], experiments were made at the trailing edge and in the near wake at 8° to 18°, which is a deep stall case, with a tripping wire.

Unstalled flow, 5° to 15° angle of attack :

Figures 1 and 15 show an overall view of the 5° to 15° case, at maximum angle of attack. The details near leading edge were already discussed in the previous section, whereas a closer look to the trailing edge is given in figures 16 and 17.

The figures a, b and c in these cases show velocity vector, chordwise turbulence intensity and Reynolds shear stress, respectively. If the flow near the leading edge separation bubble is excluded from this part

of the discussion, the maximum value of the chordwise turbulence intensity and the Reynolds shear stress invariably occurs between 5% to 10% chord downstream of the trailing edge in the pressure side of the wake. Downstream of 10% chord from the trailing edge the values of the turbulence quantities reduce as it should in the far wake. Without further analysis of the data it is not possible to say at wh distance the wake becomes self preserving and what is the effect of unsteadiness and trailing edge separation on it. However, the wake behaviour is close to a steady state wake behaviour. From the figures it is observed that :

(i) the turbulence intensity is relatively smaller near the centreline of the wake, (ii) the Reynolds shear stress is zero close to the centreline (iii) the turbulence intensity as well as the Reynolds shear stress reach a peak in the side where half-wake width is small (large transverse gradients in velocity).

In the near wake from 5% to 10% chord downstream of the trailing edge, peaks are observed at the pressure side, and these peaks do not coincide with the maximum values of velocity gradients. These peaks may be due to the effect of streamwise curvature in the flow, which is known to introduce "surprisingly large changes in the turbulence structure of shear layers" [16]. According to Bradshaw [16], "These changes are usually an order of magnitude more important than normal pressure gradients and other explicit terms appearing in the mean-motion equations for curved flows".

The trailing edge separation is detected soon after the incidence exceeds 13° (not shown). At the onset of trailing edge separation the chordwise turbulence intensity close to the surface remains unchanged but the Reynolds shear stresses drop to near zero values. With the increase of incidence the separation point moves upstream and the separated portion over the airfoil near trailing edge keeps growing even after the incidence reduces after the maximum value. More than 20% of the airfoil is separated when the incidence is 12.5° (figure 15). The activity in this separated portion of the airfoil is relatively quiet, as can be seen from figure 16. The velocity is reversed but the magnitude is very small: same order of magnitude as the turbulence intensity. The chordwise turbulence intensity falls to less than 25% of the maximum value measured at the same chordwise station (which is detected around the separation line). The Reynolds shear stress in this region is scattered around zero indicating a very small correlation between u and v. The results obtained are comparable with the wake results obtained by De Ruyck and Hirsch in [2]. A qualitative analysis of the velocity vectors near the trailing edge confirms that during increasing incidence the velocity vector at the trailing edge is tangential to the pressure surface. This is in accordance with the Geising and Maskell trailing edge condition [17], which states that the stagnation streamline at the trailing edge will be tangential to the pressure surface for positive (anticlockwise) shed vorticity and to the suction surface in the opposite case.

Stalled flow, 8° to 18° angle of attack :

Figures 18 to 25 show results of the measurements near the trailing edge for 8° to 18° incidence and with the tripping wire present at 10% chord. For a better understanding of the strong interaction between leading edge vortex and the flow at the trailing edge, the corresponding figures of the mean flow field are reproduced from [5,6] in figures d), wherever possible. It is remembered that these early experiments were performed without end-plates. The general observations at 5° to 15° incidence can also be made in this case: the maximum value of the turbulent intensity as well as the Reynolds shear stress occur near 5% chord downstream of the trailing edge in the pressure side of the wake. Severe flow turning may be the cause as can be seen in figures 21 to 23.

This series of figures starts with 17° and increasing incidence (figure 18). The trailing edge separation point in the present case has moved up to 80% chord. The separated region again is a low activity region : with lower chordwise turbulence intensity, near zero Reynolds shear stress and the reverse flow velocity of the same order of magnitude as the turbulent intensity. In figure 18d it can be seen that the leading edge vortex has just started forming at the first measuring station (15% chord). In the early experiments without end plates the trailing edge separation point has moved upstream of 60% chord position, instead of 80% in the present case. Due to the leakages at the blade tips, the opposite behaviour would normally be expected (more downwash should delay the separation), which means that the tip leakages affect the flow in a way which is more significant than just a downwash velocity. In general the earlier separation causes a general phase shift between the complete flow behaviour of the experiments with and without end-plates.

At higher incidence the separation point has moved upstream of the 80% chord and the reversed flow velocity has noticeably increased (figure 19). The chordwise turbulence intensity also slightly increases, however the Reynolds shear stresses show considerable scatter without any noticeable increase in the mean value. The scatter indicates that under these circumstances the ensemble averaging of 100 data points is not sufficient. The rolling down of the leading edge vortex sweeps the trailing edge separation point downstream of 60% chord as the incidence reduces from the maximum value (figures 20, 21). Upstream of this vortex front a strong reversed flow is build up (figure 22). The leading edge vortex itself is already away from the chord line once it leaves the trailing edge and a strong vortex of opposite vorticity forms in the near wake (figure 23). Large peak values of chordwise turbulence intensity and Reynolds shear stresses are observed during this process. After the passage of this trailing edge vortex the flow near the trailing edge and the near wake breaks down completely (figures 24). It was observed that the cycle to cycle variation of the movement of this separation point was quite large. The scatter in the velocity vector as well as in the turbulence quantities in figure 23 to 25 is a result of these non-periodicities. Figure 25 completes the cycle.

In this experiment, the flow just downstream of the trailing edge was generally found to be parallel to the non-separated side of the trailing edge. Although there is a complete breakdown of the flow in the suction side and formation of a number of large vortices close to the airfoil, the Geising and Maskell trailing edge condition can be considered as valid close to the trailing edge, since in general the velocity at the trailing edge remains tangent to the pressure side of the blade. Downstream of the trailing edge however, the separating streamline is strongly distorted by the trailing edge vortices and a complete analysis of the data including the leading edge and trailing edge vortices will be necessary. In the analysis, the indication suggested by Polling and Telionis [18] about non-zero loading in the trailing edge and in the

near wake should be taken in to account

COMPARISON WITH PREVIO'IS ;ORK

The differences between the present experimental set up and the early experiments of De Ruyck and Hirsch [1 to 6] are the presence of end-plates and the absence of a tripping wire in the 5° to 15° test case.

When comparing the data for the 5° to 15° case the observed differences are not relevant, although a significant downwash could be expected in the absence of end plates in the early experiments. This can be explained by the small size of the gaps between the blade ends and the tunnel walls (3% chord). The tripping wire was placed at 10% chord distance from the leading edge, whereas the laminar region is observed up to 15% chord.

Differences are observed at 8° to 18° angle of attack. The gaps at the blade ends enhance the separation, which may be due to an overall non-two dimensional (but still symmetric suction side flow. The earlier separation causes an overall phase shift. Stronger return flows are also observed when using end-plates.

CONCLUSIONS

In the present work experimental data are obt ined about leading edge and trailing separations. The formation of a leading edge bubble has been observed, with laminar separation, transition and turbulent reattachment. The bubble i very thin and the exact separation point is to be found by measurements very close to the wall, preferably with flush mounted sensors. Leading edge stall is f nd t be trigge ed by the bursting of the leading edge bubble, soon after the static stall limit is exceeded. No inter ction with the trailing edge separation is observed. Strong turbulence is observed in the shear layer above the bubble.

The trailing edge separation is a low speed, low turbulence event, with near zero Reynolds shear stresses. A weak vortex can be formed at high angles of attack. The passage of the leading edge vortex disturbs the trailing edge pattern into a high energy area with strong turbulence. The Geising and Maskell trailing edge condition is valid in all cas s, as far as the flow close to the trailing edge is considered.

When compared to the early experiments of De Ruyck and Hirsch [1 to 6], it is found that the presence gaps at the blade ends, and the presence of a tripping wire at 10% chord distance of the leading edge has no significant effects of the overall flow behaviour in unstalled conditions. At higher angle of attack, differences are observed due to three dimensional effects of the uncovered blade ends in the early experiments. where the separation occurs sooner and less return flow is observed.

The test case 5° to 15° delivers a complete set of data from leading edge to near wake, including data about the leading edge bubble.

Future work should be directed at an extensive analysis of the obtained data, eventually complemented by similar data at the other incidences. This should be done in connection with numerical solutions.

REFERENCES

[1] DE RUYCK J., HIRSCH C., 1981, "Turbulence Structu.e in the Wake of an Oscillating Airfoil", Report Vub-Str-12, Vrije Universiteit Brussel, Dept of Fluid Mech., 1981
[2] DE RUYCK J., HIRSCH C., 1982, "Instantaneous Turbulence Profiles in the Wake of an Oscillating Airfoil", AIAA Paper 82-035?, 1982
[3] DE RUYCK J., HIRSCH C., 1983, "Turbulence Structure in the Boundary Layer an Oscillating Airfoil", Report VUB-STR-14, Vrije Universiteit Brussel, Dept. Fluid Mech., 1983
[4] DE RUYCK J., HIRSCH C., 1984, "Instantaneous Flow Field Measurements of Stalled Regions on an Oscillating Airfoil", AIAA Paper 84-1565, 1984
[5] DE RUYCK J., HIRSCH C., 1984, "Turbulence Structure in the Boundary Layers of an Oscillat ng Airfoil", Report Vub-Str-13, Vrije Universiteit Brussel, Dept of Fluid Mechanics, 1984
[6] DE RUYCK J., HIRSCH C., 1985 "Veloc y and Turbulence Measurements in Dynamically Stalled Boundary Layers on an Oscillating Airfoil", AGARD conference proceedings CP386 on Unsteady Aerodynamics, pp 4-1, 4-13
[7] MC CROSKEY W.J., 1977, "Some Current Research in Unsteady Fluid Dynamics", Trans. ASME, Journal of Fluid Engin ering Vol. 99, pp. 8-39, 1977
[8] CARR L.W., "A Compilation of Unsteady Turbulent Boundary Layer Data", AGARDograph AG265, 1981
[9] TELIONIS D.P., "Un eady Viscous Flows", Springer Verlag, 1981
[10] BRENDEL M. and MUELLER T. J., 1988 "Boundary Layer Measurements on an Airfoil at a Low Reynolds Number in an Oscillating Freestream",AIAA Journal, vol. 23,No. 6, March 1981, pp. 257 -263
[11] EATON J.K. and JOHNSTON J.P.,1981 "A Review of Research on Sub nic Turbulent Flow Reattachment" AIAA Journal, vol. 19,No. 9, September 1981, pp. 1093-1100
[12] SERPA J. M., LESSMAN R. C. and HAGIST W. M., 1987 "Turbulent Separated and Reattached Flow Over Curved Surface", Journal of Fluids Engineering, December 1987, Vol. 109, pp 40? - 409
[13] HILLIER R. and DULAI B.S.,1985 "Pressure Fluctuation in a Turbulent Separated Flow", Fifth Symposium on Turbulent Shear Flows, Cornell University, August 1985, pp. 5.13 - 5.'3
[14] MC CROSKEY W.J., CARR L.W., MC ALISTER K.W., 1976, "Dynamic Stall Experiments on Oscillating Airfoils"

AIAA Journal, vol. 14, No. 1, January 1976, pp. 57-63.

[15] MC CROSKEY W.J., MC ALISTER K.W., CARR L.W., PUCCI S.L., LAMBERT O., INDERGRAND R.F., 1980, "Dynamic Stall on Advanced Airfoil Sections" presented at the 36th Annual National Forum of the American Helicopter Society, May 1980 - Journal of the American Helicopter Society, July 1981.

[16] BRADSHAW P., 1973 "Effect of Streamline Curvature on Turbulent Flow", AGARD-AG-169, August 1973.

[17] BASU B. C. and HANCOCK J. H., 1978 "The Unsteady Motion of a Two-dimensional Aerofoil in Incompressible Inviscid Flow", Journal of Fluid Mechanics, 1978, Vol. 87, Part 1, pp 159-178

[18] Poling D. R. and Telionis D. P., 1986 "The Response of Airfoils to Periodic Disturbances - The Unsteady Kutta Condition", AIAA Journal, vol. 24, No. 2, August 1986, pp 193 -199
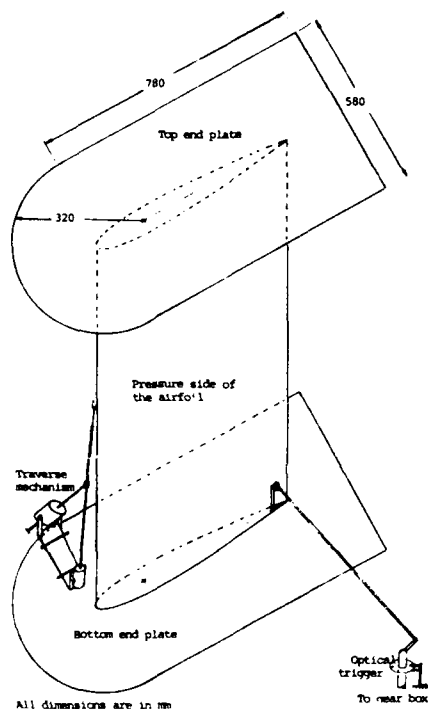
Figure 1 : Experimental set-up
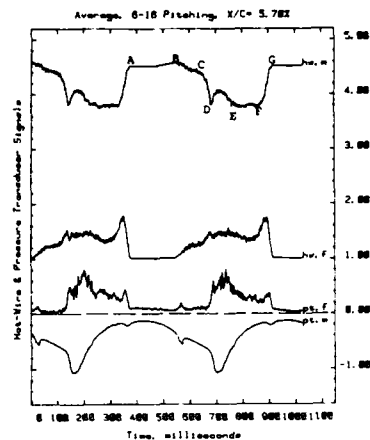
Sample of Fixed Hot-Wire and Pressure Transducer Signal

hw.m : ensemble average of hot-wire output

hw.f : rms value of hot-wire output, multiplied by 2 and shifted upwards by 1 volt

pt.m : ensemble average of pressure transducer output

pt.f : rms value of pressure transducer output, multiplied by 10

Figure 2
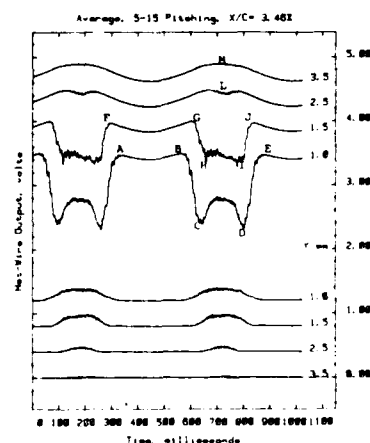
Sample of Fixed Hot-Wire Output at various Transverse Positions

The four upper curves are ensemble average, the lower curves represent rms values.

The outer curve is in the correct position, the other figures are shift towards each other by 0.5 volts each.

Figure 3

Figure 4(a) : 4 to 14°, 1.5 mm from the wall

4(b) : 5 to 15°, 1.5 mm from the wall
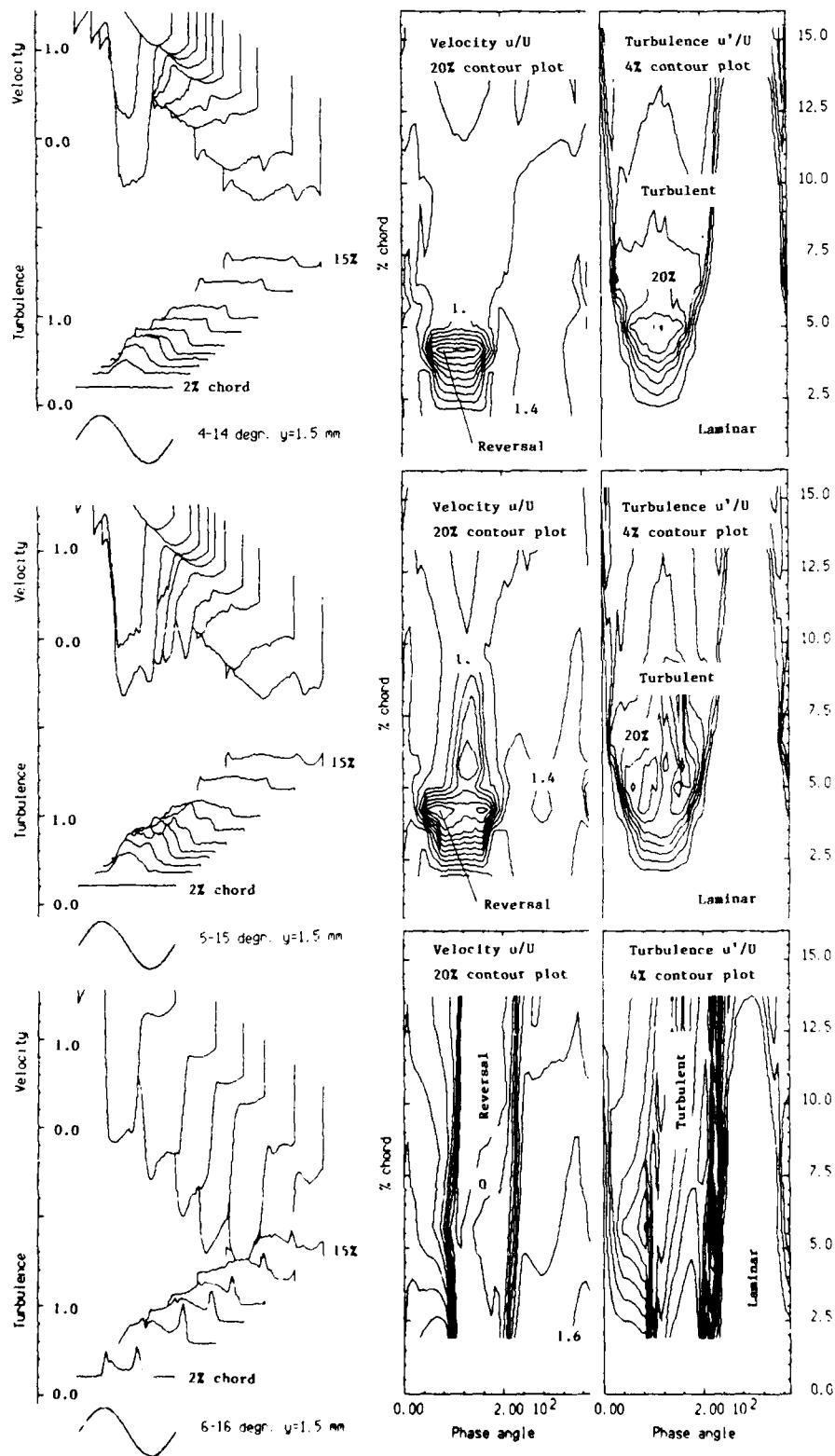
4(c) : 6 to 16°, 1.5 mm from the wall

Figure 5(a) : 5 to 15°, 1 mm from the wall

5(b) : 5 to 15°, 1.5 mm from the wall

5(c) : 5 to 15°, 2.5 mm from the wall

i= 7.36 degr. f=328.18 degr.

i= 8.14 degr. f=338.12 degr.

(d)

(e)

5   10   15

(f)

(g)
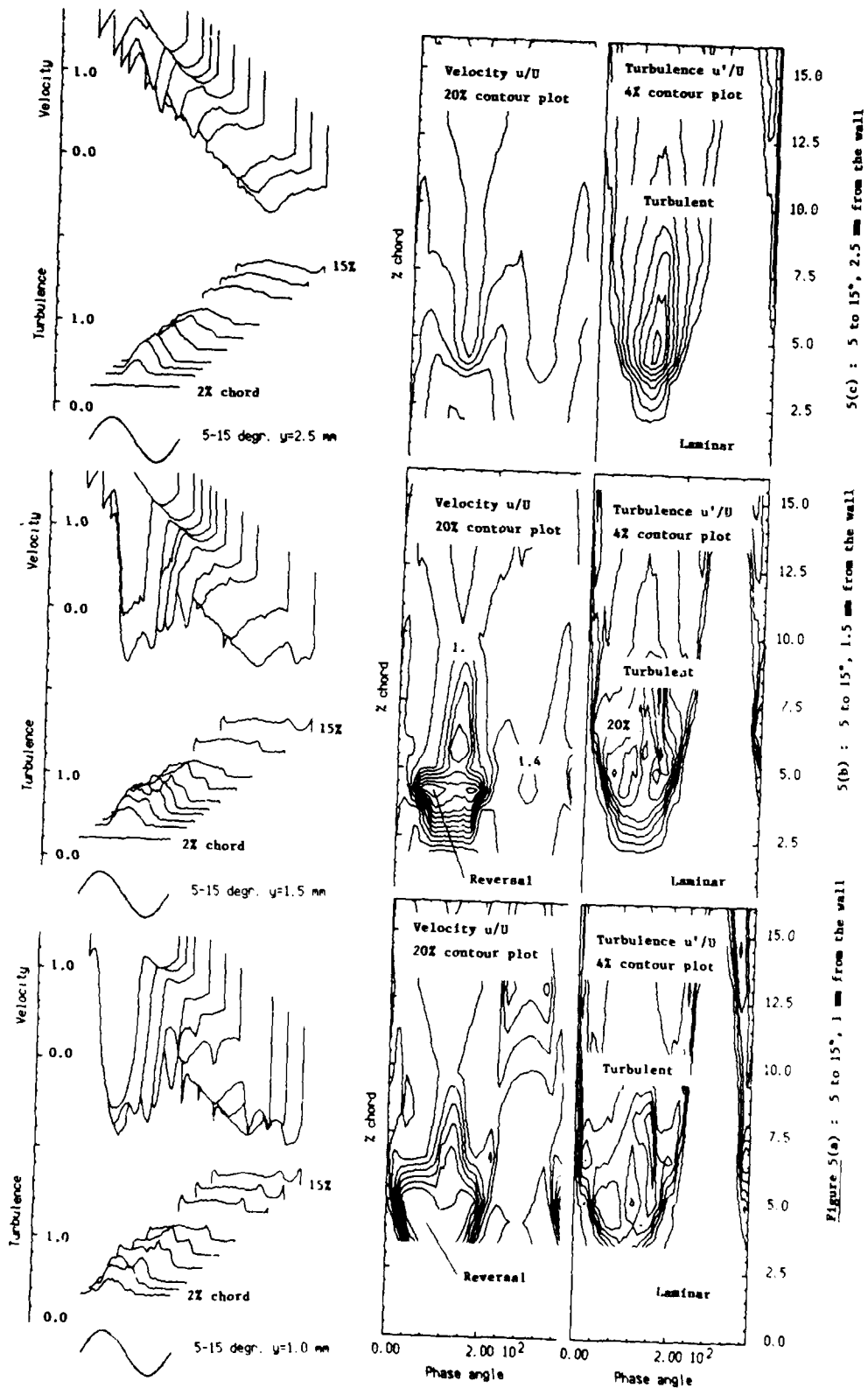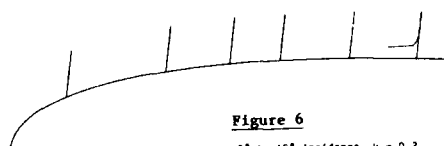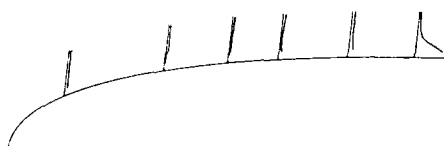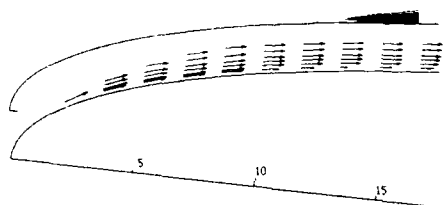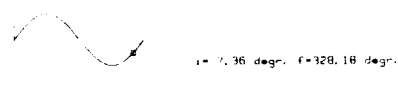
Figure 6

5° to 15° incidence, k = 0.3

(d) isoturbulence

(f) chordwise fluctuations $\sqrt{u'^2}/Q$ scale : ——— 10% Q

(g) - Reynolds stress $\overline{u'v'}/Q^2$ scale : ——— 1% Q²

Figure 7

5° to 15° incidence, k = 0.3

(d) isoturbulence

(f) chordwise fluctuations $\sqrt{u'^2}/Q$ scale : ——— 10% Q

(g) - Reynolds stress $\overline{u'v'}/_2^2$ scale : ——— 1% Q²

i= 8.97 degr. f=348.07 degr.

i=10.00 degr. f= 0.00 degr.

(d)

(e)

5   10   15

(f)
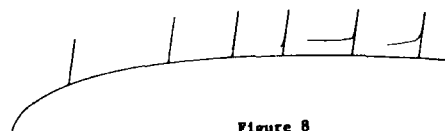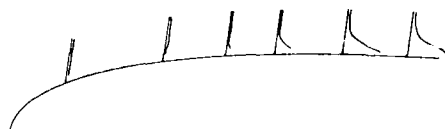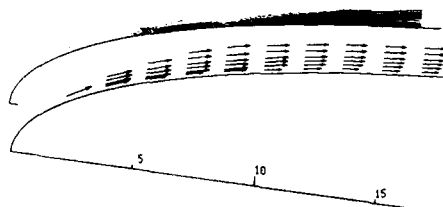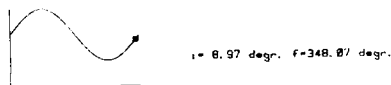
Figure 8

5° to 15° incidence, k = 0.3

(d) isoturbulence

(f) chordwise fluctuations $\sqrt{u'^2}/Q$ scale : ——— 10% Q

(g) - Reynolds stress $\overline{u'v'}/Q^2$ scale : ——— 1% Q²

(g)
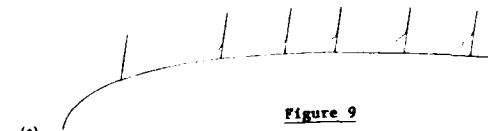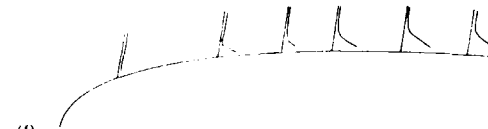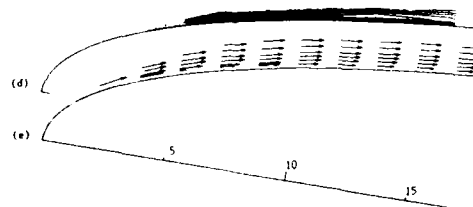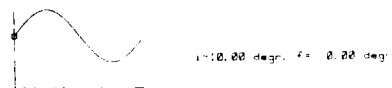
Figure 9

5° to 15° incidence, k = 0.3

(d) isoturbulence

(f) chordwise fluctuations $\sqrt{u'^2}/Q$ scale : ——— 10% Q

(g) - Reynolds stress $\overline{u'v'}/Q^2$ scale : ——— 1% Q²

i=13.28 degr. f= 39.78 degr.

i=14.3o degr. f=119.34 degr.

(d)

(e)

(f)
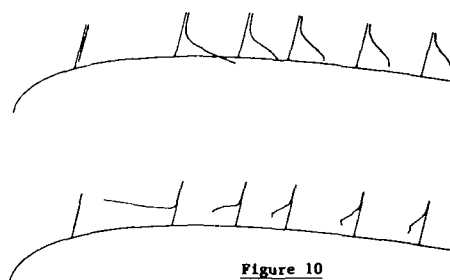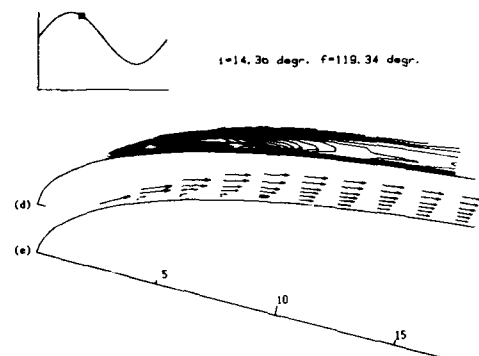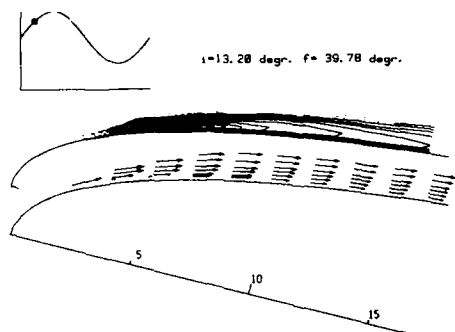
Figure 10

5° to 15° incidence, k = 0.3

(d) isoturbulence

(f) chordwise fluctuations √u'²/Q   scale :   —— 10% Q

(g) - Reynolds stress u'v'/Q²   scale :   —— 1% Q²

(g)
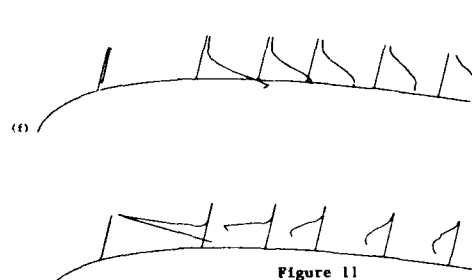
Figure 11

5° to 15° incidence, k = 0.3

(d) isoturbulence

(f) chordwise fluctuations √u'²/Q   scale :   —— 10% Q

(g) - Reynolds stress u'v'/Q²   scale :   —— 1% Q²

i=12.56 degr. f=149.17 degr.

i= 7.59 degr. f=288.84 degr.

(d)

(e)

(f)
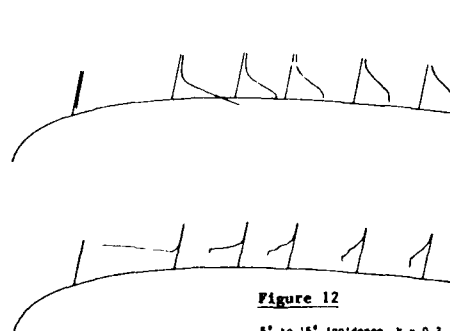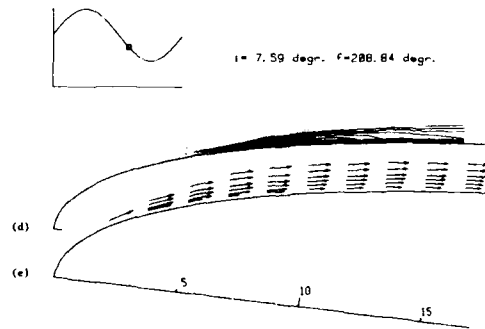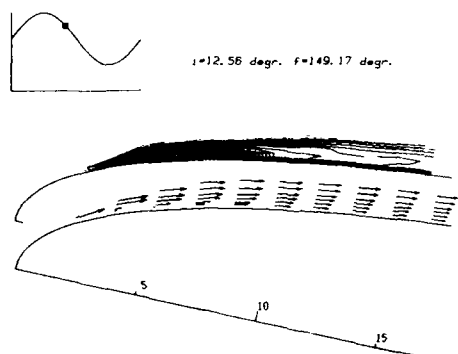
Figure 12

5° to 15° incidence, k = 0.3

(d) isoturbulence

(f) chordwise fluctuations √u'²/Q   scale :   —— 10% Q

(g) - Reynolds stress u'v'/Q²   scale :   —— 1% Q²

(g)
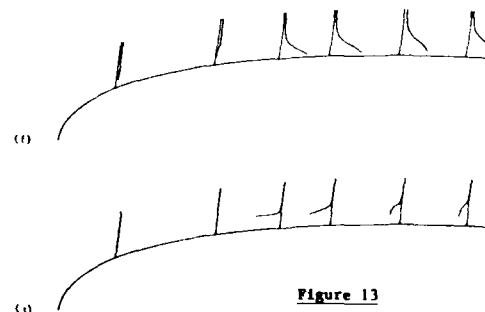
Figure 13

5° to 15° incidence, k = 0.3

(d) isoturbulence

(f) chordwise fluctuations √u'²/Q   scale :   —— 10% Q

(g) - Reynolds stress u'v'/Q²   scale :   —— 1% Q²

i=15.00 degr. f= 89.50 degr.

i=12.56 degr. f=149.17 degr.
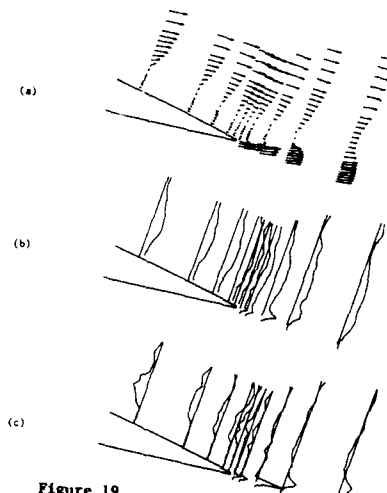
(a)

(b)

(c)
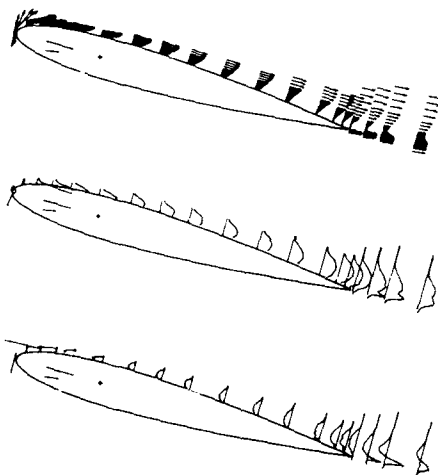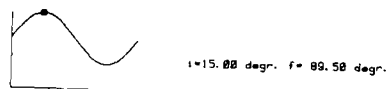
Figure 14

Figure 6.14 : 5° to 15° incidence, k = 0.3
(a) velocity vectors   scale :   — Q
(b) chordwise fluctuations √u'²/Q   scale :   — 10% Q
(c) - Reynolds stress u'v'/Q²   scale :   — 1% Q²

Figure 15

Figure 6.16 : 5° to 15° incidence, k = 0.3
(a) velocity vectors   scale :   — Q
(b) chordwise fluctuations √u'²/Q   scale :   — 10% Q
(c) - Reynolds stress u'v'/Q²   scale :   — 1% Q²

i=12.56 degr. f=149.17 degr.

i=10.86 degr. f= 9.94 degr.

(a)

(b)

(c)
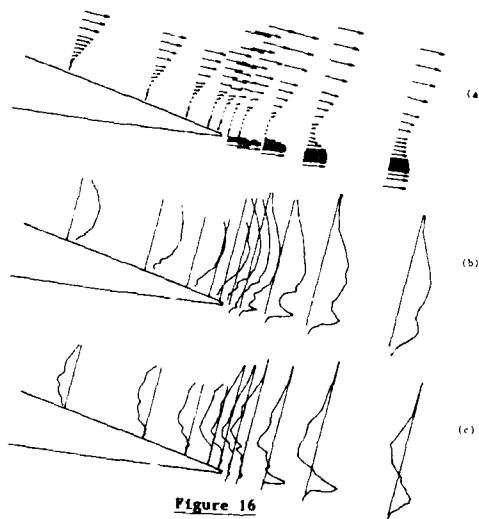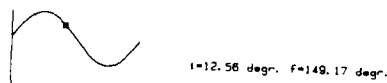
Figure 16

Figure 6.23 : 5° to 15° incidence, k = 0.3
(a) velocity vectors   scale :   — 40% Q
(b) chordwise fluctuations √u'²/Q   scale :   — 4% Q
(c) - Reynolds stress u'v'/Q²   scale :   — .1% Q²

Figure 17

Figure 6.24 : 5° to 15° incidence, k = 0.3
(a) velocity vectors   scale :   — 40% Q
(b) chordwise fluctuations √u'²/Q   scale :   — 4% Q
(c) - Reynolds stress u'v'/Q²   scale :   — .04% Q²

(d)

i=16.82 degr. f= 49.72 degr.

(d)

i=17.92 degr. f= 79.56 degr.

(a)

(b)

(c)
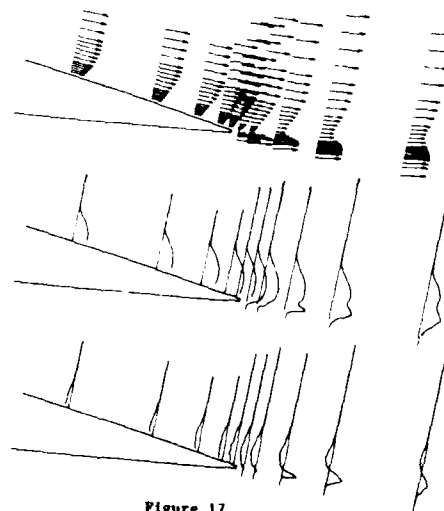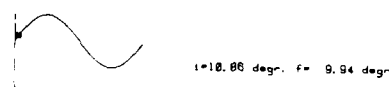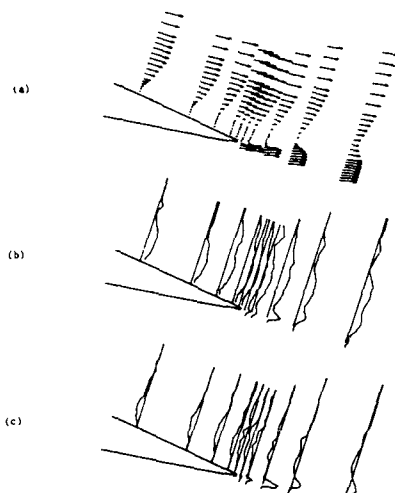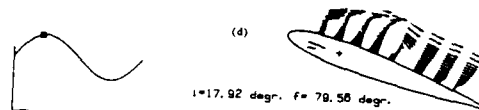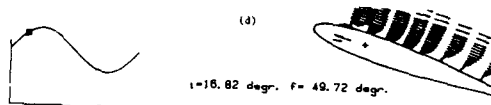
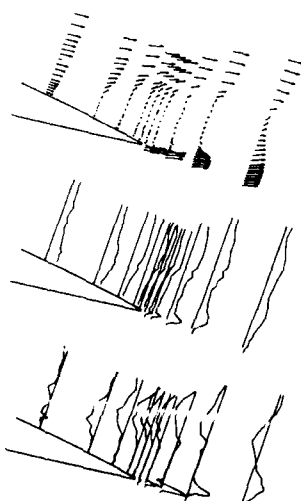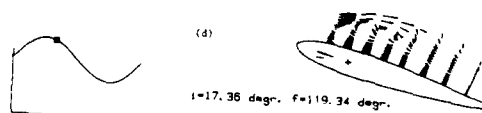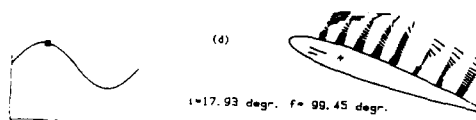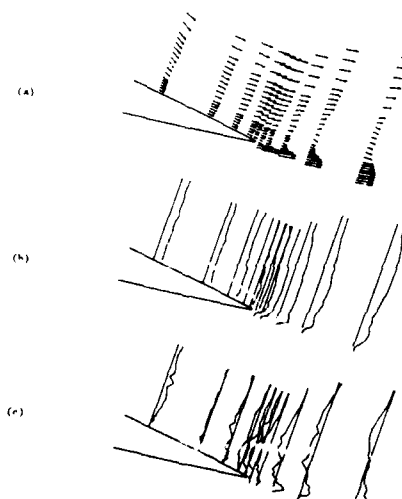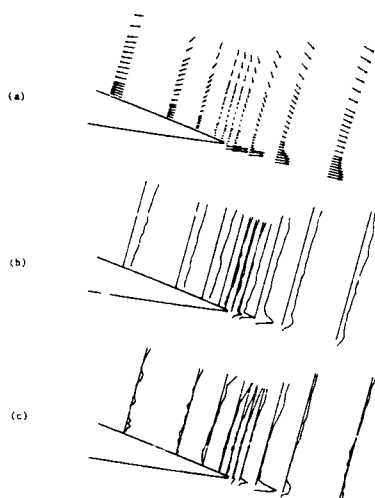**Figure 18**   8° to 18° incidence, k = 0.3

(a) velocity vectors   scale :   — 60% Q
(b) chordwise fluctuations √u'²/Q   scale :   — 20% Q
(c) - Reynolds stress u'v'/Q²   scale :   — .2% Q²

Figure 19   8° to 18° incidence, k = 0.3

(a) velocity vectors   scale :   — 60% Q
(b) chordwise fluctuations √u'²/Q   scale :   — 20% Q
(c) - Reynolds stress u'v'/Q²   scale :   — .2% Q²

(d)

i=17.93 degr. f= 99.45 degr.

(d)

i=17.36 degr. f=119.34 degr.

(a)

(b)

(c)

Figure 20   8° to 18° incidence, k = 0.3

(a) velocity vectors   scale :   — 60% Q
(b) chordwise fluctuations √u'²/Q   scale :   — 20% Q
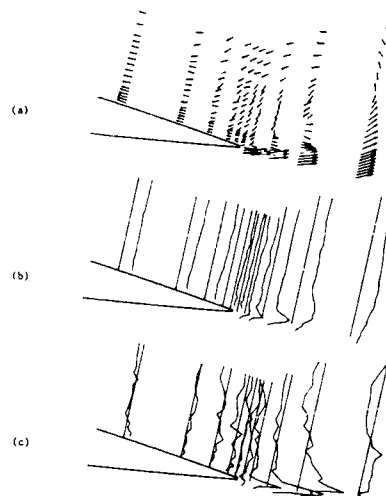(c) - Reynolds stress u'v'/Q²   scale :   — .2% Q²

Figure 21   8° to 18° incidence, k = 0.3

(a) velocity vectors   scale :   — 60% Q
(b) chordwise fluctuations √u'²/Q   scale :   — 20% Q
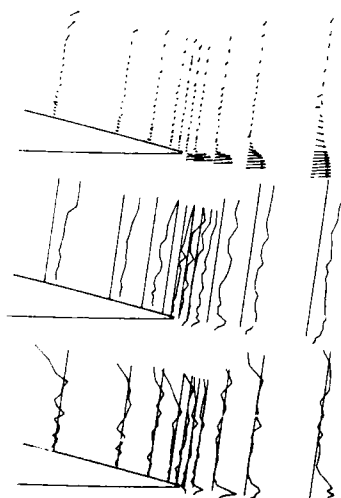(c) - Reynolds stress u'v'/Q²   scale :   — .2% Q²

(d)

i=15.56 degr. f=149.17 degr.

i=12.22 degr. f=188.95 degr.

(a)

(b)

(c)

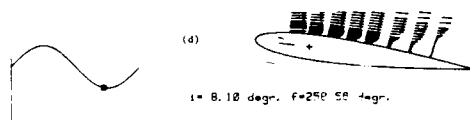**Figure 22**   8° to 18° incidence, k = 0.3

    (a) velocity vectors   scale :   — 60% Q

    (b) chordwise fluctuations $\sqrt{\overline{u'^2}}/Q$ scale :   — 20% Q

    (c) - Reynolds stress $\overline{u'v'}/Q^2$ scale :   — .2% Q²

(a)

(b)

(c)
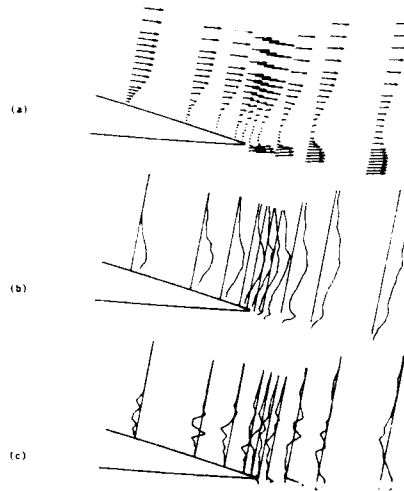
Figure 23   8° to 18° incidence, k = 0.3

    (a) velocity vectors   scale :   — 60% Q

    (b) chordwise fluctuations $\sqrt{\overline{u'^2}}/Q$ scale :   — 20% Q

    (c) - Reynolds stress $\overline{u'v'}/Q^2$ scale :   — .2% Q²

(d)

i= 8.10 degr. f=250.56 degr.

(d)

i=11.14 degr. f=338.12 degr.

(a)

(b)

(c)
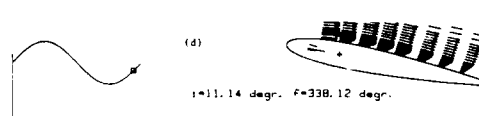
Figure 24   8° to 18° incidence, k = 0.3

    (a) velocity vectors   scale :   — 60% Q

    (b) chordwise fluctuations $\sqrt{\overline{u'^2}}/Q$ scale :   — 20% Q

    (c) - Reynolds stress $\overline{u'v'}/Q^2$ scale :   — .2% Q²

Figure 25   8° to 18° incidence, k = 0.3

    (a) velocity vectors   scale :   — 60% Q

    (b) chordwise fluctuations $\sqrt{\overline{u'^2}}/Q$ scale :   — 20% Q

    (c) - Reynolds stress $\overline{u'v'}/Q^2$ scale :   — .2% Q²

DISCUSSION

L.S.Langston, University of Connecticut, U.S.A.

Apparently the authors have used a single hot wire and have shown reverse flow in only one region, near the leading edge (a difficult thing to do without mean flow measurements, especially with a single hot wire). The results show no reverse flow in the separated regions near the trailing edge. What is the evidence that these separated regions do not contain reverse flow since a single hot wire was used and no independent flow direction measurements have been made.

Author's response :

The technique used was described in earlier papers (see ref 4 to 5 of the paper). The reverse flow was found by using a slanted wire over 360°, in such a way that it always faces both the right and the wrong flow direction. Both solutions are fully computed. The correct solutions are next found by expressing continuity in the flow angle, starting from a known direction. This is made possible by the high density of data, as well in time as in space.

The results obtained in the separated regions at the trailing edge in general show small velocity magnitude. With the present technique, this amplitude is too small to give a relevant flow direction (below about 0.3 m/s or 3% of the mainstream velocity). In this case, the region is considered as a 'dead water' zone, with no distinct 'reversal'. In some situations (see e.g. figure 9 of the paper) distinct flow reversals can be seen however.

K.Förster - University of Stuttgart,W.Germany
Could the author give
 * the reduced frequency
 * the test Mach Number

Author's response :
The reduced frequency is

$$\frac{\omega c}{2Q} = 0.3$$

where ω is the pulsation (rad/sec), c the chord and Q the main velocity (Q = 11 m/s)
The Mach Number is very small, 0.03. Hence, the compressibility effects are absent

Compressor Performance Tests in the Compressor Research Facility
by
F. R. Ostdiek, W. W. Copenhaver, D. C. Rabe
Technology Branch, Turbine Engine Division
Wright Research and Development Center (WRDC/POTX)
Wright-Patterson Air Force Base, Ohio USA 45433

SUMMARY

An advanced compressor test facility, the Compressor Research Facility (CRF), has been established at Wright-Patterson Air Force Base. The CRF is designed for exploration of steady-state and transient behavior of full-scale, multistage gas turbine engine fans and compressors. Since construction and check-out of the facility, the CRF test team has completed its first five years of testing with a variety of test articles. Customers besides the Air Force have included other Government agencies and industry.

Turbine engine technology is changing rapidly with new mission demands on the engine resulting in new aerodynamic, stability, and performance demands on each of its components. This paper describes the role of the CRF in meeting the challenges inherent in such a rapidly changing field. The facility characteristics are described along with a description of the changes, modifications, and enhancements made to the facility in its short history.

Several examples of tests performed in the CRF (both steady-state and transient) are used to demonstrate the impact of the CRF results on engine development.

Finally, the plans for further facility modifications and enhancement are given. This affords a preview of the impact which this and other test facilities will have on turbine engine technology.

INTRODUCTION

Propulsion technology for military applications is undergoing a major change from the engines of past decades. Many organizations are involved and the US Air Force Wright Research and Development Center (WRDC) is in the forefront of these changes through the Integrated High Performance Turbine Engine Technology (IHPTET) initiative (Reference 1). In this effort, the Army, Navy, and Defense Advanced Research Projects Agency have joined the Air Force in an attempt to accelerate the growth of technologies required to significantly change turbine engine performance. Consideration of the commonly used figure-of-merit for turbine engine performance, engine thrust-to-weight (T/W) ratio, shows that we have made considerable advancement in the past. Operational aircraft gas turbine engines of the '50s used the aerodynamic and structural techniques available at the end of the piston engine era and were characterized by T/W ratios in the 1-4 range. Figure 1 shows a cross-sectional view of the J79 engine of that era.

After the introduction of the gas turbine as a new engine cycle into the aircraft propulsion arena, progress was initially made by application of engineering principles to the specific problems in the engine. This led to researchers performing basic studies of the aerodynamics of the flows in each of the components, structural optimization using the available materials of the day, and aerothermodynamic cycle studies to optimize performance and develop engine designs for particular aircraft missions. Thus, steady progress was made in the performance and reliability of turbojet engines and turbofans were introduced. An example of the engines of the '70s is the F100 shown in Figure 2. This augmented engine is the most widely used engine in Air Force fighter aircraft today and, when introduced, represented a significant increase in performance and reliability over the pioneering engines. It is capable of producing nearly 25,000 pounds of thrust with an installed T/W of nearly 7.4.
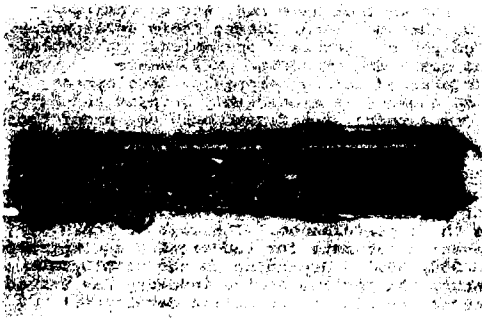
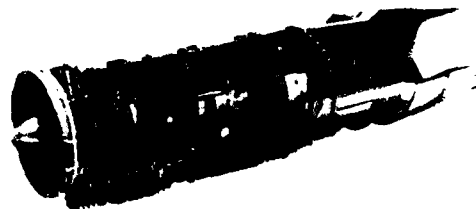Figure 1. J79 Engine Cross-Section   Figure 2. F100 Engine Cross-Section

The progress attained from the '50s through the '7Cs in building more efficient and durable engines helped define more subtle problems. This included secondary flows, transient and differential heating effects, cooling of the hot sections, interaction of multiple spools, and system stability. The stability problem has been and remains a particularly difficult one as demonstrated by the long and troublesome history of stagnation stalls. The next generation of air superiority fighters will demand a mucn wider installed performance range in terms of thrust, engine speed, and inlet conditions. The continued interest in short takeoff and vertical landing aircraft (STOVL), with the varied methods of providing vertical lift, not only widens the performance corridor wherein the aircraft with its engine is expected to operate stably, but also means that the engine now becomes a primary part of the aircraft stability/control picture. Rapid changes in flight regime which will be accomplished during thrust vectoring, thrust reversing, vertical landings, gun gas ingestion, and high speed aerobatic maneuvers will significantly increase the demand for a distortion-tolerant engine. The compression system in these new engines will therefore be required to maintain a high performance level when faced with rapid excursions in engine speed, inlet flow conditions, and pressure and temperature profile distortions.

The IHPTET goal of doubling the thrust-to-weight ratio in the next 15 years, demands that a large part of our research be spent on identifying and developing new materials for use throughout the engine. Compression systems will have shape restrictions which are wholly dependent on the structural requirements of new materials and, at the same time, compressor designs will enter into new aerodynamic regimes because of the higher temperature capability of the new materials.

Major advances in compression system aerodynamic design have been made in the past 20 years. Dr Arthur Wennerstrom of WRDC's Aero Propulsion and Power Laboratory has been a major contributor and leader in this area. Figure 3 shows one of Dr Wennerstrom's latest compressor stages which combines the high-through-flow technology he pioneered in the '70s and the swept blades in his latest research. Obviously, this rotor represents a radical change from our present operational engines, and we expect further changes in the future.

Thus, in addition to increased operability requirements from changing aircraft missions, we are faced with the struggle to obtain increased efficiency through aerodynamic research and then to retain that efficiency gain when aeromechanical requirements drive us into unknown areas. A further discussion of the revolution of turbine engine technology is contained in Reference 1.

Figure 3.   Wennerstrom Swept Rotor

HISTORICAL PERSPECTIVE OF COMPRESSOR TESTING

The turbine engine industry has been plagued with compressor problems throughout its history (Reference 2). A brief review of the history of turbine engine development indicates that virtually all of our modern turbine engines have had serious compressor problems, either mechanical or aerodynamic and sometimes both, during their development. Most of these can be traced to stringent design goals, increased operational performance requirements, complex multi-mission functional goals and transient performance requirements which were unknown or not well understood during compressor development. In addition, the aerothermodynamics of gas turbine engines is exceedingly complex and is still an emerging and expanding technology. One expects significant problems under those circumstances. The effect of these problems was manifested in slipped or cancelled programs and excessive program costs. The archives have several examples of cancelled weapon systems which can be directly related to compressor development problems. The records show that most compressors and fans go through from two (2) to eight (8) major redesigns before reaching a mature operational status. Many then go through further redesigns in an attempt to enhance or improve their performance. The cost of these redesign efforts can be staggering. A conservative estimate for redesigning a compressor is $10,000,000 and in some cases could exceed $50,000,000 depending on the development status of the engine. With this kind of impetus, the turbine engine industry has turned to component testing to help control expenditures and also to normalize development schedules.

The evolution of compressor test facilities as a tool in the development of compressors has been a steady process over the past 50 years. Test facilities at first responded to relatively unknown requirements since the turbine engine was still in its infancy. With continued use of the engine, our understanding of the flow processes and problems increased, and facilities were either constructed or converted to meet the test requirements. The usual output was an airflow-pressure ratio performance map.

Through the '70s, compressor test facilities were characterized by manual control of the drive system and support equipment. This allowed adequate test control but also meant manually monitoring, resetting, and stabilizing as test conditions changed. Thus a considerable amount of time was spent in moving from one test condition to another. Consequently, test periods were usually long and tedious. Data systems were designed to obtain steady-state information. The exceptions were strain gages and specialized test requirements when some transient pressures were recorded for later evaluation. Data systems had long sampling times and information was recorded on magnetic tapes in raw form and saved for later verification and correction. This had two effects. First, the test operator performed the test without precise knowledge of the true aerodynamic operating point. This resulted in increased test point scatter. Secondly, the reduced data was not available for days or weeks and usually not until the test was concluded. The researcher thus missed "targets of opportunity" and areas that should have been investigated.

Many tests were conducted in pairs. This was fostered by the concept of having separate aerodynamic and structural rigs because the problems were different and difficult. This generally resulted in separate tests for the two purposes and separate test teams even when using the same rig. Consequently, minimal coordination between mechanical and aerodynamic researchers occurred.

In addition to building dedicated test rigs, researchers occasionally obtained compression system data from engine operation. This testing was restrictive in that instrumentation access was often limited and operation was only on the engine operating line unless the test program could tolerate some off-schedule variable geometry rigging, in-flow bleeds, etc.

Throughout the '50s to '70s, test facilities have been built to meet the perceived needs of turbine engine development. The response has been hampered by facility construction lead time. The construction and checkout period from program initiation to fully operational status is typically 5 to 15 years (12 years for the CRF). However, the continued need for good test data still forces new facility construction.

FACILITY OVERVIEW

The CRF supports the exploratory and advanced development programs of the Aero Propulsion and Power Laboratory required to advance turbine engine technology. The facility provides the means of obtaining data required for exploration of the steady-state and transient behavior of full-scale, multistage gas turbine fans and compressors and is designed to accommodate compressors with inlet flow up to 500 lb/sec and pressure ratios of 40:1 (Reference 2, 10, 11).

The facility is an open-cycle design, in which the test compressor provides motive power to move air through the facility. The compressor is mounted inside a 20-foot diameter test chamber vessel. Filtered air is drawn from the atmosphere into the test chamber plenum through an array of five inlet control valves which provide compressor inlet pressure regulation for reduced inlet pressure testing. Mounted inside the test chamber plenum is a flow conditioning barrel with screens and honeycomb to minimize airflow distortion. A close-coupled discharge valve controls compressor pressure ratio. Discharge air passes into a collector and through a venturi flow measurement station before discharging to the atmosphere. Flow can also be measured with the inlet bellmouth.

An overall layout of the facility is shown in Figure 4. The facility actually involves space in three different buildings. The test building houses the computer and control rooms, the operations building contains the test chamber and signal conditioning room, and the electrical power conditioning equipment is located in the third building.

CRF tests are controlled from the facility control room through the CRF computer system shown in Figure 5. Commands to execute the test program are sent from the control room through a monitor computer located in the computer room to four control computers, Modcomp Classics located in the signal conditioning room. The control computers, with shared memory, control the electrical power conditioning equipment which powers the drive motors. They also control the services that support the facility and variable geometry devices on the test compressor. Auxiliary support systems, including hydraulic, test article lubrication, service air, cooling water, and fire control are controlled by programmable logic controllers monitored by these control computers. All control systems have automatic fault detection with preprogrammed facility recovery actions.

The compressor is driven at speeds up to 30,000 RPM through two speed-increasing gearboxes by either of two 30,000 HP synchronous electric motors. Various compressor speed/power ranges are available by selecting the appropriate high-speed gearbox and drive motor combination. Compressor speed is typically controlled to within ten RPM, even during stall, by controlling the frequency of the electric power supplied from the power conditioning equipment to the selected drive motor.
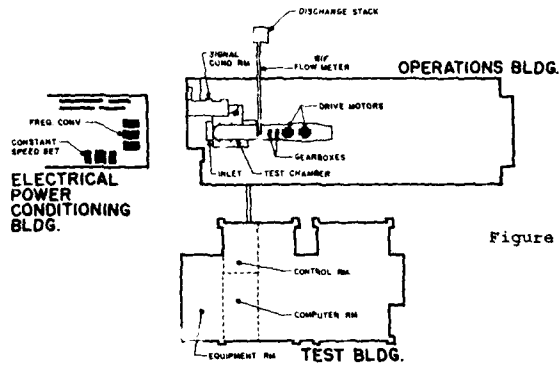
ELECTRICAL
POWER
CONDITIONING
BLDG.

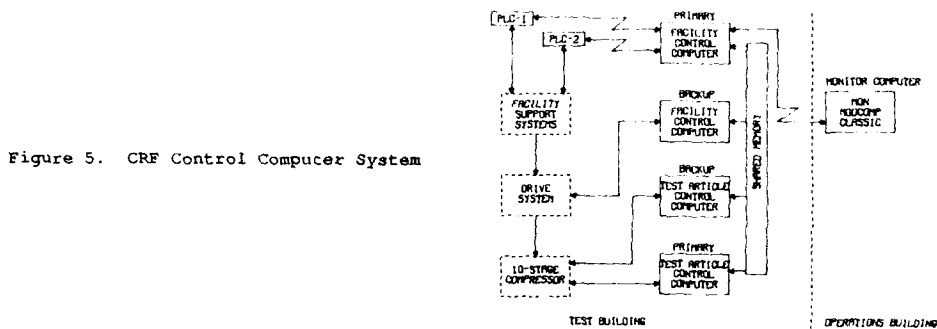Figure 4.   Compressor Research Facility Layout

Figure 5.   CRF Control Compucer System

The CRF data acquisition system is shown in Figures 6 and 7. The digital system
acquires data from a Preston analog-to-digital converter and multiplexer at a rate which
approaches 50,000 samples per second. The system can be configured to handle up to 640
amplifier channels. Data is passed from the analog-to-digital converter to a data
acquisition computer (DAC) which acquires the data and controls the data acquisition
process. A second computer (AUX) buffers the data for access by the data reduction
computer (IBM 4341 Main [MAIN]).
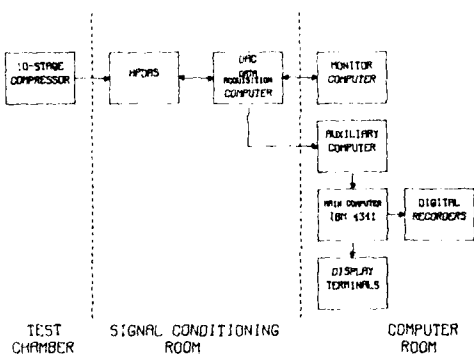
Figure 6.   CRF Data Acquisition System
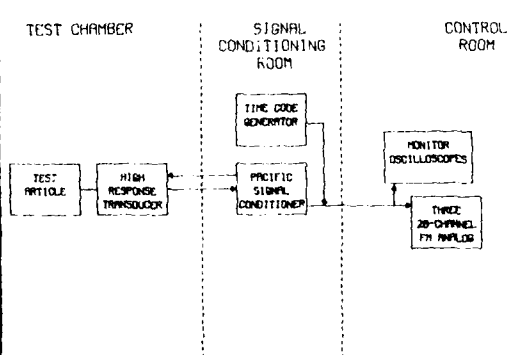   (Digital)

Figure 7.   CRF Data Acquisition System
            (Analog)

The MAIN computer is the heart of the digital data acquisition system and performs
all of the channel calibrations, engineering conversions and performance calculations.
Data is processed on-line by the MAIN computer and then transferred to monitors for
real-time use by the test team. The data is also routed to printers and storage disks and
tapes. Two important features of the MAIN computer are its ability to perform an
electronic calibration of all digital channels (channel check) and its ability to perform
an automatic five point pressure calibration of the pressure channels.

This data system has been used to measure time-averaged and unsteady pressures and temperatures during CRF tests. The pressure data acquired during the transient tests can be categorized as high-response, close-coupled, and time-averaged measurements. High-response and close-coupled methods were used for unsteady pressure measurement and time-averaged methods are used for steady and quasi-steady measurement.

Time-averaged data are acquired through real-time digital conversion and stored on digital tape or disk and are used to define time-averaged steady-state properties. A time-averaged measurement is defined as an arithmetic average of 30 samples of each channel sequentially at the maximum rate possible for analog to digital conversion, typically this requires 200 ms.

Close-coupled measurements are a subset of the time-averaged measurements and are obtained through real-time digital conversion of signals from the same transducers utilized for time-averaged measurements. These transducers are mounted as close as possible to the test compressor for unsteady tests. A close-coupled scan is defined as a single sample of all close-coupled channels whereas a time-averaged represents 30 scans.

The high-response system provides for higher frequency response than the close-coupled system and results in a more accurate characterization of pressure fluctuations. The frequency response of the high-response system is highly dependent on transducer selection and placement on the test article. High-response data are acquired in analog form and stored on tape through FM recording.

At the start of each test program in the CRF, an exhaustive checkout of the data system is performed. The channel check and pressure calibration activities ensure the proper functioning of the digital data system; however, possibilities still exist for errors. Therefore, end-to-end checks are performed from the test article to the computer readout using known pressures and temperatures. During the test program, a daily check is made of the data system and the test rig at the beginning and end of each test period by repeating a pre-selected operating condition of speed and pressure ratio to determine if the calculated parameters such as flow and efficiency have changed. Appropriate corrective action is taken. Expanded discussions of the CRF facility and data systems can be found in References 10 and 11.

DIRECT VELOCITY MEASUREMENT

The direct measurement of the velocity can provide insight into the flow behavior that cannot be achieved in any other way. Flow separation, angle of attack and deviation angles all must be detected through the direct measurement of the flow velocity vector. There are methods of calculating the velocity vector from pressure probes using multiple sensors, but generally detailed flow-field measurements are performed with the use of hot wires or laser anemometry if the test vehicle can accommodate these methods of measurement

In the CRF, the hot wire is routinely used to measure the boundary layer in the bellmouth of test compressors. With the characterization of the boundary layer, the bellmouth can be used as a second source of mass flow measurement. This measurement also characterizes the compressor inlet turbulence level. A typical boundary layer measured during a CRF compressor test is presented in Figures 8 and 9. These data show that the inlet turbulence level in this CRF test was below .5% while the boundary layer thickness was less than 25 centimeters at a location .5 diameter downstream from where the bellmouth became a constant area and with a pipe Reynolds number of approximately 5×10^6.
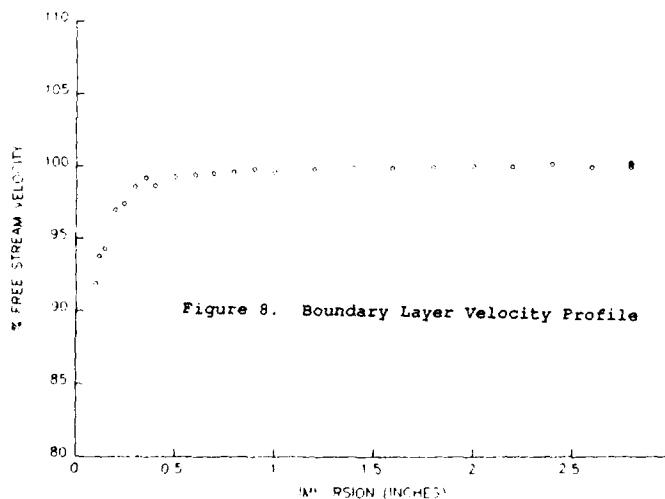

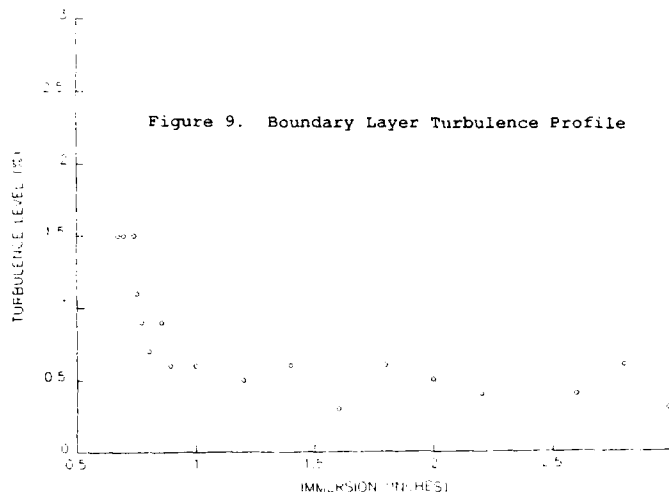Figure 8. Boundary Layer Velocity Profile

Figure 9.   Boundary Layer Turbulence Profile

Laser anemometry has also been used extensively in the CRF. Through its use, detailed measurements of the rotor flow fields are made which were not possible just a *few* years ago. Since the early '70s, laser anemometry has been refined and developed independently and commercially. There are two general techniques currently being used to investigate compressor flow fields. These include the laser fringe and laser two-focus techniques. A comparison of these two techniques was performed (Reference 8) to assess their advantages and disadvantages for use in CRF testing.

Computational and experimental laser results have been compared by many researchers (References 12 to 15). These comparisons are providing new insight into the physics of compressor flow fields. Future aerodynamic advancements in compressor performance will stem from laser and transient measurements. Further, the incorporation of on-line presentation of data in comparison with computational results will help to guide the laser and other work and improve the efficiency of test time. Two representations of laser two-focus data that are available on-line in the CRF are presented in Figures 10 and 11. This representation of the data can be achieved while a subsequent set of measurements is being obtained. With this capability the actual test data can be reviewed so laser set up conditions can be adjusted to meet the flow-field requirements.
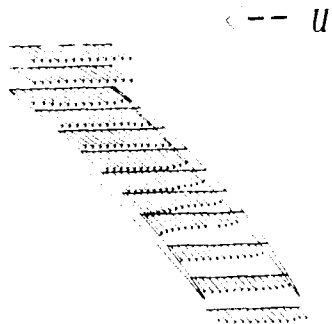
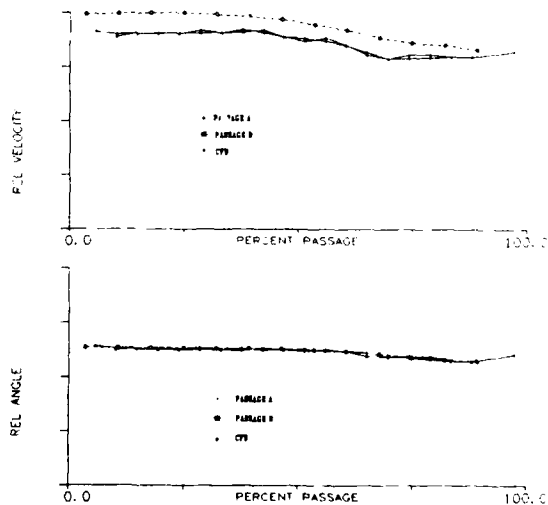Figure 10.   LTA Data Presentation in Vector Form

Figure 11.   LTA Passage Measurement Presentation

The CRF was first envisioned as an aerodynamic test facility and consequently, had minimal aeromechanic capability. Test safety, funding problems and scheduling pressures made it advisable to perform both aerodynamic and aeromechanical mapping at the same time. A new 144-channel aeromechanics workstation was designed, installed and has been operational for several years. This station includes 144 monitor oscilloscopes, digital storage of gage signals, and 182 channels of FM recording capability. This station can support four aeromechanicists during test with each having a complete set of spectrum analysis equipment. In addition, a strain gage monitoring system is being installed at the present time which will provide a watchdog function and alarm for over-limit stresses (DC to 16 Khz) for 108 channels. Since this system is computer controlled, the alarms could be used to command immediate corrective actions through the control computers.

CRF TESTS

This section shows the progression in competency of the CRF test team by presenting sample results from several tests. Through these examples, we will show the development of the facility from a purely steady-state aerodynamic test facility to a facility capable of transient testing with an aero/mechanical mix of experimentation. In addition, the capability of the facility to perform advanced laser flow measurements to characterize the details of the fluid flow will be shown. Table 1 presents an overview of the facility's test history.

TEST PROGRAM	DATE	RESULTS
J85 II	1983-84	OPERATIONAL FACILITY
HIGH TIP SPEED COMPRESSOR	1984-85	DESIGN INFORMATION GE 37 REDESIGN
FAN DISTORTION AND LASER ANEMOMETRY	1985-86	GE 37 DATA BANK
MULTISTAGE HIGH-PRESSURE COMPRESSOR	1986-87	STALL AND POST STALL DATA BANK
SWEPT ROTOR	1987-89	NEW TRANSONIC TECHNOLOGY

Table 1. CRF Test Programs

STEADY, HTSC TEST RESULTS

The first test in the facility was performed to obtain the aerodynamic performance of an advanced transonic research compressor. Limited results from this test program have been previously reported (Reference 9). The nondimensionalized compressor performance obtained for this two-stage compressor is presented in Figure 12. All of the data points taken for the map were of sufficient quality to be used on this figure. This was a direct result of performing an extensive end-to-end check audit of the instrumentation system before the test program plus daily checks to determine if channels had become inoperative. These channels were then repaired as needed. Even though the data acquired on the test compressor were essentially all steady state, the test presented the opportunity to exercise the full data acquisition system of the facility. Over 600 individual channels of pressures and temperatures were measured during the test. All of these measurements were available for review in engineering units in near real-time. They were updated on the computer terminals every one to two seconds. This provided the ability to verify the compressor performance on-line. The consistency of both the compressor and the data system was verified through the use of the daily performance checkpoints. A trend of the efficiency over the complt· est program is shown in Figure 13. This figure shows a change in the efficiency of approximately .5% near the middle of the test program. This change was considered to be outside the precision uncertainty of the data system and was therefore a change in the test system (Reference 9). The drop in efficiency was attributed to damage sustained by the second stage blades which was discovered upon post-test teardown. Although this failure mode effected only about 1% of the blade area, the data system was able to observe a change in the performance of the test compressor.
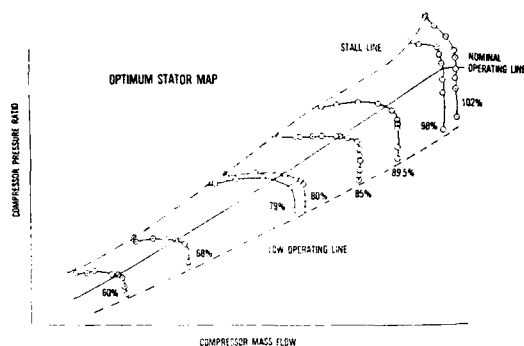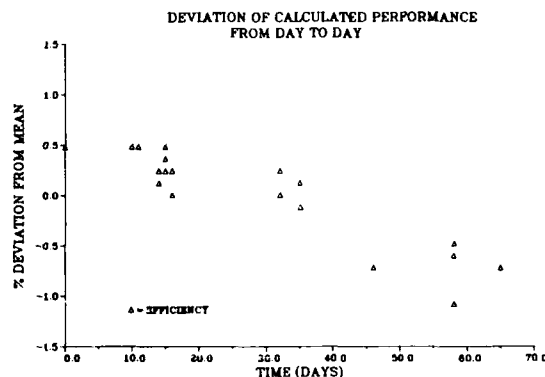
Figure 12. CRF Compressor Map

DEVIATION OF CALCULATED PERFORMANCE
FROM DAY TO DAY

Figure 13. CRF Compressor Checkpoint
History

STRUCTURAL, TEST RESULTS

During the Fan Durability Assessment (FDA) test program, the CRF demonstrated its full-scale structural testing capability. During aerodynamic testing, the structural characteristic of the test compressor had been found to be satisfactory for clean inlet flow. However, in the FDA test program, the primary objective of the test was to determine the aeromechanical response of an integrally-bladed disk to inlet flow distortion. In this program, the 16 blades of the rotor were instrumented with 20 strain gages with at least one per blade. Essentially, a classical structural test program was performed. Excessive resonant stresses were observed in the presence of some of the inlet pressure distortion patterns. These significant resonances were always in the first three natural modes. Large blade-to-blade response variations occurred even though the blades of the blisk were essentially tuned. This had not been expected prior to the test. Additional test results are presented in Reference 5. From a facility point of view, this test program basically emphasized that structural testing could be manpower intensive and it increased the risk of damage to the test compressor and the facility.

LASER TEST EXPERIENCE

Early in the facility development it was recognized that laser anemometry would play a key roll in understanding the flow physics of our advanced compressor systems. With a better understanding of the detailed flow-field behavior, computational fluid dynamics codes can be improved to provide realistic simulations of advanced compressor designs. These improved codes can be used to perform parametric analysis of current concepts and help determine better compressor design techniques.

Laser two-focus and laser fringe anemometry were both investigated (Reference 8) for use in compressor testing. These comparisons showed that the available laser two-focus system provided a mechanically more reliable flow measurement system but required more run time to acquire the test data. The laser fringe anemometer reduced run times and provided accurate measurements in higher turbulence level flows. However, its major draw back was its delicate optical system. Initially the laser two-focus system was employed in the test facility. The laser fringe system is being improved for future use.

Laser two-focus has been used in the CRF to investigate isolated flow phenomena as well as full flow-field behavior. The passage shock wave end wall boundary layer interaction in a rotor passage was investigated (References 3 and 11). Figure 14 shows this test configuration. A flat window was employed and the laser beam was transmitted through it at nearly a perpendicular angle. The magnitude and direction of the velocity component in the axial-circumferential plane was measured. The flow behavior was
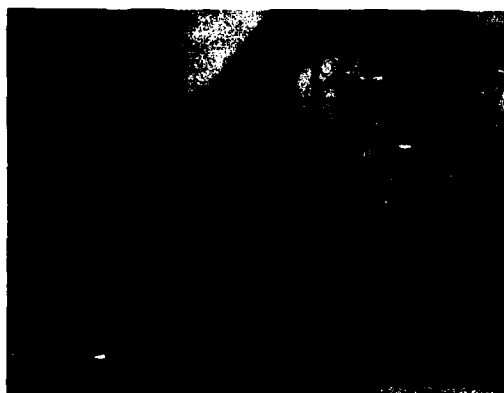
investigated in the blade tip leading edge region of the rotor passage where the passage shock wave end wall boundary layer interaction was suspected. It was discovered that the well-ordered core flow was separated from the end wall boundary layer by what appears to be a shear layer where the flow behavior changes abruptly. This shear layer appears to be at a constant depth between 12% and 22% of the axial blade chord. No evidence of this shear layer was observed at the leading edge where measurements were obtained well within the inlet boundary layer.

Figure 14.   Laser Test Configuration

The full flow field of an advanced swept rotor design has been successfully measured and the results are currently being analyzed. This test again used the laser two-focus system to obtain flow measurements. In this rotor, the blade circumferential lean prevented a view of the complete flow field if the laser was directed in a purely radial direction. Therefore, the beam penetration was changed during the test to acquire a complete view of the flow field. Near the blade tip, the beam entered the flow along the radius. When measurements were to be obtained in the hub region, the beam entered the flow at approximately 25 degrees to the radius, as seen in Figure 15. By using these two entrance angles, nearly all of the flow field could be observed. Approximately 2000 data points were acquired within the blade passage to characterize the flow field.

Figure 15.   Laser Beam Near Hub Region

In the future, the laser fringe anemometer will be developed to improve the speed of data collection. It is anticipated that the laser fringe system will improve the speed to the point that the design point condition of our advanced compression systems can be measured on a routine basis. This would require the system to be able to measure the complete flow field of a rotor in less than one test week. This requirement is leading the CRF to automatic controls of the system. The optics of the system will be mechanically improved to ensure alignment over extended periods of running in a high noise environment. Adjustments that would be performed by hand in a laboratory environment will be automatically controlled in the CRF. At the present, this laser fringe system is being configured and tested on smaller research vehicles so that it can be developed for use in the CRF.

TRANSIENT TEST EXPERIENCE

To fully characterize the performance of advanced compressor designs, testing must also include investigations into quasi-steady and unsteady compressor performance. Details of unsteady compressor phenomena provide information for designers about how a compressor transitions from a given state of operation to another, as is the case during compressor stall. When a compressor stalls, engine performance is reduced below a level that can sustain flight. Because compressor stalling does occur and aircraft have been consequently lost, the performance of a compressor operating near- and in-stall and the compressor's ability to recover from stall are extremely important considerations. Unsteady information as it relates to compressor stalling behavior can be used to develop designs that are more stall tolerant and more stall recoverable.

Transient compressor performance was investigated during the CRF multistage compressor stall recoverability test program. This CRF test program was designed to increase understanding of the details of in-stall operation and recoverability of a 10-stage, high-speed, high-pressure ratio axial-flow compressor. The test demonstrated the transient data acquisition capabilities of the CRF as well as the test team's ability

to plan and execute a test program which required the test compressor to be maintained in rotating-stall for long periods of time. During the program, approximately 10 hours were spent in rotating-stall. The test program results (Reference 4) indicated that stage matching may have a direct impact on the recoverability of a compressor from rotating-stall. The unsteady test results were also used to assist in verification of a dynamic compression system model as detailed in Reference 6.

Test program results were in the form of steady, quasi-steady and transient performance of the test compressor during the stalling process and while operating in rotating-stall. Steady-state data were obtained while the compressor was operating unstalled and in rotating-stall for five different shaft speeds as presented in Figure 16 (Reference 4). The data shown in rotating-stall is a time-averaged representation of the quasi-steady rotating-stall performance of the compressor. Each individual pressure coefficient data point is comprised of an average of 30 scans of the unsteady pressures within the compressor. Each point represented in Figure 16 was acquired after a three-minute compressor stabilization period. Steady-state data of this type provides the designer with a steady-state representation of the test compressor quasi-steady rotating-stall operating point. This steady-state representation of a compressor in an unsteady condition, rotating-stall, needs to be refined. It is useful to present results in a standard map format and at the same time, do further work to understand the details of the time-varying, rotating-stall cell.
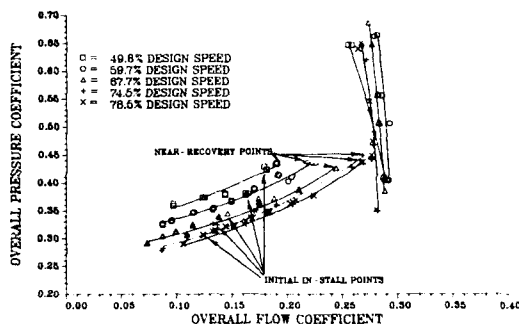

Figure 16. Test Compressor Overall Pressure Characteristics

A subset of the time-averaged measurements was the close-coupled pressure measurements a defined previously. A graphical representation of the two types of measurements is presented in Figure 17. This figure details how a time-averaged measurement would be obtained from a time-varying pressure. It also shows what information is acquired using the close-coupled digital measurement system. The difference between the two types, close-coupled and time-averaged, was the number of averages taken to make up the measurement and the rate at which the data were obtained. During the stall test program, 77 pressure channels with a nominal frequency response of 70 Hz were designated as close-coupled measurement channels. A close-coupled scan was defined as a single sample of all close-coupled channels simultaneously. All sampled signals were held until the they could be digitized and subsequently recorded. This technique eliminated the phase errors that would have been associated with sequential reading of data from individual channels of close-coupled data. Further details on the close-coupled data acquisition system are provided in Reference 10.
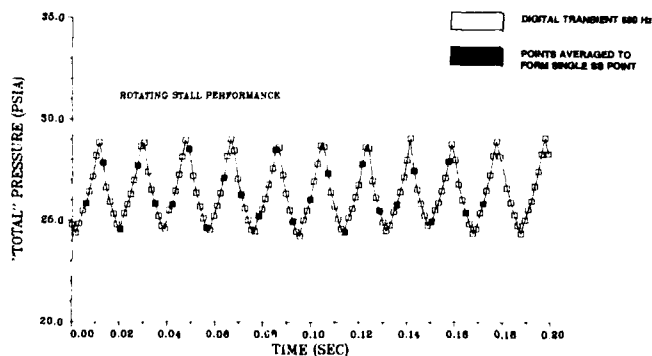

Figure 17. Time-Averaged and Time-Varying Data Acquisition

The close-coupled digital data acquired for compressor rotating-stall operation can be presented in a three-dimensional "unwrapped" condition as shown in Figure 18. This figure represents a snapshot of the pressure levels within the compressor while operating in rotating-stall. It indicates high levels of pressure fluctuations in the rear of the compressor while lower levels exist in the front stages of the compressor, suggesting that the stalled stages are isolated in the rear of the compressor. The data can be presented in an alternate fa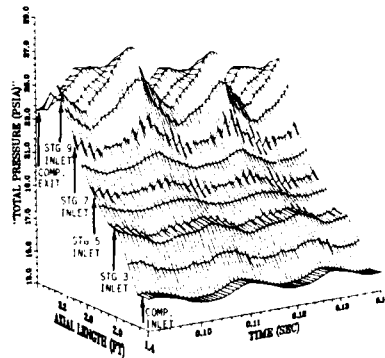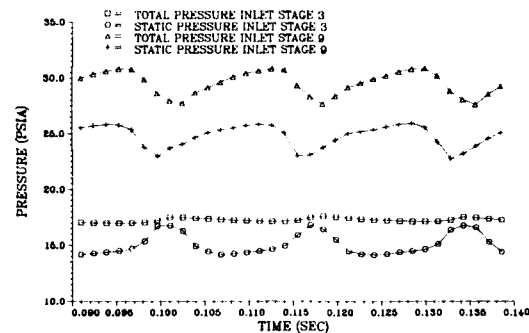shion to obtain details of the total and static pressures within the compressor while the rotating-stall cell is present within the compressor. Figure 19 shows the time-resolved total and static pressures at two axial locations in the compressor. The figure supports the concept that the stall cell is concentrated in the rear of the compressor as can be seen by the large fluctuations in both static and total pressure as the stall cell passes, while the front stages react to the cell passage in the rear with little change in total pressure and a rise in static pressure.

Figure 18.   Test Compressor In-Stall Time-
Resolved Total Pressure Rise

Figure 19.   Test Compressor 78.5% Speed Internal
Time-Resolved Pressures

□ = TOTAL PRESSURE INLET STAGE 3
○ = STATIC PRESSURE INLET STAGE 3
△ = TOTAL PRESSURE INLET STAGE 9
+ = STATIC PRESSURE INLET STAGE 9

Further details of the extent of the rotating-stall cell were obtained with the high-response analog data acquisition system described previously. The unsteady pressures were measured through a transducer/pressure tubing system that allowed for a nominal frequency response of 200 Hz. A comparison of the high-response and close-coupled methods of data acquisition is provided in Figure 20 (Reference 10). The data detailed in this figure were obtained during the transition of the test compressor from steady unstalled operation to quasi-steady in-stall operation due to exit throttle area reduction. The comparison is of two compressor exit static pressures at the same axial plane and very near to each other circumferentially. The transition into rotating-stall is characterized well by both the close-coupled and high-response systems thereby indicating high confidence in both measurement systems. As quasi-steady rotating-stall is established, the figure suggests that the close-coupled system captures the basic trend of the rotating-stall but not the details of the stall cell itself. To further investigate these details the high-response data is required.

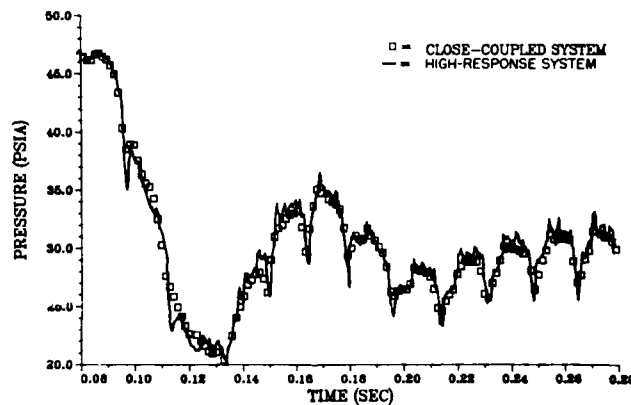

□ = CLOSE–COUPLED SYSTEM
— = HIGH-RESPONSE SYSTEM

Figure 20.   78.5% Speed Stall Inception Data Acquisition Comparison

High-response data obtained from two impact tube pressure probes positioned at the compressor exit are shown in Figure 21. The upper most curve details the time-resolved pressure during rotating-stall operation as measured from an impact probe facing upstream in the compressor, while the lower most curve is the same information, from a downstream facing probe. With this high-response information, it is possible to characterize the percentage of the compressor annulus that is blocked by the stall cell. In the blocked portion of the compressor annulus, both probes indicate pressures that are nearly equal while in the unblocked portion of the annulus, the difference is representative of reestablished through-flow velocity. Annulus blockage areas were found to vary between 60% and 15% for the in-stall throttle level tested.

Transient information of the nature presented here is essential if component tests are to continue to provide the information and insight necessary for development and improvement of design code that reliably predict high-speed axial-flow compressor stall performance and recoverability. In this test program, the CRF has demonstrated the capability to acquire accurate and reliable transient data in many forms for the advancement of future designs.
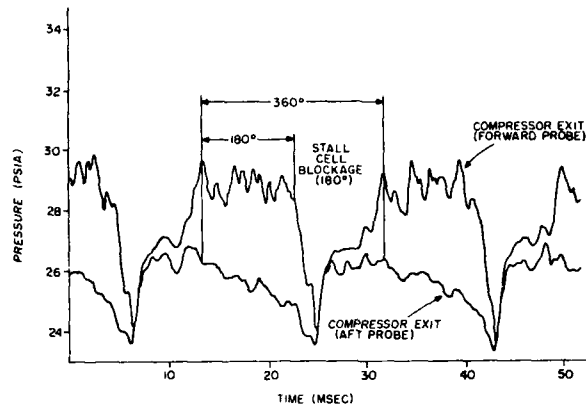
Figure 21. 78.5% Speed In-Stall High Response Data

FUTURE PLANS FOR THE CRF

The CRF has had a substantial impact on turbine engine development in the first five years of its operation. The test programs have supported exploratory research, generic system problems and advanced engine development. The facility was first envisioned as an automated facility capable of only aerodynamic investigations. During construction, the automated test function became fully integrated computer control of the test and the complete facility. After the facility was completed, an aeromechanics workstation with computer-controlled strain gage monitoring was added to allow aeromechanical investigations as well.

Many similar modifications and enhancements are planned for the CRF. A second discharge flow path, designed for 150 lb/sec, has been added and is being used for the first time. It allows testing of split-flow fans and compressors.

The CRF inlet flow system was designed to maintain the turbulence level at the compressor inlet at <0.5%. This provides a base to generate controlled pressure distortion patterns at the inlet. This has been done for several tests and will be used more frequently in the future. In addition, a hydrogen-fired heating system will be used to generate both elevated and distorted inlet temperature profiles. This unit is expected to be operational later this year and will allow us to bring increased realism to the aeromechanics testing.

A new aeromechanics effort has been started as part of the IHPTET initiative and is directed at identifying specific materials vital to engine development and then planning their development. This effort, the Core Engine Structural Assessment Research (CESAR) will utilize CRF aeromechanics testing capabilities in tests designed specifically for materials development.

New measurement techniques such as laser velocimetry, light probes for blade movement, and capacitance clearance measurements have been added to the facilities toolbag in the past few years. Further instrumentation advances for global temperature and stress measurement are being studied and will be incorporated if feasible. Precise temperature measurements are required for accurate efficiency calculations for low pressure ratio rigs. The CRF's temperature reference system will be upgraded to state-of-the-art within the next year to meet this challenge.

The F100 core test was the first transient test in the CRF. It provided a number of new insights into compressor in-stall performance and will have a significant impact on new compressor designs. Serious study of the data obtained in that test provides ample justification for more transient tests in an effort to meet the stability challenges in new high performance aircraft.

Engine operational problems are difficult to solve with rig tests even when appropriate because two to three years is usually required for rig construction, instrumentation and test. The operational Air Force cannot be grounded for that long. One solution would be to construct component test rigs during engine development and keep them up-to-date for quick response to field problems. The financial investment would be far less than we usually lose through lost and grounded aircraft and the expertise of the applied research community would be more fully utilized.

Flow-field plots obtained from computational fluid dynamic (CFD) efforts have been used very effectively as the initial velocity guess in CRF laser velocimetry studies. The rapid advancements in CFD will make possible ever more dramatic test techniques. The recent successful simulation of a core compressor transient behavior is being reported in another paper in this conference. Techniques such as these will be further exploited in the future.

Supercomputing with large memories and higher calculational speeds are helping researchers in many fields attack problems which only a few years ago were insurmountable. The CRF has initiated programs directed to near real-time comparison of analytical design code results with measured test results utilizing the power of parallel processing computers. With these computing tools, the CRF will be able to perform high-speed calculations during tests based on both analytical and test results. In addition, communications between test compressor designers' facilities and the CRF are being advanced to allow for rapid same-day transfer of information. Flow-path CFD studies, digital simulation of the test compressor, and on-line test data will be combined and presented to the test team and designers in near real-time to synergistically increase the value of the test.

CONCLUSIONS

The mission of the CRF is twofold; perform test programs which are vital to both the research and operational part of the Air Force and to devise and demonstrate leading-edge advancements in the area of test techniques and methodologies.

We started with an aerodynamic test facility and changed to a aerodynamic/aeromechanical facility with excellent test results and customer acceptance.

Within the first years of the design and construction phase, a decision was made to go to complete computer control of the test article, facility, test execution, and data system. This was an extremely fortuitous decision since it put all inputs integral to the success of the facility into a universal information system. This central data bank allows (1) rapid transfer of information between test article and facility during tests, (2) introduction of specialized data bases and algorithms for particular tests, and (3) introduction of computer simulation and computer-aided decision-making into the on-line test process.

The composition of the CRF test team has evolved to where the central core of both scientists and technicians are Government workers with significant on-site contractor effort for support services, new system detailed design, software maintenance and enhancement, hardware periodic maintenance, warehousing of parts and supplies, and for other unusual and non-periodic services. This allows the Air Force to retain responsibility and control of the daily activities in the facility and thus accrue intimate knowledge of the technology.

The Air Force has made a large investment in both dollars and manpower towards operation of the CRF. The total cost for construction, upgrades, operation, and personnel during its 18-year history is approximately $100M in terms of '89 dollars. In addition, the 50 full-time workers represent over 10% of the Aero Propulsion and Power Laboratory's work force. The magnitude and time span of this commitment indicates a firm resolve by the Air Force to continue with the CRF activity.

The results of the research tests performed in the CRF during the past five years have been excellent and have supported the IHPTET initiative. The demonstrated skills and testing precision compare favorably with other facilities.

Continuing changes in aircraft missions and engine requirements, compressed schedules, and shrinking finances combine to demand timely and incisive test data for successful engine development. The IHPTET goal of doubling T/W in the next fifteen years can only be achieved through careful and judicious use of test facilities like the CRF.

The CRF test team has been continually active in developing and using new measurement techniques and test techniques in compressor research. More facility enhancements are planned and the results will be reported in the future for consideration of use by other researchers.

REFERENCES

1. Petty, J. S. and Henderson, R. E., Advisory Group for Aerospace Research and Development, The Coming Revolution in Turbine Engine Technology, AGARD Conference Proceeding No. 421, Sep 1987.

2. Mitchell, W., Martin, R., Ostdiek, F., Rivir, R., and Shahady, P., American Institute of Aeronautics and Astronautics, Development of a National Compressor Research Facility, AIAA 77-911, 1977.

3. Rabe, D. C., Wennerstrom, A. J., and O'Brien, W. F., American Society of Mechanical Engineers, Characterization of Shock Wave End Wall Boundary Layer Interaction in a Transonic Compressor Rotor, ASME 87-GT-166, 1987.

4. Copenhaver, W. W. and Okiishi, T. H., American Institute of Aeronautics and Astronautics, Rotating Stall Performance and Recoverability of a High-Speed 10-Stage Axial-Flow Compressor, AIAA-89-2684, 1989.

5. Datko, J. D., and O'Hara, J. A., American Society of Mechanical Engineers, The Aeromechanical Response of an Advanced Transonic Compressor to Inlet Distortion, ASME 87-GT-189, 1987.

6. Boyer, K. M. and O'Brien, W. F., American Institute of Aeronautics and Astronautics, Model Prediction for Improved Recoverability of a Multistage Axial-Flow Compressor, AIAA-89-2687, 1989.

7. Dowler, C. A., Boyer, K. M. and Poti, N. D., American Institute of Aeronautics and Astronautics, Model Predictions of Fan Response to Inlet Temperature Transients and Spatial Temperature Distortion, AIAA 89-2686, 1989.

8. Rabe, D. C. and Dancey, C. L., American Institute of Aeronautics and Astronautics, Comparison of Laser Transient and Laser Doppler Anemometer Measurements in Fundamental Flaws, AIAA 86-1650, 1986.

9. Poti, N. D. and Rabe, D. C., American Society of Mechanical Engineers, Verification of Compressor Data Accuracy by Uncertainty Analysis and Testing Methods, ASME 87-GT-165, 1987.

10. Copenhaver, W. W., PhD Dissertation, Iowa State University, Stage Effects on Stalling and Recovery of a High-Speed, 10-Stage Axial-Flow Compressor, 1988.

11. Rabe, D. C., PhD Dissertation, Virginia Polytechnic Institute and State University, Shock Wave End Wall Boundary Layer Interaction in a Transonic Compressor Rotor, 1987.

12. Pierzga, M. J. and Wood, J. R., "Investigation of the Three-Dimensional Flow Field Within a Transonic Fan Rotor: Experiment and Analysis," Journal of Engineering for Gas Turbines and Power, Volume 107, April 1985, pp. 437-449.

13. McDonald, P. W., Bolt, C. R., Dunker, R. J. and Weyer, H. B., "A Comparison Between Measured and Computed Flow Fields in a Transonic Compressor Rotor," Journal of Engineering for Power, Volume 102, October 1980, pp. 683-891.

14. Dunker, R. J., Strinning, P. E. and Weyer, A. B., "Experimental Study of the Flow Field Within a Transonic Axial Compressor Rotor by Laser Velocimetry and Comparison with Through-Flow Calculations," Journal of Engineering for Power, Volume 100, April 1978, pp. 279-286.

15. Chima, R. U. and Strazisar, A. J., "Comparison of Two- and Three-Dimensional Flow Computations with Laser Anemometer Measurements in a Transonic Compressor Rotor," Journal of Engineering for Power, Volume 105, July 1983, pp. 596-605.

DISCUSSION

W. G. ALWANG, Pratt & Whitney Aircraft

    1. What digital data rates did you find were suitable for stall/surge investigations?

    2. How did you measure and control clearance during transient tests?

Author's Reply

    1. The maximum digital data rate utilized for the in-stall test program was 695 samples/second. The type of pressure fluctuation in rotating-stall characterized by this sample frequency is shown in Figure 19. This rate is sufficient to capture the fundamental stall cell characteristics that occur at around 50 to 60 Hz. To do a more detailed investigation of the stall cell as shown in Figure 21, it is recommended that sample rates higher than 700 Hz be utilized. A good comparison of the differences between analog stall inception data and digitally sampled data is provided in Figure 20. It shows that 695 Hz sampling captures the event but does miss some of the details. It should be noted that the instrumentation and connecting pressure tubes themselves often times dictated expected frequency response. This was the case for the in-stall test program as well.

    2. Clearance was neither measured or controlled for the transient test program. Rotating-stall data were obtained after a two to three minute stabilization time to assure no changes in clearance occurred while the data were being recorded.

Y. N. CHEN, SULZER BROTHERS LTD., SWITZERLAND

    The stall cells of the different stages (Figure 18) are lined up in the axial direction, confirming the measurements of Cumpsty, Day, Greitzer, Das and Ziang. According to our investigation, the boundary between the stalled and the unstalled region is a shear layer with high vortices. It is separated into individual vortices. A pair of Karman vortices with opposite rotational sense are then formed on the two ends of the stall cell. This model, which is verified in the radial compressors in our experiments, can be also derived from the MIT report of P. L. Lavrich (1988). Then, the Karman vortices form a circular Karman vortex street around the circumference of the rotor. Since a Karman vortex street induces waves with equal phase on its two sides, the vortex streets formed in the different stages are thus coupled with each other. In this way, the stall cells of the stages are lined up in the axial direction.

Author's Reply

    The transition region between the stall cells and the unstalled flow is an area of great interest. Time-dependent pressure gradients at single points and phase relationships between separate measurement points are being analyzed. The results will be used to help characterize the individual cells, indicate the cell orientation in the compressor and to guide the design of our measurement system for the next in-stall test.

R. O. BULLOCK, CONSULTANT

This is just not a question, but a comment as well. It is refreshing to learn of the capabilities of the facility described by Dr Ostdiek. Our ability to understand increases with our ability to measure and we can look forward to a better appreciation of the real aerodynamic events that take place in a compressor. It is interesting among other things, to note that Figure 18 tends to support the idea that flow takes place in parallel channels which arise from the close axial spacing of rotor and stator blades. This behavior raises a question about Figure 16. The curves on the stall branches must represent some sort of average of the widely varying pressures. If this is true, how were the averages computed and what were the tangential static pressure gradients behind the compressor?

Author's Reply

The data detailed in Figure 16 represents a time-average of impact probe measurements of the varying pressures at the compressor exit as the rotating-stall cells passed. Figure 17 is a good representation of the individual pressure signals and of the averaging technique which was used for each of the individual channels. This averaging process was performed for three circumferentially-spaced rakes, each of which had five radial measurement points. Finally, the overall compressor exit pressure was calculated from these 15 time-averaged values.

The exit static pressures at the compressor case were measured during the test at seven circumferential locations. This is part of the data being used at the present time to further characterize the rotating-stall cell and will be reported in the future.

STALL AND RECOVERY IN MULTISTAGE AXIAL FLOW COMPRESSORS

Walter F. O'Brien
J. Bernard Jones Professor of Mechanical Engineering
Virginia Polytechnic Institute and State University
Blacksburg, VA 24061
USA

Keith M. Boyer
Lt., USAF
Technology Branch, WRDC/POTX
Wright Patterson Air Force Base, OH 45433
USA

SUMMARY

At low flows relative to the design point, multistage axial-flow compressors may enter a globally-stable operational state involving rotating stall within the blade passages. For continued operation in a turbine engine, recovery of the compressor to normal operation is required. Operation in rotating stall is generally characterized by recovery hysteresis; that is, to produce recovery, compressor flow must be allowed to increase substantially beyond the initial flow level observed with rotating stall.

In turbine engine applications, it is desirable to reduce compressor recovery hysteresis to a minimum. Stage flow behavior and stage matching at low flows are shown to have major influence on recovery behavior. Conclusions are supported through the use of an analytical model recently validated with experimental data from tests of a multistage compressor in the Compressor Research Facility at Wright-Patterson Air Force Base.

INTRODUCTION

The compression system of a gas turbine engine must operate with stability and high efficiency over the range of operation of the engine. While a multistage compression system can operate stablely with one or more stages stalled, such operation is inefficient and undesirable.

At high engine speeds, reduction of compression system mass flow will generally lead to surge. While undesirable, the surge cycle includes periodic operation within the stable pressure-mass flow boundaries of the compression system, and is therefore recoverable; that is, an increase in mass flow or reduction in pressure demand will result in a return to normal operation. At lower speeds, sufficient fluid energy input and/or storage may not be available to sustain surge cycles. Reduced mass flow operation of the compression system will then take the form of globally-stable operation with at least several stages operating in stall.

This latter type of stalled compression system operation is especially undesirable in the turbine engine, because recovery to normal operation can be difficult. Since recovery hysteresis is normally evident, reduction in pressure demand may not be sufficient to produce compression system flow recovery and self-sustaining engine operation.

It is the purpose of this paper to offer a generalized concept of multistage compressor stall and recovery, utilizing a stage performance approach. Recent results from an extensive test and modeling program with a multistage compressor are employed to support an "extended starting" theory of compression system recovery hysteresis. The effects of some system design features on hysteresis and recovery behavior are examined.

BACKGROUND

Since the early investigations of axial-flow compressor stages and compression systems, the phenomena of rotating stall and surge have been observed and analyzed [1,2]. In an extensive study of compressor operation with one or more blade rows stalled, Benser [3] reported studies of stage reduceq flow and stalling behavior employing a mathematical model of a hypothetical 12-stage compressor. He observed that reduced-flow operation of the compressor led to progressive stall in the inlet stages of the compressor, and abrupt stall in middle and rear stages. Progressive stall was identified with low hub/tip ratio inlet stages, in which rotating stall developed at one end of the blade. The stalled region progressed in span and extent as mass flow was reduced, with consequent reduction in efficiency. Abrupt stall of a stage was identified as the rapid development of full-span single-cell rotating stall as mass flow was reduced, with resulting flow blockage and severe reduction in stage efficiency. In recent years, extensive studies of compression system stalling behavior have been conducted [4,5]. Generally, high pressure rise and large plenum volume have been identified with system surge, and the effect of the shape of the overall compressor characteristic on stall and recovery has been predicted. The present work primarily addresses the influence of stage behavior and interactions on compressor in-stall performance and recoverability, rather than matters relating to system performance and stall-surge boundaries.

STALL, RECOVERY, AND AERODYNAMIC STARTING

The aerodynamic starting transients of multistage compression systems are well-known. In order to obtain high efficiency and adequate stall margin at the design operating point, design procedures often lead to similar aerodynamic loadings of the several stages of the compressor at the design speed and flow. At low speeds, this design philosophy leads to increased aerodynamic loading of the front stages of the compressor, and reduced loading and choking of the rear stages. During starting (low speed operation) of the compressor, the inlet and middle stages will be driven into rotating stall, since the necessary initial compression to provide proper operation of the rear stages is not available. The resulting blockage will drive at least several of the compressor stages into deep stall, and aerodynamic starting (unstalling of the stages) will not occur unless appropriate action is taken.

To start the compression system, the initial stages must be unstalled. Conventionally, this is accomplished by bleed or variable geometry, or both. Bleeding of flow following the stalled stages will increase flow, eliminating stall and raising the pressure rise of these stages. Increased pressure rise will increase density, reducing the throughflow velocities in the rear stages. In a properly designed machine, the stage operating point changes produced by bleed will lead to aerodynamic starting.

In addition to or instead of bleed, variable geometry may be used in the initial stages. Inlet guide vanes and stators may be restaggered to reduce the stalling mass flow of the inlet. Twin spool compressor designs may also be used to produce improved starting, but these designs and their operation are not addressed in this paper.

The effects of low flow, bleed and variable geometry may be studied with the aid of Figures 1-4. Referring to Figure 1, the pressure coefficient and efficiency behavior for the stages of a hypothetical 12-stage compressor are shown as a function of flow coefficient. Since the stage characteristics shown are in coefficient form, they are theoretically speed independent. Reference point A is representative of stage operation under design conditions, with adequate stall margin for all stages and high efficiency. At reduced speed, stage operation will move to the points noted by B, with reduced stall margin in the initial stages and high velocity flow in the rear stages. This effect occurs because of the fixed annular areas of each stage and the reduced compression performance of the early stages. From continuity considerations, the result is low density and high flow velocities in the rear stages. Further reduction in mass flow at reduced speed will lead to operation at point C, with the initial stages in progressive stall. Additional reduction in mass flow will eventually lead to post stall operation at point D, with sharp reductions in pressure rise and compressor efficiency. The conditions at operating point D are representative of the stalled stage matching conditions which would exist without intervention during starting of a multistage compressor. If a valve were used to reduce the flow as described above, the compressor would not restart if the valve were opened to a position associated with an originally unstalled state; that is, recovery hysteresis would be present.
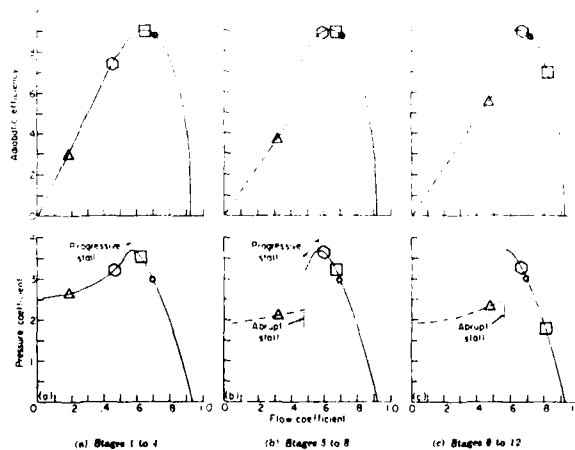
Design Speed Operation

o - Normal Operating Points

Low Speed Operation

□ - Prestall

O - Initial Stages in Progressive Stall

Δ - Poststall Operation

Figure 1.   Stage behavior for several operating
            conditions in hypothetical 12-stage
   compressor (adapted from Ref. 3)

An alternate view of the stage stalling process as a function of compressor speed is provided in Figure 2. In this hypothetical compressor, the stage stalling flow coefficients are assumed to be equal. The initial stages of the compressor are assumed to operate with progressive stall characteristics. Middle stages are assumed to begin stall with progressive behavior, then to transition to abrupt stalling. Rear stages with high hub-to-tip ratios are assumed to stall only in a full span, abrupt manner. At 80 percent speed, near the operating condition, slightly reduced flow produces only a mild, progressive stall in the front stages of the compressor. It is presumed that the compressor and turbine engine could continue operation under these conditions. Further reduction in flow would intersect the abrupt stalling boundary of the 9th stage. Because of the severe blockage produced by this event, the remaining stages of the compressor would be driven deeply into stall, and the complete compressor would be involved.

Whether the resulting global event would be a surge or a stall is conventionally assumed to depend on system dynamics. At the 80 percent speed, a surge would be the likely result, and recovery would be possible for the reasons previously discussed. If a stall resulted, the abruptly-stalling stages would exhibit hysteresis, and aerodynamic recovery of the compressor flow and pressure would be difficult. At the 50 percent speed condition of Figure 2, operating line flow involves the existence of progressive stall in the initial stages, and further reduction of flow quickly pushes all initial stages into the progressive stall region. Abrupt stall begins at the 5th stage. At this speed, the resulting complete compressor stall would very likely be a globally-stable, rotating stall. Recovery would require a large increase in mass flow, variable geometry, or bleed.

Although not the primary topic of this paper, it is interesting to note the conditions which result from reduction of flow at the 100 percent speed of the compressor. Large pressure rise in the inlet stages increases density in the rear stages, causing the initiation of abrupt stall in the last stage when flow is reduced. A compressor surge would almost certainly be the result.

The complete compressor characteristic resulting from the assumed stage characteristics is shown in Figure 3. At part speed, flattened speed lines resulting from progressive stall in the initial stages can be noted. For the lower speeds, the line of complete compressor stall corresponds to the reaching of an abrupt stall condition in a middle stage. A vertical characteristic indicates choking of the flow within the compressor.

The effect of bleed and variable vane operation on compression system stalling behavior may be studied in Figure 4. Bleed flow raises the mass flow and unstalls all stages upstream of the bleed point. The resulting increased pressure produced by the initial stages may raise the mass flow above the stalling value for downstream stages. For Case I, bleed flow is assumed at the exit of stage 4. The inlet stage flow coefficients are moved far from the stalling value. Stage 5 may or may not be in the stalling region, depending on the resulting overall compressor flow.
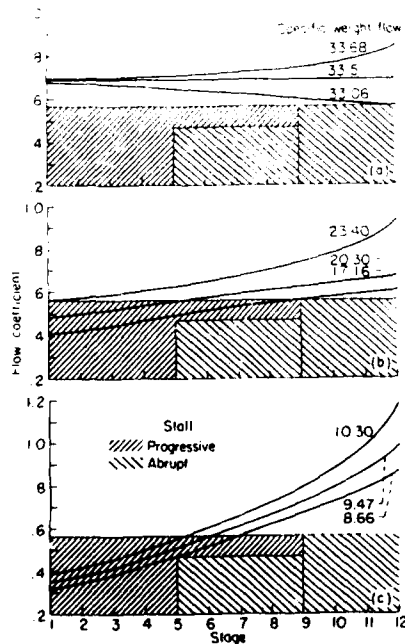
(a) Speed, 100 percent of reference.
(b) Speed, 80 percent of reference.
(c) Speed, 50 percent of reference.

Figure 2. Stage flow coefficient variation for three operating speeds in hypothetical compressor (Ref. 3)
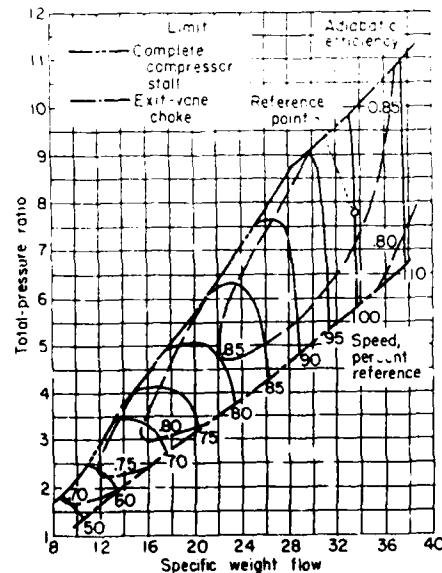
Figure 3. Computed performance for 12-stage compressor using assumed stage characteristics (Ref. 3)
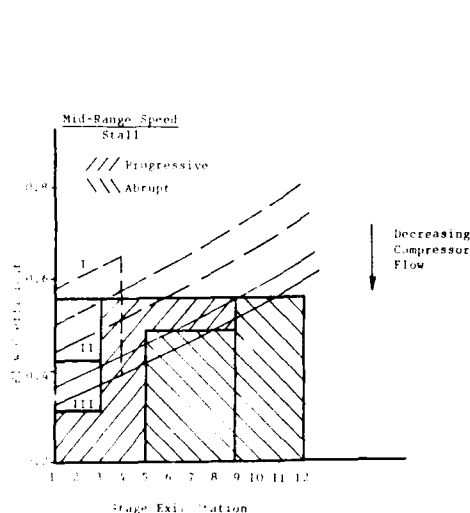
S - Stall Point

RS - Stable Rotating Stall

R - Recovery Point

Mid-Range Speed
Stall

/// Progressive

\\\ Abrupt

Decreasing
Compressor
Flow

Stage Exit Station

Figure 4. Stagewise variation of flow in hypo-
thetical compressor for Case I
(good flow) and Cases II, III
(variable geometry)

Pressure Coefficient

S

R

RS

Recovery
Hysteresis
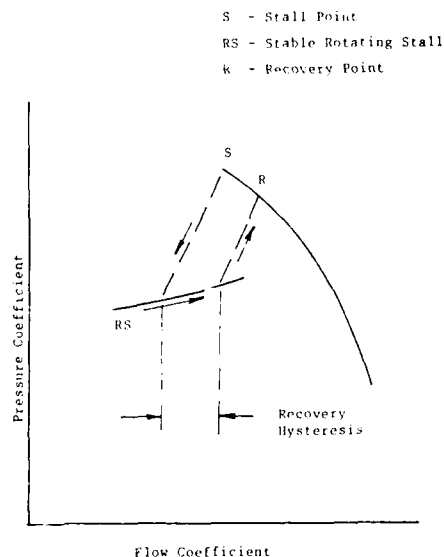
Flow Coefficient

Figure 5. Abrupt stalling stage inherent
recovery hysteresis

Variable vanes lower the stage flow coefficient at stall, and can provide for unstalled initial stage operation at reduced mass flows. Case II in Figure 4 illustrates the effect of a moderate reduction of stalling flow coefficient by variable geometry on inlet stages 1,2, and 3. While the first three stages remain unstalled for reducing mass flow, later stages may operate in progressive stall. A overly large reduction in stalling mass flow for the first three stages by means of variable geometry can extend unstalled initial stage operation to very low flow coefficients, a situation marked as Case III. As can be seen in Figure 4, stages 5 and beyond are driven into the abrupt stall region while stages 1-3 remain unstalled. As previously mentioned, this would produce severe blockage of the flow for all stages, and lead to complete compressor stall. In a starting situation, it is conventional to prevent the development of abrupt middle stage stall by proper scheduling of variable vanes and bleed in initial stages. This allows the compressor to operate without stall, and to move toward similar stage loadings as speed increases.

As a final point, it should be noted that abrupt stall of compressor stages normally involves inherent hysteresis (Figure 5); the rotating stall operating line on the characteristic is stable, and an increase in mass flow beyond that which the stalling throttling level permits is necessary for recovery [6]. Since pressure production in stall is reduced, this increased mass flow must come from additional opening of a valve, or in the case of turbine engine application, reduction of combustion temperature below the level which existed at stalling. If it is not possible to reduce downstream flow restriction sufficiently, then bleed and/or variable geometry must be applied to achieve aerodynamic starting of the compressor. When none of these measures are effective in a turbine engine, the result is "non-recoverable compressor stall".

In summary, reduced flow even at mid-range speeds in a multistage compressor can result in multiple stage stalling in a pattern which is generically similar to that of failed starting in a compressor. Scheduling of variable geometry can affect the results. By means of a model of an actual compressor, it is the intention here to show that non-recoverable stall problems experienced in some turbine engines are, in fact, extensions of the compressor starting problem with abrupt stall and resulting interaction in several compressor stages, coupled with suppression of surge in the compressor. Measures which encourage aerodynamic starting should, if properly applied, produce recovery in such compressors.

COMPRESSOR EXPERIMENTS AND MATHEMATICAL MODELS

A recent experiment was conducted to investigate the details of multistage compressor behavior in globally-stable rotating stall [7]. Stage behavior was extracted from this test, and used to create a stage-by-stage, mathematical model of the compression system [8] which has been shown to describe system and stage operation for this compressor with good fidelity. This validated model will be used to illustrate the application of the above ideas to an actual compression system. As discussed by Benser [3], it is difficult to obtain a complete

understanding of part-speed stage performance and stalling characteristics through purely exp~~~=~~..tai ap-
proaches. This difficulty arises because the inherent performance of each stage is not easily obtained when a
multistage compressor is operating in rotating stall, and because compressor surge limits the range of stage
operation that can be studied experimentally. Thus, a validated model is ideal for the present study.

Description of Modeling Technique

The theory and construction of the analytical model used in this effort are described in detail in Ref. 9.
This stage-by-stage model uses a control volume representation to simulate steady and dynamic compressor per-
formance including operation in the unstalled, globally-stable stalled (rotating stall), and transient stalled
(surge) regimes. The model can be configured to represent any compression system, given the compressor geometry
and stage characteristics as determined experimentally or estimated.

In the model, the one-dimensional forms of the mass, momentum, and energy conservation equations are solved
at each interior control volume boundary for each computational timestep. The stage forces and shaft work
required to solve the momentum and energy equations are derived from a set of steady-state pressure and tempera-
ture characteristics, respectively, specified over the entire flow range. A typical set of performance charac-
teristics, defined for a single speed and stage, are shown in Figure 6. As the flow coefficient decreases, both
the pressure and temperature coefficients increase until a stability limit is encountered. The stability or
stall limit is associated with the flow breakdown process, indicative of stage flow separation. The in-stall
portion of the characteristic represents the flow-weighted, average performance of that stage with the compres-
sor operating in rotating stall. For the present application, the unstalled and in-stall characteristics were
computed from experimental data obtained from the compressor rig represented in this study [11]. Backflow
characteristics are associated with full annulus reversed flow, and are estimated by using the overall shape
suggested by low-speed compressor rig studies and overall transient performance during surge.

The characteristics shown in Figure 6 and discussed in the preceding paragraph represent steady and quasi-
steady stage performance. During a transient event such as surge or the transition into rotating stall, the
characteristics in the rotating stall region are not applicable. When a compressor flow field becomes unstable,
there is a time lag between the onset of the instability and the establishment of the fully-developed rotating
stall pattern [4]. Thus, in the rotating stall region of the stage characteristics, stage dynamic stalling
response must be specified. This is accomplished by applying a first-order time lag on the stage forces. This
technique has been successfully used in many analytical representations, including those described in Refs. 4,
5, and 6.

Model simulation of a dynamic event is accomplished through the specification of boundary conditions as
linear functions of time. In the present application, all dynamic simulations were initiated through the use of
a throttling function. The throttling function is based on the concept of a mass flow function, and as such,
changes in the throttling function simulate changes in exit nozzle area. If the model throttling function is
sufficiently decreased, the compressor stall limit will be reached and a post-stall event will be simulated.

Application and Model Results

The 10-stage, high-speed, axial-flow compressor rig modeled in this effort was tested in the Compressor
Research Facility (CRF) at Wright Patterson Air Force Base, Ohio. The test was conducted to obtain detailed
performance data describing the behavior of each of the ten stages with the test compressor operating over a
range of conditions, with emphasis on rotating stall [7]. Data were obtained at different in-stall operating
conditions by varying compressor shaft speed, discharge throttle, and variable geometry settings. Descriptions
of the test facility and capabilities can be found in Refs. 10 and 11. A complete description of the test
compressor, compressor instrumentation, specialized test procedures, and data acquisition is contained in Ref.
11.

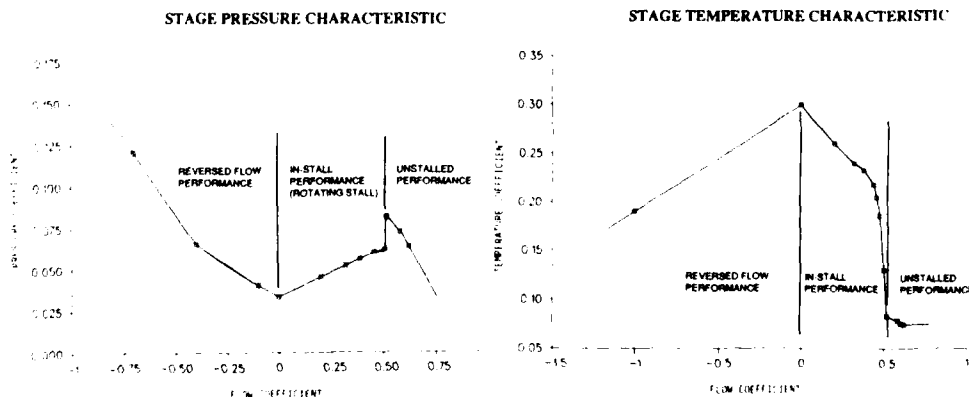**STAGE PRESSURE CHARACTERISTIC**   **STAGE TEMPERATURE CHARACTERISTIC**

Figure 6. Typical stage performance
characteristics

Figure 7 shows the model control volume arrangement and a cross section of the experimental compressor rig. Thirty-eight control volumes were used to represent the inlet ducting, compressor, and discharge volume. The number and size of control volumes are specified by the user and governed by the geometry of the represented compressor. Each compressor stage is represented by an individual control volume.

The in-stall data obtained from the CRF compressor test provided the means to validate the model on an interstage basis. The validation process for the current work involved comparisons between model output and experimental data obtained from the CRF rig test. A description of the validation efforts is found in Ref. 8. Model-predicted overall and interstage steady and transient behavior agreed well with the experimentally measured performance.

For the present study, model simulations were employed to examine unstalled and in-stall stage behavior and interaction during compressor part-speed operation at 60.0, 78.5, and 82.0 percent design corrected speed. Shown in Figure 8 is a model simulation of the large recovery hysteresis exhibited by the test compressor at 78.5% speed, the experimentally-determined rotating stall/surge boundary speed. The simulation was a result of setting the model throttling function to levels consistent with the experimental boundary conditions. As indicated in Figure 8, compressor recovery from rotating stall does not occur as the "throttle" is opened well beyond its initial stall inception value.

Model predictions of overall compressor performance during a rotating stall event at the indicated speeds are shown in Figure 9. For 60.0% and 78.5% speeds, the model was supplied with boundary conditions that were consistent with the experimental conditions. At 82.0% speed, the test compressor exhibited surge when the flow field became unstable. For the purpose of analyzing stage behavior in rotating stall at that speed, the surge behavior was suppressed; i.e. the force lagging constant was increased until the model predicted rotating stall performance. This allowed for a more complete understanding of stage stalling characteristics at speeds where this behavior under most conditions would be masked by compressor surge.
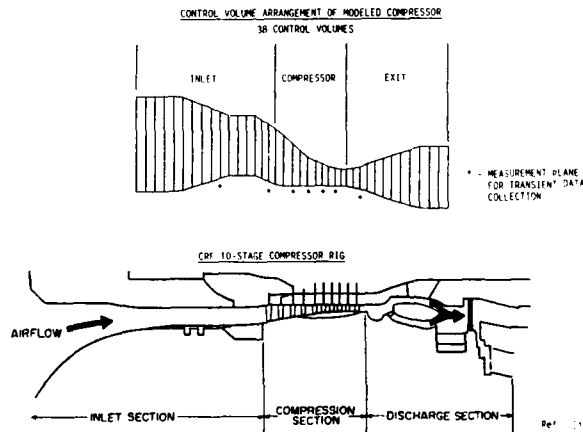
Figure 7. Model control folumes and cross
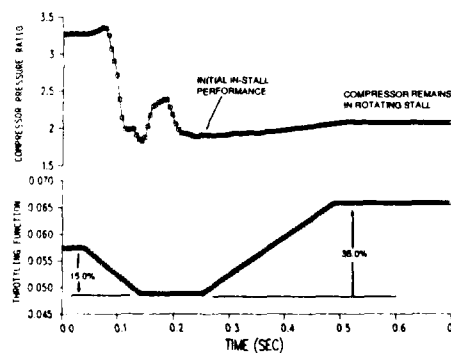section of compressor test rig

Figure 8. Model simulation of experimentally
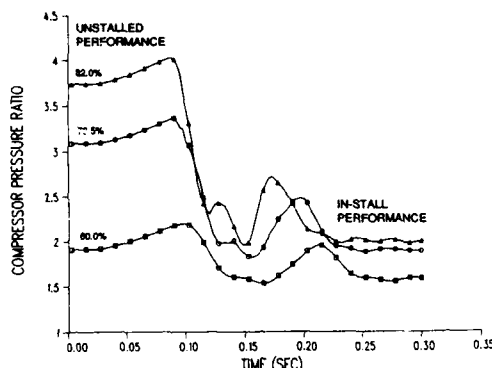determined compressor recovery
hysteresis

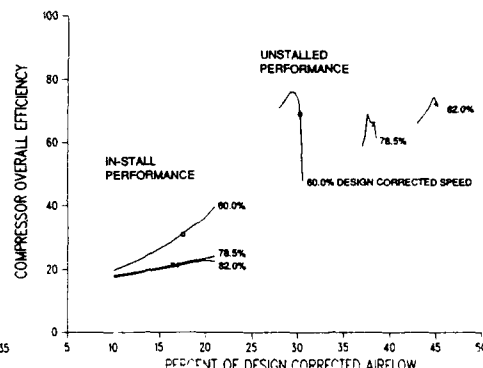Figure 9. Model-predicted overall compressor stalling behavior

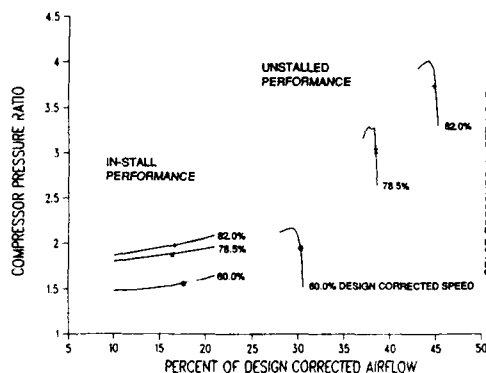Figure 11. Model-predicted overall compressor performance

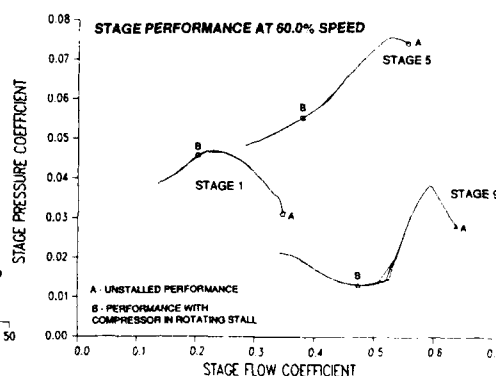Figure 10. Model predicted overall compressor performance

Figure 12. Model-predicted stage stalling behavior

Figures 10 and 11 show model predictions of overall compressor performance in the form of compressor maps (pressure ratio and efficiency versus mass flow). Indicated on the plots is the initial steady unstalled performance and the final average in-stall performance for each of the dynamic simulations shown in Figure 9. Note the extremely low efficiencies associated with the reduced performance levels, which are indicative of compressor operation in rotating stall.

An examination of individual stage unstalled and in-stall performance offers insight into the influence of stage matching on compressor rotating stall behavior and recoverability. The model-predicted performance of selected stages at the three compressor shaft speeds examined in this study is shown in Figures 12, 13, and 14. In all three figures, stage one is representative of the front stage behavior, and stages five and nine are representative of the middle and rear stage behavior, respectively.

As shown in Figure 12, at 60.0% compressor speed, the front and middle stages exhibit a progressive stalling characteristic, and the rear stages exhibit an abrupt characteristic. At the higher speeds (Figures 13 and 14), the middle and rear stages exhibit a very abrupt stalling characteristic. Additionally, at all three speeds, the front stages are operated relatively far from their stall limits.

DISCUSSION OF RESULTS

The model-generated stalling behavior of the 10-stage compressor test rig showed the classical features of a failed compressor starting situation discussed at the beginning of the paper; progressive stall in the initial stages, abrupt stall in latter stages, and recovery hysteresis. When surge was suppressed, this behavior was seen even at a speed of 82 percent of maximum, well above the starting speed range. Apparently, if surge does not occur, a multistage compression system can exhibit recovery hysteresis characteristic of starting well into the normal operating speed range. When installed in an engine, the low efficiency of the stalled compressor would lead to spool-down even with increasing turbine inlet temperatures, and a non-recoverable stall condition.

A previous study of methods to improve recoverability in this compressor rig was conducted employing the model [8]. With the low pressure rise of the initial stages in this rig, it might be expected that bleed applied to the initial stages would be ineffective in unstalling later stages so as to permit the compression system to "restart" and thus recover. In the study, a bleed flow corresponding to 15 percent of the unstalled mass flow
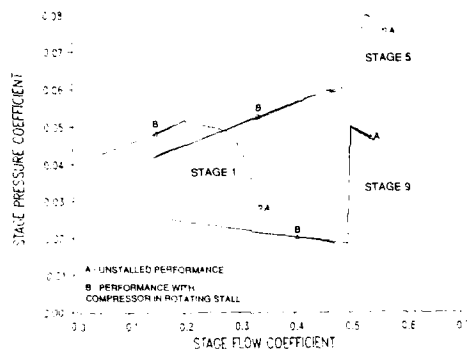
STAGE PERFORMANCE AT 78.5% SPEED   STAGE PERFORMANCE AT 82.0% SPEED

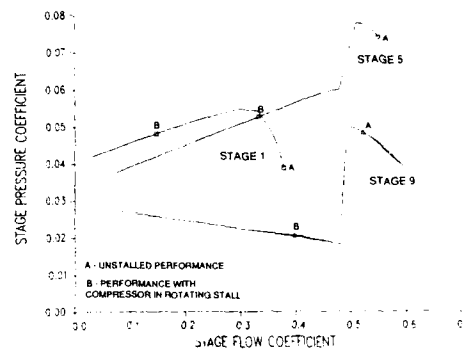Figure 13.   Model-predicted stage stalling behavior

Figure 14.   Model-predicted stage stalling behavior

of the compressor was simulated at the outlet of the 4th and 9th stages of the compressor. As shown in Figure 15, bleed at the 5th stage inlet (4th stage outlet) did not produce recovery of the 9th stage, while bleed at the 10th stage inlet (9th stage outlet) produced recovery of that stage and the entire compressor. In another study reported in Ref. 8, an increase of the 10th stage flowpath (annular area) of the compressor was simulated by shifting the stage 10 characteristic approximately 10 percent in the direction of increasing flow. Throttle opening which did not allow recovery with the original design produced recovery and return to normal operation in the modified compressor simulation, as shown in Figure 16. The results from the bleed and increased flowpath investigations are judged to support the present thesis that compressor operation in globally-stable rotating s' ". is essentially an extension of low-speed starting behavior.

When aerodynamic starting of the compressor of a turbine engine is achieved and idle speed is reached, it has been assumed that starting problems are no longer of concern. As shown in Figure 17, we may now deduce from the above evidence that the zero-bleed, globally-stable stall regime of a multistage compressor can occupy a wide region to the left and extend to the right of the compressor stall line, and that it may be reached at speeds well above those normally associated with turbine engine idle if conditions permit. Along the constant speed lines in this area, recovery requires application of bleed and/or variable geometry at a location that will benefit the stages involved in abrupt stall. The appropriate location for this bleed and variable geometry may be well downstream of the usual starting positions, depending on stage matching. Since the stalling patterns and recovery measures are similar to those seen in starting, the region is called an "extended starting" region. It is interesting to note that the entire process may be seen to have some similarities to the unstarting and restarting process for a supersonic diffuser.

It remains to speculate what conditions can lead to the situation of globally-stable rotating stall at mid-range speeds. For this particular compressor rig, it was observed that downstream volume had no effect on the stall-surge boundary [7], contrary to the usual theory. The causes of this result remain under investigation, but it is speculated that the small discharge flow area of the last stage of this rig may have prevented acoustic communication of the compressor with the downstream plenum, effectively suppressing surge. As shown in Ref. 11, the compressor exhibits a vertical speed line at the speeds in question, indicating an internal choked condition. It is clear, however, that the matter of multistage compressor non-recoverable stall is at least divided into two areas; the design and system conditions which may suppress surge at mid-range speeds, and provisions for recovery if stable stall should occur.
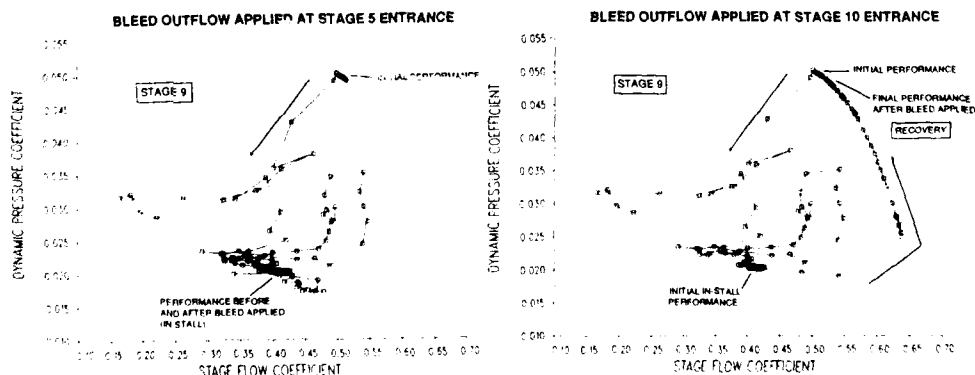
BLEED OUTFLOW APPLIED AT STAGE 5 ENTRANCE   BLEED OUTFLOW APPLIED AT STAGE 10 ENTRANCE

Figure 15.   Bleed location effect on compressor stall recovery
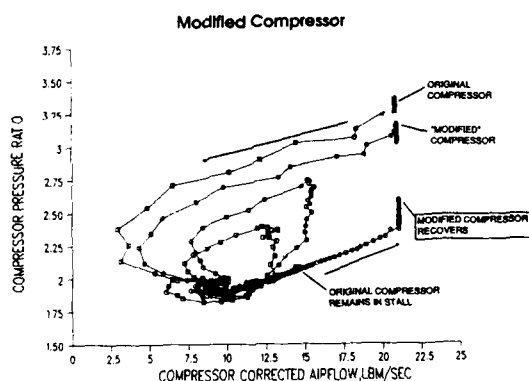
Modified Compressor

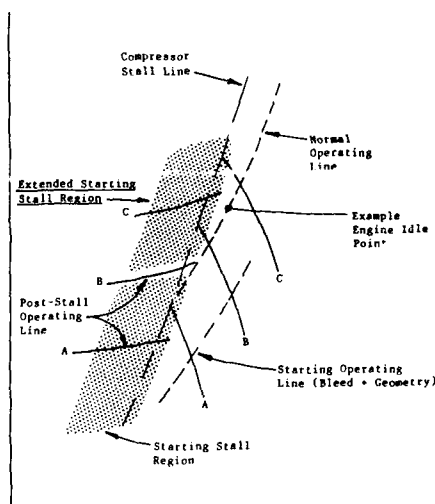Figure 16. Rear stage flowpath effect on compressor stall recovery

Figure 17. Compressor starting, operating, and extended starting region

It is also evident that the stage loading and flow coefficient distribution in a given compressor design influences both stalling and recovery. Considering recovery at mid-range speeds alone, it would appear that more uniform stage loadings, and lower design flow coefficients in latter stages favor recovery. As has been noted by others [3] and observed here, redistribution of stage pressure rise may simply move the stall problem to other stages, where provisions for recovery may not be present. The phenomenon is seen to be an inherent property of multistage compressors where flow compressibility is present.

CONCLUSIONS

The stall recovery problem in a multistage compressors at mid-range speeds has been shown to be an extension of the low-speed starting problem. To the extent that stall can occur and surge can be suppressed in a compression system, any multistage compressor may be subject to operation in the "extended starting" state.

Methods which provide for aerodynamic starting at low speeds will produce recovery at higher speeds if properly applied.

Stability, globally-steady stall, and surge are seen to be related to the details of stage design and matching in multistage compressors, as well as system considerations. To fully represent and study the phenomena, mathematical models must include representations of stage performance including compressibility effects, and experiments must include the entire multistage environment.

ACKNOWLEDGMENT

REFERENCES

1.   Iura, T, and Rannie, W. D., "Experimental Investigations of Propagating Stall in Axial-Flow Compressors, Transactions of the American Society of Mechanical Engineers, April 1954, pp. 463-471.

2.   Emmons, H. W., Pearson, C. E., and H. P. Grant, "Compressor Surge and Stall Propagation, Transactions of the American Society of Mechanical Engineers, May 1955, pp. 455-469.

3.   Johnsen, I. A. and R. O. Bullock, Eds., Aerodynamic Design of Axial-Flow Compressors, NASA SP-36, 1965, pp.341-364.

4. Greitzer, E. M., "Surge and Rotating Stall in Axial-Flow Compressors-Part 1: Theoretical Compression System Model," ASME Journal of Engineering for Power, Vol. 98, No. 2, April 1976, pp.190-198.

5. Moore, F. K., "A Theory of Rotating Stall of Multistage Axial Flow Compressors", NASA CR-3685, Lewis Research Center, Cleveland, OH, July 1983.

6. Cousins, W. T., and W. F. O'Brien, "Axial-Flow Compressor Post-Stall Analysis", AIAA Paper No. 85-1349, July 1985.

7. Copenhaver, W. W., and Okiishi, T. H., "Rotating Stall and Recoverability of a High-Speed Ten-Stage Axial-Flow Compressor, AIAA Paper No 89-2684. July 1989

8. Boyer, K.M., and W. F. O'Brien, "Model Predictions for Improved Recoverability of a Multistage Axial-Flow Compressor", AIAA Paper No. 89-2687, July 1989.

9. Davis, M. W., Jr., "A Post-Stall Compression System Modeling Technique," AEDC TR-86-34, Arnold Air Force Station, TN, February 1987.

10. Ostdiek, F. R., Copenhaver, W. W., and Rabe, D. C., "Compressor Performance Tests in the CRF," AGARD Paper 74 A-25, Propulsion and Energetics Panel 74th Specialists' Meetings, Grand Duchy of Luxembourg, 28 August-1 September 1989.

11. Copenhaver, W. W., "Stage Effects on Stalling and Recovery of a Ten-Stage Axial-Flow Compressor, Ph. D. Dissertation, Iowa State University, October 1988.

DISCUSSION

R.   BULLOCK, Consultant, US

This is only comments. As indicated by the Author, this problem arose in the past when single spool compressors having pressure ratios of 8 to 16 were wanted. The problem was made by the use of variable stators or two spool units, although intra-stage bleed was sometimes used during development. Higher pressure ratios in the single spools has naturally re-introduced the difficulty. Our improved abilities to cope with problems should provide a solution that does not impair efficiency. I don't believe that simple one-dimensional analysis of the flow will give us an accurate enough answer. *Fig 18 of A 25 suggests that compressor flow during stall has large circumferential gradients, and the resulting flow must be determined by the circumferential static pressure gradients at the exit. To attain uniform pressures, e.g. the good flow must increase which further retards the stalled flow.*

Author's reply:

The authors agree with the comments, and especially appreciate the insights offered by Mr. Bullock in this discussion.

A. SEHRA, Textron Lycoming, US

When you opened the rear stages, did you notice a reduction in the surge margin at high speed ?

Author's reply:

No model runs were made above 82% speed. Given the controlling effect of the rear stages on stall at high speed, this design change would doubtless affect stall margin in the modeled compressor at high speed.

Y.N. CHEN, Sulzer Brothers Ltd. Switzerland

The deep stall has a very large hysteresis, in combination with a very long range of recovery.
Some deep stall is initiated by light stall with very small pressure drop. In an investigation of Prof. Breugelmans, a very long range of the light stall with small multicells (7.8 or 9) was achieved.
The geometry of the blading of his rotor may serve as a guidance for keeping the light stall to extend to very low flow rate. Then, the deep stall can be shifted to this low flow rate.

Author's reply

The results reported by Prof. Breugelmans from his rotating stall
experiments will be studied to see if any particular design features
of the rig can be associated with extended stall development. In
the present paper, results reported for the 10 stage compressor rig test
did in fact show "light" or progressive stall in the initial stages of
the compressor. The observed hysteresis was associated with abrupt
stalling in the middle and dowstream stages. It is interesting to consider
design changes which might produce more progressive stall behavior in the
middle stages without affecting overall compressor performance.

PAPER A 26 by O' BRIEN (continuation)

Ph. RAMETTE, SPE, France

Have you studied the influence of the volume between the compressor
and the throttle on the stall limit, both a theoretical or an
experimental manner ?

Author's reply:

In the referenced experiment, four different downstream volumes were
attached to the compressor to study the effect on the stall-surge boundary.
In the experiment, no effect of volume was noted. We have not yet
studied this result with the model, but we plan to in the future.

REPORT DOCUMENTATION PAGE

1. Recipient's Reference	2. Originator's Reference	3. Further Reference	4. Security Classification of Document
	AGARD-CP-468	ISBN 92-835-0543-3	UNCLASSIFIED

5. Originator	Advisory Group for Aerospace Research and Development North Atlantic Treaty Organization 7 rue Ancelle, 92200 Neuilly sur Seine, France

6. Title	UNSTEADY AERODYNAMIC PHENOMENA IN TURBOMACHINES

7. Presented at	the Propulsion and Energetics Panel 74th (A) Specialists' Meeting, held in Luxembourg, 28—30 August 1989.

8. Author(s)/Editor(s)	9. Date
Various	February 1990

10. Author's/Editor's Address	11. Pages
Various	334

12. Distribution Statement	This document is distributed in accordance with AGARD policies and regulations, which are outlined on the Outside Back Covers of all AGARD publications.

13. Keywords/Descriptors	
Blades,	Transonic flow
Cascade,	Turbines
Compressors,	Turbomachines
Flutter	Unsteady aerodynamic
Oscillation	Vibration
Supersonic flow	Wakes,
	Symposia

14. Abstract

The Conference Proceedings contains the 24 papers presented at the Propulsion and Energetics Panel 74th A Specialists' Meeting on "Unsteady Aerodynamic Phenomena in Turbomachines" which was held 28—30 August 1989 in Luxembourg.

The Specialists' Meeting was arranged in the following sessions: Flutter or Oscillating Cascades (5); Wakes or Complete Stage (10); Transonic and Supersonic Unsteady Phenomena (4); and Experimental Studies and Instrumentation Problems (5). The Technical Evaluation Report is included at the beginning of the Proceedings. Questions and answers of the discussions follow each paper.

While around isolated airfoils many results on unsteady aerodynamic phenomena are available, reliable experimental data for unsteady turbomachinery flows were still missing. Therefore, the Specialists' Meeting offered a forum for experts to discuss the degree of advancements in this field. It was found that CFD with large numerical codes will be more and more developed and offer a useful tool for designers to improve their products. The experimental work for code validation is lagging somewhat behind.

AGARD Conference Proceedings No.468
Advisory Group for Aerospace Research and
Development, NATO
UNSTEADY AERODYNAMIC PHENOMENA IN
TURBOMACHINES
Published February 1990
334 pages

The Conference Proceedings contains the 24 papers presented at the Propulsion and Energetics Panel 74th A Specialists' Meeting on "Unsteady Aerodynamic Phenomena in Turbomachines" which was held 28—30 August 1989 in Luxembourg.

The Specialists' Meeting was arranged in the following sessions: Flutter or Oscillating Cascades (5); Wakes or

P.T.O.

AGARD-CP-468
Blades
Cascades
Compressors
Flutter
Oscillation
Supersonic flow
Transonic flow
Turbines
Turbomachines
Unsteady aerodynamic
Vibration
Wakes

Complete Stage (10); Transonic and Supersonic Unsteady Phenomena (4); and Experimental Studies and Instrumentation Problems (5). The Technical Evaluation Report is included at the beginning of the Proceedings. Questions and answers of the discussions follow each paper. While around isolated airfoils many results on unsteady aerodynamic phenomena are available, reliable experimental data for unsteady turbomachinery flows were still missing. Therefore, the Specialists' Meeting offered a forum for experts to discuss the degree of advancements in this field. It was found that CFD with large numerical codes will be more and more developed and offer a useful tool for designers to improve their products. The experimental work for code validation is lagging somewhat behind. ISBN 92-835-0543-3	Complete Stage (10); Transonic and Supersonic Unsteady Phenomena (4); and Experimental Studies and Instrumentation Problems (5). The Technical Evaluation Report is included at the beginning of the Proceedings. Questions and answers of the discussions follow each paper. While around isolated airfoils many results on unsteady aerodynamic phenomena are available, reliable experimental data for unsteady turbomachinery flows were still missing. Therefore, the Specialists' Meeting offered a forum for experts to discuss the degree of advancements in this field. It was found that CFD with large numerical codes will be more and more developed and offer a useful tool for designers to improve their products. The experimental work for code validation is lagging somewhat behind. ISBN 92-835-0543-3
Complete Stage (10); Transonic and Supersonic Unsteady Phenomena (4); and Experimental Studies and Instrumentation Problems (5). The Technical Evaluation Report is included at the beginning of the Proceedings. Questions and answers of the discussions follow each paper. While around isolated airfoils many results on unsteady aerodynamic phenomena are available, reliable experimental data for unsteady turbomachinery flows were still missing. Therefore, the Specialists' Meeting offered a forum for experts to discuss the degree of advancements in this field. It was found that CFD with large numerical codes will be more and more developed and offer a useful tool for designers to improve their products. The experimental work for code validation is lagging somewhat behind. ISBN 92-835-0543-3	Complete Stage (10); Transonic and Supersonic Unsteady Phenomena (4); and Experimental Studies and Instrumentation Problems (5). The Technical Evaluation Report is included at the beginning of the Proceedings. Questions and answers of the discussions follow each paper. While around isolated airfoils many results on unsteady aerodynamic phenomena are available, reliable experimental data for unsteady turbomachinery flows were still missing. Therefore, the Specialists' Meeting offered a forum for experts to discuss the degree of advancements in this field. It was found that CFD with large numerical codes will be more and more developed and offer a useful tool for designers to improve their products. The experimental work for code validation is lagging somewhat behind. ISBN 92-835-0543-3